Journal of Sensors

Advanced Sensor Technologies in Agricultural, Environmental, and Ecological Engineering

Lead Guest Editor: Yuan Li
Guest Editors: Zhenxing Zhang, Jingwei Wang, Liu Hongxiao, and Liang Xu

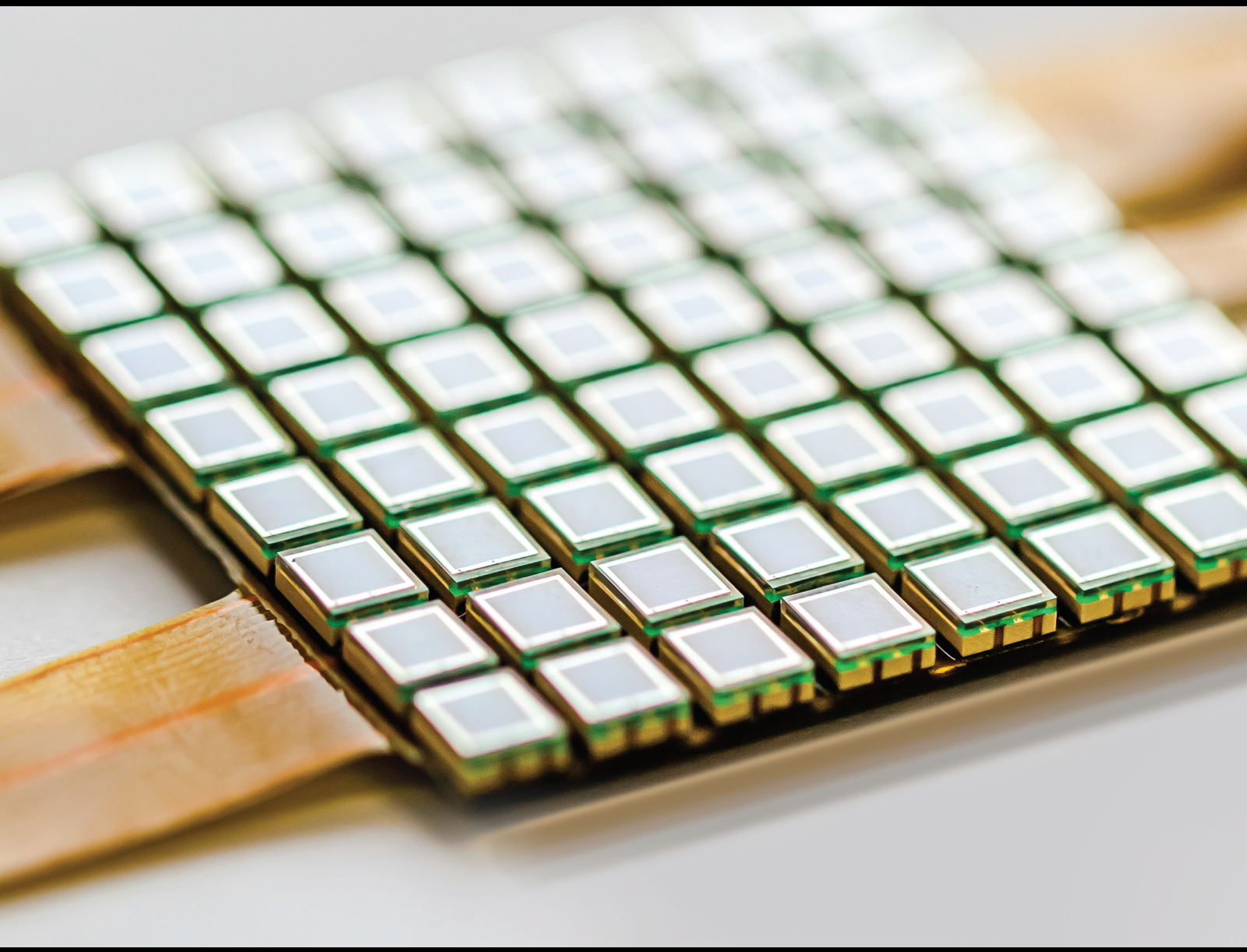

Advanced Sensor Technologies in Agricultural, Environmental, and Ecological Engineering

Journal of Sensors

Advanced Sensor Technologies in Agricultural, Environmental, and Ecological Engineering

Lead Guest Editor: Yuan Li
Guest Editors: Zhenxing Zhang, Jingwei Wang, Liu Hongxiao, and Liang Xu

Contents

Contents

Hindawi
Journal of Sensors
Volume 2021, Article ID 6668934, 12 pages
https://doi.org/10.1155/2021/6668934

Research Article

Automatic Detection and Parameter Estimation of *Ginkgo biloba* in Urban Environment Based on RGB Images

Kai Xia[1,2,3] **Hao Wang**[1,2,3] **Yinhui Yang**[1,2,3] **Xiaochen Du**[1,2,3] **and Hailin Feng**[1,2,3]

[1]*College of Mathematics and Computer Science, Zhejiang A&F University, Hangzhou, China*
[2]*Key Laboratory of State Forestry and Grassland Administration on Forestry Sensing Technology and Intelligent Equipment, Hangzhou, China*
[3]*Zhejiang Provincial Key Laboratory of Forestry Intelligent Monitoring and Information Technology, Hangzhou, China*

Correspondence should be addressed to Yinhui Yang; yhyang@zafu.edu.cn and Hailin Feng; zafu_fal@yeah.net

Received 4 November 2020; Accepted 12 July 2021; Published 6 August 2021

Academic Editor: Liu Hongxiao

Individual tree crown detection and morphological parameter estimation can be used to quantify the social, ecological, and landscape value of urban trees, which play increasingly important roles in densely built cities. In this study, a novel architecture based on deep learning was developed to automatically detect tree crowns and estimate crown sizes and tree heights from a set of red-green-blue (RGB) images. The feasibility of the architecture was verified based on high-resolution unmanned aerial vehicle (UAV) images using a neural network called FPN-Faster R-CNN, which is a unified network combining a feature pyramid network (FPN) and a faster region-based convolutional neural network (Faster R-CNN). Among more than 400 tree crowns, including 213 crowns of *Ginkgo biloba*, in 7 complex test scenes, 174 ginkgo tree crowns were correctly identified, yielding a recall level of 0.82. The precision and *F*-score were 0.96 and 0.88, respectively. The mean absolute error (MAE) and mean absolute percentage error (MAPE) of crown width estimation were 0.37 m and 8.71%, respectively. The MAE and MAPE of tree height estimation were 0.68 m and 7.33%, respectively. The results showed that the architecture is practical and can be applied to many complex urban scenes to meet the needs of urban green space inventory management.

1. Introduction

Urban trees play important roles in densely built cities, with activities that include reducing atmospheric carbon dioxide, alleviating the urban heat island effect [1, 2], isolating noise [3], alleviating urban flood risk [4], and providing shelters for wildlife [5, 6]. Detailed data on urban trees, such as species, location, number, diameter at breast height (DBH), tree height, and crown size, are essential for quantifying these benefits. Traditionally, tree attributes are obtained by field measurement, which is labor- and cost-intensive [7]. Individual tree crown detection (ITCD) technology based on remote sensing, which has the advantage of providing spatially explicit data, potentially with fine temporal resolution and low cost [6], can facilitate urban green space inventory development and monitoring.

ITCD technology has traditionally been used in forest monitoring and consists of 2 phases: (1) locating and delineating individual tree crowns and (2) classifying tree species and estimating morphological parameters such as crown size, tree height, and DBH ([8]).

In the location and delineation phase, the data source and computational methods are the two major factors dominating the results. Regardless of the data source, single tree crowns should first be detected automatically by methods such as local maxima [9], template matching [10], and image binarization [11]; then, crown edges should be delineated by various methods, such as region growing [12], watershed segmentation [13], and valley flowing [14]. Data are classified into three categories, i.e., passive sources (i.e., visible light, multispectral, and hyperspectral), active sources (i.e., LIDAR and radar), and both passive and active sources; data type has

a great impact on the results [15]. In recent decades, an increasing number of LIDAR-based ITCD studies have been carried out because LIDAR provides accurate 3D surface information. In addition, crown delineation has been carried out based on multispectral imagery involving wavelength bands crucial for the identification of vegetation characteristics [16].

In phase 2, the tree crown locations and shapes delineated in phase 1 are applied for species classification or parameter estimation. For example, tree crowns extracted from hyperspectral or multispectral images can be classified accurately based on methods such as support vector machine and random forest [6, 17, 18]. Crown size can be obtained by directly measuring tree crown shape. If the species of the tree crowns is known, we can infer some parameters, such as DBH and tree height, based on linear regression models which determine the relationships between crown size and other parameters [7]. If 3D surface information is also available, tree height can be directly extracted [19–21], as we discuss below. LIDAR data were the earliest and most accurate data type for estimating tree height. Morsdorf et al. [22] derived tree height from segmented individual trees based on LIDAR point clouds, and the accuracy evaluation revealed a strong relation between estimated and field-measured tree height. With the subsequent development of structure-from-motion (SFM) technology, 3D point clouds can be generated from remote sensing images, and it became a popular way to estimate tree height due to its lower cost and easier acquisition process than LIDAR technology. According to various studies in which tree height has been estimated based on SFM technology [7, 19, 23–25], high agreement between remote sensing estimation and field measurements can be achieved.

In contrast to forests, the focus in cities is on individual trees rather than forest stands [26]. The study of urban trees by remote sensing faces the following challenges: (1) urban trees are distributed in complex environments with interfering backgrounds, e.g., buildings, lawns, and low vegetation; (2) urban trees are unevenly distributed, vary in size, and are often in groups with heavy canopy overlap [27]; and (3) there may be many tree species in a small area [26]. In recent years, many approaches have been proposed to tackle these challenges using remote sensing data. Lin et al. [28] developed a three-step method applicable for the detection of individual trees in unmanned aerial vehicle (UAV) oblique images. Gomes et al. [29] realized individual urban tree crown detection in submeter satellite imagery using marked point processes and a geometrical-optical model. Liu et al. [6] and Mozgeris et al. [26] identified tree species in high-resolution spectral images after detecting and segmenting individual tree crowns based on LIDAR technologies. These studies indicate that the detection and classification of urban tree crowns are important but remain difficult. Some specialized methods designed according to the characteristics of the city have been proposed to estimate the morphological parameters of urban trees. Wu et al. [30] used mobile laser scanning to extract street tree height, crown size, and DBH. Jiao and Deng [31] estimated tree height based on the size of the tree shadow using sun angle and the time when the image was taken.

Previous studies on forest and urban ITCD have all demonstrated the great value of detecting tree species and estimating important morphological tree parameters accurately and automatically. However, these studies were based on different types of data sources and a variety of methods. The lack of a standardized pipeline for data acquisition and processing and an integrated computational architecture limit the practical application of current methods. Therefore, there is an urgent need to establish an integrated architecture for practical use, the design of which should be focused on solving the challenges of ITCD of urban trees via the following capabilities: (1) accurately detecting specific tree species in urban environments; (2) inferring key morphological tree parameters; (3) performing computations in a fully automatic way; and (4) performing data acquisition and processing to support the computations in a manner that is not only convenient and economical but also easy to standardize.

In recent years, deep learning approaches, especially deep convolution neural networks, have achieved great performance in object detection, and ITCD studies based on deep convolution neural networks have achieved good results. Morales et al. [32] segmented crowns of *Mauritia flexuosa* in the Amazon rainforest based on the DeepLab v3+ architecture with an accuracy of 96.60%. Ampatzidis and Partel detected citrus trees with a precision and recall of 99.9% and 99.7%, respectively, based on deep learning networks [33].

Considering the lack of an integrated architecture for ITCD with practical capabilities, this study proposes an automated urban canopy detection architecture based on deep learning that can obtain the number, location, crown size, and tree height of a given tree species from a set of RGB images. Specifically, a neural network, FPN-Faster R-CNN, is adapted in this study, and rich evaluation experiments are conducted based on high-resolution UAV images. The results indicate that the architecture is promising for ITCD studies of urban trees, although much more work is needed to further improve its performance in diverse real applications.

2. Materials and Methods

2.1. Study Sites. In this research, three study sites in Linan were selected: one on the campus of Zhejiang Agriculture and Forestry University (ZAFU), one on the west shoreline of Qingshanhu Lake, and one in a residential area (Figure 1). Linan, a typical forest city, is located in Hangzhou, Zhejiang Province, China, centered at latitude/longitude 119.72°/30.25°. It features a subtropical monsoon climate, and the vegetation is dominated by subtropical evergreen broad-leaved forest.

Ginkgo biloba, a deciduous tree distributed mainly along roadsides, was selected as the detection target. All training data and test data were collected from the three study sites, where there are many *Ginkgo biloba* trees.

2.2. Architecture. Figure 2 illustrates a general flowchart of the proposed architecture for detecting crowns and estimating morphological parameters automatically. A detailed explanation is given as follows.

Data are critical for the architecture, and the following prerequisites must be met: an orthophoto and a canopy

(a) (b) (c)

Figure 1: Study sites: (a) residential area,(b) western shoreline of Qingshanhu Lake, and (c) campus of ZAFU in Linan (top).

height model (CHM). The orthophoto, i.e., an image with a perfectly straight-down view of all objects, is needed to estimate crown size, whereas the CHM, which is a surface height distribution map, is essential for extracting tree height. Fortunately, we found that both an orthophoto and a CHM can be synthesized from a set of RGB images with a high overlap rate.

Deep learning, a general family of methods that use multilayered neural networks, has been proven effective at classifying, detecting, or segmenting objects in images. Both object detection neural networks and instance segmentation neural networks can be applied to this architecture (see Section 4.2). The deep learning system outlined in Figure 2 integrates all the functions needed, including data input, preprocessing, neural network construction, training, validation, analysis, and output. Before detection, the neural network should be trained based on training data; all trained parameters are stored in a model file. During detection, the system completes the following operations in order: preprocess the input orthophotos, build deep neural networks according to the model file, detect tree crowns in the neural network, and output the detection results. An object detection neural network, FPN-Faster-RCNN, is used to validate the architecture in this study.

The bounding box (bbox, Figure 3(a)) is the universal output form of object detection networks. (The output form of object segment networks is the bbox and mask; see Section 4.2.) We can obtain numbers and locations from the bbox statistics, which can also be used to estimate crown size and tree height.

Traditionally, crown size is represented by crown width, crown diameter, or crown area, which can be calculated by the bbox or mask. For example, crown width (a mean of two measurements made along north-south and east-west orientations; W. Lin et al. [34]; Minckler and Gingrich [35]; Vaz Monteiro et al. [36]) simply equals the average length of the sides of the bbox (see Equation (1)). (The top of all images in this study corresponds to north.)

$$\text{Crown width} = \text{average}\,(\text{length of sides of the bbox}). \quad (1)$$

The maximum pixel value of the corresponding area of a bbox (that is, the value of the brightest point in each bbox) in the CHM, a type of map named canopy height model, could be roughly estimated as the height of a tree (Figure 3(b)). It is easy to locate the position of the bbox in the CHM because the CHM and orthophoto originate from the same set of RGB images.

If the data and model are ready, the three tasks of detecting tree crowns, estimating crown widths, and estimating tree heights can be carried out continuously in one program without additional intervention.

2.3. Data Collection. The UAV used in this study was a DJI Inspire 2 (DJI Technology Co., Ltd., Shenzhen, China) and included four parts: the aircraft, remote control, camera, and power supply. All missions were flown at a height of 30-100 m above the launch site. The longitudinal overlap and side overlap were all set to 90%. The camera was set to orient vertically toward the surface. The total flight time for each individual flight was less than 15 min. All flights were conducted under light-wind or no-wind conditions.

Table 1 provides a summary of the data collected. A total of seven typical scenes, T1-T7, were chosen as test scenes (Figure 4), with T1 being from study site A (Figure 1), T2 being from study site B, and T3-T7 being from site C. Training data were also collected from sites B and C, therein excluding test scenes. To calculate crown size correctly, the images used for testing were orthophotos, which were synthesized from overlapping UAV images. However, the images used to create the training data included not only the orthophotos but also the original UAV images. Both types of images were used because the performance of a neural network typically improves as the quality, diversity, and amount of training data increase [37]. Although a large proportion of the tree crowns in the original drone images were likely to be taken from an oblique angle, the images were used to increase the data diversity and volume. Since there were few orthophotos available for training, most of the images used for training were original drone images.

The 7 test scenes are summarized in Table 2. The reference data on tree height were derived from field measurements obtained with the triangulation method using a laser rangefinder. The ground truth of the crown widths was obtained from manual measurements in the orthophotos instead of in the field because the resolution of the orthophotos was very high; thus, the data obtained from the orthophotos were expected to be more accurate than field measurements would be.

2.4. Data Processing. As shown in Figure 5, the point cloud, which is generated from overlapping images, comprises 3D point data and can be used to create orthophotos and DSMs directly. The digital terrain model (DTM), which represents the terrain surface, can be generated from point clouds by

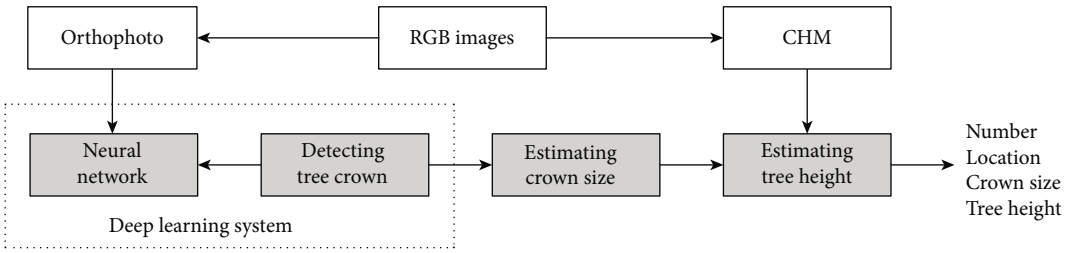

Figure 2: Flowchart of the proposed architecture: RGB: red-green-blue; CHM: canopy height model.

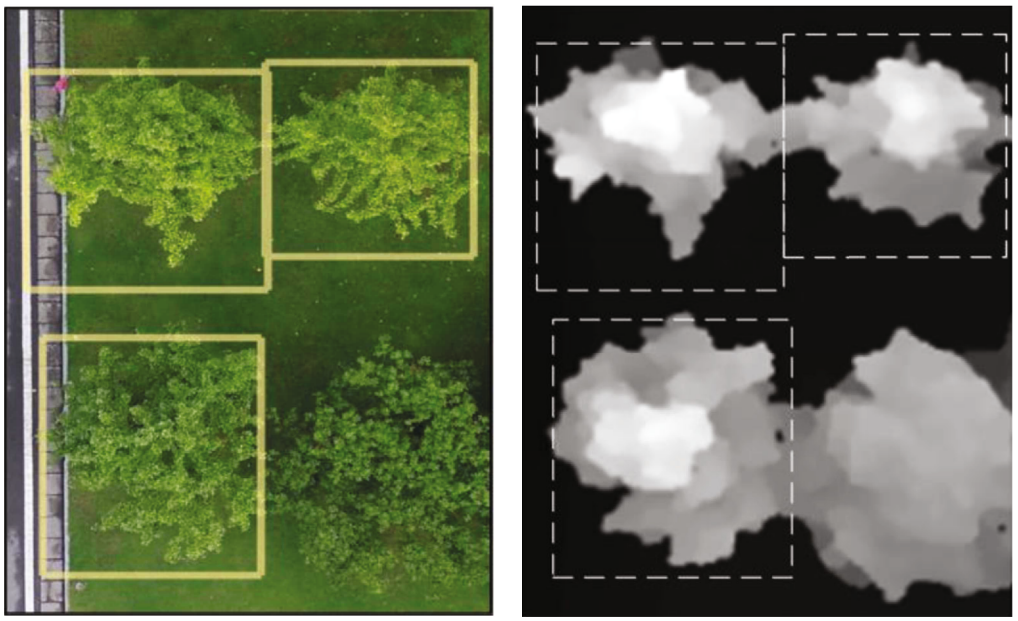

(a) (b)

Figure 3: Bounding boxes (bboxes), the output form of object detection networks: (a) bboxes in an orthophoto; (b) corresponding area in the CHM.

Table 1: Summary of data.

Data	Study sites	Acquisition time	Orthophotos	Original UAV images	Crowns
Training	B, C	2018.6/2019.6/2019.9	10	219	2593
Test	A, B, C	2019.6/2019.9	7	/	213

extracting the lowest points and interpolating them using the inverse distance weighting (IDW) method. Then, the CHM, which records tree height and other features, equals the difference between the DSM and DTM (see Equation (2)) [7]. If a point is the apex of a tree, we can obtain its elevation from the DSM, its ground elevation from the DTM, and tree height from the CHM.

$$\mathrm{CHM} = \mathrm{DSM} - \mathrm{DTM}. \quad (2)$$

The collected photos were processed with the 3D modeling software Agisoft PhotoScan Pro version 1.5.1 (Agisoft LLC, Russia). This software was chosen because it has proven effective in the production of mosaicked orthorectified imagery [38]. The data were processed with continuous operations, including photo alignment, alignment optimization, construction of dense point clouds, and orthophoto, DSM, and DTM construction. Finally, the CHM was created from ArcGIS operations.

2.5. FPN-Faster R-CNN. Faster region-based convolutional neural network (Faster R-CNN) is an object detection network based on convolutional neural networks developed by Ren et al. [39]. As shown in Figure 6, the input for Faster R-CNN is an image, and the output is bboxes around the objects identified by the Faster R-CNN program. The first module of Faster R-CNN is convnet, the output of which is a set of feature maps. The second module is the region proposal network (RPN), which generates a list of bboxes of likely positions of targets. More likely bboxes are stored in the region of interest (ROI) pool as candidate bboxes. The last module, classifier, consists of fully connected layers that

Figure 4: Detection results for ginkgo trees (yellow boxes for TP, red boxes for FP, and blue boxes for FN).

Table 2: Summary of test scenes.

Test scene	Acquisition	C1	C2	C3	C4	C5	C6	C7
T1	2019.9	14	9.07	11.00	6.56	5.21	6.52	3.72
T2	2019.9	20	8.02	11.00	5.43	3.84	4.93	2.44
T3	2019.6	42	9.36	12.40	5.78	3.62	5.85	1.26
T4	2019.6	40	9.32	13.90	5.46	3.76	6.56	1.32
T5	2019.6	22	9.69	12.50	4.91	4.29	5.32	3.42
T6	2019.6	52	10.96	14.21	6.60	4.24	6.10	2.88
T7	2019.9	23	11.29	13.82	9.10	5.64	7.37	4.25

C1: number of ginkgo trees; C2: mean tree height from field measurement; C3: maximum tree height from field measurement; C4: minimum height from field measurement; C5: mean width of measurement from orthophotos; C6: maximum width of measurement from orthophotos; C7: minimum width of measurement from orthophotos.

determine and output the optimal object categories and bboxes based on the loss function. Faster R-CNN has proven very efficient for detection, and its details can be found in the literature [39–41].

In Faster R-CNN, only the small-scale convnet feature layer is used for object detection. The layer is better at identifying simple objects than uneven distributions, different sizes, and overlapping tree crowns.

Many studies have found that small-sized feature layers are more conducive to extracting low-resolution, semantically strong features, whereas large-scale feature layers are effective at distinguishing high-resolution, semantically weak features. Feature pyramid network (FPN) is a novel structure that combines a small-scale feature layer and large-scale feature layers via a top-down pathway and lateral connections [42] (Figure 7). The top-down pathway creates large-scale feature layers by upsampling from the small-scale feature layer in higher pyramid levels. The newly created layers are then enhanced with feature layers from the bottom-up pathway via lateral connections. Each top-down feature layer can be seen as a collection of objects that can be extracted in lateral nets. This architecture can enhance the semantics of high-resolution objects, and it is very suitable for detecting uneven distributions, different sizes, and overlapping tree crowns.

FPN can be merged into other networks to improve their performance. Figure 7 illustrates the networks of FPN-Faster R-CNN that was adopted in this research to detect trees.

The training was based on a pretrained model file. Some of the hardware and software parameters for model training are shown in Table 3.

2.6. Accuracy Validation. The overall performance of tree identification and delineation was evaluated using the precision, recall, and F-score. Precision means the correct proportion of all detected objects, and recall refers to the correct proportion of all objects that should be detected. The F1-score, which is a harmonic mean of precision and recall, is used to refer to the overall accuracy [29, 43].

The overall accuracy F-score is defined by

$$\text{F-score} = \frac{2 * \text{precision} * \text{recall}}{(\text{precision} + \text{recall})}. \tag{3}$$

The precision and recall are defined as follows:

$$\begin{aligned} \text{Precision} &= \frac{\text{TP}}{(\text{TP} + \text{FP})}, \\ \text{Recall} &= \frac{\text{TP}}{(\text{TP} + \text{FN})}. \end{aligned} \tag{4}$$

TP, FP, FN, and IOU are defined as follows:

$$\begin{aligned} &\text{TP} = \text{number of detections with IOU} \geq 0.5, \\ &\text{FP} = \text{number of detections with IOU} \\ &\quad < 0.5 \text{ or detected more than once}, \\ &\text{FN} = \text{number of objects not detected}, \\ &\text{IOU} = \frac{(\text{detection result} \cap \text{ground truth})}{(\text{detection result} \cup \text{ground truth})}. \end{aligned} \tag{5}$$

The errors of the crown width and tree height estimation were evaluated by the mean absolute error (MAE), mean absolute percentage error (MAPE), and root mean square error (RMSE), which are given by Equations (6), (7), and (8) as follows (where t_i is the true value and e_i is the estimate):

$$\text{MAE} = \frac{1}{N}\sum_{i=1}^{N}|t_i - e_i|, \tag{6}$$

$$\text{MAPE} = \frac{1}{N}\sum_{i=1}^{N}\frac{|t_i - e_i|}{t_i}, \tag{7}$$

$$\text{RMSE} = \sqrt{\frac{1}{N}\sum_{i=1}^{N}(t_i - e_i)^2}. \tag{8}$$

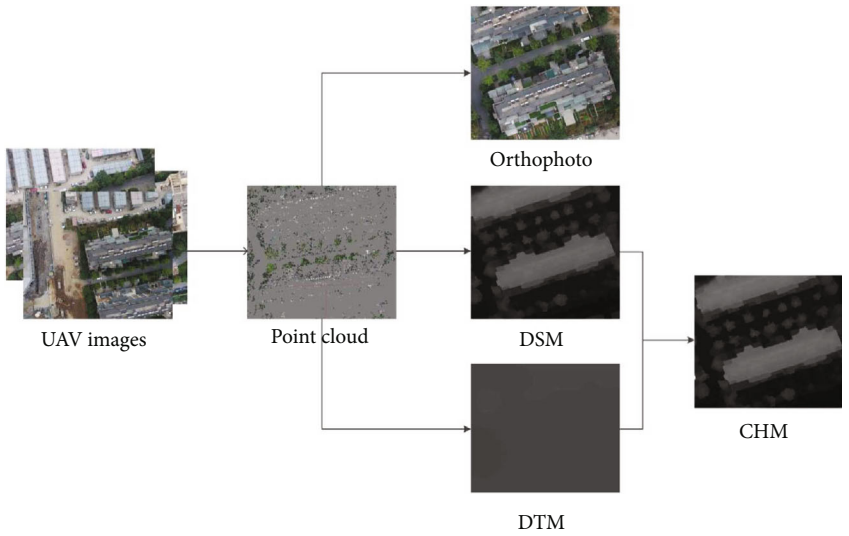

Figure 5: Data processing: DSM: digital surface model; DTM: digital terrain model; CHM: canopy height model. The DSM and DTM are both types of digital elevation model (DEM) and represent the elevation distribution of the region. They differ in that the pixel values in the DTM are the ground elevation, whereas those in the DSM are the elevation of the top surfaces of trees, buildings, and other aboveground features. Since the urban bare ground is very flat and the DTM is created by interpolation, the elevation values everywhere in the DTM are similar, and the resulting image just appears uniformly gray.

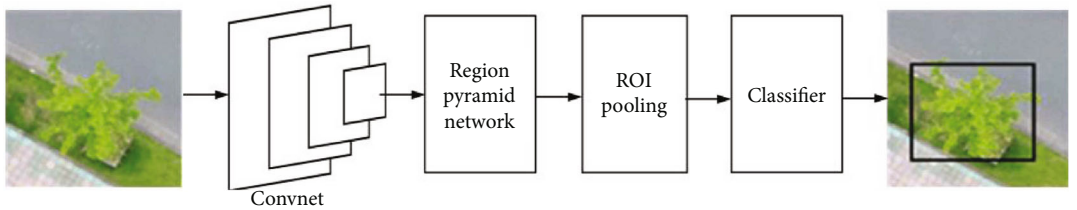

Figure 6: Faster R-CNN.

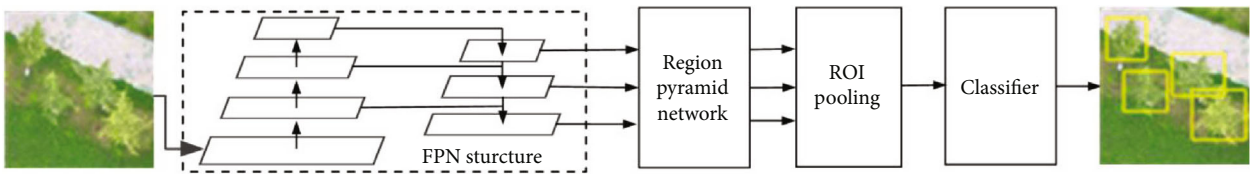

Figure 7: FPN-Faster R-CNN.

Table 3: Model training parameters.

	Parameter	Setting
Hardware	CPU	Intel Xeon E3-1225 V5 3.3 GHz
	GPU	Nvidia GeForce GTX 1080TI
	RAM	Hynix 32G
Software	Development language	Python
	Machine learning environment	TensorFlow
	Training iteration	18000

3. Results

3.1. Tree Crown Detection. In this study, 7 typical small scenes (Figure 4) were selected for testing because the use of only one large test area, as employed in previous studies, might be insufficient for representing urban landscapes. Test scene T1 represented a typical road, T2 represented a typical residential area, T3 and T4 represented areas containing tree crowns of different sizes, T5 and T6 represented areas with many overlapping canopies, and T7 represented an area where the color of the lawn background was similar to that of the crowns. Test scenes T3-T7, which were of the campus of Zhejiang A&F University and a botanical garden, were

Table 4: Detection results.

Test orthophotos	Total trees	Total detected	TP	FP	FN	Precision	Recall	*F*-score
T1	14	13	13	0	1	1	0.92	0.96
T2	20	19	19	0	1	1	0.95	0.97
T3	42	35	34	1	8	0.97	0.81	0.88
T4	40	28	28	0	12	1	0.70	0.82
T5	22	19	18	1	4	0.95	0.82	0.88
T6	52	50	44	6	8	0.88	0.85	0.86
T7	23	18	18	0	5	1	0.78	0.88
Total	213	182	174	8	39	0.96	0.82	0.88

TP = number of detections with IOU ≥ 0.5; FP = number of detections with IOU < 0.5 or detected more than once; FN = number of objects not detected; precision = TP/(TP + FP); recall = TP/(TP + FN); F-score = 2 ∗ precision ∗ recall/(precision + recall).

Table 5: Error causes.

Type	Total trees	Total detected	TP	FP	FN	Precision	Recall	*F*-score
Easy crowns	72	70	70	0	2	1	0.97	0.99
Hard crowns	141	112	104	8	37	0.93	0.74	0.78
Small crowns (width < 3 m)	28	15	15	0	13	1	0.54	0.70
Overlapping crowns	70	56	51	5	19	0.91	0.73	0.81
Lawn background	23	18	18	0	5	1	0.78	0.88

TP = number of detections with IOU ≥ 0.5; FP = number of detections with IOU < 0.5 or detected more than once; FN = number of objects not detected; precision = TP/(TP + FP); recall = TP/(TP + FN); F-score = 2 ∗ precision ∗ recall/(precision + recall).

challenging to detect. As shown in Figure 4, the results were acceptable.

Table 4 presents the detection results for each image. There were more than 400 tree crowns in the images. Comparing the detected objects with the 213 actual ginkgo trees, we found that 174 were correctly identified, with 39 false negatives; the recall was 0.82, the precision was 0.96, and the *F*-score was 0.88.

The impacts of natural factors such as crown size, canopy overlap, and background complexity on detection accuracy, which have been mentioned in previous studies, were the first issue to consider and are discussed here. For convenience, the two rows of ginkgo trees lining the roads and all the trees in T1 and T2 were classified as easy targets, and all other tree crowns were classified as hard targets. Table 5 shows the evaluation results for the easy targets and hard targets.

Most of the commission and omission errors were related to small crowns in T3 and T4 and overlapping crowns in T3, T4, T5, and T6. However, the omission errors in T7 were attributed to grass background and sunlight. In general, the results were acceptable because the overlap was so serious that we could only identify some crowns through field measurement.

Despite the problems mentioned above, our method showed very good performance: (1) regardless of the scene, the accuracy in easy target detection was very high, indicating the stability of our method. (2) Although there were many other species of trees (more than 200) in the scenes, our method incorrectly classified other species of trees as ginkgo trees only 3 times, demonstrating excellent classification performance. (3) Most artificial features, such as buildings and roads, did not interfere with the recognition of ginkgo trees. There was only one omission error due to artificial features, which was in the lower left corner in T2 and related to obstruction by a street lamp. (4) The uneven distribution of tree crowns excluding overlapping had a minimal effect on the test results.

3.2. Crown Width. Only correctly detected ginkgo trees are discussed in this section. As mentioned before, instead of field-measured crown width, manual measurements from the orthophotos were used as reference data because of the high resolution of the orthophotos. For crown width estimation, the MAE was 0.37 m, the MAPE was 8.71%, and the RMSE was 0.495 m. The largest error percentage rate of the crown width estimation was 37.2%.

Figure 8(a) shows the relationship between manually measured crown width and automatically estimated crown width. Figure 8(b) shows the percentage error (absolute (estimated – manually measured)/manually measured ∗ 100%) distribution. The results showed good agreement between the ground truth and the estimates. Some points far from the line $y = x$ correspond to overlapping crowns.

3.3. Tree Height. As in the previous section, only correctly detected ginkgo trees are discussed in this section. The largest absolute percentage error of tree height obtained by automatic detection was 67.8%, the MAE was 0.68 m, the MAPE was 7.33%, and the RMSE was 0.987 m.

Figure 8(c) presents the relationship between field measurements of tree height and automatically estimated tree height. Figure 8(d) shows the percentage error (absolute (estimated – field measured)/field measured ∗ 100

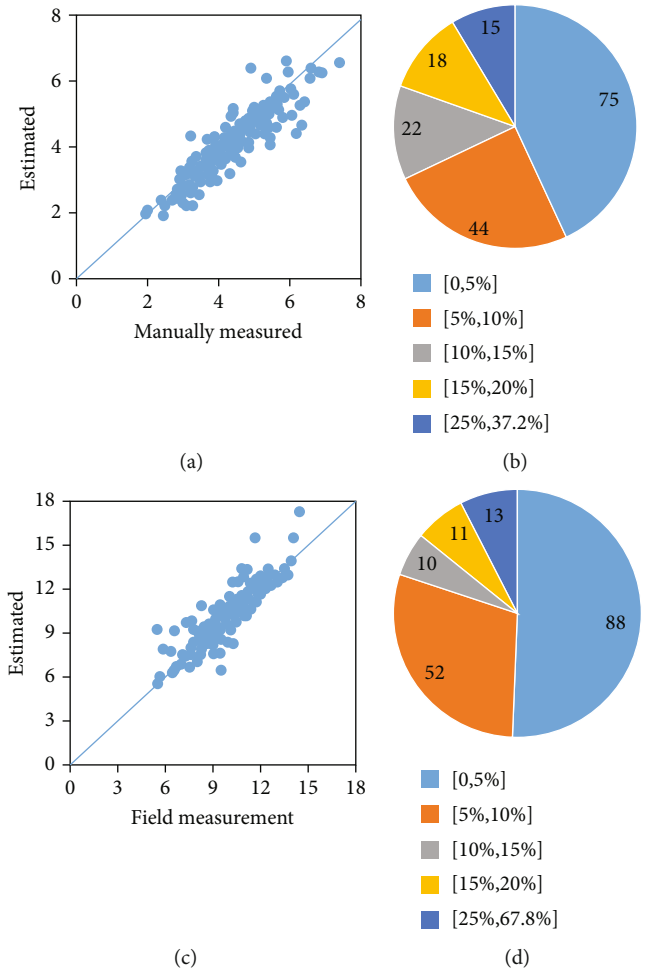

Figure 8: (a) Estimated versus manually measured crown width (both in meters); (b) percentage error distribution of crown width estimation; (c) estimated versus field-measured tree height (both in meters); (d) percentage error distribution of tree height estimation.

%) distribution. The results showed good agreement between the ground truth and the estimates. The points far from the line $y = x$ might have been caused by unpredictable interference factors.

3.4. IOU. In this study, IOU was used as an assessment criterion for determining whether a crown was detected. This criterion has been used in a few recent studies [44, 45]. The IOU threshold ultimately selected for use in this paper was 0.5, which is the general standard in deep learning studies. At higher thresholds, the detection accuracy decreased, and at a lower threshold, the detection accuracy increased (Table 6). However, the detection accuracy improved minimally when we lowered the threshold to 0, which means that very few (only 4) bbox IOUs were within [0, 0.5], illustrating the great performance of FPN-Faster R-CNN.

The IOU threshold also had a strong impact on the error statistics of crown width because crown width was calculated from the bbox. At higher thresholds, the MAE and MAPE of crown width decreased.

Table 6: Impacts of IOU.

Criterion	Detection precision	Detection recall	Detection *F*-score	MAPE of crown width	MAPE of tree height
IOU > 0	0.97	0.83	0.90	9.19%	7.50%
IOU > 0.5	0.96	0.82	0.88	8.71%	7.33%
IOU > 0.6	0.84	0.71	0.77	6.90%	7.36%
IOU > 0.7	0.67	0.57	0.61	5.97%	7.29%

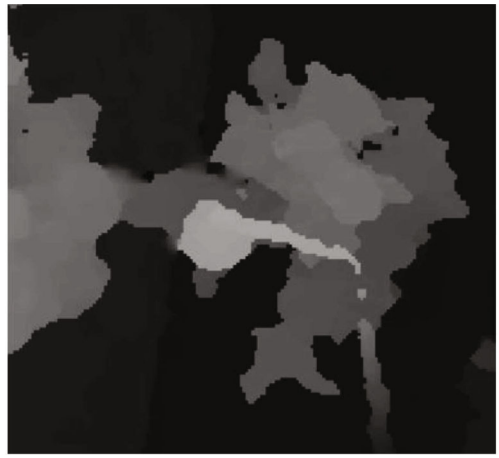

Figure 9: A street lamp above a ginkgo tree.

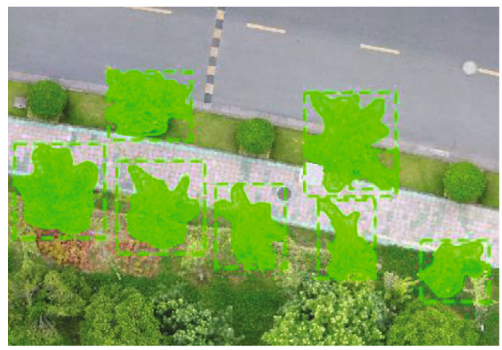

Figure 10: A result of Mask-RCNN.

We believe that the accuracy of the tree height estimation was affected mainly by the following aspects: (1) the error from the field measurement and the CHM map, (2) whether the highest point of the tree was within the bbox, and (3) interference from artificial objects. If a bbox had a large deviation (IOU < 0.5), the highest point of the tree may not be inside it, resulting in an incorrect estimation of tree height. When IOU > 0.5, the search for the highest point of a canopy usually yielded correct results and the error was mainly derived from the field measurements and CHM maps. In addition, there are countless complex scenes and unpredictable interfering factors in cities. For example, as shown in Figure 9, a large deviation in tree height estimation occurred due to a street lamp.

Table 7: Studies on individual tree detection and parameter estimation.

Study	1 [30]	2 [31]	3 [29]
Sensor	2 laser scanners, two CCD cameras	ADS40 airborne digital sensor	Submeter optical sensor
Carrying platform	Van	Plane	WorldView-2 satellite
Detection method	Voxel-based marked neighborhood searching	Classification of refined superpixels by a naive Bayes classifier	Marked point processes based on a geometrical- optical model
Study area	Small	Large	Large
Target	Individual street trees	Individual urban tree crowns	Individual urban tree crowns
Species recognition	No	No	No
Crown size	Y	Y	Y
Height	Y	Y	N
DBH	Y	N	N

4. Discussion

This paper presents a novel method to conveniently and efficiently map the individual number, locations, crown sizes, and tree heights of *Ginkgo biloba* trees.

4.1. Data Sources. Some common data sources were available for our study; for example, orthophotos can be synthesized from RGB, multispectral, or high spectral images, and LIDAR data or high overlapping RGB images are often used to create a CHM. Considering the powerful detection capabilities of deep learning, in this research, we chose a convenient, low-cost data solution in which orthophotos and CHMs are all created from highly overlapping RGB images. This approach has not often been adopted in previous studies due to the poor spectral information of such images.

However, the quality of several orthophotos was not ideal because there were some distorted crowns, especially in the dense area, due to the orthophoto synthesis process. Moreover, a few errors in the test were attributed to synthesis quality (e.g., the omission errors in the lower right corner of T6).

In addition, our program cannot yet handle large images. Therefore, if the spatial extent of an orthophoto is very large, it should be divided into small images before detection.

4.2. Flexibility of the Architecture. Any new object detection network or instance segmentation network can be applied to this architecture, such as FPN-Faster R-CNN, because object detection neural networks (such as Faster R-CNN and YOLO) output a bbox around each target, and instance segmentation networks (such as Mask R-CNN and BlendMask) all output the masks of the canopies as well as bboxes (Figure 10). We selected FPN-Faster R-CNN for our case study because of its ease of discussion, although it would have been possible for us to obtain another crown size indictor (crown area) from an instance segmentation network such as Mask-RCNN.

Therefore, the architecture has great potential for performance improvement because of this flexibility. In recent years, an increasing number of studies have focused on deep learning, and new high-performance neural networks are being continuously developed. More accurate results would be achieved if high-performance networks were adopted in this architecture.

4.3. Comparison. There have been a few schemes focused on building architectures to realize individual urban tree detection and parameter estimation simultaneously. The methods and sensors of some representative studies are listed in Table 7. In one study (study 1 in Table 7), a mobile solution with many sensors was presented; the design made it costly and limited its observable range. However, its detection of street trees (such as easy targets in Table 5) was over 98%, and the RMSE values of its estimation of tree height, DBH, and crown diameter were 0.15 m, 0.01 m, and 0.13 m, which shows its good capability in parameter estimation. While the observable range of study 2 is comparatively large, so are its costs. Additionally, there were not enough accuracy estimates suitable for comparison with our study. Given its huge coverage and the low image resolution of WorldView-2, the method presented in study 3 achieved acceptable evaluation results, with detection and delineation accuracies of 0.87 and 0.63, respectively. Compared with these schemes, our method has several benefits that cannot be ignored, such as convenience, low cost, capability of species recognition, and tremendous potential for performance improvements based on data growth and methodology evolution. Nonetheless, how to estimate DBH from the air remains an unsolved problem.

In addition to the above schemes, another scheme is available that can realize individual tree detection and parameter estimation automatically. In this scheme, both tree height estimation and tree crown detection are conducted based on CHM by using the method of local maxima. Guerra-Hernández et al. [46] validated the scheme in an area of umbrella pine afforestation, and all the trees of the plots were correctly detected. The RMSE values for the predicted heights and crown widths were 0.45 m and 0.63 m, respectively. Nonetheless, successful validation with individual urban trees has been absent, possibly due to the presence of urban infrastructure, which can result in ambiguity when height ranges are extracted to estimate tree height [6].

In addition, some studies have only focused on developing a new method to detect individual urban trees. Lin et al.

[28] developed a nondeep learning method based on UAV oblique images, and the commission and omission errors were less than 32% and 26%. Xie et al. [27] presented a two-phase deep learning method to detect urban trees based on normal height model (NHM) images, which achieved F-scores between 85% and 90%. Torres et al. [47] evaluated five deep fully convolutional networks (FCNs) for the semantic segmentation of a single tree species: SegNet, U-Net, FC-DenseNet, and two DeepLabv3+ variants. The experimental analysis revealed the effectiveness of each design, with F-scores ranging from 87.0% to 96.1%. Although all these results are based on different conditions, we believe that the accuracy of FPN-Faster RCNN adopted in this study is higher than that of the above nondeep learning method and is roughly at the same level as other deep learning networks.

4.4. Application Scenes. In general, our architecture is suitable for urban environments for 2 reasons: (1) complex urban features have little influence on deep learning-based tree canopy detection and (2) the flat terrain in urban areas is conducive to obtaining accurate tree height values. However, small patches of dense woodland in cities are a challenge for our framework, which can be attributed to its use of RGB images, which provide only color and texture information. Differences in texture and color between overlapping crowns are not obvious in many cases, which is a difficult problem for deep learning.

We believe that our method can be easily extended to plantations or sparse natural forests, grasslands, pastures, and other areas where canopy overlap is not extensive. However, if the terrain is complex, the estimation of height will be slightly affected; Guerra-Hernández et al. [48] estimated tree height based on CHM data in an area with complex terrain and obtained an RMSE of 2.84 m, which is not ideal.

We believe that in dense natural forest, severe crown overlap will affect not only the accuracy of crown detection but also the estimation accuracy of tree height and crown size. A feasible solution is to not only use CHM data for tree height estimation but also superimpose them with RGB images to train the deep learning networks. This approach is believed to be effective, although some experiments with this method show that there remains room for improvement [49].

5. Conclusions

In this paper, a novel method for automatic tree crown detection and parameter estimation using deep learning technology is proposed, and FPN-Faster R-CNN is used in a deep learning example to verify the architecture. The method realizes automatic tree crown detection and morphology parameter estimation in some complex urban scenes and is convenient and low cost. The quality of the orthophotos affected the canopy detection results. In general, deep learning is a very promising method that warrants further research, and the accuracy of the information collected by the architecture will increase as neural networks evolve.

Data Availability

The data used to support the findings of this study are available from the corresponding author upon request.

Conflicts of Interest

The authors declare no conflict of interest.

Acknowledgments

This study was supported by the National Natural Science Foundation of China (grant number U1809208); Joint Funds of the Natural Science Foundation of Zhejiang Province, China (grant number LQY18C160002); Natural Science Foundation of Zhejiang Province, China (grant number LQ20F020005); and Zhejiang Science and Technology Key R&D Program Funded Project (grant number 2018C02013).

References

[1] G. Kuchelmeister and S. Braatz, "Urban forestry revisited," *Unasylva*, vol. 44, 1993.

[2] E. G. McPherson, D. J. Nowak, and R. A. Rowntree, *Chicago's Urban Forest Ecosystem: Results of the Chicago Urban Forest Climate Project*, U.S. Department of Agriculture, Forest Service, Northeastern Forest Experiment Station, 1994.

[3] S. Roy, J. Byrne, and C. Pickering, "A systematic quantitative review of urban tree benefits, costs, and assessment methods across cities in different climatic zones," *Urban Forestry & Urban Greening*, vol. 11, no. 4, pp. 351–363, 2012.

[4] E. Zimmermann, L. Bracalenti, R. Piacentini, and L. Inostroza, "Urban flood risk reduction by increasing green areas for adaptation to climate change," vol. 161, pp. 2241–2246, 2016.

[5] M. A. Goddard, A. J. Dougill, and T. G. Benton, "Scaling up from gardens: biodiversity conservation in urban environments," *Trends in Ecology & Evolution*, vol. 25, no. 2, pp. 90–98, 2010.

[6] L. Liu, N. C. Coops, N. W. Aven, and Y. Pang, "Mapping urban tree species using integrated airborne hyperspectral and LiDAR remote sensing data," *Remote Sensing of Environment*, vol. 200, pp. 170–182, 2017.

[7] K. Iizuka, T. Yonehara, M. Itoh, and Y. Kosugi, "Estimating tree height and diameter at breast height (DBH) from digital surface models and orthophotos obtained with an unmanned aerial system for a Japanese cypress (Chamaecyparis obtusa) forest," *Remote Sensing*, vol. 10, no. 2, p. 13, 2018.

[8] J. Hyyppä and M. Inkinen, "Detecting and estimating attributes for single trees using laser scanner," *Photogramm J Finl*, vol. 16, pp. 27–42, 1999.

[9] M. Wulder, K. O. Niemann, and D. G. Goodenough, "Local maximum filtering for the extraction of tree locations and basal area from high spatial resolution imagery," *Remote Sensing of Environment*, vol. 73, no. 1, pp. 103–114, 2000.

[10] T. Brandtberg, T. A. Warner, R. E. Landenberger, and J. B. McGraw, "Detection and analysis of individual leaf-off tree crowns in small footprint, high sampling density lidar data from the eastern deciduous forest in North America," *Remote Sensing of Environment*, vol. 85, no. 3, pp. 290–303, 2003.

[11] J. Pitkänen, "Individual tree detection in digital aerial images by combining locally adaptive binarization and local maxima

methods," *Canadian Journal of Forest Research*, vol. 31, no. 5, pp. 832–844, 2001.

[12] P. Bunting and R. Lucas, "The delineation of tree crowns in Australian mixed species forests using hyperspectral Compact Airborne Spectrographic Imager (CASI) data," *Remote Sensing of Environment*, vol. 101, no. 2, pp. 230–248, 2006.

[13] L. Wang, P. Gong, and G. S. Biging, "Individual tree-crown delineation and treetop detection in high-spatial-resolution aerial imagery," *Photogrammetric Engineering and Remote Sensing*, vol. 70, no. 3, pp. 351–357, 2004.

[14] F. A. Gougeon and D. G. Leckie, "The individual tree crown approach applied to Ikonos images of a coniferous plantation area," *Photogrammetric Engineering and Remote Sensing*, vol. 72, no. 11, pp. 1287–1297, 2006.

[15] Z. Zhen, L. J. Quackenbush, and L. Zhang, "Trends in automatic individual tree crown detection and delineation-evolution of LiDAR data," *Remote Sensing*, vol. 8, no. 4, 2016.

[16] Y. Ke and L. J. Quackenbush, "A review of methods for automatic individual tree-crown detection and delineation from passive remote sensing," *International Journal of Remote Sensing*, vol. 32, no. 17, pp. 4725–4747, 2011.

[17] M. Dalponte, H. O. Ørka, L. T. Ene, T. Gobakken, and E. Næsset, "Tree crown delineation and tree species classification in boreal forests using hyperspectral and ALS data," *Remote Sensing of Environment*, vol. 140, pp. 306–317, 2014.

[18] J. Maschler, C. Atzberger, M. Immitzer, J. Maschler, C. Atzberger, and M. Immitzer, "Individual tree crown segmentation and classification of 13 tree species using airborne hyperspectral data," *Remote Sensing*, vol. 10, no. 8, p. 1218, 2018.

[19] A. C. Birdal, U. Avdan, and T. Türk, "Estimating tree heights with images from an unmanned aerial vehicle," *Hazards Risk*, vol. 8, no. 2, pp. 1144–1156, 2017.

[20] S. Koukoulas and G. A. Blackburn, "Mapping individual tree location, height and species in broadleaved deciduous forest using airborne LIDAR and multi-spectral remotely sensed data," *International Journal of Remote Sensing*, vol. 26, no. 3, pp. 431–455, 2005.

[21] Y. S. Lim, P. H. La, J. S. Park, M. H. Lee, M. W. Pyeon, and J. I. Kim, "Calculation of tree height and canopy crown from drone images using segmentation," *Journal of the Korean Society of Surveying, Geodesy, Photogrammetry and Cartography*, vol. 33, no. 6, pp. 605–614, 2015.

[22] F. Morsdorf, E. Meier, B. Kötz, K. I. Itten, M. Dobbertin, and B. Allgöwer, "LIDAR-based geometric reconstruction of boreal type forest stands at single tree level for forest and wildland fire management," *Remote Sensing of Environment*, vol. 92, no. 3, pp. 353–362, 2004.

[23] R. A. Díaz-Varela, R. de la Rosa, L. León, and P. J. Zarco-Tejada, "High-resolution airborne UAV imagery to assess olive tree crown parameters using 3D photo reconstruction: application in breeding trials," *Remote Sensing*, vol. 7, no. 4, pp. 4213–4232, 2015.

[24] P. Shin, T. Sankey, M. Moore, and A. Thode, "Evaluating unmanned aerial vehicle images for estimating forest canopy fuels in a ponderosa pine stand," *Remote Sensing*, vol. 10, no. 8, p. 1266, 2018.

[25] L. Wallace, A. Lucieer, Z. Malenovský et al., "Assessment of forest structure using two UAV techniques: a comparison of airborne laser scanning and structure from motion (SfM) point clouds," *Forests*, vol. 7, no. 12, p. 62, 2016.

[26] G. Mozgeris, V. Juodkienė, D. Jonikavičius, L. Straigytė, S. Gadal, and W. Ouerghemmi, "Ultra-light aircraft-based hyperspectral and colour-infrared imaging to identify deciduous tree species in an urban environment," *Remote Sensing*, vol. 10, no. 10, p. 1668, 2018.

[27] Y. Xie, H. Bao, S. Shekhar, and J. Knight, "A TIMBER framework for mining urban tree inventories using remote sensing datasets," in *in: 2018 IEEE international conference on data mining*, pp. 1344–1349, Singapore, 2018.

[28] Y. Lin, M. Jiang, Y. Yao, L. Zhang, and J. Lin, "Use of UAV oblique imaging for the detection of individual trees in residential environments," *Urban Forestry & Urban Greening*, vol. 14, no. 2, pp. 404–412, 2015.

[29] M. F. Gomes, P. Maillard, and H. Deng, "Individual tree crown detection in sub-meter satellite imagery using marked point processes and a geometrical-optical model," *Remote Sensing of Environment*, vol. 211, pp. 184–195, 2018.

[30] B. Wu, B. Yu, W. Yue et al., "A voxel-based method for automated identification and morphological parameters estimation of individual street trees from mobile laser scanning data," *Remote Sensing*, vol. 5, no. 2, pp. 584–611, 2013.

[31] J. Jiao and Z. Deng, "Individual building rooftop and tree crown segmentation from high-resolution urban aerial optical images," *Journal of Sensors*, vol. 2016, 13 pages, 2016.

[32] G. Morales, G. Kemper, G. Sevillano, D. Arteaga, I. Ortega, and J. Telles, "Automatic Segmentation of Mauritia flexuosa in Unmanned Aerial Vehicle (UAV) Imagery Using Deep Learning," *Forests*, vol. 9, no. 12, p. 736, 2018.

[33] Y. Ampatzidis and V. Partel, "UAV-based high throughput phenotyping in citrus utilizing multispectral imaging and artificial intelligence," *Remote Sensing*, vol. 11, no. 4, p. 410, 2019.

[34] W. Lin, Y. Meng, Z. Qiu, S. Zhang, and J. Wu, "Measurement and calculation of crown projection area and crown volume of individual trees based on 3D laser-scanned point-cloud data," *International Journal of Remote Sensing*, vol. 38, no. 4, pp. 1083–1100, 2017.

[35] L. S. Minckler and S. F. Gingrich, *Relation of Crown Width to Tree Diameter in Some Upland Hardwood Stands of Southern Illinois*, 1970.

[36] M. Vaz Monteiro, K. J. Doick, and P. Handley, "Allometric relationships for urban trees in Great Britain," *Urban Forestry & Urban Greening*, vol. 19, pp. 223–236, 2016.

[37] H. Salehinejad, S. Valaee, T. Dowdell, and J. Barfett, "Image Augmentation Using Radial Transform for Training Deep Neural Networks," in *2018 IEEE International Conference on Acoustics, Speech and Signal Processing (ICASSP)*, pp. 3016–3020, Calgary, AB, Canada, 2018.

[38] J. Dempewolf, J. Nagol, S. Hein et al., "Measurement of within-season tree height growth in a mixed forest stand using UAV imagery," *Forests*, vol. 8, no. 7, p. 231, 2017.

[39] S. Ren, K. He, R. Girshick, and J. Sun, "Faster R-CNN: towards real-time object detection with region proposal networks," *IEEE Transactions on Pattern Analysis and Machine Intelligence*, vol. 39, no. 6, pp. 1137–1149, 2017.

[40] R. Girshick, "Fast R-CNN - IEEE conference publication," in *in: 2015 IEEE International Conference on Computer Vision (ICCV)*, IEEE, 2016.

[41] K. He, X. Zhang, S. Ren, and J. Sun, "Spatial pyramid pooling in deep convolutional networks for visual recognition," *IEEE Transactions on Pattern Analysis and Machine Intelligence*, vol. 37, no. 9, pp. 1904–1916, 2015.

[42] T. Y. Lin, P. Dollár, R. Girshick, K. He, B. Hariharan, and S. Belongie, "Feature pyramid networks for object detection," in *2017 IEEE Conference on Computer Vision and Pattern Recognition (CVPR)*, pp. 936–944, 2017a.

[43] G. Goldbergs, S. Maier, S. Levick, and A. Edwards, "Efficiency of individual tree detection approaches based on light-weight and low-cost UAS imagery in Australian savannas," *Remote Sensing*, vol. 10, no. 2, p. 161, 2018.

[44] B. G. Weinstein, S. Marconi, S. Bohlman, A. Zare, and E. White, "Individual tree-crown detection in RGB imagery using semi-supervised deep learning neural networks," *Remote Sensing*, vol. 11, no. 11, p. 1309, 2019.

[45] T. Zhao, Y. Yang, H. Niu, Y. Chen, and D. Wang, "Comparing U-Net convolutional network with mask R-CNN in the performances of pomegranate tree canopy segmentation," in *Multispectral, Hyperspectral, and Ultraspectral Remote Sensing Technology, Techniques and Applications VII*, 2018.

[46] J. Guerra-Hernández, E. González-Ferreiro, A. Sarmento et al., "Using high resolution UAV imagery to estimate tree variables in Pinus pinea plantation in Portugal," *For. Syst.*, vol. 25, no. 2, 2016.

[47] D. L. Torres, R. Q. Feitosa, P. N. Happ et al., "Applying fully convolutional architectures for semantic segmentation of a single tree species in urban environment on high resolution UAV optical imagery," *Sensors (Switzerland)*, vol. 20, no. 2, 2020.

[48] J. Guerra-Hernández, D. N. Cosenza, L. C. E. Rodriguez et al., "Comparison of ALS- and UAV(SfM)-derived high-density point clouds for individual tree detection in Eucalyptus plantations," *International Journal of Remote Sensing*, vol. 39, no. 15-16, pp. 5211–5235, 2018.

[49] A. I. Pleşoianu, M. S. Stupariu, I. Şandric, I. Pătru-Stupariu, and L. Drăguţ, "Individual tree-crown detection and species classification in very high-resolution remote sensing imagery using a deep learning ensemble model," *Remote Sensing*, vol. 12, no. 15, p. 2426, 2020.

Hindawi
Journal of Sensors
Volume 2021, Article ID 6684435, 13 pages
https://doi.org/10.1155/2021/6684435

Research Article

Ecological Security Assessment Based on Remote Sensing and Landscape Ecology Model

Pei Liu,[1,2,3] **Xiaoying Zhang**,[2] **Chao Ma**,[1,2] **Hebing Zhang**,[1,2] **Ruimei Han**,[1,2] **and Xiaofeng Lu**[1]

[1]*Key Laboratory of Spatio-temporal Information and Ecological Restoration of Mines (MNR), Henan Polytechnic University, Jiaozuo, Henan 454003, China*
[2]*School of Surveying and Mapping Land Information Engineering, Henan Polytechnic University, Jiaozuo, 454003 Henan, China*
[3]*Collaborative Innovation Center of Aerospace Remote Sensing Information Processing and Application of Hebei Province, China*

Correspondence should be addressed to Ruimei Han; hrm@hpu.edu.cn

Received 23 October 2020; Accepted 1 June 2021; Published 30 June 2021

Academic Editor: Zhenxing Zhang

The various ecological processes of human beings are not only restricted by the landscape pattern on the regional scale but also affect the local and regional landscape together with global climate change. To date, most of the research on ecological security is based on the pressure-state-response (PSR) model, while there were a few studies based on the landscape ecology model approach. In addition, there has been little literature focus on the dynamic change process of ecological security, especially the simulation and prediction of the future development trend of ecological security. The purpose of this research is to establish a landscape ecological security evaluation method based on grid division, be aimed at breaking the inherent drawbacks of the administrative region as a unit mode approach, anticipated to better reflect the landscape ecological security status of the study area. A complex framework was constructed by integrating random forest algorithm, Fishnet model, landscape ecology model, and CA-Markov model. Multitemporal remote sensing data were selected as a data source, and land use maps of the study area were obtained through the random forest machine learning algorithm firstly. And then, the study area is divided into 307 grids of 2 km × 2 km using the Fishnet model. Next, the landscape disturbance index, landscape vulnerability index, and landscape loss index are used on the grid scale to establish a landscape ecological security evaluation model. Finally, ecological security assessment of Zhengzhou city was carried out, and the distribution map of the landscape ecological status in 1986, 1996, 2006, 2016, and predicted for 2026 was obtained. The results of the study showed that, as time goes by, the areas with high ecological safety gradually decrease. It is predicted that by 2026, the ecological security level of Zhengzhou will be dominated by lower ecological security areas. The research results can provide basic information and decision support for government agencies and land use planners to ensure responsible and sustainable development of the urban environment and ecology.

1. Introduction

Landscape ecology evaluates the ecological security status of a certain area through the landscape index and landscape pattern, which can provide hierarchical and integrated information data for the multiscale study of ecosystem functions [1]. Landscape pattern is the key content of landscape ecology research [2]. Landscape pattern and its corresponding changes are a comprehensive reflection of the ecological environment in a certain area due to the interaction of various factors such as natural and human factors. At the meantime, landscape pattern affects the regional ecological process [3] as well for the type, shape, size, quantity, and spatial combination of landscape patches are the interaction of various disturbing factors. Methods of landscape pattern index, which can reflect the composition and characteristics of the landscape in the spatial structure, can be used to quantitatively describe the change of landscape pattern and spatial heterogeneity [4]. Particularly, changes in landscape pattern will affect the ecological environment to a certain extent,

thereby affecting ecological security. Researches on regional landscape pattern can effectively reveal ecological status and its corresponding spatial changes. Constructing an ecological security evaluation and analytics model by quantitative evaluation of regional landscape ecological index has certain advantages in the research of regional ecosystem security [5, 6].

In the past decades, more attentions have been given to ecological security assessment, and a variety of methods have been developed to evaluate ecological security, such as ecological footprint [7, 8], PSR models [9–11], and landscape ecology models [12]; for example, Sun et al. [13] used the PSR model combined methods of AHP and FCE to assess coastal wetland ecosystem health. Yang et al. [8] further improved the ecological footprint method to evaluate ecological security, and Peng et al. [14] took Liaoyuan City as a research case to discuss the possible ecological risks of landscapes at the county scale and the resulting ecological losses. Although different ecological safety assessment methods have different focuses, most of them are based on the PSR model. While the PSR model is applicable to regional ecological evaluations with small spatial scales with a few spatial variabilities and a few influencing factors, it is not applicable to natural disasters where human activities exceed the carrying capacity of the natural environment, and it is impossible to determine ecological security risks and uncertain threats. In addition, the logical connection between pressure and state is not inevitable; it is affected by a variety of complex factors. And the PSR evaluation system overemphasizes the impact of human activities on the ecological environment, and the evaluation results are somewhat one-sided [15]. Compared with the PSR model, the landscape ecology model starts from the ecosystem itself and is based on the structure, function, landscape patch dynamics and ecological succession of the landscape, the integrity and stability of the ecosystem, anti-interference ability, and resilience; the establishment of an evaluation index system can better reflect the temporal and spatial changes of landscape patterns. The landscape ecology model is not only suitable for larger spatial scale landscape design and land use planning but also suitable for smaller scale ecological evaluation [16].

In this research, we propose an improved landscape ecology ecological security evaluation model which can break through the long-term use of administrative regions as the research unit for data collection and analysis calculation [17, 18] and can better reflect the landscape ecological security status of the research area [19]. For this purpose, multitemporal remote sensing images are used as a major data source, and a random forest algorithm machine learning algorithm is used to interpret basic information of ecological security evaluation. Next, the landscape disturbance index, vulnerability index, and loss index are integrated to establish the landscape safety index. Then, multitemporal ecological security distribution maps are obtained. Finally, with the help of the CA-Markov model, ecological security trend in future is simulated and predicted. We test the method in Zhengzhou urban area, the core city of Chinese urban concentration. The innovation of this method is as follows: (1) all the indicators used in the research are readily calculated from remote sensing satellite images; (2) the research obtained spatial distribution status of ecological security as well as the dynamic changes of ecological security; (3) simulate and predict the future development trend of ecological security; (4) break the solid-state model of data collection, analysis calculation based on administrative regions as research units in previous research.

The results will be significant to guide regional ecological planning, protection, and development and will be helpful to optimize the allocation of resources, to control the further deterioration of the ecology, and to realize regional sustainable development services [20]. The rest part of the paper is organized as follows: a brief introduction about research area, preliminary work, and preprocessing of datasets is given in Section 2. The proposed research framework based on remote sensing (RS) is drawn and applied to the research area in Section 3. The results are shown in Section 4, and analysis and discussion are given in Section 5. Finally, the conclusions are drawn in Section 6.

2. Study Area and Datasets

2.1. The General Situation of the Study Area. The study site is located in Zhengzhou city (Figure 1), the capital of Henan Province in the central part of the P.R. China, with a total area of 7507 km^2 as well as a population of 9878000 inhabitants. Zhengzhou is one of the National Central Cities in China and serves as the political, economic, technological, and educational center of the province, as well as a major transportation hub in China. The annual average temperature of the city is 14.5°C, and the general terrain trend is tilt from southwest to northeast. The study area is undergoing the accelerating of Chinese agglomeration, economic development, and urban expansion.

Zhengzhou city core area is located in the southern part of the North China Plain, the lower reaches of the Yellow River, and the north of central Henan Province, between 112°42′-114°14′ east longitude and 34°16′-34°58′ north latitude. The city is 135-143 km long from east to west. The north-south width is 70-78 km, and the total area of the city is about 7446 km^2. It has jurisdiction over 6 districts and 5 cities, 2 national-level development zones, and one national-level export processing zone. Zhengzhou city belongs to the warm temperate continental monsoon climate with four distinct seasons: spring, dry and drought; summers are hot, concentrated rainfall; autumn is cool, time is short; long winter, dry and cold, rain and snow rarely. The annual average temperature is 15.6°C, July is the hottest, and the monthly average temperature is 27.3°C. January is the coldest month, with an average monthly temperature of -0.2°C, and most of the rainfall is concentrated in July, August, and September. This paper selects the urban area of Zhengzhou city, including Huiji District, Jinshui District, Zhongyuan District, Guancheng District, and Erqi District as the study area (Figure 1).

2.2. Data Sources and Preprocessing. The selected datasets include multitemporal Landsat remote sensing images of Zhengzhou city captured on April 23, 1986, April 20, 1996, April 30, 2006, and May 11, 2016, from USGS. Images on

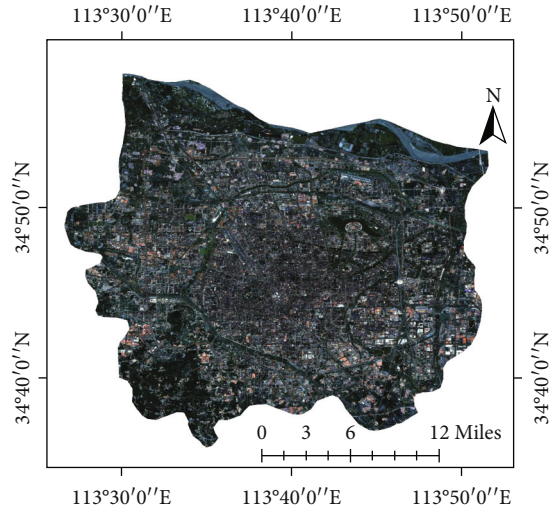

Figure 1: Location of Zhengzhou city, Henan Province, China.

April 23, 1986, April 20, 1996, and April 30, 2006, were obtained with Landsat5 TM sensor; while the image on May 11, 2016, was obtained with Landsat8 OLI sensor. The preprocessing of selected datasets includes radiation calibration, atmospheric correction, and geometric correction.

3. Methodology

3.1. Random Forest and Accuracy Assessment. Random forest (RF) is a state-of-art machine learning algorithm proposed by Leo Breiman and Adele Cutler in 2001 that combined bagging ensemble learning theory with a random subspace method [21–23]. The prediction result of the random forest algorithm is obtained by solving the mode of the decision results of multiple decision trees that make up the forest. Each time, about 2/3 of the samples from the original training dataset were extracted with bootstrap sampling technology for decision tree model training in the corresponding epoch. So some samples in the original training set may be used to perform the decision tree at the same time. The remaining about 1/3 of the samples are drawn for the out-of-bag error evaluation of the random forest model, and then, the prediction error rate of the model is calculated [24]. The basic idea of random forest classification [21, 25] can be described as three steps: (1) extracting k samples from the original training set using the bootstrap method, and ensuring the percentage of each class in subsets is the same as the original training set; (2) building k decision tree models for k sample subsets to obtain k classification results; (3) voting all classification results to obtain a final classified map. The two most important parameters in these procedures are number of trees used to construct RF and number of features selected for each individual tree. The second parameter is much more important than the first one by literature review [26–28]. In this research, the number of features is setting as $\log 2d$, where d is all features available in this research.

The evaluation of land use classification accuracy is a test of the classification results. There are two commonly used methods. One is to compare the classification results with the actual land use classification data; the other is to use high-resolution remote sensing images to select a certain proportion of training samples to test the accuracy of the classification data. At present, the most commonly used method of classification accuracy evaluation is the confusion matrix method, which is an error matrix, which is expressed by the number of correct classifications and the number of misclassifications in the experimental samples. In the confusion matrix, the overall classification accuracy (OA) and Kappa coefficient are mainly used to verify the classification results and evaluate the accuracy [23, 29].

The overall accuracy represents the probability of the number of samples that are correctly classified in the overall sample size and can reflect the overall accuracy of the classification results. As shown in

$$\mathrm{OA} = \frac{\sum_{i=1}^{q} n_{ii}}{n} \times 100\%, \tag{1}$$

where OA is the total classification accuracy, q is the number of classification categories, n is the total number of samples, and n_{ii} is the number of discriminative samples of the ith category.

The Kappa coefficient is the accuracy coefficient of the overall classification. It is a kind of ratio, which represents the ratio of error reduction between classification and completely random classification, as shown in

$$\mathrm{Kappa} = \frac{n\sum_{i=1}^{q} n_{ii} - \sum_{i=1}^{q}(n_{i+} \times n_{+i})}{n^2 - \sum_{i=1}^{q}(n_{i+} \times n_{+i})} \times 100\%, \tag{2}$$

where q is the number of classes, n represents the total number of considered pixel, n_{ii} is the diagonal element of the confusion matrix, n_{i+} represents the marginal sum of the rows in the confusion matrix, and n_{+i} represents the marginal sum of the columns in the confusion matrix.

3.2. Fishnet Model. The Fishnet model refers to the grid division of the research area based on GIS technology, where the grid scale is used as the evaluation unit to analyze the ecological security status of a selected area [30, 31]. With the continuous advancement of science and technology and the deepening of ecological safety research, the advantages of this method have become more and more obvious: it can solve the problems of data processing accuracy in space. As the smallest analysis unit is selected as a grid, the method facilitates the effective collection of relevant data and breaks the drawbacks of using only an administrative division unit as a research unit. In addition, grid division technology of the Fishnet model can treat each grid as an independent unit by establishing a grid and then calculate each grid through the establishment of an evaluation system.

In order to better reflect the landscape ecological security status of the study area, we used the grid tool in ArcGIS to divide the study area into 307 grids of 2 km × 2 km (shown in Figure 2) to break the previous inherent pattern. The division of the grid provides a more reasonable scale for the assessment of spatial change of landscape ecological security [31]. After the grid is identified, a grid layer is used to batch

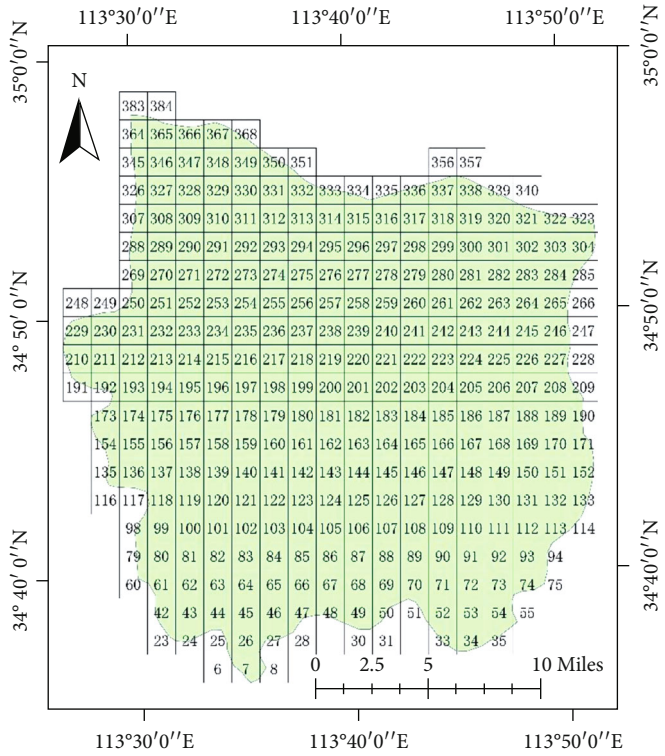

Figure 2: Fishnet grid division.

crop the land use classification data in each period to obtain corresponding grids. Land use and land cover maps of the small units are imported into the landscape pattern analysis software fragstats4.2 in batches mode for analysis. Then, landscape metrics of each grid in the study area can be obtained through calculation, and the calculated landscape metrics are used to construct the landscape ecological security index. Finally, the grid data is converted into a grid point file (located at the center of each grid), and the calculated landscape ecological safety index is assigned to the grid point file. During this process, spatial resolution is setting to 30 meters with the kriging interpolation method.

4. Landscape Ecological Model

4.1. Analysis of Landscape Pattern Changes. To analyze the changes of land use land cover landscape pattern, the ecological significance of various landscape pattern metrics in this study area was calculated [20]. By literature review [32, 33], landscape pattern can be divided into (1) patch level, which reflects the structural characteristics of a single patch in the landscape and is also the basis for calculating other landscape level indicators; (2) class level, which reflects the respective structural characteristics of different patch types in the landscape; (3) landscape level, which reflects the overall structural characteristics of the landscape. According to these landscape pattern metrics, the landscape of the study area was analyzed from a global perspective. In order to explore the structural characteristics and evolution rule of landscape pattern in various periods in Zhengzhou city, representative indicators (shown in Table 1) are selected at class level and landscape level with fully understanding the ecological significance of each landscape pattern index and the focus of the landscape structure reflected.

4.2. Analysis of Landscape Ecological Security

4.2.1. Landscape Disturbance Index. The landscape disturbance index describes the degree to which different landscape ecological environments are affected by natural and human activity factors. Its mathematical model can be described as

$$W_i = aC_i + bS_i + cD_i, \tag{3}$$

where W_i is the landscape disturbance index; a, b, and c are the landscape fragmentation index, landscape separation index, and landscape dominance index, respectively; a, b, and c represent the weight value of constructing fragmentation, separation, and dominance index, respectively. According to previous research results, and referring to the expert scoring method, the three weights are assigned as $a = 0.5$, $b = 0.3$, and $c = 0.2$.

Within this model, the mathematical expression of the landscape fragmentation index C_i is shown as

$$C_i = \frac{N_i}{A_i}, \tag{4}$$

where N_i is the number of landscape patches of type i and A_i is the total area of landscape patches of type i.

Table 1: Selected landscape metrics.

Landscape index	Meaning and value range
PLAND	The proportion of each patch area to the total area (0,100] [19, 34]
LPI	The largest patch area accounts for the proportion of the total area. The change of this value reflects the strength of human activities. It determines the abundance of dominant species in the landscape and helps determine dominant types (0,100] [35]
PAFRAC	Reflect the complexity of the shape of the landscape type on a specific scale [1,2] [36]
LSI	The degree of aggregation of patch shape features, indicating the shape of landscape [37]
CONTAG	The aggregation degree or spreading trend of different patch types in the landscape (0,100] [38]
IJI	Certain types of landscape adjacent to landscape types (0,100] [39]
SHDI	The degree of diversification of landscape types indicates the heterogeneity of the landscape and is more sensitive to the uneven distribution of various patch types, SHDI equal or greater than 0 [36, 40]
SHEI	There are no dominant types in the landscape, and the types are evenly distributed, indicating landscape diversity [0,1] [34]

The mathematical expression of the landscape separation index S_i is shown as

$$S_i = \frac{1}{2}\sqrt{\frac{C_i}{P_i}}, \quad P_i = \frac{A_i}{A}, \tag{5}$$

where P_i is the relative coverage of the i landscape and A is the total landscape area.

The mathematical expression of the landscape dominance index is shown as

$$D_i = dL_i + eP_i, \quad L_i = \frac{N_i}{N}, \tag{6}$$

where L_i is the relative density of the landscape. Related studies believe that the relative coverage has a greater contribution to the dominance of the landscape than the relative density, so the weights d and e are assigned values of 0.6 and 0.4.

4.2.2. Landscape Vulnerability Index. Different landscape plays different roles in the ecosystem and has different resistance to external pressure and sensitivity to external changes at the meantime. In research, this difference is usually associated with the vulnerability of the landscape, combined with previous research results [41]; on the basis of the actual situation of Zhengzhou city, values were assigned to corresponding land use types. For instance, unused land has the strongest vulnerability, and unused land is 5; the fragility of water is less than unused land, and water is set as 4; construction land is relatively stable which is set as -1; and the vulnerability index of cultivated land and vegetation are 3 and 2, respectively. Due to the different dimensions of each index, the normalization of the assignment of land use type is used as the vulnerability index of this type of landscape. The calculation method is shown as

$$V_i = \frac{L_i}{\sum_{i=1}^{5} L_i}, \tag{7}$$

where L_i represents the score assigned to the i type of land use and V_i represents the landscape vulnerability of the i type of land use.

4.2.3. Landscape Loss Index. The two variables of the landscape disturbance index and vulnerability index are superimposed and integrated to reflect the degree of loss of natural attributes of a certain landscape type after external disturbance. The calculation method is shown as

$$R_i = W_i \times V_i, \tag{8}$$

where the calculation method and meaning of W_i and V_i are landscape disturbance index and landscape vulnerability index, respectively.

4.2.4. Landscape Safety Index. The landscape safety index is expressed using two variables, the landscape loss index and the landscape area. The calculation method is shown in

$$\mathrm{LES}_e = \sum_{i=1}^{m} \frac{A_{ei}}{A_e}(1 - 10 \times R_i), \tag{9}$$

where LES_e represents the landscape ecological security value of the eth sampling area, e is the number of grids, A_e is the area of the eth grid, A_{ei} is the area of the ith landscape in the eth sampling area, and m is the number of land use types.

4.3. CA-Markov Model. The Markov model is a long-term prediction method based on situation and probability of a certain event at a certain moment, using the Markov chain, to predict its changes at various moments (or periods) in the future [42]. The CA model [43] has a capacity for spatial and temporal change simulation which can be defined in equation (10). The key factor of the Markov model is determining the transition probability of an event. The main components of the cellular automata model (CA) are units, states, rules, and neighborhoods. Each unit has one of a finite number of states [5, 42, 44]. The state of the unit at a certain moment depends on the current and previous moments. All unit states can be updated at the same time according to the transition rules. The principle is that the state of a cell at the next moment is a function of its neighborhood state

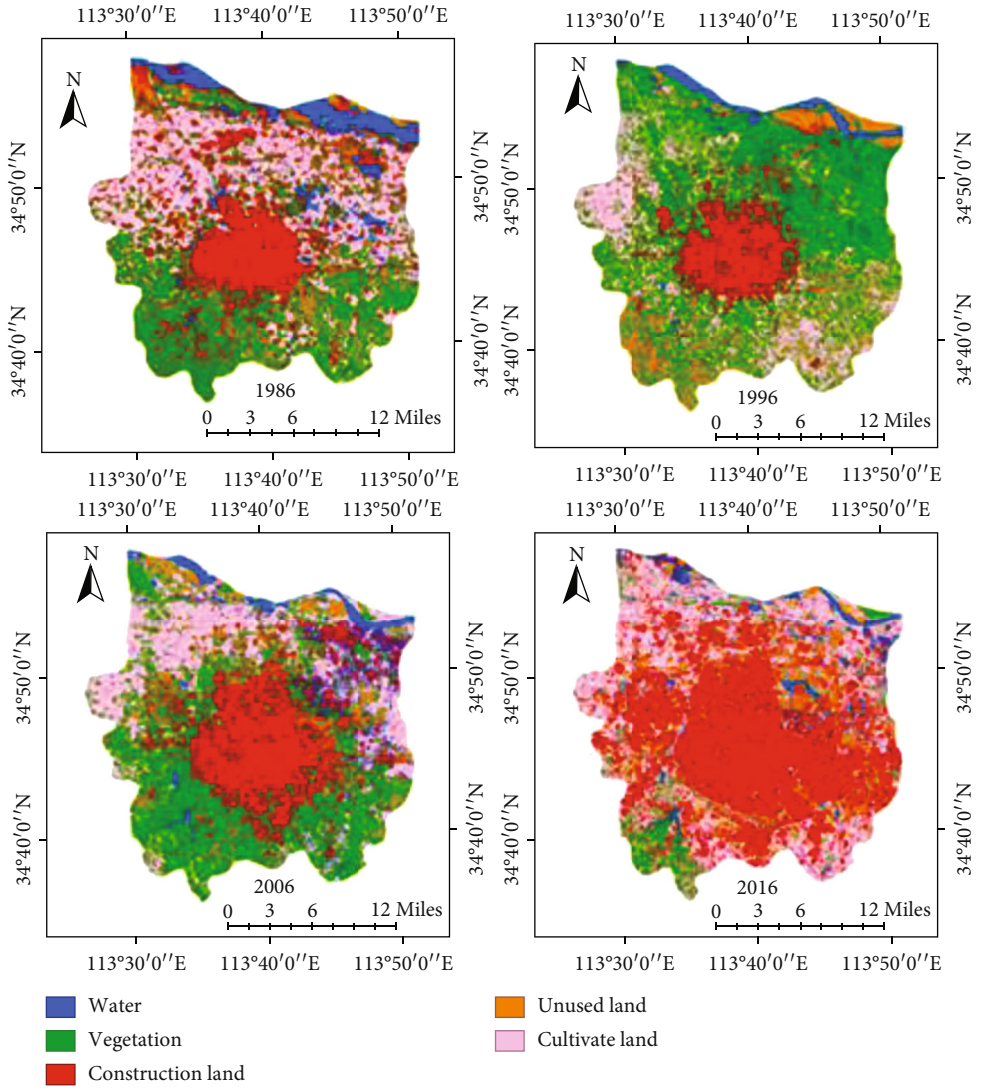

Figure 3: LULC classification results of Zhengzhou city from 1986 to 2016.

at the previous moment. The state variables are closely connected with the spatial position and have the concept of space and can be simulated. Complex changes in the spatial pattern.

$$S_{(t+1)} = f\left(S_{(t)}, N\right), \tag{10}$$

where $S_{(t+1)}$ and $S_{(t)}$ are the set of cell states at $t+1$ and t, respectively; f is the transition rule function of the state of the space cell; N is the cell field. t and $t+1$ represent start and end times. The Markov model [45] has been widely used for trend simulation at various scenarios and can be expressed as

$$S_{(t+1)} = P_{ij} \times S_{(t)}, \tag{11}$$

Table 2: LULC classification accuracy.

Parameter	1986 year	1996 year	2006 year	2016 year
OA	88.14%	81.16%	87.67%	88.79%
Kappa	0.85	0.75	0.84	0.86

where $S_{(t+1)}$ and $S_{(t)}$ are the status at time $t+1$ and t, respectively.

$$P_{ij} = \begin{pmatrix} P_{11} & \cdots & P_{1n} \\ \vdots & \ddots & \vdots \\ P_{n1} & \cdots & P_{nn} \end{pmatrix}, \left(0 \le P_{ij} < 1, \sum_{j=1}^{n} P_{ij} = 1 (i, j = 1, 2, \cdots, n)\right). \tag{12}$$

P_{ij} is the transition probability matrix in a state. The CA-Markov model is a combination of the CA model and the Markov model, both of which are dynamic models

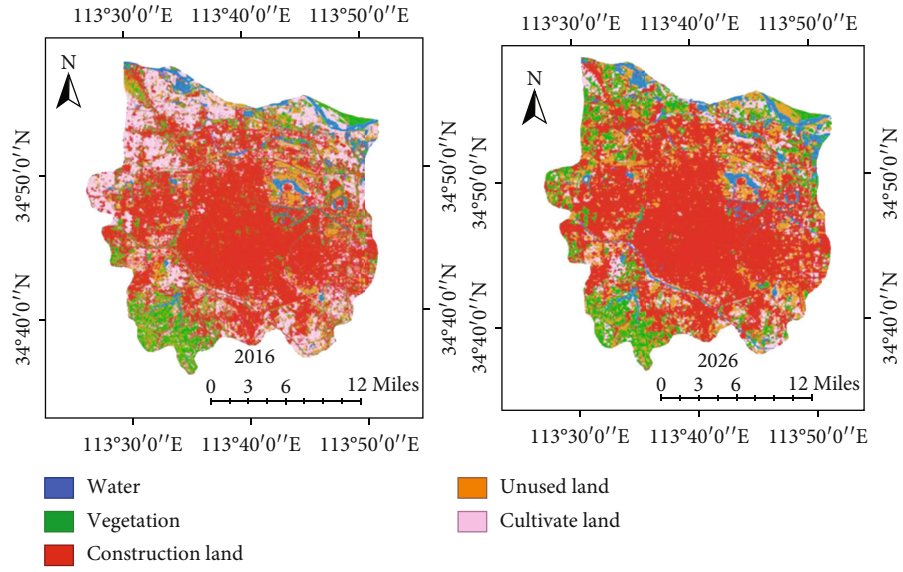

Figure 4: LULC predicted result in 2016 and 2026 with the CA-Markov model.

Table 3: Prediction accuracy of the CA-Markov model.

LULC types	2016 status/ha	2016 forecast/ha	Difference/ha	Relative error
Water	3993.39	4072.46	79.07	0.0198
Construction land	40932.9	40773.26	-159.64	-0.0039
Unused land	15114.69	16240.73	1126.04	0.0745
Cultivated land	36736.2	36115.36	-620.84	-0.0169
Vegetation	8268.03	8294.49	26.46	0.0032

with discrete states [46]. And when combined with the CA model, the CA-Markov model can overcome the limitation that the Markov model failed to catch the spatial distribution in the future and can be used to simulate spatiotemporal changes. In this research, LULC maps obtained with RF in 1986, 1996, 2006, and 2016 were selected as the study years to calculate the transition area matrix using the Markov model. And a standard 5 by 5 contiguity filter was selected for the CA model which means the condition of future pixel is not only decided by information from previous state but also considered by corresponding surrounding pixels.

5. Results and Discussion

5.1. LULC Classification Maps with Random Forest. In this research, training samples were selected by an expert. And the separability of samples was also checked to verify which is greater than 1.8 to meet the basic requirements for classification. The selected four RS images of Zhengzhou city were input to the RF classifier model to obtain classification maps of corresponding date over Zhengzhou city (Figure 3). Verification samples were selected from Google Earth to verify the accuracy of the classification results. And the total classification accuracy (OA) and Kappa coefficient were assessed with the help of selected ground truth. The total classification accuracy of the four images is greater than 80% (more details can be found in Table 2) which meet the demand of further process such as landscape pattern analysis.

5.2. Predicted Result with the CA-Markov Model. In this research, with the help of the IDRISI package, LULC results of 1996, 2006, and 2016 were selected to test and verify the prediction ability of the CA-Markov model. Firstly, the transition probability matrix and transition area matrix were calculated with images for adjacent years. And next, the transferred conditional probability image was established as the land use type transition suitability image. Then, CA filter and the number of cycles were determined. Since the image interval of each phase of this research is 10 years, the number of cycles is setting as 10, which means on the basis of LULC map of 2016 as initial to predict LULC status of 2026. Furthermore, in order to verify the reliability of the CA-Markov model, we simulated the LULC map of 2016 (shown in Figure 4) based on LULC maps of 1996 and 2006 and then calculated the accuracy of the prediction result using actually LULC maps of 2016 (Table 3). The results showed that the relative error between the predicted result and the classification result in 2016 meets the accuracy requirements. So it is scientific and reasonable to use the CA-Markov model to predict land cover in the future of the research area. So LULC map of 2026 (shown in Figure 4) was predicted with the help of the CA-Markov model and LULC results of 2006 and 2016.

Table 4: Class level landscape metrics.

Class	Year	PLAND	LPI	LSI	PAFRAC	IJI
Water	1986	7.629	2.7778	32.2845	1.3375	83.5295
	1996	5.8337	1.0263	63.1318	1.4078	67.0117
	2006	5.9512	1.2004	65.9779	1.4327	75.9909
	2016	4.6816	0.4844	55.5877	1.4377	78.8492
	2026	4.8616	0.6097	39.9916	1.3333	73.6292
Built-up	1986	20.35	9.34	122.2625	1.5138	53.8871
	1996	21.6713	8.4205	73.6836	1.4672	55.1109
	2006	22.8781	14.3014	98.2609	1.4715	80.964
	2016	38.96	30.4413	126.3306	1.4588	83.5898
	2026	55.0301	50.4739	131.2537	1.4851	91.8154
Unused	1986	9.6823	0.4096	91.3087	1.384	76.3188
	1996	9.023	1.0881	73.85	1.3822	43.5739
	2006	10.5624	0.3	86.8323	1.3848	69.1466
	2016	13.7287	0.9775	83.5122	1.4838	55.2866
	2026	14.0307	0.3944	75.2457	1.5261	53.4874
Farmland	1986	30.1118	13.0308	57.1028	1.3251	71.4841
	1996	19.9297	3.2892	121.4934	1.4745	76.2108
	2006	24.387	7.9274	99.8876	1.4846	83.589
	2016	34.7818	7.2556	122.6385	1.4875	86.2797
	2026	10.0261	6.819	113.981	1.5407	85.0774
Vegetation	1986	32.231	2.8358	167.5532	1.5353	83.4216
	1996	43.543	30.0522	166.4137	1.5291	88.8913
	2006	36.224	4.3383	147.6667	1.5098	86.2738
	2016	7.852	0.029	126.5385	1.5045	67.2062
	2026	16.0515	1.28	135.1132	1.3641	65.2682

5.3. Results of Landscape Pattern

5.3.1. Changes of Landscape Pattern in Class Level. Based on the obtained land cover classification results of each period, class level landscape pattern indexes were obtained with the help of fragstats4.2 (shown in Table 4). Results of the PLAND index showed that the dominated land cover types are farmland and built-up area in Zhengzhou city. In the period of 1986, the rank of PLAND in descending order is vegetation, farmland, built-up area, unused land, and water body. While in the period of 2016, the maximum PLAND index is built-up area and followed by farmland. The cause of these changes can be ascribed to two aspects. One is that, as the core area of national food production, governments of Henan province at all levels and the Department of Land and Resources have comprehensively strengthened the goal of arable land protection, which has further promoted the conservation and intensive use of land. The other one is that developing the economy, various provinces and cities in Henan have accelerated reclamation and at the same time high-standard farmland construction to ensure the amount of arable land; on the other hand, the rapid economic development in the urban area of Zhengzhou has resulted in continuous urban construction land expand. The PLAND index of vegetation has changed significantly, from 32.231 in 1986 to 7.852 in 2016, indicating that this type of land use type accounts for a large reduction in the overall landscape area.

Table 5: Landscape level metrics.

Year	CONTAG	IJI	SHDI	SHEI
1986	31.0152	81.8333	1.6863	0.9412
1996	33.2598	76.9566	1.5993	0.8926
2006	35.3083	74.9736	1.7025	0.9502
2016	38.2084	74.9651	1.3881	0.7747
2026	45.262	82.8463	1.4655	0.7925

Particularly, by prediction in 2026, there will be almost no changes in the area of water and unused land; the PLAND value of vegetation has increased, the area occupied by built-up area has further increased, and the PLAND index of farmland has decreased significantly. This result indicates regional urbanization and industrialization. During the process, the farmland was severely disturbed by human activities, and the farmland was squeezed by large-scale development activities by humans.

For the LPI index, the value of water has decreased greatly from 2.8 in 1986 to 0.48 in 2016, which indicated that the largest patch area of the water area has decreased,

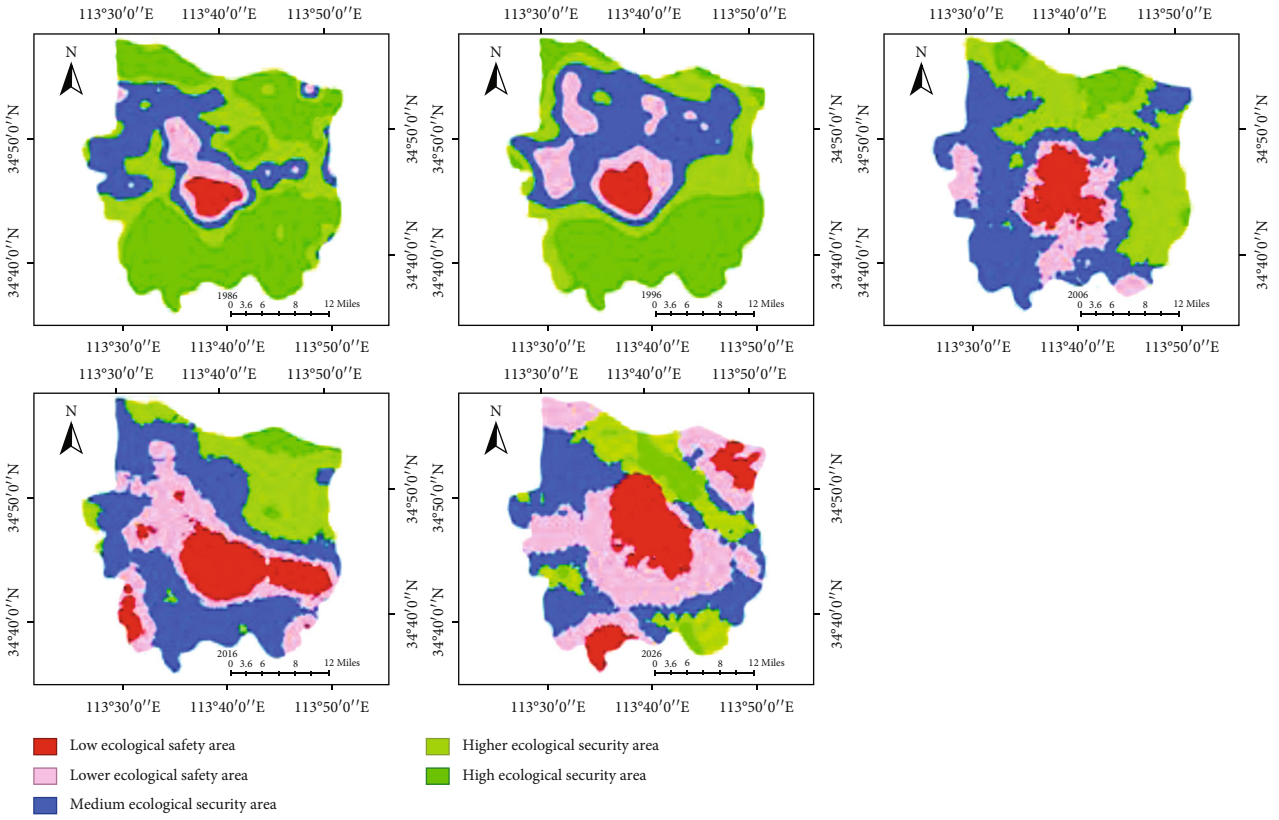

Figure 5: Ecological security distribution maps.

gradually shrinking, and the distribution is gradually fragmented; the LPI index of vegetation was 0.029 by 2016; this showed that the maximum patch area of vegetation first increases and then decreases, and its fragmentation degree first relaxes and then increases year by year. In addition, the LPI index value of built-up area increased greatly during the period from 1986 to 2016, which to a certain extent reflects that the urban construction of Zhengzhou city is more concentrated and the area of urban contiguous areas has increased significantly. The LPI index of farmland decreased from 13.03 in 1986 to 3.29 in 1996 and then increased to 7.26 in 2016, indicating that the largest patch area of farmland is fluctuating. According to the prediction results, the increase in the LPI value of water and vegetation indicates that the degree of fragmentation has decreased; the maximum patch index of unused land and farmland has decreased, and the distribution of farmland has become more concentrated.

From the perspective of the LSI index, the value of water is generally lower than that of other land types, mainly because its spatial distribution is relatively scattered, and the degree of aggregation is lower than that of other land types. During the study period, the PAFRAC index of various land use types in the urban area of Zhengzhou showed that vegetation was always the landscape with the largest PAFRAC index, indicating that the shape of vegetation in such patches was the most complicated. The PAFRAC index of built-up land has declined in fluctuations, indicating that the shape of this landscape type tends to be simple, and the

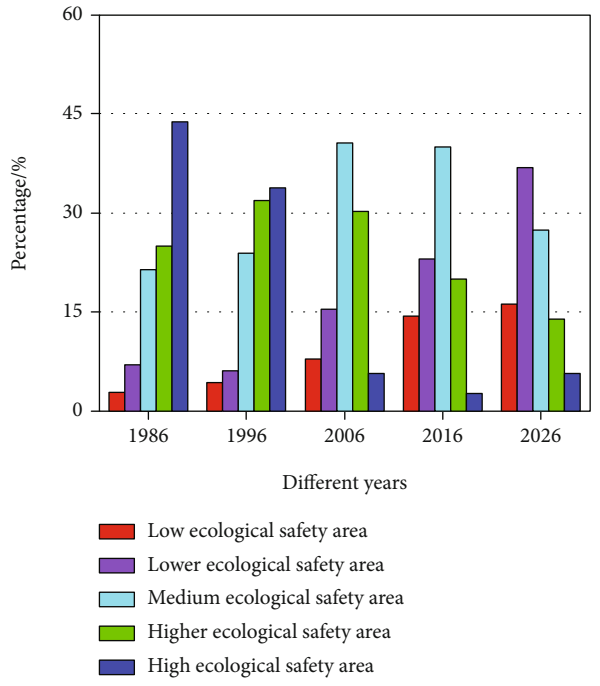

Figure 6: Percentage of ecological security levels in different years.

complexity is reduced. The PAFRAC of water, farmland, and unused land have changed, showing an increasing trend, indicating that the shapes of these three landscape types are

Table 6: Percentage of ecological security level.

Ecological security level	Percentage of each level (%)				
	1986	1996	2006	2016	2026
Low ecological security area	2.80	4.32	7.96	14.36	16.17
Lower ecological security area	6.98	6.08	15.48	22.98	36.88
Medium ecological security area	21.40	23.88	40.55	40.03	27.36
Higher ecological security area	24.97	31.96	30.26	19.95	13.90
High ecological security area	43.85	33.76	5.74	2.68	5.69

becoming more complicated. It is estimated by 2026, the LSI index of land use types other than built-up land and vegetation will decrease, indicating that the degree of aggregation is reduced; the PAFRAC of unused land and farmland has increased, indicating that the complexity of patch shape has increased, and its shape has become more and more irregular.

In terms of the IJI index, vegetation and unused land showed a downward trend, indicating that the adjacent landscape types of these two land types decreased year by year. The IJI index value of water decreased from 83.53 in 1986 to 67.01 in 1996 and increased to 78.85 in 2016 and then became relatively stable. By 2016, the IJI index of built-up land increased significantly compared to 1986, mainly due to the mutual transformation of land types around built-up land and the increase in the types of adjacent landscapes. It is estimated that by 2026, compared with 2016, the spread of land use types other than built-up land and the parallel index will change slightly, indicating that the adjacent patch types of land types other than built-up land have decreased.

5.3.2. Changes of Landscape Index Landscape Level. From the analysis of the landscape pattern in the landscape level, the calculation results of landscape metrics in different periods of Zhengzhou city are shown in Table 5.

The CONTAG index of Zhengzhou city increased from 31.02 in 1986 to 38.21 in 2016. It can be seen that the concentration of different landscape types in the study area has increased. During the study period, the IJI index of Zhengzhou city showed a decreasing trend, from 81.84 in 1986 to 74.97 in 2006, which indicated that the number of adjacent patches of a landscape type has decreased. However, the probability of all patch types adjacent to each other has stabilized after 2006. In terms of the Shannon diversity index (SHDI), whose value decreased in fluctuation, it indicated that the landscape types in the study area are gradually decreasing and the landscape diversity has decreased. In terms of the SHEI index, the uniformity of the distribution of various landscape types showed a decreasing-increasing-decreasing trend, which decreased from 0.94 in 1986 to 0.89 in 1996 and then increased to 0.95 in 2006. And SHEI increased to 0.7747 in 2016, which indicated that there were no particularly obvious advantages in the landscape in 1986, 1996, and 2006, while the advantages of landscape were obvious in 2016. According to the predicted results in 2026, SHDI and SHEI of the study area will be increased, which indicated that the intensity of human disturbance to the landscape has increased. And the predicted result also showed that the intensity of human disturbance to the landscape will increase, the diversity of the landscape will increase, and the control effect of the landscape dominance category on the overall landscape will be weakened, different land use types are more concentrated, and the types of adjacent features were increased.

5.4. Landscape Ecological Security Analysis. Due to the characteristics of spatial heterogeneity in ecological security assessment, in this study, the Fishnet tool was used to refine the units of the ecological security assessment. By calculating the corresponding landscape index in the constructed ecological security assessment model, the landscape ecological security index value of each grid is obtained, and this value is interpolated to the center of the grid using the kriging interpolation method to obtain the ecological security distribution maps.

Furthermore, according to the natural discontinuity classification method [47], the ecological security of the study area is divided into five levels: low ecological safety area, lower ecological safety area, medium ecological safety area, higher ecological safety area, and high ecological safety area (Figure 5).

From the characteristics of spatial distribution of LULC types, the high, higher, and medium security areas are mainly distributed in vegetation land cover area in the north and south, and the low and lower safety areas are distributed in the central built-up area and unused land areas.

By quantitative analysis (Figure 6 and Table 6), in 1986, the ecological security of Zhengzhou city was dominated by high-safety, higher-safety, and medium-safety areas, and the low-security zones were less distributed, indicating that the overall ecological security level of Zhengzhou city during that period was relatively high. Compared ecological security of 1996 with 1986, the medium and higher ecological security area status of ecological security in 1996 increased, while lower and low ecological security areas are almost stable. And the location of the low ecological safety zone has hardly changed when compared with 1986, and it is roughly in the center of Zhengzhou city. Compared with the ecological of 2006 to 1996, the lower and medium ecological safety zones increased significantly in 2006, and the medium ecological safety zones were widely distributed, and the high ecological safety zones decreased. This was mainly because with the rapid development of urbanization, the urban construction land expanded greatly; by 2016, the area of urban construction land will reach to 40%, frequent human activities have intensified the degree of land use, and ecological security is in a low state. Compared ecological security of 2016 with

2006, most areas are still in a state of low ecological security. The most obvious area is still located in the middle of Zhengzhou city, indicating that the urbanization of Zhengzhou city is developing rapidly, the population is growing rapidly, and human activities are frequent. Severe expansion has put a lot of pressure on the regional ecological environment, leading to a decrease in its ecological security. It is predicted that by 2026, the proportion of lower ecological safety areas will be the largest. Compared with 2016, the area of low ecological safety areas in this region has not increased much, the medium ecological safety areas have dropped by about 10%, and the percentage of higher ecological safety areas has declined, but the proportion of high ecological safety areas has increased slightly.

6. Conclusion

In this research, we have proposed an ecological security assessment framework based on random forest algorithm, Fishnet model, landscape ecology model, and CA-Markov model. With the support of multitemporal remote sensing and GIS technology, ecological security of research area in 1986, 1996, 2006, 2016, and for predicted 2026 were calculated and simulated. The research results showed that due to the significant urbanization process and certain problems in the economic development model, the largest patch area of the water has been significantly reduced, from 2.78 to 0.48. The fragmentation of water is increasing year by year. However, the construction land is more concentrated, the area of urban contiguous areas has increased significantly, and the spread and juxtaposition index value of construction land has increased from 53.8871 to 83.5898. It is predicted that by 2026, the shape of unused land and farmland will become more irregular, and the area of construction land will further increase and the distribution will be more concentrated. The results of landscape ecological security evaluation showed that between 1986 and 1996, the dominated security level is high grade, while between 2006 and 2016, the area of medium ecological security zone was in major. It is predicted that the landscape ecological security situation of Zhengzhou city will continue to decline in 2026, but the percentage of high ecological security areas will increase slightly.

The research results can provide basic information and decision support for government agencies and land use planners to ensure responsible and sustainable development of the urban environment and ecology. And the novelty of this paper is in the direction of successfully implementing the landscape ecology model for urban security assessment.

Data Availability

Researchers who are interested in this code can download it from hyperlink https://pan.baidu.com/s/1YeGDwd4DoOEkZpOh4vswKg, using password xdrg, using password i98q, or contact the corresponding author to obtain source data to conduct secondary analysis.

Disclosure

Pei Liu's current address is No. 2001 Shiji Road, Jiaozuo, Henan, China.

Conflicts of Interest

The authors declare that they have no conflicts of interest.

Authors' Contributions

P.L. contributed to the conceptualization, methodology, formal analysis, writing and preparing the original draft, and project administration; P.L., C.M., and HB. Z. wrote, reviewed, and edited the manuscript; XY. Z. and XF. L. performed the experiment. All authors contributed equally to this work.

Acknowledgments

This research was funded by the National Natural Science Foundation of China Grant number 41601450, the Outstanding Youth fund of Henan Polytechnic University Grant number J2021-3, the Key Technology R and D Program of Henan Province (No. 182102310860), and the China Scholarship Council Grant number 201808410212.

References

[1] D. Liu and Q. Chang, "Ecological security research progress in China," *Acta Ecologica Sinica*, vol. 35, no. 5, pp. 111–121, 2015.

[2] J. Wu, "Key concepts and research topics in landscape ecology revisited: 30 years after the Allerton Park workshop," *Landscape Ecology*, vol. 28, no. 1, pp. 1–11, 2013.

[3] X. Liang, X. Jin, J. Ren, Z. Gu, and Y. Zhou, "A research framework of land use transition in Suzhou city coupled with land use structure and landscape multifunctionality," *Science of the Total Environment*, vol. 737, article 139932, 2020.

[4] X. Yuantao, M. Qingwen, Y. Zheng et al., "Identifying landscape pattern metrics for the Hani terrace in Yunnan, China," *Journal of Resources and Ecology*, vol. 4, no. 3, pp. 212–219, 2013.

[5] Z. K. Motlagh, A. Lotfi, S. Pourmanafi, S. Ahmadizadeh, and A. Soffianian, "Spatial modeling of land-use change in a rapidly urbanizing landscape in Central Iran: integration of remote sensing, CA-Markov, and landscape metrics," *Environmental Monitoring and Assessment*, vol. 192, no. 11, p. 695, 2020.

[6] C. Zhu, X. Zhang, M. Zhou et al., "Impacts of urbanization and landscape pattern on habitat quality using OLS and GWR models in Hangzhou, China," *Ecological Indicators*, vol. 117, article 106654, 2020.

[7] W. Gao, G. Cheng, and C. Liu, "Incorporating carbon sink of harvested wood products into ecological footprint accounting: model and case study," *Ecosystem Health and Sustainability*, vol. 6, no. 1, article 1770629, 2020.

[8] Q. Yang, G. Liu, Y. Hao et al., "Quantitative analysis of the dynamic changes of ecological security in the provinces of China through emergy-ecological footprint hybrid indicators," *Journal of Cleaner Production*, vol. 184, pp. 678–695, 2018.

[9] Z. T. Li, M. Li, and B. C. Xia, "Spatio-temporal dynamics of ecological security pattern of the Pearl River Delta urban agglomeration based on LUCC simulation," *Ecological Indicators*, vol. 114, article 106319, 2020.

[10] J. Wu, X. Wang, B. Zhong et al., "Ecological environment assessment for Greater Mekong Subregion based on pressure-state-response framework by remote sensing," *Ecological Indicators*, vol. 117, article 106521, 2020.

[11] Y. Fan and C. Fang, "Evolution process and obstacle factors of ecological security in western China, a case study of Qinghai province," *Ecological Indicators*, vol. 117, article 106659, 2020.

[12] S. Wei, J. Pan, and X. Liu, "Landscape ecological safety assessment and landscape pattern optimization in arid inland river basin: take Ganzhou District as an example," *Human and Ecological Risk Assessment*, vol. 26, no. 3, pp. 782–806, 2020.

[13] B. Sun, J. Tang, D. Yu, Z. Song, and P. Wang, "Ecosystem health assessment: a PSR analysis combining AHP and FCE methods for Jiaozhou Bay, China," *Ocean & Coastal Management*, vol. 168, pp. 41–50, 2019.

[14] J. Peng, M. Zong, Y. Hu, Y. Liu, and J. Wu, "Assessing landscape ecological risk in a mining city: a case study in Liaoyuan City, China," *Sustainability*, vol. 7, no. 7, pp. 8312–8334, 2015.

[15] P. Liang, D. Liming, and Y. Guijie, "Ecological security assessment of Beijing based on PSR model," *Procedia Environmental Sciences*, vol. 2, pp. 832–841, 2010.

[16] T. Weber, "Landscape ecological assessment of the Chesapeake Bay watershed," *Environmental Monitoring and Assessment*, vol. 94, no. 1-3, pp. 39–53, 2004.

[17] G. Wang and W. Wu, "Assessment on ecological security spatial differences of west areas of Liaohe River based on GIS," *Huan jing ke xue= Huanjing kexue*, vol. 26, no. 5, pp. 28–33, 2005.

[18] D. Pan, H. Jia, and Y. Yuan, "A GIS-based ecological safety assessment of Wushen Banner, China," *Human and Ecological Risk Assessment*, vol. 21, no. 2, pp. 297–306, 2015.

[19] P. Parivar, D. Quanrud, A. Sotoudeh, and M. Abolhasani, "Evaluation of urban ecological sustainability in arid lands (case study: Yazd-Iran)," *Environment, Development and Sustainability*, vol. 23, no. 2, pp. 2797–2826, 2021.

[20] J. Zhang, M. Qu, C. Wang, J. Zhao, and Y. Cao, "Quantifying landscape pattern and ecosystem service value changes: a case study at the county level in the Chinese loess plateau," *Global Ecology and Conservation*, vol. 23, article e01110, 2020.

[21] B. Rasti and P. Ghamisi, "Remote sensing image classification using subspace sensor fusion," *Information Fusion*, vol. 64, pp. 121–130, 2020.

[22] S. Amini, S. Homayouni, A. Safari, and A. A. Darvishsefat, "Object-based classification of hyperspectral data using random forest algorithm," *Geo-Spatial Information Science*, vol. 21, no. 2, pp. 127–138, 2018.

[23] T. D. Acharya, A. Subedi, and D. H. Lee, "Evaluation of machine learning algorithms for surface water extraction in a Landsat 8 scene of Nepal," *Sensors*, vol. 19, no. 12, article 2769, 2019.

[24] P. Probst and A. L. Boulesteix, "To tune or not to tune the number of trees in random forest," *The Journal of Machine Learning Research*, vol. 18, pp. 6673–6690, 2017.

[25] H. Seo, M. Badiei Khuzani, V. Vasudevan et al., "Machine learning techniques for biomedical image segmentation: an overview of technical aspects and introduction to state-of-art applications," *Medical Physics*, vol. 47, no. 5, pp. E148–E167, 2020.

[26] H. Deng and G. Runger, "Gene selection with guided regularized random forest," *Pattern Recognition*, vol. 46, pp. 3483–3489, 2013.

[27] J. L. Speiser, M. E. Miller, J. Tooze, and E. Ip, "A comparison of random forest variable selection methods for classification prediction modeling," *Expert Systems with Applications*, vol. 134, pp. 93–101, 2019.

[28] P. Lou, B. Fu, H. He et al., "An optimized object-based random forest algorithm for marsh vegetation mapping using high-spatial-resolution GF-1 and ZY-3 data," *Remote Sensing*, vol. 12, no. 8, article 1270, 2020.

[29] Y. M. Asare, E. K. Forkuo, G. Forkuor, and M. Thiel, "Evaluation of gap-filling methods for Landsat 7 ETM+ SLC-off image for LULC classification in a heterogeneous landscape of West Africa," *International Journal of Remote Sensing*, vol. 41, no. 7, pp. 2544–2564, 2020.

[30] P. Šímová and K. Gdulová, "Landscape indices behavior: a review of scale effects," *Applied Geography*, vol. 34, pp. 385–394, 2012.

[31] Y. Shao, Y. Wang, and Y. Li, "Spatial-temporal response and comprehensive evaluation of ecological environment of prairie coal-electricity base development," *Journal of China Coal Society*, vol. 44, pp. 3874–3886, 2019.

[32] J. Kupfer, "Landscape ecology and biogeography: rethinking landscape metrics in a post-FRAGSTATS landscape," *Progress in Physical Geography: Earth and Environment*, vol. 36, no. 3, pp. 400–420, 2012.

[33] J. N. Inkoom, S. Frank, K. Greve, U. Walz, and C. Fürst, "Suitability of different landscape metrics for the assessments of patchy landscapes in West Africa," *Ecological Indicators*, vol. 85, pp. 117–127, 2018.

[34] Y. C. Weng, "Spatiotemporal changes of landscape pattern in response to urbanization," *Landscape and Urban Planning*, vol. 81, no. 4, pp. 341–353, 2007.

[35] Y. Song, X. Song, and G. Shao, "Effects of green space patterns on urban thermal environment at multiple spatial-temporal scales," *Sustainability*, vol. 12, no. 17, article 6850, 2020.

[36] H. Zhao, Z. Ren, and J. Tan, "The spatial patterns of land surface temperature and its impact factors: spatial non-stationarity and scale effects based on a geographically-weighted regression model," *Sustainability*, vol. 10, no. 7, article 2242, 2018.

[37] Q. Zhang, C. Chen, J. Wang et al., "The spatial granularity effect, changing landscape patterns, and suitable landscape metrics in the Three Gorges Reservoir Area, 1995-2015," *Ecological Indicators*, vol. 114, article 106259, 2020.

[38] D. Simsek and E. Sertel, "Spatial analysis of two different urban landscapes using satellite images and landscape metrics," *Photogrammetric Engineering and Remote Sensing*, vol. 84, no. 11, pp. 711–721, 2018.

[39] R. D. Bidgoli, H. Koohbanani, and M. Yazdani, "Investigation on ecosystem degradation induced by LU/LC changes using landscape pattern indices analysis," *Arabian Journal of Geosciences*, vol. 11, no. 16, 2018.

[40] L. Hou, F. Wu, and X. Xie, "The spatial characteristics and relationships between landscape pattern and ecosystem service value along an urban-rural gradient in Xi'an city, China," *Ecological Indicators*, vol. 108, article 105720, 2020.

[41] H. Xie, "Spatial characteristic analysis of land use eco-risk based on landscape structure: a case study in the Xingguo County, Jiangxi Province," *China Environmental Science*, vol. 31, pp. 688–695, 2011.

[42] A. Mohamed and H. Worku, "Simulating urban land use and cover dynamics using cellular automata and Markov chain approach in Addis Ababa and the surrounding," *Urban Climate*, vol. 31, article 100545, 2020.

[43] S. Yan, Q. Zhixin, L. Xiaoping, N. Ning, and Z. Hui, "Urban land use and land cover classification using multisource remote sensing images and social media data," *Remote Sensing*, vol. 11, no. 22, article 2719, 2019.

[44] R. Qiu, W. Xu, J. Zhang, and K. Staenz, "Modeling and simulating industrial land-use evolution in Shanghai, China," *Journal of Geographical Systems*, vol. 20, no. 1, pp. 57–83, 2018.

[45] L. Chu, T. Sun, T. Wang, Z. Li, and C. Cai, "Evolution and prediction of landscape pattern and habitat quality based on CA-Markov and InVEST model in Hubei section of three gorges reservoir area (TGRA)," *Sustainability*, vol. 10, no. 11, article 3854, 2018.

[46] Y. Yu, M. Yu, L. Lin et al., "National green GDP assessment and prediction for China based on a CA-Markov land use simulation model," *Sustainability*, vol. 11, no. 3, p. 576, 2019.

[47] X. Xu, H. Lin, and Z. Fu, "Regional ecological risk assessment of wetland in the Huanghe River Delta," *Acta Scientiarum Naturalium-Universitatis Pekinensis*, vol. 37, pp. 111–120, 2001.

Hindawi
Journal of Sensors
Volume 2021, Article ID 6659831, 14 pages
https://doi.org/10.1155/2021/6659831

Research Article

Remote Sensing Image Scene Classification Based on Fusion Method

Liancheng Yin,[1] Peiyi Yang,[2] Keming Mao,[1] and Qian Liu[1]

[1]*College of Software, Northeastern University, Shenyang, Liaoning Province 110004, China*
[2]*College of Computer Science, University of Virginia, Charlottesville, Virginia 22904, USA*

Correspondence should be addressed to Keming Mao; maokm@swc.neu.edu.cn

Received 20 October 2020; Revised 12 January 2021; Accepted 15 January 2021; Published 9 June 2021

Academic Editor: Zhenxing Zhang

Remote sensing image scene classification is a hot research area for its wide applications. More recently, fusion-based methods attract much attention since they are considered to be an useful way for scene feature representation. This paper explores the fusion-based method for remote sensing image scene classification from another viewpoint. First, it is categorized as front side fusion mode, middle side fusion mode, and back side fusion mode. For each fusion mode, the related methods are introduced and described. Then, classification performances of the single side fusion mode and hybrid side fusion mode (combinations of single side fusion) are evaluated. Comprehensive experiments on UC Merced, WHU-RS19, and NWPU-RESISC45 datasets give the comparison result among various fusion methods. The performance comparisons of various modes, and interactions among different fusion modes are also discussed. It is concluded that (1) fusion is an effective way to improve model performance, (2) back side fusion is the most powerful fusion mode, and (3) method with random crop+multiple backbone+average achieves the best performance.

1. Introduction

With explosive increasing of remote sensing data, analysis and processing remote sensing image effectively and efficiently becomes of great importance. Remote sensing image scene classification, which aims to classify remote sensing image into different types based on image content, has been attracted more and more attentions for its comprehensive application in fields of geography, ecology, city plan, forest monitor, military, etc [1].

Remote sensing image scene classification essentially belongs to domains of machine learning and computer vision. With well-organized training dataset, models can be learned through minimizing loss functions between model output and ground-truth label. According to feature extraction and representation techniques, existing methods can be categorized into three types: method based on low-level feature, method based on mid-level feature, and method based on deep feature.

Methods based on low-level feature focus on image color, texture, shape, intensity, or their combinations, which are intuitive representations of scene image. Color histogram was used to extract global feature in [2, 3]. In [4], Gabor filters with various scales and orientations were used to represent image texture. In [5], global morphological texture features were extracted with circular covariance histogram, rotation-invariant point triplets, and their extensions with Fourier power spectrum. The superpixel-based Extended Random Walker spectral–spatial classification method was proposed in [6]. It did not only incorporate superpixel to cluster local similar pixels but also build up relationship between superpixels.

Mid-level feature, such as local binary pattern (LBP), scale-invariant feature transform (SIFT), histogram of oriented gradients (HOG), and spatial envelop (Gist), was well engineered by experienced experts [7–13]. In [7], multiscale LBP features were extracted from dense patches. Fisher vector encoding and extreme learning machine were then used for the training classification model. A multineighborhood LBP method was proposed for feature extraction in small image patches [8]. Bag of visual words (BoVW) and support vector machine (SVM) were used as feature representation

and classifier. SIFT was adopted in [9] for classification of remote sensing imagery, and it showed good performance. In [10], a generalized principal component analysis (PCA) was used to reduce dimension of SIFT, and more spatial locality information can be preserved. Ship-HOG was proposed to describe target in scene image by aligning the axis to the vertical direction [11]. In [12], the rotation invariant HOG-based method was proposed by constraining the similarity between training samples with various rotations. In [13], candidate regions were obtained with segmentation. Then, gist features were extracted, and random forest classifier was trained.

Low-level feature and mid-level feature are known as traditional methods. They extract and represent features of remote sensing image in the shallow layer, and the complex structure cannot be captured. On the other hand, they treat feature extraction and classifier construction as two separate stages, which make the model suboptimal. With the breakthrough of machine learning technology [14] and massive training data (ImageNet, COCO dataset [15, 16]), deep learning models achieve great success in computer vision, including AlexNet [17], ZFNet [18], VGGNet [19], InceptionNet [20], and ResNet [21]. Deep neural network model-based methods become prevalent in field of remote sensing image scene classification. Sparse autoendocer models combined with convolutional features were proposed in [22, 23]. In [24], pairwise constraints were integrated into a stacked autoencoder, and more informative features can be extracted. The traditional BoVW method was improved in [25]. User-defined features were replaced with deep features which were extracted with an off-the-shelf CNN model. In [26], a CNN model was trained by minimizing entropy loss along with a metric learning regularization, which enforced the model more discriminative. Salient regions were extracted with visual attention, and these regions were used to learn initial parameters of the CNN model [27] which was subsequently fine tuned. Attention mechanism was also introduced in [28], which can discard unimportant information. The frequency domain was incorporated in [29], and representations of space and frequency were combined for scene classification. A knowledge distillation-based method was proposed to train a powerful light CNN model for scene classification [30]. Siamese-GAN was proposed for aerial vehicle image classification with crossdomain conditions [31]. GAN methods were also adopted in [32, 33]. Large scale of synthetic remote sensing image samples was generated, and dataset can be expanded with GAN. Comparing with traditional machine learning methods, the advantage of deep learning-based scene image classification is mainly owing to the fact that it can extract more complex and appropriate feature combination structures. Then, important and discriminate feature representation can be obtained with deep layers. and the irrelevant variants are ignored. More works about remote sensing image scene classification with deep learning can be referred to [34, 35].

Among these deep learning models, fusion-based methods are widely used and are gaining more popularity. A multiscale deep feature method was proposed in [36]. First, input satellite images were wrapped into multiple scales, and each one was represented with a deep feature through pretrained model. Then, SVM classifier was trained with using multikernel learning. Two separate nets were trained with labeled images and their rescaled samples [37]. These two models shared the same backbone network, and the similarity between them was added to loss function as a regularization term. A two-stage deep feature fusion method was proposed in [38], which focused on feature combination from various layers of deep networks. In [39], three CNN models were trained with different receptive fields. The final classification result was determined with maximum posterior probability of the outputs of three independent models. The DropBand technique was proposed in [40]. Training images were generated by dropping certain spectral bands. Images with the same spectral band set were used to train a separate CNN model. The final classification result was obtained by averaging all model outputs. A four-layer feature representation was constructed with two convolutional layers and two full connected layers of a VGGNet model [41]. Then, canonical correlation analysis (CCA) was used for feature fusion. In [42], encoded mixed-resolution representation was proposed by concatenation of low-level, mid-level, and fully connected feature. They were further encoded by locally aggregated descriptors and average pooling. In [43], each layer of the VGGNet model was extracted as separated feature descriptors. Then, they were combined to construct the final representation with CCA fusion. In [44], a feature encoding module was designed to aggregate the intermediate convolutional features into the final representation. In [45], deconvolution module was adopted to learn parameter weight in an unsupervised way, and the spatial pyramid model was used for feature aggregation. A bidirectional adaptive feature fusion strategy was investigated in [46]. Embedded deep feature and SIFT feature were fused with a recurrent neural network structure. A gradient boosting random CNN framework was adopted for efficient training multiple deep models [47]. The hydra model was proposed in [48]. Hydra's body was first designed to providing a good starting point for optimization, and then hydra's heads were trained to from the ensemble of CNNs.

Although the concept "fusion" is covered in all these works, different ways of expressions are given, i.e., "multilayer features," "feature fusion," "multi-scale deep feature," "multilevel fusion," "multi-stage feature fusion," "feature combination," "ensemble of model," and "feature aggregation." As far as we know, there is no unified and standard description, and this imprecise expression is inconvenient for further research. To address this problem, this paper makes a study on fusion-based remote sensing image scene classification in another view. According to the source of fusion (input data, feature map or vector, model output, etc.), three types of fusion modes, front side fusion mode, middle side fusion mode, and back side fusion mode, are given. In addition, typical fusion methods of three fusion modes are described. Experimental evaluations are conducted based on three widely used datasets. Comprehensive comparisons of model accuracy and efficiency are given among different fusion methods. Relationship and influence among different fusion mode are further analyzed. The main contributions of this research are twofold:

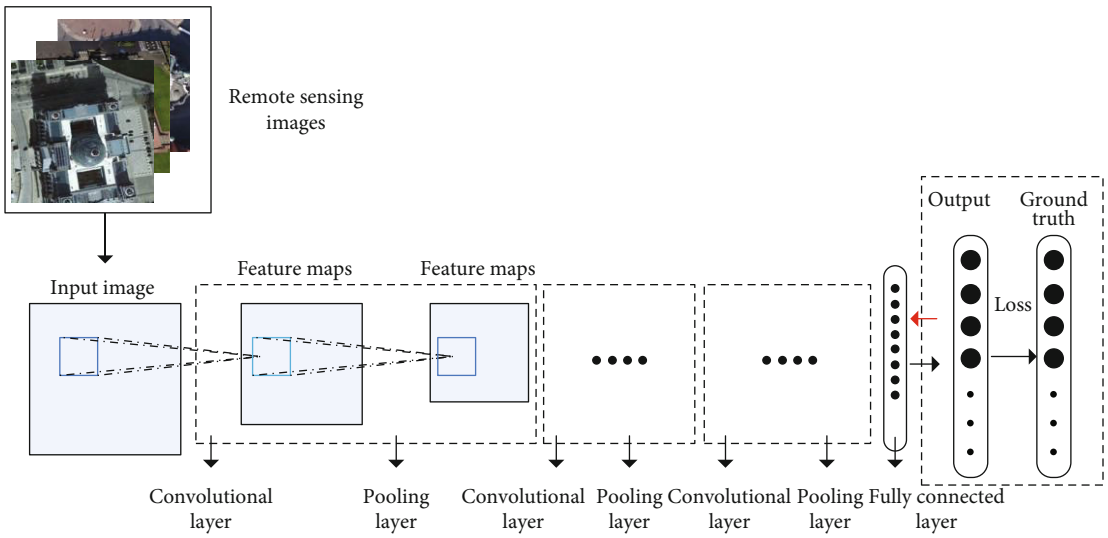

Figure 1: Typical structure of remote sensing image scene classification based on the CNN model. Blank boxes represent similar operations in CNNs.

(i) This work makes study on remote sensing image sense classification based on the origin of fusion operation. Representative works are summarized, and three types of fusion mode are defined

(ii) Extensive experimental evaluation and analysis are carried out. Importance of various fusion mode is shown quantitatively

The rest of this paper is organized as follows. Section 2 describes the workflow of remote sensing image scene classification based on the CNN model. Three types of fusion mode and their typical methods are given in Section 3. Section 4 demonstrates experimental evaluation and analysis. Section 5 concludes this paper.

2. Workflow of Remote Sensing Image Scene Classification Based on CNNs

This paper makes study on remote sensing image scene classification based on fusion methods. We first give the basic workflow based on the CNN model in this section.

Figure 1 demonstrates a typical workflow of remote sensing image scene classification based on the CNN model. The basic component of the CNN model includes convolutional layer, pooling layer, and fully connected layer. The input training image samples are fed into the CNN model, then after a series of convolutional and pooling operations, the final output is obtained with a fully connected layer using the softmax function. The loss function between model output and ground truth label is used for tuning the weight of the model parameter. The training process will be stopped when the loss value is less than a prespecified threshold. This structure can also be seen as a fundamental workflow of feature extraction and representation using the CNN model on general image classification problem. For its excellent performance, the CNN based model has become a dominant method. In this study, we only consider fusion methods that based on CNN models.

3. Fusion-Based Remote Sensing Image Scene Classification

Fusion usually incorporates information from different modalities, and they are combined for further processing. In our study, CNN models incorporated with various fusion methods are treated as a multistage procedure. These fusion methods are further divided into three types according to the stage where fusion operation works.

3.1. Remote Sensing Image Scene Classification Based on the Front Side Fusion Mode. For remote sensing image scene classification, the scale, position, and contextual information of specific object change greatly between image samples. To handle this problem, some methods focus on the input image data. It is also called multiscale, multilevel, image fusion, data fusion, etc. It is essentially a process of integrating multiple image sources to produce more consistent, accurate, and useful information than that provided by individual one. It is expected that the fused data is more informative and synthetic. In this paper, front side fusion mode is used to describe this type of fusion for the training image samples that are processed before they are fed into CNN models.

Figure 2 demonstrates remote sensing image scene classification methods based on the front side fusion mode. As is shown in Figure 2(a), original images are randomly cropped, and the patches are used as training data. This method was adopted in [37, 40]. Original images are cropped with multiple scales, and then they are resized with the same dimensions. This is shown in Figure 2(b), and it was used in [36, 39]. Figure 2(c) gives another example [40]. Original images are decomposed into many channels, such as RGB channel, HSV channel, and YCbCr channel, as well as gray and binary

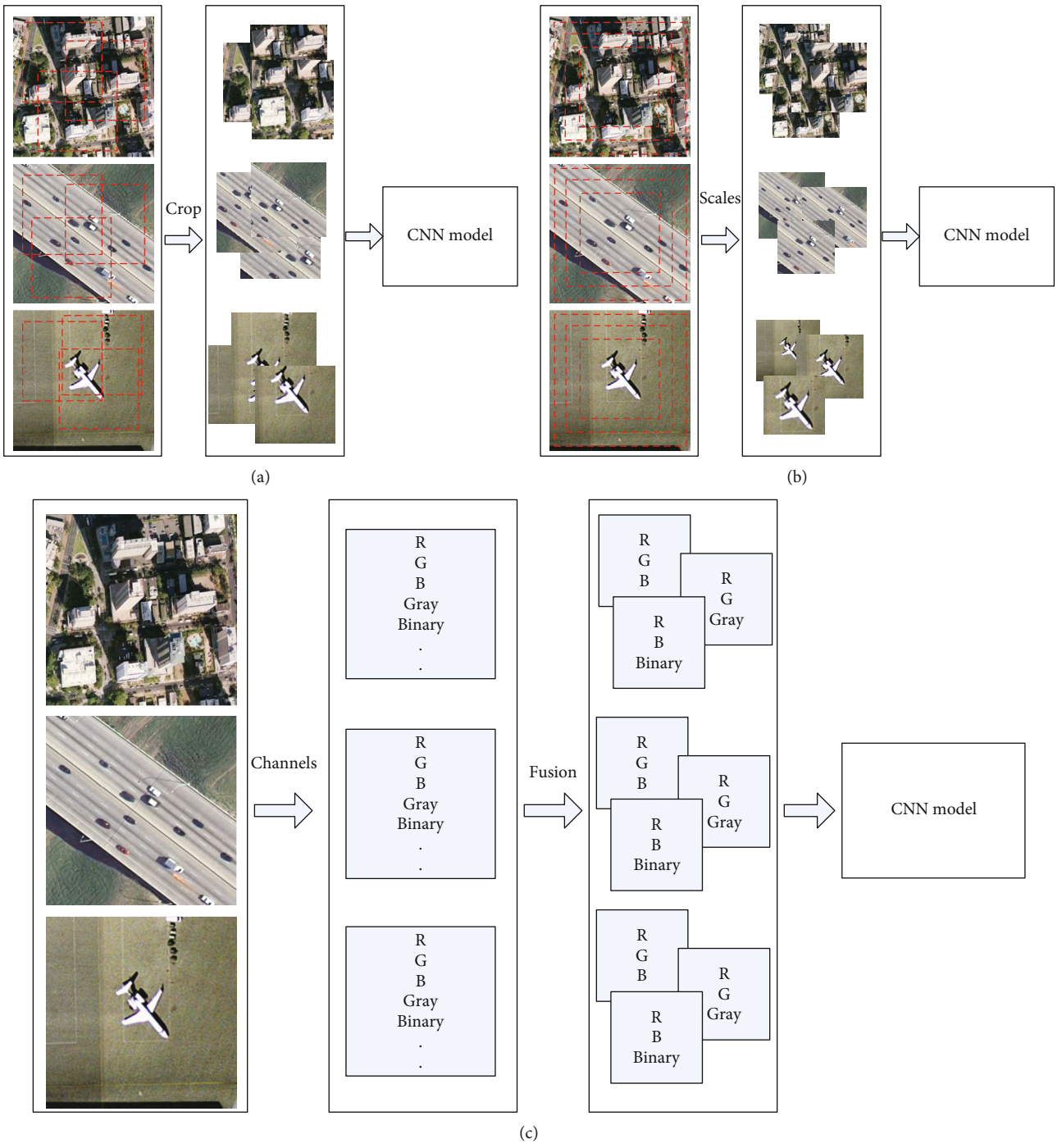

Figure 2: Demonstrations of three methods for remote sensing scene image classification based on front side fusion mode. (a) Front side fusion with random crop of input image. (b) Front side fusion with multiple scales of input image. (c) Front side fusion with channel combination of input image.

formats. Groups of channel subsets are selected to form the new training samples.

3.2. Remote Sensing Image Scene Classification Based on the Middle Side Fusion Mode. Middle side fusion can be regarded as feature level fusion. It gathers features from different paths or branches of CNN network and combines them together into a single feature map or vector. The fused feature is either fed into a classifier or used for further transformation. The difficulties for middle side fusion are the integration of heterogeneous feature.

Figure 3 demonstrates methods for remote sensing image scene classification based on middle side fusion. As is shown in Figure 3(a), C_n means nth convolutional layer, and P_n means nth pooling layer. f_n means feature map after operations of C_n and P_n. f_{n-1} and f_{n+1} are feature maps from the

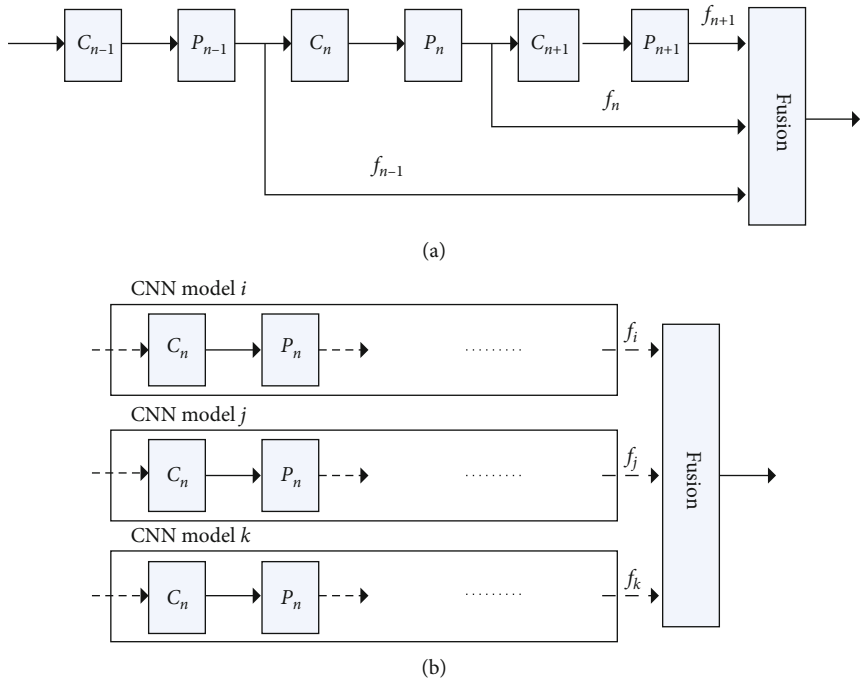

Figure 3: Demonstrations of remote sensing image scene classification based on the middle side fusion mode. (a) Middle side fusion with the single backbone network. (b) Middle side fusion with multiple backbone networks.

former and latter layers. A fused feature can be constructed by combining f_{n-1}, f_n, and f_{n+1}. This method is adopted in [38, 41]. An alternative way is shown in Figure 3(b). Feature maps f_i, f_j, and f_k are final outputs or intermediate outputs from the CNN model i, CNN model j, and CNN model k, respectively. Then, the fused feature is constructed by combining f_i, f_j, and f_k, which are from various paths. This method is adopted in [36–38, 48].

$$f_{\text{fusion}} = w_i \times f_i + w_j \times f_j + w_k \times f_k. \tag{1}$$

Equation (1) shows the linear combination of feature fusion computation. Here, feature maps f_i, f_j, and f_k are set with the same dimension. They are linearly combined at the same index, and f_{fusion} has the same dimension. w_i, w_j, and w_k are corresponding weights.

$$f_{\text{fusion}} = \text{concat}\left[f_i, f_j, f_k\right]. \tag{2}$$

Equation (2) gives another feature fusion computation and concatenation. Features are stacked instead of linear computation. f_{fusion} is the concatenation result of f_i, f_j, and f_k. If f_i, f_j, and f_k are set with dimensions of $10 \times 10 \times 3$, then f_{fusion} is a feature map set with $10 \times 10 \times 9$.

Multiple kernel learning (MKL) was also used for feature fusion computation [49]. The goal is to learn the fusion weights for each feature automatically. Let $x^i = \{x_1^i, \cdots, x_j^i, \cdots, x_n^i\}$ denote feature of an image sample i, which is composed of multiple feature x_j^i. The MKL method generates new feature vector $\{d_1 x_1^i, \cdots, d_j x_j^i, \cdots, d_n x_n^i\}$ that is optimal for training SVM classifier. It can be obtained by minimizing parameters $1/2\ \|w\|$ under constraints of $y^i(<\phi(x^i), w>+b) \geq 1$ for all training samples $\{x^i, y^i\}$. ϕ is a nonlinear mapping function. The key problem is to solve $<\phi(x^i), \phi(x^j)>$. However, it is hard to compute ϕ directly. While using kernel trick, it can be computed as follows.

$$<x^i, y^i> = K\left(x^i, x^j\right) = \sum_{m=1}^{N} d_m^2 K_m\left(x_m^i, x_m^j\right). \tag{3}$$

As shown in equation (3), $K()$ is the kernel function. Based on this scheme, d_m^2 can be computed by the gradient descend method.

3.3. Remote Sensing Image Scene Classification Based on the Back Side Fusion Mode. Back side fusion combines outputs from different models, and they are fused into a single decision. This technique does not need to consider the heterogeneity of data, and each data type can utilize exclusive classifier. It is also known as decision level fusion or late fusion [39, 40, 47].

As shown in Figure 4, label_i, label_j, and label_k are classification result by CNN model_i, model_j, and model_k, respectively. They can be fused, and a final decision output label_f can be computed.

Essentially, back side fusion mode aggregates outputs from individual classifiers to constitute a final one. Many methods are proposed to manage this problem, and two commonly used back side fusion methods are listed as below.

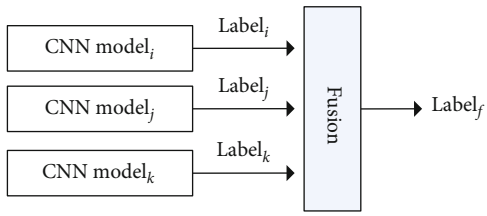

Figure 4: Demonstrations of remote sensing image scene classification based on the back side fusion mode.

3.3.1. Fusion Based on Average. Given a remote sensing image I, the classification result based on the average back side fusion method is computed as equation (4).

$$p(I) = \frac{1}{N}\sum_{i=1}^{N} p_i(I), \tag{4}$$

where $p_i()$ means ith classifier, and N is the total number. $p_i()$ gives probability value for each class label using softmax. The final result $p()$ is the value of arithmetic mean of all individual classification result [40].

3.3.2. Fusion Based on Weighted Average. Weighted average is an extension of average fusion. Weight parameters are assigned to each individual classifier [39]. It can be shown as equation (5), where w_i represents the classifier weight.

$$p(I) = \frac{1}{N}\sum_{i=1}^{N} w_i * p_i(I) \tag{5}$$

3.3.3. Using Majority Rule. In this method, the final result label_f is assigned with the one that most classifiers vote, as shown in equation (6).

$$\begin{aligned} p(e) &= \sum_{i=1}^{N} S(C_i(I) = e), \\ \text{label}_f &= \text{argmax}_j p\left(e_j\right), \end{aligned} \tag{6}$$

where C_i is ith classifier model. $S(C_i(I) = e) = 1$, if C_i classifies image I as e.

3.3.4. Using Borda Count. The Borda count for class type e is the total number of classes that ranked below e by all classifiers, as shown in equation (7).

$$\begin{aligned} p(e) &= \sum_{i=1}^{N} B_i(e), \\ \text{label}_f &= \text{argmax}_j p\left(e_j\right). \end{aligned} \tag{7}$$

$B_i(e)$ is the number of class type that ranked below e by ith classifier. The class label with maximal Borda count is regarded as the final result label_f.

4. Experiment Evaluation

To evaluate the performance and effectiveness of methods studied in this research, two widely used datasets UC Merced Land use dataset [50], WHU-RS19 dataset [51], and NWPU-RESISC45 dataset [1] are adopted in our experiments.

4.1. Dataset Description. UC Merced Land dataset is manually extracted from the USGS National Map Urban Area Imagery collection in various urban areas around the country. The pixel resolution of images in this public dataset is 1 foot. There are totally 21 classes, including agricultural, airplane, baseball diamond, beach, buildings, chaparral, dense residential, forest, freeway, golf course, harbor, intersection, medium density residential, mobile home park, overpass, parking lot, river, runway, sparse residential, storage tanks, and tennis courts. 100 images are contained in each class with size of 256×256 pixels.

The images in WHU-RS19 dataset are collected from satellite images using Google Earth. The pixel resolution of images in this public dataset is about 1.6 foot. There are totally 19 classes, including airport, beach, bridge, commercial area, desert, farmland, football field, forest, industrial area, meadow, mountain, park, parking, pond, port, railway station, residential area, river, and viaduct. 50 images are contained in each class with size of 600×600 pixels.

NWPU-RESISC45 dataset is also extracted with Google Earth. It contains 31,500 images, covering 45 scene classes, including airplane, airport, baseball diamond, basketball court, beach, bridge, chaparral, church, circular farmland, cloud, commercial area, dense residential, desert, forest, freeway, golf course, ground track field, harbor, industrial area, intersection, island, lake, meadow, medium residential, mobile home park, mountain, overpass, palace, parking lot, railway, railway station, rectangular farmland, river, roundabout, runway, seaice, ship, snowberg, sparse residential, stadium, storage tank, tennis court, terrace, thermal power station, and wetland. 700 images are contained in each class with size of 256×256 pixels.

These three datasets are public available and designed for research purposes.

4.2. Experimental Setup. In this study, fusion-based remote sensing image scene classification methods are evaluated. There are two key testings in our experiments. First, remote sensing image scene classification based on the single side fusion mode is tested (based on front side fusion mode, middle side fusion mode, and back side fusion mode). Second, remote sensing image scene classification based on the hybrid side fusion mode is tested (combination of single side fusion mode). We randomly split the datasets into two parts. 50 % is used for model training, and the rest is used for testing. This ratio is used in all experiments. Ten experiment repetitions are conducted, each having different set division. The average performance is used as final result.

We implement all the source codes. Python is used as programming language. Tensorflow and Keras are adopted as deep learning framework and library. All experiments

are tested on Pentium i5-8 series CPU, 32G RAM, Nvidia GTX 2080Ti GPU, Ubuntu OS PC.

4.3. Performance Evaluation of the Single Side Fusion Mode. In this subsection, CNN models trained with single side fusion mode are evaluated. It is further divided into front side fusion mode, middle side fusion mode, and back side fusion mode.

For the front side fusion mode, VGG16 is used. and three methods are adopted.

(a) Front side fusion with random crop of input image. Each input image sample is first randomly cropped into 4 patches with proportion of 80 % and then resized to the original image size. The original image samples are expanded for 5 times

(b) Front side fusion with multiple scales of input image. We select 3 scales for image sample generation. There are 3 generated image samples for each raw image, with scales of 50 %, 70 %, and 90 % and then resized to the original image size. The original image samples are expanded for 4 times

(c) Front side fusion with channel combination of input image sample. Red, green, blue, and gray are used as basic channels. 3 combinations of 4 basic channels are selected, and there are 4 combined image samples generated from each training image

For middle side fusion mode, there are two methods.

(a) Single backbone. VGG16 is used as the backbone network. Feature maps of 5 maxpool layers are concatenated together. For each feature map, 1×1 conv and global average pooling(GAP) operations are used. Then, there are totally 21×5 dimensions for fused feature

(b) Multiple backbones. VGG16, Mobilenet and Resnet50 are used as backbone networks. Feature maps of the last layer of three networks are concatenated together. Softmax and MKL are then trained, respectively

For the back side fusion mode, average-based and weighted-average based methods are adopted. Multiple CNN models are trained separately (VGG16, Mobilenet and Resnet50 are used). Then, the softmax results of each model are averaged or weighted averaged, and the final result can be computed. For the weighted average-based method, the weight is trained separately.

Table 1 gives the overall accuracy and standard deviation of the single side fusion mode on UC Merced and WHU-RS19 datasets. The 1st column denotes 3 types of single side fusion mode and some baseline methods. Each mode is further divided into corresponding fusion method as described above, which is listed in the 2nd column. The accuracy results are shown in the 3rd and 4th columns.

For experiment results on the UC Merced dataset, it is shown that the back side fusion mode with average method gets the best accuracy, with value of 92.85. Meanwhile, the back side fusion mode with the weighted average method and the front side fusion mode with the multiple scale method get similar performance, with values of 92.7 and 92.68. The back side fusion mode trains multiple independent CNN models, and this way essentially incorporates multiple decisions. It has a complementary effect on classification performance. Besides, methods of the front side fusion mode get better performance than those of the middle side fusion mode. The middle side fusion mode with the multiple backbone network method gets the lowest accuracy, with value of 90.74, and the gap is about 2 % compared with the best one. For the WHU-RS19 dataset, the back side fusion mode with the weighted average method gets best accuracy, with value of 89.84. The middle side fusion mode with the multiple backbone network method gets the lowest accuracy, with value of 86.39. Front side fusion methods as a whole are better than middle side fusion methods. The gap is about 3 % between the best model and worst model. For NWPU-RESISC45 dataset, there are some differences. The back side fusion mode gets the best performance, while the middle side fusion mode gets the worst performance. The gap between different fusion modes is relatively small. Some baseline methods are also evaluated. Overall, accuracies of VGG16, Mobilenet, and Resnet50 are similar. Resnet50 gets relatively higher value, with 88.87, 84.79, and 82.78 for three datasets, while they are obviously lower than fusion based methods.

From the result, we can conclude that the back side fusion mode with the average or weighted average method adopts decisions of multiple independent models and makes these decisions as complementary and therefore, the classification performance can be improved. Front side fusion methods always get better performance than those of the middle side fusion methods. This is mainly because the front side fusion mode takes best use of the sampling technique so the size of training images can be increased to some extent. Moreover, the middle side fusion mode is not a good choice compared with others. This demonstrates that the merged heterogeneous feature with the middle side fusion mode cannot make the representation optimal. Moreover, this can also be confirmed from the results of the baseline method. Model Resnet50 has a similar structure of feature fusion, but there is no superior performance compared with the VGG16 model. Moreover, evaluations on NWPU-RESISC45, which is more large and diverse, show that the gap is smaller between different fusion modes. This demonstrates that training with preferable dataset can partly compensate model defect.

Figure 5 gives the training efficiency of single side fusion methods on UC Merced dataset. Curves of testing accuracy versus training epoch are demonstrated. The back side fusion method needs to train multiple models independently and fuse the result at decision level. The middle side fusion mode with multiple backbone (MKL) treats the feature representation and classifier construction as two separate stages. Therefore, these two methods are not end-to-end form; so, they are not included in this experiment.

As can be seen obviously in Figure 5, training with the front side fusion mode is more stable while training with

Table 1: Overall accuracies (%) and standard deviations of the single side fusion mode on UC Merced, WHU-RS19, and NWPU-RESISC45 datasets.

Mode	Method	UC Merced	WHU-RS19	NWPU-RESISC45
Front side	Random crop	91.54 ± 0.72	88.24 ± 0.43	87.82 ± 0.37
	Multiscale	92.68 ± 0.65	88.78 ± 0.55	87.6 ± 0.29
	Multichannel	91.43 ± 0.68	87.71 ± 0.58	86.19 ± 0.84
Mid side	Single backbone	90.95 ± 0.73	87.52±0.29	86.76 ± 0.19
	Multibackbone	90.74 ± 0.45	86.39 ± 0.65	86.84 ± 0.32
	Multibackbone(MKL)	91.38 ± 0.37	87.47 ± 0.67	86.67 ± 0.53
Back side	Average	92.85 ± 0.76	89.67 ± 0.36	88.23 ± 0.29
	Weighted average	92.7 ± 0.56	89.84 ± 0.49	88.18 ± 0.84
Baseline method	VGG16	88.76 ± 0.63	84.76 ± 0.39	82.3 ± 0.31
	Mobilenet	87.12 ± 0.74	83.35 ± 0.27	81.21 ± 0.23
	Resnet50	88.87 ± 0.57	84.79 ± 0.51	82.78 ± 0.59

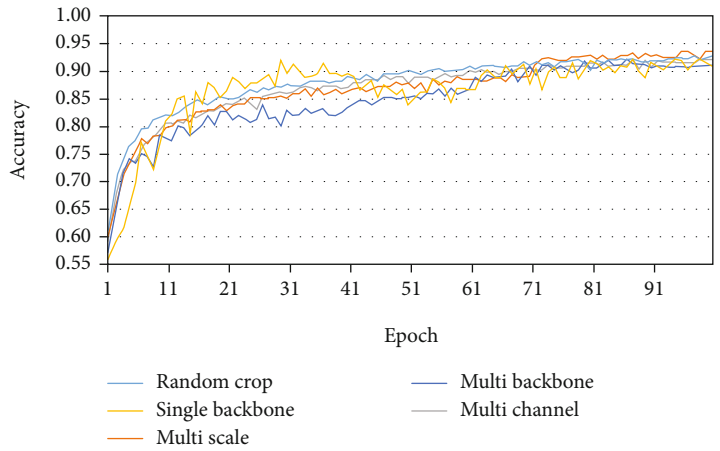

Figure 5: Training efficiency of single side fusion mode.

the middle side fusion mode is more fluctuate. The middle side fusion mode with the single backbone method combines feature from different levels of the network. The middle side fusion mode with the multiple backbone method combines feature from different CNN networks. So, the parameter tuning in these two methods is more difficult, and the models are relatively hard to train. Comparatively, the front side fusion mode adopts the same CNN network structure so the model training is relatively easy and is more stable. Similar results can be gained on the other two datasets, which are omitted here.

4.4. Performance Evaluation of the Hybrid Side Fusion Mode. In this subsection, CNN models trained with the hybrid side fusion mode are evaluated, which is designed with more than one side fusion mode. It is further divided into front+back side, front+mid side, mid + back side, and front+mid + back side fusion modes.

Table 2 gives the overall accuracy and standard deviation of hybrid side fusion methods on UC Merced, WHU-RS19, and NWPU-RESISC45 datasets. The 1st column denotes four hybrid side fusion modes. The combinations of corresponding various single side fusion methods are listed in the 2nd column. There are totally 24 models to be trained. The accuracy results are shown in the 3rd, 4th, and 5th columns. For convenience, average (w) is used to represent weighted average.

Take the result on UC Merced dataset as example. For the front+back side fusion mode, the multiscale+average method gets the best performance, 96.94. There is a slight gap compared with other methods (random crop+average or (w) average, multichannel+average or average (w)). This demonstrates the effectiveness of the back side fusion mode. For the front +middle side fusion mode, the multiscale+single backbone method gets the best performance, 96.19. The multichannel +multibackbone (MKL) method gets the worst performance, 94.49. It can also be seen that the single backbone method can better promotes performance of the front side fusion mode. For the mid + back side fusion mode, all methods get similar performance, with values range from 96.4 to 96.7. This

Table 2: Overall accuracies (%) and standard deviations of hybrid side fusion on UC Merced, WHU-RS19, and NWPU-RESISC45 datasets.

Mode	Method	UC Merced	WHU-RS19	NWPU-RESISC45
Front + back	Random crop+average	96.85 ± 0.36	92.75 ± 0.51	94.93 ± 0.87
	Multiscale+average	96.94 ± 0.41	93.14 ± 0.39	94.85 ± 0.42
	Multichannel+average	96.51 ± 0.52	91.91 ± 0.47	94.07 ± 0.63
	Random crop+average (w)	96.75 ± 0.31	92.71 ± 0.46	94.9 ± 0.56
	Multiscale+average(w)	96.84 ± 0.48	93.19 ± 0.23	94.87 ± 0.66
	Multichannel+average (w)	96.65 ± 0.45	92.03 ± 0.52	94.19 ± 0.24
Front + mid	Random crop+single backbone	96.15 ± 0.29	91.35 ± 0.51	93.46 ± 0.57
	Random crop+multibackbone	95.65 ± 0.62	90.59 ± 0.42	93.4 ± 0.32
	Random crop+multibackbone (MKL)	95.78 ± 0.75	91.02 ± 0.58	93.14 ± 0.27
	Multiscale+single backbone	96.19 ± 0.32	91.59 ± 0.62	93.56 ± 0.52
	Multiscale+multibackbone	95.34 ± 0.47	91.04 ± 0.29	93.25 ± 0.61
	Multiscale+multibackbone (MKL)	95.41 ± 0.53	90.8 ± 0.43	92.89 ± 0.62
	Multichannel+single backbone	95.51 ± 0.48	91.11 ± 0.58	93.01 ± 0.27
	Multichannel+multibackbone	94.57 ± 0.51	90.48 ± 0.45	92.96 ± 0.74
	Multichannel+multibackbone (MKL)	94.49 ± 0.45	90.54 ± 0.65	92.66 ± 0.69
Mid + back	Single backbone+average	96.55 ± 0.29	92.75 ± 0.59	94.15 ± 0.36
	Multibackbone+average	96.64 ± 0.47	92.68 ± 0.14	93.95 ± 0.52
	Multibackbone (MKL) + average	96.58 ± 0.38	92.88 ± 0.57	94.07 ± 0.32
	Single backbone+average (w)	96.45 ± 0.37	92.53 ± 0.32	94.18 ± 0.42
	Multibackbone+average (w)	96.73 ± 0.56	92.54 ± 0.29	93.87 ± 0.75
	Multibackbone (MKL) + average (w)	96.41 ± 0.51	92.65 ± 0.69	93.95 ± 0.39
Front+mid + back	Random crop+single backbone+average	97.05 ± 0.45	94.85 ± 0.55	95.45 ± 0.27
	Random crop+multibackbone+average	97.14 ± 0.32	94.74 ± 0.72	95.24 ± 0.63
	Random crop+multibackbone (MKL) + average	96.86 ± 0.37	93.76 ± 0.57	95.04 ± 0.43
	Multiscale+single backbone+average	96.87 ± 0.29	94.17 ± 0.71	95.36 ± 0.54
	Multiscale+multibackbone+average	96.74 ± 0.35	94.67 ± 0.58	95.52 ± 0.64
	Multiscale+multibackbone (MKL) + average	96.16 ± 0.31	93.42 ± 0.81	94.31 ± 0.74
	Multichannel+single backbone+average	96.79 ± 0.38	94.19 ± 0.34	94.79 ± 0.56
	Multichannel+multibackbone+average	96.54 ± 0.47	94.04 ± 0.56	94.64 ± 0.51
	Multichannel+multibackbone (MKL) + average	96.63 ± 0.42	93.83 ± 0.47	94.14 ± 0.7
	Random crop+single backbone+average (w)	97.12 ± 0.41	94.47 ± 0.75	95.57 ± 0.32
	Random crop+multibackbone+average (w)	97.04 ± 0.39	94.54 ± 0.51	95.61 ± 0.47
	Random crop+multibackbone(MKL) + average (w)	96.53 ± 0.34	93.85 ± 0.46	94.63 ± 0.27
	Multiscale+single backbone+average (w)	96.89 ± 0.43	94.25 ± 0.42	95.5 ± 0.27
	Multiscale+multibackbone+average (w)	96.77 ± 0.42	94.61 ± 0.34	95.39 ± 0.68
	Multiscale+multibackbone(MKL) + average (w)	96.09 ± 0.58	93.47 ± 0.65	94.32 ± 0.74
	Multichannel+single backbone+average (w)	96.61 ± 0.19	94.15 ± 0.39	94.52 ± 0.7
	Multichannel+multibackbone+average (w)	96.13 ± 0.68	93.75 ± 0.66	94.43 ± 0.45
	Multichannel+multibackbone(MKL) + average (w)	96.24 ± 0.47	93.61 ± 0.29	94.22 ± 0.58

demonstrates that the middle side fusion mode plays less effectiveness with regard to the back side fusion mode. For the front+mid + back fusion mode, the random crop+multiple backbone+average method gets best performance of 97.14, and multiscale+multibackbone (MKL) + average gets the worst performance of 96.16. Moreover, random crop+X + average ("X" denotes middle side fusion method) methods are generally better than other methods.

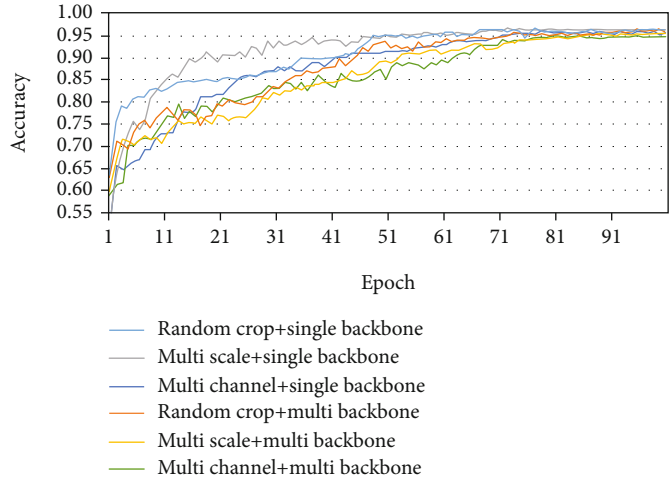

Figure 6: Training efficiency of single side feature fusion.

For comparison of the front+back side fusion mode and front+mid side fusion mode, the former is better. This indicates that the back side fusion mode is more useful than the middle side fusion mode for model performance improvement. The difference of performance between the front+back side fusion mode and middle+back side fusion mode is very small, with about 0.2 %. This indicates that the back side fusion mode is dominant for the front side fusion mode and middle side fusion mode. Front side fusion mode and middle side fusion mode are relatively unimportant for model performance boosting compared with the back side fusion mode. This may also stem from that front and middle modes play the benefit for image representation. For all fusion modes, the front+mid + back side fusion mode gets the best performance. This verifies that using all fusion techniques, including front, middle, and back side fusion, model performance is indeed increased for remote sensing image scene classification. The hybrid side fusion mode can make the best use of powerful ability for feature extraction and representation. The front+mid side fusion mode is the least efficient way compared with other modes. The essential and obvious differences stems from that it lacks the back side fusion mode, which illustrates the merit of back side fusion mode as well.

For WHU-RS19 and NWPU-RESISC45 dataset, the performance evaluation shows similar results. The front+mid + back side fusion mode works better than other fusion modes, and the front+mid side fusion mode gets the worst performance.

Figure 6 gives the training efficiency of the hybrid side fusion method. Curves of testing accuracy versus training epoch are demonstrated. Like Figure 5, fusion methods with the back side fusion mode or with multiple backbone (MKL) are not considered in this experiment.

As can be seen from Figure 6, the multiscale+single backbone method works best, and it uses minimal cost to converge. Multiscale+multibackbone and multichannel +multibackbone methods are more fluctuate and are hard to train. Single backbone is more advantageous to multiscale than the multibackbone method. This illustrates the complexity of the multibackbone method, which needs to train various inhomogeneous CNN networks simultaneously. Similar cases are demonstrated on the other two datasets, which are omitted here.

4.5. Compared with Others Methods. In this subsection, performance comparisons of other works that using fusion based method are given.

Five related fusion based methods, which are proposed in refs. [36, 37, 40, 42, 44], are used for comparison. These methods have been described in previous section. The results are given in Table 3. It can be seen that the random crop +multibackbone+average-based fusion method outperforms other methods with about 1-4 %, which demonstrates the effectiveness of our fine-tuned fusion-based method.

4.6. Performance Evaluation of Other Parameters. In this subsection, some important parameters in model training are explained, including the size of input image, optimization method, batch size, model size, and model efficiency.

4.6.1. Size of Input Image. In this testing, the random crop +multibackbone+average method is used to train the model with various sizes of input image. The results are given in Table 4.

For UC Merced dataset, training image samples are set with 128×128 pixels, 200×200 pixels, 256×256 pixels, and 300×300 pixels. Experiment evaluation shows that image samples with size of 128×128 pixels gets the best performance. It outperforms others with about 1.2 %, 0.8 %, and 1.8 %, respectively. For WHU-RS19 dataset, training image samples are set with 200×200 pixels, 300×300 pixels, 400×400 pixels, and 600×600 pixels. Experiment evaluation shows that image samples with size of 400×400 pixels get the best performance. It outperforms others with about 1.5 %, 1.1 %, and 0.8 %, respectively. For NWPU-RESISC45 dataset, training image samples are set with 128×128 pixels, 200×200 pixels, 256×256 pixels, and 300×300 pixels. Experiment evaluation shows that image samples with size

Table 3: Performance comparison with other methods.

Mode	UC Merced	WHU-RS19	NWPU-RESISC45
Method in [36]	96.18 ± 0.75	93.07 ± 0.79	91.52 ± 0.4
Method in [37]	95.76 ± 0.75	92.78 ± 0.35	91.18 ± 0.85
Method in [40]	95.59 ± 0.48	92.93 ± 0.56	91.34 ± 0.47
Method in [42]	94.50 ± 0.18	92.21 ± 0.55	90.84 ± 0.54
Method in [44]	96.37 ± 0.43	93.52 ± 0.45	92.95 ± 0.67
Random crop+multibackbone+average	97.14 ± 0.32	94.74 ± 0.72	94.14 ± 0.7

Table 4: Overall accuracies (%) and standard deviations of various input image sizes on UC Merced, WHU-RS19, and NWPU-RESISC45 datasets.

Dataset	Training image size	OAs
UC Merced	128 × 128 pixels	97.14 ± 0.32
	200 × 200 pixels	95.33 ± 0.56
	256 × 256 pixels	96.12 ± 0.45
	300 × 300 pixels	96.34 ± 0.61
WHU-RS19	200 × 200 pixels	93.23 ± 0.52
	300 × 300 pixels	93.63 ± 0.39
	400 × 400 pixels	94.74 ± 0.72
	600 × 600 pixels	93.94 ± 0.63
NWPU-RESISC45	128 × 128 pixels	94.68 ± 0.52
	200 × 200 pixels	95.14 ± 0.56
	256 × 256 pixels	95.24 ± 0.67
	300 × 300 pixels	95.02 ± 0.71

of 256 × 256 pixels get the best performance. It outperforms others with about 0.5 %, 0.1 %, and 0.2 %, respectively.

4.6.2. Optimization Method. For the optimization method, SGD, Adam, and Adagrad are evaluated. For comparison, random crop+multibackbone is used as the basic fusion method, and other parameters are set the same as Section 3.4. Among the above optimization methods, SGD is stable for training models. While for Adam and Adagrad, it illustrates that they cannot always keep smooth and steady. They are relatively hard to make the model convergence, which makes the training procedure more costly.

4.6.3. Batch Size for Model Training. Batch size is another important parameter for model training. In our research, batch size with 16, 32, 48, and 64 are evaluated. For comparison, random crop+multibackbone is used as the basic fusion method, and other parameters are set the same as Section 3.4. The experiment result shows that various batch sizes have less impact on classification accuracy of models, and the gap lies in 0.3 % It makes some influence on model training efficiency, and models with batch size 16 are easy and fast to train.

4.6.4. Model Size and Efficiency. In this testing, times for training and testing of each method are evaluated. Meanwhile, the numbers of weight parameters of each method are also reported. UC Merced dataset is used for demonstration.

Table 5 gives the evaluations of model size and efficiency of each method. The 1st and 2nd columns denote the fusion mode and method. The 3rd column gives the model size (number of weight parameters), which is measured with million. The 4th and 5th column are times for model training and testing. Training time represents the cost for one training step with batchsize 32.

For middle side fusion with multiple backbone and back side fusion with average, three CNN networks, VGG16, Resnet50, and Mobilenet, are used. So, the corresponding model sizes are all approximately 168 M. For the front side +single backbone method, the model size is approximately 138 M (We use VGG16 as single backbone network).

For front side fusion+single backbone methods, training and testing times are about 5.16 s and 0.17 s, respectively. For front side fusion+multibackbone methods, training and testing times are about 8.73 s and 0.26 s, respectively. It is more time consuming because three CNN models are combined, and more computations are needed. For front side fusion+middle side fusion+average methods, training and testing times are about 12.6 s and 0.35 s. They take the most time for three CNN models that need to be trained separately (it takes the same time for all methods combined with the back fusion mode.).

Back side fusion with average and weighted average costs the same computation and model size, and so the weighted average method is omitted. Fusion with MKL-based methods is not considered in this experiment, for it needs special libraries and cannot be evaluated on the same conditions (actually, training MKL costs quite long time).

5. Discussion

Remote sensing image scene classification is an important task for geographical analysis and region monitor. Currently, fusion-based methods are most commonly used for their excellent performance.

Among all fusion modes, back side with average is the most effective and convenient way, while the shortcoming is that it needs to training multiple independent CNN models, which may cost more resource for model training

Table 5: Model size and efficiency.

Mode	Method	Size (M)	Training (s)	Testing (s)
Front + back	Random crop+average	168	12.6	0.35
	Multiscale+average	168	12.6	0.35
	Multichannel+average	168	12.6	0.35
Front+mid	Random crop+single backbone	138	5.16	0.17
	Random crop+multibackbone	168	8.73	0.26
	Multiscale+single backbone	138	5.16	0.17
	Multiscale+multibackbone	168	8.73	0.26
	Multichannel+single backbone	138	5.16	0.17
	Multichannel+multibackbone	168	8.73	0.26
Mid + back	Single backbone+average	168	12.6	0.35
	Multibackbone+average	168	12.6	0.35
Front+mid + back	Random crop+single backbone+average	168	12.6	0.35
	Random crop+multibackbone+average	168	12.6	0.35
	Multiscale+single backbone+average	168	12.6	0.35
	Multiscale+multibackbone+average	168	12.6	0.35
	Multichannel+single backbone+average	168	12.6	0.35
	Multichannel+multibackbone+average	168	12.6	0.35

and more expensive on computation and storage. Therefore, many researches do not pay much attentions on back fusion mode in practice and real application [36, 37, 42, 44].

For the front side fusion mode, random crop and multiscale are more effective methods [36, 37, 40]. Essentially, the front side fusion mode can be seen as training data augmentation, which is a universal technique and can be used in all kinds of model training.

Middle side fusion is currently the research spot. Special architectures and complex operations are designed [42, 44]. However, in our evaluation, front side fusion mode and middle side fusion mode play similar purpose, and some methods may be offset to each other. In some cases, small cumulative effect is gained, and even duplicated objectives may take place. Moreover, single backbone and multibackbone methods are preferred to the MKL method. MKL method does not show superiority, and its training is inefficient for there is not enough libraries supporting fast parallel computing.

The aim of fusion is to learn image representation on multiple levels and degrees for key factors in scene image may appear with various scales. Fusion operations are widely adopted in state of art research. Various fusion modes (front side, middle side, and back side) are often combined to boost the model performance. In this paper, we only study common fusion methods for remote sensing image scene image classification. General trends are demonstrated by experimental evaluation. Other complex fusion methods are difficult to categorize and evaluated, and so they are not our focus and not included in this work.

6. Conclusions

This paper makes a research on the fusion-based method for remote sensing image scene classification. Three types of fusion modes, front side fusion, middle side fusion, and back side fusion, are defined. Typical methods for different fusion modes are given. Comprehensive experiments are carried out. Combinations of various fusion modes are evaluated. Results of model accuracy and training efficiency on commonly used datasets are given. It demonstrates that the random crop+multiple backbone+average method has the best performance. Characteristics of different fusion modes and their interaction are analyzed.

Our future works will focus on two aspects: (1) we will make more indepth research on the fusion-based method with specific structure. (2) External dataset should be used to improve model performance, such as webly grabbed form image engine or Google maps, for they can provide dominant training image samples.

Data Availability

The data supporting this research are from previously reported studies and datasets, which have been cited. The processed data are available at http://weegee.vision.ucmerced.edu/datasets/landuse.html, http://www.escience.cn/people/yangwen/whu-rs19.html, and https://1drv.ms/u/s!AmgKYzARBl5ca3HNaHIlzp_IXjs.

Conflicts of Interest

The authors declare no conflict of interest.

Acknowledgments

This research was supported by the Fundamental Research Funds for the Central Universities of China (Northeastern University with No. N2017007).

References

[1] G. Cheng, J. Han, and X. Lu, "Remote sensing image scene classification: benchmark and state of the art," *Proceedings of the IEEE*, vol. 105, no. 10, pp. 1865–1883, 2017.

[2] M. J. Swain and D. H. Ballard, "Color indexing," *International Journal of Computer Vision*, vol. 7, no. 1, pp. 11–32, 1991.

[3] H. Li, H. Gu, Y. Han, and J. Yang, "Object-oriented classification of high-resolution remote sensing imagery based on an improved colour structure code and a support vector machine," *International Journal of Remote Sensing*, vol. 31, no. 6, pp. 1453–1470, 2010.

[4] S. Bhagavathy and B. S. Manjunath, "Modeling and detection of geospatial objects using texture motifs," *IEEE Transactions on Geoscience and Remote Sensing*, vol. 44, no. 12, pp. 3706–3715, 2006.

[5] E. Aptoula, "Remote sensing image retrieval with global morphological texture descriptors," *IEEE Transactions on Geoscience and Remote Sensing*, vol. 52, no. 5, pp. 3023–3034, 2014.

[6] B. Cui, X. Xie, X. Ma, G. Ren, and Y. Ma, "Superpixel-based extended random walker for hyperspectral image classification," *IEEE Transactions on Geoscience and Remote Sensing*, vol. 56, no. 6, pp. 3233–3243, 2018.

[7] L. Huang, C. Chen, W. Li, and Q. du, "Remote sensing image scene classification using multi-scale completed local bBinary patterns and fisher vectors," *Remote Sensing*, vol. 8, no. 6, p. 483, 2016.

[8] S. Banerji, A. Sinha, and C. Liu, "A new bag of words LBP (BoWL) descriptor for scene image classification," *Computer Analysis of Images and Patterns*, pp. 490–497, 2013.

[9] Y. Yang and S. D. Newsam, "Comparing SIFT descriptors and gabor texture features for classification of remote sensed imagery," in *2008 15th IEEE International Conference on Image Processing*, pp. 1852–1855, San Diego, CA, USA, 2008.

[10] J. Lei, K. Xie, H. Zheng, B. Zhang, and W. Yang, "GPCA-SIFT: A New Local Feature Descriptor for Scene Image Classification," in *Pattern Recognition. CCPR 2016. Communications in Computer and Information Science*, T. Tan, X. Li, X. Chen, J. Zhou, J. Yang, and H. Cheng, Eds., vol. 2, pp. 286–295, Springer, Singapore, 2016.

[11] S. Qi, J. Ma, J. Lin, Y. Li, and J. Tian, "Unsupervised ship detection based on saliency and S-HOG descriptor from optical satellite images," *IEEE Geoscience and Remote Sensing Letters*, vol. 12, pp. 1451–1455, 2015.

[12] G. Cheng, P. Zhou, X. Yao, C. Yao, Y. Zhang, and J. Han, "Object detection in VHR optical remote sensing images via learning rotation-invariant HOG feature," in *2016 4th International Workshop on Earth Observation and Remote Sensing Applications (EORSA)*, pp. 433–436, Guangzhou, China, 2016.

[13] J. Yin, H. Li, and X. Jia, "Crater detection based on gist features," *IEEE Journal of Selected Topics in Applied Earth Observations and Remote Sensing*, vol. 8, no. 1, pp. 23–29, 2015.

[14] Y. LeCun, Y. Bengio, and G. E. Hinton, "Deep learning," *Nature*, vol. 521, no. 7553, pp. 436–444, 2015.

[15] J. Deng, W. Dong, R. Socher, L.-J. Li, K. Li, and F.-F. Li, "ImageNet: a large-scale hierarchical image database," in *2009 IEEE Conference on Computer Vision and Pattern Recognition*, pp. 248–255, 2009.

[16] T.-Y. Lin, M. Maire, S. J. Belongie et al., "Microsoft COCO: common objects in context," in *Computer Vision – ECCV 2014. ECCV 2014*, D. Fleet, T. Pajdla, B. Schiele, and T. Tuytelaars, Eds., vol. 8693 of Lecture Notes in Computer Science, pp. 740–755, Springer, Cham, 2014.

[17] A. Krizhevsky, I. Sutskever, and G. E. Hinton, "ImageNet classification with deep convolutional neural networks," *NIPS*, pp. 1106–1114, 2012.

[18] M. D. Zeiler and R. Fergus, "Visualizing and understanding convolutional networks," in *Computer Vision – ECCV 2014. ECCV 2014*, D. Fleet, T. Pajdla, B. Schiele, and T. Tuytelaars, Eds., vol. 8689 of Lecture Notes in Computer Science, pp. 818–833, Springer, Cham, 2014.

[19] K. Simonyan and A. Zisserman, "Very deep convolutional networks for large-scale image recognition," *ICLR*, pp. 1–14, 2015.

[20] C. Szegedy, W. Liu, Y. Jia et al., "Going deeper with convolutions," in *2015 IEEE Conference on Computer Vision and Pattern Recognition (CVPR)*, pp. 1–9, Boston, MA, USA, 2015.

[21] K. He, X. Zhang, S. Ren, and J. Sun, "Deep residual learning for image recognition," in *2016 IEEE Conference on Computer Vision and Pattern Recognition (CVPR)*, pp. 770–778, Las Vegas, NV, USA, 2016.

[22] E. Othman, Y. Bazi, N. Alajlan, H. Alhichri, and F. Melgani, "Using convolutional features and a sparse autoencoder for land-use scene classification," *International Journal of Remote Sensing*, vol. 37, no. 10, pp. 2149–2167, 2016.

[23] X. Han, Y. Zhong, B. Zhao, and L. Zhang, "Scene classification based on a hierarchical convolutional sparse auto-encoder for high spatial resolution imagery," *International Journal of Remote Sensing*, vol. 38, no. 2, pp. 514–536, 2017.

[24] X. Yao, J. Han, G. Cheng, X. Qian, and L. Guo, "Semantic annotation of high-resolution satellite images via weakly supervised learning," *IEEE Transactions on Geoscience Remote Sensing*, vol. 54, no. 6, pp. 3360–3671, 2016.

[25] G. Cheng, Z. Li, X. Yao, L. Guo, and Z. Wei, "Remote sensing image scene classification using bag of convolutional features," *IEEE Geoscience and Remote Sensing Letters*, vol. 14, no. 10, pp. 1735–1739, 2017.

[26] G. Cheng, C. Yang, X. Yao, L. Guo, and J. Han, "When deep learning meets metric learning: remote sensing image scene classification via learning discriminative CNNs," *IEEE Transactions on Geoscience and Remote Sensing*, vol. 56, no. 5, pp. 2811–2821, 2018.

[27] J. Chen, C. Wang, Z. Ma, J. Chen, D.-x. He, and S. Ackland, "Remote sensing scene classification based on convolutional neural networks pre-trained using attention-guided sparse filters," *Remote Sensing*, vol. 10, p. 290, 2018.

[28] Q. Wang, S. Liu, J. Chanussot, and X. Li, "Scene classification with recurrent attention of VHR remote sensing images," *IEEE Transactions on Geoscience and Remote Sensing*, vol. 57, pp. 1155–1167, 2019.

[29] J. Fang, Y. Yuan, X. Lu, and Y. Feng, "Robust space-frequency joint representation for remote sensing image scene classification," *IEEE Transactions on Geoscience and Remote Sensing*, vol. 57, no. 10, pp. 7492–7502, 2019.

[30] G. Chen, X. Zhang, X. Tan et al., "Training small networks for scene classification of remote sensing images via knowledge distillation," *Remote Sensing*, vol. 10, no. 5, p. 719, 2018.

[31] L. Bashmal, Y. Bazi, H. AlHichri, M. M. AlRahhal, N. Ammour, and N. Alajlan, "Siamese-GAN: learning invariant representations for aerial vehicle image categorization," *Remote Sensing*, vol. 10, no. 3, p. 351, 2018.

[32] S. Xu, X. Mu, D. Chai, and X. Zhang, "Remote sensing image scene classification based on generative adversarial networks," *Remote Sensing Letters*, vol. 9, pp. 617–626, 2018.

[33] D. Ma, P. Tang, and L. Zhao, "SiftingGAN: generating and sifting labeled samples to improve the remote sensing image scene classification BaselineIn vitro," *IEEE Geoscience and Remote Sensing Letters*, vol. 16, no. 7, pp. 1046–1050, 2019.

[34] G. Cheng, X. Xie, J. Han, L. Guo, and G.-S. Xia, "Remote sensing image scene classification meets deep learning: challenges, methods, benchmarks, and opportunities," *IEEE Journal of Selected Topics in Applied Earth Observations and Remote Sensing*, vol. 13, pp. 3735–3756, 2020.

[35] L. Ma, Y. Liu, X. Zhang, Y. Ye, G. Yin, and B. A. Johnson, "Deep learning in remote sensing applications: a meta-analysis and review," *ISPRS Journal of Photogrammetry and Remote Sensing*, vol. 152, pp. 166–177, 2019.

[36] Q. Liu, R. Hang, H. Song, and Z. Li, "Learning multiscale deep features for high-resolution satellite image scene classification," *IEEE Transactions on Geoscience and Remote Sensing*, vol. 56, no. 1, pp. 117–126, 2018.

[37] Y. Liu, Y. Zhong, and Q. Qin, "Scene classification based on multiscale convolutional neural network," *IEEE Transactions on Geoscience and Remote Sensing*, vol. 56, no. 12, pp. 7109–7121, 2018.

[38] Y. Liu, Y. Liu, and L. Ding, "Scene classification based on two-stage deep feature fusion," *IEEE Geoscience and Remote Sensing Letters*, vol. 15, no. 2, pp. 183–186, 2018.

[39] Y. Yu and F. Liu, "Aerial scene classification via multilevel fusion based on deep convolutional neural networks," *IEEE Geoscience and Remote Sensing Letters*, vol. 15, no. 2, pp. 287–291, 2018.

[40] N. Yang, H. Tang, H. Sun, and X. Yang, "DropBand: a simple and effective method for promoting the scene classification accuracy of convolutional neural networks for VHR remote sensing imagery," *IEEE Geoscience and Remote Sensing Letters*, vol. 15, no. 2, pp. 257–261, 2018.

[41] U. Muhammad, W. Wang, S. P. Chattha, and S. Ali, "Pre-trained VGGNet architecture for remote-sensing image scene classification," in *2018 24th International Conference on Pattern Recognition (ICPR)*, pp. 1622–1627, Beijing, China, 2018.

[42] G. Wang, B. Fan, S. Xiang, and C. Pan, "Aggregating rich hierarchical features for scene classification in remote sensing imagery," *IEEE Journal of Selected Topics in Applied Earth Observations and Remote Sensing*, vol. 10, no. 9, pp. 4104–4115, 2017.

[43] S. Chaib, H. Liu, Y. Gu, and H. Yao, "Deep feature fusion for VHR remote sensing scene classification," *IEEE Transactions on Geoscience and Remote Sensing*, vol. 55, no. 8, pp. 4775–4784, 2017.

[44] X. Lu, H. Sun, and X. Zheng, "A feature aggregation convolutional neural network for remote sensing scene classification," *IEEE Transactions on Geoscience and Remote Sensing*, vol. 57, no. 10, pp. 7894–7906, 2019.

[45] X. Lu, X. Zheng, and Y. Yuan, "Remote sensing scene classification by unsupervised representation learning," *IEEE Transactions on Geoscience and Remote Sensing*, vol. 55, no. 9, pp. 5148–5157, 2017.

[46] X. Lu, W. Ji, X. Li, and X. Zheng, "Bidirectional adaptive feature fusion for remote sensing scene classification," *Neurocomputing*, vol. 328, pp. 135–146, 2019.

[47] F. Zhang, B. du, and L. Zhang, "Scene classification via a gradient boosting random convolutional network framework," *IEEE Transactions on Geoscience and Remote Sensing*, vol. 54, no. 3, pp. 1793–1802, 2016.

[48] R. Minetto, M. Pamplona Segundo, and S. Sarkar, "Hydra: an ensemble of convolutional neural networks for geospatial land classification," *IEEE Transactions on Geoscience and Remote Sensing*, vol. 57, no. 9, pp. 6530–6541, 2019.

[49] A. Rakotomamonjy, F. R. Bach, S. Canu, and Y. Grandvalet, "SimpleMKL," *Journal of Machine Learning Research*, vol. 9, no. 3, pp. 2491–2521, 2008.

[50] Y. Yang and S. D. Newsam, "Bag-of-visual-words and spatial extensions for land-use classification," in *Proceedings of the 18th SIGSPATIAL International Conference on Advances in Geographic Information Systems - GIS '10*, pp. 270–279, 2010.

[51] G. S. Xia, W. Yang, J. Delon, Y. Gousseau, H. Maitre, and H. Sun, "Structural high-resolution satellite image indexing," in *Symposium: 100 Years ISPRS - Advancing Remote Sensing Science*, Vienna, Austria, 2010.

Hindawi
Journal of Sensors
Volume 2021, Article ID 6665829, 10 pages
https://doi.org/10.1155/2021/6665829

Research Article

Analysis of the Accuracy of an FDR Sensor in Soil Moisture Measurement under Laboratory and Field Conditions

Anzhen Qin, Dongfeng Ning, Zhandong Liu, and Aiwang Duan

Key Laboratory of Crop Water Use and Regulation, Ministry of Agriculture and Rural Affairs, Institute of Farmland Irrigation, Chinese Academy of Agricultural Sciences, Xinxiang, China 453002

Correspondence should be addressed to Dongfeng Ning; ningdongfeng@caas.cn and Zhandong Liu; liuzhandong@caas.cn

Received 11 November 2020; Revised 11 March 2021; Accepted 3 April 2021; Published 23 April 2021

Academic Editor: Jingwei Wang

Soil water content (SWC, % vol) is a key factor affecting plant growth and development. SWC measurement is vital to rational use of water resources for irrigation, and the accuracy of sensors in SWC measurement is of significant importance to smart data-driven irrigation. Here, a laboratory experiment and a field lysimetric experiment were conducted to evaluate the accuracy of Insentek sensors under various soil conditions (1.1 to 1.5 bulk densities and sand to clay soil textures) and irrigation levels (30, 45, and 60 mm), in 2018 and 2019. A microweighing lysimeter and oven-drying method were used as standard methods to compare the Insentek method. The root mean square error (RMSE, % vol) and relative prediction deviation (RPD) between the Insentek and microlysimetric SWC values were 0.89–1.04% vol and 5.6–6.8, respectively, under laboratory condition. The RPD value is larger than the threshold value of 4.0, indicating the accuracy of the Insentek sensors is reliable under laboratory condition. Except for 60 mm irrigation treatment, the RMSE between Insentek and the oven-drying method under field condition was 1.44–1.93% vol, and the RPD value was 1.56–1.93, lower than the threshold value of 4.0. The tiny gap between the Insentek sensor and soil may accelerate water infiltration along the probe 0-3 d after irrigation while increase air filling 5–7 d after irrigation, causing greater RMSE and lower RPD values. The dissatisfied performance in field condition may also be associated with the obvious drawbacks of oven-drying method, such as disturbance in soil sampling. When using oven-drying method to analyze the accuracy of the Insentek sensors in field condition, the concerns should be well addressed.

1. Introduction

Global demands for cereal grains are projected to increase by 50% by 2050. To produce more food, agriculture has become the largest water consumer accounting for more than 60% of water withdrawn from resources worldwide [1]. With the ever-increasing demands for food and water, modern agriculture should be developed toward the precision agriculture with efficient use of water and nutrient resources [2]. Nevertheless, the present efficiency of irrigation is low. In China, the mean utilization coefficient of irrigation water was 0.45 in 2019 [3]. Precision irrigation according to soil moisture dynamics is the key to achieving high water use efficiency (WUE, $kg\,m^{-3}$). However, the main difficulty for precision irrigation lies in real-time and rapid monitoring of soil water content (SWC, % vol) [4]. Over the past decades, scientists and engineers have developed various sensors to monitor the dynamics of soil moisture, including capacitive sensors (e.g., time-domain reflectometers (TDR) [5] and frequency domain reflectometers (FDR) [6]), neutron probes [7], and tensiometers [8]. TDR is a less-disturbing methodology, but the price of TDR sensor is relatively high [9]. As for neutron probes, it is difficult for the sensors to separate the signal of soil moisture from roots, giving rise to higher SWC estimates in upper soil layer [7], whereas tensiometers do not perform well in dry soil environment [8].

The Insentek sensor (Zhejiang Oriental Insentek Technology Ltd., Co, Hangzhou, China) is an FDR-type sensor that can automatically monitor SWC data. The sensor is based on the difference of relative dielectric permittivity (DP) in soils [4]. In general, DP of saturated soil at 20°C is 80, while the DP of dry soil is 2–5 [10–12]. Through detecting the DP of soil, SWC can be determined. Compared with TDR sensors, the Insentek sensor has the advantages of rapid

(a) (b)

Figure 1: (a) Insentek sensor installed in maize plots at the Qitai experimental station in 2018. (b) Thermal image (24.8–34.8°C) of soil water infiltration area along an Insentek sensor in a lysimeter experiment 2 hr after a 10 mm irrigation at Xinxiang experiment station, in June 2018.

speed of measurement, easy access to data, and low price in market [6]. The sensor is powered by a built-in lithium-polymer rechargeable battery charged by a solar panel (see Figure 1(a)). Also, a built-in GPS module with wireless communication function allows the traceability of collected data [13]. Users are able to check the real-time SWC data using their PC or cellphones. This provides convenience for users without frequent visits to experimental sites [14]. So far, the latest figure has shown that there have been more than 35,000 Insentek sensors already installed across China, forming a nationwide soil moisture monitoring network across the country. When the sensors' year-round data were checked, they showed good continuity and stability [4]. However, in practice, we did find that there was an extremely tiny gap between the probe and soil, especially when the soil was dry. The gap allows the infiltration of water immediately after irrigation or heavy precipitation, which may overestimate SWC (see Figure 1(b)). However, when soils become drier, the gap will be filled with air, causing underestimates of SWC values since the DP of air is very low [15]. The problem of the gap exists in every tube-based SWC measurement methods, and it may inevitably cause errors in data.

In addition, the measurement accuracy of FDR sensors can be affected by soil temperature [16, 17]. A temperature-dependent nonlinear model needs to be developed to compensate for the effects of temperature [18, 19]. Generally, the DP of soils decreases with increasing soil temperature, resulting in lower SWC estimates under higher temperature [20]. To minimize the negative effects, a temperature sensor and a moisture sensor were simultaneously installed in Insentek sensors. Engineers of Insentek sensors have performed thousands of experiments under various temperature and moisture levels in order to improve the accuracy of the sensors. Nevertheless, in published literature, the Insentek sensor studied in the present study has been characterized only once before [4]. In their published paper, the authors found that the Insentek sensor was an efficient tool in estimating maize evapotranspiration in the North China Plain with acceptable accuracy. However, the degree to which SWC values from Insentek sensors represent these of oven-drying method has not been well tested under both laboratory and field conditions.

In this study, the accuracy of Insentek sensors was tested both in laboratory and field conditions. We filled the gap with diluted mud in the installation of the sensors trying to exclude its adverse influences on SWC measurement. To start the experiment, a microlysimeter system was designed to test the sensors in laboratory, while in the field, a standard oven-drying method was adopted to evaluate the data of Insentek sensors. The experiment may help us validate the accuracy and reliability of Insentek sensors and better understand the uncertainty and variability in actual measurement. We hypothesized that Insentek sensors were able to monitor real-time SWC accurately both in laboratory and field conditions. The objectives of this study are (i) to validate the accuracy of Insentek sensors using microweighing lysimeters in laboratory condition and oven-drying method in field condition and (ii) to find out what factors may contribute to the variability in data if any.

2. Materials and Methods

2.1. Site Description. The experiment was carried out in June to August 2018 and 2019, at the Xinxiang experimental station of the Institute of Farmland Irrigation, Chinese Academy of Agricultural Sciences (CAAS) (35° 19′ N, 113° 53′ E, 73.2 m a.s.l.). The place has a continent temperate monsoon climate. Long-term (2009–2019) annual mean temperature is 14.1°C,

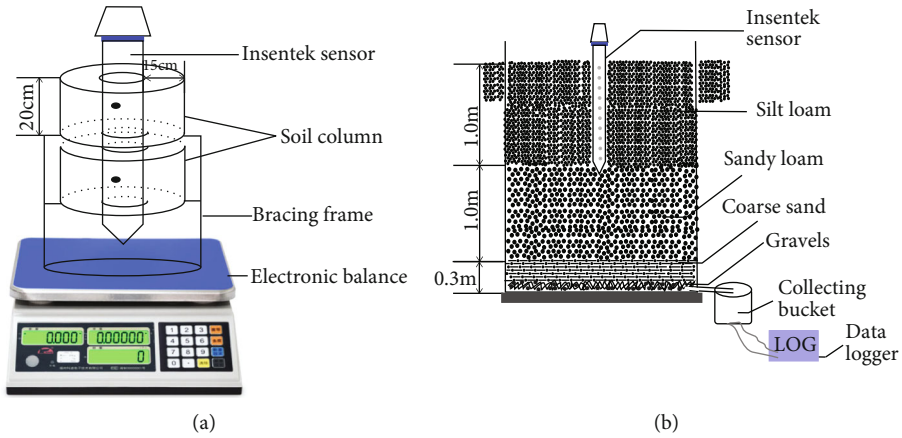

(a) (b)

Figure 2: Schematic diagram of (a) a microweighing lysimetric system and (b) a nonweighing lysimeter system.

Table 1: Soil particle size distribution for soils sampled at different locations, in April and May 2018.

Locations	Longitude	Latitude	Altitude	Sand (>0.05 mm)	Silt (0.002–0.05 mm)	Clay (<0.002 mm)	Soil texture
Huixian county	35° 30′	113° 41′	94 m	95.2%	4.8%	0	Sand
Yuanyang county	34° 59′	114° 03′	86 m	53.4%	41.2%	5.4%	Silt sand
Yanjin county	35° 14′	114° 15′	69 m	45.7%	28.6%	25.7%	Sandy loam
Muye district	35° 20′	113° 46′	73 m	41.1%	34.8%	24.1%	Silt loam
Hongqi district	35° 07′	114° 10′	71 m	37.3%	35.9%	26.8%	Silt loam
Changyuan county	35° 10′	114° 41′	62 m	17.7%	43.8%	38.5%	Loam clay
Qinyang county	35° 04′	112° 55′	126 m	8.8%	35.1%	56.1%	Clay

annual precipitation 582 mm, annual sunshine hour 2497 hr, and frost-free period 220 d. The soil is a silt loam soil [21]. Field holding capacity and permanent wilting point in 0–100 cm soil layers was 24% and 9% (by weight), average bulk density across the 0–100 cm soil depth was 1.42 g cm^{-3}, and water table was detected more than 5 m below the soil surface. Soil available N, P, and K contents were 72, 17.8, and 100 mg kg^{-1}, respectively. Soil organic carbon content was 6.54 g kg^{-1}, and soil pH was around 7.5.

2.2. Experimental Design. The experiment consisted of a microweighing lysimeter experiment in the Key Laboratory of Crop Water Use and Regulation, CAAS, from June 1st to August 30th, 2018 (see Figure 2(a)), and a nonweighing lysimeter experiment under an automatic rainproof shelter at the Xinxiang experimental station from June 1st to August 30th, 2019 (see Figure 2(b)). In the microlysimeter experiment, three microlysimetric systems were designed to evaluate the accuracy of Insentek sensors across various soil bulk densities from 1.1 to 1.5 g cm^{-3} and soil textures from sand to clay. Soils with different textures were sampled at various locations during April and May 2018 (see Table 1). When soils were collected, all stones and root debris were removed by riddling. The soils were then repacked carefully into a transparent acrylic (PMMA) tube. Different soil bulk densities were achieved by manually compacting. The Insentek sensor was installed vertically through the central circle of the soil column.

Soils collected at different locations in 2018 were classified according to their soil particle size distribution. Sand and silt sand were integrated as a sand soil, since its sand particle content was larger than 50% and clay content less than 10%. Similarly, sandy loam and silt loam were integrated as a loam soil, since its sand content was 25–50%, and silt content 25–40%; loam clay and clay were integrated as a clay soil, with its clay content larger than 35% and silt content larger than 30% [21]. The microweighing lysimetric system consisted of an electronic weighing balance, an Insentek sensor, and two soil columns. The precision of the balance was $\pm 10^{-4}$ g. Since the maximum measuring radius of an Insentek sensor was 15 cm in soils, and the diameter of the sensor was 6.5 cm, the total diameter of the soil column was designed 36.5 cm and the height 20 cm, which was considered to fully cover the measuring range of the sensor. Each type of tested soil was packed in a transparent acrylic (PMMA) tube. The junction between the sensor and the PMMA tube was sealed with glue to prevent water drainage. During the measuring period, soils were first added distilled water to holding capacity and then were air dried to wilting point under natural environment. The measurements were performed in laboratory condition at a constant temperature of 26 ± 0.5°C. After soils were mixed with water, soil columns were placed for a

period of 12 hr to obtain a uniform moisture distribution. The weight changes of soils were automatically recorded by the microweighing lysimeters. In the meantime, SWC (% vol) was monitored by Insentek sensor. The battery of the Insentek sensor was fully charged in advance. The charged battery can power the sensor to work as long as two months without recharging.

In large-scale lysimeter experiment, it consisted of nine lysimeters (3.3 m long × 2.0 m wide × 2.3 m deep) packed uniformly with silt loam soil in the 0–100 cm soil layers and sandy loam soil in the 100–200 cm soil layers. The bottom 30 cm was filled with coarse sands and <3 cm gravels to permit drainage toward lysimeter outlet. Collecting buckets were placed at the bottom side of lysimeters to hold gravity drainage effluent. These lysimeters were arranged in two rows. Between the rows, a 2.5 m wide concrete platform was constructed level with the top of the lysimeters. Nine Insentek sensors were installed at the center of each lysimeter to compare SWC measured by the standard oven-drying method. Electrically operated rainproof shelters were installed for the lysimeters. The shelters were moved over all lysimeters before precipitation happened. Three irrigation levels were arranged in a complete random design, including 30 mm, 45 mm, and 60 mm per irrigation, respectively. Each plot was irrigated separately, and different amounts of water were applied using surface irrigation, and a precision flow meter (Shanghai Water Meter Manufacturing Ltd., Co, Shanghai, China) was installed to measure and control the irrigation amounts. Preirrigation SWC was measured both by Insentek sensor and oven-drying method. After irrigation, SWC was continuously monitored by Insentek sensors at 2 hr interval. Due to the labor cost of soil-core sampling, SWC was measured by an oven-drying method at 2 hr interval for the first 8 hr after irrigation, at 4 hr interval for the next 24 hr, and 6 hr interval for the remaining days. The measurement usually lasted 7 d and repeated for three times.

2.3. Soil Water Content and Infiltration Measurements. 100 cm long Insentek sensors were used to monitor SWC (% vol) at 10 cm increment to a depth of 100 cm in field condition. 40 cm long Insentek sensors were adopted to monitor SWC at 20 cm and 40 cm depth in soil columns in laboratory condition. The sensors measured SWC every 10 min, and the average of two hours was stored in dataloggers and was transmitted to a local server via the 4G wireless network.

Microlysimeters were designed to measure the weight changes of soil column every two hours, and the data were stored in dataloggers. We used the average of a whole day to calculate daily changes of soil column weight. SWC on the ith day was derived from initial SWC and the difference in SWC (ΔSWC) using Equation (1):

$$SWC_i = SWC_{ini} - \sum_{i=1} \Delta SWC, \quad (1)$$

where SWC_i is soil water content (% vol) on the ith day, SWC_{ini} is the initial SWC at the beginning of the experiment, and ΔSWC is the daily difference between SWC on the previous and the current measurement date.

In this study, ΔSWC is derived from the changes of soil column weight (ΔWt, g) using Equation (2):

$$\Delta SWC = \frac{\Delta Wt}{H \cdot \pi \cdot \left(R^2 - r^2\right) \cdot \rho}, \quad (2)$$

where ΔSWC is the daily difference in SWC (% vol), ΔWt the daily change in soil column weight (g), H is the height of soil column (cm), R and r are the radius (cm) of the soil column and of the Insentek sensor, and ρ is the density of water ($g\,cm^{-3}$).

Soil gravimetric water content (% w/w) was measured at 10 cm increment to a depth of 100 cm using a soil auger (3 cm in diameter). Soil cores were randomly sampled about 20–30 cm away from Insentek sensor, then were oven-dried at 105°C for 8 hr after the fresh weight weighed. SWC was measured on a dry weight basis. Soil bulk density ($g\,cm^{-3}$) at the same depth and interval was determined before and after the experiment using stainless steel ring method [22]. SWC (% vol) was calculated by multiplying soil gravimetric water content with soil bulk density ($g\,cm^{-3}$) from the same layer.

In this study, infiltration area was defined as a product of infiltration depth (cm) and duration of infiltration after irrigation (d), which indicated how deep and how long irrigation amount affected SWC. The unit of infiltration area is cm d. Infiltration area was derived from pixel area estimated using the software ImageJ (NIH, Maryland, USA). Since the maximum infiltration depth was 50 cm in the present study, the area was calculated within 0–50 cm soil depth using Equation (3):

$$S_{\text{in}} = S_{\max} \frac{S_{pi}}{S_{\max-pi}}, \quad (3)$$

where S_{in} is infiltration area (cm d), $S_{\max}$ is the maximum infiltration area (350 cm d), which is a product of maximum infiltration depth (50 cm) and maximum duration after irrigation (7 d), S_{pi} is pixel area, and $S_{\max-pi}$ is the total pixel area.

2.4. Goodness-of-Fit Test. The evaluation factors include slope and coefficient of determination (R^2) for linear regression between the microlysimetric and Insentek data, and between the oven-drying and Insentek data. The slope of a line characterizes the direction of a line. The ideal slope is 1.0, indicating SWC data by the Insentek sensor are equal to those of microlysimeter or oven-drying method. The R^2 describes the proportion of variance in SWC data using microlysimeter or oven-drying method explained by the Insentek data. In addition, the root mean square error (RMSE) and relative prediction deviation (RPD) were adopted to evaluate the accuracy of Insentek sensors. The RMSE was used to investigate the differences between the microlysimeter and Insentek data, and the between oven-drying and Insentek data. The RMSE was calculated using Equation (4):

$$RMSE = \sqrt{\sum_{i=1}^{n} \left(x_{insen} - x_j\right)^2 / n}, \quad (4)$$

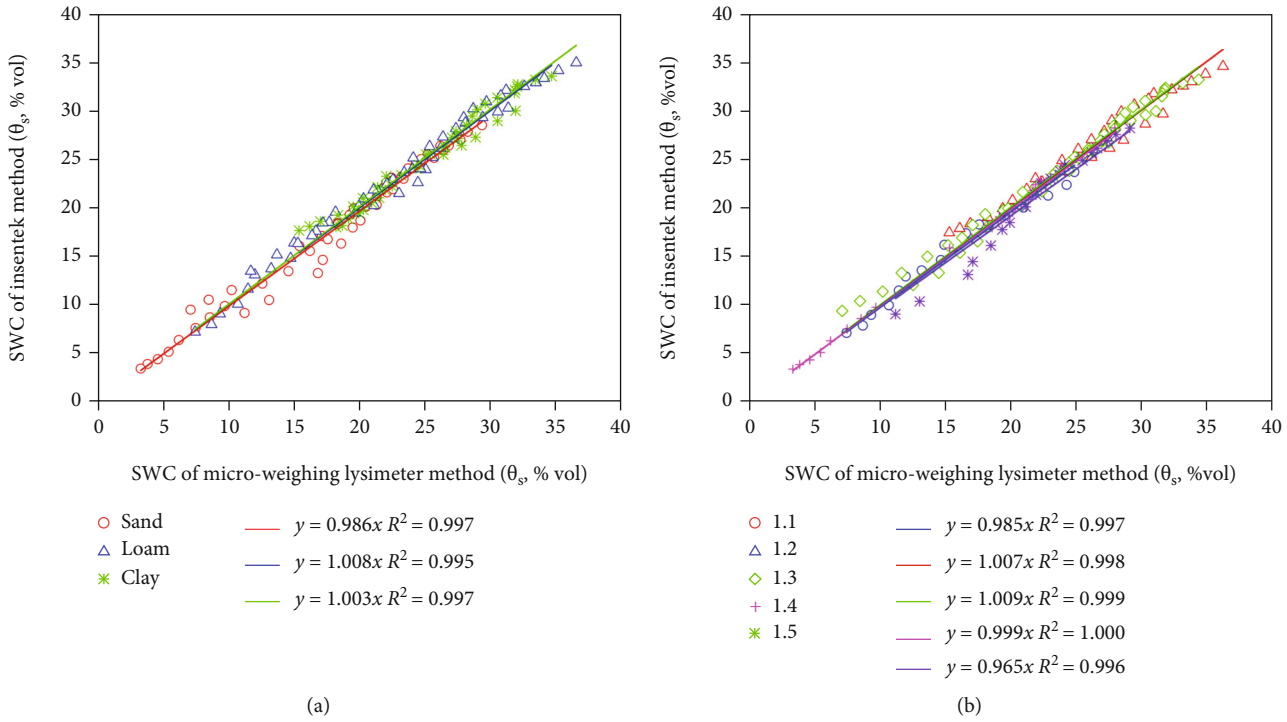

Figure 3: Linear correlation between soil water content (% vol) measured using the Insentek and microweighing lysimetric methods across (**a**) different soil textures (sand, loam, and clay) and (**b**) soil bulk densities (1.1 to 1.5 g cm^{-3}).

Table 2: Goodness-of-fit test between soil water content (SWC, % vol) calculated based on Insentek sensor and oven-drying method across different soil textures and soil bulk densities.

Treatments		Microweighing lysimetric values (% vol)			Goodness-of-fit		R^2	p
		WP	FC	Average SWC	RMSE	RPD		
Soil texture	Sand	3.46 c	28.6 b	18.09 c	1.044	6.78	0.997	0.0001
	Loam	7.26 b	35.1 a	22.71 b	0.927	7.99	0.995	0.0001
	Clay	17.7 a	33.7 a	25.35 a	0.897	5.61	0.997	0.0001
Soil bulk density (g cm^{-3})	1.1	7.47 b	25.1 c	15.6 c	0.921	5.93	0.997	0.0001
	1.2	17.7 a	35.1 a	26.4 a	1.164	4.68	0.998	0.0001
	1.3	7.14 b	33.7 a	23.8 b	0.863	7.88	0.999	0.0001
	1.4	3.46 c	28.8 b	17.9 c	0.320	22.8	1.000	0.0001
	1.5	9.22 b	28.2 b	21.1 b	1.482	3.71	0.996	0.0001

Note: WP is wilt point; FC is field holding capacity; R^2 is coefficient of determination; RMSE is root mean square error; RPD is relative prediction deviation, and values measured by Insentek sensor are reliable with RPD ≥ 4.0; and p is probability. Different letters in each column indicate significant differences at $p < 0.05$.

where *RMSE* is root mean square error, x_{Insen} and x_j are corresponding SWC values estimated by the Insentek and microlysimetric or oven-drying method, respectively, and n is the number of values evaluated. The smaller the *RMSE* values are, the more accurate the Insentek sensor is.

RPD is used to indicate the reliability of Insentek data. RPD was calculated using Equation (5):

$$RPD = STDEV(x_j)/RMSE, \quad (5)$$

where *RPD* is relative prediction deviation and $STDEV(x_j)$ is standard deviation of microlysimetric or oven-drying SWC values. $RPD \geq 4.0$ indicates Insentek data are reliable; $1.4 < RPD < 4.0$ means the data are feasible but needs to be improved; $RPD \leq 1.4$ indicates the data are unreliable [4].

2.5. Statistical Analysis. Data were analyzed using an analysis of variance with the Statistical Analysis Software (version 19.0, SPSS Inc., Chicago, IL, USA). Significance was declared at the probability level of 0.05, unless otherwise stated. Relationships among SWC by the Insentek, microlysimeter, and oven-drying methods were analyzed by means of the Levenberg–Marquardt Algorithm. Figures were plotted using Original Pro 9.1 (Origin Lab Corporation, Northampton, MA, USA).

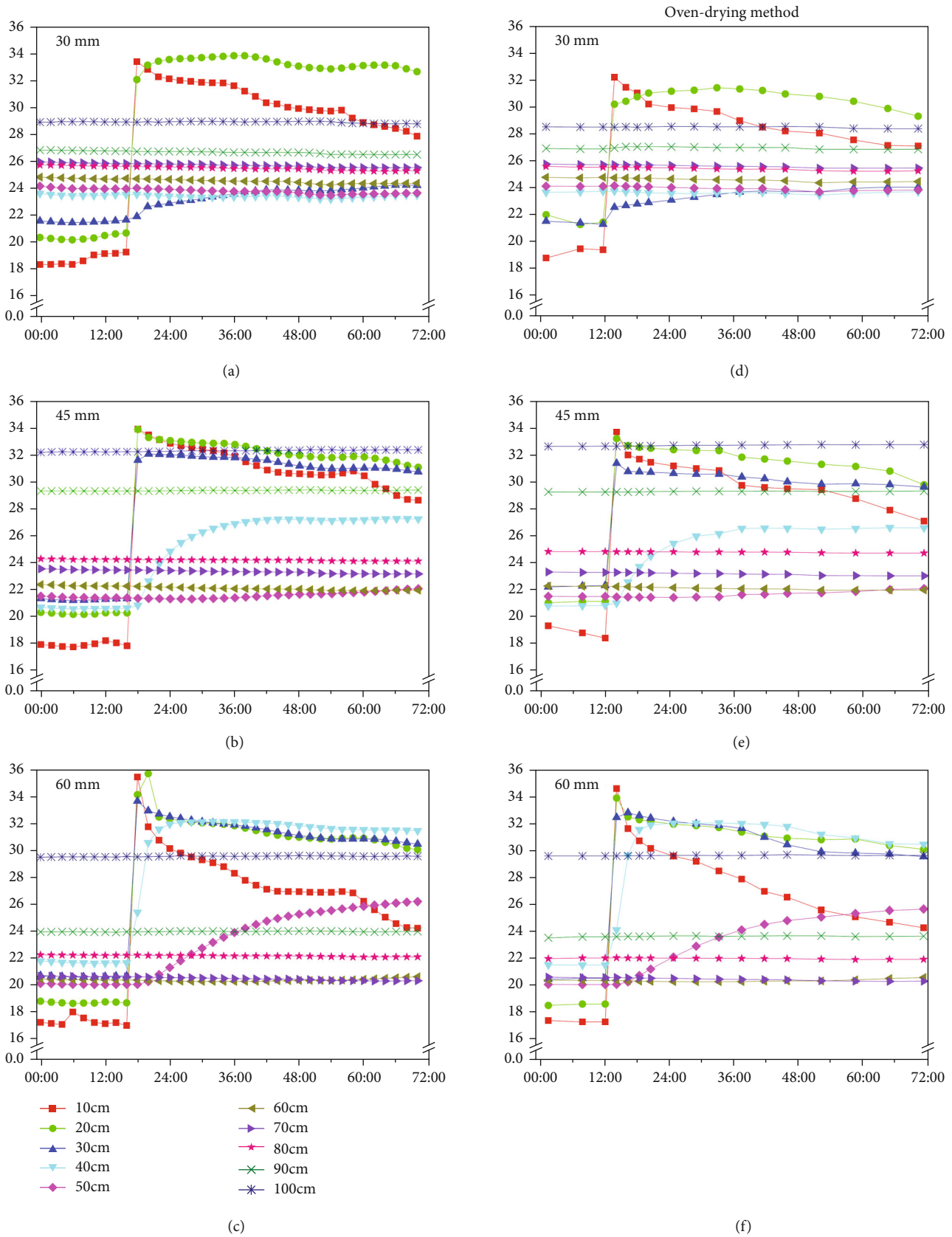

Figure 4: Dynamics of soil volumetric water content (% vol) for each 10 cm soil layer to a depth of 0–100 cm measured using the Insentek and oven-drying methods before and after irrigation events applied at the amounts of 30 mm (a, d), 45 mm (b, e), and 60 mm (c, f), respectively.

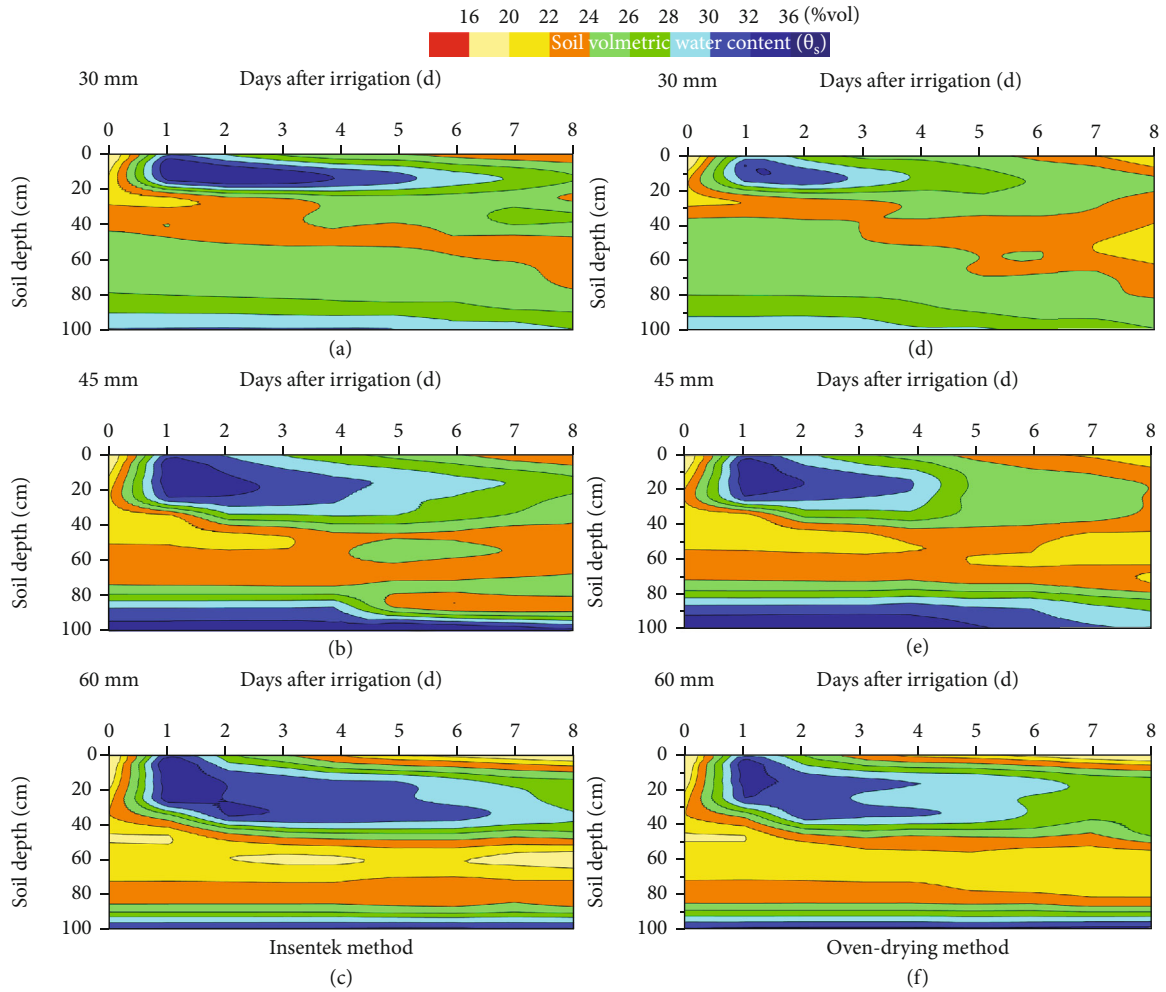

FIGURE 5: Contour plot of soil volumetric water content (% vol) in 0–100 cm soil layer measured using the Insentek and oven-drying methods before and after different irrigation events applied at the amounts of 30 mm (a, d), 45 mm (b, e), and 60 mm (c, f), respectively.

3. Results and Discussion

3.1. Comparison of Soil Water Content between Insentek and Microlysimetric Methods. SWC measured by Insentek sensor had a significant positive linear correlation with the data calculated by microlysimetric system (see Figure 3). Coefficient of determination (R^2) of the linear functions for sand, loam, and clay soils was between 0.995 and 0.997, and that for different soil bulk densities (1.1–1.5 g cm^{-3}) was between 0.996 and 1.000. The correlation between microlysimetric and Insentek data was extremely significant ($p < 0.001$). The soil physical property test showed that the wilting point of sandy and loam soil was significantly lower than that of clay, while the field holding capacity of loam and clay soil was higher than that of sandy soil (see Table 2). Consequently, the available SWC of loam soil is significantly greater than that of sandy and clay soils. According to the goodness-of-fit test, the RMSE between Insentek and microlysimetric SWC values is between 0.89 and 1.04% vol, and the RPD is between 5.6 and 6.8, larger than the threshold value (4.0), which indicates that the accuracy of Insentek sensor is high in laboratory condition. The best range of bulk density for the Insentek sensor in SWC measurement is 1.1–1.4 g cm^{-3}. Under high bulk density of 1.5 g cm^{-3}, the RMSE remains 1.48% vol, and RPD is 3.7, less than the threshold value.

So far, the standard oven-drying method is considered the most accurate method of SWC measurement [22]. Similarly, the weighing lysimetric method is regarded the most reliable approach to estimate crop evapotranspiration [6]. However, the oven-drying method is destructive, laborious, and time-consuming. That promotes the development of nondestructive, low-cost technique for SWC measurement. The Insentek sensor is an inexpensive and easy-to-use FDR probe, compared with TDR sensors. Before being applied to precision irrigation, Insentek sensors should be proven accurate and reliable in SWC measurement under a variety of field conditions. In laboratory condition, Insentek sensors have better performance in clay and loam soils compared to sandy soils, which is consistent with the results of Adla et al. [23]. The reason may be related to more reasonable range of available SWC for loam soils than sandy soils.

3.2. Comparison of Soil Water Content and Infiltration between Insentek and Oven-Drying Methods. SWC prior to

Table 3: Infiltration area (cm d) within the 0–50 cm soil depth converted using pixel area.

Treatments	Irrigation quota (mm)	Range of SWC (% vol)	Pixel area within 0–50 cm depth	Percent of total pixel area (%)	Infiltration depth (cm)	Duration after irrigation (d)	Infiltration area within 0–50 cm depth (cm d)
Maximum value		0–36	10	100	50	7.0	350
Insentek method	30	32–36	0.68	6.8	18	4.3	24
		28–32	1.63	16.3	21	5.8	57
		24–28	4.61	46.1	43	7.0	161
	45	32–36	0.65	6.5	31	1.7	23
		28–32	3.31	33.1	38	5.8	116
		24–28	3.69	36.9	48	7.0	129
	60	32–36	0.71	7.1	36	1.8	25
		28–32	4.47	44.7	42	7.0	156
		24–28	2.06	20.6	50	7.0	72
Oven-drying method	30	32–36	0.019	1.9	12	0.4	6.7
		28–32	1.04	10.4	19	2.7	36
		24–28	4.28	42.8	39	7.0	150
	45	32–36	0.41	4.1	25	1.1	14
		28–32	2.05	20.5	33	3.3	72
		24–28	4.17	41.7	45	6.9	146
	60	32–36	0.23	2.3	26	0.6	8
		28–32	3.98	39.8	41	5.6	139
		24–28	3.81	38.1	50	7.0	133

Note: maximum infiltration depth is 50 cm under the three irrigation treatments. Pixel area is calculated using the software ImageJ (NIH, Maryland, USA). Infiltration area is the product of infiltration depth (cm) and duration after irrigation (d).

Table 4: Goodness-of-fit test for soil water content (% vol) between the Insentek and oven-drying methods.

Treatments		Linear regression equation	Average SWC (% vol)		Goodness-of-fit		R^2	p
			Insentek	Oven-drying	RMSE	RPD		
Irrigation amount (mm)	30	$y = 0.9623\,x$	24.7	23.8	1.436	1.56	0.778	0.01
	45	$y = 0.9671\,x$	26.2	25.3	1.930	1.93	0.784	0.01
	60	$y = 0.9819\,x$	25.2	24.8	0.977	4.04	0.912	0.001

Note: y is soil water content (SWC, % vol) of Insentek method; x is SWC of oven-drying method; RMSE is root mean square error (% vol); RPD is relative prediction deviation; R^2 is coefficient of determination; and p is probability.

irrigation was similar between Insentek and oven-drying methods (see Figure 4). However, postirrigation SWC measured by Insentek sensors was larger than that of oven-drying method. Specifically, SWC in 0–10 cm soil layer decreased noticeably with time under 60 mm treatment. For 30 mm treatment, SWC in 10–20 cm layer remained stable within 1.0 d after irrigation and then gradually declined. As for SWC in 20–30 cm soil layer, it increased gradually and reached the maximum SWC values 2 d after irrigation under 30 mm treatment, while for SWC in 0–30 cm soil layer, it reached the maximum values within 1 d after irrigation under 45 and 60 mm treatments and remained stable for the remaining 6 d. Under 45 mm and 60 cm treatments, the mean SWC in 30–50 cm soil layers increased gradually with time and eventually reached the maximum values 3.0 d after irrigation. Averaged across the three irrigation treatments, postirrigation SWC of 10–20 cm layer measured by Insentek sensors is 7.0% higher than that of oven-drying method (33.3% vs. 31.1%). Similarly, SWC of 20–30 cm soil layer measured by Insentek sensors is 5.6% higher, and that of 30–50 cm layer is 4.8% higher ($p < 0.05$), respectively, than that of the oven-drying method. Irrigation treatments showed nonsignificant effect ($p < 0.05$) on SWC below 50 cm soil layer. Besides, SWC below 50 cm layer was similar between the Insentek and oven-drying methods.

Figure 5 shows the differences in infiltration area between the Insentek and oven-drying methods. The maximum infiltration depth was detected 50 cm under the three irrigation treatments. Although the infiltration depth measured by the two methods was generally the same, the duration of infiltration (d) after irrigation measured by the oven-drying method was much shorter than that of the Insentek method, especially for the 30 mm treatment. Under the 30 mm treatment, the duration of infiltration for SWC ranging from 32 to 36% vol was 4.3 d by the Insentek method, 3.9 d longer than that of the oven-drying method (see Table 3).

In this study, the difference in infiltration area between the Insentek and oven-drying methods was larger in the upper 0–10 cm depth, but it became smaller with soil depth. The result was consistent with the findings of Domínguez–Niño et al. [24]. In addition, other factors, such as soil temperature, were considered attributable to influence sensor accuracy [25]. Diurnal variations in soil temperature are heterogeneous across different soil depths [26] and are generally larger in the upper soil layer, resulting in disturbance in sensor measurement. To solve the problem, a temperature sensor and a moisture sensor have been installed in the Insentek sensors, and then, thousands of experiments were performed to develop proper temperature compensation models to improve the accuracy of the sensors [27]. In laboratory with a constant temperature, our results proved that soil texture and bulk density had little impact on the accuracy of Insentek sensors, except sandy soil with high bulk density. The result was consistent with Domsch et al. [28]. In general, sandy soil texture and high bulk density are associated with high thermal conductivity of soil [29], which negatively affects the soil dielectric constant [30], and thus SWC data.

3.3. Goodness-of-Fit Test between the Insentek and Oven-Drying Methods. Slopes for equations between Insentek and oven-drying methods were <1.0, indicating SWC measured by the oven-drying method was constantly lower, which was probably due to the destruction of soils causing increases in soil evaporation in upper soils and thus leading to lower SWC (see Table 4). In soil sampling, great efforts were made to reduce destructive effects on soils, leaving soils within the measuring radius (15 cm) of the Insentek sensor unchanged. During the experiment, sampling locations were kept a distance of 20–30 cm away from the Insentek sensor. After soil sampling, holes were filled with original soils. However, some artificial factors such as compactness of soil and destruction of macro soil pores inevitably contributed to the variability of experimental results. We suggest that disturbance to the soils should be minimized when choosing the oven-drying method to calibrate SWC sensors. The overestimates of SWC and infiltration area may also be associated with the tiny gap between the tube and soil. It has been learned that the outer layer of the Insentek sensor was made of chlorinated polyvinyl chloride with high chlorinated polyethylene (HCPE) coating, which helped improve the corrosion resistance to soil chemicals. To eliminate the impact of the gap on SWC measurement, it is suggested to adopt proper chemical material that has the same thermal expansion coefficient as soils.

4. Conclusions

We performed a comparative study using microweighing lysimeter and oven-drying methods to assess the accuracy of Insentek sensors in SWC measurement under laboratory and field conditions. The results showed that, in laboratory condition, the SWC of Insentek sensors had a significant ($p < 0.001$) positive correlation to that of microweighing lysimeter across various soil textures and bulk densities, except sandy soil with high bulk density. In field condition, the Insentek method monitored the same infiltration depth as the oven-drying method did, but the duration of infiltration after irrigation was longer by the Insentek method. The accuracy of the Insentek sensor tested by the microlysimetric method in laboratory condition was higher than that of oven-drying method in field condition. The discrepancy in the SWC data between the Insentek and oven-drying methods was likely attributable to the tiny gap between the tube and soil. Also, the disturbance to soils in the oven-drying method may also contribute to variability in SWC data. Compared with the microlysimetric method, the oven-drying method with continuous disturbance in soil sampling may have drawbacks in assessing the accuracy of Insentek sensor in field conditions. We consider the microweighing lysimetric method an appropriate approach to assess the accuracy and reliability of the SWC measurement sensors.

Data Availability

The data used to support the findings of this study have not been made available because it is only available for researchers and collaborators of Key Laboratory of Crop Water Use and Regulation, CAAS.

Conflicts of Interest

The authors declare that they have no conflicts of interest.

Acknowledgments

This research was funded by the National Key Research and Development Program of China (2017YFD0301102), the Central Public Interest Scientific Institution Basal Research Fund (Farmland Irrigation Research Institute, CAAS, FIRI2020–02), the Agricultural Science and Technology Innovation Program (ASTIP) of Chinese Academy of Agricultural Sciences, the China Agriculture Research System (CARS–02), and the Scientific and Technological Project of Henan Province (212102110069).

References

[1] D. K. Ray, N. Ramankutty, N. D. Mueller, P. C. West, and J. A. Foley, "Recent patterns of crop yield growth and stagnation," *Nature Communications*, vol. 3, no. 1, 2012.

[2] P. Placidi, L. Gasperini, A. Grassi, M. Cecconi, and A. Scorzoni, "Characterization of low–cost capacitive soil moisture sensors for IoT networks," *Sensors*, vol. 20, no. 12, 2020.

[3] A. Guo, D. Jiang, F. Zhong et al., "Prediction of technological change under shared socioeconomic pathways and regional differences: a case study of irrigation water use efficiency changes in Chinese provinces," *Sustainability*, vol. 11, no. 24, 2019.

[4] A. Qin, D. Ning, Z. Liu et al., "Insentek sensor: an alternative to estimate daily crop evapotranspiration for maize plants," *Water*, vol. 11, no. 1, 2019.

[5] Y. Zhu, S. Irmak, A. Jhala, M. Vuran, and A. Diotto, "Time–domain and frequency–domain reflectometry type soil

moisture sensor performance and soil temperature effects in fine– and coarse–textured soils," *Applied Engineering in Agriculture*, vol. 35, no. 2, pp. 117–134, 2019.

[6] A. Qin, D. Ning, Z. Liu et al., "Structural equation modeling of soil moisture effects on evapotranspiration of maize in the North China plain," *National Academy Science Letters*, vol. 43, no. 3, pp. 219–224, 2020.

[7] M. Duygu and Z. Akyürek, "Using cosmic–ray neutron probes in validating satellite soil moisture products and land surface models," *Water*, vol. 11, no. 7, 2019.

[8] R. Muñoz-Carpena, Y. Li, W. Klassen, and M. Dukes, "Field comparison of tensiometer and granular matrix sensor automatic drip irrigation on tomato," *HortTechnology*, vol. 15, no. 3, pp. 584–590, 2005.

[9] J. Oliveira, E. Pinto, V. Silva Neto, and A. D'Assunção, "CSRR–based microwave sensor for dielectric materials characterization applied to soil water content determination," *Sensors*, vol. 20, no. 1, 2020.

[10] K. Kupfer, E. Trinks, N. Wagner, and C. Hübner, "TDR measurements and simulations in high lossy bentonite materials," *Measurement Science and Technology*, vol. 18, no. 4, pp. 1118–1136, 2007.

[11] G. Topp, S. Zegelin, and I. White, "Impacts of the real and imaginary components of relative permittivity on time domain reflectometry measurements in soils," *Soil Science Society of America Journal*, vol. 64, no. 4, pp. 1244–1252, 2000.

[12] C. Gao, Y. Zhao, and Y. Zhao, "A novel sensor for noninvasive detection of in situ stem water content based on standing wave ratio," *Journal of Sensors*, vol. 2019, Article ID 3594964, 10 pages, 2019.

[13] S. Zang, K. Hou, and S. Nguang, "Underground communications using capacitive data transfer devices," *Journal of Sensors*, vol. 2020, Article ID 8849618, 11 pages, 2020.

[14] J. Jabro, W. Stevens, W. Iversen, B. Allen, and U. Sainju, "Irrigation scheduling based on wireless sensors output and soil–water characteristic curve in two soils," *Sensors*, vol. 20, no. 5, 2020.

[15] R. Aroca, A. Hernandes, D. Magalhães, M. Becker, C. Vaz, and A. Calbo, "Calibration of passive UHF RFID tags using neural networks to measure soil moisture," *Journal of Sensors*, vol. 2018, Article ID 3436503, 12 pages, 2018.

[16] M. Lu, J. Kapilaratne, and I. Kaihotsu, "A data-driven method to remove temperature effects in TDR-measured soil water content at a Mongolian site," *Hydrological Research Letters*, vol. 9, no. 1, pp. 8–13, 2015.

[17] E. Nagahage, I. Nagahage, and T. Fujino, "Calibration and validation of a low–cost capacitive moisture sensor to integrate the automated soil moisture monitoring system," *Agriculture*, vol. 9, no. 7, 2019.

[18] L. Lin, Y. He, Z. Xiao, K. Zhao, T. Dong, and P. Nie, "Rapid–detection sensor for rice grain moisture based on NIR spectroscopy," *Applied Sciences*, vol. 9, no. 8, 2019.

[19] J. Kapilaratne and M. Lu, "Automated general temperature correction method for dielectric soil moisture sensors," *Journal of Hydrology*, vol. 551, pp. 203–216, 2017.

[20] D. Xiao, J. Feng, N. Wang, X. Luo, and Y. Hu, "Integrated soil moisture and water depth sensor for paddy fields," *Computers and Electronics in Agriculture*, vol. 98, pp. 214–221, 2013.

[21] National Standards of China (NSC), "China Soil Classification and Code (GB/T 17296–2009)," NSC, Beijing, China, 2009.

[22] A. Qin, Y. Fang, D. Ning et al., "Incorporation of manure into ridge and furrow planting system boosts yields of maize by optimizing soil moisture and improving photosynthesis," *Agronomy*, vol. 9, no. 12, 2019.

[23] S. Adla, N. Rai, S. Karumanchi, S. Tripathi, M. Disse, and S. Pande, "Laboratory calibration and performance evaluation of low–cost capacitive and very low–cost resistive soil moisture sensors," *Sensors*, vol. 20, no. 2, 2020.

[24] J. Domínguez-Niño, J. Oliver-Manera, G. Arbat, J. Girona, and J. Casadesús, "Analysis of the variability in soil moisture measurements by capacitance sensors in a drip–irrigated orchard," *Sensors*, vol. 20, no. 18, 2020.

[25] S. Evett, N. Agam, W. Kustas, P. Colaizzi, and R. Schwartz, "Soil profile method for soil thermal diffusivity, conductivity and heat flux: comparison to soil heat flux plates," *Advances in Water Resources*, vol. 50, pp. 41–54, 2012.

[26] G. Kargas and K. Soulis, "Performance analysis and calibration of a new low-cost capacitance soil moisture sensor," *Journal of Irrigation and Drainage Engineering*, vol. 138, no. 7, pp. 632–641, 2012.

[27] M. Oates, A. Fernández-López, M. Ferrández-Villena, and A. Ruiz-Canales, "Temperature compensation in a low cost frequency domain (capacitance based) soil moisture sensor," *Agricultural Water Management*, vol. 183, pp. 86–93, 2017.

[28] H. Domsch and A. Giebel, "Estimation of soil textural features from soil electrical conductivity recorded using the EM38," *Precision Agriculture*, vol. 5, no. 4, pp. 389–409, 2004.

[29] J. Triantafilis and S. Lesch, "Mapping clay content variation using electromagnetic induction techniques," *Computers and Electronics in Agriculture*, vol. 46, no. 1–3, pp. 203–237, 2005.

[30] M. Mojid, D. Rose, and G. Wyseure, "A model incorporating the diffuse double layer to predict the electrical conductivity of bulk soil," *European Journal of Soil Science*, vol. 58, no. 3, pp. 560–572, 2007.

Hindawi
Journal of Sensors
Volume 2021, Article ID 6649498, 11 pages
https://doi.org/10.1155/2021/6649498

Research Article

Effects of Herbicides on the Microbial Community and Urease Activity in the Rhizosphere Soil of Maize at Maturity Stage

Jie Chen,[1] **Wenping Yang**,[2] **Jin Li**,[1] **Sumera Anwar**,[3] **Kai Wang**,[1] **Zhenping Yang**,[1] **and Zhiqiang Gao**[1]

[1]*College of Agriculture, Shanxi Agricultural University, Taigu 030801, China*
[2]*College of Life Sciences, North China University of Science and Technology, Caofeidian 063210, China*
[3]*Institute of Molecular Biology and Biochemistry, The University of Lahore, Lahore 54000, Pakistan*

Correspondence should be addressed to Zhenping Yang; yangzp.2@163.com

Received 19 November 2020; Revised 4 February 2021; Accepted 5 April 2021; Published 22 April 2021

Academic Editor: Jingwei Wang

Studying the effects of herbicides on microbial community and urease activity in the rhizosphere soil of maize is helpful to clarify the mechanisms herbicides used to affect soil microbial environment. In this research, four common preemergence maize specific herbicides, nicosulfuron+atrazine (A1), alachlor+acetochlor+atrazine (A2), propisochlor+atrazine (A3), and acetochlor+atrazine (A4), were selected to use in a pot trial. A preemergence herbicide nonspecific for maize, dinitraniline (A0), was used as the positive control, whereas water instead of herbicide was considered as the negative control (CK). At the maturity stage, the microbial communities and urease activity in the 0-20 cm, 20-40 cm, and 40-60 cm rhizosphere soils of maize were analyzed. Results showed that A0 dramatically suppressed maize growth, with no grain got finally, while A1 displayed the weakest effect. The tested herbicides affected the microbial community in the 0-20 cm layer greater than in the 20-60 cm ones, with A1 displaying the greatest effect. In the 0-20 cm soil, A1 largely reduced the relative abundance of the top three dominant genera, *Prevotella*, *Barnesiella*, and *Lactobacillus* in the CK soil, by 99.0%, 98.7%, and 79.2%, and made *Pseudomonas*, *Gemmatimonas*, and *Sphingomonas* became the new dominant genera, while A2 and A3 displayed similar but slighter effects. All herbicides dramatically reduced the relative abundance of the top one dominant fungal phylum (Ascomycota) and genus (*Diatrype*) in the CK soil, from 45% to 5.2%-7.9% and 42% to 2.1%-3.2%. A0 dramatically dropped the urease activity in the 0-60 cm soils, by 30.5%-33.1%, whereas A1-A4 displayed an unsignificant effect. In conclusion, A1 is a suitable herbicide for maize. Both the bacterial community and urease activity in the 0-20 cm rhizosphere soil are suitable indices to evaluate the effects of preemergence herbicides on maize growth and soil microbial environment.

1. Introduction

Maize (*Zea mays* L.) plays a key role in keeping food security and agricultural production especially in the developing countries and is the third important cereal crop in the world [1, 2]. In China, maize has become the first grain crop with the largest planting area and total yield [3]. Weed is one of the most important factors restricting both the yield and quality of maize. It is reported that about half of the maize field faces weed damage in different levels in China [4]. The annual yield loss of maize caused by weed in China has reached to 20% [5]. Herbicides have many merits such as time-saving, economy, and high-efficiency, Therefore, the use of herbicides is still one of the most important measures to control weed in the fields of grain crops including maize [6]. However, together with the economic benefit, herbicides also bring adverse effects to the soil environment [7–9]. After entering into soils, herbicides may influence the soil environment through the processes of sorption-desorption, transformation, transporting to groundwater, or degradation [10]. Evaluating the effects of herbicides on the soil environment is crucial for the reasonable use of herbicides. The preemergence herbicide is a kind of herbicide that is sprayed directly on the soil surface before the emergence of crops and, hence,

affects soil chemical and microbial environment deeper than the postemergence ones. However, the effects of preemergence herbicides on soil microbial environment still need more researches.

Microorganisms play key roles in nutrient cycling and energy flow in soil and are important indicators for soil health, soil pollution, and ecological restoration [11, 12]. Herbicides application may inhibit, activate, or show no effects to soil microorganisms. Xu et al. reported that sterane first decreased soil bacterial diversity and abundance in maize field at 10 days but increased them at 60 days after application [13], Bezuglova et al. demonstrated that foliar application of sulfonylurea herbicide decreased the abundance of bacteria especially for the quickly growing ones on winter wheat soil [14], whereas Kepler et al. found that glyphosate did not affect the overall microbial community composition in maize or soybean grown soil [15].

Except for microorganisms, enzymes also are important evaluation indicators for soil quality as they are directly involved in the biochemical process and nutrient cycle [16]. Soil enzymes may catalyze organic substances into inorganic nutrients or assist the degradation of exogenous harmful compounds to promote plant growth [17, 18], which can then regulate the soil microbial community. Moreover, soil enzymes mainly come from soil microorganisms [19]; hence, the activity of soil enzymes is correlated with the soil microbial environment. Among soil enzymes, urease mainly participates in hydrolyzing urea into CO_2 and NH_3, regulating the soil nitrogen cycle [20]. Herbicides affect the soil urease activity had been reported. Xie et al. [21] found that applying a high dose of either bensulfuron-methyl·butachlor or quinclorac in pot paddy soil suppressed the soil urease activity. Du et al. applied mesotrione on a laboratory cultured soil and found that the soil urease was less affected than β-glucosidase [16]. Researches from Aruna Kumari et al. showed that the soil urease activity can be affected by herbicide type, concentration, and application time [2].

The rhizosphere soil is closely in contact with roots and shows a larger influence on plant growth than the nonrhizosphere soil. After entering into soil, herbicides interacted with soil microorganisms and plant roots, hence showed different effects to soil environment when compared with the nonrhizosphere soil. Studying the effects of herbicides on the microorganisms and enzyme activity in rhizosphere soil is helpful to elucidate the mechanisms of herbicides affecting both plant growth and soil environment [22–24]. However, until now, studies about the effects of herbicides on soil microorganisms and urease activity mainly focus on the nonrhizosphere soils [25–28]. Moreover, both the degradation and migration rates of herbicides in soil differ the influence degree to soil environment caused by herbicides. Effects of herbicides on soil microorganisms or enzymes in 0-20 cm soils after a short time application had been studied [13, 29, 30]. How did herbicides affect soil microbial environment in soils at different depths after a much longer time application (such as after planting a season of crop) is still unclear.

In this study, five preemergence herbicides: four maize-specific herbicides and one nonspecific herbicide for maize were sprayed on the potted soil surface immediately after sowing maize. At the maturity stage, the effects of herbicides on the total bacterial and fungal community structures in the 0-20, 20-40, and 40-60 cm rhizosphere soils were analyzed by high-throughput sequencing technology, and the soil urease activities in the same soil layers were determined. The weight and number of maize grains were also recorded. Results from this study may help enlighten the effects of preemergence herbicides on the microbial environment in rhizosphere soil at different layers after planting a season crop and provide guides for selecting suitable herbicides for maize.

2. Materials and Methods

2.1. Materials. The maize hybrid "Bingdan 16" used in this study was provided by the Institute of Crop Science, Shanxi Academy of Agricultural Sciences. The growth period of Bingdan 16 is 120 days. The five preemergence herbicides commonly sold in market that were selected to use in this experiment (Table 1) were bought from Shanxi Taigu County Yirong Seed Industry Co., LTD, and applied based on the instructors. Dinitraniline (A0) is a nonspecific herbicide for maize, and nicosulfuron+atrazine (A1), alachlor+acetochlor +atrazine (A2), propisochlor+atrazine (A3), and acetochlor +atrazine (A4) are specific herbicides for maize.

2.2. Soil. The raw soil sample was taken from a 2 m layer from an uncultivated land in Taigu County, Shanxi Province, China. The soil was air-dried, sieved (1 mm), and evenly mixed before use. Nutrient status of the soil was as follows: 0.2 g kg^{-1} total nitrogen, 19.8 mg kg^{-1} available nitrogen, 2.9 mg kg^{-1} available phosphorus, 30.3 mg kg^{-1} available potassium, and 1.2 g kg^{-1} organic matter.

2.3. Experimental Methods. The experiment was conducted from June 3, 2014, to October 1, 2014, at the Loess Plateau Crop Research Institute, Shanxi Agricultural University, China. A special root tube device (25 cm diameter, 200 cm length) that consists of two semicylinders fixed with iron wire and steel plates was used. Soil bulk density in 0-200 cm soil layer was measured for local maize field by 20 cm interval. Based on the soil bulk density, soil mass was calculated and weighted for every 20 cm length in the tube. The soil prepared above was added to the root tube devices and compacted by every 20 cm layer. The top 0-20 cm soil was added after mixing with NPK nutrients (urea, 170 mg kg^{-1}; superphosphate, 560 mg kg^{-1}; potassium chloride, 170 mg kg^{-1}). All root tube devices were placed vertically in the grooves in a way that the soil surface inside the tubes was leveled to the outer soil surface. Five maize seeds were sown in each tube on June 3, 2014. Herbicide solutions (100 ml) were then sprayed evenly based on the dosage as mentioned in Table 1. A nonspecific herbicide for maize (A0) was sprayed as the positive control and an equal volume water instead of herbicide was considered as the negative control (CK). Each treatment was repeated three times, and all tubes were randomly placed. After emergence, seedlings were thinned to one seedling per tube and watered as needed.

2.4. Soil Sample Collection. On October 1, 2014 (at the maturity stage), the aboveground maize plants were cut and all tubes were opened. The rhizosphere soils from 0-20, 20-40,

Table 1: The tested herbicides information.

Number	Effective components and content	Actual dosage (μl tube^{-1})	Water dosage (ml pot^{-1})
A0	48% dinitraniline	14.7	100
A1	2% nicosulfuron+20% atrazine	14.7	100
A2	10% alachlor+14% acetochlor+18% atrazine	22.1	100
A3	16% propisochlor+26% atrazine	17.7	100
A4	26% acetochlor+26% atrazine	14.7	100

and 40-60 cm layer from the soil surface were collected using a banister brush from the root surface after the untight soil was removed. All soil samples were collected into seal bags and divided into two parts: one was stored in -80°C before sending to the Sangon Biological Engineering Co. Ltd. Shanghai to analyze the bacterial and fungal community structures, while the other part was used to determine the urease activity.

2.5. Measured Indices

2.5.1. Growth Indices. The grain number and weight per plant were recorded, and the thousand grains weight was calculated at the maturity stage.

2.5.2. Soil Microorganisms

(1)DNA Extraction and Gene Amplification. The collected soil samples were sent to Sangon Biotech (Shanghai) Co., Ltd., for the study of the bacterial and fungal community. Briefly, 5.0 g soil was used for DNA extraction by the PowerSoil® DNA extraction kit (MoBio, USA) following the instructions. The Qubit2.0 DNA detection kit was performed to detect the concentration and quality of the extracted DNA. The bacterial community was estimated on the V3-V4 region of the 16S rRNA gene using the primers 338F (5′-ACTCCTACGGGAGGCAGCAG-3′) and 806R (5′-GGACTACHVGGGTWTCTAAT-3′). The fungal community based on the NS1-FUNG region of the 18S DNA gene was analyzed using the primers NS (5′-CCTACA CGACGCTCTTCCGATCTN GTAGTCATATGCTTGT CTC-3′) and FUNG (5′-GACTGGAGTTCCTTGGCAC CCGAGAATTCCAATTCCCCGTTACCCGTTG-3′). The purified PCR products were then sequenced using the Illumina Miseq platform.

(2)Sequencing Analysis. The obtained sequences were quality controlled through truncating the overlapped of low-quality bases in the 3′ end using the PRINSEQ-lite 0.19.5, and then, the bases in the double ends were combined to one complete sequence using FLASH v1.2.7. The obtained sequences were checked by MOTHUR (pre. cluster), and the chimeras were removed by UCHIME, and finally, the high-quality sequences were obtained. These sequences were clustered by UCLUST v1.1.579 and generated into operational taxonomic units (OTUs) at 0.97 similarity. One sequence with the highest abundance for each OTU was chosen as the representative sequence. Taxonomy was assigned using the RDP classifier and Greengenes database. The Alpha diversity indices (Shannon index, ACE index, and Alpha index) and were calculated using Mothur (http://www.mothur.org/).

2.5.3. Soil Urease Activity. For each layer of soil in each pot, the collected soil samples at the maturity stage used for analyzing urease activity were divided into two even parts, and the total of six replicated soil samples were air-dried and sieved. The urease activity was analyzed by the indigo colorimetry method [19] and calculated based on the content of NH_3-N (mg g^{-1}) released from one-gram soil within the cultivated time.

2.6. Data Analysis. The Microsoft Excel 2016 software was used to analyze the data, and the Origin 9 was used to draw bar charts. The SPSS 18.0 software was used to analyze the differences between treatments or soil layers based on the least significant difference (LSD) method at the level of $P = 0.05$.

3. Results

3.1. Effects of Herbicides on the Grain Weight of Maize. Among the tested herbicides, nicosulfuron+atrazine (A1) did not affect either the early growth of maize seedlings or the grain structures during the maturity stage, whereas dinitraniline (A0) dramatically inhibited the growth of maize seedlings, and with no grain at the maturity stage (Table 2, Figure 1). The grain weight and number per plant were not significantly reduced by alachlor+acetochlor+atrazine (A2), propisochlor+atrazine (A3), or acetochlor+atrazine (A4), whereas a 27.0%-39.9% reduction in thousand-grain weight was recorded compared to the control (Table 2).

3.2. Effects of Herbicides on the Microbial Diversity in the Rhizosphere Soil of Maize. The total number of effective bacterial and fungal OTUs was 5075-6757 and 1103-1673, respectively, from different soils. Shannon index reflects the diversity degree of microorganisms, and ACE and Chao 1 indices reflect the richness of the microbial community. For bacteria, the five tested herbicides had little effect on the bacterial Shannon index in the 0-60 cm rhizosphere soil of maize. The effects of herbicides on ACE and Chao1 indices in the 0-20 cm rhizosphere soil were also weak, with only A1 changing the ACE index by more than 20% (20.9%). In the 20-40 cm rhizosphere soil, A0 and A3 reduced the ACE and Chao 1 indices, to 28.3%-40.4%, whereas increased these indices by 24.3%-55.2% in the 40-60 cm rhizosphere soil compared with the control. A5 also increased the ACE and Chao1 indices in the 40-60 cm rhizosphere soil by 46.7% and 36.8% than that of the control, respectively (Table 3).

Table 2: Effects of herbicides on the grain structures of maize.

Treatment	Grain weight (g plant^{-1})		Grain number (plant^{-1})		Thousand grain weight (g)	
	Measured value	△CK (%)	Measured value	△CK (%)	Measured value	△CK (%)
CK	67.1 ± 44.0a	—	177.0 ± 120.3ab	—	395.7 ± 41.0a	—
A0	0.0 ± 0.0b	-100.0	0.0 ± 0.0c	-100.0	0.0 ± 0.0d	-100.0
A1	41.1 ± 25.0ab	-38.7	121.7 ± 54.1b	-31.3	321.2 ± 57.5ab	-18.8
A2	58.7 ± 3.1a	-12.5	241.0 ± 4.0a	36.2	243.5 ± 8.7c	-38.5
A3	62.3 ± 25.8a	-7.1	215.3 ± 84.3ab	21.7	288.9 ± 52.6bc	-27.0
A4	43.3 ± 1.8a	-35.4	188.3 ± 40.1ab	6.4	237.8 ± 57.2c	-39.9

Notes: data in the table are X ± SD ($n = 3$), different lowercase letters in the same column indicate significant difference ($P < 0.05$) based on the LSD test.

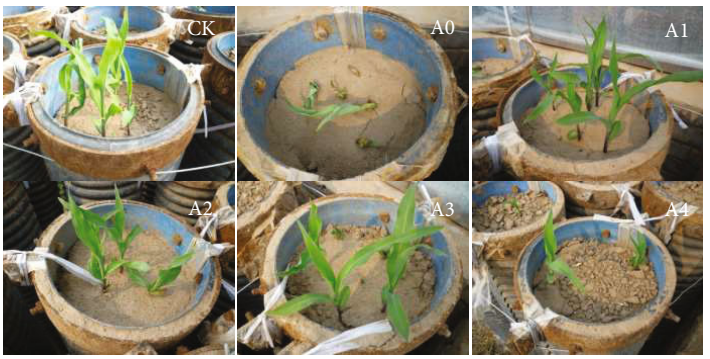

Figure 1: Effects of herbicides on the growth of maize seedlings. Note: CK, the no herbicide negative control; A0, a preemergence nonspecific herbicide for maize, dinitraniline (the active control); A1-A4: four preemergence maize specific herbicides, nicosulfuron+atrazine, alachlor +acetochlor+atrazine, propisochlor+atrazine, and acetochlor+atrazine, respectively.

Table 3: Effects of herbicides on the alpha diversity of bacteria in the rhizosphere soil of maize.

Soil layer (cm)	Treatment	Shannon		ACE		Chao 1	
		Measured value	△CK (%)	Measured value	△CK (%)	Measured value	△CK (%)
0-20	CK	7.6	—	26109.7	—	15204.3	—
	A0	7.6	0.9	30042.1	15.1	16573.7	9.0
	A1	7.5	-1.2	20645.4	-20.9	13299.7	-12.5
	A2	7.7	2.3	25091.6	-3.9	15564.7	2.4
	A3	7.8	3.2	27539.3	5.5	16687.2	9.8
	A4	7.5	-0.2	29388.9	12.6	16735.1	10.1
20-40	CK	7.6	—	31795.4	—	17283.6	—
	A0	7.5	-1.6	21090.5	-33.7	12400.6	-28.3
	A1	7.4	-3.1	24043.1	-24.4	14098.2	-18.4
	A2	7.4	-2.3	30041.6	-5.5	16472.0	-4.7
	A3	7.4	-2.4	18942.7	-40.4	11330.8	-34.4
	A4	7.6	-0.3	33844.3	6.4	17851.1	3.3
40-60	CK	7.5	—	19817.4	—	12125.5	—
	A0	7.8	4.1	30746.0	55.2	18073.9	49.1
	A1	7.3	-3.2	21884.8	10.4	13089.6	8.0
	A2	7.6	1.5	22149.7	11.8	13397.3	10.5
	A3	7.5	0.5	25644.3	29.4	15070.1	24.3
	A4	7.5	-0.3	29077.7	46.7	16219.4	33.8

Note: CK, the no herbicide negative control; A0, a preemergence nonspecific herbicide for maize, dinitraniline (the active control); A1-A4: four preemergence maize-specific herbicides, nicosulfuron+atrazine, alachlor+acetochlor+atrazine, propisochlor+atrazine, and acetochlor+atrazine, respectively.

In contrast to bacteria, the Shannon index of fungi in the herbicides treated 0-20 cm soil was increased by 21.0%-39.9% than that of the control. In the 0-20 cm soils, the fungal ACE and Chao1 indices in the A3 and A4 treated soils were higher than other herbicides. For the 20-40 cm soil, A0 increased the fungal ACE and Chao1 indices by 32.8% and 29.8%, respectively, over that of the control, while the other four herbicides showed negligible effects. A0, A1, A3, and A4 increased the fungal ACE and Chao1 indices by 21.4%-62.1% in the 40-60 cm soil than the nonherbicide control treatment (Table 4).

3.3. Effects of Herbicides on the Composition of the Microbial Community in the Rhizosphere Soil of Maize

3.3.1. Bacterial Community. At the phylum level, herbicides affected the bacterial community composition in the 0-20 cm soil greater than in the 20-40 and 40-60 cm soils, with A1 showing the greatest effect. In the 0-20 cm soil, Bacteroidetes, Firmicutes, and Proteobacteria were the top three dominant phyla in the CK treatment. A1 decreased the relative abundance of Bacteroidetes and Firmicutes greatly, from 27.8% and 26.0% in the CK soil to 5.5% and 4.4%, whereas increased the relative abundance of Proteobacteria, from 22.3% in the CK soil to 37.7%. The relative abundance of Actinobacteria in the A1 treated 0-20 cm soil was 693.0% more than that in the control and made Actinobacteria become the second dominant phylum. The relative abundances of Gemmatimonadetes and Planctomycetes in the A1 treated 0-20 cm soil were also 423.5% and 225.0% more than that in the control. Compared with A1, A3 and A2 showed similar but weaker effects on the 0-20 cm soil bacterial community. A0 displayed the weakest effect on the 0-20 cm soil among the five tested herbicides. In the 20-40 cm and 40-60 cm soil, all herbicides showed weak effects on the bacterial community, with A1 and A0 displaying much greater effect than other herbicides, respectively (Figure 2(a)).

At the genus level, similar to the phylum level, A1 showed the greatest effect on the bacterial composition in the 0-20 cm soil and followed by A3 and A2. A1 reduced the relative abundance of *Prevotella*, *Barnesiella*, and *Lactobacillus*, the top three dominant genera in the 0-20 cm CK soil, from 11.3%, 7.5%, and 5.3% to 0.1%, 0.1%, and 1.1%, respectively. The relative abundance of *Clostridium* IV was also dropped from 2.1% in the CK soil to only 0.1%. In contrast, A1 increased the relative abundance of *Pseudomonas*, *Sphingomonas*, *Gemmatimonas*, Gp6, and *Aciditerrimonas* by 225.7%-1153.3% more when compared with no herbicide control. Similar with A1, A3 and A2 also increased the relative abundance of these above five bacterial genera by 118.2%-446.9% more when compared with the control. In the 20-40 cm and 40-60 cm soils, all herbicides displayed weak effects on the bacterial community, while also with A0 showed much greater effect than the other herbicides in the 40-60 cm soil. A0 reduced the relative abundances of *Pseudomonas* and *Barnesiella* by 27.9% and 27.4% when compared with the control, whereas increased the relative abundances of *Sphingomonas*, *Gemmatimonas*, *Subdivision3_genera_incertae_sedis*, and *Clostridium* IV, by 36.7%-230.3% than that in the no herbicide control (Figure 2(b)).

3.3.2. Fungal Community. At the phylum level, a total of seven phyla were classified. Different from those in the bacterial community, all the five tested herbicides showed similar and great effects on the fungi community in the 0-20 cm rhizosphere soil. Ascomycota was the top one dominant fungal phylum in the CK soil at 0-20 cm layer, accounting for 45.0% of the total fungal community. Herbicides reduced the relative abundance of this phylum to 5.2%-7.9%. The relative abundance of the unclassified fungal phylum (Others) was also increased greatly, from 9.6% in the no herbicide control soil to 44.0%-67.9% in the herbicide-treated soils. A1 also increased the relative abundance of Basidiomycota greatly, by 202.4% than that in the CK treatment. A1 and A2 also reduced the relative abundance of Glomeromycota, and Chytridiomycota, by 32.5%-43.7% than that in the no herbicide control. In the 20-40 cm soil, A0 and A2 increased the relative abundance of Glomeromycota but reduced the relative abundance of the unclassified phylum, with the variation being 31.9%-82.4% when compared with the control. The relative abundance of Basidiomycota in the A3-treated soil and Ascomycota in the A4-treated soil was 194.6% and 189.5%, respectively, more than that in the control treatment. In the 40-60 cm soil, A0 and A1 displayed similar effects on the fungal community, with increasing relative abundance of Glomeromycota, Chytridiomycota, and Basidiomycota, whereas reducing relative abundance of the unclassified phyla (Others), whereas A2 showed opposite effects (Figure 3(a)).

At the genus level, similar to the phylum level, all herbicides displayed great and similar effects on the fungal community in the 0-20 cm soil, but different effects in the 20-60 cm soils. *Diatrype* was the top one dominant genus in the CK soil at 0-20 cm layer. Herbicides reduced the relative abundance of *Diatrype* from 42.0% in CK to only 2.1%-3.2%. In contrast, the relative abundance of the other genera in the herbicides applied 0-20 cm soil was increased from 18.2% in the control soil to 56.6%-73.9%. *Funneliformis* and *Powellomyces* were the third and fourth dominant fungal genus in the CK soil, accounting for 6.5% and 3.6% of the total fungal community. All herbicides reduced the relative abundance of *Funneliformis* and *Powellomyces*, with A2 and A3 showing greater reduction effects (42.9% and 55.5%, respectively) than the other three herbicides. Additionally, A1 also increased the relative abundance of *Stephanospora* greatly, from 0.1% in the control to 4.7%. In the 20-40 cm soil, A0 and A2 increased the relative abundance of *Rhizophagus*, the top one dominant genus in the CK soil, greatly, by 84.8% and 42.3% than that in the control, respectively. A0, A1, A2, and A3 reduced the relative abundance of *Diatrype*, the second dominant genus in the CK soil, with 61.3%, 67.9%, 37.6%, and 23.4% less than the control, respectively, whereas A4 increased it by 245.3% when compared with the control. In the 40-60 cm soil, A0 and A1 displayed similar effects on the fungal community, by increasing the relative abundance of *Rhizophagus*, *Funneliformis*, *Powellomyces*, and *Glomus*, whereas A2 showed opposite effects. A4 also greatly increased the relative abundance of *Diatrype* in the 20-40 cm and 40-60 cm soils, with 245.3% and 129.0% than that in the CK soil (Figure 3(b)).

Table 4: Effects of herbicides on the alpha diversity of fungi in the rhizosphere soil of maize.

Soil layer (cm)	Treatment	Shannon		ACE		Chao 1	
		Measured value	△CK (%)	Measured value	△CK (%)	Measured value	△CK (%)
0-20	CK	4.1	—	2952.8	—	2328.9	—
	A0	5.6	38.1	3190.9	8.1	2572.6	10.5
	A1	5.6	36.7	2978.8	0.9	2589.3	11.2
	A2	4.9	21.0	3043.3	3.1	2303.8	-1.1
	A3	5.7	39.9	3987.5	35.0	3026.1	29.9
	A4	5.4	31.8	3488.6	18.1	2825.7	21.3
20-40	CK	4.8	—	3373.7	—	2575.8	—
	A0	5.2	10.2	4479.9	32.8	3343.4	29.8
	A1	5.1	7.2	3495.0	3.6	2760.6	7.2
	A2	5.4	13.2	3637.7	7.8	2679.6	4.0
	A3	5.4	13.6	3261.7	-3.3	2707.8	5.1
	A4	4.8	1.1	3019.6	-10.5	2463.6	-4.4
40-60	CK	5.2	—	2584.1	—	2181.4	—
	A0	5.3	1.9	3621.1	40.1	2647.5	21.4
	A1	5.3	2.9	4189.2	62.1	2806.1	28.6
	A2	4.5	-12.5	2337.6	-9.5	1843.0	-15.5
	A3	5.4	3.7	3508.7	35.8	2670.5	22.4
	A4	5.3	1.7	3522.1	36.3	2875.7	31.8

Note: CK, the no herbicide negative control; A0, a preemergence nonspecific herbicide for maize, dinitraniline (the active control); A1-A4: four preemergence maize specific herbicides, nicosulfuron+atrazine, alachlor+acetochlor+atrazine, propisochlor+atrazine, and acetochlor+atrazine, respectively.

3.4. Effects of Herbicides on the Urease Activity in the Rhizosphere Soil of Maize. A0 significantly decreased the urease activity in the 0-60 cm layer rhizosphere soil by 30.6%-38.6% than the control, whereas A1 did not affect the urease activity in the same layer soils. A2, A3, and A5 did not significantly affect the urease activity in the 0-20 and 20-40 cm rhizosphere soils, whereas A2 and A3 increased the urease activity in the 40-60 cm rhizosphere soil, by 27.1% and 19.8% than that in the CK soils. As the layer increased, the urease activity did not change significantly in the A0, A1, and CK treatments but significantly increased in the A2- and A3-treated soils. The urease activity in the A4-treated 40-60 cm soil was also 24.2% higher than that in the 0-20 cm soil (Table 5).

4. Discussion

4.1. Herbicides Affected Rhizosphere Soil Microbial Structure. Soil microorganisms are the main components of the agricultural microbial system, play key roles in nutrient cycling and energy flow, and are considered as indicators to reflect the effects of herbicides on the soil environment [2, 6, 16, 31]. Rhizosphere soil connected with plant roots tightly; hence, the change of rhizosphere soil environment influences plant growth stronger than the nonrhizosphere ones. Rhizosphere environment, herbicides, and microorganisms interacted with each other closely [24]. Studying the effects of herbicides on the microbial communities in rhizosphere soils contributes to reveal the effective mechanisms of herbicides on both microbial environment and plant growth. At present, the effects of herbicides on microorganisms in nonrhizosphere maize soil had been reported widely. Niewiadomska et al. found that a mixed herbicide (containing nicosulfuron or mesotrione) increased the total number of cultivable microorganisms in 0-20 cm maize soil under field condition [30]. Borowik et al. sprayed a mixture herbicide of terbuthylazine, mesotrione, and S-metolachlor to potted maize soil, and found that herbicides altered both the population and ecophysiological diversity of the cultivatable soil bacteria, actinomycetes, and fungi [19]. Xu et al. also analyzed the effects of starane on 0-15 cm maize soil on field scale that used the high-throughput sequencing technology [13]. However, few studies had been done to clarify the effects of herbicides on maize rhizosphere soil at different depths. In this present study, we tested the effects of five preemergence herbicides on maize rhizosphere soil at the maturity stage and found that the tested herbicides affected both the bacterial and fungal communities in the rhizosphere soil of maize in general, with nicosulfuron+atrazine (A1) displaying the greatest effect on bacteria, whereas dinitraniline (A0) showed the weakest effect, while all herbicides displayed similar effects on fungi diversity and community structure in the 0-20 cm soil. In our study, herbicides altered both the dominant microbial groups and abundance largely. Considering that A1 did not significantly reduce the maize grain weight but A0 application got no grain (Table 2), it indicates that the microbial community, especially the bacterial community structure in the 0-20 cm rhizosphere soil adjusted by herbicides contributes to the alleviation of the harmful effects on maize caused by herbicides.

After entering into soils, herbicides affect the growth of soil microorganisms either by directly feed soil microorganisms as

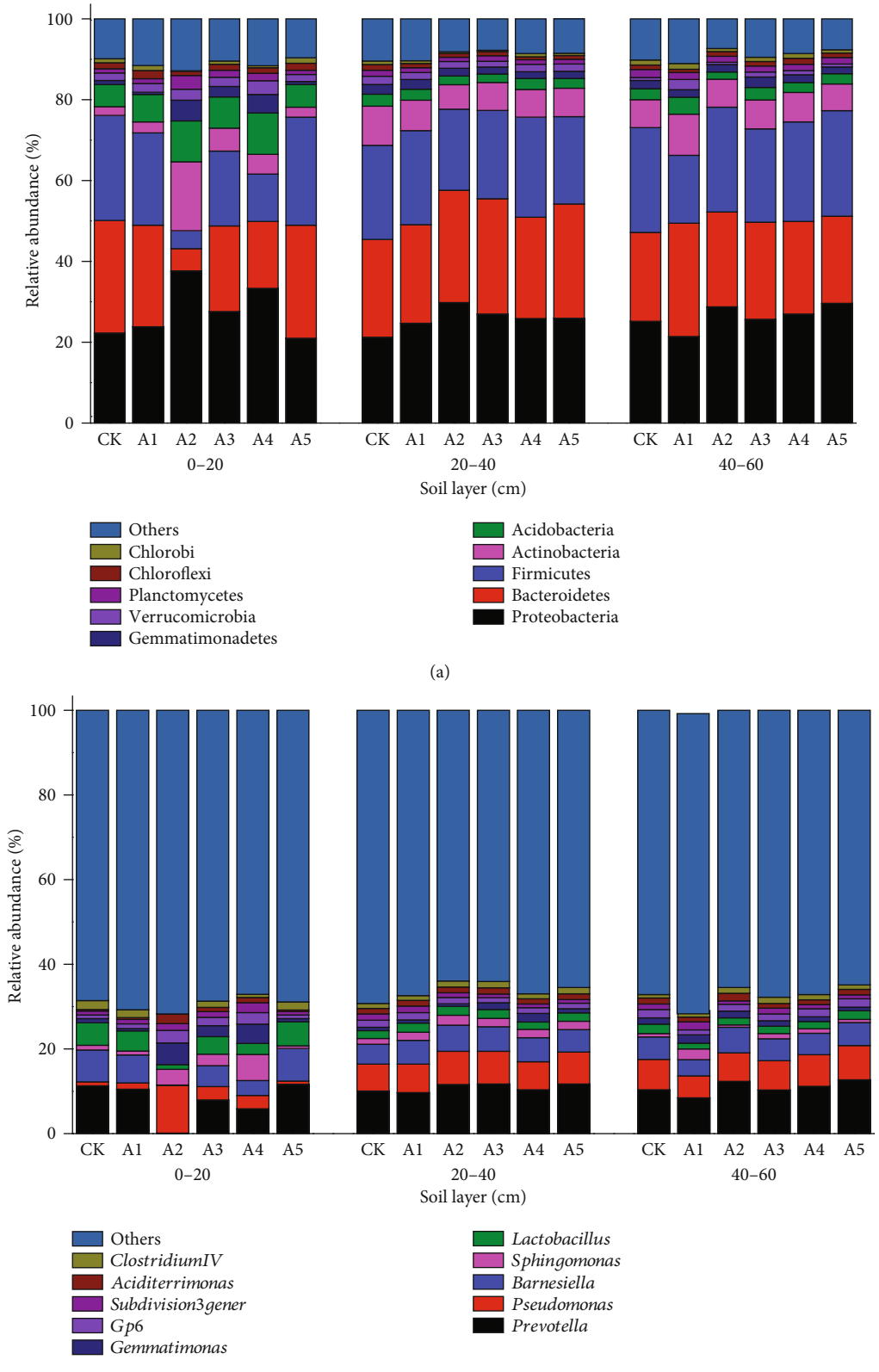

Figure 2: Relative abundance of the top ten bacteria in the phylum (a) and genus (b) level in the 0-20 cm, 20-40, and 40-60 cm rhizosphere soils. Note: CK, the no herbicide negative control; A0, a preemergence nonspecific herbicide for maize, dinitraniline (the active control); A1-A4: four preemergence maize specific herbicides, nicosulfuron+atrazine, alachlor+acetochlor+atrazine, propisochlor+atrazine, and acetochlor+atrazine, respectively.

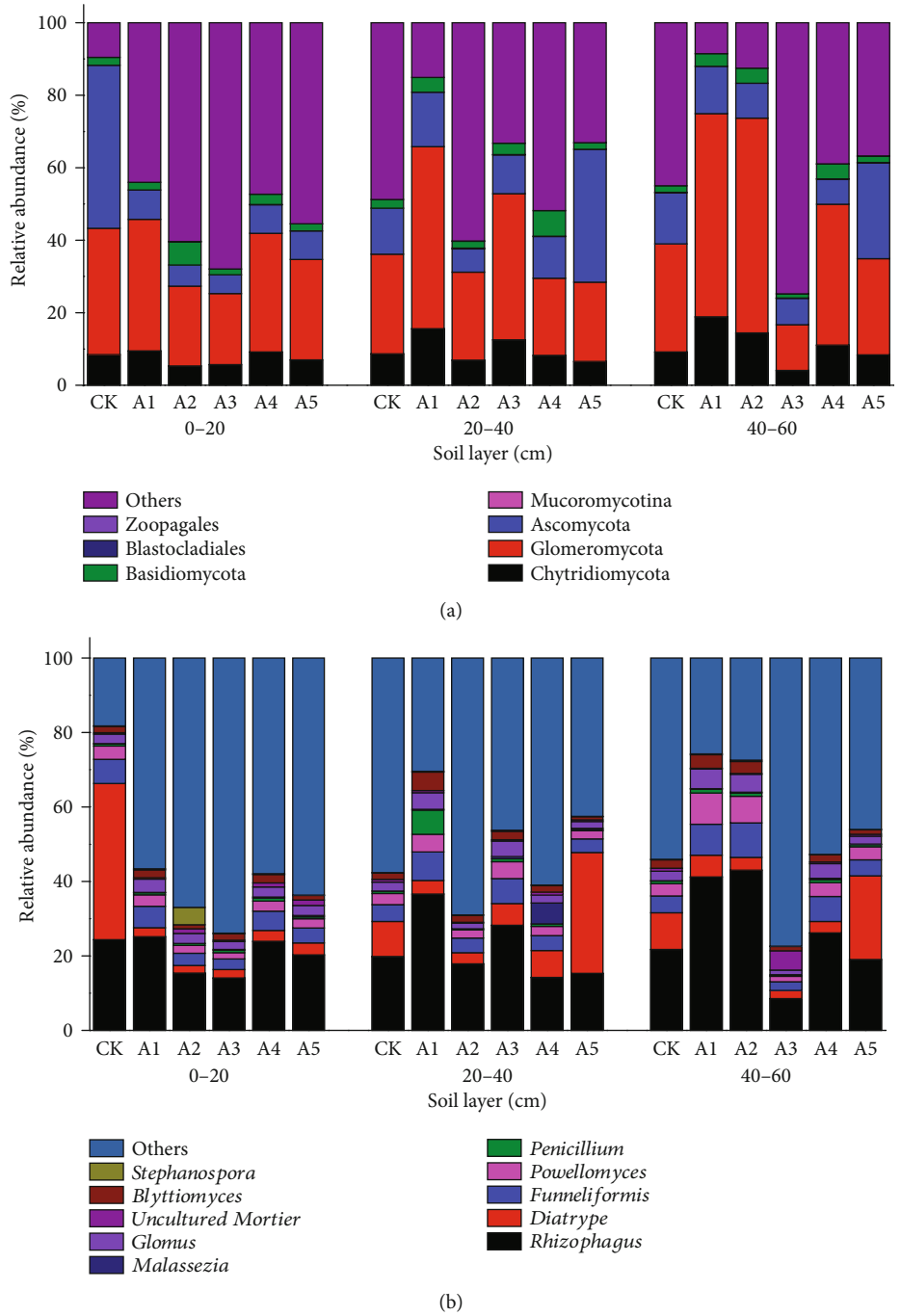

Figure 3: Relative abundance of the top ten fungi in the phylum (a) and genus (b) level in the 0-20, 20-40, and 40-60 cm rhizosphere soils. Note: CK, the no herbicide negative control; A0, a preemergence nonspecific herbicide for maize, dinitraniline (the active control); A1-A4: four preemergence maize specific herbicides, nicosulfuron+atrazine, alachlor+acetochlor+atrazine, propisochlor+atrazine, and acetochlor +atrazine, respectively.

an energy source, or indirectly by influencing the chemical environment, and then regulating the growth of soil microorganisms [32]. Zhou et al. thought that the increase of bacteria in soybean rhizosphere soil under fomesafen treatment might due to this herbicide provided more energy substances for some bacterial growth [24]. The application of sulfonylurea herbicide into winter wheat soil induced a chemical stress on soil and, then, influenced both the plants and the soil bacteria [14]. As it is well known that soil microbial community is regulated by plant root exudates, hence, herbicides may also influence soil microbial community through altering the growth of plant roots and the secretion of root exudates. This speculation still needs further researches.

Soil microorganisms may also reversely regulate the effects of herbicides on the soil environment by degrading the harmful active substances of herbicides. These herbicide-degrading microorganisms include *Bacillus* spp., *Pseudomonas* sp., and arbuscular mycorrhizal fungi [33–36]. In our research, the

Table 5: Effects of herbicides on the urease activity in the rhizosphere soil of maize.

Treatment	Soil layer (cm) 0-20 Measured value (mg g^{-1})	△CK%	20-40 Measured value (mg g^{-1})	△CK %	40-60 Measured value (mg g^{-1})	△CK %
CK	132.1 ± 6.6aA	—	130.1 ± 2.4abA	—	122.2 ± 12.6bcA	—
A0	81.1 ± 35.2bA	-38.6	87.0 ± 40.9cA	-33.1	84.9 ± 35.0dA	-30.5
A1	107.3 ± 42.3abA	-18.8	109.9 ± 44.8bcA	-15.6	114.5 ± 41.6cA	-6.3
A2	135.7 ± 14.3aB	2.7	149.7 ± 4.6aA	15.0	155.4 ± 7.9aA	27.1
A3	121.5 ± 15.2aB	-8.0	143.4 ± 9.8aA	10.2	146.3 ± 16.8abA	19.8
A4	111.8 ± 14.9aB	-15.4	127.2 ± 28.4abAB	-2.2	138.8 ± 8.1abcA	13.6

Note: CK, the no herbicide negative control; A0, a preemergence nonspecific herbicide for maize, dinitraniline (the active control); A1-A4: four preemergence maize specific herbicides, nicosulfuron+atrazine, alachlor+acetochlor+atrazine, propisochlor+atrazine, and acetochlor+atrazine, respectively. Data in the table are X ± SD ($n = 6$), different lowercase letters in the same column indicate significant difference ($P < 0.05$) between treatments, and different capital letters in the same row indicate significant difference ($P < 0.05$) between layers based on the LSD test.

relative abundance of *Pseudomonas* in the A1-treated soil was far higher than that in the control soil. The harmful components in A1 were degraded into unharmful ones by soil microorganisms such as *Pseudomonas* may partly illustrate the weakest effect displayed by A1 on maize growth.

4.2. Herbicides Affected the Activity of Soil Urease. Soil enzymes take part in the biochemical process and nutrient cycling in soil, which influence soil microecology environment [37, 38]. Urease enzyme is related to the nitrogen transformation in soil and has been used to evaluate the effects of herbicides on soil biochemical environment [2, 24]. Borowik et al. demonstrated that a mixture of herbicide (containing terbuthylazine, mesotrione, and S-metolachlor) inhibited the activity of urease in 0-20 cm maize soil [19]. Results from Du et al. and Sun et al. showed that urease activity did not change much in the soil treated with mesotrione [16, 29]. In this present study, different herbicides showed different effects on urease activity in the rhizosphere soil at different layers, among which A0 significantly decreased the activity of urease in the 0-60 cm rhizosphere soil, and other herbicides did not affect urease activity largely in general, except for alachlor+acetochlor+atrazine (A2) significantly increased the urease activity in the 40-60 cm soil. A large part of soil enzymes are extracellular metabolites secreted by soil microorganisms [39]. Herbicides application altered both the structure and abundance of the soil microbial community, which affect the activity of soil enzymes. Herbicides may also affect the activity of soil enzymes by changing the cell lysis and cell membrane permeability [40, 41]. Herbicides may also act as substrates or inhibitors for the catalytic reaction of soil enzymes, which directly affect the activity of soil enzymes [24]. In addition, some researchers reported that herbicides may influence the activity of soil enzymes by regulating the growth of plant roots, altering the absorbing ability of roots to soil nutrient elements and the root activity [24]. Whether the tested herbicides displayed similar mechanisms on the activity of urease in maize rhizosphere soil still needs more studies.

In general, the effects of herbicides on soil microbial environment varied based on herbicide species and soil depths. Among the five tested herbicides, only A0 contains dinitraniline, and the other four herbicides all contain atrazine. Among the four maize-specific herbicides, only A1 contains a sulfonylurea component (nicosulfuron), whereas the other three herbicides instead with chloroacetamide ones (alachlor, acetochlor, or propisochlor). When considering soil depth, the tested herbicides affected the microbial community stronger in the 0-20 cm layer than in the 20-60 ones, whereas A0 and A1 showed consistent effects, but A2-A4 first showed insignificant effect but, then, increased the activity of soil urease with the soil depth increased. The differences in chemical characteristic, degradation, and migration rates of active components in the five tested herbicides may partly explain these inconsonant results among different soil layers. Further experiments still need to be done to confirm this speculation.

4.3. Conclusions. The use of herbicide is still a common measure to control weed damage in maize field. Herbicides affect both soil microbial environment, and the activity of soil enzymes has been reported. However, the effects of preemergence herbicides on the microbial environment of maize rhizosphere soil after applying for a relatively long time are still unclear. In this research, we applied five preemergence herbicides on maize soil and investigated the effects of herbicides on microbial community and urease activity in the rhizosphere soil of maize in different layers at the maturity stage. We found that among the five tested herbicides, nicosulfuron+atrazine (A1) largely altered the bacterial community structure especially in the 0-20 cm layers and showed insignificant effect on the activity of urease in the 0-60 cm rhizosphere soils, with other three maize-specific herbicides (A2-A4) displayed mild effects. The nonspecific herbicide of maize, A0, changed the microbial community slightly but dramatically dropped the activity of urease in the 0-60 rhizosphere soils. Considering that A1 did not affect the grain yield of maize, but A0 totally suppressed the development of maize grain, we proposed that A1 was a suitable herbicide for maize, and both the bacterial community structure and the urease activity in the rhizosphere soil at 0-20 cm layers are suitable indicators for evaluating the effects of herbicides on maize plant growth and soil microbial environment. The differences in active components may contribute to explain the differences among herbicide species and soil depths.

Data Availability

The data used to support the findings of this study are available from the corresponding author upon request.

Conflicts of Interest

The authors declare no conflict of interest.

Acknowledgments

This work was financially supported by the Key Project of Shanxi Key R&D Program of China (201703D211001-02), the Special Plan of Scientific Research for Shanxi Agriculture Valley of China (SXNGJSKYZX 201701), the Shanxi Collaborative Innovation Centre of Featured Crops High-quality and Efficiency Production in Loess Plateau ([2016]5), the "1331 Project" Crop Ecology and Dry Cultivation Physiology Key Laboratory of Shanxi Province (201705D111007, [2017]14), the "1331 Project" Organic Dry Farming and Cultivating Physiology Innovation Team Project of Shanxi Province ([2018]4), the Modern Agriculture Industry Technology System Construction (CARS-03-01-24), the Science and Technology Innovation Foundation of Shanxi Agricultural University (2019002), and the University Science and Technology Innovation Foundation of Shanxi Province (2020L0159).

References

[1] B. Mitra, P. M. Bhattacharya, A. Ghosh, K. Patra, A. K. Chowdhury, and M. K. Gathala, "Herbicide options for effective weed management in zero-till maize," *Indian Journal of Weed Science*, vol. 50, no. 2, pp. 137–141, 2018.

[2] J. A. Kumari, P. C. Rao, M. Madhavi, and G. Padmaja, "Effect of herbicides on the activity of soil enzymes urease in maize crop," *Indian Journal of Agricultural Research*, vol. 52, no. 3, pp. 300–304, 2018.

[3] T. J. Xu, T. F. Lv, J. R. Zhao et al., "Effects of herbicides on growth, development and yield of different maize varieties," *Chinese Journal of Eco-Agriculture*, vol. 26, no. 8, pp. 1159–1169, 2018.

[4] L. T. Qi, Z. Q. Li, X. Q. Li et al., "Effect of 4 herbicides on weed control and the growth, yield of maize," *Journal of Shanxi Agricultural Sciences*, vol. 44, no. 10, pp. 1519–1521, 2016.

[5] H. Yan, L. J. Wang, and H. Y. Dong, "Control effects of six herbicides on weed in maize field," *Liaoning Agricultural Sciences*, vol. 2, no. 2, pp. 64–67, 2017.

[6] C. Thiour-Mauprivez, F. Martin-Laurent, C. Calvayrac, and L. Barthelmebs, "Effects of herbicide on non-target microorganisms: Towards a new class of biomarkers?," *Science of the Total Environment*, vol. 684, pp. 314–325, 2019.

[7] H. Fang, J. Lian, H. Wang, L. Cai, and Y. Yu, "Exploring bacterial community structure and function associated with atrazine biodegradation in repeatedly treated soils," *Journal of Hazardous Materials*, vol. 286, pp. 457–465, 2015.

[8] J. L. Pereira, S. C. Antunes, B. B. Castro et al., "Toxicity evaluation of three pesticides on non-target aquatic and soil organisms: commercial formulation versus active ingredient," *Ecotoxicology*, vol. 18, no. 4, pp. 455–463, 2009.

[9] F. Ackerman, "The economics of atrazine," *International Journal of Occupational and Environmental Health*, vol. 13, no. 4, pp. 437–445, 2007.

[10] A. Chowdhury, S. Pradhan, M. Saha, and N. Sanyal, "Impact of pesticides on soil microbiological parameters and possible bioremediation strategies," *Indian Journal of Microbiology*, vol. 48, no. 1, pp. 114–127, 2008.

[11] X. N. Wu, J. J. Sun, Y. Y. Lu, W. J. Liu, and J. Yao, "Effect of glyphosate on energy metabolism of soil microorganisms," *Chemistry and Bioengineering*, vol. 4, no. 5, pp. 18–21, 2016.

[12] B. B. Liu, D. Chen, Q. Y. Kang, M. Q. Liu, H. X. Li, and J. G. Jiao, "The biological indication of soil organisms to soil environment of insecticide factory," *Chinese Journal of Soil Science*, vol. 44, no. 5, pp. 1210–1217, 2013.

[13] Y. R. Xu, Z. J. Fang, X. P. Lu, and L. J. Hao, "Effects of starane on maize soil bacterial diversity analyzed by high-throughput sequencing technology," *Acta Microbiologica Sinica*, vol. 57, no. 7, pp. 985–993, 2017.

[14] O. S. Bezuglova, A. V. Gorovtsov, E. A. Polienko et al., "Effect of humic preparation on winter wheat productivity and rhizosphere microbial community under herbicide-induced stress," *Journal of Soils and Sediments*, vol. 19, no. 6, pp. 2665–2675, 2019.

[15] R. M. Kepler, D. J. Epp Schmidt, S. A. Yarwood et al., "Soil microbial communities in diverse agroecosystems exposed to the herbicide glyphosate," *Applied and Environmental Microbiology*, vol. 86, no. 5, p. e01744, 2020.

[16] Z. Du, Y. Zhu, L. Zhu et al., "Effects of the herbicide mesotrione on soil enzyme activity and microbial communities," *Ecotoxicology and Environmental Safety*, vol. 164, pp. 571–578, 2018.

[17] A. T. Adetunji, F. B. Lewu, R. Mulidzi, and B. Ncube, "The biological activities of β-glucosidase, phosphatase and urease as soil quality indicators: a review," *Journal of Soil Science and Plant Nutrition*, vol. 17, no. 3, pp. 794–807, 2017.

[18] Z. Hao, W. Mu, Z. Hou, X. Wu, and S. Zhang, "Biodegradation of nicosulfuron by the bacterium Serratia marcescens N80," *Journal of Environmental Science and Health. Part. B, Pesticides, Food Contaminants, and Agricultural Wastes*, vol. 47, no. 3, pp. 153–160, 2012.

[19] A. Borowik, J. Wyszkowska, J. Kucharski, M. Baćmaga, and M. Tomkiel, "Response of microorganisms and enzymes to soil contamination with a mixture of terbuthylazine, mesotrione, and S-metolachlor," *Environmental Science Pollution Research*, vol. 24, no. 2, pp. 1910–1925, 2017.

[20] Q. Zhang, L. Zhu, J. Wang et al., "Effects of fomesafen on soil enzyme activity, microbial population, and bacterial community composition," *Environmental Monitoring and Assessment*, vol. 186, no. 5, pp. 2801–2812, 2014.

[21] Z. J. Xie, H. L. Li, C. X. Xu, Q. Zhang, and G. R. Liu, "Effects of two kinds of herbicides on paddy soil ecology and growth of succeeding crops," *Acta Pedologica Sinica*, vol. 51, no. 4, pp. 880–887, 2014.

[22] M. M. Hart, J. R. Powell, R. H. Gulden et al., "Separating the effect of crop from herbicide on soil microbial communities in glyphosate-resistant corn," *Pedobiologia*, vol. 52, no. 4, pp. 253–262, 2009.

[23] A. Singh, M. L. Kewat, and S. Sondhia, "Studies on the effect of day time application of herbicide mesosulfuronmethyl on soil microbial communities of wheat rhizosphere," *Journal of Environmental Biology*, vol. 39, no. 1, pp. 59–65, 2018.

[24] S. X. Zhou, Z. J. Wei, H. Y. Hu, B. J. Gao, and Z. J. Li, "Effects of fomesafen on soil microorganisms, soil enzyme activities and its degradation in soybean rhizosphere," *Journal of Plant Nutrition and Fertilizers*, vol. 24, no. 1, pp. 203–211, 2018.

[25] B. Yan, Y. Qi, G. Fu, J. He, N. W. Xiao, and J. S. Li, "Effects of atrazine on soil microbial functional diversity of wild weed communities," *Research of Environmental Sciences*, vol. 30, no. 8, pp. 1246–1254, 2017.

[26] J. L. Xu, N. J. Hu, Z. W. Zhang, B. R. Tao, and L. Q. Zhu, "Effects of two herbicides on soil microbes and enzyme activities in a paddy field," *Bulletion of Soil and Water Conservation*, vol. 35, no. 4, pp. 168–171, 2015.

[27] J. G. Zaller, C. Cantelmo, G. D. Santos et al., "Herbicides in vineyards reduce grapevine root mycorrhization and alter soil microorganisms and the nutrient composition in grapevine roots, leaves, xylem sap and grape juice," *Environmental Science and Pollution Research*, vol. 25, no. 23, pp. 23215–23226, 2018.

[28] K. Mandl, C. Cantelmo, E. Gruber, F. Faber, B. Friedrich, and J. G. Zaller, "Effects of glyphosate-, glufosinate- and flazasulfuron-based herbicides on soil microorganisms in a vineyard," *Bulletin of Environmental Contamination and Toxicology*, vol. 101, no. 5, pp. 562–569, 2018.

[29] Y. B. Sun, R. L. Wang, Y. M. Xu, X. F. Liang, L. Wang, and G. L. Zhang, "Ecological effects of herbicide mesotrione on soil microbial communities," *China Environmental Science*, vol. 36, no. 1, pp. 190–196, 2016.

[30] A. Niewiadomska, H. Sulewska, A. Wolna-Maruwka, Z. Waraczewska, A. Budka, and K. Ratajczak, "AN assessment of the influence of selected herbicides on the microbial parameters of soil in maize (*Zea mays*) cultivation," *Applied Ecology and Environmental Research*, vol. 16, no. 4, pp. 4735–4752, 2018.

[31] L. Z. Han, D. G. Zhao, and X. X. Luo, "Effects of herbicide 2,4-D on soil microbial population," *Guizhou Agricultural Sciences*, vol. 42, no. 2, pp. 85–88, 2014.

[32] M. E. Pampulha and A. Oliveira, "Impact of an herbicide combination of bromoxynil and prosulfuron on soil microorganisms," *Current Microbiology*, vol. 53, no. 3, pp. 238–243, 2006.

[33] J. Liu, S. H. Chen, J. Ding, Y. Xiao, H. Han, and G. Zhong, "Sugarcane bagasse as support for immobilization of Bacillus pumilus HZ-2 and its use in bioremediation of mesotrione-contaminated soils," *Applied Microbiology and Biotechnology*, vol. 99, no. 24, pp. 10839–10851, 2015.

[34] L. Carles, M. Joly, F. Bonnemoy, M. Leremboure, I. Batisson, and P. Besse-Hoggan, "Identification of sulfonylurea biodegradation pathways enabled by a novel nicosulfuron-transforming strain *Pseudomonas fluorescens* SG-1: toxicity assessment and effect of formulation," *Journal of Hazardous Materials*, vol. 324, Part B, pp. 184–193, 2017.

[35] L. Carles, M. Joly, F. Bonnemoy et al., "Biodegradation and toxicity of a maize herbicide mixture: mesotrione, nicosulfuron and S-metolachlor," *Journal of Hazardous Materials*, vol. 354, no. 15, pp. 42–53, 2018.

[36] X. Gao, X. Fan, S. Zhang, and F. Song, "The effect of herbicide application on arbuscular mycorrhizal fungi in farmland: a review," *Chinese Agricultural Science Bulletin*, vol. 36, no. 27, pp. 129–134, 2020.

[37] W. P. Yang, C. H. Wang, and Z. G. Ru, "Effect of returning straw to field on rhizosphere microorganisms and soil enzyme activity of winter wheat cultivar bai-nong ai-kang 58," *Journal of Northeast Agricultural University*, vol. 42, no. 7, pp. 20–24, 2011.

[38] G. F. Ge, Z. J. Li, J. Zhang et al., "Geographical and climatic differences in long-term effect of organic and inorganic amendments on soil enzymatic activities and respiration in field experimental stations of China," *Ecological Complexity*, vol. 6, no. 4, pp. 421–431, 2009.

[39] C. Follmer, "Insights into the role and structure of plant ureases," *Phytochemistry*, vol. 69, no. 1, pp. 18–28, 2008.

[40] E. Romero, J. Fernández-Bayo, J. M. C. Díaz, and R. Nogales, "Enzyme activities and diuron persistence in soil amended with vermicompost derived from spent grape marc and treated with urea," *Applied Soil Ecology*, vol. 44, no. 3, pp. 198–204, 2010.

[41] S. Hussain, T. Siddique, M. Saleem, M. Arshad, and A. Khalid, "Chapter 5 impact of pesticides on soil microbial diversity, enzymes, and biochemical reactions," *Advances in Agronomy*, vol. 102, no. 1, pp. 159–200, 2009.

Hindawi
Journal of Sensors
Volume 2021, Article ID 6692333, 11 pages
https://doi.org/10.1155/2021/6692333

Research Article

Analysis of Land Use Changes and Driving Forces in the Yanhe River Basin from 1980 to 2015

Zhihong Yao,[1] **Bo Wang**,[1] **Jie Huang**,[2] **Yu Zhang**,[1] **Jianchen Yang**,[1] **Rongxin Deng**,[1] **and Qinke Yang**[3]

[1]*School of Surveying, Mapping and Geographic Information, North China University of Water Resource and Electric Power, Zhengzhou 450046, China*
[2]*China Construction Bank Co., Ltd., Zhengzhou Railway Sub Branch, Zhengzhou 450000, China*
[3]*Department of Urban and Resource Sciences, Northwest University, Xi'an, 710069 Shaanxi, China*

Correspondence should be addressed to Qinke Yang; qkyang@126.com

Received 24 November 2020; Revised 7 March 2021; Accepted 2 April 2021; Published 21 April 2021

Academic Editor: Yuan Li

Based on the support of RS and GIS technology, this paper analyzes the spatial and temporal variation characteristics and driving forces of land use in the Yanhe River Basin through the processing and interpretation of remote sensing images in different periods from 1980 to 2015 and the methods of the land use transfer matrix and dynamic attitude. The results show that cropland, grassland, and forest land are the three types of land use with the most obvious changes, while urban land and water body have relatively small changes in the Yanhe River Basin. The transfer between cropland, forest land, and grassland and urban land is very obvious, among which the conversion rate of cropland is the highest. During the 15 years from 2000 to 2015, the land use types of the Yanhe River Basin changed by 13.17%, with an average annual growth rate of 0.88%. The implementation of ecological restoration and governance policy is the direct driving force of land use change in the Yanhe River Basin. The results obtained in this study can provide reference basis for land use planning and management and land use structure optimization in the Yanhe River Basin in the future.

1. Introduction

Land use change is an important manifestation of human activities on terrestrial surface ecosystems [1]. It mainly changes the nature of the surface through the joint action of climate change and human activities. Land use patterns are constantly changing with the rapid development of human society, so the change of land use is also an important way to reflect the impact of human activities on the natural environment [2]. Since the 21st century, lots of studies show that land use change has caused natural disasters, energy shortage, food shortage, economic crisis, and other social and ecological problems [3]. Therefore, the international geosphere biosphere program (IGBP) and the humanity factor in global environmental change program (IHDP) proposed the research on the rules of land use change and driving force analysis as the core research direction in order to reduce the negative impact of land use change on natural and social [4]. This is of great significance to the sustainable development of the society [5]. At present, human researches on land use change mainly focus on the speed of land use type change, direction of land use type transfer, degree of land use, and driving factors [6, 7]. In terms of research methods, scholars usually use mathematical statistics and establish the corresponding mathematical model by remote sensing images [8]. Many scholars in China have studied land use change in different scales by using different indicators. For the study of large-scale areas, Liu et al. [9, 10] analyzed the spatial and temporal change characteristics of large-scale regional land use in China in the early 21st century by

using the indicators of comprehensive land use dynamic attitude and land use degree change and revealed the spatial pattern and major driving factors of land use change in China through the dynamic land use zoning map. And they analyzed the temporal and spatial pattern and new characteristics of land use change in China from 2010 to 2015 by comparing with the temporal and spatial pattern of land use change in the early 21st century. For the study of small and medium scale areas, Liao et al. [11] analyzed the rate of change of land use in the Yellow River Basin based on the land use data in the six phases from 1980 to 2015 and analyzed the transfer types and quantities of land use in the whole basin and provinces within the basin from 1980 to 2000 and from 2000 to 2015 by using the land use transfer matrix, and finally pointed out that the most important factors driving the land use change in the Yellow River Basin were climate change, population increase, and economic development.

The Yanhe River Basin is a large tributary of the middle reaches of the Yellow River and also a key basin of sediment source of the Yellow River [12]. As a typical representative of hilly and gully region on the Loess Plateau, it has suffered serious soil erosion for a long time. Due to the overexploitation and utilization of land resources by human being and some nature factors, the ecological system in this region is very fragile and highly sensitive to external disturbance [13]. With the rapid development of social economy, especially after the implementation of the ecological policy of "returning farmland to forest" in China at the end of 1999, great changes have taken place in the land use structure of Yan River Basin and remarkable achievements have been made in soil and water conservation measures [14]. At present, abundant achievements have been made in the study of land use change in the Yanhe River Basin. For example, Li et al. [15] discussed the impact of land use change in the Yanhe River Basin on the ecological service value of the basin. Ran et al. [16] analyzed the scale conversion method of land use/cover change model in the Yanhe River Basin. Li et al. [17] analyzed the impact of soil and water conservation measures on runoff and sediment in the Yanhe River Basin. Wei et al. [18] and Xie et al. [19], respectively, revealed the impact of the policy of " returning farmland to forest" on the temporal and spatial change of land use and soil erosion in the Yanhe River Basin. However, there are relatively few researches on the land use change in the Yanhe River Basin in the longer time series. This study analyzed the temporal and spatial variation characteristics of land use in the Yanhe River Basin from 1980 to 2015 and analyzed the driving factors of land use change in the Yanhe River Basin in the past 35 years on this basis, so as to grasp the overall trend of land use change in the Yanhe River Basin in the past 35 years correctly and provide reference basis for land use planning and management and land use structure optimization in the Yanhe River Basin.

2. Data and Methods

2.1. Study Area. The Yanhe River Basin is located in the central loess Plateau in northern Shaanxi Province, the geographic coordinates are 36°21′-37°19′N and 108°38′-110°29′E (Figure 1). The basin covers a total area of 7,725 square kilometers, with a total length of 286.9 km, and is the second largest river in northern Shaanxi. The basin belongs to the continental semiarid climate of warm temperate zone, with annual rainfall of about 510 mm and average annual temperature of 9°C. The topographic conditions in the basin are complex, mainly loess hilly gully topography; soil and water loss is very serious. Natural disasters also occur frequently in the river basin, mainly including heavy rains, sandstorms, droughts, and frosts.

2.2. Data. In this study, seven stages of multispectral remote sensing images are selected for the Yanhe River Basin in 1980, 1990, 1995, 2000, 2005, 2010, and 2015. They are all from the geospatial data cloud (http://www.gscloud.cn), including Landsat3 (MSS), Landsat5 (TM), Landsat7 (ETM+), and Landsat8 (OLI). The operability of remote sensing images and the clarity of ground features should be taken into account when the classification system of land use change is established. According to the national general land use classification system and the actual situation of the Yanhe River Basin, combined with the related research of previous scholars, considering the weak changes of bare land and the possible influence on the accuracy of the supervised classification of remote sensing images, five main land use types, including cropland, forest land, grassland, urban land, and water area, were selected (Table 1).

Taking 2015 Landsat8 image pretreated as an example, band 5, band 4, and band 3 were selected for synthesis. Firstly, radiation calibration, atmospheric correction, and geometric correction were carried out for the images by ENVI processing tool. But the area of Yanhe River Basin is very large; three overlapped remote sensing images of each other need to be downloaded to cover it completely at least. And the vector boundary of the basin was used for clipping; the three images were joined by the seamless mosaic tool. Finally, visual interpretation was performed by combining topographic map, Google Earth and other tools with the SVM supervised classification method. According to the confusion matrix table, the overall classification accuracy is 95.87% and the kappa coefficient is 0.92, indicating good interpretation accuracy (Figure 2). At last, we obtained land use types maps of the Yanhe River Basin in seven stages (Figure 3).

2.3. Analysis Methods

2.3.1. Land Use Transfer Matrix. Land use transfer matrix is the application of the Markov model in land use change. The Markov model can not only quantitatively show the conversion between different land use types but also reveal the transfer rate between different land use types. Transfer matrix is the main method to conduct quantitative research on the quantity and direction characteristics of the mutual transformation between land use types, which can specifically reflect the structural characteristics of land use change and the direction of transfer among different

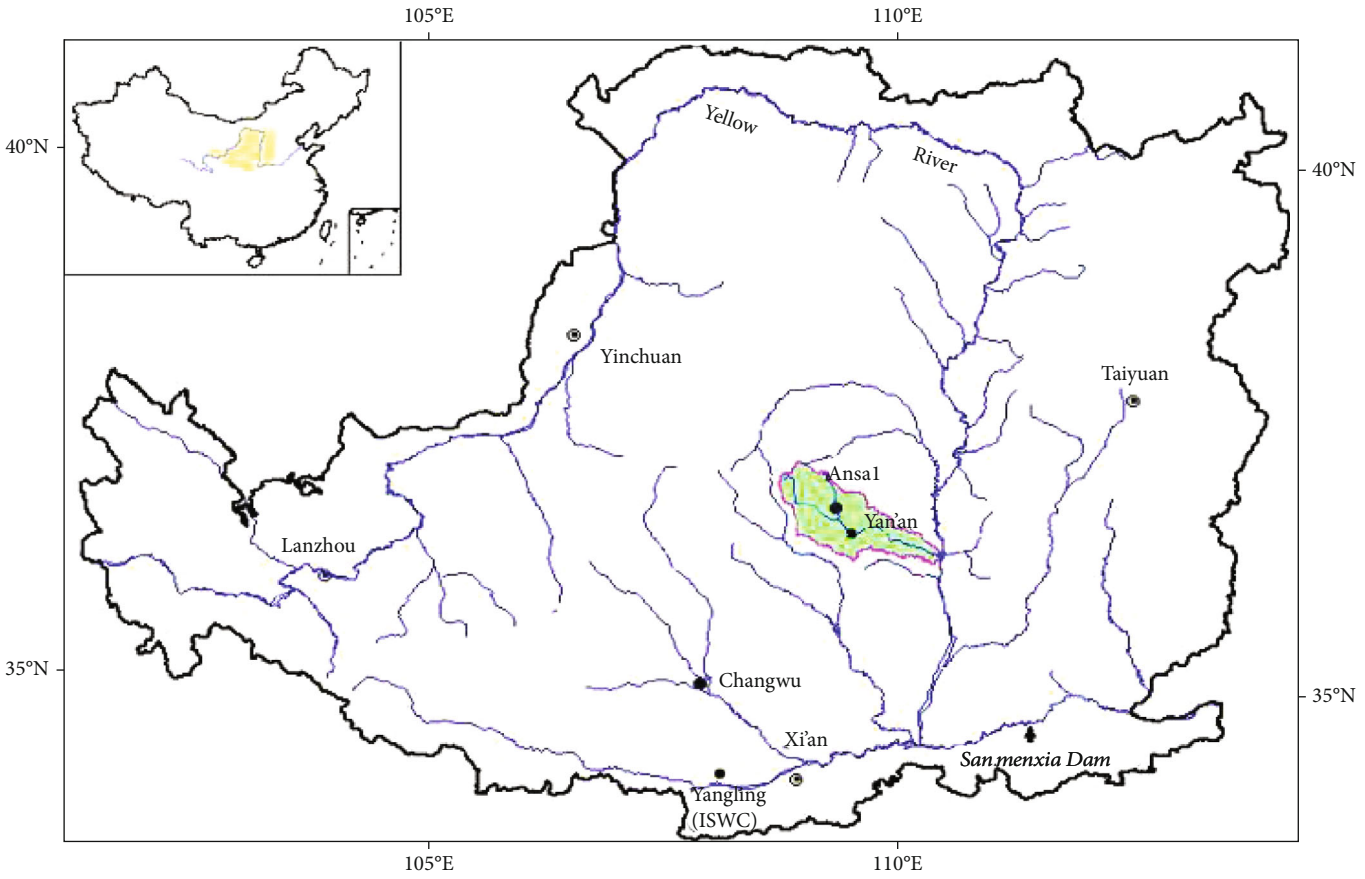

Figure 1: Location of the study area.

Table 1: Land use types.

Land use types	Meaning
Cropland	Refers to land planted with crops, including cultivated land, newly developed land, land for consolidation, and land for leisure
Forest land	Refers to the land where trees, bamboos, and shrubs grow and the land along the coast where mangroves grow
Grassland	Refers to the growth of herbaceous plants which is given priority to land
Water body	Refers to land water, ditches, hydraulic structures, and other land
Urban land	Refers to land used for industrial, mining, transportation, and other purposes outside counties and towns as well as other land used for construction purposes

types [20]. Its mathematical expression is as follows:

$$S_{ij} = \begin{Bmatrix} S_{11} & S_{12} & S_{13} \cdots & S_{1n} \\ S_{21} & S_{22} & S_{23} \cdots & S_{2n} \\ S_{31} & S_{32} & S_{33} \cdots & S_{3n} \\ \cdots & \cdots & \cdots \cdots & \cdots \\ S_{n1} & S_{n2} & S_{n3} \cdots & S_{nn} \end{Bmatrix}, \quad (1)$$

where S is the variation area of each land use type, n is total types of land use, and i and j are the types of land use at the beginning and end of the study.

2.3.2. Land Use Dynamic Attitude

(1) Single land use type dynamic attitude: it refers to the quantitative change of a certain land use type within a certain research area within a certain period [21], which is usually expressed by percentage, and its expression is as follows:

$$K_T = \frac{U_b - U_a}{U_a} \times 100\%, \quad (2)$$

where K_T is the dynamic attitude of a certain type of land use in the research area and U_a and U_b are the

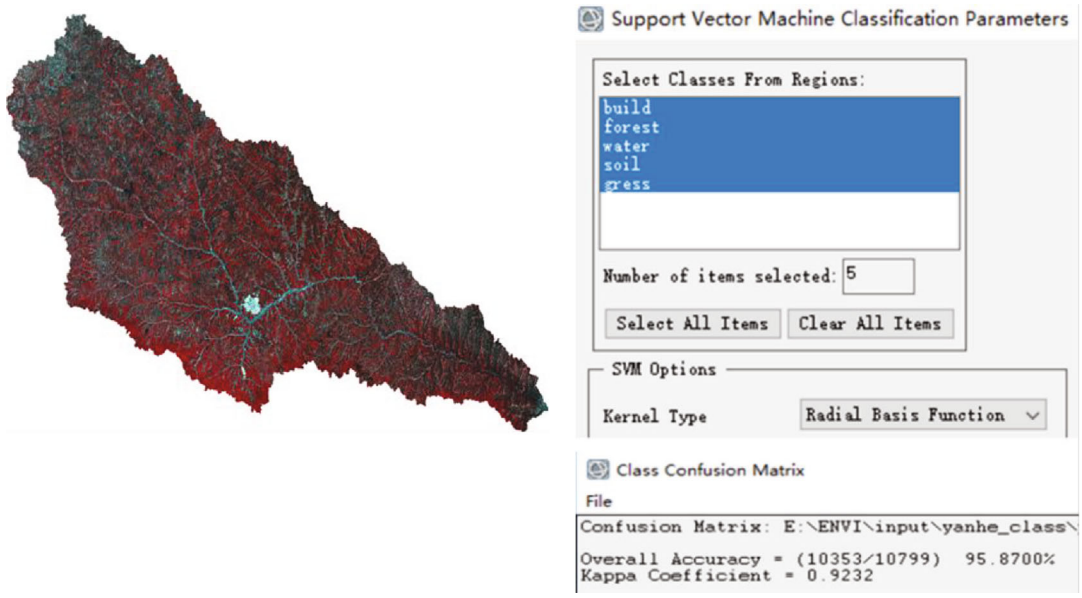

Figure 2: Processing and classification precision of remote sensing image in 2015.

areas of a certain type of land use at the beginning and end of the study.

(2) Comprehensive land use dynamic attitude: it reflects the total land activity attitude in the study area and refers to the percentage of the total area of each land use type changed in the study area [22]. Its expression is follows:

$$LC_T = \left(\frac{\sum_{i=1}^{n} \Delta LU_{ij}}{\sum_{i=1}^{n} LU_i} \right) \times 100\%, \quad (3)$$

where LC_T is comprehensive land use dynamic attitude, ΔLU_{ij} is the area of i land use types converted to non-$j(j = 1 \cdots n)$ land types during the study period, LU_i is the area of type I land use at the beginning of the study, and n is total types of land use.

3. Results and Analysis

3.1. General Characteristics of Land Use Change. According to the seven stages land use type maps, based on the initial implementation of the policy of returning farmland to forest (grass) in 2000, the land use change maps of the Yanhe River Basin from 1980 to 2000 and from 2000 to 2015 (Figures 4 and 5) and total land use change area of the Yanhe River Basin (Table 2) are obtained using Arcgis10.2, respectively.

Table 2 shows that the overall change range of land use types in the Yanhe River Basin was very small from 1980 to 2000. Forest land and grassland were the land types with the biggest change in area, and cropland, water body, and urban land had little change in area. The types of land use with increased area were forest land and urban land, respectively, and the types with decreased area were grassland, cropland, and water body. The area of forest land increased from 826.78 km^2 in 1980 to 857.77 km^2 in 2000, with an increase of 30.99 km^2, meanwhile the overall proportion of the Yanhe River Basin increased from 10.82% to 11.22%, with the largest increase of 0.4%. The area of grassland decreased from 3,473.14 km^2 in 1980 to 3,443.63 km^2 in 2000, with a decrease of 29.51 km^2. The overall proportion of the Yanhe River Basin decreased from 45.45% to 45.06%, with the largest decrease of 0.39%.

And from 2000 to 2015, cropland was the land with the largest area change, followed by the forest land and grassland, the water body with the smallest in the Yanhe River Basin. The types of land use with increased area were forest land, grassland, and urban land, and the types with decreased area were cropland and water body, respectively. The area of cropland decreased by 863.18km^2 from 3,289.13 km^2 in 2000 to 2,425.95 km^2 in 2015. The overall proportion of the Yanhe River Basin decreased from 43.04% to 31.74%, and the area decreased by 11.3%, with the largest reduction. The area of grassland increased from 3,443.63 km^2 in 2000 to 4,016.95 km^2 in 2015, with an increase of 573.32 km^2. The overall proportion of the Yanhe River Basin increased from 45.06% to 52.56%, and the area increased by 7.5%, with the largest increase. The area of forest land increased from 857.77 km^2 in 2000 to 1,127.50 km^2 in 2015, with an increase of 269.73 km^2. The overall proportion of the Yanhe River Basin increased from 11.22% to 14.75%, and the area increased by 3.53%, with an obvious increase. The area of urban land increased from 26.73 km^2 in 2000 to 46.93 km^2 in 2015, with an increase of 20.2 km^2. The overall proportion of the Yanhe River Basin increased from 0.35% to 0.61%, and the area increased by 0.26%, with an obvious increase.

3.2. Land Use Change Transfer Matrixes from 1980 to 2015. In order to explore the internal structure and characteristics of land use types in the Yanhe River Basin, four land use transfer matrixes are generated by superposition analysis of Arcgis10.2 (Table 3–6), so as to analyze the inflow and

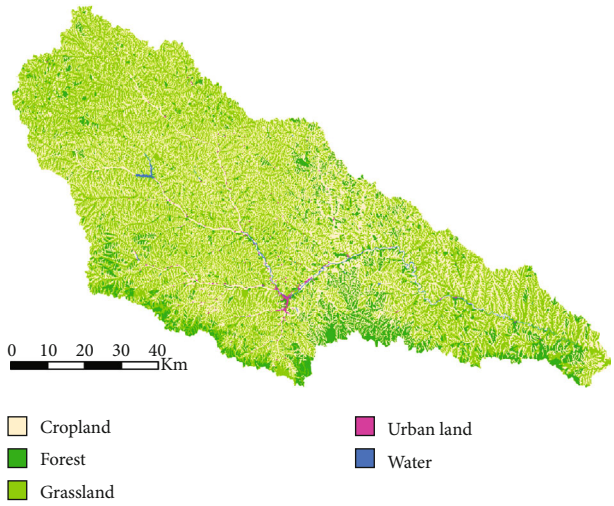

(a) Land use types of the Yanhe River Basin in 1980

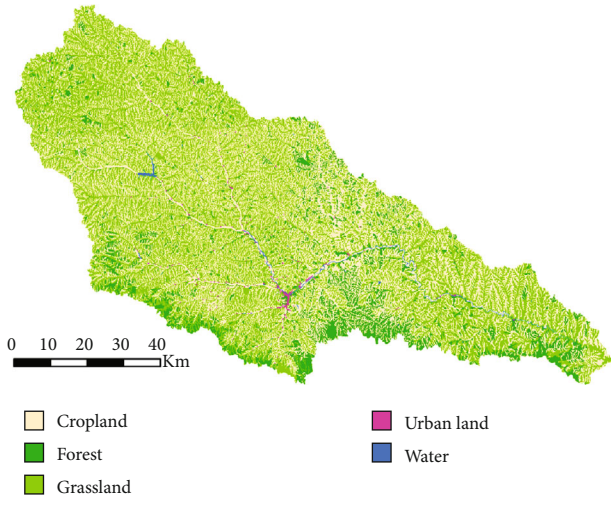

(b) Land use types of the Yanhe River Basin in 1990

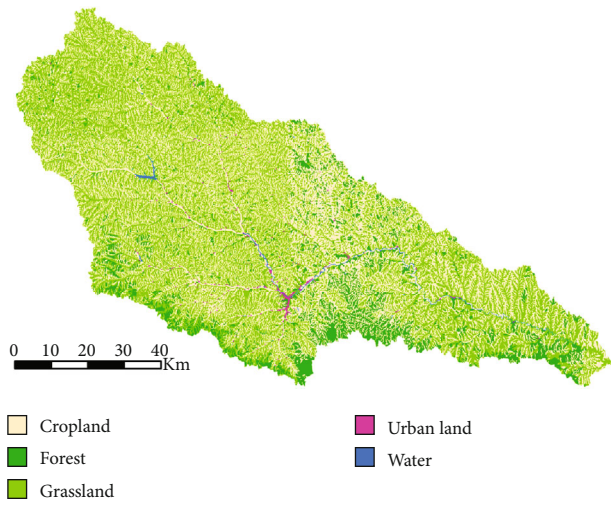

(c) Land use types of the Yanhe River Basin in 1995

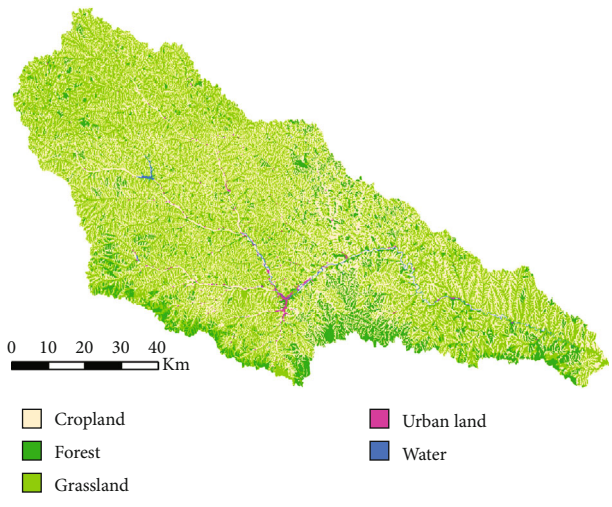

(d) Land use types of the Yanhe River Basin in 2000

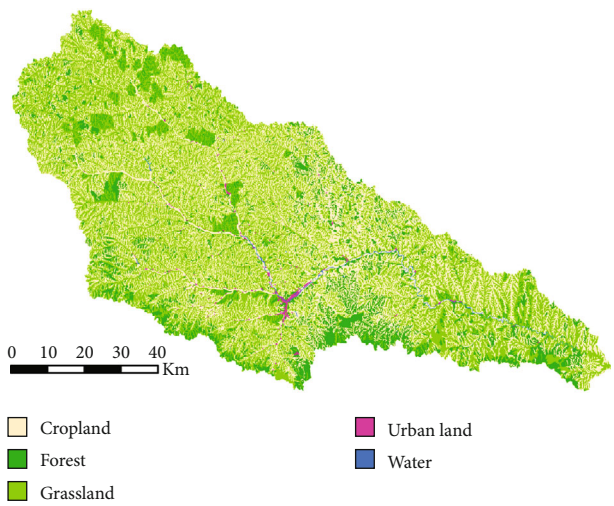

(e) Land use types of the Yanhe River Basin in 2005

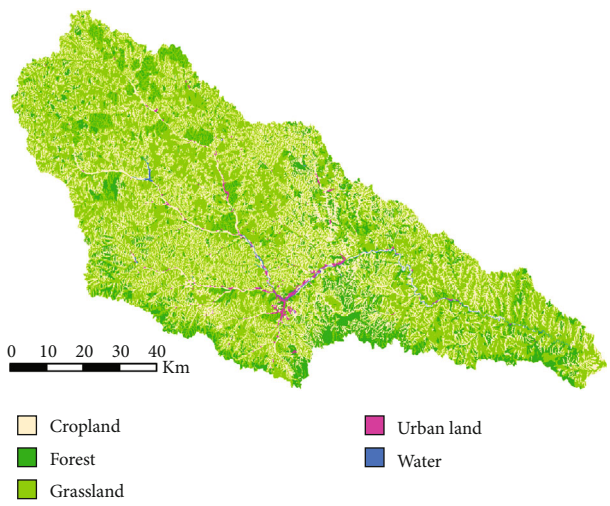

(f) Land use types of the Yanhe River Basin in 2010

Figure 3: Continued.

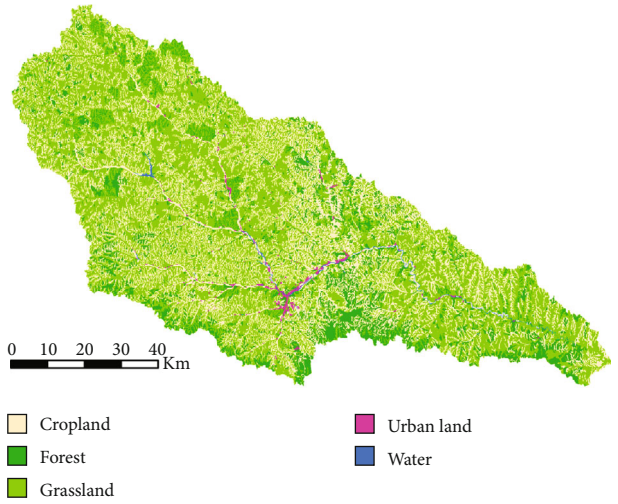

(g) Land use types of the Yanhe River Basin in 2015

Figure 3: Land use types in the Yanhe River Basin from 1980 to 2015.

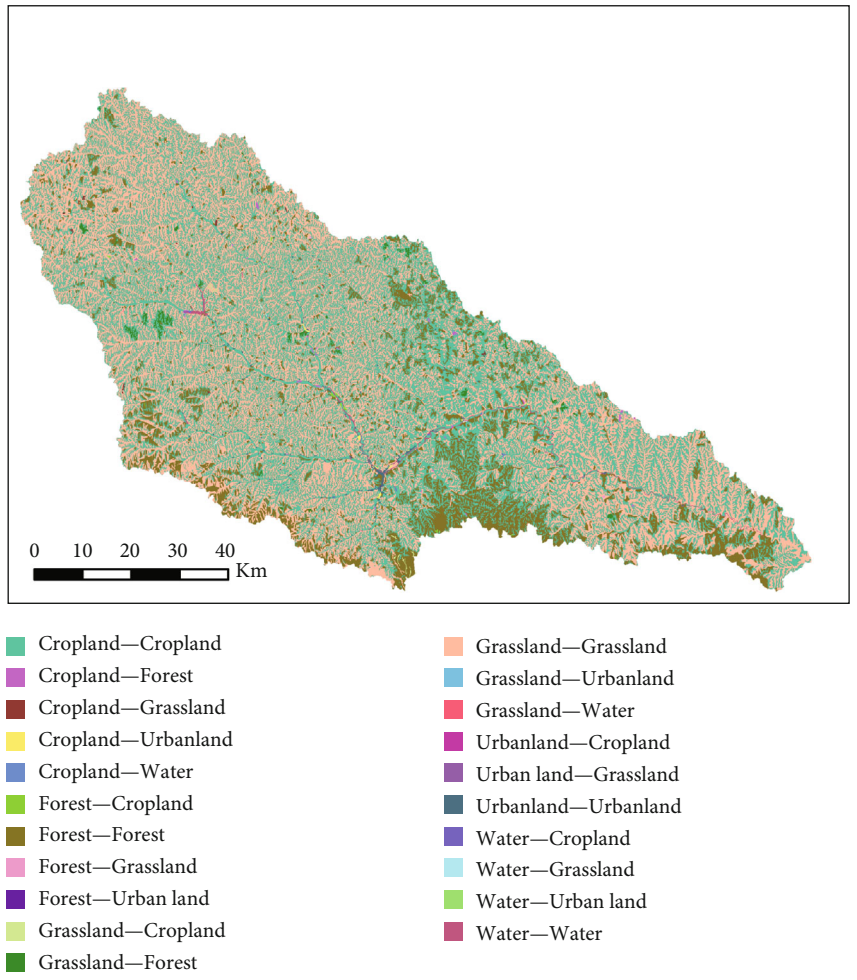

Figure 4: Land use changes of the Yanhe River Basin from 1980 to 2000.

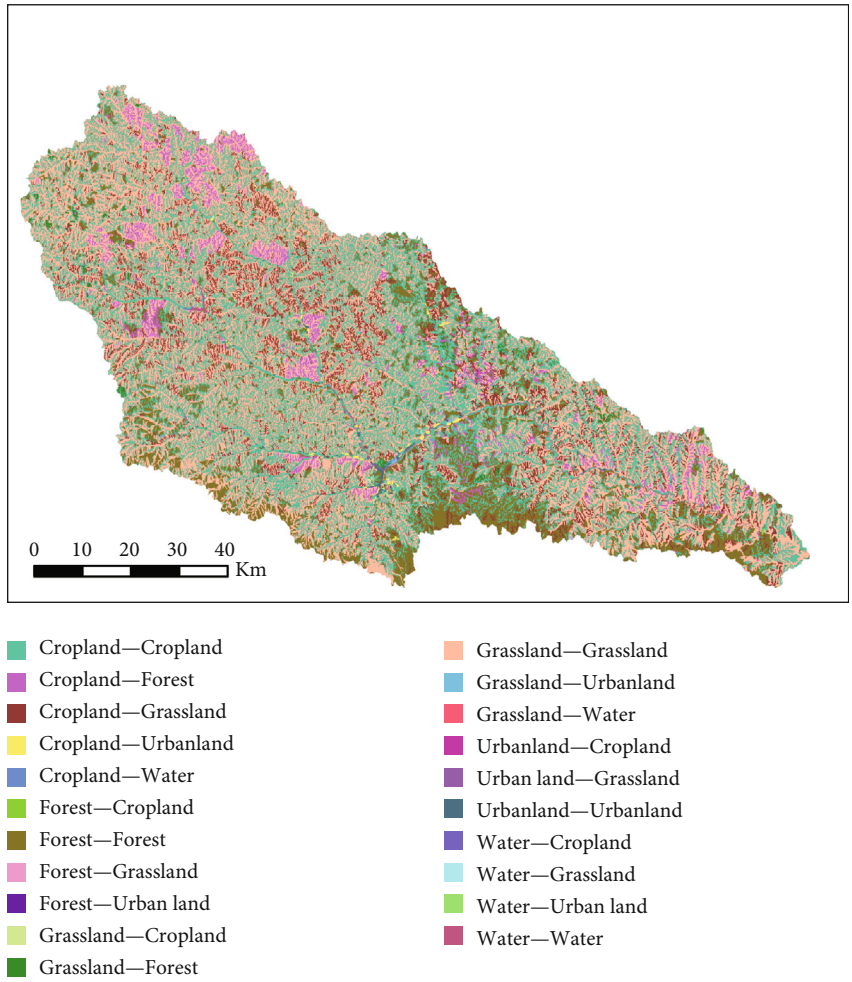

Figure 5: Land use changes of the Yanhe River Basin from 2000 to 2015.

Table 2: Statistics for land use changes of the Yanhe River Basin from 1980 to 2015 (km^2, %).

Land use type	1980		2000		2015	
	Area	Ratio	Area	Ratio	Area	Ratio
Cropland	3292.12	43.08	3289.13	43.04	2425.95	31.74
Forest	826.78	10.82	857.77	11.22	1127.50	14.75
Grassland	3473.14	45.45	3443.63	45.06	4016.95	52.56
Water	27.15	0.36	25.08	0.33	25.01	0.33
Urban land	23.16	0.30	26.73	0.35	46.93	0.61
Total	7642.35		7642.34		7642.34	

outflow of different land use types in the Yanhe River Basin from 1980 to 2015.

From Table 3, for the three major land use types from 1980 to 1990, the conversion area of grassland was 144.94 km^2, and the conversion rate was 4.17%, among which 3.94% was converted into cropland and 0.2% into forest land. The conversion area of cropland was 158 km^2, and the conversion rate was 4.8%, among which 4.17% was converted to grassland and 0.58% to forest land. The conversion area of forest land was 28.33 km^2, and the conversion rate was 3.42%, among which 0.9% was converted to grassland and 2.5% to cropland. During this period, all land use types in the Yanhe River Basin did not change significantly.

The transition matrix of land use change in Table 4 explains some changes in the Yanhe River Basin from 1990 to 2000 in detail. The conversion area of grassland was 175.65 km^2, and the conversion rate was 5.33%, among which 4.21% was converted into cropland and 1.07% into forest land. The conversion area of cropland was165.35 km^2, and the conversion rate was 5.29%, among which 4.35% was converted to grassland and 0.81% to forest land. The conversion area of forest land was 27.57 km^2, and the conversion rate was 3.46%, among which 2.48% was converted to cropland and 0.92% to grassland. The result showed that all land use types in the Yanhe River Basin changed little during this period. During this period, the land use types of the Yanhe River Basin mainly changed from grassland to forest land. It was related to the implementation of various soil and water conservation measures in the Yanhe River Basin at the end of the 20th century, which indicated that the comprehensive management of fragile ecological environment had achieved certain results.

From Table 5, the conversion area of grassland was 88.47 km^2, and the conversion rate was 2.64%, among which 1.47% was converted into cropland and 1.01% into forest

Table 3: The transition matrix of land use change of the Yanhe River Basin from 1980 to 1990 (km^2).

		1980					
		Grassland	Urban land	Cropland	Forest	Water	Total
1990	Grassland	3328.18	0.48	137.21	7.45	0.80	3474.12
	Urban land	0.41	21.95	0.70	0.08	0.05	23.18
	Cropland	136.84	0.60	3134.09	20.67	1.08	3293.28
	Forest	6.96	0.08	19.17	798.40	0.13	824.73
	Water	0.73	0.06	0.92	0.13	25.09	26.93
	Total	3473.12	23.16	3292.09	826.73	27.15	7642.24

Table 4: The transition matrix of land use change of the Yanhe River Basin from 1990 to 2000 (km^2).

		1990					
		Grassland	Urban land	Cropland	Forest	Water	Total
2000	Grassland	3298.48	0.40	136.01	7.34	1.38	3443.61
	Urban land	0.68	22.22	3.42	0.34	0.07	26.73
	Cropland	138.86	0.45	3127.93	19.75	2.12	3289.10
	Forest	35.22	0.07	25.13	797.17	0.13	857.72
	Water	0.89	0.05	0.79	0.13	23.22	25.08
	Total	3474.12	23.18	3293.28	824.73	26.93	7642.24

Table 5: The transition matrix of land use change of the Yanhe River Basin from 2000 to 2010 (km^2).

		2000					
		Grassland	Urban land	Cropland	Forest	Water	Total
2010	Grassland	3355.16	0.32	654.53	4.22	0.60	4014.83
	Urban land	4.61	25.92	15.45	0.80	0.11	46.89
	Cropland	49.12	0.43	2368.02	8.71	1.91	2428.19
	Forest	33.84	0.03	250.34	843.96	0.16	1128.33
	Water	0.90	0.03	0.80	0.08	22.29	24.10
	Total	3443.63	26.73	3289.13	857.77	25.08	7642.34

Table 6: The transition matrix of land use change of the Yanhe River Basin from 2010 to 2015 (km^2).

		2010					
		Grassland	Urban land	Cropland	Forest	Water	Total
2015	Grassland	3977.69	0.21	31.48	7.41	0.17	4016.95
	Urban land	0.22	46.33	0.26	0.07	0.05	46.93
	Cropland	30.14	0.27	2390.31	5.09	0.14	2425.95
	Forest	6.52	0.06	5.19	1115.70	0.03	1127.50
	Water	0.26	0.02	0.96	0.05	23.72	25.01
	Total	4014.83	46.89	2428.19	1128.32	24.10	7642.33

land from 2000 to 2010. And the conversion area of cropland was 921.12 km^2, and the conversion rate was 38.90%, among which 27.64% was converted to grassland and 10.57% to forest land. The conversion area of forest land was 13.81 km^2, and the conversion rate was 1.64%, among which 0.50% was converted to grassland and 1.03% to cropland. The conversion area of urban land was 0.81 km^2, and the conversion rate was 3.11%, among which 1.23% was converted to grassland and 1.68% to cropland. The conversion area of water was 2.78 km^2, and the conversion rate was 12.49%, among which 2.70% was converted to grassland and 8.56% to cropland. During this period, the cropland area of the Yanhe River Basin decreased significantly and most of it was converted to grassland and forest land, which was mainly related to the vigorous implementation of ecological restoration policy of returning farmland to forest (grass) since 1999. Moreover, the area of urban land began to increase compared with the previous stage, and part of grassland and cropland began to transfer to urban land, which also indicated that the growth rate of residential area in the Yanhe River Basin was accelerated and the level of urbanization was further improved. The ecological environment of the basin had

achieved obvious effects through comprehensive treatment. The result was mainly due to the ecological policy of returning farmland to forest (grass) and the implementation of water conservation measures such as the World Bank loan Phase II project in the Yanhe River Basin in 2002.

According to Table 6, the conversion area of grassland was 37.14 km^2, and the conversion rate was 0.93%, among which 0.76% was converted into cropland and 0.16% into forest land from 2010 to 2015. The conversion area of cropland was 37.88 km^2, and the conversion rate was 1.56%, among which 1.3% was converted to grassland and 0.21% to forest land. The conversion area of forest land was 12.63 km^2, and the conversion rate was 1.12%, among which 0.66% was converted to grassland and 0.45% to cropland. During this period, all land use types in the Yanhe River Basin did not change significantly. But the area of forest land decreased for the first time since 2000 after the implementation of the policy of returning farmland to forest. And the urban land and water area increased slightly, which was mainly due to the large-scale development and construction in Yan'an New Area in 2012, and a lot of farmland, forest land, and grassland were used for urbanization construction.

In conclusion, the conversion rate of cropland in the Yanhe River Basin increased greatly from 1980 to 2015, indicating that cropland transferred to other land use types continuously. There was no significant change in the conversion rate of forest land, indicating that the forest land did not transfer to other land use types, and the increase of forest land mainly came from cropland and grassland. The conversion rate of grassland decreased slightly with the increase of time, indicating that the transfer rate of grassland area to other land use types became slower and slower. Moreover, the conversion rate of cropland to grassland and forest land also indicated that the area transferred from cropland to grassland was larger than that transferred from forest land.

3.3. Land Use Dynamic Attitude. According to formulas (2) and (3), dynamic land use attitudes in the Yanhe River Basin from 1980 to 2000 and from 2000 to 2015 can be obtained (Tables 7 and 8).

Tables 7 and 8 describe that 0.69% of the land use in the Yanhe River Basin changed with an average annual growth rate of 0.03%, with little overall change from 1980 to 2000. The land types with an increased dynamic land use attitude were urban land and forest land, while the land types with a negative dynamic land use attitude were cropland, grassland, and water body, respectively, indicating that the area showed a trend of continuous decrease. The most obvious increase of dynamic attitude was in urban land, up to 15.41%, with an average annual increase rate of 0.77%. The most obvious decrease of dynamic attitude was in water body, up to -7.62%, with an average annual decrease rate of 0.38%. The three main types of land use (cropland, forest land, and grassland) had no significant change in their dynamic attitude, indicating that their overall change degrees were not significant. On the contrary, during the 15 years from 2000 to 2015, 13.17% of the land use was changed, with an average annual growth rate of 0.88%, nearly 30 times of the average annual growth rate in the previous 20 years, indicating that the land use type of the Yanhe River Basin had significantly changed in the 15 years. The land use types with increasing land use attitude from large to small were urban land, forest land, and grassland, which was 75.57%, 31.45%, and 16.65%, respectively, with annual growth rates of 5.04%, 2.1%, and 1.11%, respectively. The land use types with decreased dynamic attitude to land use were cultivated land and water body (-26.24% and -0.28%, respectively), and the average annual reduction rate was 1.75% and 0.02%, respectively. It was revealed that the area of forest land and grassland in the Yanhe River Basin increased greatly during the 15 years, the area of residential land and traffic land also increased rapidly, and the area of cropland decreased greatly, which was closely related to the vigorous construction of Yan'an New Area and the remarkable achievements of ecological management in the Yanhe River Basin.

Table 7: The land use dynamic degree of the Yanhe River Basin from 1980 to 2000 (%).

	Cropland	Forest	Grassland	Water	Urban land	LC_T
K_T	-0.09	3.75	-0.85	-7.62	15.41	0.69
$K_T/20$	0.00	0.19	-0.04	-0.38	0.77	0.03

Table 8: The land use dynamic degree of the Yanhe River Basin from 2000 to 2015 (%).

	Cropland	Forest	Grassland	Water	Urban land	LC_T
K_T	-26.24	31.45	16.65	-0.28	75.57	13.17
$K_T/15$	-1.75	2.10	1.11	-0.02	5.04	0.88

3.4. Driving Forces of Land Use Change. Land use change generally refers to the underlying surface change caused by the simultaneous action of natural factors and cultural factors. Natural factors mainly include climate, soil, topography, and other aspects; cultural factors mainly include population change, economic growth, and national policies. Generally speaking, land use change caused by natural factors in a certain period is relatively weak, while cultural factors are the leading driving force for land use change [23]. This paper analyzes the driving force of land use change in the Yanhe River Basin from three aspects: population and urbanization, regional economic development, and ecological restoration and governance policies, thus revealing the causes of land use change in the Yanhe River Basin in the past 35 years, so as to provide a basis for comprehensive land resource management of the basin in the future.

Population is one of the most direct driving forces of land use change; population growth not only affects the change of agricultural products demand to influence the change of land use spatial pattern but also causes a direct impact on land use change to some extent [24]. From 1980 to 2015, the population of the Yanhe River Basin kept expanding rapidly and people's demands for residential land also increased continuously, so the area of urban land also increased significantly. At the same time, due to the development of urban surrounding areas and the construction of urban infrastructure in the basin, a large number of cropland and forest land resources

were occupied and turned to urban land. In addition, as the development of science and technology and the traditional agricultural production cannot meet the needs of the people's daily life, the gradual decline of cropland was also natural. Thus, it can be seen that the large increase of population will lead to the increase of urban land and also affect the reduction of cropland.

During the 35 years from 1980 to 2015, the economy of the Yanhe River Basin developed rapidly, and the total GDP of the basin increased by more than 10 times since 2000. The continuous and rapid development of economy and the improvement of people's living quality have accelerated the change of land use type in the Yanhe River Basin. The number of people engaged in the primary industry in the Yanhe River Basin continued to decrease with the improvement of living standard, while with the rapid development of the petroleum industry and the red tourism industry in Yan'an, the proportion of the third industry in the total GDP of the basin was gradually increasing. With the development of urbanization and the adjustment of industrial structure, the construction of a large number of infrastructure needed to occupy the land resources in the basin, which promoted the change of land use type in the Yanhe River Basin.

In order to ensure the healthy and stable development of the watershed ecological environment, the Chinese government began to establish the corresponding land use policies to devote itself to the ecological restoration and treatment of the watershed environment since 1970. The Yanhe River Basin began to implement the construction of the three-north shelterbelt system and other related ecological projects in 1978; the World Food Program approved the implementation of the Integrated watershed management project of the Xingzi River which was a tributary of the Yanhe River Basin in 1988; the Yanhe River Basin Governance Project, financed by the World Bank, was born and implemented in 1994; the natural forest protection project was implemented in 1998; the project of returning farmland to forest (grass) was fully implemented at the end of 1999. The implementation of these policies in the Yanhe River Basin has caused the rapid decrease of the cropland and the large increase of forest and grassland, and the land use type has changed from agricultural production land to ecological restoration land. The ecological environment of the Yanhe River basin has been greatly improved since 2000. Therefore, the implementation of ecological restoration and governance policies is the direct driving force of land use change in the Yanhe River Basin from 1980 to 2015.

4. Discussion

In this study, remote sensing data and GIS technology are used to obtain the results of the land use change of the Yanhe River Basin from 1980 to 2015. The cropland area has been greatly reduced and has been transferred to grassland and forest land, grassland and forest land increased in a large area, and urban land continued to increase. This research result is basically consistent with the previous scholars [13, 16] in the same basin. In addition, the area of cropland and forest land in the Yanhe River Basin began to change significantly since 2000. From 2000 to 2010, the area of cropland in the basin continued to decrease, while the area of forest land and grassland increased significantly. This research result is also consistent with the previous scholar [12], indicating that ecological policies such as returning farmland to forest (grass) in the Yanhe River Basin in the past ten years have achieved obvious effects, and vegetation coverage increased significantly. From 2010 to 2015, the area of forestland in the basin decreased relatively, the decrease rate of cropland also decreased significantly compared with the previous period, and the grassland, water body, and urban land increased slightly, which was mainly related to the small scale of ecological policy of returning farmland to forest (grass) and the slow progress of project implementation.

In addition, driving force analysis is an important part of the study of land use change, and human factors are the most core driving factors among all the driving forces. Some scholars [24] have explored the land use change and driving force in the Yanhe River Basin from 1985 to 2000, but the time series was short and only factors of population, policy, and agricultural production mode were taken into account in the analysis of driving forces, while factors of socioeconomic development were not taken into account. It is clear that the adjustment of land use structure in the Yanhe River Basin is closely related to the sustained and rapid development of social economy in these 35 years by analyzing the social and economic situation of the Yanhe River Basin combined with national policies in the long time series from 1980 to 2015 in this paper. Due to the support of economic policies and the change of people's ideas, more and more people left the countryside and started to work in the secondary and tertiary industries, which is one of the important reasons for the change of land use types in the Yanhe River Basin.

At the same time, there are also many limitations in this study. Quantitative research on land use change involves some technical problems such as continuous acquisition and interpretation of multispectral remote sensing images and elimination of errors, and quantitative analysis of driving forces also requires more detailed and practical socioeconomic data, which are both difficult to complete in a practical work. Therefore, such problems need to be further considered in future researches.

5. Conclusions

Some important conclusions can be drawn from this study: (1) cropland, grassland, and forest land are the three most obvious types of land use changes, while the change of urban land and water area is relatively small. (2) It can be seen that the transfer between cropland, forest land, grassland and urban land was very obvious during 1980-2015, among which the conversion rate of cropland was the highest, forest land did not change significantly, grassland decreased slightly with the growth of time, and urban land conversion rate increased significantly since 2000. (3) During the 15 years from 2000 to 2015, the land use types of the Yanhe River Basin changed by 13.17%, with an average annual growth rate of 0.88%, indicating that the land use types of the Yanhe River Basin changed significantly. (4) In addition, the main driving forces of land use change in the Yanhe River Basin

include population and urbanization; regional, social, and economic development; and ecological restoration and governance policies. The implementation of ecological restoration and governance policy is the direct driving force of land use change in the Yanhe River Basin. The results obtained in this study can provide reference basis for land use planning and management and land use structure optimization in the Yanhe River Basin in the future.

Data Availability

The data used to support the findings of this study are available from the corresponding author upon request.

Conflicts of Interest

The authors declare no conflict of interest.

Acknowledgments

This work was supported by the National Natural Science Foundation of China (Grant number 31971723) and National Key Research Priority Program of China-Variation Mechanism and Trend Prediction of Water and Sediment in the Yellow River Basin (2016YFC0402402).

References

[1] L. N. Wu, S. T. Yang, X. Y. Liu, Y. Luo, X. Zhou, and H. G. Zhao, "Response of land use change in the Beiluo River Basin to human activity level since 1976," *Journal of Geographical Sciences*, vol. 69, no. 1, pp. 54–63, 2014.

[2] J. Yang, G. X. Xu, J. Yao, and J. K. Luan, "Analysis of land use change and driving force in the Weihe River Basin," *Pearl River*, vol. 38, no. 7, pp. 22–26, 2017.

[3] S. S. Xiao, C. D. Wu, and J. Y. Chu, "Analysis of land use change and driving factors in Taihu Lake region from 1980 to 2005," *Transactions of the Chinese Society of Agricultural Engineering*, vol. 28, no. 23, pp. 1–11+293, 2012.

[4] B. Turner, D. Skole, S. Sanderson, D. Fischer, and R. Leemans, "Land-use and land-cover change: science/research plan," *Global Change Report (Sweden)*, vol. 43, pp. 669–679, 1995.

[5] P. H. Verburg, B. Eickhout, and H. van Meijl, "A multi-scale, multi-model approach for analyzing the future dynamics of European land use," *Annals of Regional Science*, vol. 42, no. 1, pp. 57–77, 2008.

[6] F. Lambin, H. J. Geist, and E. Lepers, "Dynamics ofland-use andland-coverchange intropicalregions," *Annual Review of Environment and Resources*, vol. 28, no. 1, pp. 205–241, 2003.

[7] K. Biro, B. Pradhan, M. Buchroithner, and F. Makeschin, "Land use/land cover change analysis and its impact on soil properties in the northern part of Gadarif region, Sudan," *Land Degradation & Development*, vol. 24, no. 1, pp. 90–102, 2013.

[8] L. Yu, W. He, Y. F. Yao, Y. Q. Huang, K. C. Huang, and L. W. Zhou, "Land use/cover change and driving force analysis in Li River Basin from multiple perspectives," *Soil and Water Conservation in China*, vol. 454, no. 1, pp. 5+44–5+48, 2020.

[9] J. Y. Liu, Z. X. Zhang, X. L. Xu et al., "Spatial pattern and driving force analysis of land use change in China in the early 21st century," *Journal of Geographical Sciences*, vol. 64, no. 12, pp. 1411–1420, 2009.

[10] J. Y. Liu, J. Ning, W. H. Kuang et al., "The spatial and temporal pattern and new features of land use change in China from 2010 to 2015," *Journal of Geographical Sciences*, vol. 73, no. 5, pp. 789–802, 2018.

[11] H. Liao, Z. K. Shu, J. L. Jin, C. G. Yang, and G. Q. Wang, "Characteristics and driving force of land use change in the Yellow River Basin from 1980 to 2015," *South-to-North Water Transfers and Water Science & Technology(Chinese and English)*, vol. 19, no. 1, pp. 129–139, 2021.

[12] H. Z. Lou, S. T. Yang, Q. W. Zhou, Y. Luo, and L. P. Hou, "Analysis of land use/cover change and driving force in Yanhe River Basin from 2000 to 2010," *Journal of Arid Land Resources and Environment*, vol. 28, no. 4, pp. 15–21, 2014.

[13] W. S. Zhang, F. Wang, X. M. Mu, R. Li, and Y. He, "Spatial-temporal characteristics of land use/cover change in the Yanhe River Basin in recent 25 years," *Research of Soil and Water Conservation*, vol. 19, no. 5, pp. 148–152+157+291, 2012.

[14] H. X. Xie, Q. K. Yang, R. Li, X. P. Zhang, L. Cheng, and G. W. Pang, "Analysis of erosion reduction effect of soil and water conservation measures in the Yanhe River Basin," *Science of Soil and Water Conservation*, vol. 8, no. 4, pp. 13–19, 2010.

[15] J. P. Li, F. Wang, X. M. Mu, and Q. K. Yang, "Effects of land use change on ecological service value in the Yanhe River Basin," *Research of Soil and Water Conservation*, vol. 17, no. 3, pp. 110–114, 2010.

[16] S. H. Ran, K. Zhang, and C. H. Lu, "Scale transformation method of land use/cover change model in the Yanhe River Basin," *Progress in Geography*, vol. 29, no. 11, pp. 1414–1419, 2010.

[17] C. Z. Li, H. Wang, F. L. Yu, A. M. Yang, and D. H. Yan, "Effects of soil and water conservation on runoff and sediment in the Yanhe River Basin," *Science of Soil and Water Conservation*, vol. 9, no. 1, pp. 1–8, 2011.

[18] J. J. Wei, X. P. Li, Q. K. Yang, and W. Liang, "Research on spatio-temporal change of land use and conversion of farmland to forest based on remote sensing – a case study of the lower reaches of the Yanhe River Basin," *Bulletin of Soil and Water Conservation*, vol. 27, no. 2, pp. 87–90, 2007.

[19] H. X. Xie, R. Li, Q. K. Yang, J. Li, and W. Liang, "Effects of returning farmland to forest (grassland) and rainfall changes on soil erosion in the Yanhe River Basin," *Scientia Agricultura Sinica*, vol. 42, no. 2, pp. 569–576, 2009.

[20] F. P. Ren, Y. Jiang, X. Xiong, M. Y. Dong, and B. Wang, "Analysis of spatial-temporal differences in land use changes in the Dongjiang River Basin in recent 20 years," *Resources Science*, vol. 33, no. 1, pp. 143–152, 2011.

[21] L. Cheng, Z. X. Xu, R. Luo, and Y. J. Mi, "Spatial and temporal variation characteristics and driving force analysis of LUCC in Weihe River Basin from 1980 to 2000," *Research of Soil and Water Conservation*, vol. 16, no. 5, pp. 1–6+30+287, 2009.

[22] W. Li, J. Chen, L. Li, and H. Chen, "Analysis of land use change in the Yangtze River Basin from 1980 to 2015," *Yangtze River*, vol. 51, no. 2, pp. 49–57, 2020.

[23] J. Ren, J. Y. Jiang, Z. H. Zhao, L. Xu, and M. Cheng, "Study on land use/cover change and driving force in Yili Basin from 1980 to 2015," *Science Technology and Engineering*, vol. 20, no. 21, pp. 8480–8488, 2020.

[24] H. F. Zhu, W. W. Zhao, M. Y. Kang, and W. W. Guo, "Spatial and temporal changes of land use patterns and driving factors in the Yanhe River Basin," *Journal of Arid Land Resources and Environment*, vol. 22, no. 8, pp. 17–22, 2008.

Hindawi
Journal of Sensors
Volume 2021, Article ID 6638728, 11 pages
https://doi.org/10.1155/2021/6638728

Research Article

Spatial-Temporal Simulations of Soil Moisture Content in a Large Basin of the Loess Plateau, China

Zhiqi Wang,[1,2,3] Xiaobo Feng,[3] Zhihong Yao,[2] Zhaolong Ma,[4,5] and Guodong Ji[1]

[1]*Key Laboratory of Water and Sediment Sciences, Ministry of Education, Department of Environmental Engineering, Peking University, Beijing 100871, China*
[2]*School of Surveying, Mapping and Geographic Information, North China University of Water Resource and Electric Powder, Zhengzhou 450000, China*
[3]*River and Lake Protection Center of Ministry of Water Resources, Beijing 100038, China*
[4]*Department of Hydraulic Engineering, Tsinghua University, Beijing, China 100084*
[5]*China Institute of Water Resource and Hydropower Research, No. 20 Chegongzhuang West Road, Haidian District, Beijing 100044, China*

Correspondence should be addressed to Guodong Ji; jiguodong@pku.edu.cn

Received 24 November 2020; Revised 28 February 2021; Accepted 26 March 2021; Published 14 April 2021

Academic Editor: Yuan Li

Soil moisture is a crucial factor limiting the growth and survival of plants on the Loess Plateau. Its level has a severe impact on plants' growth and development and the type and distribution characteristics of communities. This study area is the Jihe Basin in the Loess Plateau, China. Multiple linear regression models with different environmental variables (land use, topographic and meteorological factors, etc.) were developed to simulate soil moisture's spatial and temporal changes by integrating field experiments, indoor analysis, and GIS spatial analysis. The model performances were evaluated in the Jihe Basin, with soil moisture content measurements. The result shows that soil moisture content is positively correlated with soil bulk density, monthly rainfall, topographic wetness index, land use coefficient, and slope aspect coefficient but negatively correlated with the monthly-averaged temperature and the relative elevation coefficient. The selected variables are all related to the soil moisture content and can account for 75% of the variations of soil moisture content, and the remaining 25% of the variations are related to other factors. Comparing the simulated and measured values at all sampling points shows that the average error of all the simulated values is 0.09, indicating that the simulation has high accuracy. The spatial distribution of soil moisture content is significantly affected by land use and topographic factors, and seasonal variation is remarkable in the year. Seasonal variation of soil moisture content is determined by the seasonal variation of rainfall and the air temperature (determining evaporation) and vegetation growth cycle. Therefore, the proposed model can simulate the spatial and temporal variation of soil moisture content and support developing the soil and water loss model on a basin scale.

1. Introduction

The Loess Plateau of China, situated in the upper and middle reaches of the Yellow River, covers about 630,000 km^2, has an elevation of 1200–1600 m above sea level and is predominantly covered by loess deposits. This region has been prone to severe soil erosion that is a consequence of both natural factors (e.g., the unique geology and landforms, climate conditions, and vegetation coverage due to water resource constraints) and anthropic factors (e.g., poor land use management) [1]. Intensive soil erosion has resulted in the decline of land productivity and environmental degradation [2–4]. The key to ecological environment construction and sustainable agricultural development is to protect and rationally utilize water and land resources. As a significant limiting factor for plant growth and development in the Loess Plateau, soil moisture is of critical importance to hydrological processes at a variety of scales, and it is an essential factor affecting rainfall infiltration, runoff, and sediment yield [5–9]; therefore, objective estimation of the soil moisture is

fundamental. However, the measured data of soil moisture content is very few, and it is more difficult to obtain at the moment before rainfall in a basin. The soil moisture model is usually constructed by the empirical relationship of antecedent rainfall [10, 11] or calculated using a daily model based on the antecedent rainfall [12]. The model can reflect soil dryness/wetness, but it does not reflect the real soil moisture content, so it has a significant impact on the results simulated and predicted with the model. Particularly at the regional scale, there are many factors affecting soil moisture content, such as rainfall, evaporation, soil type, land use, and topography [13–15]; all the factors interact with each other, and some factors are difficult to quantitatively express their influence on soil moisture content, which makes it difficult to simulate soil moisture content. Hence, simulation of soil moisture content still lacks for large-scale basins. Based on previous studies [16–22] and research results of small watersheds [23], the objective of this study was to estimate the soil moisture content in large-scale basins considering various factors affecting soil moisture content [24–26]. It would lay a foundation for studying the regional soil and water loss model and provide a scientific basis for soil and water conservation and ecological restoration in the Loess Plateau, China.

2. Materials and Methods

2.1. Study Area. The study area is the Xihe Basin located in the region of 34°20′19″ N~34°38′59″ N and 105°07′50″ E~106°00′45″ E, belonging to the third subregion of the Loess Hilly-gully region. The overview of the Xihe Basin is shown in Figure 1. The basin has an area of 1276.73 km^2, with an average annual rainfall of 558.9 mm. Rainfall varies greatly annually and is unevenly distributed during a year, mainly from July to September. The terrain is fragmented, and ravines crisscross. It is high in the northwest and low in the southeast, at altitudes between 1069 and 2717 m. Soil and water loss occurs in a wide range and large areas; the erosion types are complex and varied; the erosion process is concentrated with large intensity. Water resources are still the main restricting factors of soil and water conservation and ecological environment construction in the basin.

2.2. Data Sources

2.2.1. Digital Elevation Model (DEM). The original data used was a 1 : 50,000 topographic map (1954 Beijing coordinate system, 1956 Yellow Sea elevation system, contour interval 20 m, reference ellipsoid Krasovsky). The topographic map was scanned, and Geoway was used for vectorization to generate the required layers of contour lines, elevation points, and slopes, and then, E00 was derived after splicing, which was transformed into coverage format in ArcInfo, and topological relations are constructed. Finally, the professional ANUDEM interpolation software is used to set parameters according to existing studies to generate HC-DEM with 10 m resolution (Figure 1) [27]. The DEM projection was Gaussian projection, which was transformed into the unified projection information in this study— ALBERS projection using ArcGIS.

2.2.2. Meteorological Data. The daily rainfall and temperature data were provided by the China Meteorological Data Network (http://data.cma.cn/site/index.html) and the book of Hydrological Data of the Yellow River Basin. The monthly-averaged rainfall and temperature in November 2007 and May 2008 were calculated using the Inverse Distance Weighting (IDW) interpolation method.

2.2.3. Topographic Wetness Index. Based on DEM and by using multiple flow algorithm, topographic wetness index was calculated as shown in Figure 2 according to the calculation formula of "$w = \ln(\alpha/\tan\beta)$" [28], where w is the topographic wetness index; α is the confluence area in a unit contour length or a unit grid; β is the local slope gradient. Among them, α is calculated by the formula "$\alpha = A/L$," where A is the total upstream catchment area of the grid, and L is the effective contour length in the inflow direction around the grid.

2.2.4. Land Use Coefficient. The land use map of the Xihe Basin is obtained by interpreting the TM remote sensing images acquired in 2005. According to current research results [23], the significant coefficients of farmland, barren grassland, and woodland on soil moisture content were 1.06, 1.0, and 0.65, respectively, and the coefficients of residential land and water body were set as 0. The land use coefficient map was obtained by reassigning the land use map, as shown in Figure 3.

2.2.5. Slope Aspect Coefficient. The result of a representative study on small watershed [23] showed that in the eight slope aspects (north, northeast, east, southeast, south, southwest, west, and northwest), the slope aspect coefficients affecting the soil moisture content are 1, 0.90, 0.77, 0.81, 0.75, 0.79, 0.89, and 0.87, respectively. We have reassigned the slope aspect map, and the slope aspect coefficient map is illustrated in Figure 4.

2.2.6. Relative Elevation Coefficient. Owing to the ravines crisscross in the Loess Hilly-gully region, the landform is complex, and the upper, middle, and lower parts of ridge, hills, and gully cannot be quantitatively represented accurately. Therefore, each sampling point's relative elevation coefficients in a small watershed are selected to represent the slope position quantitatively. The calculation formula is shown in equation (1).

$$X_{Er} = \frac{E - E_0}{E_{\max} - E_0}, \tag{1}$$

where X_{Er} is the relative elevation coefficient, E is the elevation of the sampling point, $E_{\max}$ is the maximum elevation in the watershed, and E_0 is the elevation at the watershed outlet. The calculation results of relative elevation coefficient are shown in Figure 5.

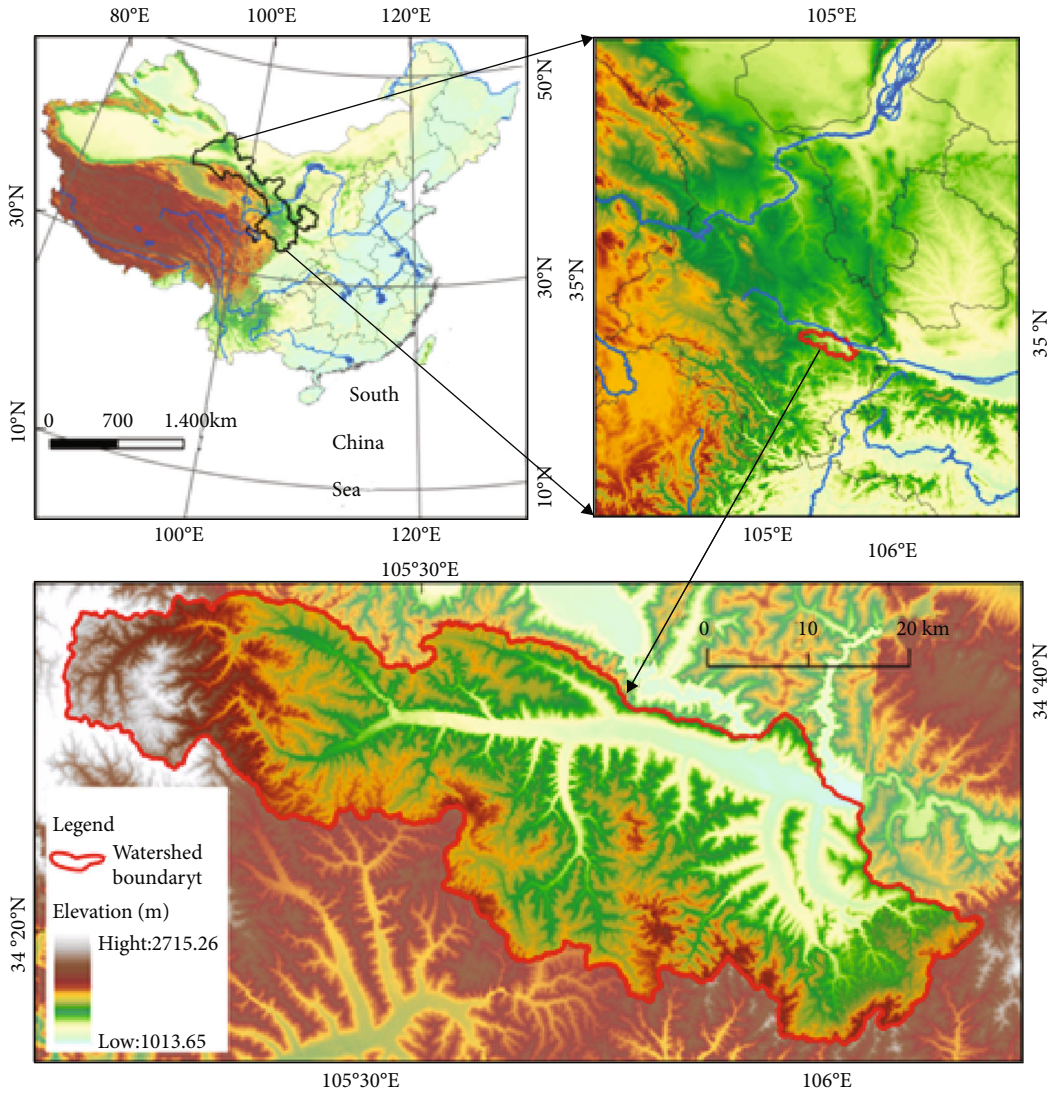

Figure 1: The location and Digital Elevation Model (DEM) of the Xihe River Basin.

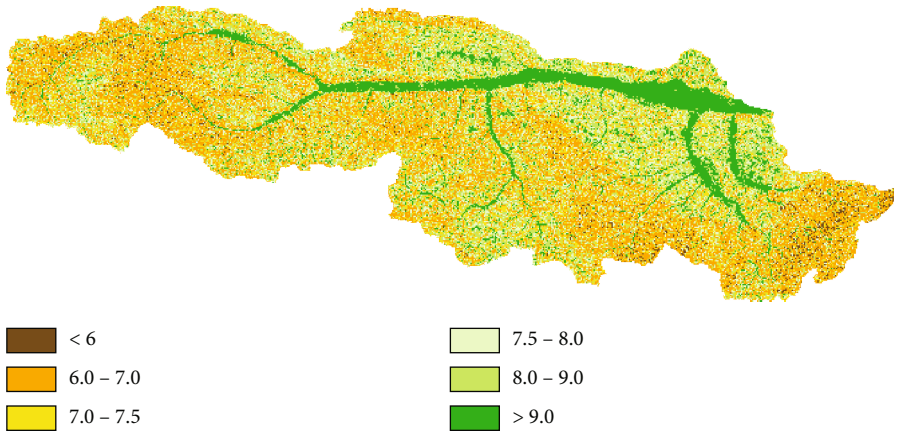

Figure 2: Topographic wetness index of the Xihe River Basin.

2.2.7. Field Collection of Soil Moisture Content. The layout of sampling points: sampling points are collected according to the combination of land use and landform type, the sampling points cover the primary land use types, prominent small- and medium-sized landforms, different slope aspects, different gradient grades, and slope positions, and a total of

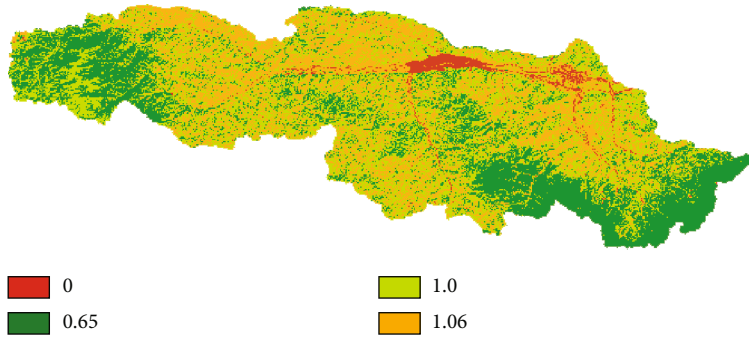

Figure 3: Land use coefficient of Xihe River Basin in 2005.

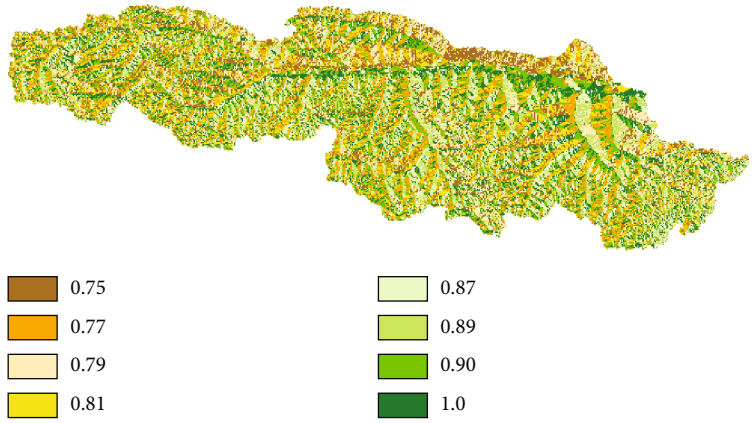

Figure 4: Slop aspect coefficient of Xihe River Basin.

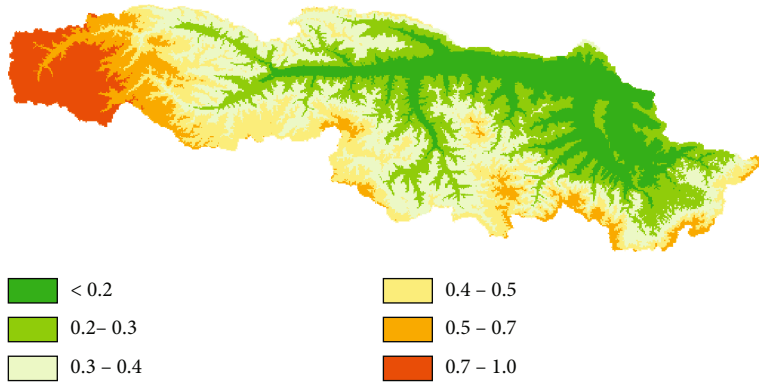

Figure 5: Relative elevation coefficient of the Xihe River Basin.

70 points are selected. Because the study area was large, data were collected at 43 sampling points in November 2007 and 27 sampling points in May 2008. At each sampling point, handheld GPS is used to record the longitude, latitude, and altitude. The soil properties, including the moisture content and dry bulk density, and the topography near the site, soil erosion, and land use type are recorded. Measurement of soil moisture content: considering that near-surface soil is the central origin of the erosion-induced sediment yield, only the soil at a depth of 0-50 cm is taken as the research subject. When sampling, a ring knife is used to collect soil at a depth of 0-50 cm, and the interval between samples is 10 cm. The samples are sealed and then taken back to the laboratory, and the moisture contents of the samples are determined with the drying method (105°C, 10 h). The average soil moisture content in the depth of 0-50 cm at each sampling site is taken as the mean of soil moisture content in each soil layer $\bar{W}$.

The mass content of moisture was converted into the thickness of soil water.

$$W_H = \bar{W} \times \rho_\theta \times 50 \times 10, \quad (2)$$

where W_H, $\bar{W}$, and ρ_θ refer to the thickness of soil water in 0-50 cm depth soil layer (mm), the average mass moisture content of 0-50 cm depth soil, and the average dry volume weight of the 0-50 cm depth soil at each sampling point (g/cm^3), respectively.

3. Model Evaluation Method

3.1. Regression Analysis. Regression analysis is the most basic quantitative analysis method. According to the data statistics principle, the regression analysis method can help process a large number of statistical data mathematically, determine the correlation between dependent variables and some independent variables, and establish a regression equation (function expression) with good correlation. Besides, it can also help find a good regression coefficient and then carry out a correlation test to determine the correlation coefficient, which can predict the change of dependent variables after meeting the correlation requirements.

In this study, the multivariate regression analysis method in Excel is used to analyze the relationship between the soil moisture content (mm) (the dependent variable) and the soil bulk density, monthly-averaged rainfall, monthly-averaged temperature, topographic wetness index, land use coefficient, slope aspect coefficient, and relative elevation coefficient (7 independent variables).

Multivariate regression analysis gives the following evaluation indexes: multiple correlation coefficient R, determinant coefficient R^2, and the P value of F statistics. The multiple regression analysis results were completed by analyzing the variable coefficient, multiple correlation coefficient R, decision coefficient R^2, and P value of F statistics, etc.

3.2. Relative Error. The ratio of the absolute error caused by measurement over the measured true value (in agreement) is the relative error, which can better reflect the credibility of measurement.

$$\Delta_k = \left| \frac{(x(k) - \hat{x}(k))}{x(k)} \right|, \tag{3}$$

where Δ_k is the relative error; $x(k)$ is the measured value; $\hat{x}(k)$ is the simulated value.

In order to reflect the overall reliability of measurement, the average relative errors at all points are obtained by the following formula:

$$\Delta = \frac{1}{n} \sum_{k=1}^{n} \Delta_k, \tag{4}$$

where Δ is the averaged relative error; Δ_k is the relative error; n is the number of sampling points.

4. Results and Discussion

4.1. Construction of Soil Moisture Content Model. The soil moisture content (mm) is taken as the dependent variable, and the soil bulk density, monthly-averaged rainfall, monthly-averaged temperature, land use coefficient, topographic wetness index, slope aspect coefficient, and relative elevation coefficient are the independent variables. Use the regression function in the data analysis tool of Excel to carry out multivariate regression analysis. Some data required for regression analysis and simulated results are shown in Table 1.

(1) The model equation obtained through multivariate linear regression analysis is

$$Y = 66.06 \times X_1 + 0.16 \times X_2 - 2.99 \times X_3 + 0.13 \times X_4 + 9.34 \times X_5 + 48.36 \times X_6 - 18.54 \times X_7 + 15.7, \tag{5}$$

where Y is the moisture content of soil (mm); X_1 is the volume density of soil (g/cm^3); X_2 is the monthly-averaged rainfall (mm); X_3 is the monthly-averaged temperature (°C); X_4 is the topographic wetness index; X_5 is the land use coefficient; X_6 is the slope aspect coefficient; X_7 is the relative elevation coefficient.

The main statistical parameters of the model equation are shown in Table 2.

(2) The result of regression analysis shows that the multiple correlation coefficient R is 0.84, and the determinant coefficient R^2 is 0.75. It implies that the variables under consideration account for 75% of the variations of soil moisture content, and the remaining 25% of variations have to be caused by other factors. This indicates that the factors affecting soil moisture are complex

(3) The P value of the F statistics is 1.843×10^{-11}, which is much smaller than the significant level of 0.05. It shows that the regression effect of the equation is remarkable, and the selected variables are all related to the soil moisture content

(4) The P value of the t-test corresponding to the regression coefficient indicates that the regression coefficient is significantly away from zero, and it can be used to explain the change of soil moisture content. The regression coefficients of the variables (soil bulk density, monthly rainfall, topographic wetness index, land use coefficient, and slope aspect coefficient) are positive, indicating that soil moisture content is positively correlated with these variables. The regression coefficients of the monthly-averaged temperature and the relative elevation coefficient are negative, indicating that soil moisture content is negatively correlated with these two variables

(5) Analysis of the errors in simulation results

If we substitute the data at each measuring point in Table 1 into equation (5), the soil moisture content at each measuring point can be simulated and shown in Table 1 (column 10). Substitute the simulated and measured values into equation (3) to calculate the relative error of the sampling

Table 1: Parameter attribute value of the samples.

Sampling point number (1)	Soil moisture content (2)	Volume density (3)	Rainfall (4)	Average air temperature °C (5)	Topographic humidity index (6)	Land use coefficient (7)	Slope aspect coefficient (8)	Relative elevation coefficient (9)	Simulated result (10)	Relative error (11)
1	129.68	1.25	84.50	10.44	6.27	1.06	0.89	0.25	129.97	0.0022
2	138.07	1.38	84.51	10.44	9.35	1.00	0.89	0.24	138.34	0.0020
3	134.90	1.40	84.52	10.44	7.21	1.06	0.81	0.24	136.13	0.0091
4	148.72	1.27	84.51	10.44	5.98	1.00	0.79	0.26	125.40	0.1568
5	76.60	1.24	84.50	10.44	8.12	1.06	0.79	0.26	124.08	0.6198
6	135.61	1.16	84.90	10.33	8.04	1.00	0.90	0.23	124.34	0.0831
7	154.36	1.30	84.93	10.32	6.77	0.65	0.87	0.20	129.87	0.1587
8	134.10	1.26	84.94	10.32	5.75	0.65	0.90	0.20	128.30	0.0433
9	150.96	1.38	84.25	10.52	7.21	1.00	1.00	0.08	146.22	0.0314
10	141.29	1.33	84.25	10.52	19.62	0.00	0.77	0.07	124.25	0.1206
11	112.93	1.14	84.65	10.40	8.22	0.65	0.90	0.26	119.29	0.0563
12	111.27	1.25	84.64	10.40	8.20	1.06	1.00	0.28	134.73	0.2108
13	93.63	1.25	84.61	10.39	5.44	1.06	0.79	0.17	126.73	0.3535
14	118.21	1.19	84.62	10.39	8.78	1.06	0.75	0.14	121.71	0.0296
15	111.83	1.19	84.26	10.51	8.14	1.00	0.81	0.22	122.09	0.0917
16	123.72	1.22	84.26	10.51	5.80	1.06	0.79	0.23	122.72	0.0081
17	138.85	1.50	84.48	10.39	6.72	0.65	0.81	0.22	139.00	0.0011
18	145.66	1.48	84.48	10.39	8.53	1.00	0.89	0.24	144.60	0.0073
19	144.87	1.34	84.43	10.40	6.85	1.00	0.79	0.16	132.38	0.0862
20	144.22	1.47	84.43	10.39	14.63	1.00	1.00	0.16	151.94	0.0535
21	148.92	1.43	84.44	10.33	6.47	1.00	0.90	0.23	142.18	0.0453
22	139.84	1.40	84.50	9.86	6.92	1.00	0.77	0.18	136.67	0.0227
23	122.13	1.25	84.42	10.38	8.02	1.06	0.89	0.27	129.43	0.0598
…	…	…	…	…	…	…	…	…	…	…
70	85.81	1.24	34.57	18.59	19.69	1.06	0.77	0.41	92.79	0.0813

Table 2: The parameters associated with regression analysis.

R	R^2	P value of F statistics	P value of regression coefficients						
			X_1	X_2	X_3	X_4	X_5	X_6	X_7
0.84	0.75	1.843×10^{-11}	0.00038	0.9	0.71	0.79	0.54	0.064	0.41

point's simulated soil moisture content, as shown in Table 1 (column 11). Finally, all points' mean relative error was calculated by the formula (4), $n = 70$, and the mean relative error is 0.09. The results showed that the simulation accuracy of soil moisture content was high.

4.2. Simulation of Soil Moisture Content in the Study Area. Considering that the seasonal variation of soil moisture content is mainly affected by rainfall and air temperature (evaporation), land use, soil factor, and topographic factors are relatively stable, the rainfall and temperature of each month in the year are inserted in equation (5), and the other variables remain unchanged. The seasonal variations of the soil moisture content were simulated from April to October 2005, and the simulated results are shown in Figure 6.

According to the simulated results shown in Figure 6, the average monthly soil water content from April to October is 110.03, 107.02, 94.79, 104.06, 101.81, 109.68, and 125.90 mm, respectively. Combining changes of the average rainfall and temperature from April to October 2005 in the Xihe Basin (Figure 7), it can be seen that the rainfall is the lowest in April and the highest in July, with no significant difference in other months, but the temperature rises gradually from May to August and drops gradually from August to October. The simulated monthly soil moisture content shows that the seasonal variation of soil moisture content is determined by the seasonal variation of rainfall and the temperature (controlling evaporation) and vegetation growth cycle. In April, although rainfall was less, the soil moisture content was not the lowest because the temperature was relatively low and

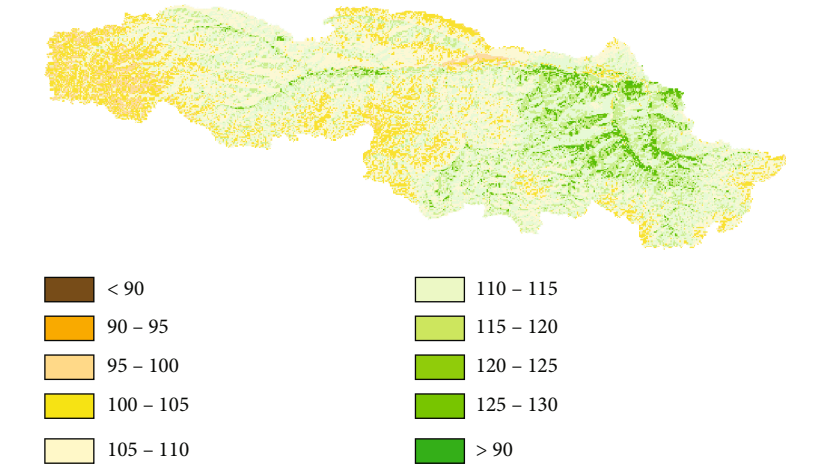

(a) The soil moisture content in Apr. 2005

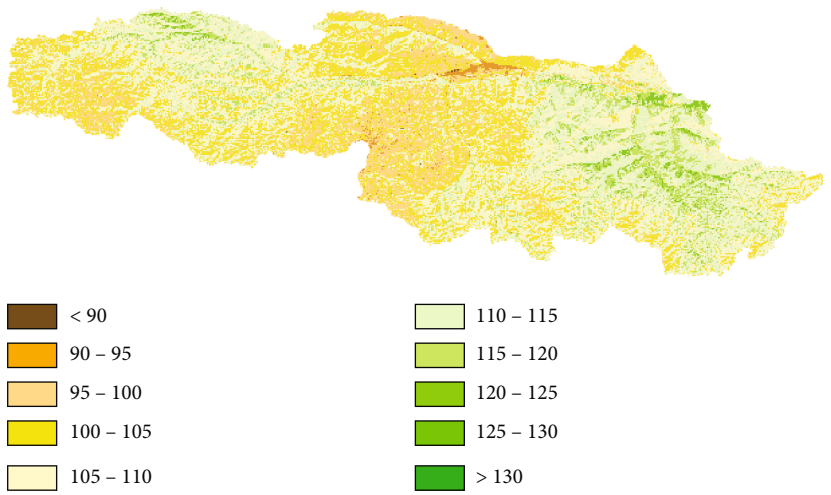

(b) The soil moisture content in May 2005

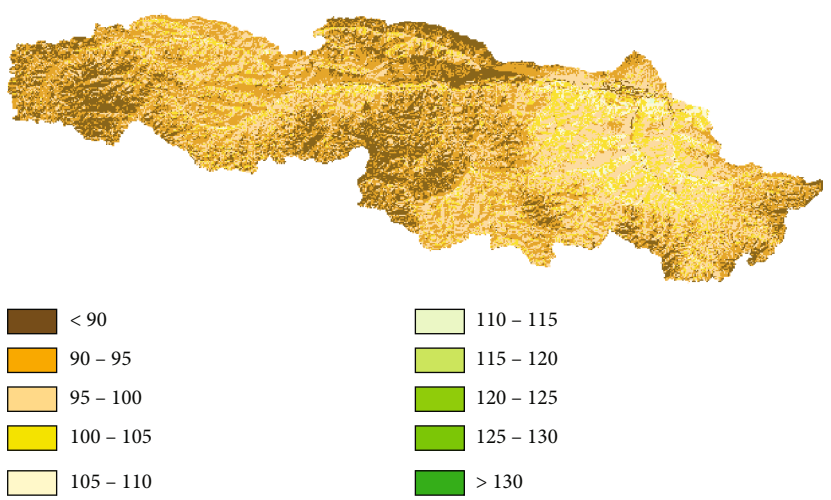

(c) The soil moisture content in Jun. 2005

Figure 6: Continued.

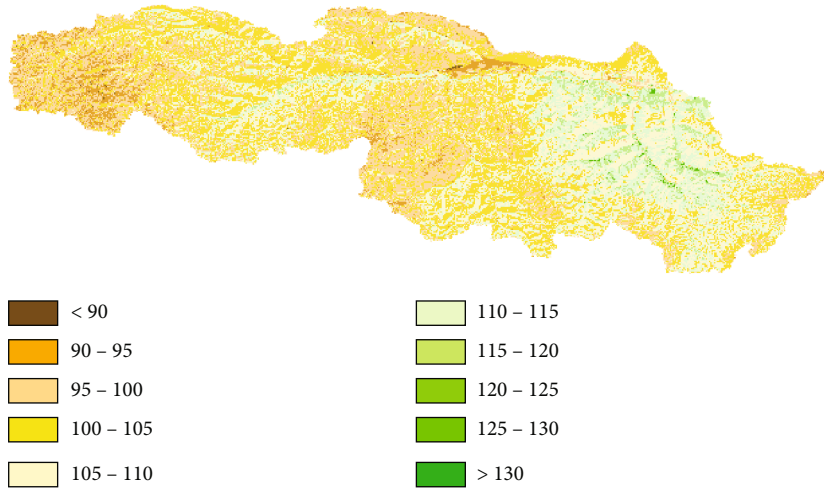

(d) The soil moisture content in Jul. 2005

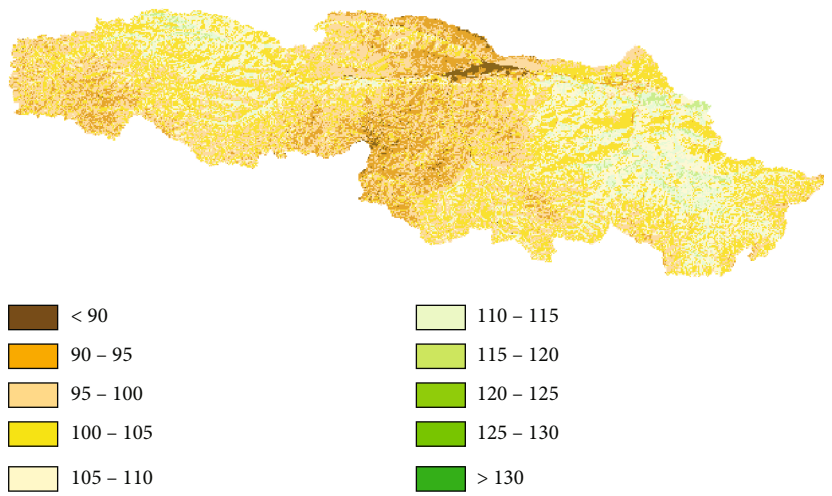

(e) The soil moisture content in Aug. 2005

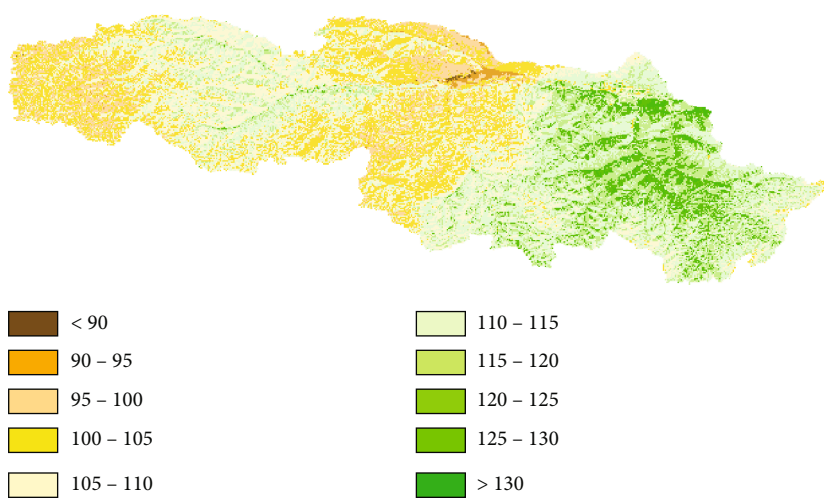

(f) The soil moisture content in Sep. 2005

Figure 6: Continued.

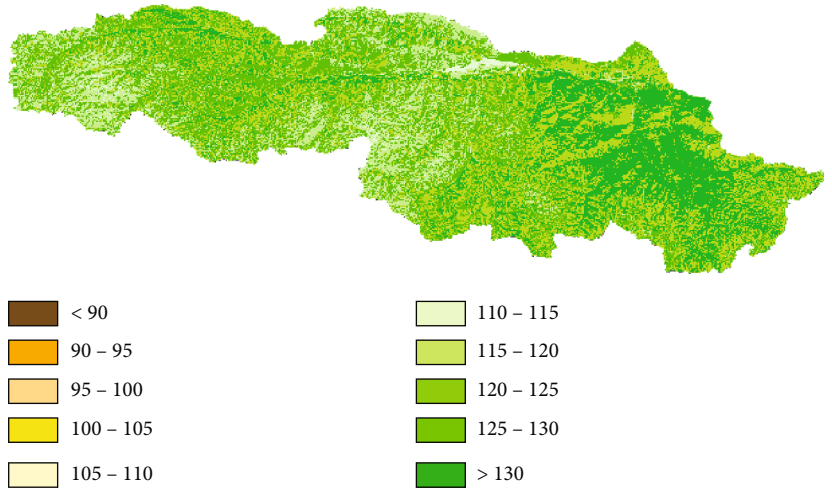

(g) The soil moisture content in Oct. 2005

Figure 6: The soil moisture content in from Apr. to Oct. in 2005.

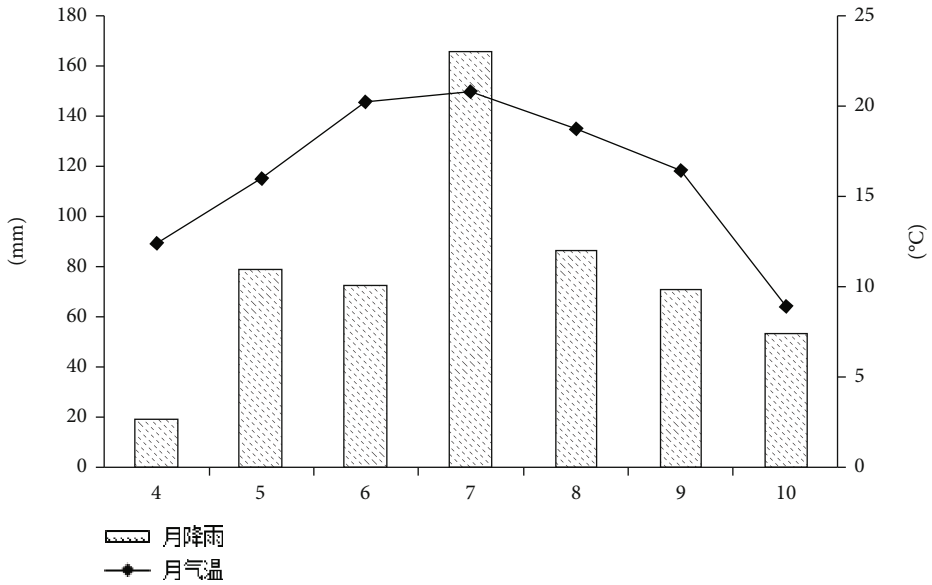

Figure 7: The average temperature and rain from Apr. to Oct. in 2005.

evaporation was less. Rainfall is then increased in May, but owing to the increase of temperature and evaporation, vegetation growth gradually becomes vigorous, and the soil moisture content is lower than that in April. From June to August, the temperature rises rapidly. Vegetation thrives, and evaporation increases. Additionally, because the rainfall in June is relatively small, June's soil moisture content is the lowest; when the rainfall increases in July, the soil moisture content is increased accordingly; however, the soil moisture content is decreased in August. From September to October, the temperature declines significantly, and the water consumption of vegetation and evaporation is decreased significantly; the soil moisture content is increased gradually, so the soil moisture content in October was higher (118.30 mm). These indicated that the seasonal variation of soil moisture content is not synchronous with the rainy season in climate [24] and is also affected by the temperature and vegetation growth cycle [25]. This is consistent with the conclusions of previous studies [29–32]. Therefore, it can be concluded that the proposed model equation can satisfactorily simulate the spatial and temporal variation of regional soil moisture content.

5. Conclusions

Based on the measured data, multiple linear regression analysis was carried out to obtain the simulated equation of soil water content, and the equation was applied in the study area.

The specific conclusions are given below: (1) The simulation method of antecedent soil moisture content in watershed scale was explored. The multiple regression equation of soil moisture content was established, which could simulate soil moisture content's spatial and temporal distribution.

(2) The proposed method produces reasonable estimates of soil moisture content. The average error of all the simulated values is 0.09, indicating that the simulation has high accuracy. (3) The map of soil moisture content in April-October 2005 obtained by the proposed method to the study area shows that the spatial distribution of soil moisture content is significantly affected by land use and the topographic index; seasonal variations in the year are significantly affected by the temperature (evaporation). The result can reflect the spatial and temporal variation of regional soil moisture content. This study provides methodological support for estimating regional soil moisture content and can be used to study regional soil erosion models.

Data Availability

The data used to support the findings of this study are available from the corresponding author upon request.

Conflicts of Interest

The authors declare no conflict of interest.

Acknowledgments

This study was supported by the National Key Research and Development Project of China (No. 2019YFC0409202), the Foundation for Innovative Research Groups of the National Natural Science Foundation of China (No. 51721006), High-level talent support program of North China University of water resources and electric power, and Special support for an innovative scientific and technological team of water ecological security in the water source area of the middle route of South to North Water Diversion in Henan Province.

References

[1] Y. Qiu, B. J. Fu, J. Wang, and L. D. Chen, "Soil moisture variation in relation to topography and land use in a hillslope catchment of the Loess Plateau, China," *Journal of Hydrology*, vol. 240, no. 3-4, pp. 243–263, 2001.

[2] H. Shi and M. A. Shao, "Soil and water loss from the Loess Plateau in China," *Journalof Arid Environments*, vol. 45, no. 1, pp. 9–20, 2000.

[3] L. D. Chen, W. Wei, B. J. Fu, and Y. H. Lü, "Soil and water conservation on the Loess Plateau in China: review and perspective," *Progress in Physical Geography*, vol. 31, no. 4, pp. 389–403, 2007.

[4] G. Lacombe, B. Cappelaere, and C. Leduc, "Hydrological impact of water and soil conservation works in the Merguellil catchment of central Tunisia," *Journal of Hydrology*, vol. 359, no. 3–4, pp. 210–224, 2008.

[5] C. Fitzjohn, J. L. Ternan, and A. G. Williams, "Soil moisture variability in a semi-arid gully catchment: implications for runoff and erosion control," *Catena*, vol. 32, no. 1, pp. 55–70, 1998.

[6] E. Meyles, A. Williams, L. Ternan, and J. Dowd, "Runoff generation in relation to soil moisture patterns in a small Dartmoor catchment, Southwest England," *Hydrological Processes*, vol. 17, no. 2, pp. 251–264, 2003.

[7] B. M. Wyatt, T. E. Ochsner, E. S. Krueger, and E. T. Jones, "In-situ soil moisture data improve seasonal streamflow forecast accuracy in rainfall-dominated watersheds," *Journal of Hydrology*, vol. 590, no. 1, pp. 125404–125412, 2020.

[8] H. Wang, J. Q. Wang, and M. A. Shao, "Simulation experiment of effect of antecedent soil moisture content on characteristics of runoff and sediment from two soil sloping lands," *Transactions of the Chinese Society of Agricultural Engineering*, vol. 24, no. 5, pp. 65–68, 2008.

[9] V. Castillo, A. GomezPlaza, and M. MartinezMena, "The role of antecedent soil water content in the runoff response of semiarid catchments: a simulation approach," *Journal of Hydrology*, vol. 284, no. 1-4, pp. 114–130, 2003.

[10] G. A. Hongbei and S. H. Mingan, "Effect of rainfall on soil water and soil temperature in arid region," *Journal of Irrigation and Drainage*, vol. 30, no. 1, pp. 40–45, 2011.

[11] H. Wang, X. Lei, D. Qin, J. H. Wang, and Z. H. Zhou, "Basin runoff yielding model construction based on human activities," *Resources Science*, vol. 6, pp. 14–18, 2003.

[12] J. Luo, Z. Zheng, T. Li et al., "Quantifying the contributions of soil surface microtopography and sediment concentration to rill erosion," *Science of the Total Environment*, vol. 752, no. 141886, pp. 1–11, 2021.

[13] L. Yang, W. Wei, L. Chen, F. Jia, and B. Mo, "Spatial variations of shallow and deep soil moisture in the semi-arid Loess Plateau, China," *Hydrology and Earth System Sciences*, vol. 16, no. 9, pp. 3199–3217, 2012.

[14] Z. Jin, L. Guo, Y. L. Yu, D. Luo, B. Fan, and G. Chu, "Storm runoff generation in headwater catchments on the Chinese Loess Plateau after long-term vegetation rehabilitation," *Science of the Total Environment*, vol. 748, article 141375, 2020.

[15] J. M. Tadros, N. K. al-Mefleh, A. Y. Othman, and A. al-Assaf, "Water harvesting techniques for improving soil water content, and morpho- physiology of pistachio trees under rainfed conditions," *Agricultural Water Management*, vol. 243, article 106464, 2021.

[16] C. X. Zhang, *Extraction and Application of Topographic Wetness Index Based on DEM. Master*, Northwest A&F University, 2006.

[17] H. M. Wang, Q. K. Yang, and Z. H. Yao, "Correlation of soil moisture and topographic wetness index at a scale of small watershed," *Bulletin of Soil Water Conservation*, vol. 29, no. 4, pp. 110–113, 2009.

[18] T. C. Li, M. A. Shao, Y. H. Jia, X. Jia, and L. Huang, "Profile distribution of soil moisture in the gully on the northern Loess Plateau, China," *Catena*, vol. 171, pp. 460–468, 2018.

[19] B. W. Yu, G. H. Liu, Q. S. Liu, X. Wang, J. Feng, and C. Huang, "Soil moisture variations at different topographic domains and land use types in the semi-arid Loess Plateau, China," *Catena*, vol. 165, pp. 125–132, 2018.

[20] S. Wang, B. J. Fu, and J. B. Liu, "Soil moisture temporal stability analysis for typical hilly and gully re-vegetated catchment in the Loess Plateau, China," *Environmental Earth Sciences*, vol. 75, no. 9, 2016.

[21] H. X. Bi, J. J. Zhang, J. Z. Zhu et al., "Spatial dynamics of soil moisture in a complex terrain in the semi-arid Loess Plateau region, China," *Journal of the American Water Resources Association*, vol. 44, no. 5, pp. 1121–1131, 2008.

[22] Y. Qiu, B. J. Fu, J. Wang, and L. Chen, "Spatial variability of soil moisture content and its relation to environmental indices in a semi-arid gully catchment of the Loess Plateau, China," *Journal of Arid Environments*, vol. 49, no. 4, pp. 723–750, 2001.

[23] Z. H. Yao, Y. Q. Wang, and R. Li, "Modeling soil moisture based on GIS in small watershed of Loess Hilly area," *Acta Agrestia Sinica*, vol. 19, no. 3, pp. 525–530, 2011.

[24] S. H. Sadeghi, G. A. Ghaffari, A. Rangavar, Z. Hazbavi, and V. P. Singh, "Spatiotemporal distribution of soil moisture in gully facies," *International Soil and Water Conservation Research*, vol. 8, no. 1, pp. 15–25, 2020.

[25] E. Sachs and P. Sarah, "Combined effect of rain temperature and antecedent soil moisture on runoff and erosion on Loess," *Catena*, vol. 158, pp. 213–218, 2017.

[26] M. Lal, S. K. Mishra, and M. Kumar, "Reverification of antecedent moisture condition dependent runoff curve number formulae using experimental data of Indian watersheds," *Catena*, vol. 173, pp. 48–58, 2019.

[27] Q. K. Yang, L. T. Li, T. R. McVicar, T. G. Van Niel, and C. X. Zhang, "ANUDEM—a professional DEM interpolation software package," *Agricultureal Research in the Arid Areas*, vol. 24, no. 3, pp. 36–41, 2006.

[28] K. J. Beven and M. J. Kirkby, "A physically based, variable contributing area model of basin hydrology," *Hydrological Sciences Bulletin*, vol. 24, pp. 43–68, 1979.

[29] J. Y. Li, F. B. Zhang, S. W. Wang, and M. Yang, "Combined influences of wheat-seedling cover and antecedent soil moisture on sheet erosion in small-flumes," *Soil and Tillage Research*, vol. 151, no. 8, pp. 1–8, 2015.

[30] J. Fortesa, J. Latron, J. García-Comendador, J. Company, and J. Estrany, "Runoff and soil moisture as driving factors in suspended sediment transport of a small mid-mountain Mediterranean catchment," *Geomorphology*, vol. 368, no. 11, article 107349, 2020.

[31] B. Wang, F. X. Wen, J. T. Wu, X. Wang, and Y. Hu, "Vertical profiles of soil water content as influenced by environmental factors in a small catchment on the hilly-gully Loess Plateau," *Plos One*, vol. 9, no. 10, article e109546, 2014.

[32] Y. Q. Wang, J. Yang, Y. N. Chen, A. Wang, and P. de Maeyer, "The spatiotemporal response of soil moisture to precipitation and temperature changes in an arid region, China," *Remote Sensing*, vol. 10, no. 3, p. 468, 2018.

Hindawi
Journal of Sensors
Volume 2021, Article ID 6639668, 8 pages
https://doi.org/10.1155/2021/6639668

Research Article

Development of Capacitive Rain Gauge for Marine Environment

Hui Chai, Shixuan Liu, Xianglong Yang, Xiaozheng Wan, Shizhe Chen, Jiming Zhang, Yushang Wu, Liang Zheng, and Qiang Zhao

Institute of Oceanographic Instrumentation, Qilu University of Technology (Shandong Academy of Sciences), Qingdao 266061, China

Correspondence should be addressed to Shizhe Chen; hcszom@163.com

Received 24 November 2020; Revised 19 February 2021; Accepted 12 March 2021; Published 7 April 2021

Academic Editor: Yuan Li

At present, the methods and instruments for measuring the precipitation on land may not effectively work in the offshore corrosion environment which is characterized by salt and humid. The research look at investigating the reliable and precision approach of measuring rainfall and a capacitive rain gauge for the marine environment is developed. Firstly, according to the working principle and performance requirements of the capacitive rain gauge, the modular mechanical structure and capacitance voltage conversion circuit of the rain gauge are designed, and the calibration and stability experiments of the prototype are tested to evaluate the measurement error and exam the accuracy of the rain gauge measurement results changing over time. Then, environmental adaptability experiment is carried out on the capacitive rain gauge to explore its performance in the environment of temperature and humidity changes as well as salt spray. Finally, the feasibility of the rain gauge used in the marine environment is verified by the sea test of the prototype. The measurement error of the developed capacitive rain gauge is less than 1 mm, which provides a realization method for the measurement of precipitation in the marine environment.

1. Introduction

The measurement for oceanic precipitation is one of the basic elements of marine meteorological observation, which is significant to the study of marine weather and climate change, water, and energy cycle system as well as numerical weather forecast [1–3]. Rainfall measurement can be obtained directly by rain gauge [4, 5] and can also be indirectly estimated by weather radar [6] and retrieved by satellite remote sensing [7] and microwave link attenuation [8, 9]. Compared with radar estimation, satellite remote sensing, and microwave link attenuation retrieval of rainfall, the accuracy of rainfall measured by rain gauge is the highest and is usually used as a comparison benchmark for evaluating other precipitation measurement methods [10–12]. However, the rain gauge is a single point precipitation measurement tool and unable to obtain the precipitation in a large area. To solve this problem, the rainfall station network is designed for measuring regional precipitation, and this network has been widely used on land [13, 14].

The main methods of measuring precipitation by rain gauge mainly include water-holding method [15], optical method [16], acoustic method [17], and piezoelectric effect method [18]. The water-holding method obtains rainfall by measuring the change of water weight or volume in the container, optical method adopts the principle of diffuse reflection caused by raindrop passing through laser or infrared light to predict rainfall, acoustic method uses acoustic reflection to measure precipitation, and the rain gauge applying piezoelectricity effect estimates raindrop spectrum and precipitation through perception raindrop momentum changing. Among these methods, the optical method, acoustic method, and piezoelectric effect method apply optics lens, acoustic probe, and piezoelectric patches as perception elements, respectively, and these sensing parts or elements are susceptible to the surrounding environment such as noise, dust, and corrosive; so, these methods are easy to cause measurement error and rarely used in rough environmental conditions [19, 20]. The rain gauge adopting the water-holding method has few environment sensitive parts comparing with other types of rain gauge; so, it has advantages in high

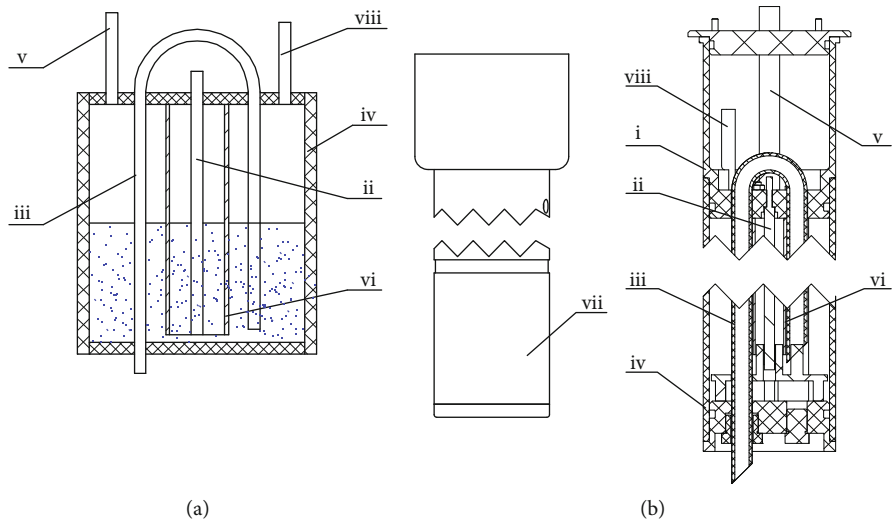

Figure 1: Schematic diagram (a) and structure diagram (b) of the capacitive rain gauge with (i) water inlet support, (ii) electrode rod, (iii) drainage pipe, (iv) water container, (v) water inlet pipe, (vi) electrode pipe, (vii) shell, and (viii) vent pipe.

accuracy and adaptability and is widely used for measuring rainfall.

There are mainly three kinds of rain gauges for measuring precipitation by the water-holding method: tipping bucket type [21], siphon type [22], and weighting type [23]. The performance of these rain gauges varies according to the measure principle, and there exists certain deficiencies among these rain gauges when they are used in different conditions. For example, the tipping bucket rain gauge is easy to be affected by rain intensity, and its measurement error increases with rain intensity increasing [24]. When the rain intensity is small, a measure error will happen for siphon rain gauge [25]. In the case of heavy rainfall, the weighting rain gauge is prone to miss precipitation data; so, the stability of measurement results is insufficient [26]. In addition, the tipping bucket rain gauge and siphon rain gauge have mechanical transmission parts, which are difficult to work stably and reliably in the marine environment with the characteristic of humidity and salt spray, and for this reason, the rain gauges need to be regularly maintained. However, the maintenance for the rain gauge used in severe or unattended environment is difficult. Hence, the measure accuracy and operation reliability in various environment are needed to give serious consideration when a rainfall measuring apparatus is developed.

It has been utilized in rain gauge to compose network on land to measure rainfall in large area; however, the rainfall monitoring about a large area at sea using rain gauge is not implemented. So far, the use of rain gauge to measure precipitation at sea mainly relies on ship [19, 27] and ocean buoy [28, 29]. However, the ship route selection, ship movement, and ship superstructure all affect the rainfall measurement area and results [19, 27]. The density of the buoy in the sea is still low, and the spatial distribution is uneven, which cannot meet the needs of large-scale regional rainfall monitoring. With the exploitation of marine resources and development of ocean observation technology, more and more drilling platforms, wind and ocean energy power generation devices, and ocean observation equipment will be deployed near-globe seas, and these ocean platforms will become the ideal platform to carry rain gauge; so, it can be predicted that an increasing number of rain gauge will be installed on ocean platforms to carry out large-scale marine precipitation measurement in the future. Although some technologies based on the methods mentioned above for measuring rainfall at sea have been carried out, and the measurement accuracy is similar to that of used on land, the weatherability, environment adaptability, and data integrity still need to be further verified or perfected [18, 19]. Therefore, it is necessary to pay close attention to study the feasibility method for measuring precipitation and elaborate a rain gauge that works precisely and reliably in the marine corrosive environment for a long-term application.

From the point of technical feasibility and working reliability, a type of capacitive rain gauge that is able to adapt to the marine environment was developed in this paper. The modular mechanical structure, circuit design, laboratory performance trial, and offshore test of the rain gauge were systematically studied, which provided an effective and feasible technical method and selection scheme for obtaining the marine precipitation.

2. Materials and Methods

This part first introduces the working principle of the capacitive rain gauge, then describes the hardware composition of the developed capacitive rain gauge, and finally shows the performance test method of the rain gauge.

2.1. Working Principle. The rainfall measure method of the gauge presented in this paper is based on the principle of capacitive sensor for liquid level measurement [30]. The schematic diagram of the capacitive rain gauge is shown in Figure 1(a). The electrode rod, electrode tube, and the air and the water between the electrode rod and electrode tube constitute a cylindrical capacitor, and the axe of the water

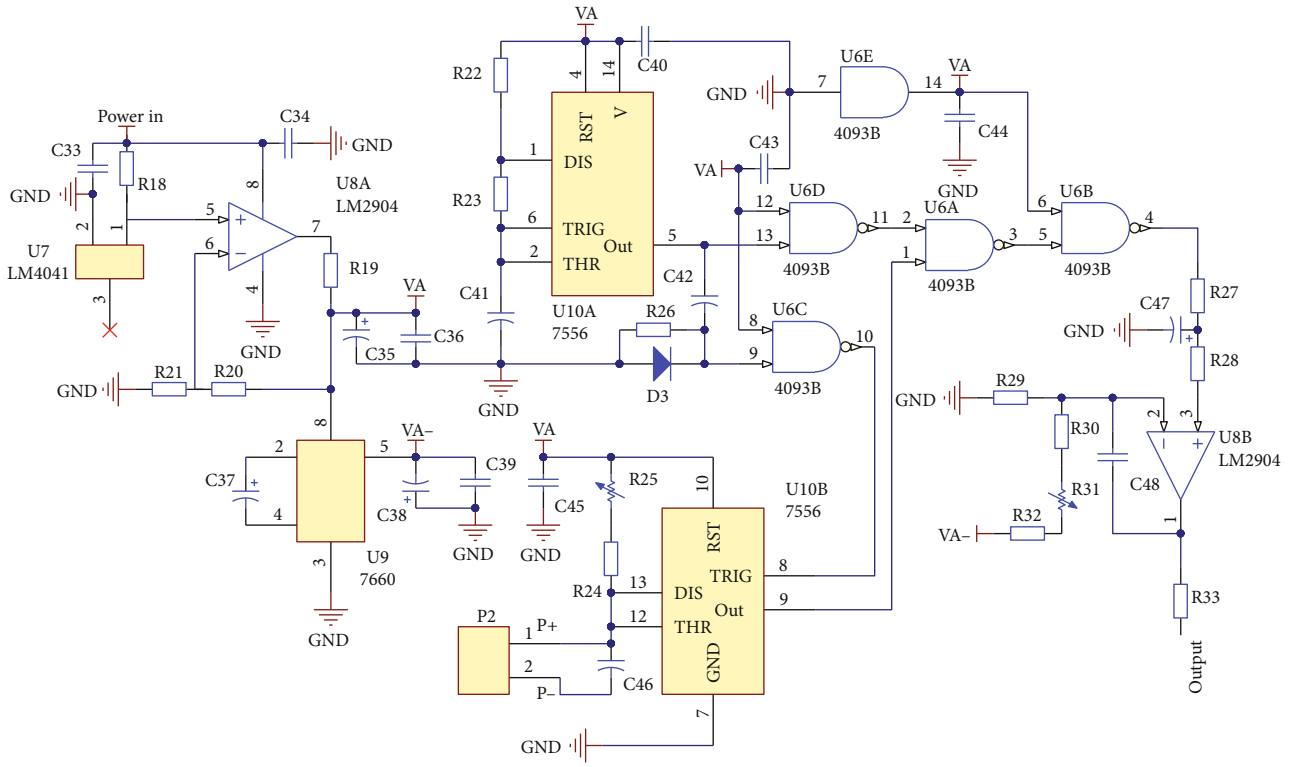

Figure 2: Circuit design of the capacitive rain gauge.

container, electrode tube, and electrode rod is colinear. When rain falls, the precipitation enters into the water container through the water inlet pipe and as a result, the water level in the electrode tube will change, which will cause the change of capacitance value. The precipitation can be measured by measuring the changed capacitance value.

The whole cylinder capacitor can be regarded as the capacitor c_1 (F) with water as its dielectric and the capacitor c_2 (F) with air as its dielectric in parallel. The inner circle radius of the electrode tube is r_1 (mm), the radius of the electrode rod is r_0 (mm), the height of water container is L (mm), and the height of the internal water level is l (mm). The dielectric constants of vacuum, water, and air are ε_0, ε_1, and ε_2, respectively. The theoretical values of c_1 and c_2 are

$$c_1 = \frac{2\pi\varepsilon_0\varepsilon_1 l}{\ln(r_1/r_0)}, c_2 = \frac{2\pi\varepsilon_0\varepsilon_2(L-l)}{\ln(r_1/r_0)}. \quad (1)$$

The capacitance c (F) of the whole cylinder capacitor can be expressed as

$$c = c_1 + c_2 = \frac{2\pi\varepsilon_0\varepsilon_2 L}{\ln(r_1/r_0)} + \frac{2\pi\varepsilon_0(\varepsilon_1-\varepsilon_2)}{\ln(r_1/r_0)} l. \quad (2)$$

According to Equation (2), the capacitance c is a linear function of the water level height l, and there is a one-to-one match between the capacitance value and water level height. When the water level rises to the top of U-shaped drainage pipe, the precipitation value is the maximum, and the siphon phenomenon will occur at this time. As a result, the precipitation in the water container is discharged by the drainage pipe, the measured value of rainfall returns to zero, and the measurement of precipitation starts again for next cycle.

2.2. Hardware System Design

2.2.1. Mechanical Structure Design. The capacitive rain gauge is composed of mechanical part and circuit part. As shown in Figure 1(b), the modular mechanical part is mainly composed of outside shell and internal structure. The internal structure is the core part of the rain gauge and mainly includes water inlet support, water container, drainage pipe, electrode rod, electrode tube, and circuit. The shell, on one hand, is used to protect and seal the internal parts, and on the other hand, it is used to accommodate precipitation and to provide a mounting location with offshore platform. The circuit elements are installed in the water inlet support of the internal structure.

The maximum volume of the water container V (ml), the maximum precipitation H (mm) in one measuring cycle, and the effective cross-sectional area S (mm^2) of the water container are all set values according to the designed requirements. The diameter of shell upper end D (mm) and the height of water container L (mm) can be expressed as follows:

$$D = \frac{2}{\sqrt{\pi}}\sqrt{\frac{V}{H}}, L = \frac{V}{S} = \frac{\pi D^2}{4S} H. \quad (3)$$

Equation (3) can also be used to characterize the relationship between the water level changing Δl (mm) and

precipitation h (mm) over a period of time:

$$\Delta l = \frac{\pi D^2}{4S} h. \quad (4)$$

Compared with the existing tipping bucket rain gauge and siphon rain gauge, the proposed capacitive rain gauge has no mechanical transmission parts, which can effectively improve the reliability of the system in the oceanic environment. In addition, all parts of the rain gauge are made of ant-corrosion and weather resistance materials considering the corrosive environment of high salt and humidity on the sea: except for the electrode rod, electrode tube, and fastening connector which are made of stainless steel, and the other parts are made of polycarbonate or polymethyl methacrylate. The circuit components and wiring points are treated with moisture proof, salt fog proof, and mould proof technology.

2.2.2. Circuit Design. In order to achieve high-precision measurement, the circuit of the rain gauge is meticulously designed. The circuit diagram of the system is shown in Figure 2. Because there is a one-to-one correspondence between capacitance and precipitation, the capacitance is output in the form of voltage. It is the key of circuit design to accurately measure the capacitance value of the capacitor composed of electrode tube, electrode rod, and dielectric between them and convert the capacitance value into the voltage value. The circuit system is mainly composed of reference oscillation circuit, oscillation modulation circuit, phase discrimination shaping circuit, and integral amplifier circuit. The reference oscillation circuit and the oscillation modulation circuit preprocess the input capacitance data and modulate pulse width, respectively, and then generate rectangular pulse through the phase discrimination and shaping circuit. Finally, the corresponding voltage signal is obtained through the integral amplifier circuit.

According to Equations (2) and (4), the relationship between capacitance change Δc (F) and precipitation h (mm) for a precipitation process can be obtained:

$$\Delta c = \frac{2\pi\varepsilon_0\varepsilon_2 L}{\ln(r_1/r_0)} + \frac{\pi^2\varepsilon_0(\varepsilon_1 - \varepsilon_2)D^2}{2\ln(r_1/r_0)S} h. \quad (5)$$

The relationship between output voltage u (V) and capacitance c (F) according to circuit analyses can be expressed as follows:

$$u = \mathrm{A}c + \mathrm{B}, \quad (6)$$

where A (V/F) and B (V) are constants related to circuit parameters.

According to Equations (5) and (6), the relationship between output voltage u and capacitance c is linear. The precipitation in a certain period can be obtained by calculating the change value of output voltage. The input voltage of the system is 12 V, and the output voltage is 0–5 V, corresponding to 0–50 ml precipitation.

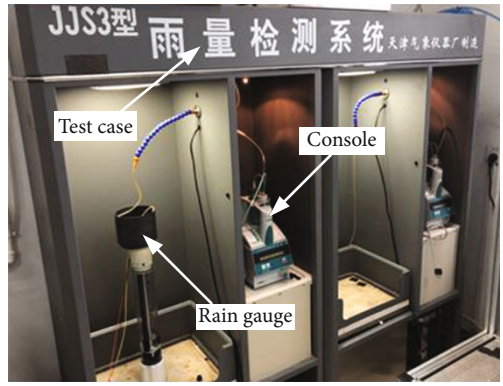

Figure 3: Calibration test and stability experiment of the rain gauge.

2.3. Experiments

2.3.1. Calibration Experiment. In order to determine the relationship between the precipitation and the output voltage value of the capacitive rain gauge and even evaluate the measurement error and test the accuracy of the measurement results, the developed rain gauge was calibrated. The calibration experiment of rain gauge is shown in Figure 3, and it can be seen that the rain gauge calibration system is composed of two parts: test case and console. The test case is used to place the rain gauge and add water to the rain gauge. The console is used to precisely control the amount of water added and process the output voltage value.

The calibration method is as follows: the test case injects ration water into the rain gauge from 0 ml to the maximum value of 500 ml by 50 ml interval, which corresponds the precipitation increasing correspondingly from 0 mm to 50 mm by 5 mm interval, and the interval time of adjacent water injection is 3 minutes. At the same time, the output voltage is collected by data collector of console. Once the water capacity reaches 500 ml, siphon will occur, and the water injection and measurement process will be repeated after emptying. The process of water injection and measurement is carried out for three times, and for the same volume injection, the average value of the three output voltage values is taken as the measurement voltage.

2.3.2. Stability Experiment. In order to test the stability of measurement results of the developed capacitive rain gauge over time, the stability experiment was carried out using the same experiment system shown in Figure 3. The test method is as follows: the water in the rain gauge is drained and injects 50 ml, 150 ml, 250 ml, 350 ml, and 450 ml water orderly into the rain gauge every 5 days to simulate the precipitation of 0 mm, 5 mm, 15 mm, 25 mm, 35 mm, and 45 mm. For each water injection point, the output voltage is collected at a sampling interval of 10 minutes for 5 days, and the change of voltage data during the period is recorded.

2.3.3. Environmental Adaptability Experiment. The developed capacitive rain gauge is mainly used in the marine environment. In order to investigate the possible issues of the prototype and test the adaptability and reliability of the rain

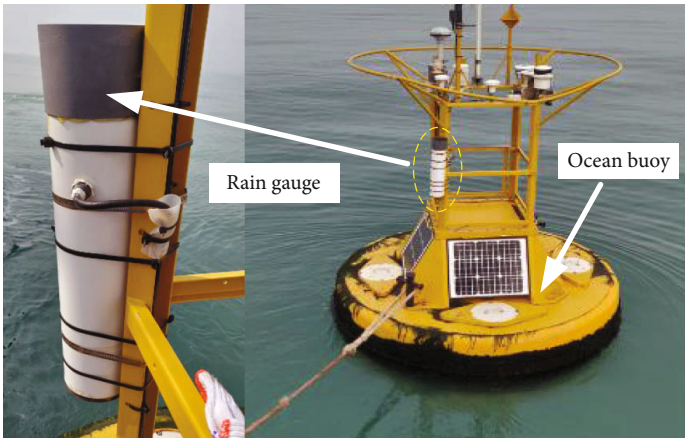

Figure 4: Offshore experiment of the rain gauge.

Table 1: Calibration data of rain gauge.

Measuring point [ml]	Nominal voltage [V]	Measuring voltage [V]	Precipitation error [mm]	Uncertainty [mm]
0	0	0.008	0.08	0.001
50	0.5	0.551	0.51	0.001
100	1.0	1.071	0.71	0.001
150	1.5	1.532	0.32	0.001
200	2.0	2.010	0.10	0.002
250	2.5	2.501	0.01	0.002
300	3.0	2.980	-0.20	0.002
350	3.5	3.480	-0.20	0.003
400	4.0	4.001	0.01	0.003
450	4.5	4.510	0.10	0.003
500	5.0	4.990	0.10	0.003

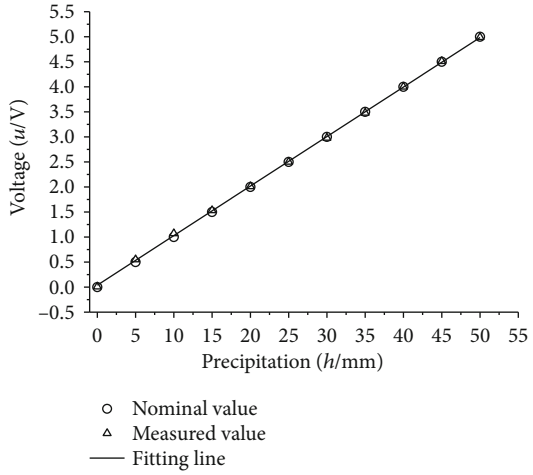

Figure 5: Calibration curve of output voltage with precipitation.

gauge in the marine environment, the environmental adaptability experiment of the rain gauge is carried out. Environmental adaptability experiment for oceanic rain gauge includes temperature test and salt spray test. During the temperature test, the working capacitive rain gauge is placed in a constant temperature and humidity box. The humidity is set to 95% RH, and the temperature varies from −10°C to 50°C by 10°C interval. The temperature test for each temperature point lasts 72 hours. During the salt spray test, the cleaned capacitive rain gauge is put into the salt spray box, and 5% sodium chloride solution (pH value between 6.5 and 7.2) is atomized by ultrasonic cavitation to simulate the salt spray corrosion environment. The salt spray experiment lasts for 48 hours. After the test, the salt deposits on the surface of the shell are washed with flowing water, and the rain gauge is placed in the indoor environment for 1-2 hours to observe its appearance structure.

2.3.4. Offshore Experiment. In order to exam the performance of the developed capacitive rain gauge in the marine environment, the developed rain gauge is installed on the marine monitoring buoy which is 1.8 kilometers out of the land in Weihai on the coast of the Yellow Sea for offshore experiment as shown in Figure 4. The power supply of the rain gauge is provided by solar battery on the buoy, and the output voltage data is processed by the buoy control system and then transmitted back to land by the communication system in real time.

3. Results and Discussion

The designed capacitive rain gauge is mainly used in the marine environment, which requires high reliability and measurement accuracy. The specific performance requirements are as follows: precipitation measurement range is 0–50 mm, and measurement accuracy is 1 mm.

According to the calibration method mentioned above, the calibration is carried out, and the calibration data are shown in Table 1. It can be seen from Table 1 that when the water volume increases from 0 ml to 500 ml by 50 ml interval, the measurement error of each calibration point is within ±1 mm, and the maximum measurement error and maximum uncertainty are 0.71 mm and 0.003 mm, respectively, which meet the designed requirements of the capacitive rain gauge. However, the calibration results about the

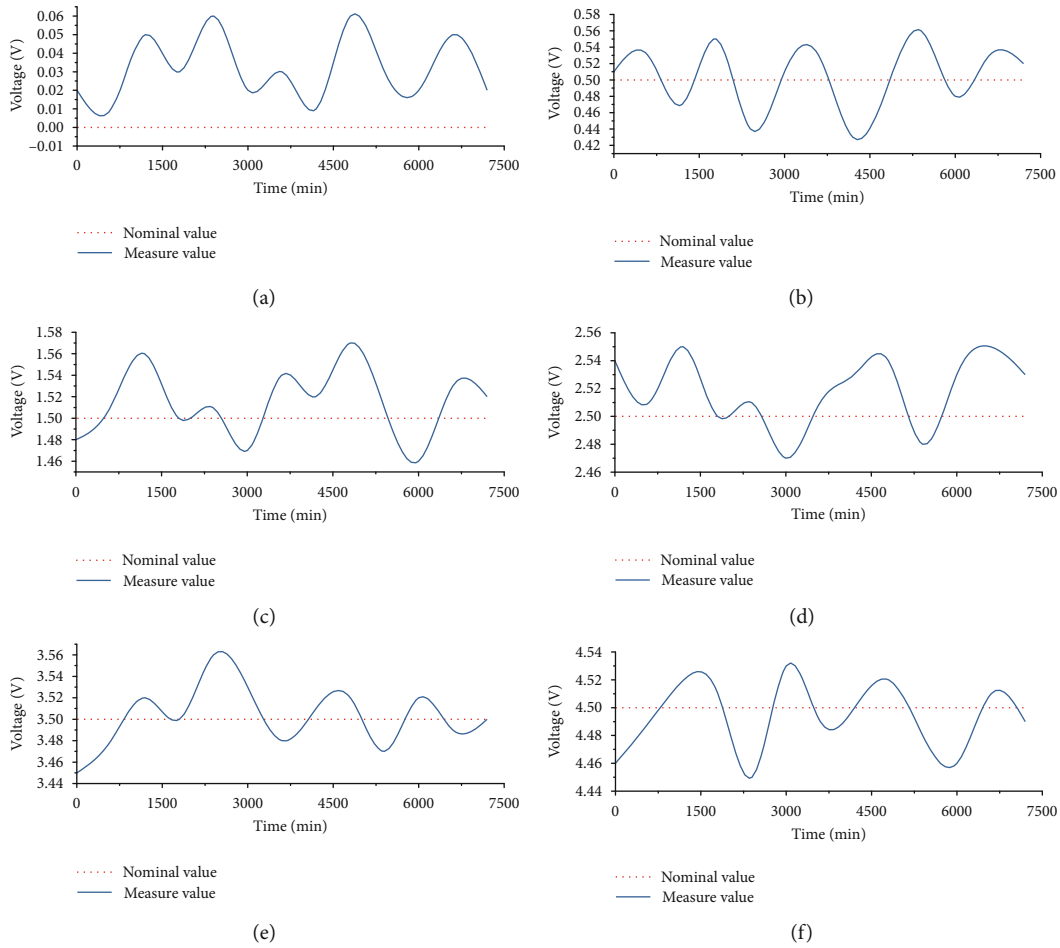

Figure 6: Voltage of measured point over time in the stability test with precipitation (a) 0 mm, (b) 5 mm, (c) 15 mm, (d) 25 mm, (e) 35 mm, and (f) 45 mm.

Table 2: The maximum voltage deviation and precipitation error of stability experiment.

Measuring point [ml]	Nominal voltage [V]	Maximum deviation voltage [V]	Maximum error of precipitation [mm]
0	0	0.008	0.08
50	0.5	0.567	0.67
150	1.5	1.552	0.52
250	2.5	2.541	0.41
350	3.5	3.476	-0.24
450	4.5	4.543	0.43

rain gauge are confined only to the date of test points showed in Table 1. In order to obtain the relationship between the measuring voltage and the precipitation for any point within the range, the least square method is used to fit the measured values in Table 1 to obtain the calibration curve, and the calibration curve is shown in Figure 5.

The expression of the calibration curve is

$$u = 0.0989h + 0.0394. \quad (7)$$

According to Figure 5 and Equation (7), the relationship between output voltage u and precipitation h is linear, which verifies the correctness of theoretical analysis of Equations (5) and (6) about circuit design. Equation (7) is the basis for setting the output voltage of the designed rain gauge.

In the stability experiment, the output voltage curves of each measuring point over time are shown in Figure 6. It can be seen from Figure 6 that the output voltage of each measured point fluctuates around the nominal value during the test process, and there is no gradual increase or decrease trend, indicating that the rain gauge measurement result is stable and reliable.

The maximum deviation voltage of each measuring point and the corresponding precipitation error during the stability trial are shown in Table 2. It can be seen from Table 2 that the maximum measurement error of precipitation is less than 1 mm. When the precipitation is 50 mm, the maximum error of the measured value is 0.67 mm. The stability experiment results show that the rain gauge meets the requirements of stability and measurement accuracy.

In the process of environmental adaptability experiment, the output voltage of rain gauge has no change, which shows that the rain gauge has good adaptability and reliability under different temperature and humidity environments. After the

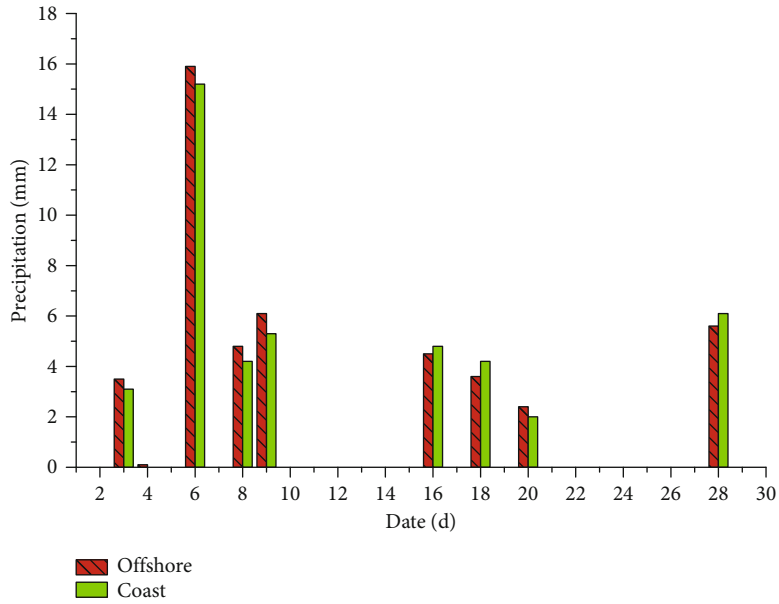

Figure 7: Precipitation comparison of offshore trial and coast observation.

salt spray experiment, there is no pitting corrosion and crack on the surface of rain gauge, which indicates that the rain gauge is able to resist salt spray corrosion.

The rain gauge was installed on the buoy platform for sea trial in May 2019. The daily measured offshore precipitation data from June 1st, 2019 to June 30, 2019, is shown in Figure 7. The coast precipitation in the same period is also given in Figure 7 to compare with the offshore precipitation to verify the measurement performance of the developed capacitive rain gauge in the marine environment. It can be seen from Figure 7 that the difference between the offshore precipitation and the coast precipitation offered by local meteorological observation is small, and the maximum difference is 0.8 mm. The results show that the capacitive rain gauge can accurately measure the offshore precipitation.

4. Conclusions

A capacitive rain gauge is developed in this paper, which has been tested in laboratory and marine environment, and the performance of the rain gauge has met the design requirements. The following conclusions can be obtained: the hardware system in the mechanical structure and circuit board design of the rain gauge adopts anticorrosive material and technology, which exhibits good environmental adaptability in different temperature and humidity environments as well as salt fog environment. The relationship between the output voltage and precipitation is linear in theory and is proved by calibration and stability experiment. It also shows in the calibration test that the precipitation measurement accuracy of the rain gauge is less than 1 mm, which achieves the design requirement. Based on the marine monitoring buoy, the capacitive rain gauge was tested in the marine environment. The rain gauge can measure the offshore precipitation with high accuracy and reliability comparing with the precipitation data observed on the coast. The developed capacitive rain gauge has obtained the calibration certificate and has valuable in onshore and offshore application.

Data Availability

The data used to support the findings of this study are available from the corresponding author upon request.

Conflicts of Interest

The authors declare no conflict of interest.

Acknowledgments

This research is supported by the National Natural Science Foundation of China (41976179), National Key Research and Development Project (2017YFC1403303), Natural Science Foundation of Shandong Province (ZR2019MF022), and Integration of Defence and Civilian Technologies Project of Shandong (2019JMRH0105).

References

[1] C. Kummerow, W. Barnes, T. Kozu, J. Shiue, and J. Simpson, "The tropical rainfall measuring mission (TRMM) sensor package," *Journal of Atmospheric and Oceanic Technology*, vol. 15, no. 3, pp. 809–817, 1998.

[2] K. Trenberth, L. Smith, T. Qian, A. Dai, and J. Fasullo, "Estimates of the global water budget and its annual cycle using observational and model data," *Journal of Hydrometeorology*, vol. 8, no. 4, pp. 758–769, 2007.

[3] S. Michaelides, V. Levizzani, E. Anagnostou, P. Bauer, T. Kasparis, and J. E. Lane, "Precipitation: Measurement, remote sensing, climatology and modeling," *Atmospheric Research*, vol. 94, no. 4, pp. 512–533, 2009.

[4] A. Molini, L. G. Lanza, and P. La Barbera, "The impact of tipping-bucket raingauge measurement errors on design rainfall for urban-scale applications," *Hydrological Processes*, vol. 19, no. 5, pp. 1073–1088, 2005.

[5] C. Frei and C. Schär, "A precipitation climatology of the Alps from high-resolution rain-gauge observations," *International Journal of Climatology*, vol. 18, no. 8, pp. 873–900, 1998.

[6] L. L. Yang, Y. Yang, Y. C. Qi, X. X. Qiu, and Z. Q. Gong, "A case study of radar-derived quantitative precipitation estimation," *Advanced Materials Research*, vol. 726-731, pp. 4541–4546, 2013.

[7] C. Kummerow, Y. Hong, W. S. Olson et al., "The evolution of the Goddard profiling algorithm (GPROF) for rainfall estimation from passive microwave sensors," *Journal of Applied Meteorology*, vol. 40, no. 11, pp. 1801–1820, 2001.

[8] M. F. R. Gaona, A. Overeem, T. H. Raupach, H. Leijnse, and R. Uijlenhoet, "Rainfall retrieval with commercial microwave links in São Paulo, Brazil," *Atmospheric Measurement Techniques*, vol. 11, no. 7, pp. 4465–4476, 2018.

[9] Y. Xue, X. C. Liu, T. C. Gao, C. Y. Yang, K. Song, and H. K. Gao, "Regional attenuation correction of weather radar using a distributed microwave-links network," *Advances in Meteorology*, vol. 2017, 8 pages, 2017.

[10] Y. X. Qin, Z. Q. Chen, Y. Shen, S. P. Zhang, and R. H. Shi, "Evaluation of satellite rainfall estimates over the Chinese mainland," *Remote Sensing*, vol. 6, no. 11, pp. 11649–11672, 2014.

[11] K. U. V. Murali, S. K. Das, S. M. Deshpande, S. L. Doiphode, and G. Pandithurai, "The assessment of global precipitation measurement estimates over the Indian subcontinent," *Earth and Space Science*, vol. 4, no. 8, pp. 540–553, 2017.

[12] S. Prakash and R. M. Gairola, "Validation of TRMM-3B42 precipitation product over the tropical Indian Ocean using rain gauge data from the RAMA buoy array," *Theoretical and Applied Climatology*, vol. 115, no. 3-4, pp. 451–460, 2014.

[13] R. Xu, F. Q. Tian, L. Yang, H. C. Hu, H. Lu, and A. Z. Hou, "Ground validation of GPM IMERG and TRMM 3B42V7 rainfall products over southern Tibetan plateau based on a high-density rain gauge network," *Journal of Geophysical Research: Atmospheres*, vol. 122, no. 2, pp. 910–924, 2017.

[14] A. Baronetti, F. Acquaotta, and S. Fratianni, "Rainfall variability from a dense rain gauge network in north-western Italy," *Climate Research*, vol. 75, no. 3, pp. 201–213, 2018.

[15] M. D. Pollock, G. O'Donnell, P. Quinn et al., "Quantifying and mitigating wind-induced undercatch in rainfall measurements," *Water Resources Research*, vol. 54, no. 6, pp. 3863–3875, 2018.

[16] M. Löffler-Mang and J. Joss, "An optical disdrometer for measuring size and velocity of hydrometeors," *Journal of Atmospheric and Oceanic Technology*, vol. 17, no. 2, pp. 130–139, 2000.

[17] E. M. Trono, M. L. Guico, N. J. C. Libatique, G. L. Tangonan, and A. P. F. Parrenas, "Rainfall monitoring using acoustic sensors," in *TENCON 2012 IEEE Region 10 Conference*, pp. 1–6, Cebu, 2012.

[18] J. Förster, G. Gust, and S. Stolte, "A piezoelectrical rain gauge for application on buoys," *Journal of Atmospheric and Oceanic Technology*, vol. 21, no. 2, pp. 179–193, 2010.

[19] G. D. Quartly, T. H. Guymer, and K. G. Birch, "Back to basics: measuring rainfall at sea: part 1 - *In situ* sensors," *Weather*, vol. 57, no. 9, pp. 315–320, 2002.

[20] A. W. Jayawardena and R. B. Rezaur, "Measuring drop size distribution and kinetic energy of rainfall using a force transducer," *Hydrological Processes*, vol. 14, no. 1, pp. 37–49, 2000.

[21] G. J. Ciach, "Local random errors in tipping-bucket rain gauge measurements," *Journal of Atmospheric and Oceanic Technology*, vol. 20, no. 5, pp. 752–759, 2003.

[22] H. Y. Li, Q. Li, X. Li, and J. L. Song, "Discussion on the algorithms of a new siphon rain gauge," *WSEAS Transactions on Circuits and Systems*, vol. 9, no. 6, pp. 389–398, 2010.

[23] M. Colli, L. G. Lanza, and P. La Barbera, "Performance of a weighing rain gauge under laboratory simulated time-varying reference rainfall rates," *Atmospheric Research*, vol. 131, pp. 3–12, 2013.

[24] S. Iida, D. F. Levia, K. Nanko et al., "Correction of canopy interception loss measurements in temperate forests: a comparison of necessary adjustments among three different rain gauges based on a dynamic calibration procedure," *Journal of Hydrometeorology*, vol. 19, no. 3, pp. 547–553, 2018.

[25] V. Kvicera and M. Grabner, "Dynamic calibration of tipping-bucket raingauges and rainfall intensity data processing," in *2006 First European Conference on Antennas and Propagation*, pp. 1–5, Nice, France, 2006.

[26] X. Zhang, H. Y. Zhao, H. Y. Liang, and Y. J. Wang, "Analysis of precipitation measuring accuracy between weighing type and siphon type rain gauge," *China Flood & Drought Management*, vol. 30, no. 3, pp. 32–36, 2020.

[27] S. E. Yuter and W. S. Parker, "Rainfall measurement on ship revisited: the 1997 PACS TEPPS cruise," *Journal of Applied Meteorology*, vol. 40, no. 6, pp. 1003–1018, 2001.

[28] K. P. Bowman, "Comparison of TRMM precipitation retrievals with rain gauge data from ocean buoys," *Journal of Climate*, vol. 18, no. 1, pp. 178–190, 2005.

[29] Q. Y. Wu and Y. L. Wang, "Comparison of oceanic multisatellite precipitation data from tropical rainfall measurement Mission and global precipitation measurement mission datasets with rain gauge data from ocean buoys," *Journal of Atmospheric and Oceanic Technology*, vol. 36, no. 5, pp. 903–920, 2019.

[30] P. Azimi and H. Golnabi, "Precise formulation of electrical capacitance for a cylindrical capacitive sensor," *Journal of Applied Sciences*, vol. 9, no. 8, pp. 1556–1561, 2009.

Hindawi
Journal of Sensors
Volume 2021, Article ID 6664933, 17 pages
https://doi.org/10.1155/2021/6664933

Research Article

Time Series Deformation Monitoring over Large Infrastructures around Dongting Lake Using X-Band PSI with a Combined Thermal Expansion and Seasonal Model

Liang Bao,[1,2] **Xuemin Xing**,[1,2] **Lifu Chen**,[1,3] **Zhihui Yuan**,[1,3] **Bin Liu**,[1,2] **Qing Xia**,[1,2] **and Wei Peng**[1,2]

[1]*Laboratory of Radar Remote Sensing Applications, Changsha University of Science & Technology, Changsha 410014, China*
[2]*School of Traffic and Transportation Engineering, Changsha University of Science & Technology, Changsha 410014, China*
[3]*School of Electrical and Information Engineering, Changsha University of Science & Technology, Changsha 410014, China*

Correspondence should be addressed to Xuemin Xing; xuemin.xing@csust.edu.cn

Received 26 November 2020; Revised 5 March 2021; Accepted 10 March 2021; Published 31 March 2021

Academic Editor: Zhenxing Zhang

The long-term spatial-temporal deformation monitoring of densely distributed infrastructures near the lake area is of great significance to understand the urban health status and prevent the potential traffic safety problems. In this paper, the permanent scatterer interferometry (PSI) technology with TerraSAR-X imagery over the area around Dongting Lake was utilized to generate the long-term spatial-temporal deformation. Since the X-band SAR interferometric phases are highly influenced by the thermal dilation of the observed objects, and the deformation of large infrastructures are highly related to external temperature, a combined deformation model considering the thermal expansion and the seasonal environmental factors was proposed to model the temporal variations of the deformation. The time series deformation and the thermal dilation parameter over the area were obtained, and a comparative study with the traditional linear model was conducted. The Dongting Lake Bridge and the typical feature points distributed around the lake were analyzed in details. In order to compensate for the unavailability of external in situ measurements over the area, phase residuals and the subsidence generated through Differential Interferometric Synthetic Aperture Radar (D-InSAR) were utilized to verify the accuracy of the obtained deformation time series. Experiment results suggested that the proposed model is suitable and suggested for the selected study site. The root mean square error (RMSE) of the residual phase was estimated as 0.32 rad, and the RMSE compared with D-InSAR derived deformation was ±1.1 mm.

1. Introduction

Dongting Lake is located at the South Bank of Yangtze River in the north of Hunan Province, China, which is a tectonic lake with the characteristics of barrier lake. With the well-developed surrounding water system, Dongting Lake is adjacent to Yangtze River to the north, with its river water flowing into the Xiang River. Yueyang is a lakeside city of Hunan Province next to Dongting Lake, which is under the combined geological structure characteristics of intermittent uplift denudation and intermittent stable uplift deposition (i.e., uplift and stable alternating) [1]. As a city with a population of 5.8 million, plenty of residential areas and developed transportation network are distributed in Yueyang. Every flood season, the residential areas around Dongting Lake are under high potential danger of accumulated deformation, collapse of ground surface, or even landslides of the slope, which greatly endangers the safety of the area. The stability control of the densely distributed infrastructures near the Lake area is of remarkable importance. Therefore, the long-term spatial-temporal deformation monitoring over this area is of great significance to understand its health status and prevent the potential traffic safety problems.

Permanent scatterer interferometry (PSI) has proven to be an effective tool to obtain time series deformation results through extracting and processing those PS points, which can always keep long-term stable backscatter characteristics over multi-SAR images [2]. It can detect information of

ground displacement with millimeter precision, showing high potential ability for the application to large traffic infrastructures (i.e., railways, highways, and bridges) [3–6]. Earlier study shows that bridge railings, curbs, and pavements can be treated as artificial corner reflector structures, which are easily to be identified as PS points in SAR images [7]. Successful cases also proved the applicability using PSI technology with high-resolution SAR images to monitor slow deformation of large-scale bridges and other artificial structures [8, 9].

Deformation modeling determines the functional relationship between the displacement phase component and deformation parameters at each high coherence point. The deformation model not only determines the accuracy of displacement estimation but also directly affects the subsequent progress such as phase unwrapping and the interpretation of the final deformation results [10]. Earlier studies showed that the linear model (LM) is the most commonly used temporal model in PSI processing, which has been successfully applied in a large amount of cases [11, 12]. However, the deformation over large infrastructures (especially bridges) is related to complicated factors, such as the pile foundation, steel structure, and bridge cable, which are highly influenced by external temperatures [13]. Specifically, the upward accumulative effect of the thermal expansion can counteract the downward movement caused by land subsidence, which leads to the underestimation of land subsidence estimation [14]. Moreover, as introduced in [15], the X-band SAR interferometric phases are highly influenced by the thermal dilation of the observed objects. The thermal component of a given interferogram shows the displacement caused by thermal dilation, which is a consequence of temperature differences in the imaged area between two SAR acquisitions. These factors have a clear impact on the deformation velocity map. In particular, these factors can be remarkably severe if the observed period is relatively short (e.g., less than a year) [16]. Moreover, considering that the deformation of steel bridges is highly related to external temperature, some researchers introduced the thermal expansion model into the deformation estimation of large infrastructures [17–19].

Based on the above background, considering the unavoidable influences by the thermal dilation of the observed objects for X-band SAR images and the special hydrological environment of Donting Lake area, the thermal expansion and the participation were introduced into the seasonal model (TESM), which are used to model the low-pass components in PSI. With use of 24 high-resolution TerraSAR-X images acquired from December 2011 to April 2013, covering the area around Dongting Lake, two groups of time series deformation results, generated by both LM and TESM, have been obtained. Subsequently, a comparative investigation between the two deformation sequences was conducted, and the time series deformation results of Dongting Lake Bridge were analyzed in detail.

2. Methods

2.1. Standard LM of PSI. A master image should be selected from the time series SAR images in the experiment, and then all the slave images are coregistered and resampled to the master image. An external SRTM DEM data is utilized to remove the topographic phase and, consequently, phase filtering, and temporal-spatial unwrapping is carried out for each interferometric pair.

For each baseline in the PS network (connecting i-th and j-th PS candidates), the interferometric phase difference can be expressed as [20]

$$\Delta\phi_{i,j}^{m} = 2\pi\Delta k_{i,j}^{m} + \frac{4\pi}{\lambda}\bullet\frac{B_{\perp}^{m}}{R_{i,j}^{m}\sin\theta_{i,j}^{m}}\cdot\Delta\delta H_{i,j} + \frac{4\cdot\pi\cdot t^{m}}{\lambda}\Delta v_{i,j} + \Delta\phi\mathrm{res}_{i,j}^{m}, \tag{1}$$

where m represents the index number of the interferometric pair, $\Delta\phi_{i,j}^{m}$ and $\Delta k_{i,j}^{m}$ are the differences of the interferometric phase and the integer phase ambiguity between neighboring PS targets, respectively, $\Delta v_{i,j}$ defines the increments of linear displacement rates along the line of sight (LOS), and $\Delta\delta H_{i,j}$ represents the increment of elevation error. t^{m} and $B_{\perp}^{m}$ represent the temporal baseline and normal baseline of the m-th interferogram, respectively, $R_{i,j}^{m}$ defines the slant range distance, and $\theta_{i,j}^{m}$ defines the incident angle; $\Delta\phi\mathrm{res}_{i,j}^{m}$ is the residual phase, including the contribution of atmospheric delay phase, decorrelation noise, and high-pass deformation component.

According to formula (1), $\Delta k_{i,j}^{m}$, $\Delta\delta H_{i,j}$, and $\Delta v_{i,j}$ are unknown. The LAMBDA (Least Squares Ambiguity Correlation Adjustment) method proposed by Teunissen of Delft University in the Netherlands for the GPS dual differential phase observation model can be used here to unwrap the temporal differential phases [21]. This technique was introduced into InSAR processing to search the integer ambiguity in PSI in 2003 [22]. In order to ensure the accuracy of the temporal unwrapping results, it is necessary to evaluate the quality of each PS points and delete those of poor quality. We choose baseline correlation coefficient as the baseline accuracy index, which was introduced by Ferretti [20, 23]. It can be written as

$$\gamma_{\mathrm{base}} = \frac{1}{n}\sum_{i=1}^{n}(\cos(\Delta w_{i}) + j\sin(\Delta w_{i})), \tag{2}$$

where n is the total number of baselines, and Δw_{i} is the residual phase for each baseline (equals to $\Delta\phi\mathrm{res}_{i,j}^{m}$ in equation (1)).

The absolute deformation rate and elevation error at each PS points are calculated through spatial phase unwrapping. The specific processing flow is shown in Figure 1.

2.2. Seasonal Model of PSI. The seasonal model supposes the low-pass component as the sum of the linear and periodic subsidence, which has been widely used in describing the deformation related to seasonal factors. Seasonal model can be written as [24]

$$\Delta\phi_{i,j}^{m} = 2\pi\Delta k_{i,j}^{m} + \frac{4\pi}{\lambda}\bullet\frac{B_{\perp}^{m}}{R_{i,j}^{m}\sin\theta_{i,j}^{m}}\Delta\delta H_{i,j} + \frac{4\pi}{\lambda}\Delta t^{m}\Delta v_{i,j} + \frac{4\pi}{\lambda}\left[\Delta A_{i,j}\cos\left(\frac{2\pi}{T}t^{m}\right) + \Delta B_{i,j}\sin\left(\frac{2\pi}{T}t^{m}\right)\right] + \Delta\phi\mathrm{res}_{i,j}^{m}, \quad (3)$$

where T defines the seasonal deformation period ($T = 365$ days); $\Delta A_{i,j}, \Delta B_{i,j}$, and $\Delta v_{i,j}$ are the unknown parameters.

2.3. Extended TESM of PSI. The TESM introduces the thermal expansion component into the seasonal model, which can be written as:

$$\Delta\phi_{i,j}^{m} = 2\pi\Delta k_{i,j}^{m} + \frac{4\pi}{\lambda}\bullet\frac{B_{\perp}^{m}}{R_{i,j}^{m}\sin\theta_{i,j}^{m}}\Delta\delta H_{i,j} + \frac{4\pi}{\lambda}\Delta\mathrm{Temp}^{m}\Delta Th_{i,j} + \frac{4\pi}{\lambda}\Delta\mathrm{Prec}^{m}\Delta P_{i,j} + \frac{4\pi}{\lambda}\Delta t^{m}\Delta v_{i,j} + \frac{4\pi}{\lambda}\cdot\left[\Delta A_{i,j}\cos\left(\frac{2\pi}{T}t^{m}\right) + \Delta B_{i,j}\sin\left(\frac{2\pi}{T}t^{m}\right)\right] + \Delta\phi\mathrm{res}_{i,j}^{m}, \quad (4)$$

where $\Delta\mathrm{Temp}^{m}$ and $\Delta\mathrm{Prec}^{m}$ are the differential temperature and precipitation between the two SAR image acquisitions of the m-th interferogram, respectively, and $\Delta Th_{i,j}$ and $\Delta P_{i,j}$ are the increments of the thermal dilation parameter and the precipitation coefficient between the two adjacent PS targets separately. The unknown parameters in equation (4) are extended as $\Delta k_{i,j}^{m}$, $\Delta\delta H_{i,j}$, $\Delta A_{i,j}$, $\Delta B_{i,j}$,$\Delta P_{i,j}$, $\Delta v_{i,j}$, and $\Delta Th_{i,j}$. It can be seen from equation (4) that the interferometric phase varies linearly with the unknown parameters. Therefore, similar algorithms as introduced in equation (1) can be utilized to solve the unknown parameters. Subsequently, the low-pass (LP) deformation component at each target can be obtained. Considering that the atmospheric delay phase component is a temporally random high frequency signal, it is spatially related to low frequency signal. In contrast, the nonlinear residual deformation phase is a high frequency signal both spatially and temporally [25]. Accordingly, in order to extract the high-pass (HP) deformation component from the residual phase, a temporal HP filtering and a spatial LP filtering can be utilized [23]. Through summarizing the LP and HP deformation components, the final time series deformation at each PS point can be acquired.

2.4. Experiment

2.4.1. Geological Background of the Study Area. The surrounding area of Dongting Lake was selected as the study area. As a city with a population of 5.8 million, plenty of residential areas and developed transportation network are distributed in Yueyang. Hangzhou-Ruili Expressway, passing through Dongting Lake Bridge and Dongting Lake super bridge, is an important transportation hub connecting Junshan district and Yueyang Tower District in the northwest of Yueyang City. Dongting Lake Bridge is located at the downstream of Northern Gate Ferry in Yueyang City, which

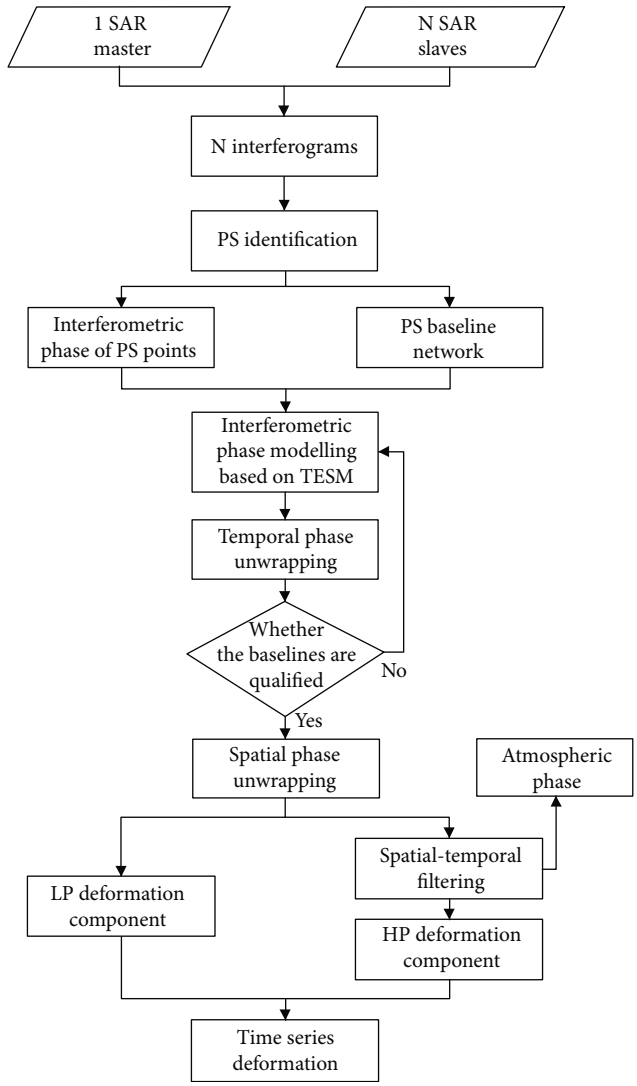

Figure 1: PSI data processing flow chart.

was built on 19 December 1996, and opened to traffic on 26 December 2000. As an urban expressway connecting Junshan district and Yueyang Tower District, Dongting Lake Bridge is a super huge bridge crossing Dongting Lake on the North Hunan trunk line. With a total length of 5784.5 m, the width of the main water level of Dongting Lake bridge is about 1400 m. Equipped with a 10×50 m continuous box girder, it is an 880 m long-span cable-stayed bridge with three towers and a double inclined-plane cable floating system. Three tower long-span cable-stayed bridge is the first structural form adopted in China, which is the most important structural characteristic of Dongting Lake Bridge [26].

The spatial coverage of the selected TerraSAR-X image is outlined by red rectangle in Figure 2(a). The green rectangle in Figure 2(b) defines the test area of Donting Lake of interest in our experiment. The location of Dongting Lake Bridge with the average amplitude image as background is shown in Figure 2(b). The territory of China is shown in Figure 2(c), and the in situ picture of the bridge is shown in Figure 2(d). According to our in situ geological investigation, the surface water system around Dongting Lake Bridge is

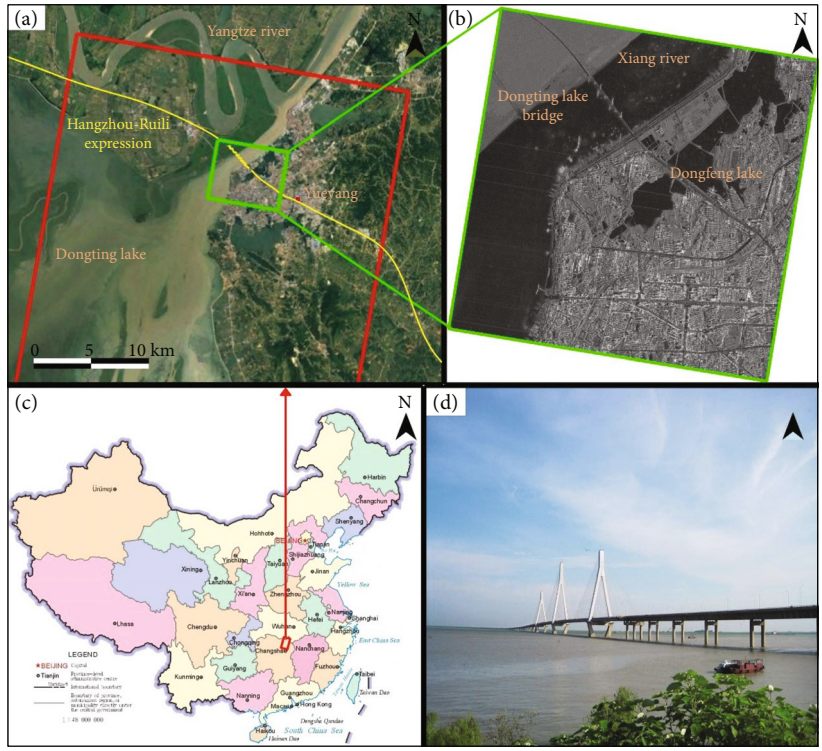

Figure 2: Study area features at different scales: (a) regional scale in China, (b) an amplitude image of the study area, (c) location of the study area in China, and (d) in situ picture of Dongting Lake Bridge.

developed, and the aquifer is extensive, which is prone to subsidence. Therefore, the long-term deformation monitoring of this area is of great significance.

2.4.2. SAR Acquisition and Data Processing. In this paper, 24 TerraSAR X-band Stripmap descending images covering Dongting Lake Bridge from December 2011 to April 2013 were collected (the parameters of these images are listed in Table 1). The pixel spacing of selected images is 1.364 m along the range direction and 1.849 m along the azimuth direction. The polarization mode of these images is HH polarization. The radar processing module of Sarscape 5.2 was used for the interferometric processing. In order to conduct a more precise observation over the bridge, no multilooking was conducted to constrain the original resolution. And the 9-th image in Table 1 represents the selected master image, whereas the rest ones are slave images. In the interferometric processing, the topographic phase was eliminated with use of SRTM DEM data (with 30 m spatial resolution provided by NASA). The orbit error is removed by the polynomial fitting method [27]. Thus, 23 differential interferograms are generated without spatial-temporal phase unwrapping.

According to equation (4), in order to model the thermal expansion phase component, the differential temperature and the differential precipitation of the interferometric period are necessary. The external air average temperature of Yueyang City is shown in Figure 3 (obtained on the website of China Meteorological Administration [28]), which was treated as the surface temperature in equation (4). The

Table 1: List of the interferometric pairs and their parameters with image number 9 as the master (strip no. 011, descending).

Image no.	Acquisition dates (yyyy/mm/dd)	Temporal baseline (days)	Normal baseline (m)
1	2011/12/28	-264	-95
2	2012/2/10	-220	-26
3	2012/3/3	-198	-100
4	2012/3/25	-176	-17
5	2012/4/16	-154	35
6	2012/5/8	-132	58
7	2012/5/30	-110	58
8	2012/8/26	-22	61
9	2012/9/17	0	0
10	2012/10/9	22	-145
11	2012/10/31	44	16
12	2012/11/11	55	52
13	2012/11/22	66	-32
14	2012/12/14	88	144
15	2012/12/25	99	3
16	2013/1/5	110	-71
17	2013/1/16	121	-38
18	2013/1/27	132	-94
19	2013/2/7	143	70
20	2013/2/18	154	-47
21	2013/3/1	165	-206
22	2013/3/12	176	-120
23	2013/3/23	187	133
24	2013/4/3	198	-125

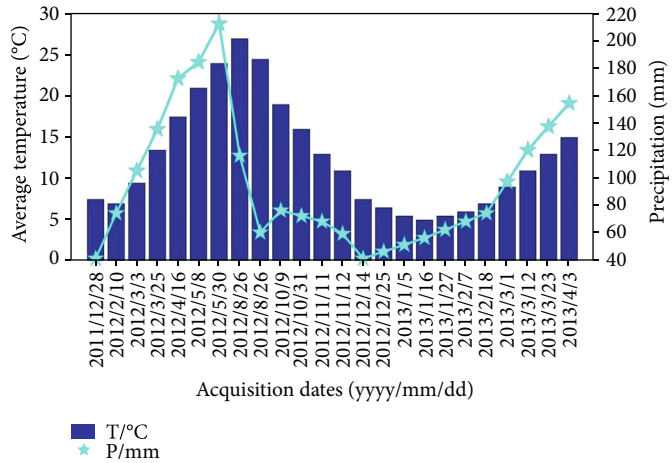

Figure 3: The average temperature and precipitation of Yueyang city (from 28 December 2011 to 3 April 2013).

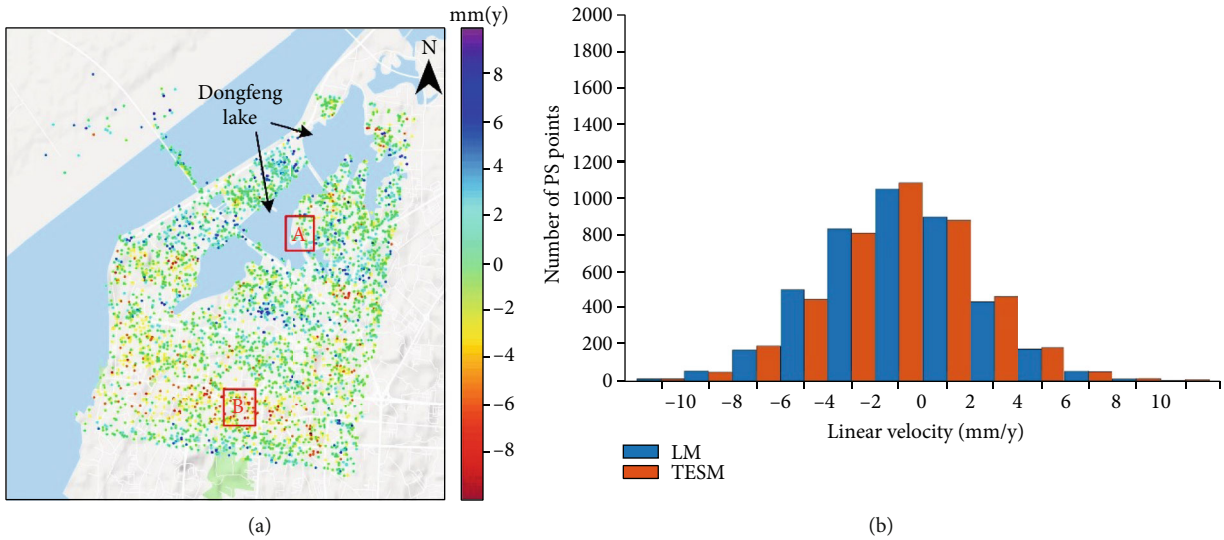

Figure 4: (a) Linear velocity map generated by TESM (with Google map as background). (b) PS point distribution comparison of the deformation velocity for the two models.

processes including the PS recognition [29], PS baseline network construction, parameter estimation, and time series deformation generation were conducted by the MATLAB software. 4420 PS points and 9224 triangle network baselines were generated.

2.5. Experimental Results

2.5.1. Linear Deformation Velocities. Two groups of experiments for both two models were carried out, with two groups of deformation parameters generated, respectively. The average linear velocities were generated by the TESM (Figure 4(a)). And the comparison for the number of the PS point distribution for the two models is shown in Figure 4(b). All the geocoded results in this paper were transferred to the vertical direction according to $S_v = S_{LOS}/\cos\theta$, where S_v and S_{LOS} represent the vertical and LOS subsidence, respectively.

According to our experiment, the experimental results show that the PS number distribution of the two models shows good consistency (Figure 4(b)). The results show that the linear velocity of TESM is consistent in the spatial distribution,and the deformation rate is generally between -2 mm/year and -10 mm/year, the maximum deformation rate is -13 mm/year, and the color range is from yellow to orange. The model has a slight uplift point near the Dongfeng Lake, and its velocity is mainly between 2 mm/year and 6 mm/year. It is considered that the uplift is related to the geological structure and terrain type of Jianghan-Dongting Basin where Yueyang City is located. This area is located in the margin of the geological structure between Yuanjiang depression and Fushan uplift [1]. In order to further analyze the results, two main deformation regions (red rectangles A and B in Figure 4(a)) are extracted. The uplift rate of area A is 8 mm/year. In contrast, area B is dominated by subsidence, and the maximum subsidence rate is 13 mm/year. The total

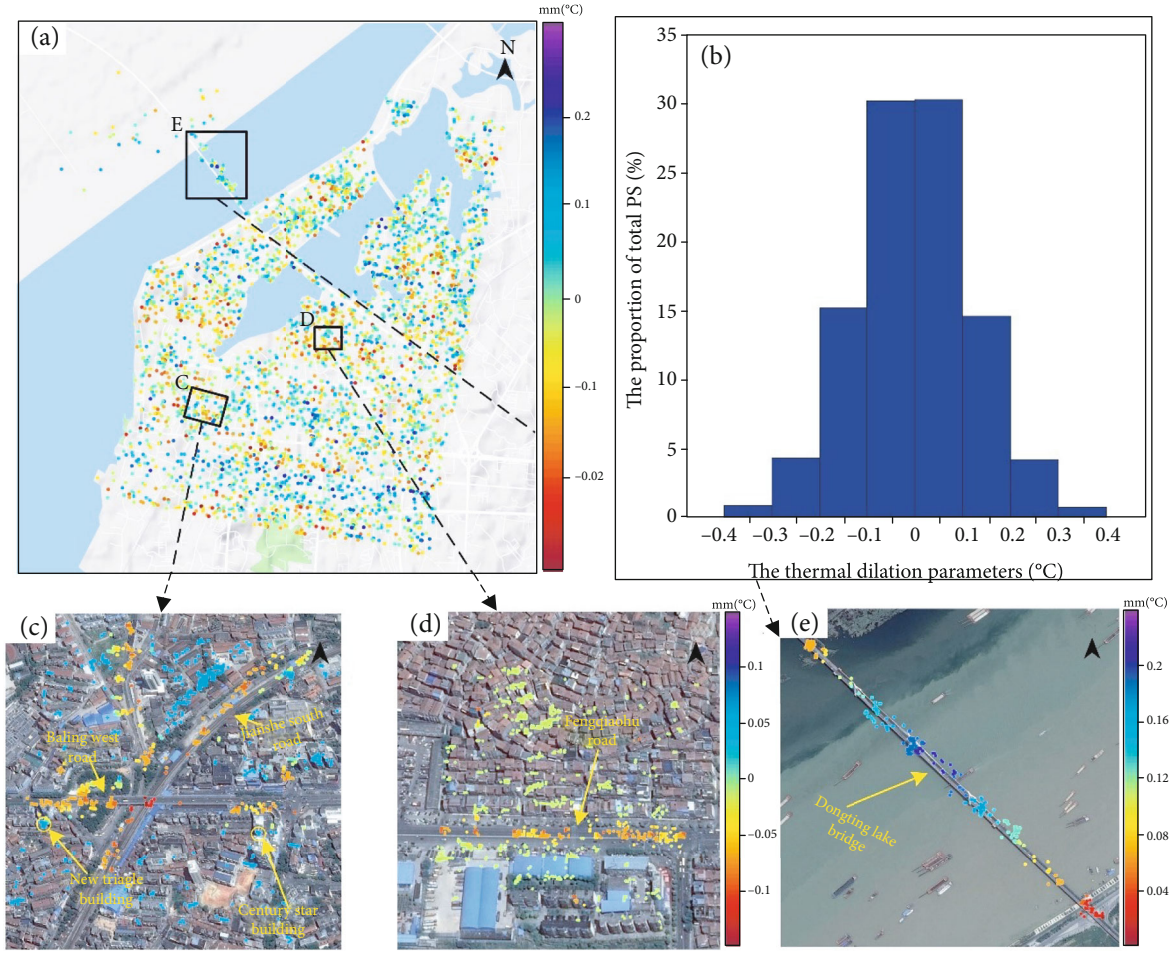

FIGURE 5: (a) Thermal dilation parameter map. (b) The proportion of thermal dilation parameter distribution on PS targets. (c), (d), and (e) are enlarged maps of area C, D, and E in Figure 5(a) (with optical image as background).

average deformation velocity of Dongting Lake Bridge is -5 mm/year.

2.5.2. Thermal Map. The obtained thermal dilation parameters in equation (4) are shown in Figure 5(a). It can be seen that the points within rectangle C were with relatively higher values, with the maximum value of 0.3 mm/°C. The suggested reason is related to the heights of the infrastructures in this area. According to equation (5) introduced in [16] (which will be described later), with a constant thermal expansion (considered constant when different infrastructures are made of similar materials), the thermal dilator parameter is directly proportional to the height of the buildings. The quantitative distribution of all the thermal dilation parameters is shown in Figure 5(b). It is easy to find that the values for 60% of PS points ranged within the interval of [-0.1 0.1] mm/°C, whereas 90% of PS points within the interval of [-0.2 0.2] mm/°C and 98% of PS points within the interval of [-0.3 0.3] mm/°C. As our in situ investigation, the typical buildings distributed in C are the New Triangle Building and the Century Star Building, both of which were with higher height (as shown in Figure 5(c)). According to our estimation, the highest thermal dilation parameter in area C was the Century Star Building, with a value of 0.17 mm/°C, which was supposed to be made of quartzite aggregate cement concrete. In contrast, area D shown in Figure 5(a) near Dongfeng Lake in the north was mainly distributed with old residential areas and hotels (the enlarged map is shown in Figure 5(d)). With a lower height, the thermal dilation parameters over this area were relatively low or even negative (the mean thermal dilation parameter of Fengqiaohu Road is estimated as -0.12 mm/°C) (see Figure 5(d)). As introduced in [14, 16], when a point moves away from the SAR sensor along the LOS direction, the horizontal deflection of the point performs to be negative. Consequently, a negative thermal expansion coefficient indicates a greater horizontal deflection away from the SAR sensor than the positive vertical deflection, which leads the comprehensive negative deformation away from the sensor. With a higher horizontal deflection and a lower vertical deflection for a tall building, the total deflection induced by thermal expansion performs positive. In contrast, the thermal expansion of a low and long road is mainly with a negative deflection. Accordingly, the points with negative coefficient of thermal expansion perform to concentrate along the road. This is why the negative thermal expansion points distributed mainly along the road in Figure 5(d).

The thermal dilation parameters for the PS points distributed at Dongting Lake Bridge (area E in Figure 5(a))

Figure 6: Time series deformation around Dongting Lake based on LM (referenced to 28 December 2011, *F* represents a typical uplift area, which will be discussed later).

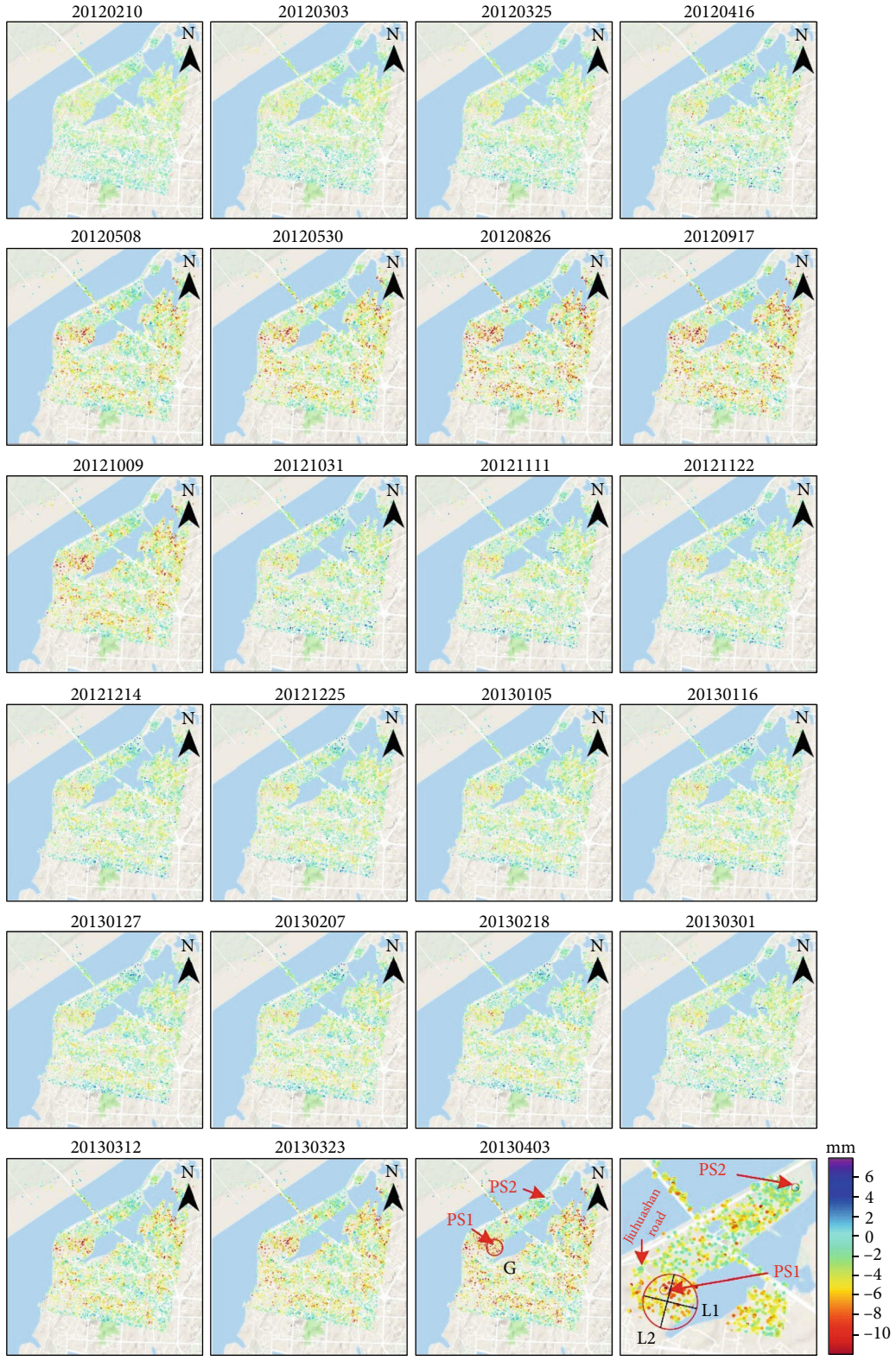

Figure 7: Time series deformation around Dongting Lake based on TESM (referenced to 28 December 2011, *G* is a typical subsidence bowl with transversal line L1 and longitudinal line L2, which will be discussed later).

were also obtained, which is displayed clearly in Figure 5(e). As the generated thermal dilation parameters can reflect the physical property of the observed objects, a rough function was used to estimate the corresponding thermal expansion coefficient of the bridge material, which can be expressed as [16]

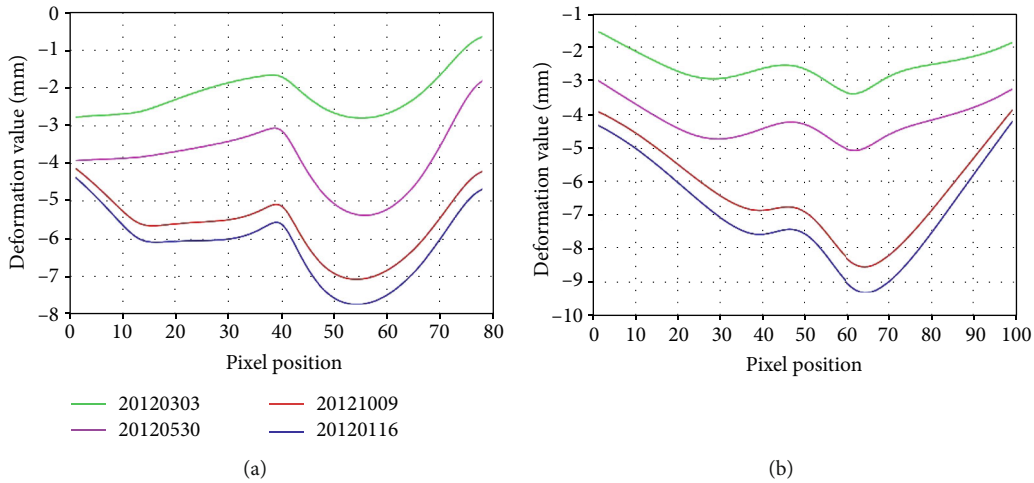

Figure 8: Profiles of the subsidence bowl in Figure 7. (a) Along the $l1$ direction. (b) Along the $l2$ direction.

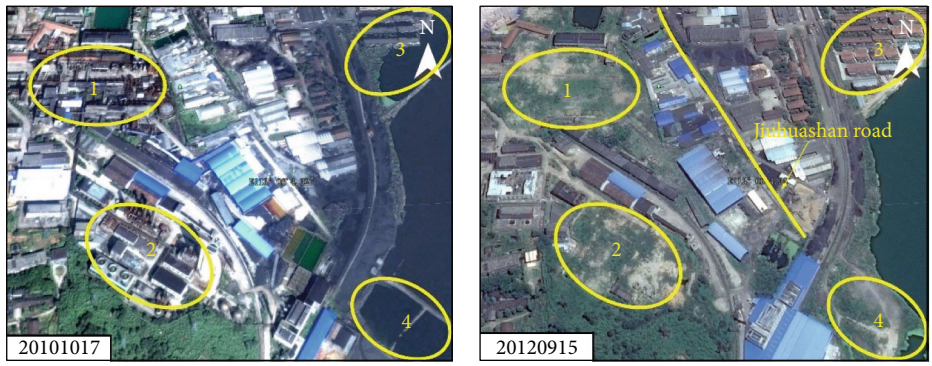

Figure 9: Enlarged map of the uplift area G in Figure 7 with the optical map as background.

$$K = \frac{\mathrm{Th}}{H}, \tag{5}$$

where K and Th define the coefficient of thermal expansion and thermal dilation parameter, respectively; H represents the height of main girder of the bridge reference to the bottom of pier. According to our estimation, the average expansion coefficient of the bridge materials is $11.6 \times 10^{-6}/°\mathrm{C}$. According to the collected construction design materials, the main girder of Dongting Lake bridge is made of C50 prestressed concrete with a continuous ribbed plate structure. The thermal expansion coefficient of this kind of concrete is approximately ranging from $6 \times 10^{-6}/°\mathrm{C}$ to $13 \times 10^{-6}/°\mathrm{C}$. Therefore, our estimations show good consistency with the physical properties of bridge materials [30].

2.5.3. Overall Time Series Deformation. The generated two groups of overall time series deformation maps based on the LM and TESM are shown in Figures 6 and 7, respectively. From the spatial distribution, the surface deformation of LM along Dongfeng Lake (black ellipse F) shows slight uplift, approximately within the range of 3 mm to 7 mm, while the urban hinterland was dominated by land subsidence, within the range of 5 mm to 13 mm. The results based on the TESM were mainly orange, and the corresponding subsidence was approximately ranging from 2 mm to 6 mm. In addition, it can be found from Figure 7 that there is an obvious subsidence funnel (see the red ellipse G) locates close to Dongfeng Lake and Jiuhuashan Road (shown in Figure 7), which was hidden in the generated results by LM. To further discuss and analyze the growing process of the typical subsidence bowls, profile analysis along the transversal and longitudinal directions (see the transversal line $l1$ and longitudinal line $l2$ in the last image of Figure 7) was carried out. The results are shown in Figure 8. According to our measurements, the peak subsidence along the $l1$ direction was 6 mm and 8 mm on the 15th and 54th pixels, whereas 7 mm and 9 mm at the 38th and 63th pixels along $l2$ direction. The maximum subsidence of 8 mm and 9 mm was detected at the 54th and 63th pixels along $l1$ and $l2$ directions, respectively. According to our investigation for the temporal optical images (shown as Figure 9) and the collected historical engineering materials of this area, we found that demolishment of some factory buildings (shown as areas 1 and 2 in Figure 9) and the lake reclamation project on some areas (shown as areas 3 and 4 in Figure 9) occurred during the period from 17 October 2010 to 15 September 2012. The subsiding phenomenon for

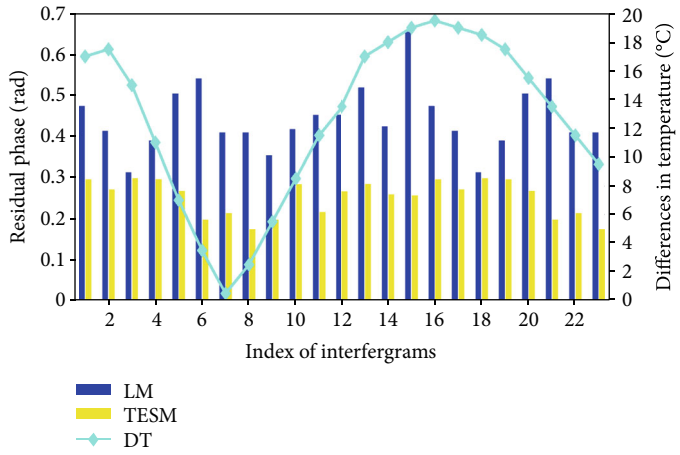

Figure 10: RMS of residual phases of a 23-interferogram comparison for TESM and LM (DT means the difference of temperature for each interferogram).

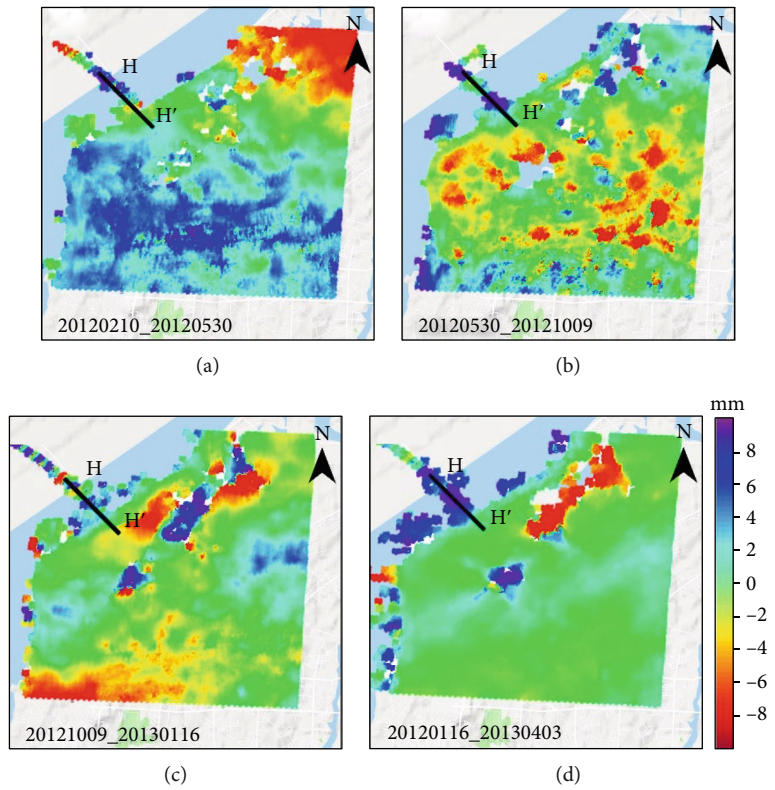

Figure 11: D-InSAR generated deformation pairs.

this area is suggested related to those engineering projects during this period.

2.5.4. Accuracy Assessment. In order to compensate for the unavailability of the external in situ deformation measurements over this area, the residual phase of each interferogram obtained through the TESM was compared with that of LM. According to [31], the fitting accuracy of a deformation model can be reflected by the residue phase ($\Delta\phi$res in equation (1)). The smaller the residual phase is, the higher the accuracy of the selected model is. The root mean square (RMS) of the residual phases for all the interferograms is shown in Figure 10. It can be seen that for the two models, the total RMS of the residual phase is less than 0.7 rad, which indicates a good accuracy of deformation modeling. Comparatively, for the 6^{th}, 7^{th},8^{th},21^{th},22^{th}, and 23^{th} images, the RMS of TESM was obviously lower than that of LM, and the total RMS for the TESM is 0.32 rad, whereas LM is 0.46 rad. It shows that the temporal evolution of deformation in this study area can be modeled more accurately by adding

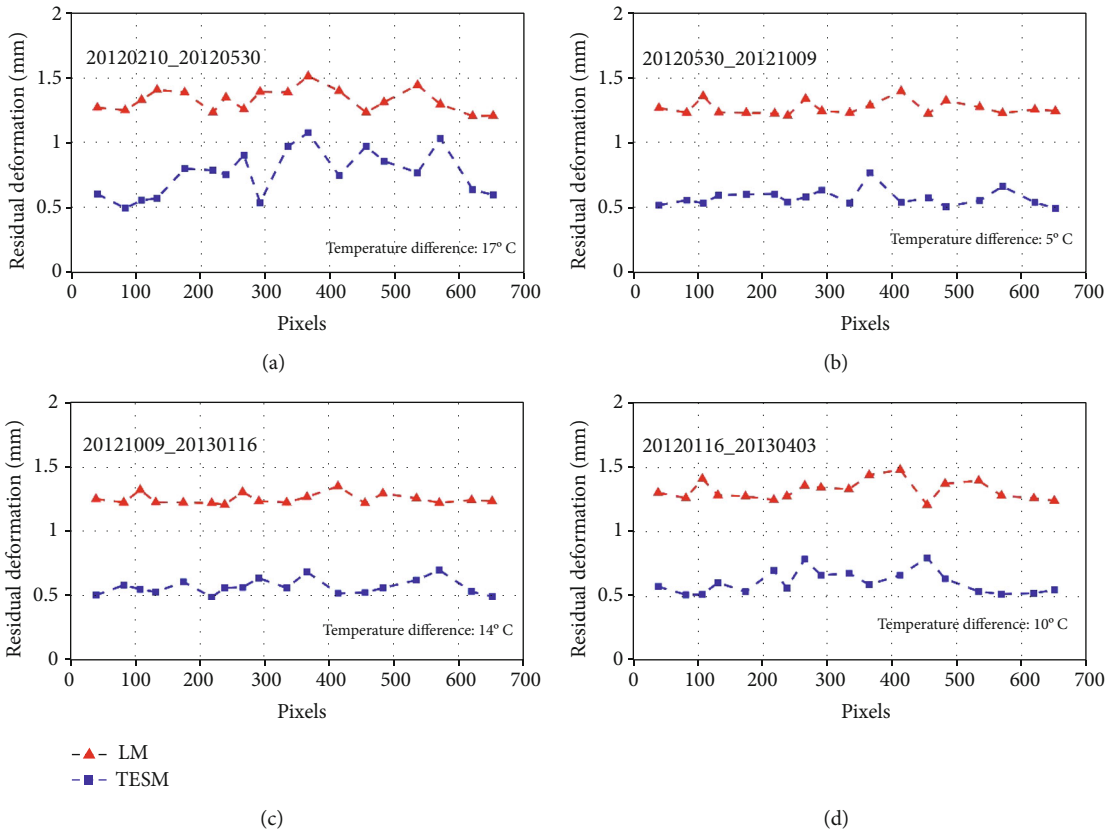

Figure 12: Residual deformation comparison of the two models along Section H-H′.

a thermal expansion component into the traditional seasonal model.

To further evaluate the accuracy of the obtained deformation time series, the PSI derived deformation was compared with the results of D-InSAR processing. Four periods were selected, and the corresponding D-InSAR generated deformation pairs are displayed as Figure 11. The D-InSAR results along the section H-H′ were extracted to compare with the PSI generated results, which are demonstrated in Figure 12. It can be noticed that the residual deformation of the TESM was obviously lower than that of LM. The deviation of TESM was lower than 0.8 mm, while for LM, most of the pixels were higher than 1.2 mm. The quantitative calculation of the mean value and root mean square error (RMSE) of the residuals are summarized in Table 2. It is easy to find that TESM shows a better performance, with a total RMSE of ±1.1 mm for the entire observation period and an improvement of about 33%. Moreover, earlier study introduced that the subsidence magnitude around Dongting Lake area was within 1 cm, which is consistent with the magnitude obtained in this paper [32].

Table 2: Mean residual and RMSE with comparison to D-InSAR derived subsidence (DT represents the differences of temperature).

Interferometric pairs	DT (°C)	Mean residual (mm)		RMSE (mm)	
		LM	TESM	LM	TESM
20120210-20120530	17.0	1.3	0.8	1.9	1.5
20120530-20121009	-5.0	1.2	0.6	1.3	0.8
20121009-20130116	-14.0	1.2	0.6	1.3	0.7
20130116-20130403	10.0	1.3	0.7	1.7	1.1

3. Discussions

3.1. Temporal Deformation Characteristics Based on TESM. From the temporal evolution shown by the time series deformation maps generated by TESM (see Figure 7), it can be seen that the results show a periodic temporal evolution. From 3 March 2012 to 26 August 2012, a temporally subsiding trend dominated this area, with the accumulated subsidence up to 13 mm until 26 August 2012. From 26 August 2012 to 14 December 2012, a slow uplift trend dominated the deformation, with the maximum recovery accumulated to 14 mm. The main reason for this periodic variation was supposed related to the local hydrogeological conditions and climatic factors. According to the working data of 402 geological team in Hunan Province, this area was with extremely well-developed water system and rick groundwater resources [32]. According to our in situ investigation, the shallow groundwater is closely connected with the major water systems. In rainy seasons, the water volume of rivers and lakes was increased by the precipitation. According to the statistics of the Meteorological Bureau, the precipitation from April to July in Yueyang was obviously serious, with

Table 3: The proportion of each deformational component on PS1 and PS2.

Feature points	Seasonal component	Thermal expansion component	Precipitation related component	Linear component	Residual component
PS1	79.7%	11.2%	3.2%	1.7%	4.2%
PS2	32.3%	56.1%	5.3%	2.6%	3.7%

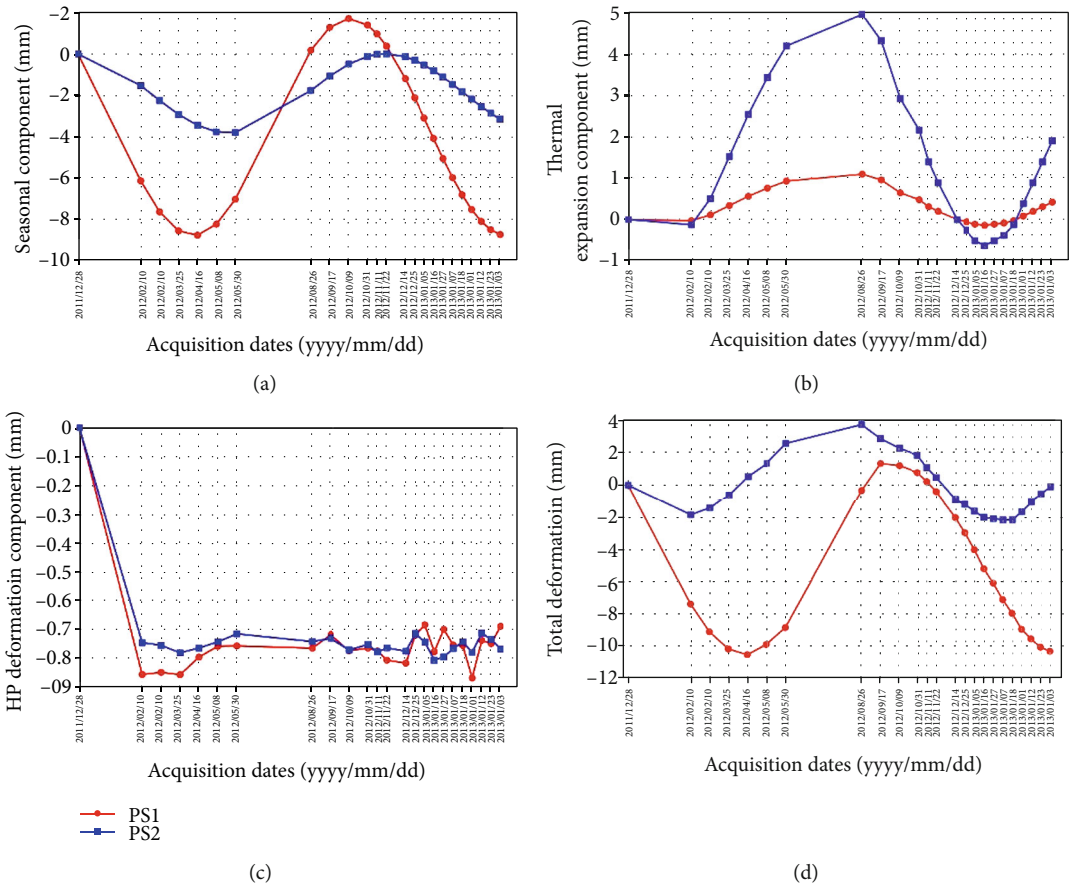

Figure 13: Time series deformation of the two feature points in Figure 7: (a) seasonal deformation component, (b) thermal expansion deformation component, (c) HP deformation component, and (d) total deformation.

the average precipitation higher than 150 mm (see Figure 3). Due to the increase of precipitation in summer, the groundwater was increased by the surrounding water system and the precipitation supply, which lead to obvious ground surface uplift around the lake area.

In order to clearly show the temporal evolution of deformation, two feature points located in the subsidence funnel and the uplift area were selected, respectively. The proportion of each component is shown in Table 3. For instance, for PS1, the deformation component related to the seasonal component accounted for 79.7%, whereas the component related to the thermal expansion accounted for 11.2%, and the precipitation deformation component occupied 3.2%, the linear component accounted for 1.7%, and the HP-deformation 4.2%. For PS2, the isolated deformation component related to the seasonal component accounted for 32.3% of the total deformation, and the component related to thermal expansion accounted for 56.1%. The precipitation deformation component and the linear component only accounted for 5.3% and 2.6%, respectively. The HP-deformation isolated from the residual phase only occupied 3.7%. We can see that the seasonal component and the thermal expansion component dominated the total deformation, followed with the precipitation deformation component, which indicate that the deformation of soft clay in the area was most significantly affected by the seasonal component and the thermal expansion. The time series deformation for the seasonal component and thermal expansion component of the two points is shown in Figure 13 quantitively. It can be seen that the deformation of PS1 is mainly subsiding with periodical fluctuation. The seasonal component dominated the total deformation of PS1, accounting for approximately 80%. The max subsidence for PS1 was 10 mm occurred on 3 April 2013. In contrast, PS2 was dominated by the thermal expansion component (accounting for 56%), thus following a temporal periodic variation, with the peak value accumulated to 4 mm on

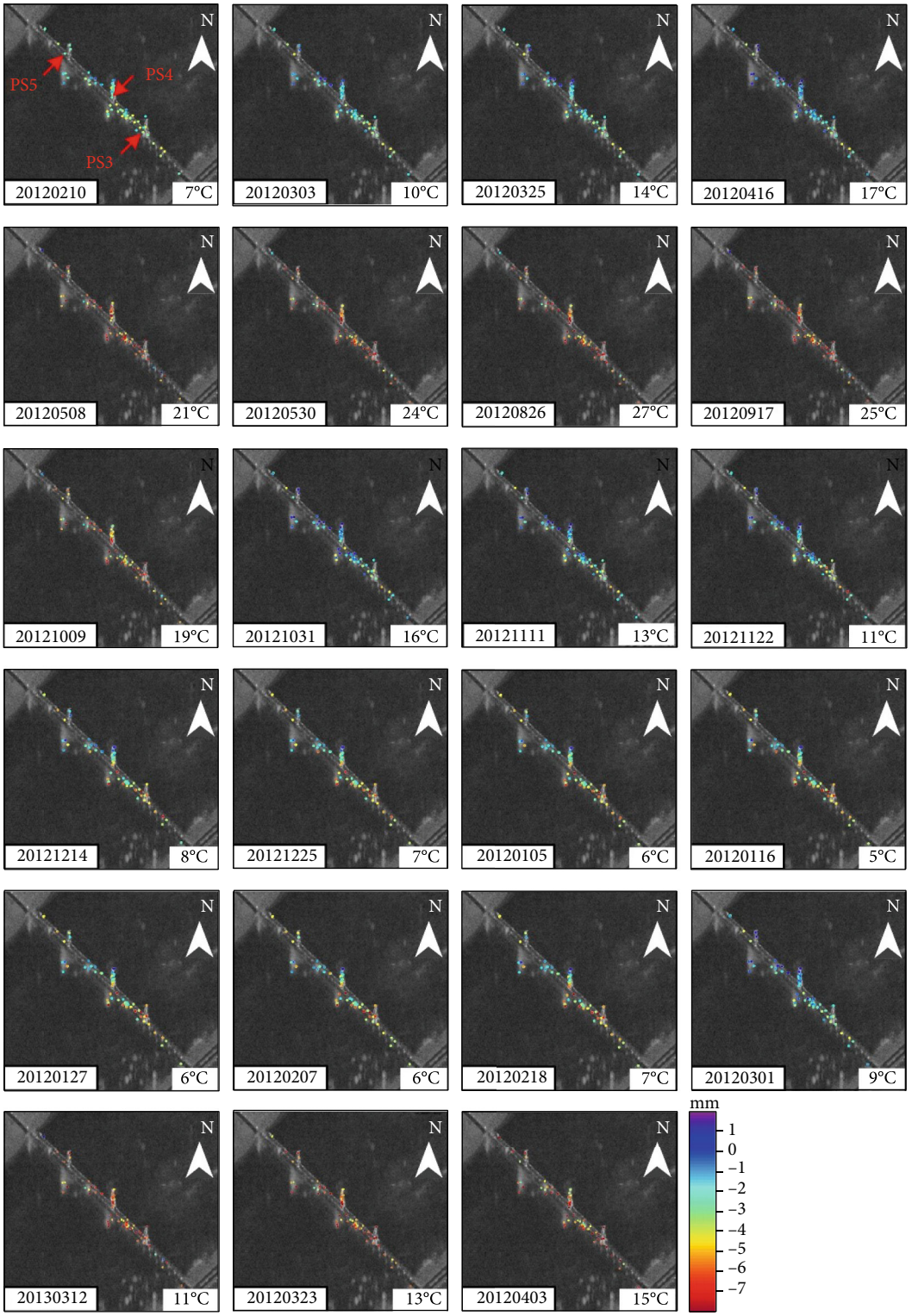

Figure 14: Overall deformation time series of Dongting Lake Bridge.

26 August 2012 and the max subsidence of 2 mm on 14 December 2012.

3.2. Deformation over Dongting Lake Bridge Based on TESM. During our experiment, 191 PS points were extracted from Dongting Lake Bridge, and the time series deformation is shown in Figure 14. The temperature mark for each sub-Figure in Figure 14 is the temperature difference for each interferometric period, which is used to get the average temperature in function (4). It is easy to find that the color of the PS points on the whole bridge was mainly yellow, which indicates a settlement trend, with the max subsidence of 12 mm

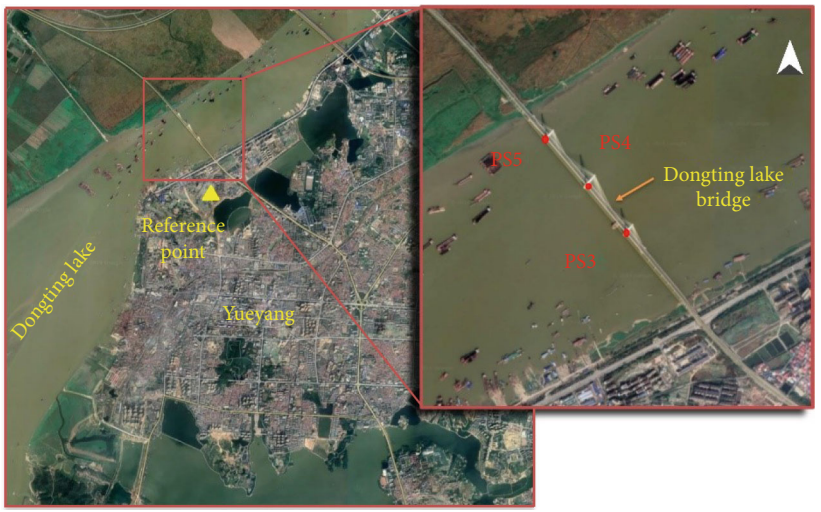

Figure 15: Location of feature points on Dongting Lake Bridge.

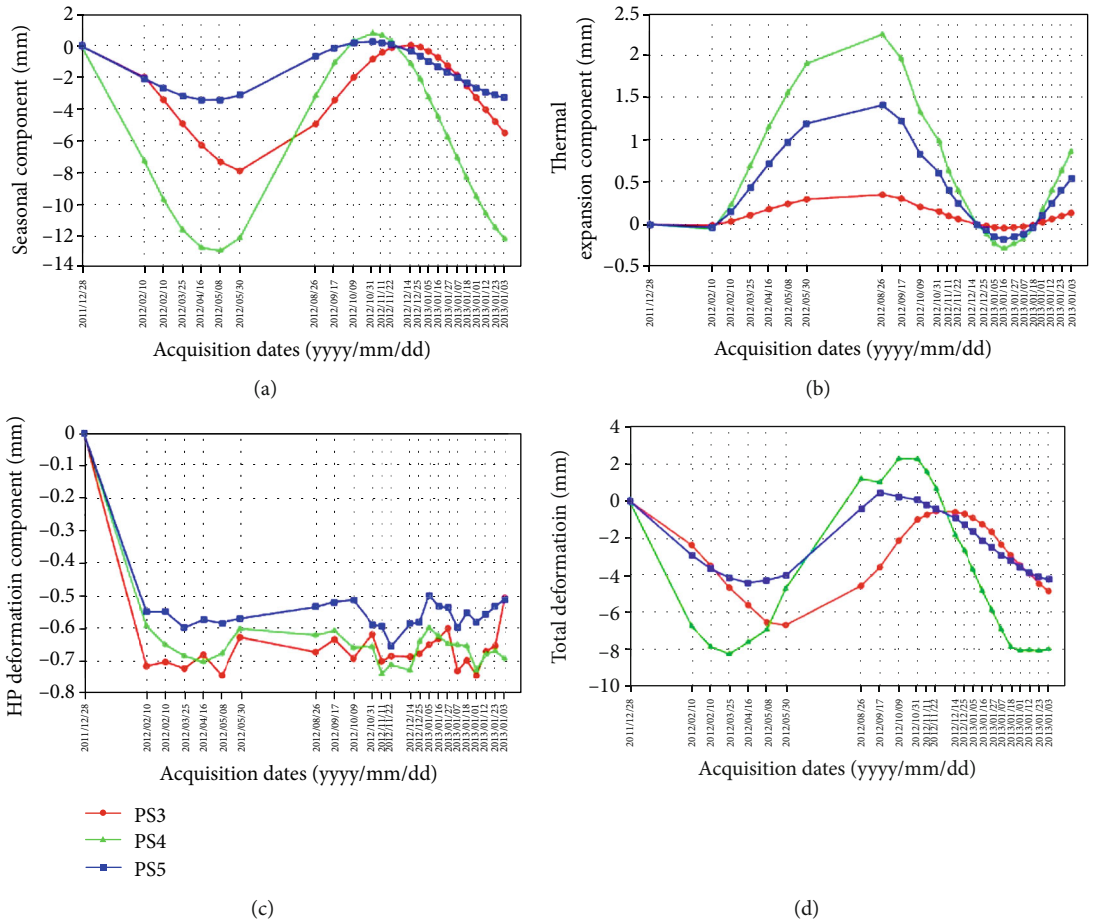

Figure 16: Time series deformation components at feature points on Dongting Lake Bridge: (a) seasonal deformation component, (b) thermal expansion deformation component, (c) HP deformation component, and (d) total deformation.

occurred at 26 August 2012. This is suggested related to the vertical expansion of the bridge pier as the increase of temperature. Moreover, the points at the top of the middle bridge tower showed a dominantly blue color while the points along the lower part of the bridge tower were yellow and red. This phenomenon suggested that the top of the middle bridge tower was affected by the tension of the stay cables on both sides, which induced a mainly horizontal movement rather than subsidence. Since we roughly treated the 3D deformation as the contribution of a single LOS deformation

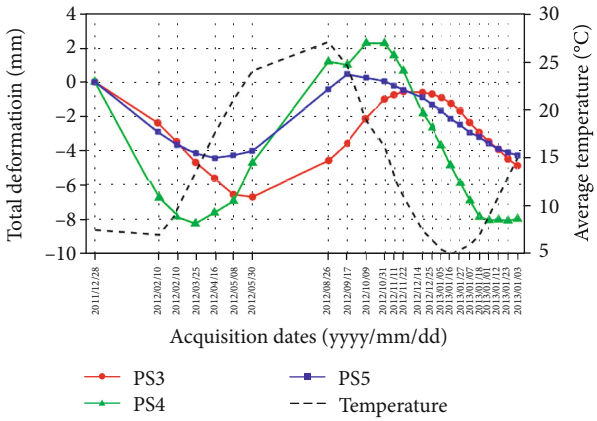

Figure 17: Correlation between the deformation of the feature points and the ambient temperature.

component, the final transferred vertical deformation of the points at the top of the middle tower showed a relatively uplift trend. From 9 October 2012, more orange points appeared at the segment from the middle tower to the south tower, with the max subsidence of 6 mm, which occurred on 26 August 2012. Moreover, our results reflect that the PS points located close to both riversides were more stable than those at the center segment, which was related to the more steadily support of the piers in riversides. According to the design standard of the bridge, the maximum downward deflection of the middle span is 33.8 cm, and the maximum downward deflection of the side span is 12.8 cm. Consequently, according to the magnitude of our estimation, the total deformation induced by thermal expansion was within a controllable range, which indicates the bridge was under a relatively stable condition.

In order to further analyze the temporal evolution of the deformation along the bridge, three feature points were selected on three piers, which were indexed as PS3, PS4, and PS5 from the south to north (see the locations for the three PSs on Figure 15). PS3 is located at the south bridge tower, and the obtained time series deformation at PS3 is shown in Figure 16. It can be noticed that the deformation at PS3 is mainly subsidence. The seasonal component accounts for 80% of the total deformation, with the max value up to -8 mm. In contrast, the thermal expansion component accounts for 10% of the total deformation. The peak uplift of the thermal expansion component was up to 0.4 mm on 26 August 2012, whereas the maximum subsidence was 0 mm on 5 January 2013. According to our estimation from Figure 5(a), the thermal dilation parameter at point PS3 was 0.178 mm/°C. The total deformation shows an obvious periodical evolution, with the max subsidence of 6 mm on 30 May 2012.

Comparatively, PS4 and PS5 which are located at the middle and north bridge tower show a generally time series subsidence with periodical fluctuation. The thermal expansion component accounts for more than 30% of the total deformation, up to 2 mm for both the two targets. The maximum uplift of the thermal expansion component was 2.3 mm for PS4, whereas 1.5 mm for PS5, which occurred on 30 May 2012, respectively. The thermal dilation parameters for those two points were 0.323 mm/°C and 0.294 mm/°C, respectively. The total deformation for the two points reached a maximum of 8 mm and 4 mm in August, respectively. Similarly, with an approximately 7 mm recovery, the total deformation was only 1 mm on 14 December 2012. Obviously, the periodical fluctuation of the deformation time series depended on the seasonal component.

As shown in Figure 14, we found that the total deformation shows relationship with the temperature difference for each interferometric period. In order to further explore the correlation between the total deformation and the temperature, we carried out a correlation analysis, which is shown in Figure 17. Due to the unavailability of detail bridge surface temperature, we only collected external air temperature in Yueyang City to conduct the study. It can be noticed from the figure that the vertical deformation of the bridge was highly correlated with the temperature, with the correlation coefficients of 0.89, 0.87, and 0.79, respectively, for the three targets.

4. Conclusions

A long-term deformation investigation over the area with densely distributed infrastructures around Dongting Lake was presented based on PSI technology using 24 TerraSAR-X images from December 2011 to April 2013. Considering the unavoidable influence of the thermal expansion over the infrastructures for TerraSAR X satellite image and the seasonal environmental factors for the lakeside area, TESM was proposed to replace the traditional LM. A comparative analysis has been conducted for the spatial-temporal investigation for the deformation time series. Spatially, subsidence mainly dominated the inland area on the north part of the study area, while the area along Dongfeng Lake performed a slight uplift trend. An obvious subsidence funnel, located close to Jiuhuashan Road in Yueyang Tower District, was detected in the result of TESM, which was hidden in that of LM. In addition, a generally periodical subsiding variation was detected through TESM, with a maximum subsidence up to 18 mm occurred on 26 August 2012. From the generated thermal dilator parameter map, the thermal expansion coefficient for Dongting Lake Bridge was estimated as 11.6 $\times 10^{-6}$/°C, which is consistent with the physical properties of the bridge concrete. The results of three feature points at the bridge show that the maximum subsidence value of the bridge was 8 mm, which occurred on 26 August 2012, showing the whole bridge was under a stable condition during the entire observation period.

In order to compensate for the unavailability of external in situ geodetic measurements over this area, the phase residuals and D-InSAR generated subsidence were utilized to verify the accuracy of the obtained deformation time series. The results show that with adding the thermal expansion component, the RMS of the residual phase performed an improvement of 30%. The RMS compared to the DInSAR results for the two models is 1.7 mm and 1.1 mm, respectively, which indicated an increasement of 33% for TESM. The consistence with the settlement magnitude over this area

introduced in earlier study work also verified the reliability of our result.

Data Availability

The TerraSAR-X satellite images used in this paper are provided by the German Space Center (DLR) (Data Order Program Project: MTH3393).

Conflicts of Interest

The authors declare no conflict of interest.

Acknowledgments

This work was supported by the National Natural Science Foundation of China under Grant (No. 41701536, No. 61701047, and No. 41904003), Natural Science Foundation of Hunan Province under Grant (No. 2017JJ3322, No. 2019JJ50639), Key Project of Education Department of Hunan Province under Grant (No. 18A148), Project of Education Department of Hunan Province under Grant (No. 16C0034), and Open Fund of Engineering Laboratory of Spatial Information Technology of Highway Geological Disaster Early Warning in Hunan Province under Grant (No. kfj190601).

References

[1] D. Bai, J. Li, T. Ma et al., "Tectonic-sedimentary landforms classification of middle segment of east quaternary Jianghan-Dongting Basin," *Scientia Geographica Sinica*, vol. 30, no. 2, pp. 236–241, 2010.

[2] W. Tang, M. Liao, and P. Yuan, "Atmospheric correction in time-series SAR interferometry for land surface deformation mapping - a case study of Taiyuan, China," *Advances in Space Research*, vol. 58, no. 3, pp. 310–325, 2016.

[3] Z. Yang, F. Schmid, and C. Roberts, "Assessment of railway performance by monitoring land subsidence," in *Proc. IET-RCM*, Birmingham, UK, September 2014.

[4] D. Perissin, Z. Wang, and H. Lin, "Shanghai subway tunnels and highways monitoring through Cosmo-SkyMed persistent Scatterers," *ISPRS Journal of Photogrammetry and Remote Sensing*, vol. 73, pp. 58–67, 2012.

[5] S. W. Kim, S. Wdowinski, T. H. Dixon, F. Amelung, J. W. Kim, and J. S. Won, "Measurements and predictions of subsidence induced by soil consolidation using persistent scatterer InSAR and a hyperbolic model," *Geophysical Research Letters*, vol. 37, no. 5, article L05304, 2010.

[6] F. Chen, H. Lin, Z. Li, Q. Chen, and J. Zhou, "Interaction between permafrost and infrastructure along the Qinghai-Tibet Railway detected via jointly analysis of C- and L-band small baseline SAR interferometry," *Remote Sensing of Environment*, vol. 123, pp. 532–540, 2012.

[7] D. Cusson, K. Trischuk, D. Hébert, G. Hewus, M. Gara, and P. Ghuman, "Satellite-Based InSAR monitoring of highway bridges: validation case study on the North Channel Bridge in Ontario, Canada," *Transportation Research Record: Journal of the Transportation Research Board*, vol. 2672, no. 45, pp. 76–86, 2018.

[8] P. Ma, T. Li, C. Fang, and H. Lin, "A tentative test for measuring the sub-millimeter settlement and uplift of a high-speed railway bridge using COSMO-SkyMed images," *ISPRS Journal of Photogrammetry and Remote Sensing*, vol. 155, pp. 1–12, 2019.

[9] Y. Zhao, L. Wang, Y. Liu, Z. Tian, and Y. Peng, "Study on the monitoring of urban bridge shape variables based on remote sensing data and PS-InSAR," *Construction Science and Technology*, vol. 4, pp. 55–58, 2016.

[10] X. Xing, L. Chen, Z. Yuan, and Z. Shi, "An improved time-series model considering rheological parameters for surface deformation monitoring of soft clay subgrade," *Sensors*, vol. 19, no. 14, article 3073, 2019.

[11] C. Qu, X. Shan, X. Song, G.-F. Zhang, G.-H. Zhang, and L. Guo, "The PSInSAR technique and its application to the study on crustal deformation of the Haiyuan fault zone," *Chinese Journal of Geophysics*, vol. 54, no. 4, pp. 984–993, 2011.

[12] D. Ge, W. Yan, X. Guo, W. Yi, and X. Ye, "Land subsidence investigation along railway using permanent scatterers SAR interferometry," in *Proc. IEEE-IGARSS*, Boston, MA, USA, July 2008.

[13] T. Li, G. Liu, H. Jia et al., "An improved multi-temporal InSAR method for increasing spatial resolution of surface deformation measurements," *ISPRS-SSG*, vol. XL-7/W2, pp. 145–150, 2013.

[14] P. Ma, H. Lin, H. Lan, and F. Chen, "Multi-dimensional SAR tomography for monitoring the deformation of newly built concrete buildings," *ISPRS Journal of Photogrammetry and Remote Sensing*, vol. 106, pp. 118–128, 2015.

[15] X. Qin, L. Zhang, X. Ding, M. Liao, and M. Yang, "Mapping and characterizing thermal dilation of civil infrastructures with multi-temporal X-band synthetic aperture Radar interferometry," *Remote Sensing*, vol. 10, no. 6, p. 941, 2018.

[16] O. Monserrat, M. Crosetto, M. Cuevas, and B. Crippa, "The thermal expansion component of persistent scatterer interferometry observations," *IEEE Geoscience and Remote Sensing Letters*, vol. 8, no. 5, pp. 864–868, 2011.

[17] M. Crosetto, O. Monserrat, M. Cuevas-González, N. Devanthéry, G. Luzi, and B. Crippa, "Measuring thermal expansion using X-band persistent scatterer interferometry," *ISPRS Journal of Photogrammetry and Remote Sensing*, vol. 100, pp. 84–91, 2015.

[18] X. Qin, M. Liao, M. Yang, and L. Zhang, "Monitoring structure health of urban bridges with advanced multi-temporal InSAR analysis," *Annals of GIS*, vol. 23, no. 4, pp. 293–302, 2017.

[19] J. Jiang, Q. Huang, Y. Wang, Q. Wang, and J. Guo, "Application of InSAR Technology in Deformation Monitoring of Yangtze River Bridge of Anqing Railway," *Journal of Gansu Sciences*, vol. 30, no. 6, pp. 73–77, 2018.

[20] A. Ferretti, C. Prati, and F. Rocca, "Permanent scatterers in SAR interferometry," *IEEE Transactions on Geoscience and Remote Sensing*, vol. 39, no. 1, pp. 8–20, 2001.

[21] P. J. G. Teunissen, "The least-squares ambiguity decorrelation adjustment: a method for fast GPS integer ambiguity estimation," *Journal of Geodesy*, vol. 70, no. 1-2, pp. 65–82, 1995.

[22] B. M. Kampes and R. F. Hanssen, "Ambiguity resolution for permanent scatterer interferometry," *IEEE Transactions on Geoscience and Remote Sensing*, vol. 42, no. 11, pp. 2446–2453, 2004.

[23] A. Ferretti, C. Prati, and F. Rocca, "Nonlinear subsidence rate estimation using permanent scatterers in differential SAR

interferometry," *IEEE Transactions on Geoscience and Remote Sensing*, vol. 38, no. 5, pp. 2202–2212, 2000.

[24] S. S. Li, Z. W. Li, J. Hu, Q. Sun, and X. Y. Yu, "Investigation of the seasonal oscillation of the permafrost over Qinghai-Tibet Plateau with SBAS-InSAR algorithm," *Chinese Journal of Geophysics*, vol. 56, no. 5, pp. 1476–1486, 2013.

[25] J. Wei, Z. Li, J. Hu, G. Feng, and M. Duan, "Anisotropy of atmospheric delay in InSAR and its effect on InSAR atmospheric correction," *Journal of Geodesy*, vol. 93, no. 2, pp. 241–265, 2019.

[26] J. Liao, D. Li, J. Hu, and H. Zhou, "Design of three tower cable-stayed bridge of Dongting Lake Bridge in Yueyang," in *Proc. AEM-CHS*, pp. 222–228, Yinchuan, Ningxia, China, 2001.

[27] J. H. T. Bbates, "A polynomial method for fitting continuous distributions of exponentials with positivity constraint," *IEEE Transactions on Biomedical Engineering*, vol. BME-32, no. 7, pp. 478–484, 1985.

[28] China Meterological Administration, "Historical weather in Yueyang," http://lishi.tianqi.com/yueyang/index.html.

[29] M. Esmaeili and M. Motagh, "Improved persistent scatterer analysis using amplitude dispersion index optimization of dual polarimetry data," *ISPRS Journal of Photogrammetry and Remote Sensing*, vol. 117, pp. 108–114, 2016.

[30] J. Huang, S. Wu, and D. Shen, "E xperimental study on thermal expansion coefficient of different type coarse aggregates concrete at early ages," *Structural Engineers*, vol. 26, no. 3, pp. 154–158, 2010.

[31] X. Xing, H. C. Chang, L. Chen, J. Zhang, Z. Yuan, and Z. Shi, "Radar interferometry time series to investigate deformation of soft clay subgrade settlement—a case study of Lungui Highway, China," *Remote Sensing*, vol. 11, no. 4, p. 429, 2019.

[32] D. Jiang, S. Huang, W. Zhang, and D. Yu, "A discussion on the evolution of the Dongting Lake based on geo-environmental remote sensing investigation and monitoring data," *Remote Sensing for Land & Resources*, vol. 22, Supplement 1, pp. 124–129, 2010.

Hindawi
Journal of Sensors
Volume 2021, Article ID 6694407, 13 pages
https://doi.org/10.1155/2021/6694407

Research Article

Exploring the Variations of Redbed Badlands and Their Driving Forces in the Nanxiong Basin, Southern China: A Geographically Weighted Regression with Gridded Data

Gusong Luo[1], **Hua Peng**[1], **Shaoyun Zhang**[1], **Luobin Yan**[2] and **Yuxiang Dong**[1,3]

[1]*School of Geography and Planning, Sun Yat-sen University, Guangzhou, Guangdong 510275, China*
[2]*School of Geography Sciences, Southwest University, Chongqing 400700, China*
[3]*Department of Resources and the Urban Planning, Xinhua College of Sun Yat-sen University, Guangzhou, Guangdong 510520, China*

Correspondence should be addressed to Yuxiang Dong; eesdyx@mail.sysu.edu.cn

Received 30 October 2020; Revised 1 February 2021; Accepted 15 February 2021; Published 10 March 2021

Academic Editor: Yuan Li

At present, most of the international research cases on badlands are based on semiarid regions, while there are few studies on badlands in humid regions. Therefore, the research on badlands in humid regions has strong theoretical and practical significance. By taking the Nanxiong Basin, which is located in the humid regions of southern China as the research object, this paper analyzes the scale and spatial distribution variation characteristics of redbed badlands and builds a set of factors that influence redbed badlands to explore the driving forces influencing the variation of redbed badlands based on remote sensing images of the American KH-4A satellite from 1969 and a Landsat 8 image from 2017. The result shows that the scale of redbed badlands in the Nanxiong Basin had generally decreased from 1969 to 2017. The area of redbed badlands decreased from 1693.97 hm^2 in 1969 to 127.4 hm^2 in 2017, with a decrease of 92.48%. The spatial distribution of redbed badlands had gradually changed from the contiguous planar distribution form in 1969 to the dispersed island distribution form in 2017, forming four agglomerations. The influence degree of the driving forces for the scale variation of redbed badlands is in the order of lithology > road > aspect > residential locations > slope > water system > vegetation > garden plots. Among these driving forces, except vegetation and garden plots, which have a negative correlation with the variation of redbed badlands, other factors have a positive correlation. Lithology is positively correlated with the variation of redbed badlands and has the strongest influence on the redbed badlands of all the influencing factors. The road factor is second to the lithological factor; the more accessible an area is, the stronger the human influence will be and the more serious the damage to vegetation will be, which easily cause surface vegetation damage, induce land degradation, and form redbed badlands.

1. Introduction

Badlands represent a type of surface landscape cut by strong running water, and they are barren areas that feature dense ravines without vegetation coverage [1, 2]. The problems of badlands make them research hotspots domestically and internationally. The research direction mainly involves the material basis of badlands [3, 4], development and influencing factors [5–8], influence of human activities [9, 10], badland erosion [11, 12], badland ecology [13, 14], and other aspects. At present, most of the international research cases on badlands are based on semiarid regions, while there are few studies on badlands in humid regions [15]. Therefore, research on badlands in humid regions has strong theoretical and practical significance.

A redbed badland is a geomorphologic shape developed based on the characteristics of the parent rocks of redbeds, which has typical characteristics such as the loss of the topsoil layer, the direct exposure of contiguous redbed bedrock or thin weathered crust of redbed, and the dense distribution of chicken feet-shaped erosion ditches [16]. The redbed badland may occur in any climatic region, and it is especially

Figure 1: Typical redbed badlands in the Nanxiong Basin.

worthy of people's attention when it occurs in humid regions [16]. At present, scholars have conducted an in-depth study on the development process of redbed badlands and their influencing factors. Among them, Zhu and Cui [17], Cui [18], and Tian et al. [19] mainly focused on soil and water loss in redbed zones from the perspectives of the water erosion desertification and red desertification in humid areas. Peng et al. [16, 20] believed that the redbed was the extreme form of redbed land degradation and a special type of desertification. Yan [21] analyzed the characteristics of "badland-style redbed desertification" from the perspectives of landscape, geomorphic, soil, and ecological features. In addition, Deng believed that the causes of the redbed degradation in humid regions include both natural and human aspects. Natural causes include climate, soil geology, vegetation, and other factors, while human causes include excessive deforestation, overloading of the land carrying capacity, and blind scale reclamation [22]. Lu believed that lithology is the internal factor for redbed badland formation, but the slope, aspect, and cultivation methods also have a strong influence [23]. Peng et al. believed that the degradation of redbeds is a result of comprehensive action of multifactors. They believed that the initial cause of redbed degradation is the destruction of vegetation and erosion of the soil shell. After the vegetation is destroyed, the protection function of the vegetation to the soil shell decreases continuously, and the splash erosion ability of raindrops leads to the dispersion of soil particles [24–27], thus forming favorable conditions for the dispersion and erosion of soil particles. However, the research can be further extended to the aspects of the variations in the redbed badland degradation process and the quantitative identification and systematic research of their driving forces.

Redbeds in China's humid regions are mainly distributed in the intermountain small and medium basins in central China and southern China [28, 29], such as Hengyang Basin, Ganzhou Basin, and Nanxiong Basin. Among them, the Nanxiong Basin is located in the humid region of southern China, and the redbed region in Guangdong, Hunan, and Jiangxi is one of the hardest hit areas of soil erosion in China, which is the representative of redbed badland regions in China [21] (Figure 1). Therefore, based on the satellite image data from 1969 and 2017, this research uses RS and GIS spatial analysis methods to analyze the landscape pattern variation characteristics of redbed badlands in the Nanxiong Basin and adopts the geographically weighted regression method to quantitatively analyze the influencing factors of redbed badlands, so as to explore the variation characteristics

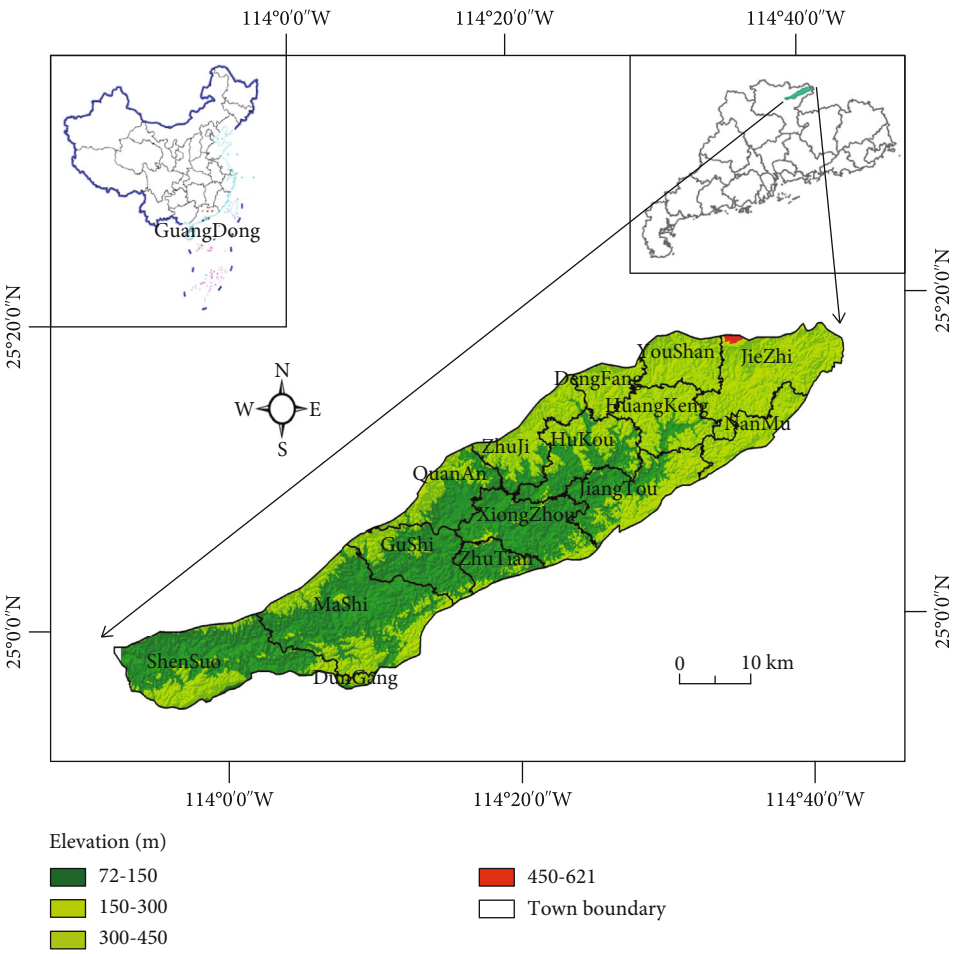

Figure 2: Location of the Nanxiong Basin. Note: the map of China in this figure is based on the standard map with the drawing approval number GS (2020) No. 4619 downloaded from the website of the Standard Map Service of the Ministry of Natural Resources, and the base map has not been modified.

and mechanism of redbed badlands in representative regions of China and provide a basis for scientific prevention and control.

2. Overview of the Research Area

The Nanxiong Basin is located in the northeast part of Shaoguan, Guangdong Province, at the border of Guangdong, Jiangxi, and Hunan Provinces. The latitude and longitude range from 113°50′-114°44′E to 24°35′-25°24′N. The basin has a total area of 4500 km^2, and the redbeds are distributed over an area of 1800 km^2 (Figure 2), accounting for 40%. The geomorphic form of the basin features in low mountains and hills has high terrain in the northeast and low terrain in the southwest, whose altitude ranges from 72 to 621 m. This region has a subtropical wet monsoon climate, with an average annual rainfall of 1535.6 mm, average annual temperature of 19.7°C, and good hydrothermal conditions [21]. The Nanxiong Basin is a typical redbed soft-rock basin, and its redbed belongs to the continental sedimentary rock series formed at the Cretaceous-Paleogene transition between the Meso-Cenozoic and Cenozoic in a dry and hot climate with short intervals of humid and hot climates. The redbed rocks in the Nanxiong Basin are low in maturity; rich in calcite and feldspar; low in weathering resistance; soft in lithology, generally containing calcareous nodules, purple-red and brown-red in color; poor in diagenesis, and weak in weathering erosion resistance [30]. This city is a key control area of soil erosion in Guangdong Province. The regional GDP of this city achieved 11.384 billion yuan in 2019, with a resident population of 333,300 people.

3. Methodology and Data

3.1. Methodology

3.1.1. Geographically Weighted Regression Model. The factors influencing the development of redbed badlands have spatial characteristics, and the relationship between them changes with the change of geographical location. The general global regression model cannot consider the spatial heterogeneity of regression parameters of spatial data, so it cannot accurately describe the relationship between variables. The geographically weighted regression (GWR) model integrates the spatial attributes of data into the regression model to estimate local parameters, which has been widely used in revealing the

relationship between variables changing with spatial location. Based on this, this paper selects the GWR model to analyze the influencing factors of the development and change of redbed badlands, and the specific formula is [31]

$$y_i = \beta_0(u_i, v_i) + \sum_k a_k(u_i, v_i)x_{ik} + \varepsilon_i. \quad (1)$$

In this formula, y_i is the dependent variable at point i, β_0 is the intercept, x_{ik} is the value of the kth independent variable at point i, k is the independent variable count, i is the sample point count, ε_i is the residual error, (u_i, v_i) is the spatial coordinate of the ith sample point, and $a_k(u_i, v_i)$ is the local regression coefficient at point i.

3.1.2. Selection of Driving Force Indicators. Based on the grid scale, this paper discusses the driving force of changes of redbed badlands. The research area was divided into 1 km × 1 km unit grids, and the area variation of each grid from 1969 to 2017 was considered to be the dependent variable in the regression model. The redbed badlands are explained as being caused by the joint action of natural factors and human factors. Among the natural factors, lithology, rainfall, slope, and aspect have a strong influence, while the human factors are mainly various human disturbances caused by construction and cultivation. Lithology, slope, and aspect can be directly quantified [21]. Rainfall is a homogeneous index over a small area, so it cannot be used directly and is replaced by the water system. The construction behavior in Nanxiong is mainly reflected by the residential locations and roads. The cultivation behavior mainly takes place in and garden locations. The farmlands in the Nanxiong Basin are paddy fields with no redbed badlands. Therefore, garden locations were used as a symbol of cultivation behavior. To sum up, lithology, slope, aspect, water system, vegetation, residential locations, garden plots, and roads are selected for use as indexes in this paper, and their substitute indexes are lithology, average slope, average aspect, average distance of the water system, average of the garden area, average density of residential locations, average density of garden plots, and average road distance (Table 1).

3.2. Data Sources and Processing

3.2.1. Information Extraction of Redbed Badlands. The basic data sources used in the research are images from the keyhole satellite KH-4B image (focal length: 61 cm; image coverage area per frame: 13.8 × 188 km) from 1969 with spatial resolution of 1.8 m × 1.8 m and the Landsat 8 remote sensing image from 2017. ENVI software was used to merge the Landsat 8 multispectral images with Google Earth orthographic images, and the spatial resolution after the fusion reached 0.61 m × 0.61 m.

An early image processing step was to select a specific band sequence in ArcGIS 10.8 for RGB synthesizer rendering and stretching processing and to obtain images with obvious hues, clear hierarchies, and significant color differences among ground objects. Combining the features of color, morphology, texture, and other auxiliary materials, corresponding interpretation marks were established between the remote sensing image features and corresponding Google Earth image features, and visual interpretation and artificial vectorization were carried out in the redbed-poor areas. Some inferior patches with unclear boundaries were verified in the field in October 2017 and June 2018, and the redbed badland distribution map of the Nanxiong Basin was finally generated. In the images from 1969 and 2017, 707 and 331 patches of the red substratum were acquired, respectively (Figure 3).

3.2.2. Other Relevant Data Acquisition. The DEM for the Nanxiong Basin was downloaded through BIGEMAP, and the projection grid and resampling processing were carried out in ArcGIS. The resolution was 30 m, and the slope and aspect information was obtained by using ArcGIS. The current land use status used the land survey data from 2014, from which the river system and residential location elements were obtained. The road network data were obtained from the OpenStreetMap official website. The projection coordinate system (WGS_1984_UTM_Zone_49N) was used for conversion, correction, and spatial matching of the above data.

4. Results

4.1. Spatial-Temporal Variation Features of Redbed Badlands

4.1.1. Scale Variation Characteristics. From 1969 to 2017, the scale of redbed badlands in the Nanxiong Basin generally showed a decreasing trend. Specifically, the patch number of redbed badlands in the Nanxiong Basin decreased from 707 in 1969 to 331 in 2017, with a decrease of 53.18%. The area of redbed badlands decreased from 1693.97 hm^2 in 1969 to 127.4 hm^2 in 2017, with a decrease of 92.48%. The monomer scale of redbed badlands also decreased greatly (Figure 4). The average monomer area in 1969 and 2017 was 2.4 hm^2 and 0.38 hm^2, respectively, with a decrease of 84.17%. In terms of the largest area of redbed badlands, it was 12.69 hm^2 in 1969 and 2.05 hm^2 in 2017, with a decrease of 83.85%. Among the redbed badlands in 1969, there were 252 areas that were larger than the largest area in 2017 (2.05 hm^2), which accounted for 35.64% of the total quantity of redbed badlands in that year. In 2017, 93.05% of the redbed badlands were smaller than 1 hm^2 and showed a fragmented distribution pattern.

4.1.2. Spatial Distribution and Its Change. In 1969, the redbed badlands showing a continuous plane distribution trend were mainly distributed in the northeast part of the Nanxiong Basin. In the Nanxiong Basin, Huangkeng Town boasts the largest number of redbed badlands accounting for 27.58% of the total number. Hukou Town has the largest redbed badland area accounting for 20.34% of the total area. The redbeds show a decentralized island distribution and form four distinct agglomerations (Figure 5). (1) The Youshan agglomeration is located in the northeastern part of the basin and includes Shangjiang Village, Aijing Village, and Gaosu Village in Youshan Town. In 1969 and 2017, this region belonged to agglomerations, with little change in the agglomeration scope. In 2017, 127 redbed badlands were distributed

Table 1: Independent variables and their substitute indexes.

Type of independent variables	Indicators	Index definition	Calculation method	Index definition
Natural factors	Lithology	Influence of different geological group types on the spatial pattern of redbed badlands	$y = \frac{S_i}{S} \times 100$	s_i is the area of the lithologic group type in the unit grid, and S is the area of the unit grid
	Average slope	Influence of slope on the spatial pattern of redbed badlands	$y = \text{atan}\left(\sqrt{\left(\frac{d_z}{dx}\right)^2 + \left(\frac{d_z}{dy}\right)^2}\right) * 57.29578$	d_z/dx is the horizontal change rate of the central pixel, and d_z/dy is the vertical change rate of the central pixel
	Average aspect	Influence of aspect on the spatial pattern of redbed badlands	$y = 57.29578 * \text{atan}^2\left(\left[\frac{\partial z}{\partial x}\right], -\left[\frac{\partial_2}{\partial x}\right]\right)$	$\partial z/\partial x$ is the change rate of the unit pixel in the x direction, and $\partial z/\partial y$ is the change rate of the unit pixel in the y direction
	Average distance of the water system	Influence of the water system on the spatial pattern of redbed badlands	$d = \frac{\sum_n^{i=1} d_i}{n}, d_i = \sqrt{(x_0 - \chi_i)^2 + (y_0 - y_i)^2}$	x_0 and y_0 are vertical coordinates of badlland and the nearest river, χ_i and y_i are centroid coordinates of the nearest badland, d_i is the distance from any badland to the nearest river in the unit grid, n is the number of badlands in the unit grid, and d is the average water system distance in the unit grid
	Average forestland area	Influence of forestland on the spatial pattern of redbed badlands	$y = \frac{\sum_{i=1}^{n} S_i}{n} \times 100\%$	s_i is the area of vegetation in the unit grid, and S is the area of the unit grid
Human factors	Average density of residential locations	Influence of human activities on the spatial pattern of redbed badlands	$D = \frac{3(1 - \text{scale}^2)}{\pi r^2}$	scale is the area unit scale factor of residential locations in each grid, r is the neighborhood radius, and D is the average density of residential locations in the unit grid
	Average density of garden plots		$D = \frac{3(1 - \text{scale}^2)}{\pi r^2}$	scale is the area unit scale factor of residential locations in each grid, r is the neighborhood radius, and D is the average density of residential locations in the unit grid
	Average road distance		$d = \frac{\sum_n^{i=1} d_i}{n}, d_i = \sqrt{(x_0 - \chi_i)^2 + (y_0 - y_i)^2}$	x_0 and y_0 are vertical coordinates of badlland and the nearest river, χ_i and y_i are centroid coordinates of the nearest badland, d_i is the distance from any badland to the nearest river in the unit grid, n is the number of badlands in the unit grid, and d is the average water system distance in the unit grid

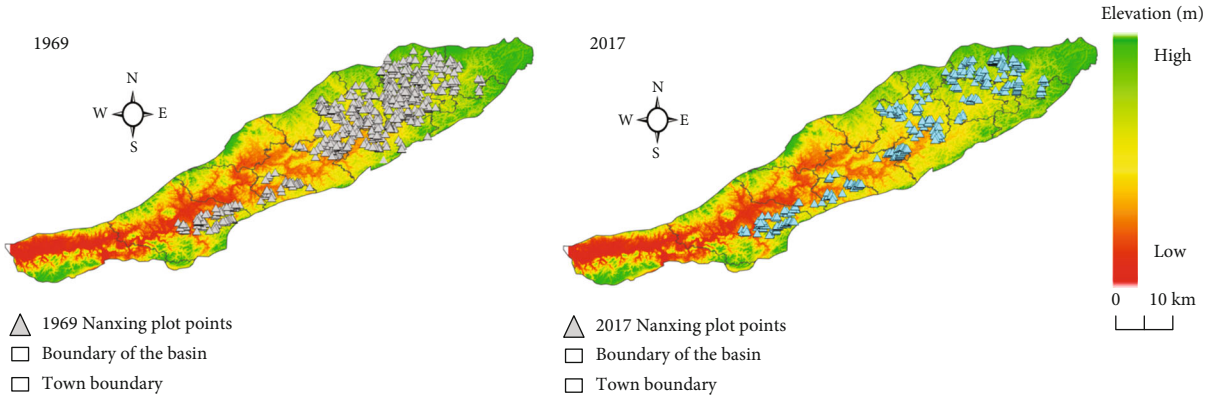

Figure 3: Distribution of redbed badlands in the Nanxiong Basin in different years.

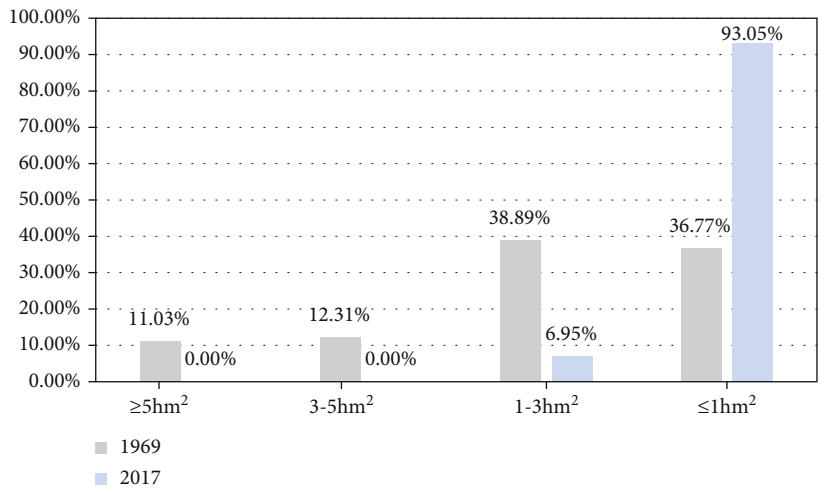

Figure 4: Comparison of the monomer scale of redbed badlands.

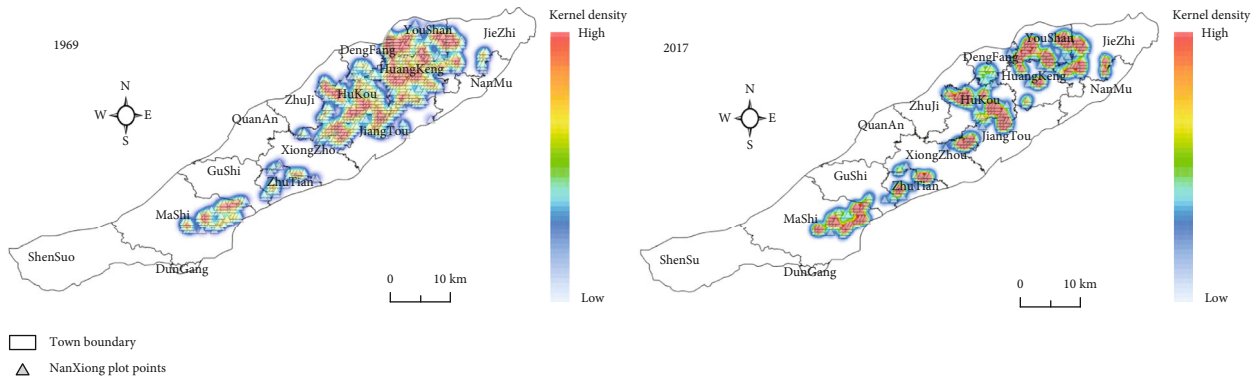

Figure 5: Density distribution of redbed badlands in the Nanxiong Basin.

in the area, which accounted for 38.37% of the total quantity of redbed badlands and 45.56% of the total area. (2) The Hukou agglomeration is located in the northeastern part of the basin and includes Hukou Village, Xinjing Village, and Xiahu Village in Hukou Town. In 2017, 108 redbed badlands were distributed in the area, which accounted for 33.83% of the total quantity of redbed badlands and 28.59% of the total area. (3) The Dungang agglomeration is located in the southwest part of the basin and includes Dutang Village and Yuanjing Village. In 1969, the agglomeration degree of this area was not high. In 2017, 60 redbed badlands were distributed in this area, which accounted for 18.13% of the total quantity of redbed badlands and 20.26% of the total area. (4) The Zhutian agglomeration is located in the southwestern part of the basin and includes

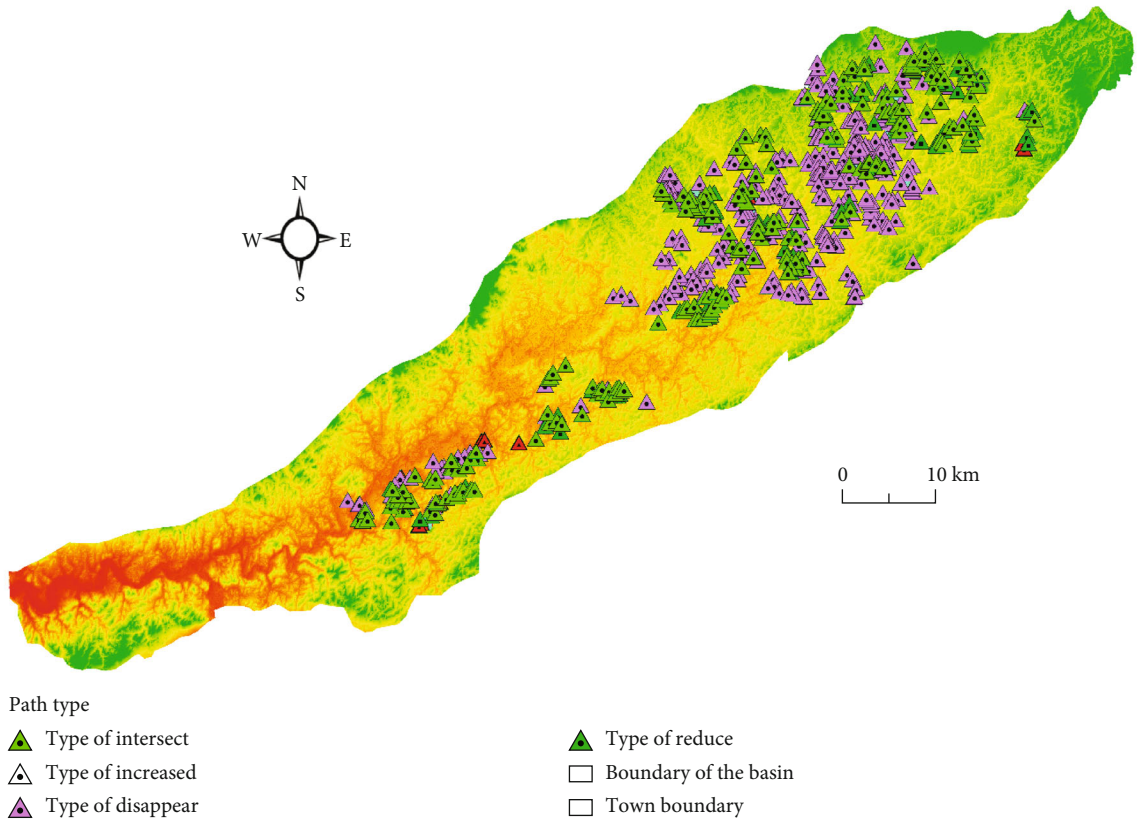

Figure 6: Types of redbed badlands in the Nanxiong Basin.

Wuzhou Village and Shing Mun Village in Zhutian Town. Different from the Donghang agglomeration area, the agglomeration degree of this area was not high in 1969, and in 2017, it had become an agglomeration area; however, its scale was small. In 2017, 32 redbed badlands were distributed in the area, which accounted for 9.67% of the total quantity of redbed badlands and 5.59% of the total area.

According to the spatial variation characteristics of redbed badlands from 1969 to 2017, the redbed badlands in the Nanxiong Basin can be divided into four types (Figure 6). (1) Type of increased: redbed badlands only existed in 1969. There were 389 redbed badlands with an area of 782.89 hm^2. (2) Type of reduce: redbed badlands existed in both 1969 and 2017, but the area of the redbed badlands decreased significantly. There were 67 redbed badlands with an area of 463.89 hm^2. (3) Type of intersect: redbed badlands in 2017 partly overlap with the redbed badlands in 1969, but the redbed badlands in 2017 were not completed within the redbed badlands in 1969. There were 236 badlands in total, and the area was 33.78 hm^2. (4) Type of disappear: redbed badlands only existed in 2017. There were 19 new redbed badlands with an area of 58.66 hm^2.

4.2. Influencing Factors and Spatial Heterogeneity of Redbed Badland Changes

4.2.1. Analysis of Influencing Factors Based on the OLS Model. Before taking the GWR model as the method of analysis, the global regression OLS model must be used to test the relationship between the change scale of redbeds and the explanatory variables determined above. The operation results of the OLS model are shown in Table 2. The adjusted determination coefficient of the model is 0.576, which indicates that the global OLS model can account for 57.6% of the change of redbed badlands. Specifically, except that the garden density and the proportion of forestland are negatively correlated with the change of the redbed badland area, other explanatory variables are positively correlated with the change of the redbed badland area. The positive correlation coefficients of lithology, road, and slope are large, and the robust probability statistics are significant, which indicates that these three types of variables are the main factors affecting the research on changes of redbed badlands. The VIF values of all eight explanatory variables are less than 7.5, and there are no redundant explanatory variables. Meanwhile, the Koenker test shows that the global regression OLS model is unstable in the study area; that is, the relationship between the change of the redbed badland area and explanatory variables in the study area is spatially heterogeneous, which requires an analysis conducted by using the GWR model.

4.2.2. Influencing Factors and Spatial Heterogeneity Based on the GWR Model. The GWR model is analyzed by ArcGIS 10.2, in which the core type adopts the "fixed core" method, and the common Akaike information criterion (AICc) method is adopted to determine the model bandwidth. The

Table 2: OLS regression model results.

Explanatory variables	Estimation coefficient	Standard deviation	T statistical value	Robust probability	VIF
Intercept	-0.297470	0.250484	-1.187578	0.235955	—
Lithology	0.643417	0.035579	18.084160	0.000000*	1.069833
Average density of residential locations	0.214968	0.108997	1.972239	0.049511*	1.526899
Average density of garden plots	-0.105391	0.067333	-1.565223	0.118615	1.388346
Average aspect	0.218043	0.212271	1.196011	0.305163	1.175888
Average slope	0.122078	0.115866	1.053615	0.292913	2.472239
Average distance of water system	0.072180	0.041420	1.742632	0.082447	1.436574
Average road distance	0.293969	0.041704	7.048899	0.000000*	1.425976
Proportion of the forestland area	-0.008057	0.002583	-3.119311	0.002002*	2.186504
R^2	0.587				
Adjusted R^2	0.576				
AICc	443.340				
Koenker (BP) statistics	20.517				

Table 3: Descriptive statistical analysis of the regression coefficients of the GWR model.

Independent variable	Minimum	25% quantile	Median	75% quantile	Maximum
Constant term	-0.370	0.304	0.572	0.828	4.689
Lithology	0.643301	0.643388	0.64341	0.643435	0.643474
Average density of residential locations	0.214747	0.214941	0.215	0.215043	0.215113
Average density of garden plots	-0.105454	-0.105435	-0.105417	-0.1054	-0.105337
Average aspect	0.217806	0.217859	0.21791	0.21796	0.21814
Average slope	0.121726	0.121846	0.121931	0.122023	0.122358
Average distance of water system	0.071938	0.072142	0.072196	0.072249	0.07232
Average road distance	0.2940	0.294014	0.294024	0.294034	0.29407
Proportion of the forestland area	-0.00806	-0.008056	-0.008055	-0.008055	-0.008055
R^2	0.587				
Adjusted R^2	0.576				
Local R^2	0.587				
AICc	443.348				
Bandwidth	569385.634				

calculation results are shown in Table 3. The determination coefficient and adjusted determination coefficient of the model are 0.587 and 0.576, which are equal to the corresponding values of the global regression OLS model. The AICc value is slightly higher than that of the OLS model, with a difference of 0.008. Within the allowable error range, it can be considered that the performance of the two models is the same, but the local goodness of fit (local R^2) of the GWR model is 0.587, higher than the adjusted determination coefficient (0.576) of the OLS model, indicating that the GWR model is more explanatory in the heterogeneity of the local fit space, the number of conditions of the GWR model is less than 30, and there is no local multicollinearity in the model. Based on the regression coefficient of the GWR model to the influencing factors of each grid, Table 3 makes statistics on the mean value, minimum value, maximum value, upper and lower quartile value of each factor, etc. The median order of the regression coefficients for each factor is lithology > road > residential locations > aspect > water system > slope > garden plots. From Table 3, it can be seen that from 1969 to 2017, the lithology, aspect, and water system among the natural factors and residential locations and roads among the human factors have a stable positive influence on the variations in the redbed badlands in the Nanxiong Basin. Among them, the median value of the regression coefficient of the lithological factor is approximately 0.643, which is much higher than that for the six other independent variables, followed by roads, residential locations, and slope. The regression coefficients of these three factors are close, ranging from 0.21 to 0.29. The influence of the water system factor is smaller, at only approximately 0.07. The slope and garden plot factors have a negative influence on the variations in the redbed badlands, with regression coefficients between -0.105 and 0.008.

(1) The Lithological Factor (Figure 7(a)). Lithology is positively correlated with the variation of redbed badlands and has the strongest influence on the redbed badlands of all the influencing factors. The regression coefficient showed an increasing trend from southwest to northeast in the area from Dungang Town to Youshan Town, indicating that lithology promoted the formation of redbed badlands, which was most significant in the northeast area around Youshan Town. Lithology is the material basis for redbed badland formation. The redbeds in the Nanxiong Basin mainly formed in the Cretaceous and Paleogene, and a total of nine groups are divided into two groups. The area of redbed badlands in the Zhutian, Zhenshui, and Shanghu Formations is as high as 87.98%, while the other redbed badlands are relatively less developed, which results from the main compositions of the redbeds in the Zhutian, Zhenshui, and Shanghu Formations which are argillaceous siltstone, silty mudstone, and silty mudstone, whose components are muddy cementation. The clay mineral content is as high as 28.4-50.3%. Clay minerals are mainly illite and illite-montmorillonite mixed layer, with weak cementation, high clay mineral content, and low degree of compaction. The redbeds are more prone to differential disintegration than other lithologies [30].

(2) The Aspect Factor (Figure 7(b)). Aspect is positively correlated with the variations of the redbed badlands; the regression coefficient indicated an increasing trend to the southwest from Youshan Town to Dungang Town, indicating that the influence of aspect on redbed badlands was most significant in the southwest area of Dungang Town. The Nanxiong Basin is located at 24°35′-25°24′N, the southeast direction, which is the aspect that receives the most solar radiation. According to the research of Li et al., increases in temperature accelerate the disintegration of redbed rocks, and the higher the average temperature is, the higher the erosion rate of redbed badlands will be and vice versa [32]. The fractured rock is exposed to the bedrock under rain wash, which is conducive to badland formation. Compared to the eastern slope, the northern slope receives less light, and the possibility of producing badlands decreases.

(3) The Slope Factor (Figure 7(c)). Slope is positively correlated with the changes in redbed badlands. The regression coefficient showed an increasing trend to the southwest from Youshan Town to Dungang Town. Badland formation is the extreme result of soil erosion, and the intensity of soil erosion is closely related to the slope. According to the statistics, the slopes in the Nanxiong Basin are between 0 and 51.73°. In 2017, 251 redbed badlands in the Nanxiong Basin were distributed on slopes of 0-5°, accounting for 75.83% of the total quantity. There were 71 badlands on slopes of 5-8°, which accounted for 21.45% of the total quantity. There were 9 badlands on slopes of 8°-15°, which accounted for 2.72% of the total land quantity. From large to small, the distribution of badlands was as follows: 0-5° > 5-8° > 8-15°. No badlands developed on other slopes. The reason is that the rocks comprising the redbeds in the Nanxiong Basin mainly consists of soft rocks, such as siltstones and mudstones. These soft rocks are characterized by low strength, high porosity, and poor cementation and are significantly affected by structural surface cutting and weathering. The presence of loose, soft, and weak rocks causes the slopes in redbed areas to be relatively slow. However, due to the existence of slope, the gravity will be beneficial to the erosion and movement of weathered soft rock and the formation of redbeds.

(4) The Water System Factor (Figure 7(d)). The water system is positively correlated with changes in redbed badlands but has the least influence of all the influencing factors. The regression coefficient showed an increasing trend to the northeast from Dungang Town to Youshan Town. The material foundation of redbeds is soft rock, which is prone to disintegration under a water system and can be completely disintegrated after half an hour of immersion [33]. Due to the existence of soft rocks, such as siltstone and argillaceous rock, when rainfall gathers on the surface, rainfall rarely penetrates into the ground and rapidly gathers and forms small streams of water to erode the surface. With continuous erosion, the parent rock outcrops and, finally, promotes the formation and development of badlands. However, the existence of water is also conducive to soil formation from the weathered debris of soft rock. Under a favorable set of hydrothermal conditions, vegetation recovery is faster, which makes it easy for redbed badlands to naturally recover vegetation or be governed.

(5) The Residential Location Factor (Figure 7(e)). The residential location is positively correlated with the changes in redbed badlands and has a strong impact on redbed badlands. The regression coefficient showed an increasing trend to the northeast from Dungang Town to Youshan Town and thus indicated that residential locations have a promoting effect on redbed badlands in all towns, and this effect is most significant in the northeast area around Youshan Town. It is estimated that the average distance between residential areas in the grid and redbed badlands is 405.29 m. In the grid of the redbed badland distribution, the average proportion of construction land is 0.57% and the maximum proportion is 27.54%, which shows that the denser the residential areas are, the more frequent the production and living activities of human beings are and the more serious the damage to vegetation may be. Once the surface vegetation is destroyed, an irreversible degradation process may occur, which becomes an important factor for redbed badland formation.

(6) The Garden Plot Factor (Figure 7(f)). The median value of the regression coefficient of garden plots was approximately -0.105, which was negatively correlated with the land changes of redbed badlands and was the same as the forestland factor. The regression coefficient showed an increasing trend to the southwest from Youshan Town to Dungang Town. The reason for this trend is that garden land is mainly a sentry land for redbed badlands. In the same area, if the land can be well utilized, then the possibility of redbed badland development will be decreased, leading to a negative correlation between the two.

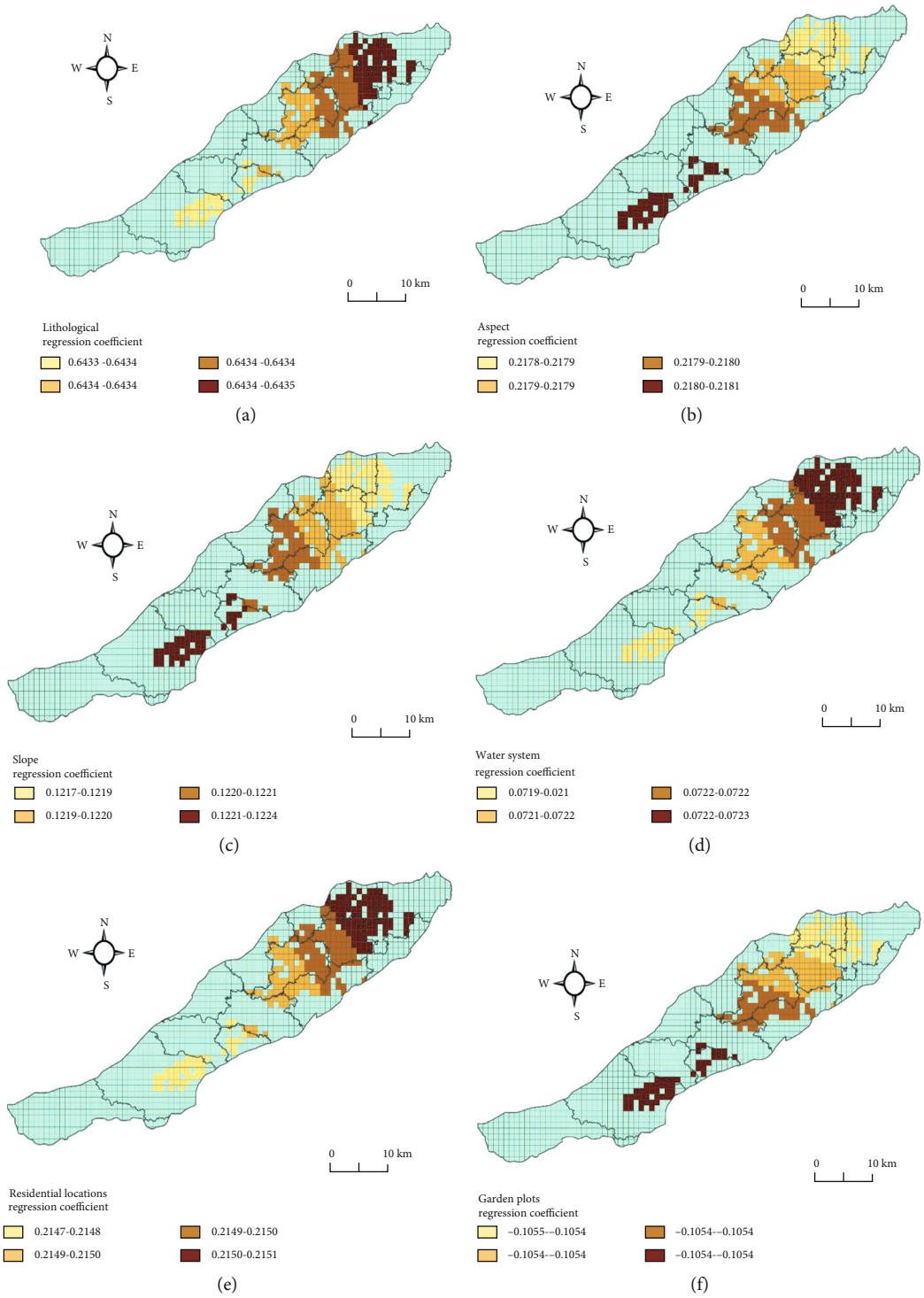

Figure 7: Continued.

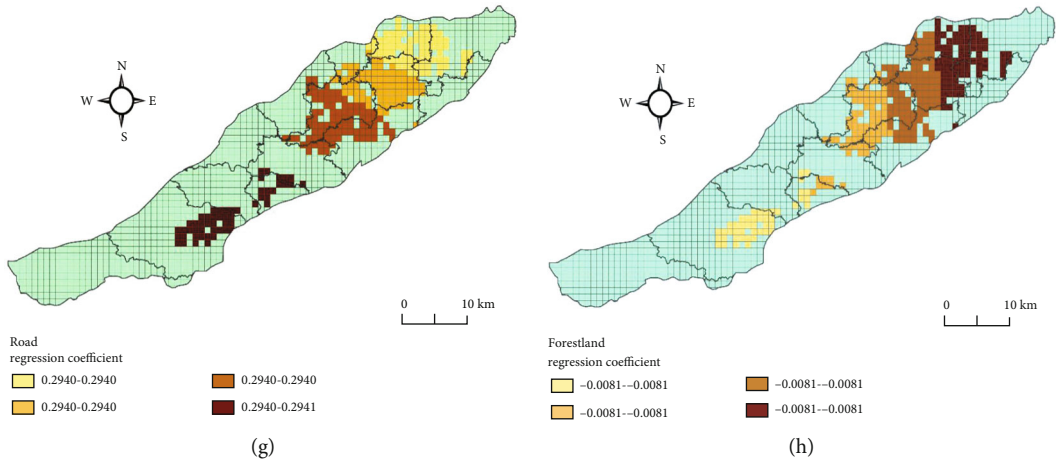

Figure 7: GWR model analysis.

(7) The Road Factor (Figure 7(g)). The road factor is second to the lithological factor but is also close to the strength of the aspect and residential location factors, indicating that the road factor is positively correlated with the changes in redbed badlands and has a strong influence on redbed badlands. The regression coefficient showed an increasing trend to the southwest from Youshan Town to Dungang Town, indicating that roads promoted redbed badlands in all towns, and it was most significant in the southwest area of Dungang Town. It is calculated that the average distance between roads in the grid and redbed badlands is 342.68 m. In the grid of the redbed badland distribution, the average proportion of road land is 0.56% and the maximum proportion is 5.14%, which is much higher than the grid without redbed badlands, which indicates that the more accessible an area is, the stronger the human influence will be and the more serious the damage to vegetation will be, which easily cause surface vegetation damage, induce land degradation, and form redbed badlands

(8) The Forestland Factor (Figure 7(h)). The same as the garden factor, the forestland factor is one of the two negatively related to the change of redbed badlands, but its negative influence is smaller than that of the garden factor. From 1969 to 2017, the Nanxiong Basin continued to carry out governances for redbed badlands, in which afforestation was an important task. By 2018, the number of the forestland area had reached 445,800 hectares. The restoration of vegetation plays a good role in resisting erosion and conserving water for the degradation of redbeds and effectively inhibits the increase in redbed badlands. There is a trade-off between the two.

The analysis above indicates that the change of redbed badland is a multifactor comprehensive process based on lithology, induced by human activities, a joint action of natural factors such as rainfall, slope, and aspect and human factors such as residential areas and roads.

5. Discussion

A redbed badland is a geomorphologic shape developed based on the characteristics of the parent rocks of redbeds, which has typical characteristics such as the loss of the topsoil layer, the direct exposure of contiguous redbed bedrock or thin weathered crust of redbed, and the dense distribution of chicken feet-shaped erosion ditches. The research should be further extended to the aspects of the variations in the redbed badland degradation process and the quantitative identification and systematic research of their driving forces.

In this paper, based on the remote sensing images data of American KH-4A from 1969 and Landsat 8 from 2017, the scale and spatial distribution characteristics of redbed badlands are analyzed, and the driving factors of redbed badlands are analyzed by the geographically weighted regression. We found that the landscape index of the redbed badlands generally showed a trend of reduction from 1969 to 2017. The influence degree of the driving factors of the scale change of the redbed badlands is lithology > road > residential locations > aspect > water system > slope > garden plots.

In previous studies, Deng believed that the causes of the redbed degradation in humid regions include both natural and human aspects. Natural causes include climate, soil geology, vegetation, and other factors, while human causes include excessive deforestation, overloading of the land carrying capacity, and blind scale reclamation [22]. Lu believed that lithology is the internal factor for redbed badland formation, but the slope, aspect, and cultivation methods also have a strong influence [23]. Peng et al. believed that the degradation of redbeds is a result of comprehensive action of multifactors. They believed that the initial cause of redbed degradation is the destruction of vegetation and erosion of the soil shell. After the vegetation is destroyed, the protection function of the vegetation to the soil shell decreases continuously, and the splash erosion ability of raindrops leads to the dispersion of soil particles [24–27], thus forming favorable conditions for the dispersion and erosion of soil particles. The conclusion of this paper is consistent with these studies. Furthermore, the research has been extended to the aspects of the variations in the redbed badland degradation process and the quantitative identification and systematic research of their driving forces. At the same time, the importance of the index is further studied.

It should be said that the selection of driving factors is not systematic enough, the analysis is relatively simple, and the quantitative analysis needs to be further strengthened. In addition, not only the plane variations of redbed badlands but also the variations of their height and shape deserve our attention. Based on a comprehensive consideration of the three-dimensional morphology of redbed badlands, future studies need to continuously improve the set of influencing factors and conduct a more in-depth modeling analysis of the factors that influence the development and evolution of redbed badland to clarify its influencing mechanism.

6. Conclusion

At present, most of the international research cases on badlands are in the semiarid areas, while the research on badlands in wet areas are less, so it is of great theoretical and practical significance to carry out the research on badlands in wet areas. Taking redbeds in the Nanxiong Basin located in the humid area of South China as the research target, this paper uses remote sensing images of the American KH-4A satellite from 1969 and Landsat 8 images from 2017 to analyze the scale and spatial distribution characteristics of redbeds, builds a set of factors that influence redbed badlands, and discusses the driving factors of changes of redbed badlands. The results show the following:

(1) From 1969 to 2017, the landscape index of the redbed badlands generally showed a trend of reduction. In particular, the number of the patches of redbed badlands in the Nanxiong Basin had decreased from 707 in 1969 to 331 in 2017, with a decrease of 53.18%. The area of redbed badlands had decreased from 1693.97 hm^2 in 1969 to 127.4 hm^2 in 2017, with a decrease of 92.48%. In terms of spatial distribution, the spatial distribution of redbeds has gradually changed from the planar distribution pattern in 1969 to the island distribution pattern in 2017, forming 4 distinct agglomerations

(2) The influence degree of the driving factors of the scale change of the redbed badlands is lithology > road > residential locations > aspect > water system > slope > garden plots. Except that the factors of forestlands and gardens are negatively correlated with changes of redbed badlands, other factors are positively correlated with each other

(3) Lithology is positively correlated with the variation of redbed badlands and has the strongest influence on the redbed badlands of all the influencing factors. Redbeds are mainly composed of argillaceous siltstone, silty mudstone, and silty mudstone, whose components are muddy cementation. The clay mineral content is as high as 28.4-50.3%. Clay minerals are mainly illite and illite-montmorillonite mixed layer, with weak cementation, high clay mineral content, and low degree of compaction. The redbeds are more prone to differential disintegration than other lithologies

(4) The road factor is positively correlated with the changes in redbed badlands, whose influence on redbed badlands is second to the lithological factor. The more accessible an area is, the stronger the human influence will be and the more serious the damage to vegetation will be, which easily cause surface vegetation damage, induce land degradation, and form redbed badlands

Data Availability

The datasets used in the experiments and discussed in the paper will be available if requested.

Conflicts of Interest

The authors declare no conflict of interest.

Acknowledgments

This work was supported by the National Natural Science Foundation of China (grant number 41771088) and the Special Project for Key Basic Research of the Chinese Ministry of Science and Technology (grant number 2013FY111900).

References

[1] R. Faribridge, *Encyclopaedia of Geomorphology*, vol. 1295, New York: Reinhold Book Corp, 1968.

[2] K. Higuchi, M. Chigira, and D. H. Lee, "High rates of erosion and rapid weathering in a Plio-Pleistocene mudstone badland, Taiwan," *Catena*, vol. 106, no. 3, pp. 68–82, 2013.

[3] Y. Cantón, A. Solé-Benet, I. Queralt, and R. Pini, "Weathering of a gypsum-calcareous mudstone under semi-arid environment at Tabernas, SE Spain: laboratory and field-based experimental approaches," *Catena*, vol. 44, no. 2, pp. 111–132, 2001.

[4] M. Kasanin-Grubin and R. Bryan, "Lithological properties and weathering response on badland hillslopes," *Catena*, vol. 70, no. 1, pp. 68–78, 2007.

[5] I. A. Campbell, "Badlands and badland gullies," in *Arid Zone Geomorphology*, D. S. G. Thomas, Ed., pp. 159–183, Belhaven Press, London, 1989.

[6] D. E. Alexander, "Difference between "calanchi" and "biancane" badlands in Italy," in *Badlands Geomorphology and Piping*, R. B. Bryan and A. Yair, Eds., pp. 71–87, Geo Books, Norwich, 1982.

[7] A. Courtney, "Morphology and development of selected badlands in southeast Spain: implications of climatic change," *Earth Surface Processes and Landforms*, vol. 21, no. 8, pp. 725–735, 1996.

[8] M. L. Clarke and H. M. Rendell, "Process-form relationships in Southern Italian badlands: erosion rates and implications for landform evolution," *Earth Surface Processes and Landforms*, vol. 31, no. 1, pp. 15–29, 2006.

[9] K. Hall and M.-F. André, "New insights into rock weathering from high-frequency rock temperature data: an Antarctic study of weathering by thermal stress," *Geomorphology*, vol. 41, no. 1, pp. 23–35, 2001.

[10] C. Y. Zhou, Y. M. Deng, X. S. Tan, Z. Q. Liu, W. Shang, and S. Zhan, "Experimental research on the softening of mechanical properties of saturated soft rocks and application," *Chinese*

Journal of Rock Mechanics and Engineering, vol. 24, no. 1, pp. 33–38, 2005.

[11] E. Nadal-Romero, J. F. Martínez-Murillo, M. Vanmaercke, and J. Poesen, "Scale-dependency of sediment yield from badland areas in Mediterranean environments," *Progress in Physical Geography*, vol. 35, no. 3, pp. 297–332, 2011.

[12] A. E. Godfrey, B. L. Everitt, and J. F. M. Duque, "Episodic sediment delivery and landscape connectivity in the Mancos Shale badlands and Fremont River system, Utah, USA," *Geomorphology*, vol. 102, no. 2, pp. 242–251, 2008.

[13] W. E. H. Culling, "Soil creep and the development of hillside slopes," *The Journal of Geology*, vol. 71, no. 2, pp. 127–161, 1963.

[14] W. E. Dietrich, R. Reiss, M. L. Hsu, and D. R. Montgomery, "A process-based model for colluvial soil depth and shallow landsliding using digital elevation data," *Hydrological Processes*, vol. 9, no. 3-4, pp. 383–400, 1995.

[15] A. Young, "Present rate of land erosion," *Nature*, vol. 224, no. 5222, pp. 851-852, 1969.

[16] H. Peng, L. Yan, Z. Chen, S. Simonson, and G. Luo, "A preliminary study of desertification in red bedsin the humid region of southern China," *Acta Geographica Sinica*, vol. 70, no. 11, pp. 1699–1707, 2015.

[17] Z. Zhu and C. Shuhong, "Desertification in southern China," *China Desert*, vol. 16, no. 4, pp. 331–337, 1996.

[18] C. Shuhong, "Desertification in humid areas," *Quaternary Research*, no. 2, pp. 173–181, 1998.

[19] Y. Tian, P. E. N. G. Buzhuo, and T. Xie, "Discussion on red desertification prototype," *Resources and environment of the Yangtze river basin*, vol. 10, no. 4, pp. 380–384, 2001.

[20] H. Peng, Z. X. Pan, L. B. Yan, and S. Simonson, "A review of the research on red beds and Danxia landform," *Scientia Geographica Sinica*, vol. 68, no. 9, pp. 1170–1181, 2013.

[21] Y. Luobin, "Study on red-bed land degradation and its driving mechanism under humid environment in southeast China," in *A Case Study of Nanxiong Basin in Guangdong*, School of Geographic Science and Planning, Sun Yat-sen University, Guangzhou, 2017.

[22] L. Deng, "Soil and water loss and its control countermeasures in purple sand shale area of Nanxiong County," *Water and Soil Conservation Bulletin*, vol. 6, no. 11, pp. 30–34, 1991.

[23] S. Lu, "Soil erosion and comprehensive control of purple sand shale area in Nanxiong City," *Soil and Water Conservation in China*, no. 9, pp. 16-17, 2011.

[24] A. J. Parsons, A. D. Abraham, and J. Wainwright, "Rainsplash and erosion rates in an interrill area on semi-arid grassland, southern Arizona," *Catena*, vol. 22, no. 3, pp. 215–226, 1994.

[25] P. P. Sharma, A. C. Gupta, and G. R. Foster, "Raindrop-induced soil detachment and sediment transport from interrill areas," *Soil Science Society of America Journal*, vol. 59, no. 3, pp. 727–734, 1995.

[26] A. I. J. M. Dijk, "A methodology to study rain splash and wash processes under natural rainfall," *Hydrological Processes*, vol. 17, no. 1, pp. 153–167, 2003.

[27] K. Nanko, S. Mizugaki, and Y. Onda, "Estimation of soil splash detachment rates on the forest floor of an unmanaged Japanese cypress plantation based on field measurements of throughfall drop sizes and velocities," *Catena*, vol. 72, no. 3, pp. 348–361, 2008.

[28] P. Hua and Z. Wu, "Preliminary discussion on the characteristics and distribution of red layer," *Journal of sun yat-sen university*, vol. 42, no. 5, pp. 109–113, 2003.

[29] P. Hua, "Perspectives on the red beds landforms in humid area of southern China and some related problems," *Geographical Research*, vol. 30, no. 10, pp. 1739–1752, 2011.

[30] Z. Xianqiu, Z. Ximan, H. Mingcai, L. Gang, and L. Hanmin, "Stratigraphic division of red strata in the Nanxiong Basin," *Journal of stratigraphy*, vol. 37, no. 4, pp. 441–451, 2013.

[31] A. S. Fotheringham, M. Charlton, and C. Brunsdon, "The geography of parameter space: an investigation in-to spatial nonstationarity," *International Journal of Geographical Information Systems*, vol. 10, pp. 605–627, 1996.

[32] L. Peixian, Z. Cheng, Z. Zhijun, and F. Xiaosi, "Nanxiong Formation and Danxia Formation in Nanxiong Basin, Guangdong," *Acta Geographica Sinica*, vol. 28, no. 2, pp. 181–189, 2007.

[33] C. Zhi, *Study on the Weathering, Disintegration and Erosion of Soft Rock with Inferior Red Beds in Nanxiong Basin*, School of Geographic Science and Planning, Sun Yat-sen University, Guangzhou, 2017.

Hindawi
Journal of Sensors
Volume 2021, Article ID 6625774, 14 pages
https://doi.org/10.1155/2021/6625774

Research Article

The Potential Scattering Model for Oil Palm Phenology Based on Spaceborne X-, C-, and L-Band Polarimetric SAR Imaging

Soni Darmawan[1], **Ita Carolita**[2], **Rika Hernawati**[1], **Dede Dirgahayu**[2], **Agustan**[3], **Didin Agustian Permadi**[1], **Dewi Kania Sari**[1], **Widya Suryadini**[1], **Dhimas Wiratmoko**[4] **and Yohanes Kunto**[1]

[1]*Institut Teknologi Nasional Bandung (ITENAS), PKH. Mustofa 23. Bandung 40124, Indonesia*
[2]*Remote Sensing Applications Center of National Institute of Aeronautics and Space (LAPAN), Kalisari 8, Pekayon, Pasar Rebo, East Jakarta 13710, Indonesia*
[3]*Agency for the Assessment and Application of Technology (BPPT), M.H Thamrin 8 Jakarta 10340, Indonesia*
[4]*Indonesian Oil Palm Research Institute, Brigjen Katamso 51, Medan 20158, Indonesia*

Correspondence should be addressed to Soni Darmawan; soni_darmawan@itenas.ac.id

Received 27 November 2020; Revised 20 January 2021; Accepted 7 February 2021; Published 8 March 2021

Academic Editor: Zhenxing Zhang

Information about oil palm phenology is required for oil palm plantation management, but using spaceborne polarimetric radar imagery remains challenging. However, spaceborne polarimetric radar on X-, C-, and L-band is promising on structure vegetation and cloud area. This study investigates the scattering model of oil palm phenology based on spaceborne X-, C-, and L-band polarimetric Synthetic Aperture Radar (SAR) imaging. The X-, C-, and L-band polarimetric SAR are derived from spaceborne of TerraSAR-X, Sentinel-1A, and ALOS PALSAR 2. Study area is located in oil palm plantations, Asahan District, North Sumatra, Indonesia. The methodology includes data collection, preprocessing, radiometric calibration, speckle filtering, terrain correction, extraction of scattering value, and development of scattering model of oil palm phenology. The results showed different scattering characteristics for the X-, C-, and L-band polarimetric SAR of oil palm for age and found the potential of the scattering model for oil palm phenology based on the X-band on HH polarization that showed a nonlinear model with $R^2 = 0.65$. The C-band on VH and VV polarization showed a nonlinear model with $R^2 = 0.56$ and $R^2 = 0.89$. The L-band on HV and HH polarization showed a logarithmic model with $R^2 = 0.50$ and $R^2 = 0.51$. In this case, the most potential of the scattering model of oil palm phenology based on$R^2$is using C-band on VV polarization. However, the scattering model based on X-, C-, and L-band is potentially to be used and applied to identify the phenology of oil palm in Indonesia, which is the main parameter in yield estimation. For the future phenology model needs to improve accuracy by integrating multisensors, including different wavelengths on optical and microwave sensors and more in situ data.

1. Introduction

Oil palm (Elaeis guineensis) is a palm tree that is generally planted in Southeast Asia, particularly in Malaysia, Indonesia, and Thailand. Oil palm can produce cooking oil, mechanical oil, and fuel, widely utilized in daily life and industry [1, 2]. Oil palm obtained from seeds or portions in a hard mesocarp shell produces around 80% saturated fat that can be utilized as a raw material for the production of soap, cleansers, and other substances in the oleochemical industry [3–5]. Oil palm has an exceptional potential to be used as a biofuel in the future [6]. High yields and low production costs from oil palm are the reasons that encourage commercial plantation companies to develop oil palm trees for a considerable scope [7]. Because of expanding worldwide interest for nourishment and fuel, oil palm cultivation has been extended exponentially [8], and nowadays, oil palm is one of the most consumed vegetable oils in the world [9].

Southeast Asia has the ideal condition for oil palm cultivation because it needs the moist equatorial condition [10].

Oil palm is adapting to the tropical atmosphere with a high precipitation rate, high intensity of global radiation, and warm temperature of 24–32°C [11]. The regular dry season in the tropical areas could significantly reduce oil palm yields [3]. The oil palms are generally planted in triangular patterns with a nine-meter interplanting distance (see Figure 1), following an industry standard to maximize yield with optimal sunlight penetration [3]. A planting density of 130–140 palms for each is the general practice. However, it varies according to the planting conditions and oil palm breed type [9, 12, 13]. Terrace planting usually facilitates a countermeasure to run off water and maximizing planting density in hilly areas [14].

Oil palm plantations are planted per block so that all plants in each block have a uniform age. The age of oil palm is the main parameter in yield estimation. Oil palm age is one of the significant variables affecting the production of fruit bunches [3, 10]. Age information of oil palm is a good indicator of yield prediction as it influences the quality and quantity of the fresh fruit bunches [16]. Besides, age information is essential to precision agriculture to recognize anomalies among oil palms inside a specific age group to plan counteractive management practices and optimize management resources [10, 17]. In other cases, oil palm age information is required for the tax estimation, replanting time, and identification of oil palm diseases [15]. Organization or plantation management favors such useful data for maximizing oil palm yield, one of the most important influencing benefits [10]. According to Tan et al. [10], collecting age information on oil palm trees is time-consuming and costly, particularly on a large or regional scale. The age of oil palm growth affects the physical and environment of the oil palm plantation itself. According to Tan et al. [10] and Chemura et al. [16], canopy height and size of oil palms have a strong correlation with age.

Spaceborne technology has been commonly applied in the agriculture and forestry sectors. These technologies are proven to provide a precise, affordable, and efficient solution for agricultural and forestry planning, monitoring, and management [18]. According to Henderson and Lewis [19], although sensors in the optical range of the electromagnetic spectrum have gotten the best consideration and have widely used, considerable effort has been invested into the utilization of radar sensors. Microwave sensors have become a promising technology in the application of remote sensing due to their cloud penetration ability and their capability to obtain data in all-weather day-night conditions. The microwave sensor also relies on its internal energy source, unlike the optical sensors, which rely on sunlight's external energy source. Scatter radar is very sensitive to the dielectric properties (soil moisture and vegetation) and attributes of the geometric conditions (surface roughness) of objects on the surface of Earth [20].

Many regions in the world (e.g., areas covered by clouds and lacking light), radar is the only sensor that can reliably provide consistent and periodic data. A radar sensor can obtain information in the electromagnetic spectrum bands K (1.1–1.7 cm), X (2.4–3.8 cm), C (3.8–7.5 cm), L (15–30 cm), and P (30–100 cm) [20], with the polarization of Horizontal to Horizontal (HH), Vertical to Vertical (VV), Horizontal to Vertical (HV), or Vertical to Horizontal (VH), which have varying ranges and azimuth resolutions [21]. Each of these wavelengths has a unique characteristic related to the reflection from forest stands [22]. The X-band interacts with leaves and canopy cover surfaces; hence, it is very suited for information on the tree canopy surface layer [23]. The C-band can penetrate through the leaves and spread to small branches and other underlying objects [24]. The L-band, which has a higher penetration capability, can penetrate the surface layer and spread to the stems and main branches [25, 26]. The P-band has the highest penetration capability and can penetrate the canopy covers [27].

Many studies developed the model of oil palm phenology derived from scattering characteristics and any parameter, such as derived from biomass [27], leaf area index (LAI) [10, 17], height tree and tree diameter [10], crown projection area (CPA) [16], scattering [28], NDVI [10, 17, 29–31], and spectral band [10, 17, 28, 32]. However, to our best knowledge, information about phenology based on spaceborne X-, C-, and L-band polarimetric SAR has been limited and fragmented in Indonesia. In this study, we pioneered to investigate the scattering model of oil palm phenology in Indonesia based on spaceborne X-, C-, and L-band polarimetric SAR simultaneously.

2. Materials and Methods

2.1. Study Area. Study area in Asahan Regency, North Sumatra, Indonesia. This regency has the capital of Kisaran City and covers an area of 3702.97 km^2. A part of Asahan regency was selected as the study area, which is an oil palm plantation area located in Hessa Plantation, Simpang Empat, Asahan Regency, 2.98° east longitude and 99.67° north latitude and 2.92° east longitude and 99.75° north latitude (Figure 2).

The Asahan Regency is in the central part of the North Sumatra Province eastern coast. The district is mainly agricultural, and the primary land uses are oil palm and rubber plantations inland, with coconut groves and aquaculture ponds by the sea [33]. The first Indonesian oil palm plantation was founded in Asahan [34]. In 1911 during the Dutch colonial era, a Belgian company opened the first commercial oil palm plantation [35], and Asahan was a pioneer in the East Coast area of Sumatra [34, 36]. The large plantation area owned by many private companies and the state-owned Perkebunan Nusantara Company contributes a great deal to most Asahan citizens' economic needs. The plasma plantation scheme is owned by a smallholder whose management is supported by the company (as a central plantation) [34].

Asahan District has a factory capacity of 50 tons of fresh fruit bunch (FFB) per hour [37]. According to Budidarsono et al. [38], on the eastern coast of Sumatra, oil palm production (CPO) increased drastically. The area of the first farm, which was built in 1910–1914, was 2620 ha. The location biophysics is suitable for oil palm growing, with high rainfall (minimum 1600 mm/year) and a tropical climate within 10° of the equator. Land and labor, the most significant inputs, were available [38].

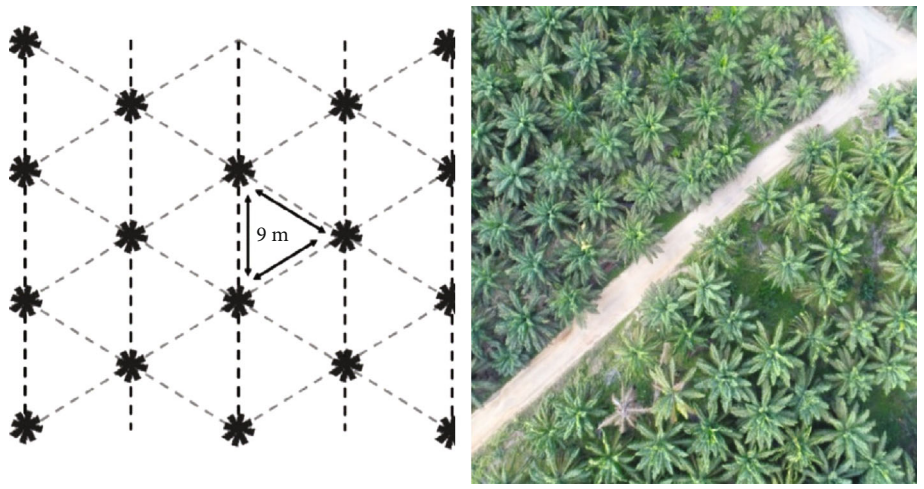

Figure 1: The oil palms planted in triangular patterns (source: [9, 15]).

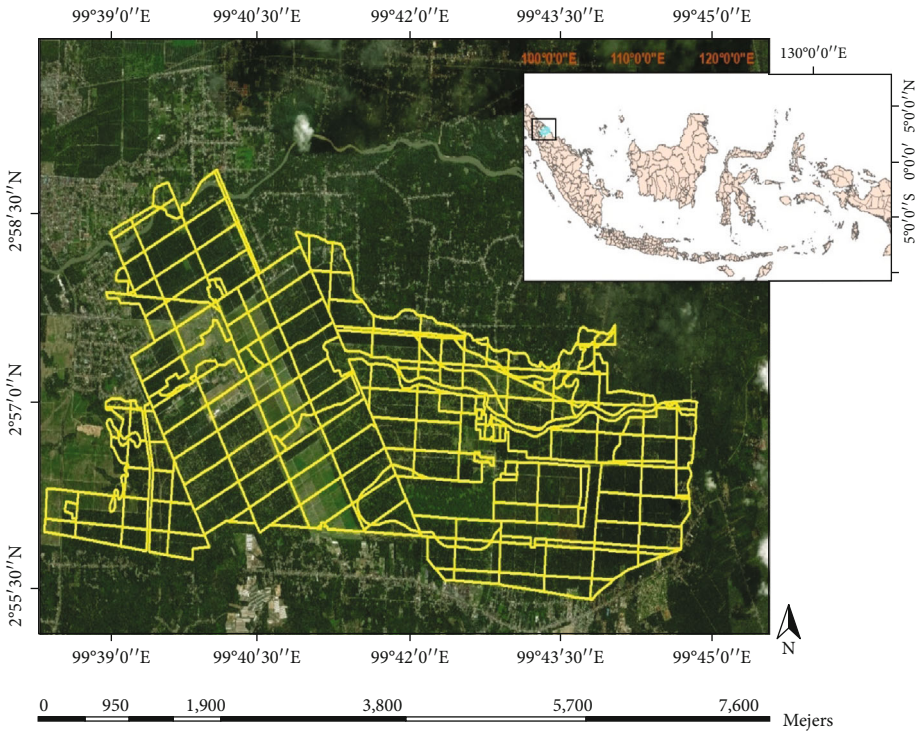

Figure 2: Study Area in Asahan Regency, North Sumatra, Indonesia.

2.2. Methodology. The methodology includes data collection, preprocessing, radiometric calibration, speckle filtering, terrain correction, extracting scattering value, and development scattering model based on spaceborne X-, C-, and L-band polarimetric SAR (Figure 3).

2.2.1. Data Collection. Collecting of variety polarimetric SAR imaging, including TerraSAR-X (X-band), Sentinel-1A (C-band), and ALOS PALSAR 2 (L-band) (Figure 4). TerraSAR-X and ALOS PALSAR-2 data were obtained from the National Institute of Aeronautics and Space-Indonesia (LAPAN), while Sentinel-1A data were collected from the European Space Agency (ESA) Copernicus. The details of the SAR imaging are presented in Table 1.

The topography elevation data were derived from Shuttle Radar Topographic Mission (SRTM), which has a spatial resolution of around 90 meters, and were processed by the National Aeronautics and Space Administration (NASA) and the United States Geological Survey (USGS). The data were projected in a geographic (Lat/Lon) projection, with the WGS84 horizontal datum. Field data collection was conducted in 2020 that collected planting age blocks of oil palm and some photograph in the study area (Figures 5 and 6). In this study area, we used 174 blocks, which represent 11 varieties of oil palm age from 0 to 25 years. This planting age

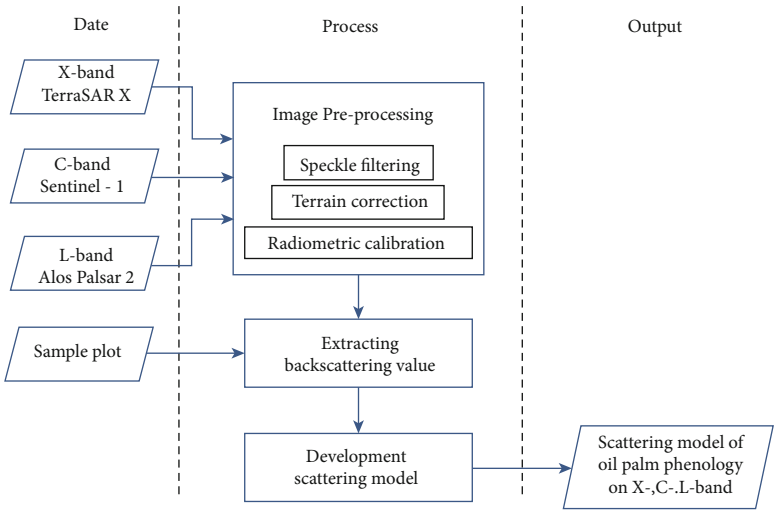

Figure 3: Methodology.

block data is used as a boundary in taking the region of interest (ROI) based on the scattering value with totally around 44,000 pixels.

2.2.2. Preprocessing

(1) Speckle Filtering. SAR imaging interpretation and classification principal problem is the speckle effect caused by wave coherent interference reflected from many primary scatterers [39]. Speckle appears in SAR imaging as granular noise due to waves interference reflected from many basic scatterers [40]. Speckle filtering is a procedure to increase image quality by reducing speckle. The enhanced Lee filter with a window size of 7×7 has been chosen in this study to minimize speckle effect on the images [41, 42], also to remove noise in the edge and high contrast area [40] without loss of information [43], because previous research showed reduction in speckles on SAR data using the Lee Filter before extracting the scattering value [24]. According to Lee et al., this algorithm is the best algorithm for segmentation crop filed purpose [40].

(2) Terrain Correction. The preprocessed image was also terrain correction to eliminate the distortion introduced by the topographical variations. The purpose of terrain correction for SAR imaging is to minimize the SAR geometry effects (foreshortening, layover, and shadow) towards radar images [24]. The Shuttle Radar Topography Mission (SRTM) was used as the Digital Elevation Model (DEM) to provide height information [44] using Range-Doppler Terrain Correction [24]. The geometric corrections were performed on all SAR (X-, C-, and L-band) data of the study area. All images were rectified, and the data were projected in geographic (Lat/-Long) projection, with the WGS84 datum.

(3) Radiometric Calibration. Calibration of the scattering values is necessary for the intercomparison of radar images acquired with different sensors or images obtained by the same sensor if acquired in different modes or processed with different processors [45]. Radiometric calibration resulting in sigma naught (σ°) [45].

The radiometric calibration process for X-band first calculated the radar brightness $\beta^{\circ}_{\mathrm{dB}}$ (beta zero, as contained in dB) derived from the polarization-specific calibration factor k_S (in equation (1)) and converted from digital numbers (DN) to sigma naught (σ°) using equation (2) [39, 46]:

$$\beta\circ_{\mathrm{dB}} = 10 \times \log_{10}\left(K_S \mathrm{DN}^2\right). \tag{1}$$

The final radiometric calibration was performed by calculating sigma naught (σ°) using

$$\sigma^{\circ} = \beta\circ_{\mathrm{dB}} + \log_{10}(\sin\theta_{\mathrm{loc}}). \tag{2}$$

where θ_{loc}, the local incident angle image, is defined for the four scenes' angle position, based on 2D interpolation across the performed image dimensions. The interpolation method applied is based on Delaunay's triangulation of data using the Qhull algorithm [47]. In conclusion, the local incident image has the same dimensions as the scene image and produces specific information about each pixel's local incident angle [39].

While the scattering value of the C-band is transforming the gamma-calibrated scattering coefficient [48], the C-band product uses a radiometric calibration look-up table (LUT) to do the calibration [49]. The essential conversion of amplitude to DN and from DN to sigma naught was done automatically on SNAP, and once the sigma naught values were obtained [41, 50], the computation of scattering ($\sigma^{\circ}_{\mathrm{dB}}$) can be performed in

$$\sigma\circ_{\mathrm{dB}} = 10 \cdot \log_{10}[\gamma_i], \tag{3}$$

where γ_i is the gamma-calibrated scattering coefficient of the C-band [48].

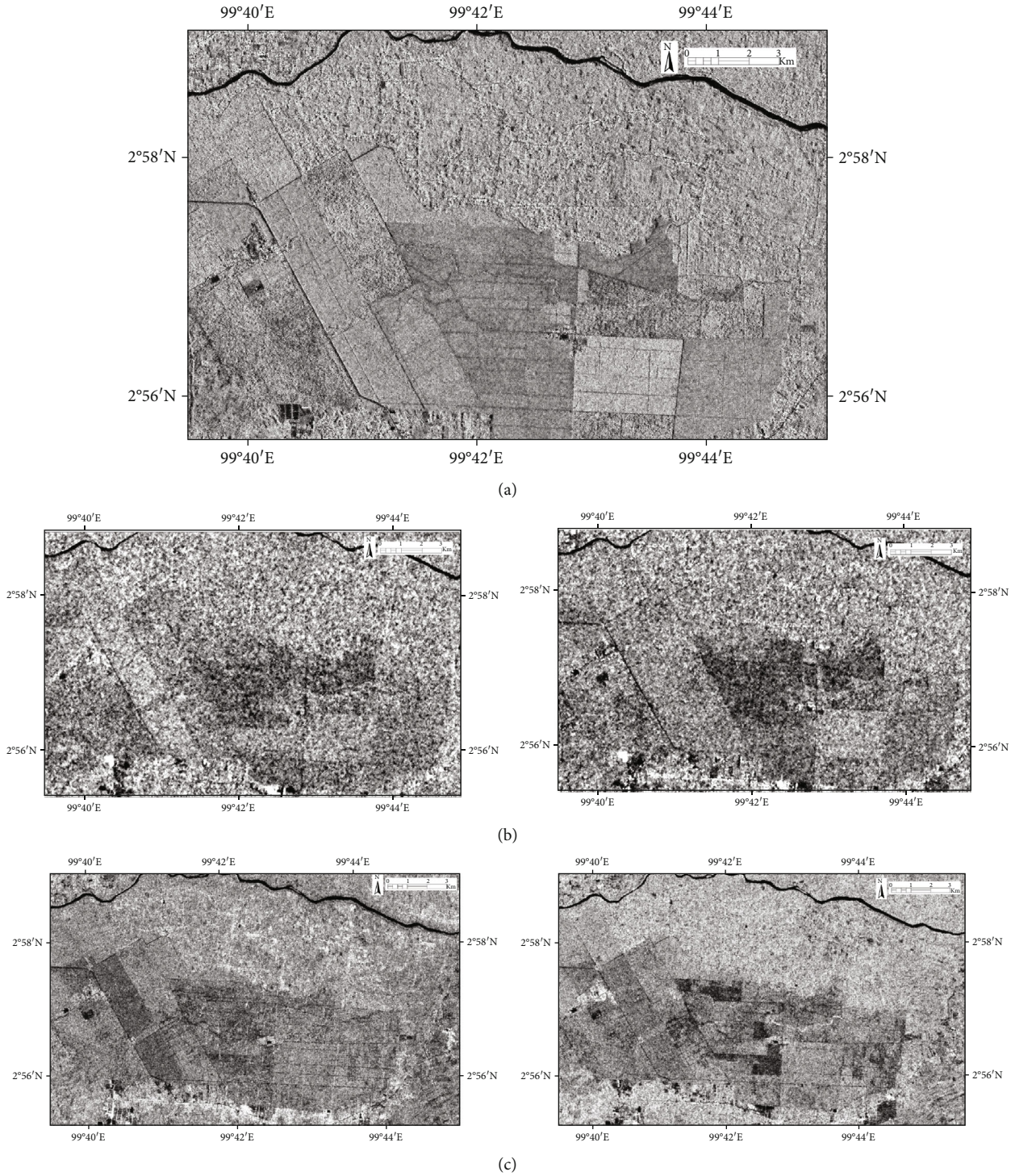

Figure 4: SAR imaging on TerraSAR-X on HH (a), Sentinel-1 on VV and VH (b), and ALOS PALSAR on HH and HV (c).

The L-band was built on a 16-bit data type, and all pixels have digital numbers (DN) ranging from 0 to 65,535 [41]. The DN has to be converted to scattering (i.e., the reflected radar signals) recognized as Normalized Radar Cross Section (NRCS) and expressed in σ° in decibels (dB) [41]. The conversion of HH (DN_{HH}) and HV (DN_{HV}) scattering intensities into NRCS (that is $\sigma^\circ{}_{HH}$ and $\sigma^\circ{}_{HV}$) [28, 51] was based on Shimada's study [51] shown in

$$\sigma^\circ{}_{HH}\,(\mathrm{dB}) = 10 \times \log_{10}\left(\mathrm{DN}_{HH}^2\right) - \mathrm{CF}, \tag{4}$$

$$\sigma^\circ{}_{HV}\,(\mathrm{dB}) = 10 \times \log_{10}\left(\mathrm{DN}_{HV}^2\right) - \mathrm{CF}, \tag{5}$$

where σ° is the scattering coefficient and CF is the calibration

Table 1: The characteristics of SAR data.

Sensor	TerraSAR-X	Sentinel-1A	ALOS PALSAR-2
Wavelength	X-band $\lambda = 3.1$ cm	C-band $\lambda = 5.6$ cm	L-band $\lambda = 23.5$ cm
Frequency	8-12 GHz	4-8 GHz	1-2 GHz
Polarization	Single HH	Dual VV/VH	Dual HH/HV
Resolution	Stripmap: 3×3 m	Interferometric Wide Swath (IW): 5×20 m	Stripmap: 3-10 m
Frame size	Stripmap: 50×30 km	IW: 250 km	Stripmap: 55×70 - 70×70 km
Temporal	11 days	12 days	14 days
Date of acquisition	29 August 2017	15 July 2018	17 January 2015
Incidence angle range	28.7°	39°	34.9°

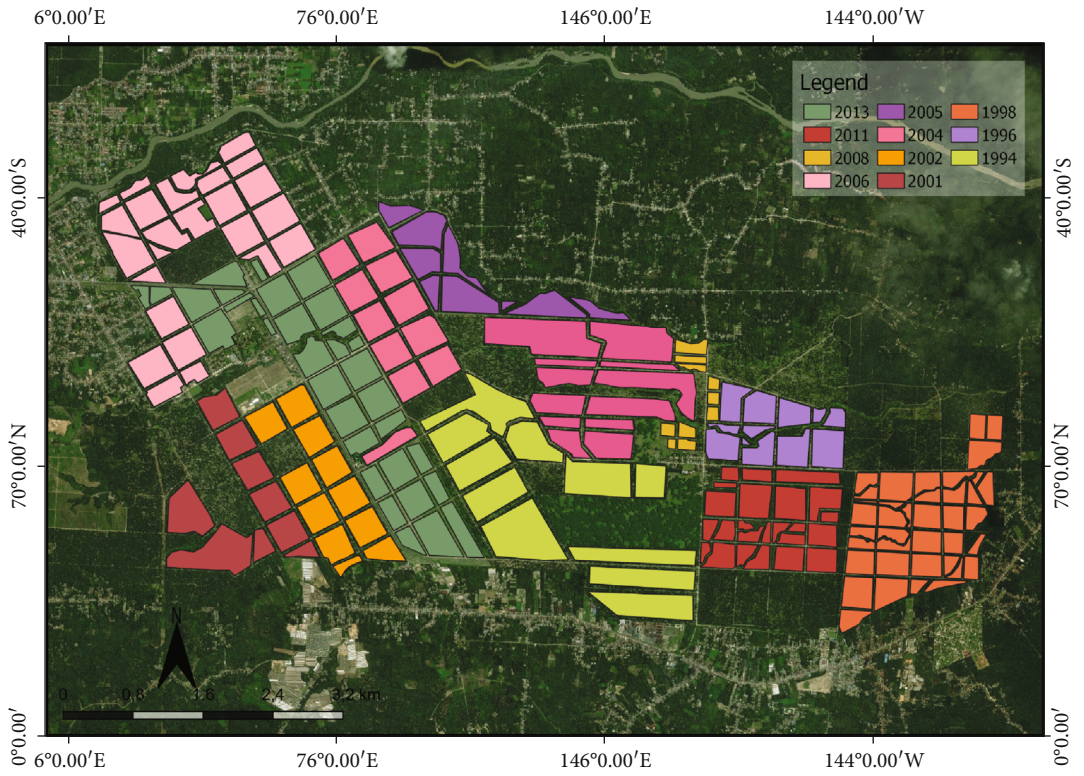

Figure 5: The planting age blocks of oil palm in the study area.

factor. The CF is dependent on the processing date. In this study, CF is equal to -83.0 both for HH and HV [28].

2.2.3. Extracting Scattering Characteristic. We created a region of interest (ROI) for area sampling; also the ROI was calculated to determine the scattering characteristics of X-, C-, and L-band polarimetric SAR imaging with the age of the oil palm in the forms of mean and standard deviation values using the algorithm as follows (equation (6) and (7)) [52]:

$$\bar{\mathbf{x}} = \frac{\sum_{j=1}^{n} x_j}{n}, \tag{6}$$

$$s^2 = \frac{\sum_{j=1}^{n} (x_i - \bar{\mathbf{x}})^2}{n-1}, \tag{7}$$

where n is the number of samples taken, x_i is the sample value, $\bar{\mathbf{x}}$ is the average of the samples, and s is the standard deviation.

2.2.4. The Development of Scattering Model. We analyzed the relationship between the scattering value of SAR imaging polarization (X-band on HH, C-band on VV and VH, and L-band on HH and HV) and the age of oil palm plantation. The scattering response from oil palm areas depends on the structure and density of the oil palms. All oil palm ranges, and even under those circumstances, the various structures, and densities have different scattering patterns and textures at various wavelengths [28]. Analyzing the relationship between scattering and age is using the Pearson correlation coefficient (equation (8)). Pearson's method assumed that if the coefficient is similar to one, it implies a strong correlation

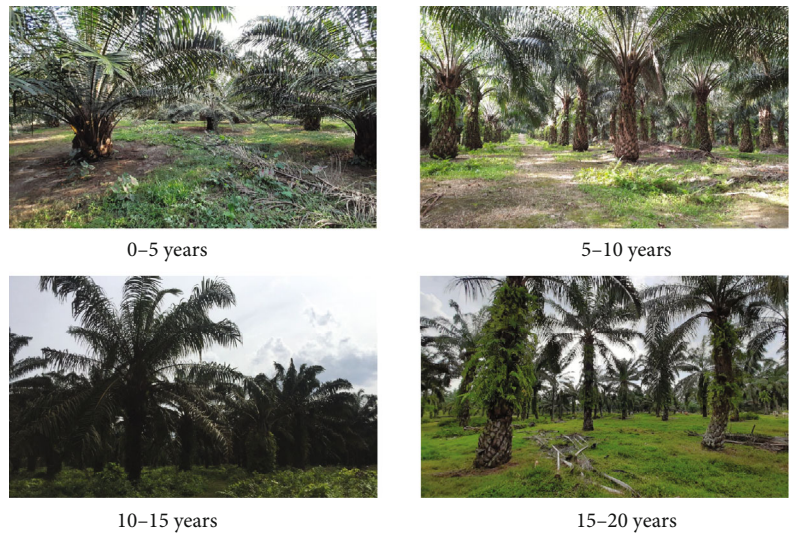

Figure 6: Oil palm age in study area.

between the two variables [53].

$$\sqrt{R^2} = r = \frac{\sum (X_i - \bar{X})(Y_i - \bar{Y})}{\left[\sum (X_i - \bar{X})^2 \sum (Y_i - \bar{Y})^2\right]^{1/2}}, \quad (8)$$

where $\bar{X}$ is the mean of the X variable and $\bar{Y}$ is the mean of the Y variable. In this study, the first variable is the oil palm age, and the second variable is scattering polarization value. The coefficient of determination (R^2) is an indication of the regression model [54]. The R^2 value will show the percentage of variation as a regression model variable [55]. Several methods have been proposed to interpret the correlation coefficient into descriptors like "weak," "moderate," or "strong" relationship [56].

3. Results

The X-, C-, and L-band polarimetric SAR imaging was filtered using the Lee filter for each polarization. The scattering model of oil palm phenology was based on an empirical model derived from the relationship between oil palm age and scattering value of X-, C-, and L-band SAR imaging. In this study, ranges of oil palm age were divided for five years: 0-5, 5-10, 10-15, 15-20, and 20-25.

3.1. The Scattering Model of Oil Palm Phenology Based on X-Band. The scattering model of oil palm phenology was based on X-band with HH polarization. The value starts at the age of 0-5 years around -6.8 dB, of 5-10 years around -5.7 dB, of 10-15 years around -5 dB, and of 20-25 years around -6.4 dB (Figure 7). On HH polarization, the scattering model has nonlinear regression on $y = -0.0114x2 + 0.2741x - 7.2823$ with $R^2 = 0.65$ (Figure 7).

3.2. The Scattering Model of Oil Palm Phenology Based on C-Band. The scattering model of oil palm plantation was based on C-band with VH and VV polarization. On VH polarization, the value starts in the age of 0-5 years around -14 dB, age of 5-10 years around -15 dB, age of 10-15 years around -14 dB, age of 15-20 years around -15 dB, and age of 20-25 years around -16 dB (Figure 8(a)). On VH polarization, the scattering model has nonlinear regression $y = -0.0055x^2 + 0.1248x - 15.785$ with $R^2 = 0.56$ (Figure 8(a)).

On VV polarization, the value starts at the age of 0-5 years around -7.8 dB, at the age of 5-10 years around -7.4 dB, at the age of 10-15 years around -6.5 dB, at the age of 15-20 years around -7.4 dB, and at the age of 20-25 years around -8.0 dB (Figure 8(b)). On VV polarization, the scattering model has nonlinear regression $y = -0.0117x^2 + 0.3006x - 8.9534$ with $R^2 = 0.89$ (Figure 8(b)).

3.3. The Scattering Model of Oil Palm Phenology Based on L-Band. The scattering model of oil palm plantation based on L-band with HH and HV polarization. On HH polarization, the value starts at the age of 0-5 years around -12.6 dB, at the age of 5-10 years around -11 dB, at the age of 10-15 years around -11.3 dB, at the age of 15-20 years around -11.5 dB, and at the age of 20-25 years around -11.9 dB (Figure 9(a)). The scattering model has logarithmic regression $y = 0.5293 \ln(x) - 12.616$ with $R^2 = 0.51$ (Figure 9(a)).

On HV polarization, the value starts at the age of 0-5 years around -22 dB, at the age of 5-10 years around -18 dB, at the age of 10-15 years around -19 dB, at the age of 15-20 years around -18.9 dB, and at the age of 20-25 years around -18.5 dB (Figure 9(b)). The scattering model has logarithmic regression $y = 1.1555 \ln(x) - 21.815$ with $R^2 = 0.50$ (Figure 9(b)).

4. Discussion

Two significant characteristic categories determine the SAR scattering values are the sensor and the target characteristics [57]. The sensor category includes the frequency/wavelength of the SAR, the polarization of the transmitted and received SAR signal, the incident angle of the ground-interacting radar beam, and the sensor looking position [57]. According to Henderson and Lewis [19], the target characteristic

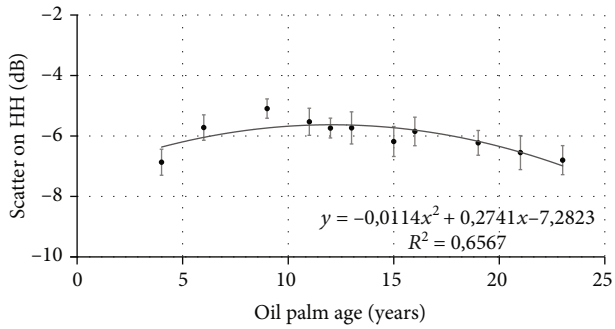

Figure 7: Scattering model of oil palm phenology on X-band with HH polarization.

influence varied with (1) vegetation type, (2) stand structure, and (3) canopy composition.

4.1. Characteristics Age of Oil Palm Based on SAR Imaging. The scattering characteristics of the forest vegetation are influenced by the thickness of the volume, density of the component particles (or scatters), size distribution of the component particles, shape distribution of the component particles, orientation distribution of the component particles, and dielectric properties of the component particles [58]. It is essential to know the polarization from which the SAR image obtained because signals at different polarizations interact differently with objects on the ground, which affects the brightness of the radar recorded in a particular polarization channel [59]. For simplicity, it is assumed that a natural scene can be described as a combination of three types of scatterers: (1) rough surface scatterers, (2) double-bounce scatterers, and (3) volume scatterers [60].

4.1.1. On the X-Band. The scattering characteristics of the oil palm at the X-band of the young oil palm have the lowest scattering value as seen in Figure 10 of the 4-year-old histogram which is caused by rough surface scatters. The mature oil palm has a higher scattering value as seen in Figure 10 on the 6 to 15-year-old histogram which is caused by double-bounce scattering. The old oil palm has a lower scattering value as seen in Figure 10 of the 16 to 23-year-old histogram which is caused by volume scatters.

According to Martinis and Rieke [61], adopting the X-band, canopy attenuation, volume, and surface scattering from the top layer of the forest canopy is generally higher [62] because the X-band is sensitive to canopy surface scattering [63]. Hence, the same canopy surface seems rough for X-band wavelength causing high scattering values [64]. According to Rosenqvist [65], the X-band instrument clear relationship between canopy growth area and threshold ambiguity for trees.

4.1.2. On the C-Band. The scattering characteristics of oil palm at the C-band on VV and VH polarization on the young oil palm have the lowest scattering value as seen in Figures 11 and 12 on the histogram for 2 to 4-year-old histogram which is caused by rough surface scattering. The mature oil palm has a higher scattering value as seen in Figures 11 and 12 of the 7 to 14-year-old histogram which is caused by double-bounce scattering. The old oil palm has a lower scattering value as seen in Figures 11 and 12 of the 17 to 21-year-old histogram which is caused by volume scatters.

According to Carolita et al. [15], increase and decrease in the scattering value occur because at the planting new age of trees height was relatively low and the size of the canopy is still small when the tree reached into productive age, the scattering value will rise because of the difference in the height of tree and soil. C-band data has a short wavelength, causing the scattering values for canopy density to become smaller. According to Teng et al. [6], there was also a significant contribution from the trunks to the surface volume scattering component, although this was not the dominant component. Also, at the shorter C-band wavelength, volume scattering can occur within the canopies of lower or sparse vegetation types, such as bushes, shrubs, or crops. According to Rignot et al. [66], radar signals were expected to be dominantly scattered by the foliage and the top branches and twigs of the canopy at the C-band.

4.1.3. On the L-Band. The scattering characteristics of oil palm at the L-band on HH and HV polarization on the young oil palm have the lowest scattering value as seen in Figures 13 and 14 on the 5-year-old histogram which is caused by in surface scattering. The mature oil palm has a higher scattering value as seen in Figures 13 and 14 of the 7 to 14-year-old histogram which is caused by double-bounce scattering. The old oil palm has a lower scattering value, as seen in Figures 13 and 14 of the 16 to 24-year-old histogram which is caused by volume scatters.

According to Toh et al. [67], the scattering increased with age for all polarization in general for the L-band frequency. The L-band scattering coefficient showed the trend increasing with the age of oil palm more than 20 years. Besides that, according to Teng et al. [6], the scattering value for HH polarization using the L-band was increasing attenuation of waves propagating through to the soil surface and back, as the leaves, fronds, and trunks are growing larger.

The scattering value for each polarization (HH and HV) among the age of oil palm was increasing; according to Darmawan et al. [28], it was hypothesized that the growth of oil palms was caused by higher trunks, more leaves, more branches, and larger canopy followed by the condition of scattering value. In any case, the scatter values derived from the L-band are depending on wavelengths, polarization, incident angle, and temporal data; environments such as land moisture and landscape [25, 28, 68]; and the structure of oil palms such as size, geometry, and orientation of leaves, trunks, branches, and aerials or stilt roots [28, 68, 69].

4.2. Coefficient Determination of Scattering Model of Oil Palm Phenology. The scatter model of oil palm phenology was performed separately for each radar wavelength (X-, C-, and L-band). In this study, the X-band showed the nonlinear oil palm phenology model in HH polarization with coefficient determination $R^2 = 0.65$, which means the model has moderate correlation. The C-band showed the nonlinear or quadratic model of oil palm phenology in VH polarization with coefficient determination $R^2 = 0.56$, which means the model

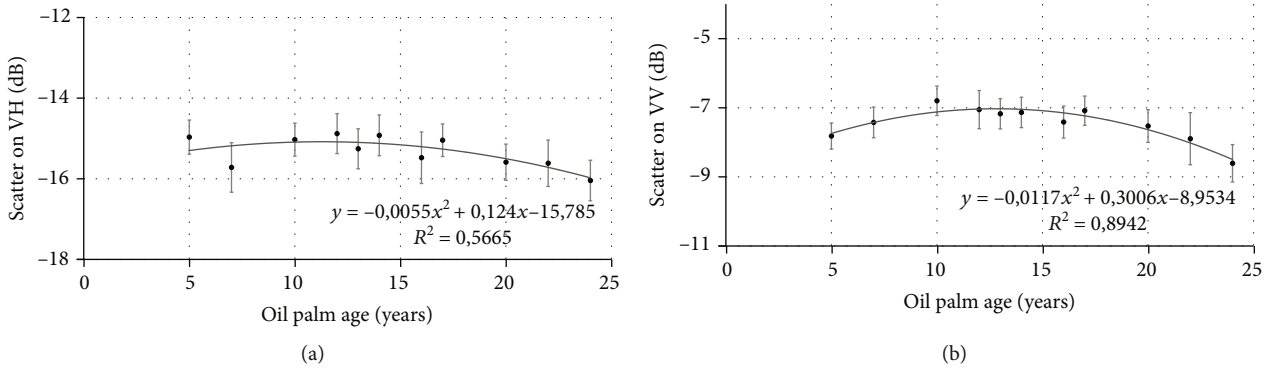

Figure 8: Scattering model of oil palm phenology on C-band with VH polarization (a) and VV polarization (b).

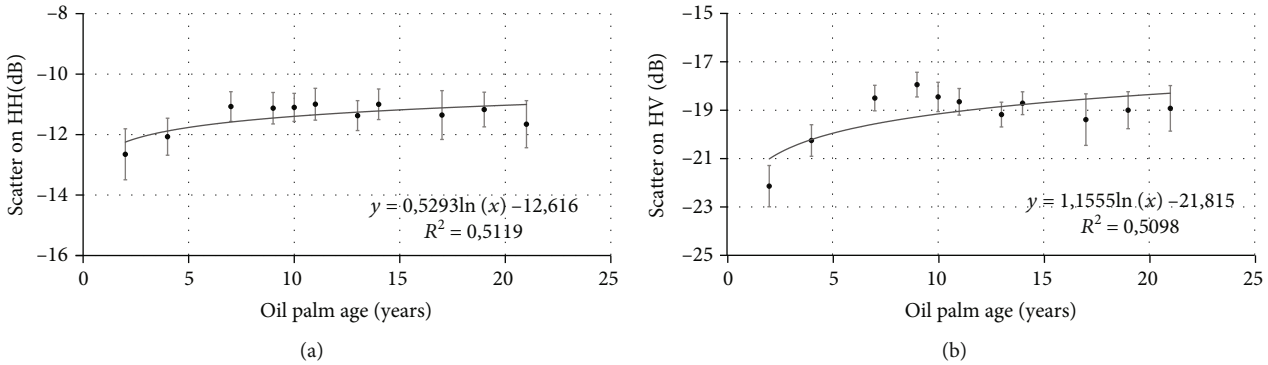

Figure 9: Scattering model of oil palm phenology on L-band with HH polarization (a) and HV polarization (b).

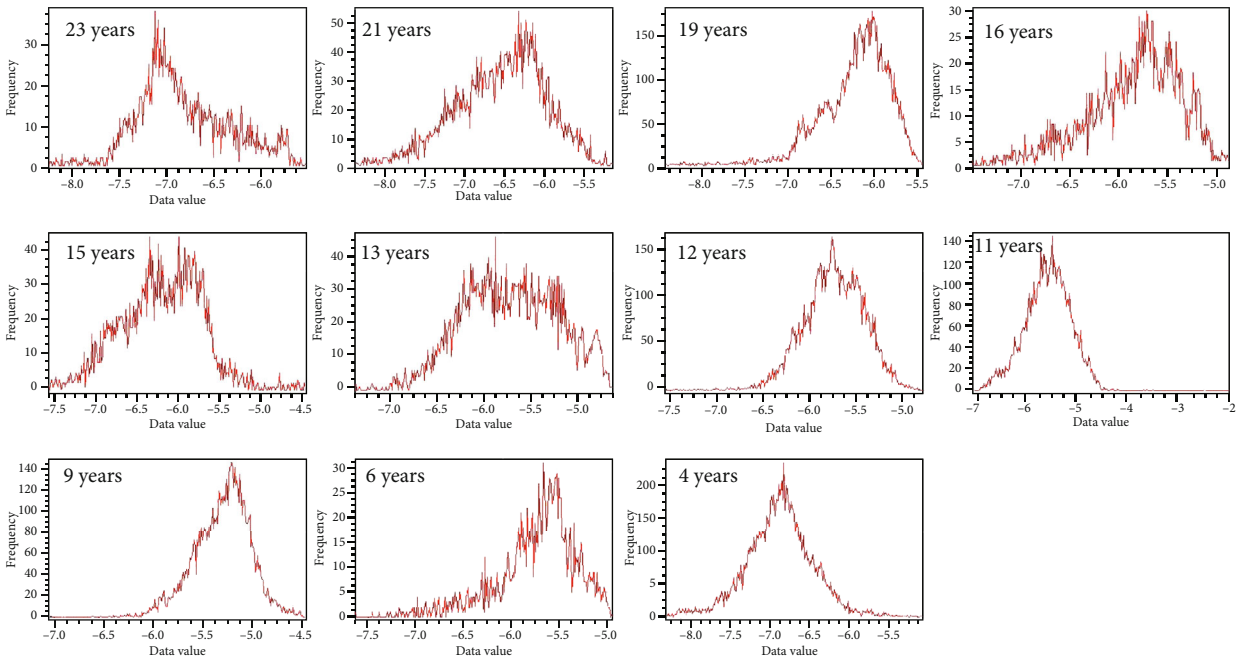

Figure 10: Histogram X-band for each age of oil palm.

has moderate correlation, and while on VV polarization with coefficient determination $R^2 = 0.89$, it means the model has strong correlation. The L-band showed the logarithmic model of oil palm phenology in HV polarization with coefficient determination $R^2 = 0.50$, which means the model has moderate correlation, and while on HH polarization with coefficient determination $R^2 = 0.51$, it means the model has moderate correlation. In this case, the more potential of scattering model of oil palm phenology based on R^2 is using C-band on VV polarization.

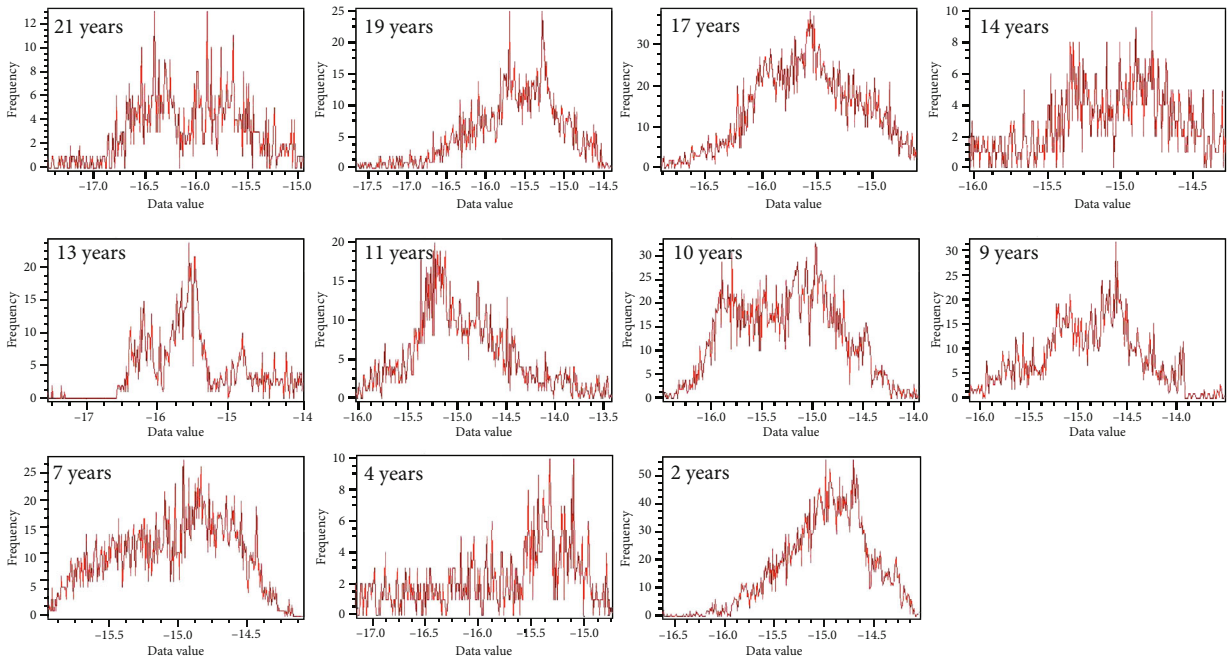

Figure 11: Histogram C-band on VH for each age of oil palm.

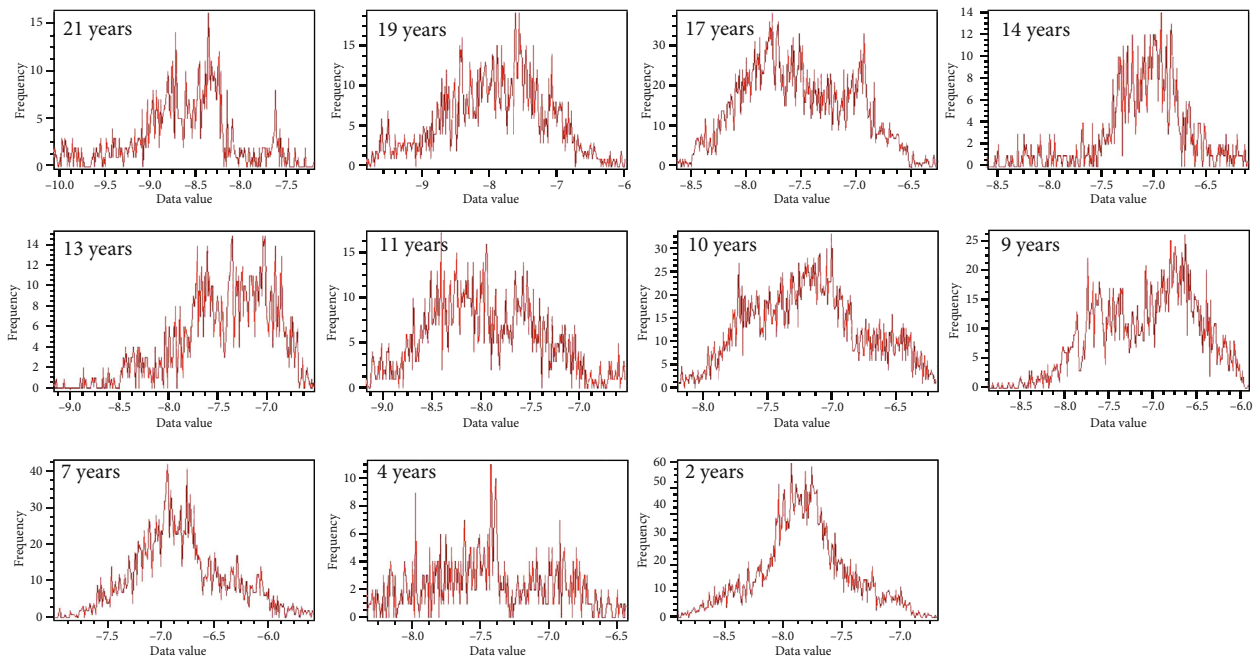

Figure 12: Histogram C-band on VV for each age of oil palm.

The scattering model with the moderate correlation also found by other researchers such as Tan et al. [10] has logarithmic regression for the correlating scattering value with oil palm age using ALOS PALSAR-2 with coefficient determination on HH polarization$R^2 = 0.49$, HV polarization with$R^2 = 0.27$, and ratio of HH/HV polarization with$R^2 = 0.26$, for study case in the southern part of peninsular Malaysia. Darmawan et al. [28] also used ALOS PALSAR-2 on HH and HV polarization having a logarithmic regression model with coefficient determination $R^2 = 0.62$ and 0.41 for study case area in Jerantut, Pahang, Malaysia. In other cases, Avtar et al. [70] for study area near Miri City, Sarawak, Malaysia, showed a logarithmic regression model for a variety of SAR data including TerraSAR-X (X-band) on HH polarization with coefficient determination $R^2 = 0.075$; Radarsat-2 (C-band) on HH, HV, and VV polarization with coefficient determination $R^2 = 0.39$, 0.49, and 0.39; and ALOS PALSAR-2 (L-band) on HH and HV polarization with coefficient determination $R^2 = 0.62$ and 0.77. Okarda et al. [32] studied the relationship between the age

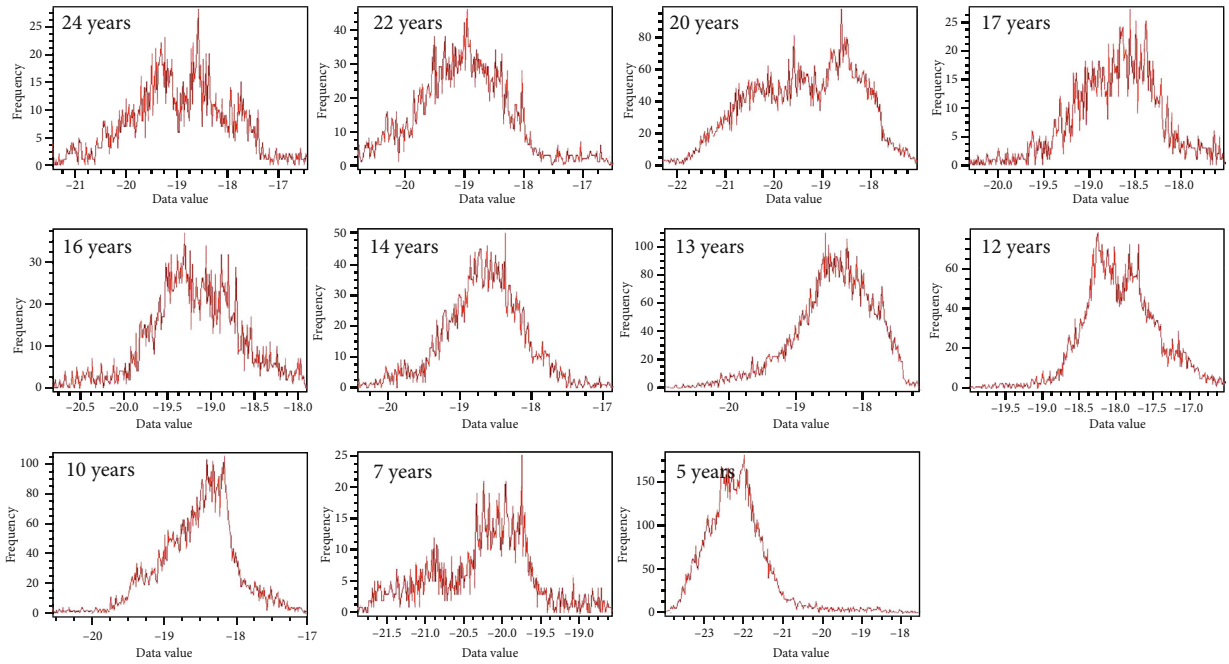

Figure 13: Histogram L-band on HV for each age of oil palm.

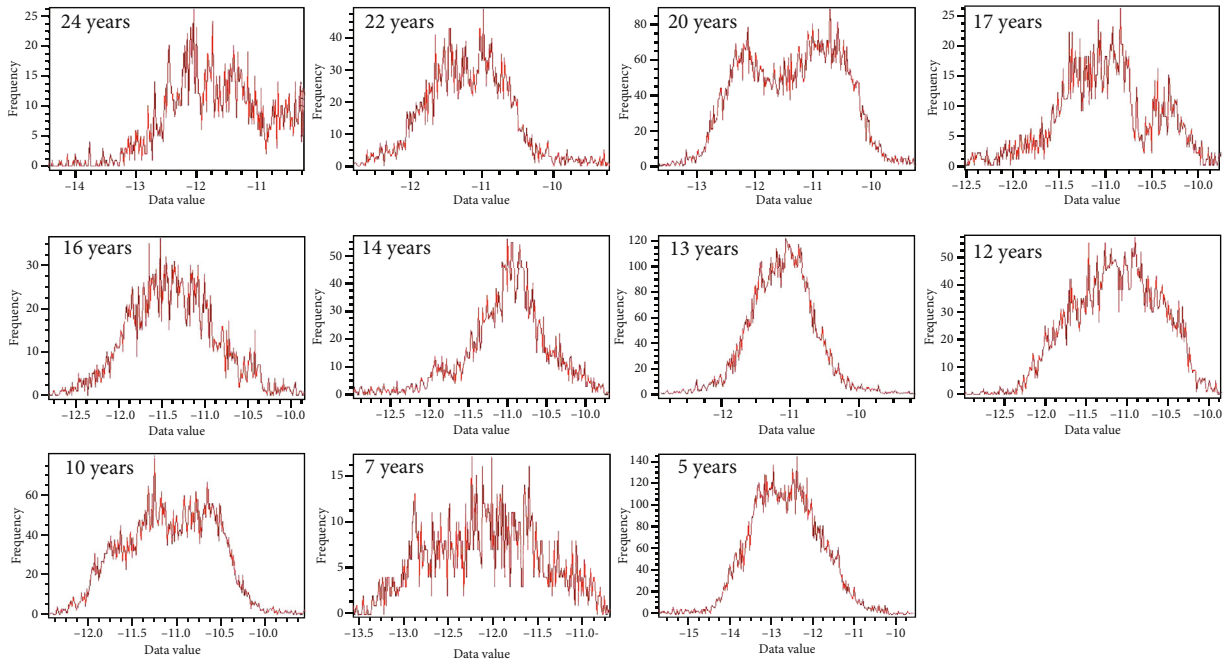

Figure 14: Histogram L-band on HH for each age of oil palm.

of oil palm in mineral soil and age and peatland in Central Kalimantan, Indonesia, using ALOS PALSAR-2 on HH and HV polarization. The scattering model has linear regression with coefficient determination on HH and HV between age and mineral soil with $R^2 = 0.55$ and 0.37 and age and peatland on HH and HV with $R^2 = 0.36$ and 0.28. For C-band data, it was studied by Carolita et al. [15] using Sentinel-1A on HH and HV polarization. The scattering model has nonlinear regression (quadratic model) with coefficient determination $R^2 = 0.68$ for HH and HV with $R^2 = 0.77$ for study case area in Asahan, North Sumatra Indonesia.

5. Conclusions

This study investigated the scattering model of oil palm phenology based on X-, C-, and L-band polarimetric SAR imaging in Asahan Regency, North Sumatra, Indonesia. We generated scattering values for different ranges of oil palm

age: 0-5, 5-10, 10-15, 15-20, and 20-25 years, with different scattering characteristics for each X-, C-, and L-band polarimetric SAR imaging depending on the wavelength and age ranges of oil palm. Finally, we found the scattering model of oil palm phenology based on the X-band on HH polarization which is $y = -0.0114x^2 + 0.2741x - 7.2823$ with $R^2 = 0.65$. The C-band on VH polarization is $y = -0.0055x^2 + 0.1248x - 15.785$ with $R^2 = 0.56$, while that on VV polarization is $y = -0.0117x^2 + 0.3006x - 8.9534$ with $R^2 = 0.89$. The L-band on HH polarization is $y = 0.5293 \ln(x) - 12.616$ with $R^2 = 0.51$, while that on HV polarization is $y = 1.1555 \ln(x) - 21.815$ with $R^2 = 0.50$. In this case, the more potential of the scattering model of oil palm phenology based on R^2 is using C-band on VV polarization. However, the scattering model can be used and applied to identify the phenology of oil palm in Indonesia, which is the main parameter in yield estimation, also required for the tax estimation, replanting time, and identification of oil palm diseases. The scattering model being developed needs to improve accuracy by integrating multisource-multispectral data, including different wavelengths on optical data and microwaves and more in situ data.

Data Availability

The data used to support the findings of this study are not yet available because other research work requiring data remains incomplete.

Conflicts of Interest

The authors declare no conflict of interest.

Acknowledgments

This research was funded by the Ministry of Research and Technology/National Research and Innovation (Kemenristek/BRIN) and Agency Indonesia Endowment Fund for Education (LPDP), with Contract No. 249/E1/PRN/2020. In addition, the researchers would like to thank Kemenristek/-BRIN, LPDP, LAPAN, PPKS, and LPPM Itenas Bandung.

References

[1] W. Li, H. Fu, L. Yu et al., "Stacked autoencoder-based deep learning for remote-sensing image classification: a case study of African land-cover mapping," *International Journal of Remote Sensing*, vol. 37, no. 23, pp. 5632–5646, 2016.

[2] R. Dong, W. Li, H. Fu et al., "Oil palm plantation mapping from high-resolution remote sensing images using deep learning," *International Journal of Remote Sensing*, vol. 41, no. 5, pp. 2022–2046, 2020.

[3] Y. Basiron, "Palm oil production through sustainable plantations," *European Journal of Lipid Science and Technology*, vol. 109, no. 4, pp. 289–295, 2007.

[4] R. Härdter, W. Y. Chow, and O. S. Hock, "Intensive plantation cropping, a source of sustainable food and energy production in the tropical rain forest areas in Southeast Asia," *Forest Ecology and Management*, vol. 91, no. 1, pp. 93–102, 1997.

[5] D. Sheil, A. Casson, E. Meijaard et al., *Oil Palm Basics; What Do we Know and What Do we Need to Know?*, Center for International Forestry Research, 2009.

[6] K. C. Teng, J. Y. Koay, S. H. Tey, K. S. Lim, H. T. Ewe, and H. T. Chuah, "A dense medium microwave backscattering model for the remote sensing of oil palm," *IEEE Transactions on Geoscience and Remote Sensing*, vol. 53, no. 6, pp. 3250–3259, 2015.

[7] H. Aholoukpè, B. Dubos, A. Flori et al., "Estimating aboveground biomass of oil palm: Allometric equations for estimating frond biomass," *Forest Ecology and Management*, vol. 292, pp. 122–129, 2013.

[8] E. Fitzherbert, M. Struebig, A. Morel et al., "How will oil palm expansion affect biodiversity?," *Trends in Ecology & Evolution*, vol. 23, no. 10, pp. 538–545, 2008.

[9] K. L. Chong, K. D. Kanniah, C. Pohl, and K. P. Tan, "A review of remote sensing applications for oil palm studies," *Geo-Spatial Information Science*, vol. 20, no. 2, pp. 184–200, 2017.

[10] K. P. Tan, K. D. Kanniah, and A. P. Cracknell, "Use of UK-DMC 2 and ALOS PALSAR for studying the age of oil palm trees in southern peninsular Malaysia," *International Journal of Remote Sensing*, vol. 34, no. 20, pp. 7424–7446, 2013.

[11] R. H. Corley and P. B. Tinker, *The Oil Palm*, John Wiley & Sons, 2008.

[12] R. H. V. Corley, *Oil Palm Physiology: A Review*, Incorporated Society of Planters, 1973.

[13] G. Squire, "The Oil Palm. 4th Edition. Edited by R. H. V. Corley and P. B. Tinker. Oxford: Blackwell Publishing (2003), pp. 284, £115.00. ISBN 0-632-05212-0," *Experimental Agriculture*, vol. 41, no. 1, pp. 121–121, 2005.

[14] H. Z. M. Shafri, N. Hamdan, and M. I. Saripan, "Semi-automatic detection and counting of oil palm trees from high spatial resolution airborne imagery," *International Journal of Remote Sensing*, vol. 32, no. 8, pp. 2095–2115, 2011.

[15] I. Carolita, S. Darmawan, R. Permana et al., "Comparison of optic Landsat-8 and SAR Sentinel-1 in oil palm monitoring, case study: Asahan, North Sumatera, Indonesia," *IOP Conference Series: Earth and Environmental Science*, vol. 280, 2019.

[16] A. Chemura, I. van Duren, and L. M. van Leeuwen, "Determination of the age of oil palm from crown projection area detected from WorldView-2 multispectral remote sensing data: the case of Ejisu-Juaben district, Ghana," *ISPRS Journal of Photogrammetry and Remote Sensing*, vol. 100, pp. 118–127, 2015.

[17] J. McMorrow, "Linear regression modelling for the estimation of oil palm age from Landsat TM," *International Journal of Remote Sensing*, vol. 22, no. 12, pp. 2243–2264, 2010.

[18] S. Darmawan, D. K. Sari, K. Wikantika, A. Tridawati, R. Hernawati, and M. K. Sedu, "Identification before-after forest fire and prediction of mangrove forest based on Markov-cellular automata in part of Sembilang national park, Banyuasin, South Sumatra, Indonesia," *Remote Sensing*, vol. 12, no. 22, pp. 3700–3725, 2020.

[19] F. M. Henderson and A. J. Lewis, "Radar detection of wetland ecosystems: a review," *International Journal of Remote Sensing*, vol. 29, no. 20, pp. 5809–5835, 2008.

[20] N. M. Yusoff, F. M. Muharam, W. Takeuchi, S. Darmawan, and M. H. Abd Razak, "Phenology and classification of abandoned agricultural land based on ALOS-1 and 2 PALSAR multi-temporal measurements," *International Journal of Digital Earth*, vol. 10, no. 2, pp. 155–174, 2017.

[21] S. Darmawan, D. K. Sari, W. Takeuchi, K. Wikantika, and R. Hernawati, "Development of aboveground mangrove forests' biomass dataset for Southeast Asia based on ALOS-PALSAR 25-m mosaic," *Journal of Applied Remote Sensing*, vol. 13, no. 4, 2019.

[22] S. Darmawan, I. Carolita, and E. Ananta, "Identification of oil palm plantation on multiscatter and resolution of SAR data using variety of classifications algorithm (case study: Asahan District, North Sumatera Province)," *In Proceedings of the IOP Conference Series: Earth and Environmental Science*, vol. 500, 2020.

[23] B. Brisco, "Mapping and monitoring surface water and wetlands with synthetic aperture radar," in *Remote Sensing of Wetlands*, pp. 119–136, Natural Resources Canada, 2015.

[24] N. E. Mohd Najib, K. D. Kanniah, A. P. Cracknell, and L. Yu, "Synergy of active and passive remote sensing data for effective mapping of oil palm plantation in Malaysia," *Forests*, vol. 11, no. 8, p. 858, 2020.

[25] S. Darmawan, W. Takeuchi, Y. Vetrita, K. Wikantika, and D. K. Sari, "Impact of topography and tidal height on ALOS palsar polarimetric measurements to estimate aboveground biomass of mangrove forest in Indonesia," *Journal of Sensors*, vol. 2015, 13 pages, 2015.

[26] Y. Qin, X. Xiao, J. Dong et al., "Mapping forests in monsoon Asia with ALOS PALSAR 50-m mosaic images and MODIS imagery in 2010," *Scientific Reports*, vol. 6, no. 1, pp. 1–10, 2016.

[27] L. Nordin, "Application of Airsar data to oil palm tree," in *Proceedings of the Proceedings of the Asian Conference on Remote Sensing*, pp. 5–9, Kathmandu, India, 2002.

[28] S. Darmawan, W. Takeuchi, A. Haryati, R. A. M. Najib, and M. Na'Aim, "An investigation of age and yield of fresh fruit bunches of oil palm based on ALOS PALSAR 2," *Proceedings of the IOP Conference Series: Earth and Environmental Science*, vol. 37, 2016.

[29] I. Carolita, D. Yudhatama, D. Dirgahayu et al., "Silvia Informasi Spasial Tematik Klasifkasi Tanaman Sawit Berdasarkan Umur," in *Pusat Pemanfaatan Penginderaan Jauh*, LAPAN, Jakarta, 2019.

[30] I. Carolita, J. Sitorus, J. Manalu, and D. Wiratmoko, "Growth profile analysis of oil palm by using spot 6 the case of North Sumatra," *International Journal of Remote Sensing and Earth Sciences (IJReSES)*, vol. 12, no. 1, p. 21, 2017.

[31] J. Sitoms, P. Bidang, and P. Daia, "Pengembangan model estimasiumur tanaman sawit dengan menggunakan data landsat-Tm," *Jauh dan Pengolahan Data Citra Digital*, vol. 1, pp. 14–19, 2004.

[32] B. Okarda, I. Carolita, T. Kartika, and H. Komarudin, "Mapping of smallholder oil palm plantation and development of a growth model," *Proceedings of the IOP Conference Series: Earth and Environmental Science*, vol. 169, 2018.

[33] A. C. Crossland, S. A. Sinambela, A. S. Sitorus, and A. W. Sitorus, "The coastal zone of Asahan regency: an area of international importance for migratory waders in North Sumatra province, Indonesia," *Stilt*, vol. 55, pp. 8–12, 2009.

[34] A. Ma, "Agro-pastoral and preservation of local wisdom Bondang for agricultural sustainability in Asahan, North Sumatra," *Agricultura*, vol. 105, pp. 110–113, 2018.

[35] *The Recent Development of the Indonesian Palm Oil Industry | Indonesian Palm Oil Association (GAPKI IPOA)*, October 2020, https://gapki.id/en/news/18397/the-recent-development-of-the-indonesian-palm-oil-industry.

[36] D. Rutz and R. Janssen, "Socio-economic impacts of bioenergy production," *Socio-Economic Impacts of Bioenergy Production*, pp. 1–297, 2014, 9783319038.

[37] M. Masril, Nazaruddin, and J. Hidayati, "Improving the utilization of palm oil mill through fulfillment of fresh fruit bunch," *IOP Conference Series: Materials Science and Engineering*, vol. 801, 2020.

[38] S. Budidarsono, A. Susanti, and A. Zoomers, "Oil palm plantations in Indonesia: the implications for migration, settlement/resettlement and local economic development," in *Biofuels - Economy, Environment and Sustainability*, pp. 173–193, 2013.

[39] S. Gebhardt, J. Huth, L. D. Nguyen, A. Roth, and C. Kuenzer, "A comparison of TerraSAR-X Quadpol backscattering with RapidEye multispectral vegetation indices over rice fields in the Mekong Delta, Vietnam," *International Journal of Remote Sensing*, vol. 33, no. 24, pp. 7644–7661, 2012.

[40] J. S. Lee, L. Jurkevich, P. Dewaele, P. Wambacq, and A. Oosterlinck, "Speckle filtering of synthetic aperture radar images: a review," *Remote Sensing Reviews*, vol. 8, no. 4, pp. 313–340, 1994.

[41] H. Omar, M. Misman, and A. Kassim, "Synergetic of PALSAR-2 and sentinel-1A SAR polarimetry for retrieving aboveground biomass in dipterocarp forest of Malaysia," *Applied Sciences*, vol. 7, no. 7, p. 675, 2017.

[42] J.-S. Lee, J.-H. Wen, T. L. Ainsworth, K.-S. Chen, and A. J. Chen, "Improved sigma filter for speckle filtering of SAR imagery," *IEEE Transactions on Geoscience and Remote Sensing*, vol. 47, no. 1, pp. 202–213, 2009.

[43] J. Amini and J. T. Sri Sumantyo, "SAR and optical images for forest biomass estimation," *Biomass - Detection, Production and Usage*, Darko Matovic, Ed., pp. 53–74, 2011.

[44] J. Hu, P. Ghamisi, and X. Zhu, "Feature extraction and selection of Sentinel-1 dual-pol data for global-scale local climate zone classification," *ISPRS International Journal of Geo-Information*, vol. 7, no. 9, p. 379, 2018.

[45] R. Düring, F. N. Koudogbo, M. Weber, and I. Gmbh, "TerraSAR-X and TanDEM-X : Revolution in spaceborne radar," in *Proceedings of the The International Archives of The Photogrammetry, Remote Sensing and Spatial Informastion Sciences*, pp. 227–234, Beijing, 2008.

[46] *Airbus Defence and Space, Radiometric Calibration of TerraSAR-X Data, Beta Naught and Sigma Naught Coefficient Calculation*, Innfoterra GMBH, Friedrichshafen, Germany, 2008.

[47] C. B. Barber, D. P. Dobkin, and H. Huhdanpaa, "The Quickhull algorithm for convex hulls," *ACM Transactions on Mathematical Software*, vol. 22, no. 4, pp. 469–483, 1996.

[48] Y. W. Kee, A. R. M. Shariff, A. M. Sood, and L. Nordin, "Application of SAR data for oil palm tree discrimination," *IOP Conference Series: Earth and Environmental Science*, vol. 169, 2018.

[49] A. Schubert, N. Miranda, D. Geudtner, and D. Small, "Sentinel-1A/B combined product geolocation accuracy," *Remote Sensing*, vol. 9, no. 6, pp. 607–616, 2017.

[50] F. Filipponi, "Sentinel-1 GRD preprocessing workflow," *Proceedings*, vol. 18, no. 1, p. 11, 2019.

[51] M. Shimada, "Model-based polarimetric SAR calibration method using forest and surface-scattering targets," *IEEE Transactions on Geoscience and Remote Sensing*, vol. 49, no. 5, pp. 1712–1733, 2011.

[52] T. F. Chan, G. H. Golub, and R. J. Leveque, "Statistical computing: algorithms for computing the sample variance: analysis

and recommendations," *American Statistician*, vol. 37, pp. 242–247, 1983.

[53] A. S. Hess and J. R. Hess, "Linear regression and correlation," *Transfusion*, vol. 57, no. 1, pp. 9–11, 2016.

[54] J. P. Holcomb, N. R. Draper, H. Smith, J. O. Rawlings, S. G. Pantula, and D. A. Dickey, "Applied regression analysisapplied regression analysis," *A Research Tool*, vol. 53, 1999.

[55] A. C. Cohen, "On estimating the mean and standard deviation of truncated normal distributions," *Journal of the American Statistical Association*, vol. 44, no. 248, pp. 518–525, 1949.

[56] P. Schober, C. Boer, and L. A. Schwarte, "Correlation coefficients: appropriate use and interpretation," *Anesthesia & Analgesia*, vol. 126, no. 5, pp. 1763–1768, 2018.

[57] A. I. Flores-Anderson, K. E. Herndon, R. B. Thapa et al., *THE SAR HANDBOOK: Comprehensive Methodologies for Forest Monitoring and Biomass Estimation*, SERVIR Global, Sparkman Drive, Huntsville, 2019.

[58] J. van der Sanden, *Radar Remote Sensing to Support Tropical Forest Management*, Tropenbos-Guyana Programme and the Wageningen Agricultural University, 1997.

[59] R. Bamler, "Principles of synthetic aperture radar," *Surveys in Geophysics*, vol. 21, pp. 147–157, 2000.

[60] J. J. Van Zyl and Y. Kim, *Synthetic Aperture Radar Polarimetry*, J. H. Yuen, Ed., A John Wiley and Sons, Inc., Publication, California, 2011.

[61] S. Martinis and C. Rieke, "Backscatter analysis using multitemporal and multi-frequency SAR data in the context of flood mapping at river Saale, Germany," *Remote Sensing*, vol. 7, no. 6, pp. 7732–7752, 2015.

[62] J. A. Richards, P. W. Woodgate, and A. K. Skidmore, "An explanation of enhanced radar backscattering from flooded forests," *International Journal of Remote Sensing*, vol. 8, no. 7, pp. 1093–1100, 2007.

[63] E.-M. Bernhard, A. Twele, and M. Gähler, "Brandflächendetektion auf Basis von X-band Radarsatellitendaten im Europäischen Mittelmeerraum," *Photogrammetrie - Fernerkundung - Geoinformation*, vol. 2011, no. 4, pp. 261–270, 2011.

[64] T. M. Lillesand and R. W. Kiefer, *Remote Sensing and Image Interpretation.*, Wiley, 1979.

[65] A. Rosenqvist, *Analysis of the Backscatter Characteristics of Rubber , Oil palm and Irrigated rice in Multi-band Polarimetric Synthetic Aperture Radar Imagery*, Institute of Industrial Science, University of Tokyo, Tokyo, Japan, 1997.

[66] E. J. M. Rignot, C. L. Williams, J. Way, and L. A. Viereck, "Mapping of forest types in Alaskan boreal forests using SAR imagery," *IEEE Transactions on Geoscience and Remote Sensing*, vol. 32, no. 5, pp. 1051–1059, 1994.

[67] C. M. Toh, H. T. Ewe, S. H. Tey, and Y. H. Tay, "A study on oil palm remote sensing at L-band with dense medium microwave backscattering model," *IEEE Transactions on Geoscience and Remote Sensing*, vol. 57, no. 10, pp. 8037–8047, 2019.

[68] R. Lucas, J. Armston, R. Fairfax et al., "An evaluation of the ALOS PALSAR L-band backscatter—above ground biomass relationship Queensland, Australia: impacts of surface moisture condition and vegetation structure," *IEEE Journal of Selected Topics in Applied Earth Observations and Remote Sensing*, vol. 3, no. 4, pp. 576–593, 2010.

[69] A. C. Morel, S. S. Saatchi, Y. Malhi et al., "Estimating aboveground biomass in forest and oil palm plantation in Sabah, Malaysian Borneo using ALOS PALSAR data," *Forest Ecology and Management*, vol. 262, no. 9, pp. 1786–1798, 2011.

[70] R. Avtar, R. Ishii, H. Kobayashi, H. Fadaei, R. Suzuki, and S. Herath, "Efficiency of multi-frequency, multi-polarized SAR data to monitor growth stages of oilpalm plants in Sarawak, Malaysia," in *2013 IEEE International Geoscience and Remote Sensing Symposium - IGARSS*, pp. 2137–2140, Melbourne, VIC, Australia, 2013.

Hindawi
Journal of Sensors
Volume 2021, Article ID 6662769, 12 pages
https://doi.org/10.1155/2021/6662769

Research Article

A Novel Sensor for In Situ Detection of Freeze-Thaw Characteristics in Plants from Stem Temperature and Water Content Measurements

Chao Gao[1,2], **Hao Tian**[1,2] **and Yandong Zhao**[3,4]

[1]*School of Artificial Intelligence, Beijing Technology and Business University, Beijing 100048, China*
[2]*Beijing Key Laboratory of Big Data Technology for Food Safety, Beijing Technology and Business University, Beijing 100048, China*
[3]*School of Technology, Beijing Forestry University, Beijing 100083, China*
[4]*Beijing Laboratory of Urban and Rural Ecological Environment, Beijing Municipal Education Commission, Beijing 100083, China*

Correspondence should be addressed to Hao Tian; thc_1015@foxmail.com

Received 22 October 2020; Revised 21 January 2021; Accepted 28 January 2021; Published 15 February 2021

Academic Editor: Jingwei Wang

Freezing is a typical abiotic stress on plants, which can induce physiological damages of plants. A better understanding of plant freeze-thaw characteristics contributes to solving some hot issues in plant physiology, such as cold resistance and cold acclimation. This article presents a novel sensor for in situ detection of freeze-thaw characteristics in plants based on stem temperature and water content. The measuring circuit of stem temperature was designed based on constant current source and platinum resistance. The measuring circuit of stem water content was designed based on standing wave ratio and the dielectric properties of stem tissue. The temperature resolution of the compound sensor is less than 0.1°C. The MAE and RMSE of temperature measurement are approximately 0.57°C and 0.65°C, respectively. The volumetric water content resolution of the compound sensor is less than 0.05%. The MAE and RMSE of volumetric water content measurement are approximately 1.59% and 1.81%, respectively. Moreover, a mathematical model for describing the freeze-thaw characteristics of plant stem was established and solved based on the compound sensor. Then, some freeze-thaw indicators including stem water content, ice content, freezing depth, freezing velocity, thawing depth, and thawing velocity were solved and used to interpret the freeze-thaw rules of plant stem. It can be concluded that the freeze-thaw velocity is closely related to the physicochemical properties of plant stem which also change dynamically in the freeze-thaw cycle.

1. Introduction

Freezing is a typical abiotic stress on plants. From the microperspective, freezing stress can induce various damages for plants, such as cellular dehydration, structural changes in tissues or organs, and embolisms in xylem vessels [1, 2]. From the macroperspective, freezing stress can inflict the reduction of crop yields and limit the distribution of plant species [3, 4]. Therefore, it is significant to accurately detect freeze-thaw characteristics which can quantify freezing stress on plants.

Some early detection methods of freeze-thaw characteristics in plants were indirect and assumed that plant tissue fluid had freeze-thaw properties of ideal solutions [5]. Ideal freeze-thaw curves can be calculated by measuring cell solute concentrations, hydrostatic pressures, and the amounts of bound water [6]. With the development of electronic detection technology, some of direct detection methods have been used to study freeze-thaw characteristics in plants, mainly including calorimetric method, spectrometric method, and electron microscopy. Calorimetric method basically involves the detection of exothermic and endothermic events by monitoring relative temperature changes in plant tissue fluid. Based on different thermal analysis techniques, common calorimetric methods include conventional thermal analysis, differential thermal analysis (DTA) [7], and differential scanning calorimetry (DSC) [8]. Conventional thermal analysis is primarily used to determine the freezing and thawing points of plant tissue fluid by inserting a thermocouple in a stem and

monitoring stem temperature during freeze-thaw cycles. Compared with conventional thermal analysis, DTA has a higher resolution of temperature by comparing the output from two thermocouples inserted in a sample and reference [3, 4]. Combined with the heat of fusion of water and the heat capacities of water and ice, DSC can quantify the amount of frozen or thawed water by measuring differences in heat evolution or absorption between the sample and reference during freeze-thaw cycles. But it is difficult to choose the correct heat of fusion and heat capacity for plant tissue fluid, thus limiting the further application of DSC. Based on different spectral bands, common spectrometric methods include infrared video thermography (IRVT) [9], nuclear magnetic resonance (NMR) [10], and magnetic resonance imaging (MRI) [11]. Compared with the above calorimetric methods, IRVT can provide a real-time heat map of the temperature of the plant surface, thus revealing the distribution and evolution of ice. NMR provides a method to quantify the liquid water content of partially frozen plant tissues. In contrast, MRI is a major improvement to NMR and has sufficient resolution to observe liquid water in the dimension of plant tissues or organs. Based on different treatment processes, common electron microscopy methods include cryoscanning electron microscopy (CSEM) [12] and freeze-substitution electron microscopy (FSEM) [13]. CSEM shows ice by the appearance of fracture faces during the sublimation process of ice. FSEM shows ice by the appearance of cavities during the dissolution process of ice. Both methods have sufficient resolution to identify ice in the dimension of cells or molecules.

These methods differ greatly in temporal resolution: calorimetric method > spectrometric method > electron microscopy. And the calorimetric methods can realize in situ measurement of the freezing and thawing points of plant tissue fluid. However, the disadvantage of calorimetric methods is that it is difficult to quantify the amount of freezing or thawing that takes place. In the meanwhile, considering that the measuring method of standing wave ratio has been used to quantify stem water content with high performance [14], hence, a novel method combining calorimetric method and standing wave ratio was proposed to detect the freeze-thaw characteristics of plant stem in this study. The main research contents in this paper are as follows: (1) developing a compound sensor for detecting stem temperature and water content, (2) analyzing the measurement performance of the compound sensor, (3) establishing a mathematical model for describing the freeze-thaw characteristics of plant stem, and (4) interpreting the freeze-thaw characteristics of plant stem based on the freeze-thaw model.

2. Materials and Methods

2.1. Measuring Principle of Stem Temperature. The measuring circuit of stem temperature was designed based on constant current source and platinum resistance [15]. As illustrated in Figure 1, initially, the reference voltage V_{ref} is converted to the constant current source with the value of $V_{\text{ref}}/R_{\text{ref}}$ via the operational amplifier U1 and the reference resistance R_{ref}. As the current I flows through the platinum resistance R_{Pt100}, a tiny voltage difference is generated on R_{Pt100}. Ultimately, the tiny voltage difference is amplified into the standard voltage output signal V_{out1} by the operational amplifier U2. Hence, the output of stem temperature measuring circuit can be calculated by

$$V_{\text{out1}} = \beta_2 I R_{\text{Pt100}} = \frac{\beta_2 V_{\text{ref}} R_{\text{Pt100}}}{R_{\text{ref}}} \tag{1}$$

where β_2 is the amplification coefficient of the operational amplifier U2.

There is a linear relationship between R_{Pt100} and the temperature T, which can be expressed as

$$T = kR_{\text{Pt100}} + b \tag{2}$$

where k is the proportionality coefficient and b is the bias coefficient. In accordance with Formula (1), Formula (2) can be rewritten as

$$T = \frac{kR_{\text{ref}}}{\beta_2 V_{\text{ref}}} V_{\text{out1}} + b \tag{3}$$

As the parameters including R_{ref}, V_{ref}, β_2, k and b are determined, it can be concluded from Formula (3) that the stem temperature can be calculated by measuring the output voltage of U2.

2.2. Measuring Principle of Stem Volumetric Water Content. The measuring circuit of stem water content was designed based on standing wave ratio [16] and the dielectric properties of stem tissue [17]. As illustrated in Figure 2, initially, a high-frequency electromagnetic wave generated by the 100 MHz oscillator spreads along the transmission line. But there is an impedance mismatch between the impedance of the transmission line Z_0 and the impedance of the annular electrodes Z_l, causing partial incident wave to be reflected back towards the source. Then, the incident wave and the reflected waveform a stable standing wave on the transmission line. Both terminal voltages of the transmission line V_a and V_b are measured by two wave detectors separately. Ultimately, the voltage difference between V_a and V_b is amplified into the standard voltage output signal V_{out2} by the operational amplifier U. Hence, the output of stem water content measuring circuit can be calculated by

$$V_{\text{out2}} = \beta(V_a - V_b) = 2\beta A\rho = 2\beta A \frac{(Z_l - Z_0)}{(Z_l + Z_0)} \tag{4}$$

where β is the amplification coefficient of the operational amplifier U, A is the amplitude of the oscillator, and ρ is called the reflection coefficient.

As the parameters including β, A, and Z_0 are determined, it can be concluded from Formula (4) that the impedance of the annular electrodes Z_l can be calculated by measuring the output voltage of U. Since stem water content mainly depends on Z_l, it can be derived from V_{out2} based on a

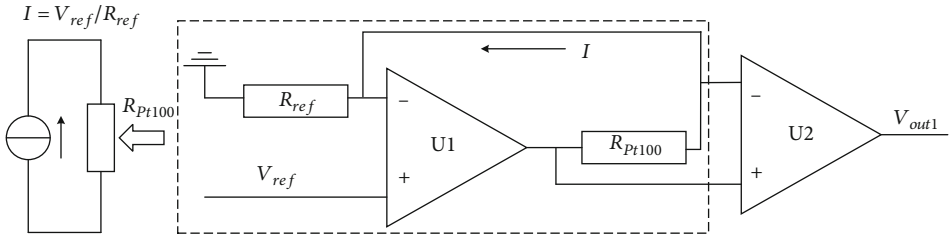

Figure 1: Schematic diagram of stem temperature measuring circuit.

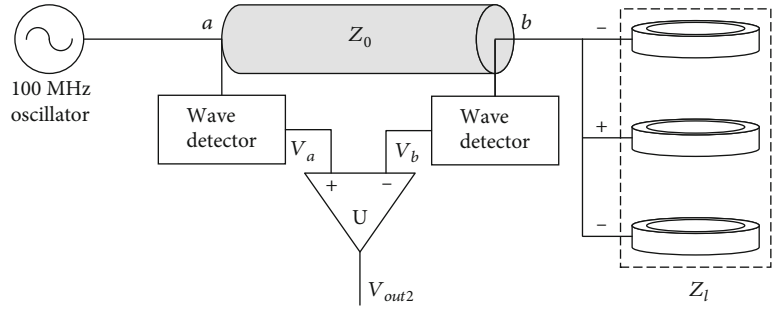

Figure 2: Schematic diagram of stem water content measuring circuit.

definite function which can be obtained by drying calibration method.

2.3. Measuring Electrodes of the Compound Sensor. In the structure diagram of measuring electrodes shown in Figure 3(a), stem temperature electrodes are composed of two stainless-steel probes with embedded Pt100 platinum resistance. The diameter of the probe is set to 1 mm to reduce the damages to stem tissue, and the length of the probe can be customized according to stem diameter. Stem water content electrodes consist of three elastic stainless-steel rings, the diameter of which can be customized according to stem diameter and adapt to the changes of stem growth. The thickness and width of the ring are 0.2 mm and 8 mm, respectively. The lower and upper electrodes are negative, and the middle electrode is positive. The spacing of adjacent electrodes is 10 mm. In the material object of measuring electrodes shown in Figure 3(b), the stainless-steel probe is inserted into the elastic stainless-steel ring through a connector. The installation process of the compound sensor is divided into three steps. First, the connection position between the compound sensor and the stem is polished into a standard ring. Second, a mounting hole with a diameter of 1 mm is drilled in the stem. Third, the probe is knocked into the sapwood by a rubber hammer, and the elastic ring is snugly wrapped around the stem.

2.4. Hardware System of the Compound Sensor. The hardware system of the compound sensor mainly consists of detection units and collection units. As shown in Figure 4(a), detection units include temperature detection unit and water content detection unit, and the other functional units can be collectively called collection units. The high-performance microcontroller STM32 was chosen as the hardware platform. The 12-bit analog-to-digital converter with a reference voltage of 3.3 V can achieve the sampling of two detection units at the resolution of 0.8 mV. The technique of time-sharing power supply was adopted to avoid the electromagnetic interference between two detection units. The compound sensor can communicate with upper-computer software through the RS485 interface. Moreover, the measured data can be stored on a local SD card and transmitted to a remote server through the GPRS module. As shown in Figures 4(a) and 4(c), the printed circuit boards of detection and collection units were designed separately according to the hardware system of the compound sensor.

2.5. Freeze-Thaw Model of Plant Stem. In order to quantify the freeze-thaw characteristics of plant stem through the compound sensor, the freeze-thaw model of plant stem was established according to the physical structure of plant stem. Then, some freeze-thaw indicators were defined and derived based on the freeze-thaw model. The volumetric ice content θ_{ice} of the stem can be calculated by

$$\begin{aligned}\theta_{\text{ice}} &= \frac{m_{\text{ice}}}{\rho_{\text{ice}} V_{\text{stem}}} \\ &= \frac{\rho_{\text{liquid}} \left(\theta_{\text{threshold}} - \theta_{\text{liquid}}\right) V_{\text{stem}}}{\rho_{\text{ice}} V_{\text{stem}}} \\ &= \frac{\rho_{\text{liquid}} \left(\theta_{\text{threshold}} - \theta_{\text{liquid}}\right)}{\rho_{\text{ice}}},\end{aligned} \tag{5}$$

where m_{ice} is the ice mass in stem, ρ_{ice} is the ice density ($0.9\,\text{g cm}^{-3}$), ρ_{liquid} is the water density ($1\,\text{g cm}^{-3}$), $\theta_{\text{threshold}}$ is the initial volumetric water content of stem at the critical freezing temperature at which stem tissue fluid begins to

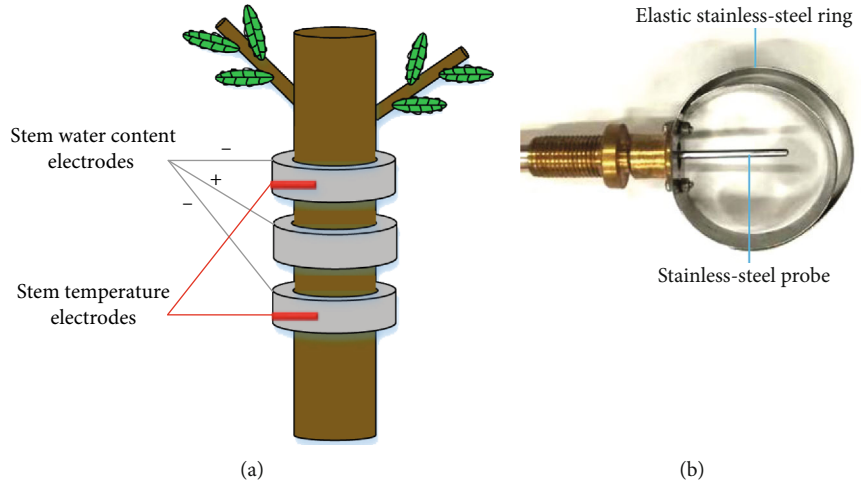

FIGURE 3: (a) Structure diagram of measuring electrodes. (b) Material object of measuring electrodes.

freeze, θ_{liquid} is the volumetric water content of stem during the freezing process, and V_{stem} is the volume of the stem.

Considering that the stem usually consists of multiple growth rings with different radius and wood in the same growth ring has the same physicochemical properties, it can be assumed that the stem segment is a cylinder and the water in stem freezes or thaws evenly from the outer growth ring to the inner growth ring. According to the freezing model of stem segment shown in Figure 5(a), the volume of stem segment V_{stem} and the ice volume V_{ice} in stem segment can be expressed by

$$V_{stem} = \pi R_{stem}^2 L_{stem}, \tag{6}$$

$$V_{ice} = \frac{m_{ice}}{\rho_{ice}} = \frac{\rho_{liquid}\pi\left(R_{stem}^2 - R_{UFA}^2\right)L_{stem}\theta_{threshold}}{\rho_{ice}}, \tag{7}$$

where R_{stem} is the radius of stem segment, L_{stem} is the length of stem segment, and R_{UFA} is the radius of the unfrozen area. According to Formula (6) and (7), θ_{ice} can be rewritten as

$$\theta_{ice} = \frac{V_{ice}}{V_{stem}} = \frac{\rho_{liquid}\left(R_{stem}^2 - R_{UFA}^2\right)\theta_{threshold}}{\rho_{ice}R_{stem}^2}. \tag{8}$$

The radius of the unfrozen area R_{UFA} can be derived based on Formula (5) and (8), and

$$R_{UFA} = R_{stem}\sqrt{1 - \frac{\rho_{ice}\theta_{ice}}{\rho_{liquid}\theta_{threshold}}}. \tag{9}$$

The freezing depth of stem segment D_{freeze} was defined as the difference between R_{stem} and R_{UFA}. The freezing velocity of stem segment v_{freeze} was defined as the variation of D_{freeze} per unit time. The two indicators of freezing information can be calculated by

$$D_{freeze} = R_{stem} - R_{UFA} = R_{stem}\left(1 - \sqrt{1 - \frac{\rho_{ice}\theta_{ice}}{\rho_{liquid}\theta_{threshold}}}\right),$$
$$v_{freeze} = \frac{\Delta D_{freeze}}{\Delta t}, \tag{10}$$

where ΔD_{freeze} is the variation of D_{freeze} at the interval of Δt.

The thawing model of stem segment was established and analyzed in the same way as the freezing model. According to the thawing model of stem segment shown in Figure 5(b), the ice volume V_{ice} in stem segment can be expressed by

$$V_{ice} = \frac{m_{ice}}{\rho_{ice}} = \frac{\rho_{liquid}\pi\left[\left(R_{stem} - D_{thaw}\right)^2 - R_{UFA}^2\right]L_{stem}\theta_{threshold}}{\rho_{ice}}, \tag{11}$$

where D_{thaw} is the thawing depth of stem segment. According to Formula (6) and (11), θ_{ice} can be rewritten as

$$\theta_{ice} = \frac{V_{ice}}{V_{stem}} = \frac{\rho_{liquid}\left[\left(R_{stem} - D_{thaw}\right)^2 - R_{UFA}^2\right]\theta_{threshold}}{\rho_{ice}R_{stem}^2}. \tag{12}$$

The quadratic equation with one variable about D_{thaw} can be derived based on Formula (5) and (12), and

$$D_{thaw}^2 - 2R_{stem}D_{thaw} + \left(1 - \frac{\rho_{ice}\theta_{ice}}{\rho_{liquid}\theta_{threshold}}\right)R_{stem}^2 - R_{UFA}^2 = 0. \tag{13}$$

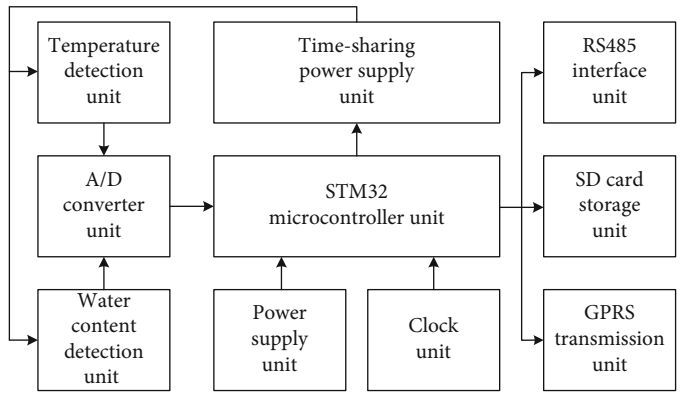

(a)

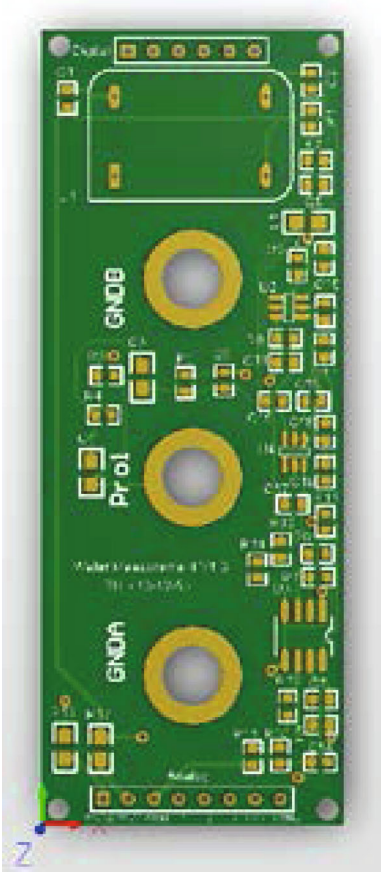

(b)

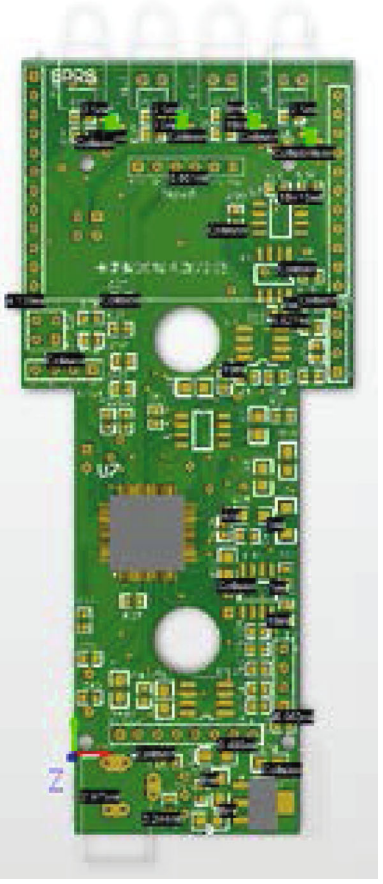

(c)

Figure 4: (a) Structure diagram of hardware system. (b) Printed circuit board of detection units. (c) Printed circuit board of collection units.

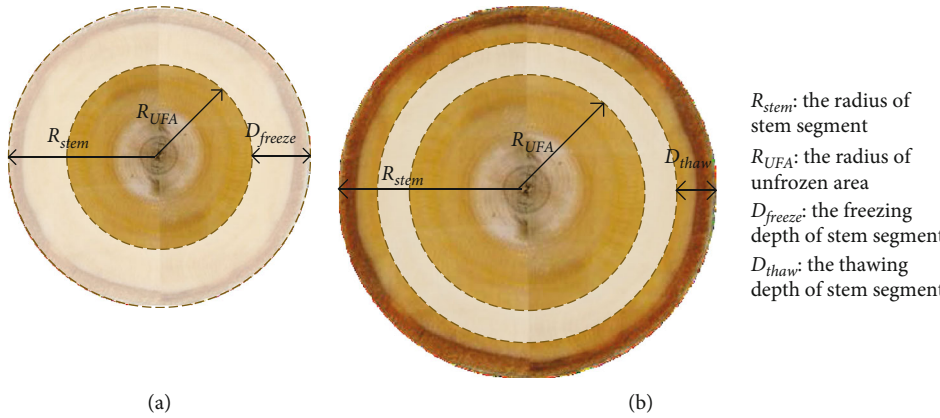

Figure 5: (a) Freezing model of stem segment. (b) Thawing model of stem segment.

The thawing depth of stem segment can be calculated by solving Equation (13), and

$$D_{\text{thaw}} = R_{\text{stem}}\left(1 - \sqrt{\frac{\rho_{\text{ice}}\theta_{\text{ice}}}{\rho_{\text{liquid}}\theta_{\text{threshold}}} + \left(\frac{R_{\text{UFA}}}{R_{\text{stem}}}\right)^2}\right). \quad (14)$$

The thawing velocity of stem segment v_{thaw} was defined as the variation of D_{thaw} per unit time. The indicator of thawing information can be calculated by

$$v_{\text{thaw}} = \frac{\Delta D_{\text{thaw}}}{\Delta t}, \quad (15)$$

where ΔD_{thaw} is the variation of D_{thaw} at the interval of Δt.

2.6. Calibration Experiments of the Compound Sensor. In order to obtain the functional relationships between output voltages of the compound sensor and two measured variables, the calibration experiments of stem temperature and water content were carried out separately. In the calibration experiment of stem temperature, the compound sensor was placed in the high-low temperature alternating test chamber (GDJ-1500B, HASUC, China, range: -40~150°C, accuracy: ±0.1°C) and the temperature of which increased evenly from -30 to 80°C. Each temperature level lasted for half an hour. In the meanwhile, the temperature of the test chamber and the corresponding output voltage of the compound sensor were recorded. In the calibration experiment of stem water content, the fresh stem segment of *Pachira glabra* with 6 cm in diameter and 106 cm^3 in volume was selected as the test sample. The diameter of the ring was adjusted to 6 cm, and the length of the probe was customized to 15 mm which is close to the sapwood depth of test sample. Then, the stem segment connected with the compound sensor was placed in the blast drying oven (DHG-9030A, HASUC, China, range: 35~250°C, accuracy: ±0.5°C) whose temperature was set at 45°C. During the drying process, the mass of the stem segment and the corresponding output voltage of the compound sensor were recorded at the interval of 6 hours until the stem segment was thoroughly dried. Then, the records of stem mass were converted to the records of stem volumetric water content according to stem volume.

2.7. Freezing Experiments of the Solutions. In order to verify the technical feasibility of the compound sensor to detect the freezing point, the freezing experiments of the solutions with different freezing temperature were conducted separately. Considering that most of the freezable water in a plant crystallizes between 0 and -4°C [18, 19], the sodium chloride solutions with theoretical freezing temperature of 0 (mass concentration 0%) and -4°C (mass concentration 6.4%) were selected as the test samples. Then, the plastic beaker filled with the solution was placed in the low-temperature refrigerator (DW-40W100, Haier, China, range: -20~-40°C, accuracy: ±1°C) and connected with the compound sensor. During the freezing process, the temperature of the refrigerator was set at -25°C, and the output voltages of the compound sensor were recorded at the interval of 1 minute until the solution was thoroughly frozen.

2.8. Freeze-Thaw Experiments of the Plant Stem. In order to observe the freeze-thaw characteristics of the plant stem, the *Pachira glabra* with 6 cm in diameter (R_{stem}=3 cm) and 40 cm in height (L_{stem}=40 cm) was selected as the test sample. The diameter of the ring was adjusted to 6 cm, and the length of the probe was customized to 15 mm which is close to the sapwood depth of test sample. Then, the tree connected with the compound sensor was placed in the low-temperature refrigerator. In the freezing stage, the temperature of the refrigerator was set at -25°C, and this stage lasted for 550 minutes. In the thawing stage, the temperature of the refrigerator was consistent with room temperature (appr. 25°C), and this stage lasted for 880 minutes. During the whole process, the output voltages of the compound sensor were recorded at the interval of 1 minute and converted to stem temperature and water content based on the acquired calibration functions which were described in Section 3.1. Finally, some freeze-thaw indicators including stem water content, ice content, freezing depth, freezing velocity, thawing depth, and thawing velocity were calculated based on the freeze-thaw model.

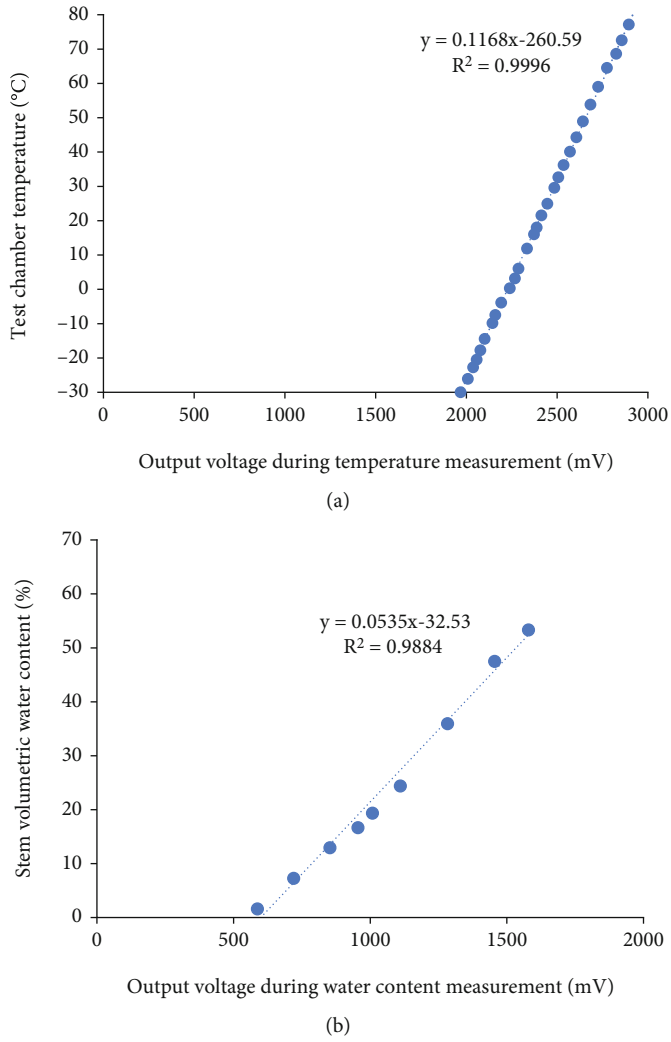

Figure 6: (a) Calibration equation of stem temperature. (b) Calibration equation of stem water content.

3. Results and Discussion

3.1. Calibration of Stem Temperature and Water Content. The calibration equations between output voltage and two measured variables are shown in Figure 6. As can be seen from Figure 6(a), the plot of test chamber temperature versus output voltage is a straight line with the slope of 0.1168°C mV^{-1} and the determination coefficient of 0.9996. Combining the resolution of A/D convertor mentioned above, the temperature resolution of the compound sensor can be calculated and it is less than 0.1°C, indicating that the compound sensor is able to measure stem temperature with high sensitivity. In addition, two error indicators of temperature measurement were calculated based on the calibration equation. The mean absolute error (MAE) is approximately 0.57°C, and the root mean square error (RMSE) is about 0.65°C, revealing that the compound sensor has high measuring accuracy and stability in terms of stem temperature detection. As can be seen from Figure 6(b), there is a linear relation between stem volumetric water content and output voltage with the slope of 0.0535% mV^{-1} and the determination coefficient of 0.9884. Then, we calculated the volumetric water content resolution and two error indicators in the same way. The volumetric water content resolution of the compound sensor is less than 0.05%, indicating that the compound sensor is able to measure stem volumetric water content with high sensitivity. The MAE and RMSE of volumetric water content measurement are approximately 1.59% and 1.81%, respectively, revealing that the compound sensor has high measuring accuracy and stability in terms of stem water content detection. The calibration equations were used to observe solution freezing point and stem freeze-thaw characteristics in the next two sections.

3.2. Detection of Solution Freezing Point. The frozen temperature curves of sodium chloride solutions with theoretical freezing temperature of 0 and -4°C are shown in Figure 7 in which the solution temperature is the calibrated value and the water content is directly the voltage value of sensor output. Before the solution temperature drops to the supercooling point (-1.9°C in Figure 7(a) and -6.1°C in Figure 7(b)), the output voltage during water content measurement remains virtually unchanged. When the solution temperature breaks through the supercooling point and jumps to the freezing

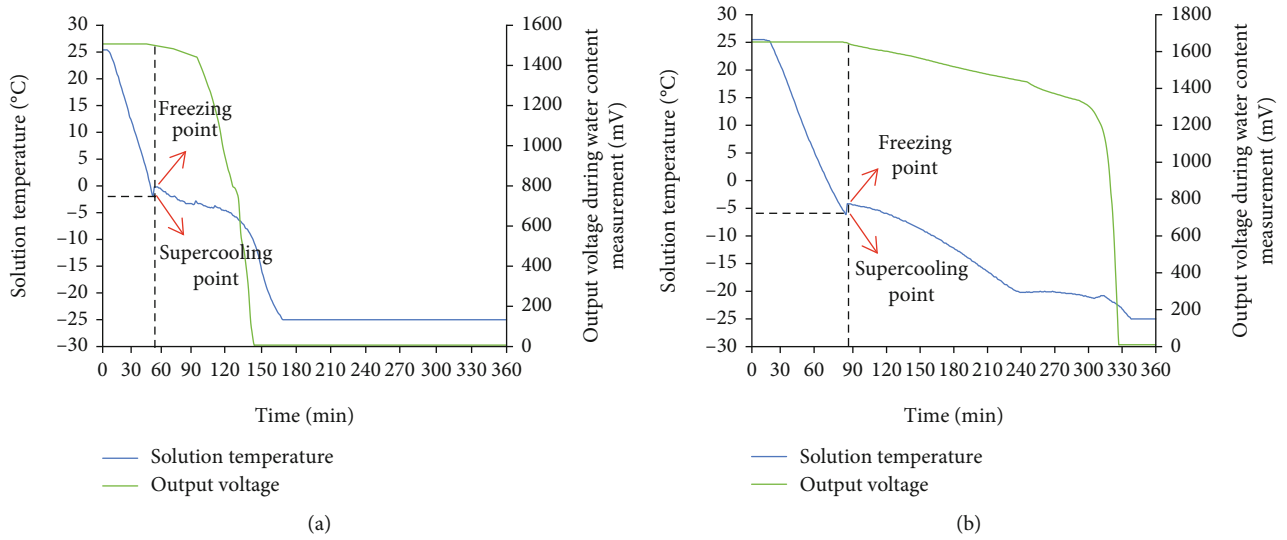

FIGURE 7: (a) Frozen temperature curve of sodium chloride solution with the freezing temperature of 0°C. (b) Frozen temperature curve of sodium chloride solution with the freezing temperature of -4°C.

point (-0.2°C in Figure 7(a) and -4.2°C in Figure 7(b)) under the effect of freezing latent heat [20], the output voltage during water content measurement begins to decline slowly due to the formation of ice crystals, indicating that the compound sensor is able to accurately detect solution freezing point based on latent heat effect. We assumed that the gradient of water content can be regarded as the freezing velocity of the solution. It can be concluded that during the freezing process of the solution, there exists a significant negative correlation between solution temperature and freezing velocity. It should be pointed out that the deficit of stem water content is related to various biotic and abiotic factors, such as insects, viruses, fungi, drought, salt, irradiation, and freezing stress [21, 22]. But the phenomenon of temperature jump from supercooling point to freezing point is a typical symbol of freezing stress, which can be used to determine the initial volumetric water content of stem at the beginning of the freezing process, namely $\theta_{\text{threshold}}$ in Formula (5).

3.3. Observation of Stem Freeze-Thaw Characteristics. The changes in stem volumetric water content, stem temperature, and temperature gradient during the freezing process are shown in Figure 8. As can be seen from Figure 8(a), the stem volumetric water content begins to decline at the point A (appr. 0.4°C) which is the freezing point of stem tissue fluid. But comparing Figures 7 and 8, we do not observe the phenomenon of temperature jump from supercooling point to freezing point in stem. It is mainly caused by the fact that the thermal conductivity of wood is significantly smaller than that of water [23, 24]. As can be seen from Figure 8(b), the stem temperature is relatively stable and the temperature gradient is less than 0.05°C mm^{-1} during the period from point A to B. It is mainly caused by the relative balance between ambient temperature and the release of latent heat during freezing process. Therefore, we can also determine the freezing point of stem by observing the temperature gradient. Considering that the place where the freezing started to take place may be outside the sensitive distance of the temperature probe, the mean temperature during the period from point A to B (appr. -0.5°C) can be regarded as the freezing temperature of stem tissue fluid. In the meanwhile, we can find that the stem temperature begins to drop rapidly during the period from point B (appr. -1.9°C) to the end. It is mainly caused by two factors. One is that the release of latent heat reduced with the decrease of freezing radius. The other is that the sensitivity of the temperature probe declined with the increase of freezing depth when the freezing depth exceeded half of the probe length (7.5 mm).

The changes in stem volumetric water content, stem temperature, and temperature gradient during the thawing process are shown in Figure 9. As can be seen from Figure 9(a), the stem volumetric water content begins to rise at the point C (appr. -5.8°C) which is the thawing point of stem tissue fluid. As can be seen from Figure 9(b), the stem temperature is relatively stable and the temperature gradient is less than 0.05°C mm^{-1} during the period from point C to D. It is mainly caused by the relative balance between ambient temperature and the absorption of latent heat during thawing process. Therefore, we can also determine the thawing point of the stem by observing the temperature gradient. Considering that the place where the thawing started to take place may be outside the sensitive distance of the temperature probe, the mean temperature during the period from point C to D (appr. -2.3°C) can be regarded as the thawing temperature of stem tissue fluid. In the meanwhile, we can find that the stem temperature begins to rise rapidly during the period from point D (appr. -0.5°C) to the end. It is mainly caused by two factors. One is that the absorption of latent heat reduced with the decrease of thawing radius. The other is that the sensitivity of the temperature probe declined with the increase of thawing depth when the thawing depth exceeded half of the probe length (7.5 mm). Comparing Figures 8 and 9, we can observe that the thawing temperature of stem tissue fluid is significantly lower than the freezing temperature of

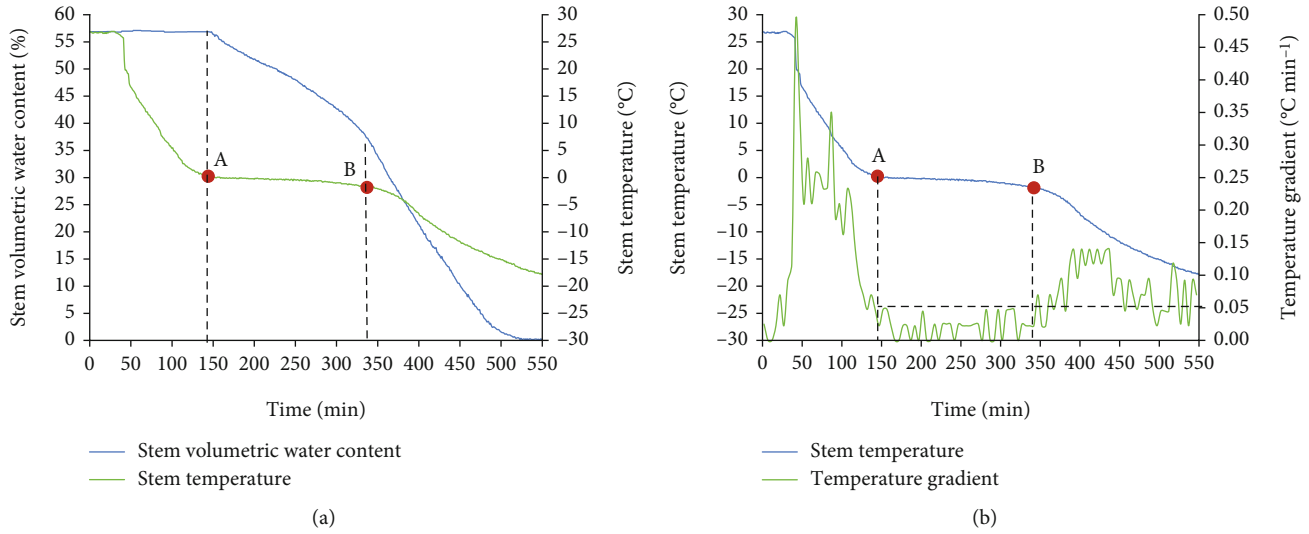

Figure 8: (a) Changes of stem volumetric water content and stem temperature during the freezing process. (b) Changes of stem temperature and temperature gradient during the freezing process.

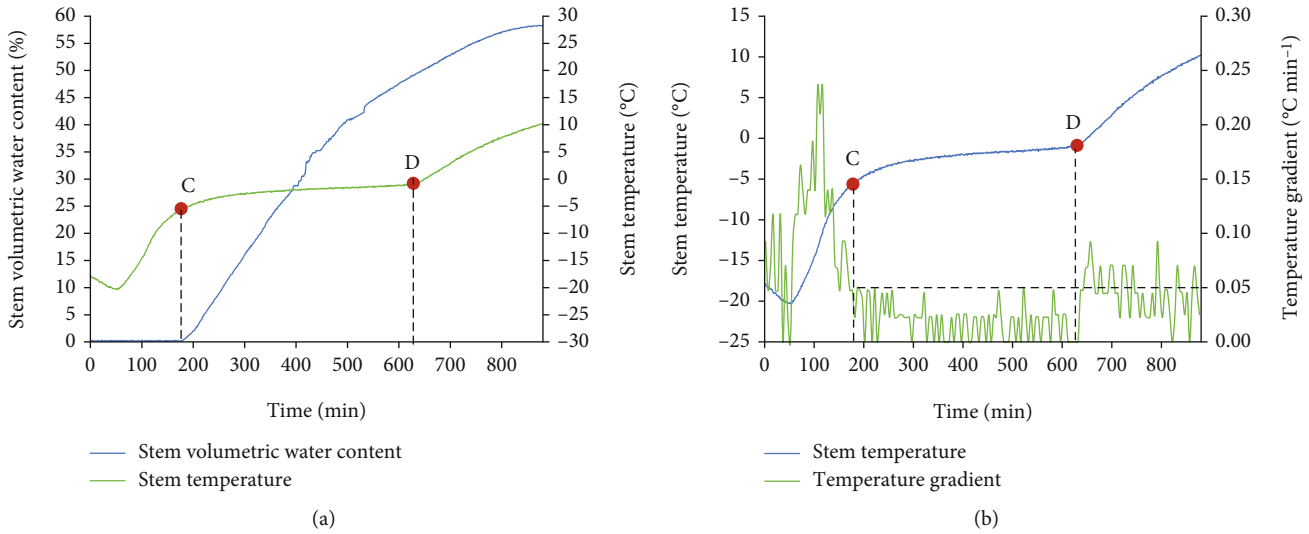

Figure 9: (a) Changes of stem volumetric water content and stem temperature during the thawing process. (b) Changes of stem temperature and temperature gradient during the thawing process.

stem tissue fluid. The reason is that some cytoplasmic components such as soluble sugars and electrolytes leaked out of cells during the freezing process, thus resulting in the decline of stem thawing temperature [25, 26].

The changes in stem volumetric water content and ice content during the freeze-thaw process are shown in Figure 10. As can be seen from Figure 10(a), the stem volumetric water content is 56.86% when the water began to freeze, namely $\theta_{threshold} = 56.86\%$, and the stem volumetric ice content is 63.01% when the water was completely frozen. The numerical difference between two indicators is due to the difference in density between water and ice. As can be seen from Figure 10(b), the stem volumetric water content is 58.27% which is slightly higher than $\theta_{threshold}$ when the ice was completely melted. It is mainly caused by the phenomenon that the moisture in the air condensed on the surface of stem water content electrodes, thus resulting in the increase of measured value. Comparing Figures 10(a) and 10(b), we can find that the duration of the freezing process (appr. 390 minutes) is shorter than that of the thawing process (appr. 624 minutes). It is mainly due to the fact that the thermal conductivity of ice is four times greater than that of water at the same temperature [27].

The changes in stem freeze-thaw depth and velocity during the freeze-thaw process are shown in Figure 11. As can be seen from Figure 11(a), there is a significant difference between the stem freezing velocity in sapwood and heartwood. When the freezing depth is less than 6 mm, the mean freezing velocity is about 0.03 mm mim^{-1}. When the freezing depth is more than 6 mm, the mean freezing velocity is about

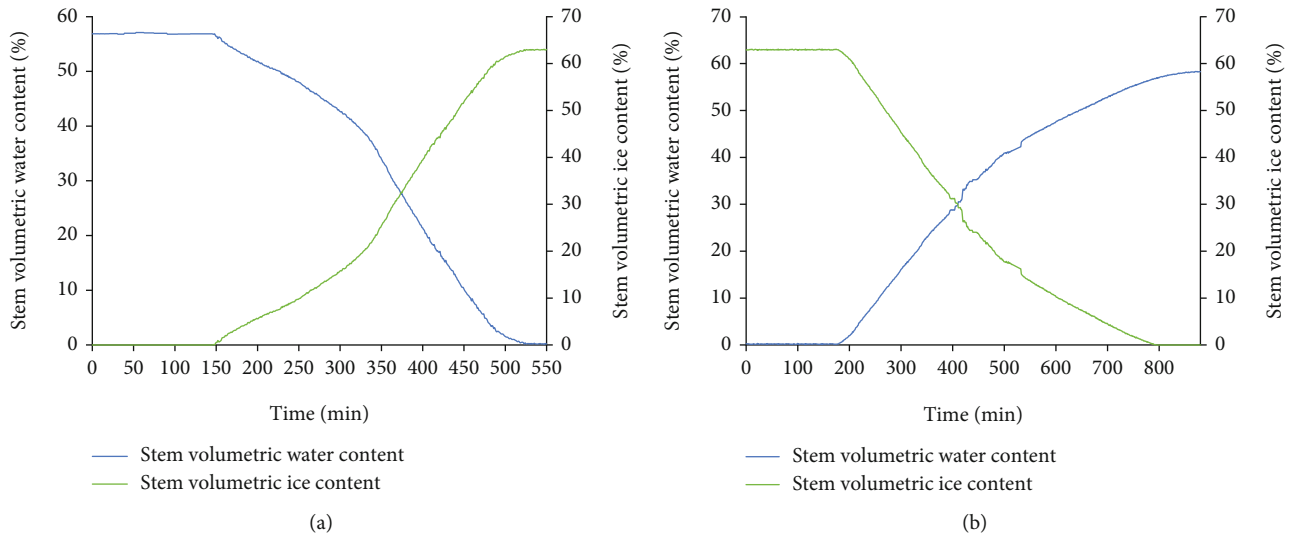

Figure 10: (a) Changes of stem volumetric water content and ice content during the freezing process. (b) Changes of stem volumetric water content and ice content during the thawing process.

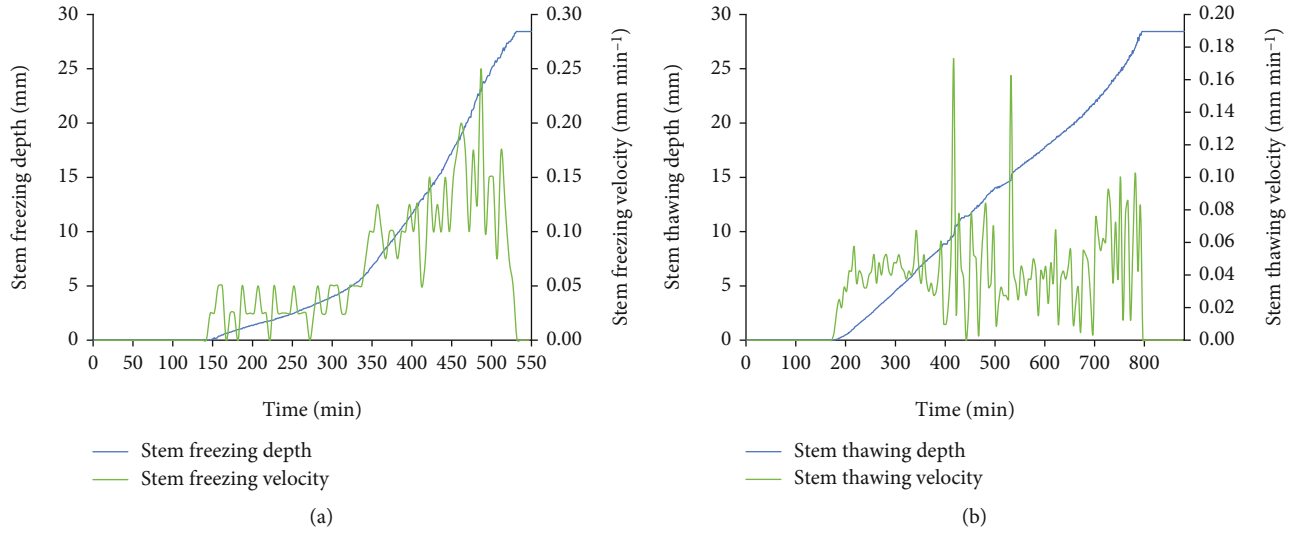

Figure 11: (a) Changes of stem freezing depth and velocity during the freezing process. (b) Changes of stem thawing depth and velocity during the thawing process.

0.12 mm min^{-1}. It is mainly due to the fact that the sapwood has some special pore structures including conduits and sieve tubes, thus causing the lower thermal conductivity in sapwood [28, 29]. The maximum freezing depth calculated by the freeze-thaw model of plant stem is 28.43 mm which is slightly less than the stem radius. This error can be explained by the fact that the stem water content is not uniformly distributed in radial direction and the water content in sapwood is usually greater than that in heartwood [30]. Hence, the more accurate freeze-thaw model needs to be built in future work. As can be seen from Figure 11(b), there is no significant difference between the stem thawing velocity in sapwood and heartwood and the mean thawing velocity is about 0.04 mm mim^{-1}. It is mainly caused by the fact that ice masses can separate cell layers and create cavities which are distributed throughout sapwood and heartwood, thus causing the decrease of thermal conductivity in the whole stem [31, 32]. The maximum thawing depth calculated by the freeze-thaw model of plant stem is still 28.43 mm which is equal to the maximum freezing depth, indicating that the model has high consistency in the freeze-thaw cycle.

3.4. Performance Comparison between Conventional Measurement Methods and the Compound Sensor. The conventional methods for detecting the freeze-thaw characteristics in plants can be divided into three categories: calorimetric method, spectrometric method, and electron microscopy. The differential scanning calorimetry is a typical calorimetric method and can quantify the amount of water that freezes or thaws. The amount of water which is frozen is determined by measuring the heat released during freezing process, or absorbed during thawing process, and by making calculations based on the heat of fusion of water and the heat capacities of ice and liquid water. The major weakness in

using differential scanning calorimetry for determining ice content is in choosing the correct heat of fusion and heat capacity for stem tissue fluid. When most of the water in a stem is still liquid, it has a heat of fusion near that of pure water. As the amount of frozen water increases, such unfrozen water will have a high solute concentration, thus causing the decrease of the heat of fusion [33]. However, there is no appropriate method to measure the heat of fusion for stem tissue fluid in real time during freeze-thaw process. Ultimately, the uncertainty of the heat of fusion will greatly affect the measurement accuracy of differential scanning calorimetry. The compound sensor can measure stem water content with high accuracy by using the calibration equation and does not need to pay attention to the varying physicochemical indicators of stem tissue fluid during freeze-thaw process. Spectrometric method and electron microscopy can provide the distribution maps of liquid water and ice on the cross section of stem, respectively. But both methods require sampling and belong to destructive measurements. The compound sensor can realize in situ real-time measurement for water and ice content in the stem. Compared with the above three methods, the compound sensor has a better practical application value. However, the compound sensor has only a separate temperature probe which cannot accurately reveal the distribution and evolution of ice on the cross section of stem. Therefore, an ideal freeze-thaw model of plant stem was proposed to explain the freeze-thaw characteristics including stem water content, ice content, freezing depth, freezing velocity, thawing depth, and thawing velocity.

4. Conclusions

In order to explore the freeze-thaw characteristics of plant stem, a compound sensor for detecting stem temperature and water content in situ was designed and developed in this paper. The length of the temperature electrode and the diameter of the water content electrode can be customized to match different sizes of plant stems. The resolution, MAE, and RMSE of the compound sensor when measuring stem temperature are approximately 0.1, 0.57, and 0.65°C, respectively. The resolution, MAE, and RMSE of the compound sensor when measuring stem water content are approximately 0.05, 1.59, and 1.81%, respectively. Considering that the compound sensor cannot accurately reveal the distribution and evolution of ice on the cross section of stem, we proposed an ideal freeze-thaw model of plant stem based on the physicochemical properties of plant stem. Moreover, six freeze-thaw indicators including stem water content, ice content, freezing depth, freezing velocity, thawing depth, and thawing velocity were defined to describe the freeze-thaw characteristics of plant stem based on the compound sensor and the freeze-thaw model.

Data Availability

The data used to support the findings of this study are available from the corresponding author upon request.

Conflicts of Interest

The authors declare no conflicts of interest.

Authors' Contributions

For this research article, Chao Gao and Yandong Zhao conceived and designed the experiments; Hao Tian performed the experiments; Chao Gao and Hao Tian analyzed the data; Chao Gao wrote the paper.

Acknowledgments

This research was supported by the Beijing Natural Science Foundation (Grant No. 6214034), Fundamental Research Funds for Science and Technology Innovation Service Ability Construction (Grant No. PXM2020_014213_000017), National Key Research and Development Program of China (Grant No. 2017YFD0600901), and Beijing Municipal Science and Technology Commission (Grant No. Z161100000916012).

References

[1] M. J. Burke, L. V. Gusta, H. A. Quamme, C. J. Weiser, and P. H. Li, "Freezing and injury in plants," *Annual Review of Plant Physiology*, vol. 27, no. 1, pp. 507–528, 1976.

[2] R. S. Pearce, "Plant freezing and damage," *Annals of Botany*, vol. 87, no. 4, pp. 417–424, 2001.

[3] G. S. Sanghera, S. H. Wani, W. Hussain, and N. B. Singh, "Engineering cold stress tolerance in crop plants," *Current Genomics*, vol. 12, no. 1, pp. 30–43, 2011.

[4] J. Zhu, C. H. Dong, and J. K. Zhu, "Interplay between cold-responsive gene regulation, metabolism and RNA processing during plant cold acclimation," *Current Opinion in Plant Biology*, vol. 10, no. 3, pp. 290–295, 2007.

[5] C. B. Rajashekar and M. J. Burke, "Freezing characteristics of rigid plant tissues (development of cell tension during extracellular freezing)," *Plant Physiology*, vol. 111, no. 2, pp. 597–603, 1996.

[6] L. V. Gusta, M. J. Burke, and A. C. Kapoor, "Determination of unfrozen water in winter cereals at subfreezing temperatures," *Plant Physiology*, vol. 56, no. 5, pp. 707–709, 1975.

[7] O. M. Lindstrom, N. P. A. Huner, and J. V. Carter, "Differential thermal analysis of the freezing of water in leaves of cold-hardened and nonhardened Puma rye," *Botanical Gazette*, vol. 144, no. 2, pp. 234–239, 1983.

[8] R. V. Devireddy, D. Raha, and J. C. Bischof, "Measurement of water transport during freezing in cell suspensions using a differential scanning calorimeter," *Cryobiology*, vol. 36, no. 2, pp. 124–155, 1998.

[9] M. Wisniewski, S. E. Lindow, and E. N. Ashworth, "Observations of ice nucleation and propagation in plants using infrared video thermography," *Plant Physiology*, vol. 113, no. 2, pp. 327–334, 1997.

[10] M. Ishikawa, W. S. Price, H. Ide, and Y. Arata, "Visualization of freezing behaviors in leaf and flower buds of full-moon maple by nuclear magnetic resonance microscopy," *Plant Physiology*, vol. 115, no. 4, pp. 1515–1524, 1997.

[11] H. Ide, W. S. Price, Y. Arata, and M. Ishikawa, "Freezing behaviors in leaf buds of cold-hardy conifers visualized by

NMR microscopy," *Tree Physiology*, vol. 18, no. 7, pp. 451–458, 1998.

[12] S. Fujikawa and K. Kuroda, "Cryo-scanning electron microscopic study on freezing behavior of xylem ray parenchyma cells in hardwood species," *Micron*, vol. 31, no. 6, pp. 669–686, 2000.

[13] S. Hillmer, C. Viotti, and D. G. Robinson, "An improved procedure for low-temperature embedding of high-pressure frozen and freeze-substituted plant tissues resulting in excellent structural preservation and contrast," *Journal of Microscopy*, vol. 247, no. 1, pp. 43–47, 2012.

[14] C. Gao, Y. Zhao, and Y. Zhao, "A novel sensor for noninvasive detection of in situ stem water content based on standing wave ratio," *Journal of Sensors*, vol. 2019, Article ID 3594964, 10 pages, 2019.

[15] V. M. Malygin, "Design of a platinum resistance thermometer temperature measuring transducer and improved accuracy of linearizing the output voltage," *Measurement Techniques*, vol. 38, no. 1, pp. 84–88, 1995.

[16] S. Roberts and A. Von Hippel, "A new method for measuring dielectric constant and loss in the range of centimeter waves," *Journal of Applied Physics*, vol. 17, no. 7, pp. 610–616, 1946.

[17] F. T. Ulaby and R. P. Jedlicka, "Microwave dielectric properties of plant materials," *IEEE Transactions on Geoscience and Remote Sensing*, vol. GE-22, no. 4, pp. 406–415, 1984.

[18] M. P. Fuller and P. L. Grice, "A chamber for the simulation of radiation freezing of plants," *Annals of Applied Biology*, vol. 133, no. 1, pp. 111–121, 1998.

[19] M. F. Thomashow, "Role of cold-responsive genes in plant freezing tolerance," *Plant Physiology*, vol. 118, no. 1, pp. 1–8, 1998.

[20] A. Gholaminejad and R. Hosseini, "A study of water supercooling," *Journal of Electronics Cooling and Thermal Control*, vol. 3, no. 1, pp. 1–6, 2013.

[21] A. Kadioglu, R. Terzi, N. Saruhan, and A. Saglam, "Current advances in the investigation of leaf rolling caused by biotic and abiotic stress factors," *Plant Science*, vol. 182, pp. 42–48, 2012.

[22] P. E. Verslues, M. Agarwal, S. Katiyar-Agarwal, J. Zhu, and J. K. Zhu, "Methods and concepts in quantifying resistance to drought, salt and freezing, abiotic stresses that affect plant water status," *The Plant Journal*, vol. 45, no. 4, pp. 523–539, 2006.

[23] J. Zhou, H. Zhou, C. Hu, and S. Hu, "Measurements of thermal and dielectric properties of medium density fiberboard with different moisture contents," *BioResources*, vol. 8, no. 3, pp. 4185–4192, 2013.

[24] E. Troppová, M. Švehlík, J. Tippner, and R. Wimmer, "Influence of temperature and moisture content on the thermal conductivity of wood-based fibreboards," *Materials and Structures*, vol. 48, no. 12, pp. 4077–4083, 2015.

[25] J. Klotke, J. Kopka, N. Gatzke, and A. G. Heyer, "Impact of soluble sugar concentrations on the acquisition of freezing tolerance in accessions of Arabidopsis thaliana with contrasting cold adaptation—evidence for a role of raffinose in cold acclimation," *Plant, Cell and Environment*, vol. 27, no. 11, pp. 1395–1404, 2004.

[26] M. E. S. Nunes and G. R. Smith, "Electrolyte leakage assay capable of quantifying freezing resistance in rose clover," *Crop Science*, vol. 43, no. 4, pp. 1349–1357, 2003.

[27] E. J. Rosenbaum, N. J. English, J. K. Johnson, D. W. Shaw, and R. P. Warzinski, "Thermal conductivity of methane hydrate from experiment and molecular simulation," *The Journal of Physical Chemistry B*, vol. 111, no. 46, pp. 13194–13205, 2007.

[28] T. Hölttä, M. Mencuccini, and E. Nikinmaa, "Linking phloem function to structure: Analysis with a coupled xylem-phloem transport model," *Journal of Theoretical Biology*, vol. 259, no. 2, pp. 325–337, 2009.

[29] S. D. Wullschleger, K. W. Childs, A. W. King, and P. J. Hanson, "A model of heat transfer in sapwood and implications for sap flux density measurements using thermal dissipation probes," *Tree Physiology*, vol. 31, no. 6, pp. 669–679, 2011.

[30] J. H. Fromm, I. Sautter, D. Matthies, J. Kremer, P. Schumacher, and C. Ganter, "Xylem water content and wood density in spruce and oak trees detected by high-resolution computed tomography," *Plant Physiology*, vol. 127, no. 2, pp. 416–425, 2001.

[31] J. Farrant, C. A. Walter, H. Lee, and L. E. McGann, "Use of two-step cooling procedures to examine factors influencing cell survival following freezing and thawing," *Cryobiology*, vol. 14, no. 3, pp. 273–286, 1977.

[32] M. E. McCully, M. J. Canny, and C. X. Huang, "The management of extracellular ice by petioles of frost-resistant herbaceous plants," *Annals of Botany*, vol. 94, no. 5, pp. 665–674, 2004.

[33] M. J. Burke, R. G. Bryant, and C. J. Weiser, "Nuclear magnetic resonance of water in cold acclimating red osier dogwood stem," *Plant Physiology*, vol. 54, no. 3, pp. 392–398, 1974.

Hindawi
Journal of Sensors
Volume 2021, Article ID 6610178, 11 pages
https://doi.org/10.1155/2021/6610178

Research Article

The Release of Endogenous Nitrogen and Phosphorus in the Danjiangkou Reservoir: A Double-Membrane Diffusion Model Analysis

Zhiqi Wang,[1,2,3] Hongxin Ren,[2] Zhaolong Ma,[3,4,5] Zhihong Yao,[2] Pengfei Duan,[6] and Guodong Ji[1]

[1]*Key Laboratory of Water and Sediment Sciences, Ministry of Education, Department of Environmental Engineering, Peking University, Beijing 100871, China*
[2]*School of Surveying, Mapping, and Geographic Information, North China University of Water Resource and Electric Powder, Zhengzhou 450000, China*
[3]*River and Lake Protection Center of Ministry of Water Resources, Beijing 100038, China*
[4]*Department of Hydraulic Engineering, Tsinghua University, Beijing 100084, China*
[5]*China Institute of Water Resource and Hydropower Research, No. 20 Chegongzhuang West Road, Haidian District, Beijing 100044, China*
[6]*Key Laboratory of Ecological Security in Water Source Area of the Middle Route of South-to-North Water Transfer Project in Henan Province, Nanyang Normal University, 473000, China*

Correspondence should be addressed to Guodong Ji; jiguodong@pku.edu.cn

Received 9 November 2020; Revised 12 January 2021; Accepted 25 January 2021; Published 13 February 2021

Academic Editor: Yuan Li

Endogenous contamination from the newly submerged sediment may have an impact on the water quality of the Danjiangkou Reservoir, the water source of the middle route of the South-to-North Water Diversion Project. In this study, in situ sediment samples were collected at different locations (Guojiashan (DJK1), Kongqueyuan (DJK2), Shijiagou (DJK3), Shiqiao Wharf (DJK4), and Songgang Wharf (DJK5) from the north to the south) of the Danjiangkou Reservoir and the upstream tributary using a columnar sediment sampler and statically cultured in laboratory, and the distribution and release of endogenous N and P from the sediment were investigated based on a double-membrane diffusion model. The results showed that the P contents in the main reservoir and the upstream tributary followed the order of inorganic phosphorus (IP) > organic phosphorus (OP) > calcium – phosphorus (Ca – P) > iron – phosphorus (Fe – P) > labile phosphorus (LP). IP accounted for the largest proportion (47.10-59.70%) of total phosphorus (TP), while LP accounted for only a small proportion (0.10-0.90%) of TP. There is a significant difference in the spatial distribution of P at different sampling points, especially for the OP content (226.90 $mg \cdot kg^{-1}$) with a coefficient of variation of 26.90%. The contents of different forms of P and NH_4^+-N decreased from the upstream tributary to the main reservoir, which was mainly attributed to the land use type. In the vertical distribution, the contents of different forms of P in DJK4 and DJK5 decreased with the increase of sediment depth. The contents of NH_4^+-N and PO_4^{3-}-P in the sediment interstitial water of DJK4 and DJK5 were higher than those in the overlying water. In addition, the contents of NH_4^+-N and PO_4^{3-}-P were higher in DJK5 than that in DJK4. The static culture experiments showed that N and P were mainly released from the sediment-overlying water interface to the overlying water. The release rate of NH_4^+-N and PO_4^{3-}-P ranged from 13.08 $mg \cdot (m^2 \cdot d)^{-1}$ to 21.39 $mg \cdot (m^2 \cdot d)^{-1}$ and from 3.06 $mg \cdot (m^2 \cdot d)^{-1}$ to 6.02 $mg \cdot (m^2 \cdot d)^{-1}$, and the release amount calculated based on the double-membrane diffusion model was 1.17×10^3 $t \cdot a^{-1}$ and 0.53×10^3 $t \cdot a^{-1}$, respectively. Thus, endogenous contamination from the newly submerged land is an important factor affecting the water quality of the Danjiangkou Reservoir.

1. Introduction

Reservoir sediment is considered to be an important sink of various nutrients in the overlying water [1] and thus even a small change of reservoir sediment can have a substantial impact on the quality of the overlying water [2]. The nutrients accumulated in the sediment such as nitrogen (N) and phosphorus (P) can be released from the sediment back to the overlying water through the interstitial water as a result of convection, diffusion, and resuspension, causing secondary pollution of the overlying water [3]. For instance, the release rate of NH_4^+-N from the sediment is still as high as 3.31×10^3 t·a^{-1} in the Dianchi Lake of Yunnan Province, China, after dredging and sewage interception [4], and resuspension of nutrient-rich sediment causes eutrophication for several decades even when external nutrient loads are curtailed [5]. In this case, endogenous release of nutrients from the sediment is the main factor affecting the water quality [6]. Therefore, a better understanding of the distribution of nutrients in the sediment and their release fluxes is essential to take steps to reduce endogenous nutrient load and improve reservoir water quality [7].

The Danjiangkou Reservoir is the main water source of the middle route of the South-to-North Water Transfer Project of China, and thus the water quality has been maintained at a high level for years. However, evidence has emerged that there is an increasing risk of endogenous contamination that can seriously affect the water quality of the reservoir [8]. The overflow weir crest of the Danjiangkou Reservoir was heightened in 2012, resulting in an increase in the storage capacity from 17.45 billion m^3 to 29.05 billion m^3 [9] and consequently inundation of 17333 ha of farmland [10]. The newly formed sediments contain a higher amount of organic matter compared with the original sediments, which implies a higher risk of endogenous release and contamination. N is more likely to be released from the newly submerged farmland and orchard of the Danjiangkou Reservoir [11], and P loss is more prominent in the new riparian zone compared with that in the existing riparian zone [12]. Thus, endogenous release of nutrients such as N and P from the sediment in the newly submerged area may pose a threat to the water quality of the reservoir. A number of studies have been conducted to investigate the factors affecting the release of nutrients from the sediment, such as existing states and seasonal variations of nutrients, dissolved oxygen, and temperature [13], but little is known about the release of nutrients from the sediment in the newly submerged area.

A number of models have been proposed to describe the release of nutrients from the lake sediment, such as the permeation model, the double-membrane diffusion model, and the surface renewal model. Among them, the double-membrane diffusion model is particularly suitable to characterize the flux of endogenous nutrients from the kinetic perspective, as it uses mathematical conversion to obtain the double film thickness that is difficult to measure by other models and generalizes the actual complex release process. However, there are three theoretical premises: both water and sediment phases are single homogeneous phases, transmission takes place by means of molecular diffusion, and the total amount of sediment nutrients remains unchanged. It avoids the influence of complicated environmental factors and allows for the estimation of the release of sediment nutrients in a large reservoir area. The K value is calculated from the data obtained from the simulated release experiment, which is the net release coefficient derived from the actual sediment adsorption, precipitation, and microbial action [14].

In this study, in situ sediment samples were collected at different locations of the Danjiangkou Reservoir and statically cultured in laboratory, and the distribution and release of endogenous N and P from sediments were investigated based on the double-membrane diffusion model. The results of this study may provide important insights into how to improve the water quality of the reservoir.

2. Materials and Methods

2.1. Study Area and Sampling Sites. The Danjiangkou Reservoir is located in the northwest of Hubei province and the southwest of Henan province and consists of Hanjiang and Danjiang reservoirs. The annual average inflow is about 39.48 billion m^3 from the Hanjiang River and its tributary Danjiang River, and the terrain is high in the northwest but low in the southeast. The reservoir was put into operation in 1973, and the overflow weir crest was heightened in 2012. Now, it is the largest artificial freshwater lake in Asia, with a water area of about 102275 ha and a storage capacity of about 29.05 billion m^3 [15].

In this study, five representative sampling sites were established at Guojiashan (DJK1; 33°02′39″N and 111°28′46″E), Kongqueyuan (DJK2; 33°0′51″N and 111°27′11″E), Shijiagou (DJK3; 32°54′42″N and 111°30′47″E), Shiqiao Wharf (DJK4; 32°49′23″N and 111°34′28″E), and Songgang Wharf (DJK5; 32°46′02″N and 111°38′50″E), as shown in Figure 1. These sampling sites were about 0.5 km away from the reservoir shore with a water depth of about 2 m. The overlying water and sediment samples were collected in March and August, 2018. The longitude and latitude of the sampling sites were determined by GPS (see Table 1). AD, DJK 4, and DJK 5 were continuous farmland since 2012 where a large amount (188-356 kg·ha^{-1}) of chemical fertilizers (mainly potash and phosphate fertilizers) were used with a maximum of 646 kg·ha^{-1} [16]. Thus, the double-membrane diffusion model was used to investigate the effect of the release of endogenous N and P on the overlying water at these two sampling sites based on the data collected in March, 2018.

2.2. Sample Collection and Analysis. Columnar sediment samples were collected using a columnar sampler with an organic glass tube (90 mm × 500 mm), and three parallel samples were collected at each sampling site for static culture experiments. The overlying water samples were also collected at each sampling site without disturbing the sediment. A portion of water samples was encapsulated in 5 L plastic bottles to supplement the water in static culture experiments, while the rest was encapsulated in 500 ml polyethylene bottles for the measurement of N and P concentrations in the overlying

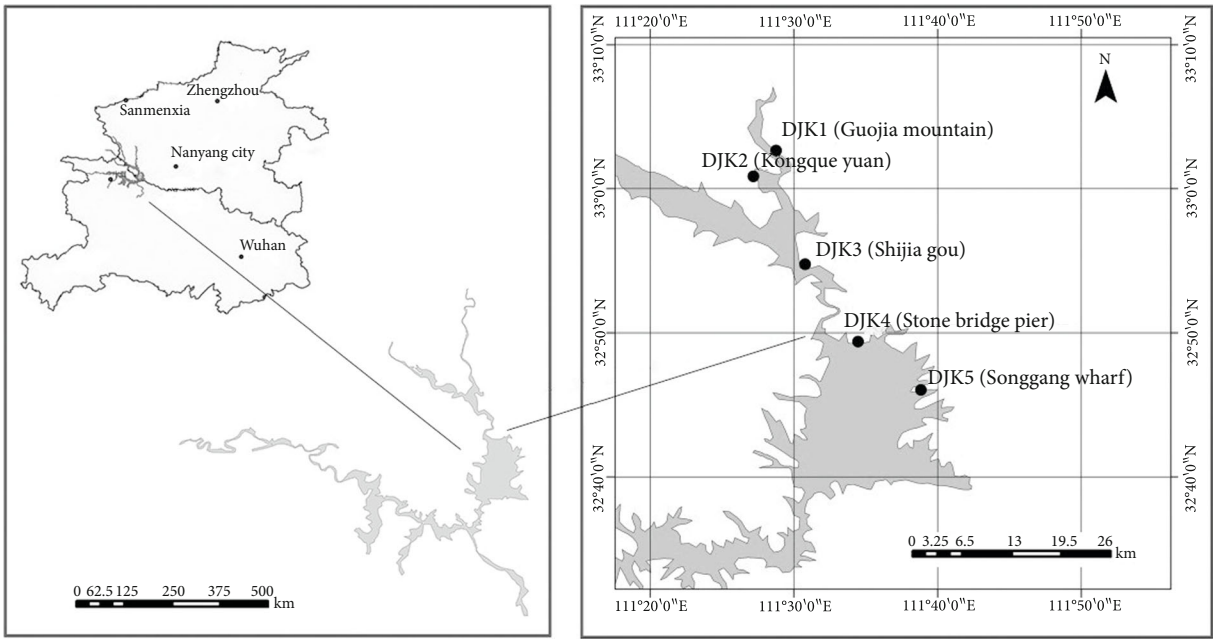

Figure 1: The sampling sites in the Danjiangkou Reservoir.

Table 1: N and P contents in the overlying water at each sampling site and the original land use type.

Sampling sites	Background concentration in the overlying water ($mg \cdot L^{-1}$)		Land use type	Longitude	Latitude
	NH_4^+-N	PO_4^{3-}-P			
DJK1	1.08	0.12	Farmland (corn field)	E 111°28′46″	N 33°02′39″
DJK2	0.59	0.08	Farmland	E 111°27′11″	N 33°00′51″
DJK3	0.56	0.06	Moving the topsoil to cultivate fertility	E 111°30′47″	N 32°54′45″
DJK4	0.35	0.02	Farmland and woodland	E 111°34′27″	N 32°49′23″
DJK5	0.53	0.02	Farmland	E 111°38′50″	N 32°46′02″

water, and several drops of concentrated sulfuric acid were added to reach a pH value of 2 and shaken uniformly in order to inhibit the microbial activity. Statically cultured samples were cut according to the depth (0-1 cm, 1-2 cm, 2-3 cm, 3-4 cm, 4-5 cm, 5-6 cm, 6-7 cm, 7-8 cm, 8-9 cm, and 9-10 cm) and centrifuged at 5000 r/min for 20 min. Sediment interstitial water was obtained and filtered using a 0.45 μm fiber filtration membrane for the measurement of NH_4^+-N and PO_4^{3-}-P concentrations in the sediment interstitial water.

2.3. Static Culture Experiments. The overlying water was removed from columnar sediment samples by siphonage, and then the original overlying water was filtered using the 0.45 μm fiber filtration membrane and carefully introduced into the columnar sediment samples along the wall by siphonage. In order to better simulate the field environment of the Danjiangkou Reservoir (the annual average temperature is about 16°C), all columnar sediment samples were placed vertically in a culture vessel with a water depth of 0.40 m in dark at 16°C for 10 days. Water samples were collected at the middle of the sample at the beginning of the experiment and then every 8 h during the culture. Prior to each sampling, the overlying water was stirred slowly using a slender glass rod in order to ensure uniform sampling and to avoid sediment resuspension. After sampling, an equal amount of original overlying water was supplemented. All samples were kept in a constant temperature incubator at 4°C.

2.4. Analysis Methods. The contents of NH_4^+-N in the overlying water, sediment, and sediment interstitial water were measured using Nessler's reagent colorimetric method (GB7479-87, National Standards of People's Republic of China), KCl extraction-distillation method [17], and Nessler's reagent colorimetric method [17], respectively, while those of PO_4^{3-}-P were measured using molybdenum-antimony anticolorimetry (GB11893-89, National Standards of People's Republic of China) and the molybdenum blue coloration method [17], respectively. The states of P were determined as described in using the Standards, Measurements, and Testing (SMT) method (Standards Measurements and Testing Program of the European Commission) [18] (see Figure 2). Labile phosphorus (LP) was extracted

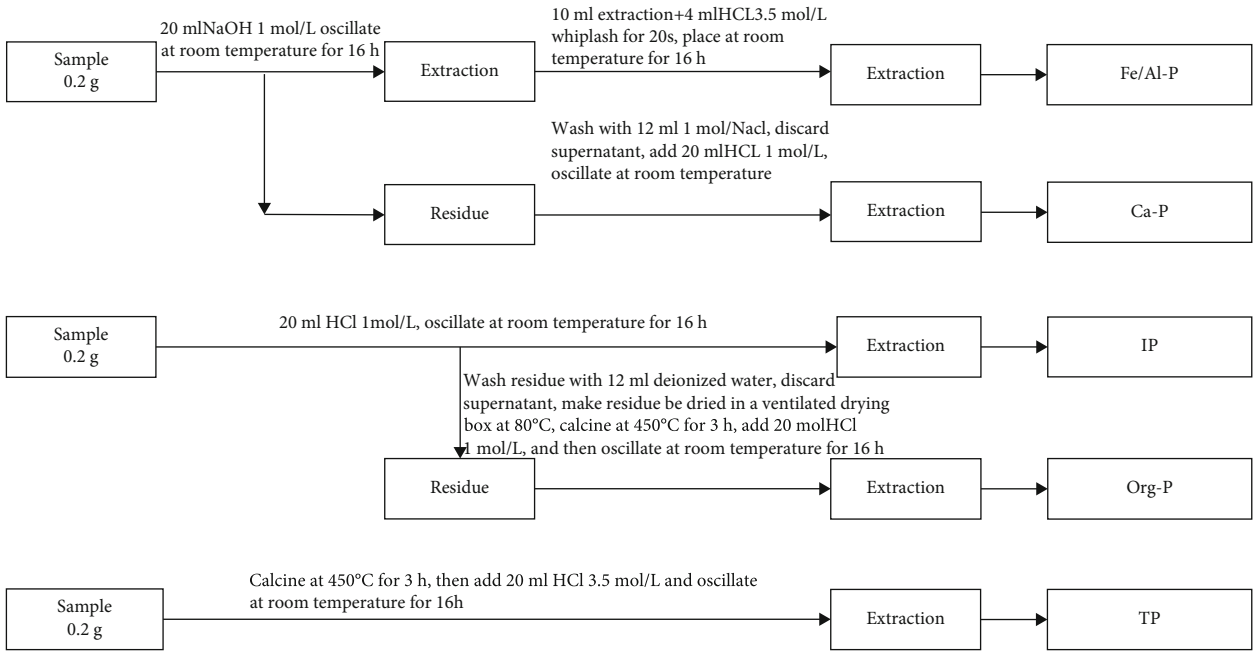

Figure 2: Extraction of P from the sediment by the SMT method.

using 1 mol/L NH_4Cl [19]: 1 g of sediment was placed in a centrifuge tube, and 25 ml of NH_4Cl (1 mol/L) was added, oscillated for 0.5 h, and centrifuged. The LP content in the supernatant was measured using molybdenum blue colorimetry. All measurements were repeated three times, and the average was reported (the error was within <5%). The significance of spatial difference was analyzed by one-way ANOVA using SPSS 19.0, and figures were plotted using Origin 9.0 and ArcGIS 10.2. Error bars represented the standard deviations (SD) throughout the paper.

2.5. Calculation of Experimental Results

2.5.1. Double-Membrane Diffusion Model. A number of models have been proposed to describe the release of contaminants from the lake sediment, such as the permeation model, the double-membrane diffusion model, and the surface renewal model. In this study, the double-membrane diffusion model is used, in which the molecular diffusion coefficient and the ratio of the thickness of double membranes (K) are used instead of the thickness of double membranes that is difficult to determine [20]. Three assumptions are made in this model: (1) both the overlying water and sediment are single homogeneous phases, and the overlying water is well mixed, (2) the mass transfer between the sediment and the overlying water takes place only through molecular diffusion, and (3) the nutrient content is relatively high in the sediment compared with that in the overlying water, and thus nutrient loss due to sediment release is negligible throughout the study. The release processes of nutrients from the sediment into the overlying water consist of (1) migration of nutrients from the interior to the surface of the sediment, (2) interfacial transfer of nutrients to the water side, (3) diffusion through the liquid membrane, and (4) uniform mixing in the overlying water. Given the above three assumptions, steps 1, 2, and 4 are assumed to occur instantaneously, and thus step 2 is the controlling step of the release processes [21].

According to the double-membrane diffusion model, the transfer flux N should be proportional to the molecular diffusion coefficient D and the concentration gradient in the double membrane, the latter of which is the concentration difference between the two sides of the membrane divided by the thickness of the double membrane δ:

$$N = \mathrm{D}\frac{(Cw - C)}{\delta}, \tag{1}$$

where C is the contaminant concentration on the water side ($mg{\cdot}L^{-1}$), and Cw is the equilibrium concentration of contaminants in the water phase ($mg{\cdot}L^{-1}$).

Let the transfer velocity constant be $\mathrm{K} = \mathrm{D}/\delta$. According to the double-membrane diffusion model and the dynamics theory,

$$\mathrm{K}V(Cw - C) = V \times \frac{dc}{dt}. \tag{2}$$

Thus, the dynamics of contaminant concentration in the water phase can be described as follows:

$$C = Cw\left(1 - e^{-\frac{KA}{V}\times t}\right), \tag{3}$$

where A is the release area (m^2), and V is the volume of the overlying water (m^3).

Eq. (3) can be transformed into

$$\frac{V}{A} \times \mathrm{Ln}\left(\frac{Cw}{Cw - C}\right) = \mathrm{K}t, \quad (4)$$

where V/A is the depth of the overlying water in the experimental column [22].

The plot of $(V/A) \times \mathrm{Ln}(Cw/Cw - C)$ against time t is a straight line through the origin of coordinates, and the slope is the K value [21]. The K values calculated from experimental results are shown in Table 2.

According to the double-membrane diffusion model, the release flux of contaminants from the sediment is

$$N = \mathrm{K}(Cw - C). \quad (5)$$

The release rate of contaminants is

$$\frac{dC}{dt} = \mathrm{K}A(Cw - C), \quad (6)$$

where A is the sediment area (m^2).

Thus, the annual diffusion amount W is

$$\mathrm{W} = \mathrm{K}(Cw - C) \times V \times t, \quad (7)$$

where V is the volume of the overlying water (m^3), $V = AH$, H is the depth of the overlying water (m), and t is the diffusion period [21].

2.5.2. Release Rate of Nutrients in Statically Cultured Sediments. The release rate of contaminants can be calculated according to the mass conservation principle:

$$R = \frac{\left[V(\rho_n - \rho_0) + \sum_{j=1}^{n} v_{j-1}\left(\rho_{j-1} - \rho_\alpha\right)\right]}{\mathrm{A}t}, \quad (8)$$

where R is the release rate of contaminants from sediment samples, mg/(m^2·d); V is the volume of the overlying water (L); ρ_0, ρ_n, and ρ_{j-1} are the contents of contaminants collected at the beginning of the experiment, time n and $j - 1$, respectively (mg/L); ρ_α is the contaminant content in the added water (mg·L^{-1}), v_{j-1} is the volume of $j - 1$ samples (L); A is the contact area between the sediment and the overlying water (m^2); and t is the release time (d) [22].

3. Results and Discussion

3.1. Distribution of Different Forms of P and N in the Sediment. There is a significant difference in total phosphorus (TP) contents (402.40-560.30 mg·kg^{-1}) among the five sampling sites (DJK 1-5) with a coefficient of variation of 14.4% ($p < 0.01$), which is consistent with the previous finding in the Danjiangkou Reservoir (530 mg·kg^{-1}) [15] but lower than that in the Three Gorges Reservoir (1189 mg·kg^{-1}) [23]. In sampling sites from DJK1 to DJK5, a great amount of P in chemical fertilizers and crop residues can be fixed in the soil by adsorption, sedimentation, and microbial immobilization [24]. However, the TP contents in DJK 1-5 seem to be less affected by agricultural practices compared with that in the Three Gorges Reservoir. The highest TP content is found in DJK 1, which is 1.34 times that in DJK 4. In general, the TP content decreases from the upstream tributary to the main reservoir, which may be associated with the original land use type [25] and the amount of chemical fertilizers used (see Table 1).

Table 2: Contaminant migration velocities (K) in the sediment.

Sampling sites	K values
DJK4-NH_4^+-N	0.06
DJK5-NH_4^+-N	0.06
DJK4-PO_4^{3-}-P	0.15
DJK5-PO_4^{3-}-P	0.12

The contents of different forms of P follow the order of IP > OP > Ca − P > Fe − P > LP. Thus, IP accounts for the largest proportion (47.10-59.70%) of TP in the five sampling sites, while the LP content is only 0.98-3.50 mg·kg^{-1}, accounting for a small proportion (0.10-0.90%) of TP (see Figure 3). However, it is noted that LP is a weakly bound phosphate on the sediment surface that is readily exploitable by aquatic organisms, and P is most easily released from the sediment in the form of LP [26]. The vertical distribution of various forms of P in DJK 4 shows a decreasing trend with sediment depth and the contents of Fe-P, which can also be easily utilized by aquatic organisms, range from 1.70 mg·kg^{-1} to 4.70 mg·kg^{-1}, while that in DJK 5 shows a W-shaped decreasing trend and the Ca-P contents range from 9.30 to 28.50 mg·kg^{-1}. The vertical distribution of P may be associated with the environment, sedimentation rate, and age. The greater the sediment depth is, the lower the contents of various forms of P will be [27]. Fertilizers containing P were not allowed in early years, thus resulting in less accumulation of nutrients in the sediment; whereas an increasing amount of P fertilizers are used in recent years, thus resulting in an increase in P contents in the sediment.

Inorganic N exists in the sediment and overlying water mainly in the form of NH_4^+-N [28]. Table 3 shows that the NH_4^+-N content ranges from 173.00 mg·kg^{-1} to 208.10 mg·kg^{-1} in the five sampling sites, which is slightly higher than that obtained in a previous study (142.30 mg·kg^{-1}) [29]. In line with the study of the Yuqiao Reservoir [30], the NH_4^+-N content also decreases from the upstream tributary to the main reservoir. Compared with the reservoir, the tributary river is characterized by smaller bed slopes and flow velocities, making it easier to accumulate organic matter [31]. The spatial distribution of P is also affected by agricultural practices at the five sampling sites due to extensive use of chemical fertilizers. In the vertical distribution, the NH_4^+-N content increases as the sediment depth increases (see Figure 3), because NH_4^+-N can be easily diffused from the sediment surface to the overlying water through complex physical, chemical, and biological exchanges [32]. However, the NH_4^+-N content is increased at 4-12 cm. Organic N is mineralized at an increasing rate in the deep sediment under the effect of ammonifiers, and

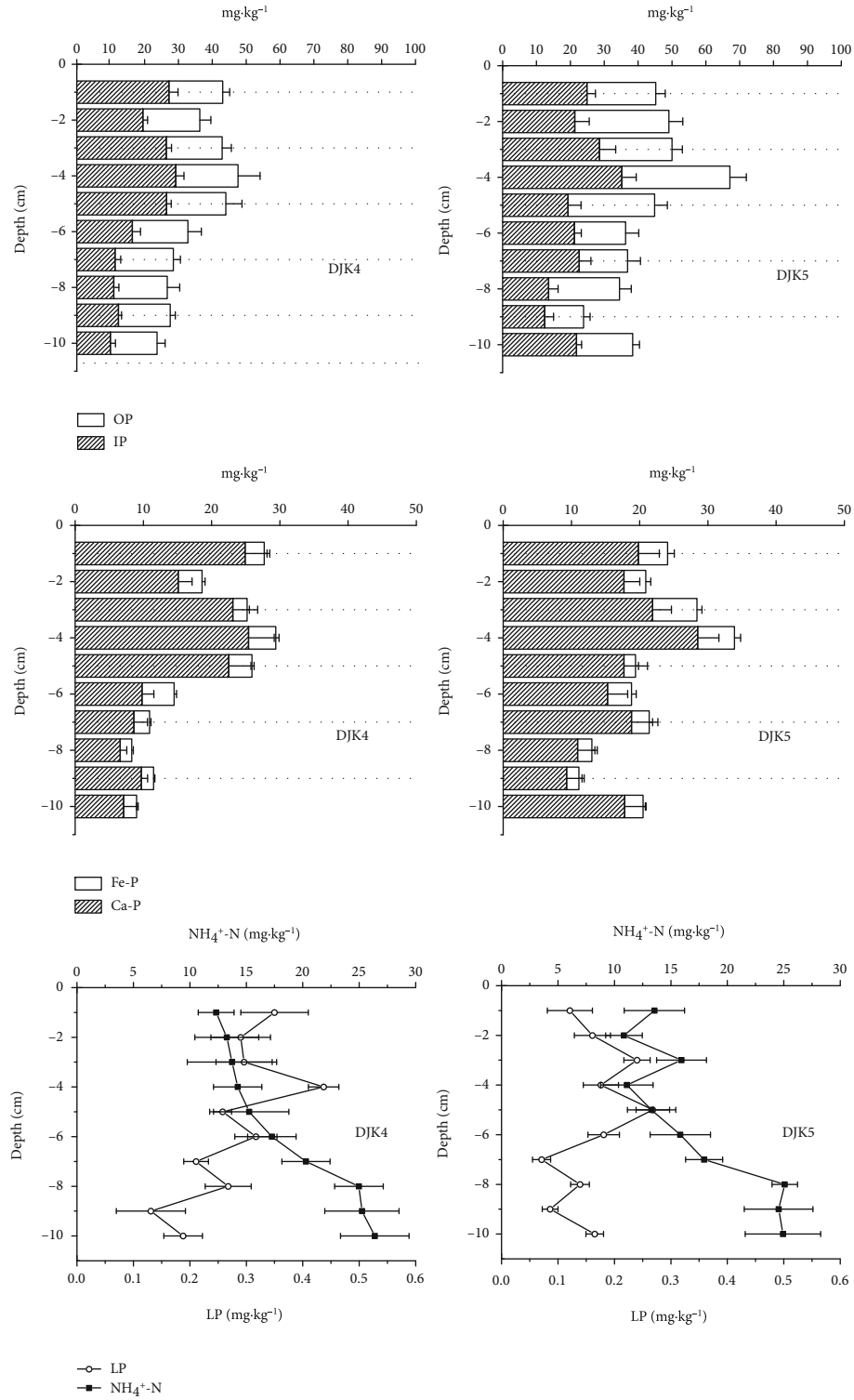

Figure 3: Vertical distribution of various forms of P and NH_4^+-N in the sediments collected from sites DJK4 and DJK5.

more importantly, less oxygen is available as the sediment depth increases, resulting in inhibition of nitrification and thus transformation of less NH_4^+-N into other forms of N. As a consequence, an increase in the NH_4^+-N content is observed at 4-12 cm [33].

The contents of NH_4^+-N and PO_4^{3-}-P in the sediment interstitial water of DJK 4 and DJK 5 increase with increasing depth (see Figure 4), and they are significantly higher in DJK4 than in DJK5 ($p < 0.01$). The average NH_4^+-N content in the interstitial water at a depth of 10 cm in samples from DJK4 and DJK5 is 16.00 mg·L^{-1} and 3.50 mg·L^{-1} with a coefficient of variation of 42.50% and 107.70%, respectively. Thus, the NH_4^+-N content varies more dramatically in DJK5 [34]. In DJK5, the NH_4^+-N content increases as the

Table 3: Average contents of P in the surface sediments of different sampling sites.

Sampling sites	LP/(mg·kg^{-1})	Fe-P/(mg·kg^{-1})	Ca-P/(mg·kg^{-1})	OP/(mg·kg^{-1})	IP/(mg·kg^{-1})	TP/(mg·kg^{-1})	NH_4^+-N/(mg·kg^{-1})
DJK1	3.50 ± 0.51a	59.40 ± 5.33a	265.50 ± 25.83a	226.90 ± 18.56a	334.60 ± 20.28a	560.30 ± 28.55a	208.10 ± 27.40a
DJK2	0.98 ± 0.14b	57.01 ± 4.37b	194.60 ± 14.00b	230.90 ± 21.06a	279.70 ± 18.13b	516.50 ± 24.71b	198.30 ± 24.50a
DJK3	2.94 ± 0.35ab	48.72 ± 3.47bc	180.30 ± 10.58b	165.20 ± 11.91b	245.50 ± 17.14b	452.90 ± 21.72b	186.40 ± 26.50b
DJK4	2.75 ± 0.42b	28.85 ± 4.67c	152.90 ± 9.42c	163.60 ± 14.58c	189.40 ± 11.45c	402.40 ± 16.72c	182.90 ± 23.80c
DJK5	1.61 ± 0.12b	33.99 ± 3.42bc	177.80 ± 7.96c	205.40 ± 11.23b	220.50 ± 9.33c	439.00 ± 16.73b	173.00 ± 22.90c

Note: different letters after the values indicate significant differences ($p < 0.01$), means ± standard deviations.

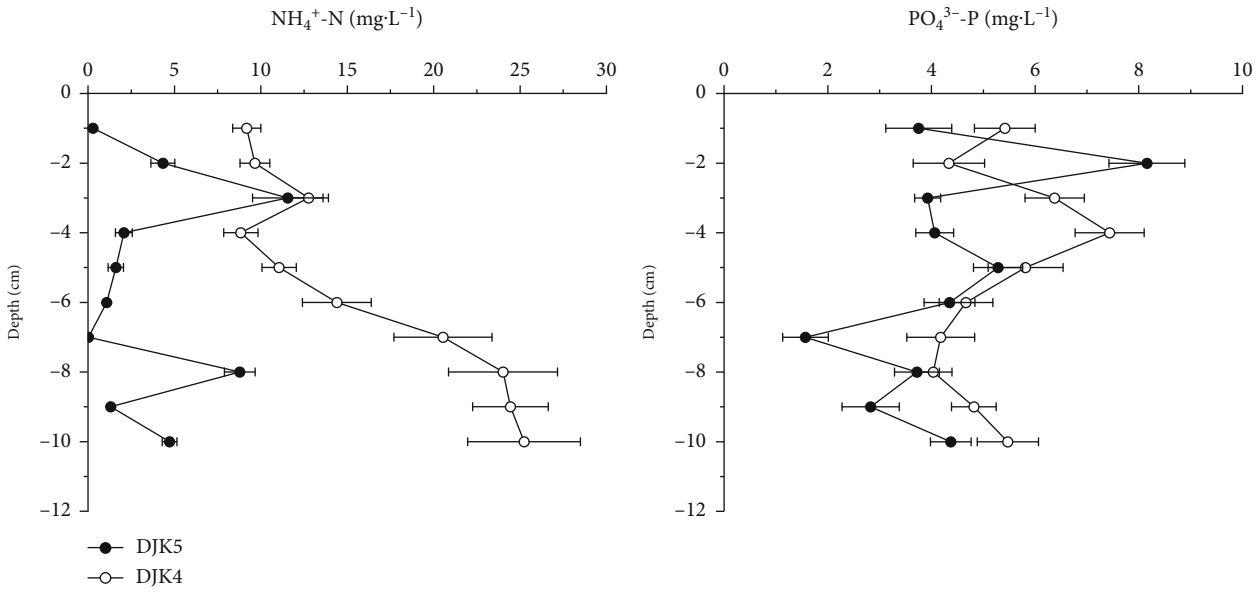

Figure 4: Variation of NH_4^+-N and PO_4^{3-}-P contents in the sediment interstitial water.

depth increases until a maximum of 12.75 mg·L^{-1}is reached at 3 cm, after which it decreases with further increase of the depth. This agrees well with the study of Liu et al. about the Beili Lake of the Hangzhou West Lake [35] and the study of Wang et al. about the Nansi Lake [36]. The significant difference in the NH_4^+-N content at 4-10 cm between DJK 4 and DJK 5 can be attributed to the presence of more iron and manganese oxides in DJK5, which act as electron acceptors of NH_4^+ for conversion of NH_4^+ into NH_3 gas under anaerobic conditions [37]. It is also noted that the higher NH_4^+-N content in the interstitial water of DJK 4 is consistent with the NH_4^+-N content in the sediment.

The average PO_4^{3-}-P content in the interstitial water at a depth of 10 cm in samples from DJK4 and DJK5 is 5.26 mg·L^{-1} and 4.30 mg·L^{-1} with a coefficient of variation of 20.50% and 36.20%, respectively, which is related to the high P content in DJK 4. In DJK 5, the PO_4^{3-}-P content first increases and then decreases with increasing depth, and the maximum of 8.16 mg·L^{-1} is reached at 2 cm; while in DJK 4, the PO_4^{3-}-P content is maximized at 4 cm (7.45 mg·L^{-1}) and 10 cm (5.47 mg·L^{-1}). This is because the PO_4^{3-}-P in the surface interstitial water can be easily diffused into the overlying water, resulting in a lower PO_4^{3-}-P content compared with that in the deep interstitial water [38]. In both DJK 4 and DJK 5, the PO_4^{3-}-P content is decreased at 4-7 cm, at which there is a transition from aerobic to anaerobic conditions that can inhibit the effect of aerobic microbes on the active organic detritus and increase the dissolution of iron and manganese oxides under anaerobic conditions, and consequently result in the release of adsorbed P.

3.2. Release of NH_4^+-N from Statically Cultured Sediments. NH_4^+-N is released from the sediment-overlying water interface into the overlying water in March in DJK1-5 (see Figure 5), which is in good agreement with that of the Danjiangkou Reservoir in August [11]. The release rate ranges from 13.08 mg·(m^2·d)$^{-1}$ to 21.39 mg·(m^2·d)$^{-1}$, and the maximum is observed in DJK3 (21.39 mg·(m^2·d)$^{-1}$), which is 1.32 times of the average. It is higher than that in the Meiliang Bay of the Tai Lake at 15°C (12.60 mg·(m^2·d)$^{-1}$) [39], but lower than that in the Fubao Bay of the Dianci Lake at 14-16°C (93.03 mg·(m^2·d)$^{-1}$) [40], because organic matter is released in a larger amount from the sediment to the overlying water in DJK3. In the spatial distribution, the coefficient of variation of the NH_4^+-N content is 50.60% in DJK 4 and 74.30% in DJK 5, both of which are higher than that in DJK1-DJK3 (18.70%, 20.90%, and 20.10%, respectively) which were predominantly used for agricultural purposes.

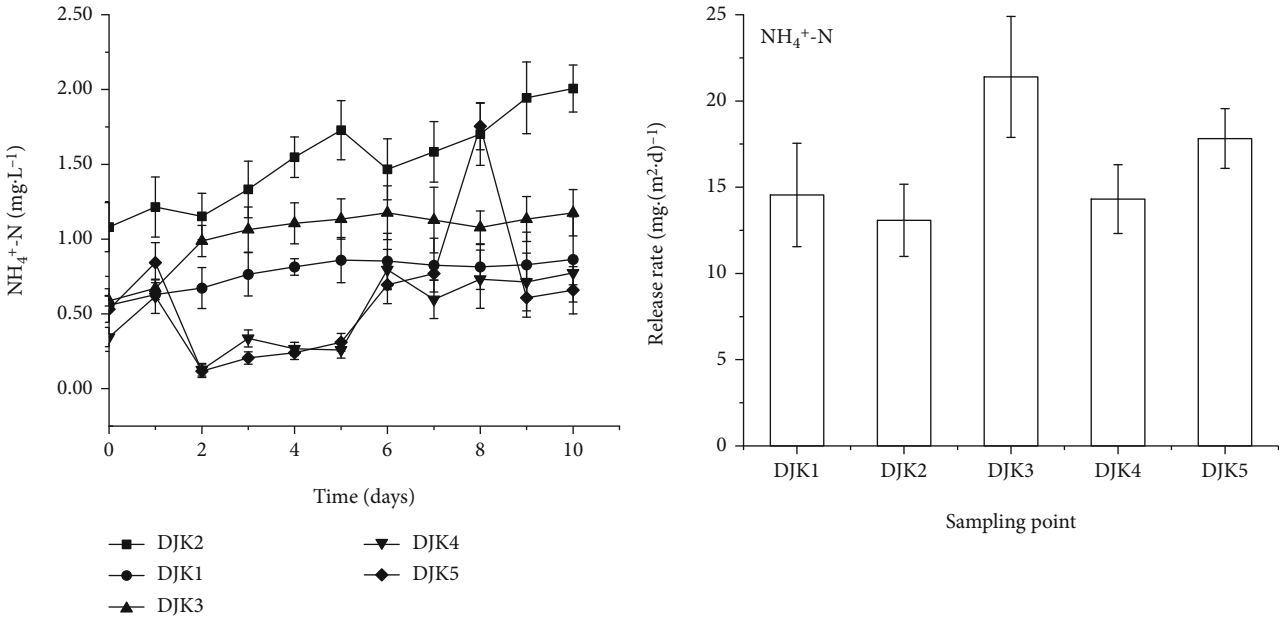

Figure 5: The content and release rate of NH_4^+-N in the overlying water.

The flow velocity is generally low at the bottom of the reservoir, making it difficult for nutrients to migrate to the overlying water through the sediment-interstitial water-overlying water interface. Under oxygen-rich conditions, the organic N in the sediment can be converted into inorganic ions such as NH_4^+ and NO_3^- by nitrification, which in turn can be diffused to the interstitial water and then to the overlying water and, as a result, have an effect on the NH_4^+-N content in the overlying water [37]. It is also noted that more NH_4^+ would be released under anaerobic conditions compared with that under aerobic conditions [41]. In addition, the decomposition of organic N results in the formation of NH_3 under hypoxia conditions but NH_4^+-N under acidic conditions. The NH_4^+ in the overlying water can also be diffused back to the sediment. The activities of microorganisms in the sediment and subsequent ammonification are reduced in an anoxic environment, and the reducing environment can also promote the denitrification, and finally, N is released into the atmosphere.

3.3. Release of PO_4^{3-}-P from Statically Cultured Sediments. The PO_4^{3-}-P concentration in the overlying water of five sampling points (DJK1-5) tends to increase over time in March, and the coefficient of variation in the reservoir (35.40% and 64.70% in DJK 4 and DJK 5, respectively) is significantly higher than that in the upstream tributary (21.40%, 15.80%, and 26.70% in DJK1-DJK3, respectively) (see Figure 6). The same phenomenon is also observed for the NH_4^+-N content in the overlying water. The release rate of PO_4^{3-}-P ranges from 3.06 mg·(m^2·d)$^{-1}$ to 6.02 mg·(m^2·d)$^{-1}$ with an average of 4.65 mg·(m^2·d)$^{-1}$, which is lower than that in the Meiliang Bay of the Tai Lake in July (76.55 mg·(m^2·d)$^{-1}$) [42], but slightly higher than that in the Wuli Lake of the Tai Lake (2.05 mg·(m^2·d)$^{-1}$) [43]. The highest release rate is found in DJK1, which is 1.29 times the average. The release rate of PO_4^{3-}-P decreases from the upstream tributary to the main reservoir, which is consistent with the contamination extent of the sediment. However, the release potential of P from the sediment is not entirely determined by the TP amount in the sediment. The release rate of P is high in water with severe organic contamination, which is related to the presence of a large amount of easily degradable matter [44]. At the beginning of the experiment when there is rich oxygen, the active organic debris in the sediment can release a large amount of PO_4^{3-} under the effect of microorganisms. PO_4^{3-} can be diffused to the interstitial water and then to the overlying water driven by the concentration gradient, forming the first release peak of PO_4^{3-}. On the other hand, an anaerobic environment would be formed under the effect of aerobic microbes, and iron and manganese oxides can be easily reduced to increase the solubility, resulting in the release of adsorbed P and thus the formation of the second release peak of PO_4^{3-}.

3.4. Annual Release Amount of N and P from the Sediment and Risk Evaluation. The increase of dam height in 2012 results in a total reservoir area of 1023 km^2, a storage capacity of 29.05 billion m^3 and an average water depth of about 30 m. After interception of contaminants, the annual release amount of PO_4^{3-}-P and NH_4^+-N from the newly submerged sediment into the overlying water is calculated to be 0.53×10^3 t and 1.17×10^3 t, respectively, using formula (7) based on the migration coefficient (K) obtained in experiments and the double-membrane diffusion model at an average temperature of 16°C for the Danjiangkou Reservoir. This differs substantially from the release amount of TP based on the SWAT model (1.86×10^4 t) [45], probably because some management practices such as moving the topsoil to cultivate fertility can reduce the endogenous contaminants in the sediment and consequently the release amount of TP. The

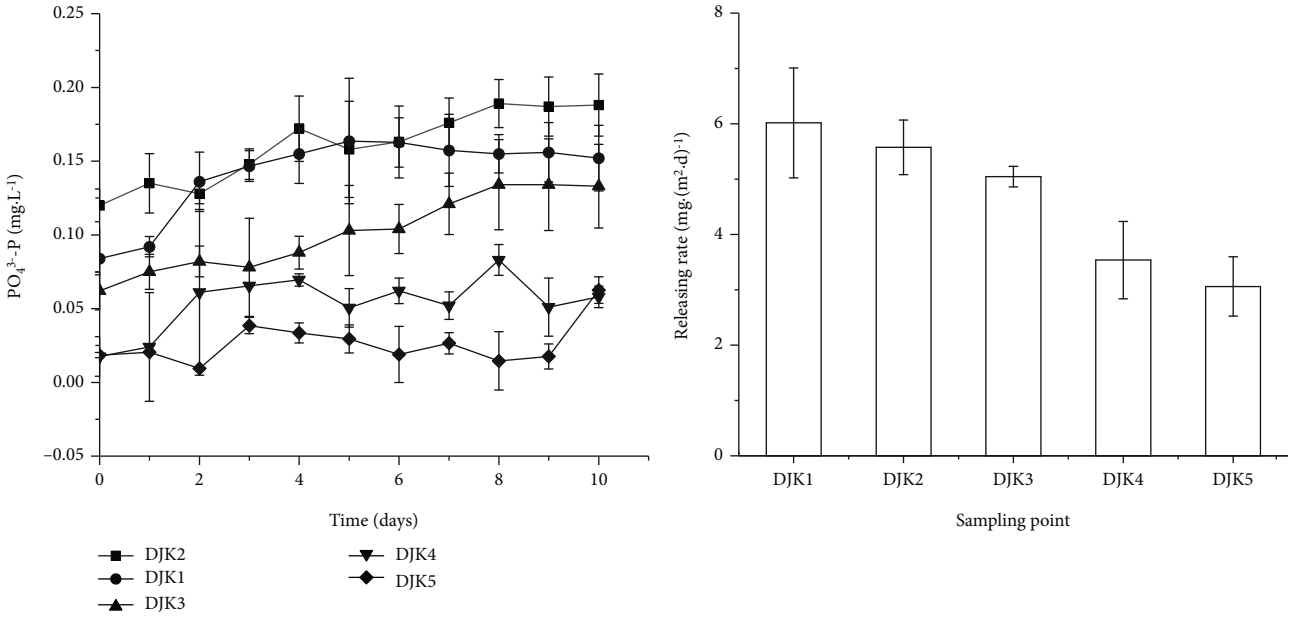

Figure 6: The content and release rate of PO_4^{3-}-P in the overlying water.

amounts of NH_4^+-N and PO_4^{3-}-P would be increased from 0.44 mg·L^{-1} and 0.02 mg·L^{-1} to 0.57 mg·L^{-1} and 0.02 mg·L^{-1} according to the average annual inflow (39.48 billion m^3) and to 0.62 mg·L^{-1} and 0.03 mg·L^{-1} according to the total reservoir storage (29.05 billion m^3), respectively. In theory, the water quality is between mesotrophy and eutrophication (0.03-0.05 mg·L^{-1} for TP and 0.31-0.65 mg·L^{-1} for TN) [46]. The reservoir storage is increased in the wet season from May to October, and the increase of temperature leads to an increase in dissolved carbon and microbial activities in the soil. As a result, a large amount of N and P accumulated in the soil would migrate to the overlying water, which is now the main factor affecting the water quality of the Danjiangkou Reservoir. In addition, the newly submerged area is often in alternative submergence-dry states, and land is cultivated for agricultural production under dry conditions [16], thus resulting in an increase in the diffusion of P and N from the sediment into the overlying water.

4. Conclusions

(1) The TP contents in the 0-10 cm sediment samples collected in the Danjiangkou Reservoir and its upstream tributary range from 402.40 mg·kg^{-1} to 560.30 mg·kg^{-1}, and the contents of different forms of P follow the order of IP > OP > Ca − P > Fe − P > LP. The spatial difference in P contents among the five sampling points may be related to the original land use type

(2) The average PO_4^{3-}-P and NH_4^+-N contents in the interstitial water of DJK 4 and DJK 5 are higher than those in the overlying water, and thus PO_4^{3-}-P and NH_4^+-N are likely to be released from the sediment to the overlying water

(3) Both experimental and calculation results show that N and P are easily released from the sediment to the overlying water, and thus endogenous contamination from the newly submerged sediment is an important factor affecting the water quality of the Danjiangkou Reservoir

Data Availability

The data used to support the findings of this study are available from the corresponding author upon request.

Conflicts of Interest

The authors declare no conflict of interest.

Acknowledgments

This study was supported jointly by the National Key Research and Development Project of China (No. 2019YFC0409202), the Foundation for Innovative Research Groups of the National Natural Science Foundation of China (No. 51721006), High Level Talent Support Program of North China University of Water Resources and Electric Power, and Special Support for Innovative Scientific and Technological Team of Water Ecological Security in the water source area of the middle route of South-to-North Water Diversion in Henan Province.

References

[1] C. X. Fan, L. Zhang, J. J. Wang, C. H. Zheng, G. Gao G, and S. M. Wang, "Process and mechanism of the effects of lake sediment dredging on endogenous release," *Science Bulletin*, vol. 3, no. 15, pp. 1523–1528, 2004.

[2] X. Li, L. X. Song, D. B. Ji et al., "Characteristics of nitrogen release at the sediment-water interface in the typical tributaries of the three gorges reservoir during the sensitive period in spring," *Environmental Science*, vol. 39, no. 3, pp. 1113–1121, 2018.

[3] W. Qu, L. L. Gong, Z. Y. Deng et al., "Estimation of nitrogen diffusion flux at the interface between sediment and overlying water before and after desilting in the South Han dyke channel in 2017," *Wetland Science*, vol. 18, no. 4, pp. 468–474, 2020.

[4] W. Wang, H. Yan, L. X. Jiao et al., "Characteristics and influencing factors of nitrogen endogenous load in sediments of Dianchi Lake," *China Environmental Science*, vol. 35, no. 1, pp. 218–226, 2015.

[5] K. R. Reddy, M. M. Fisher, and D. Ivanoff, "Resuspension and diffusive flux of nitrogen and phosphorus in a hypereutrophic lake," *Journal of Environmental Quality*, vol. 25, no. 2, pp. 363–371, 1996.

[6] Z. H. Zhibo, L. I. Tao, C. A. Qimeng, Z. H. Ju, and D. E. Huanguang, "Spatial distribution and stoichiometric characteristics of carbon, nitrogen and phosphorus in sediment Potamogeton crispus system of Dongping Lake," *Environmental Chemistry*, vol. 39, no. 8, pp. 2263–2271, 2020.

[7] H. Cui, S. Chen, C. Yang, W. Y. Tang, P. Ying, and H. B. Yi, "Characteristics of endogenous pollution and release of sediments from Hengshan reservoir in Yixing City," *Environmental Science*, vol. 425, no. 3, pp. 1–14, 2020.

[8] S. B. Liu, N. X. Chen, S. L. Hao, L. Yang, and Q. G. Chang, "Evaluation of ecological service value of soil and water conservation in Danjiangkou Reservoir area and its upper reaches," *Yellow River*, vol. 40, no. 2, pp. 88–92, 2018.

[9] H. Liu, J. Wu, J. Yin, M. Wang, and X. L. Chen, "Estimation and change of dynamic storage capacity of Danjiangkou Reservoir," *Chinese Journal of Applied Ecology*, vol. 29, no. 8, pp. 2658–2666, 2018.

[10] J. Z. Li, X. Jiang, S. H. Wang, W. W. Wang, and J. Y. Chen, "Characteristics and distribution of heavy metals in sediments of Danjiangkou reservoir," *China Environmental Science*, vol. 36, no. 4, pp. 1207–1217, 2016.

[11] Z. X. Zeng, P. Lei, H. Zhang, B. Q. Shan, and Y. H. Ye, "Nitrogen and phosphorus fractions and releasing characteristics of the soils from the representative water-level-fluctuating zone of Danjiangkou reservoir," *Journal of Environmental Science*, vol. 35, no. 5, pp. 1383–1392, 2015.

[12] W. Yin, W. Zhu, J. S. Lei, H .Y. Jia, and Z. X. Zeng, "Soil nutrient distribution of different land use types in typical watershed of Danjiangkou reservoir," *Journal of Yangtze River Basin Resources and Environment*, vol. 24, no. 7, pp. 1185–1191, 2015.

[13] Y. Wang, W. Xu, and W. Hu, "Distribution and pollution assessment of nitrogen and phosphorus in sediments of Chaohu Lake," *Environmental Science*, vol. 621, no. 6, pp. 1–17, 2020.

[14] J. F. Wang, J. G. Chen, W. Luo, H. Zhang, and P. P. Yu, "Comparative study on estimation methods of endogenous phosphorus release flux in sediments of Hongfeng Lake," *Earth and Environment Earth Environment*, vol. 46, no. 1, pp. 1–6, 2018.

[15] B. Li, Y. Wang, Y. Zheng et al., "Temporal and spatial variation of nutrients and heavy metals in surface sediments before and after water transfer in Danjiangkou Reservoir," *Environmental Science*, vol. 39, no. 8, pp. 3591–3600, 2018.

[16] L. Q. Zhang, M. Wu, and Y. S. Wan, "Study on countermeasures for water quality security of the Danjiangkou Reservoir," *Chinese Water Conservancy*, vol. 36, no. 1, pp. 44–47, 2018.

[17] S. D. Bao, *Soil Agrochemical Analysis*, China Agricultural Press, Beijing, China, 3rd edition, 1999.

[18] V. Ruban and P. Pardo, "Harmonized protocol and certified reference material for the determination of extractable contents of phosphorus in freshwater sediments: a synthesis of recent works. Fresenius," *Journal of Analytical Chemistry*, vol. 78, no. 5, pp. 125–136, 2001.

[19] K. Pettersson, "Phosphorus characteristics of settling and suspended particles in Lake Erken," *Science of the Total Environment*, vol. 266, no. 1-3, pp. 79–86, 2001.

[20] C. L. Jin, Z. Q. Guo, D. C. Wang, and W. B. Zhu, "Brief introduction to water resources quality," *Assessment of China*, vol. 45, no. 5, pp. 58–66, 1996.

[21] L. Zhang, *Study on Water Quality Model of Nanhu Lake*, Wuhan University of Technology, 2006.

[22] B. Li, S. M. Ding, C. X. Fan et al., "Estimation of releasing fluxes of sediment nitrogen and phosphorus in Fubao Bay in Dianchi Lake," *Environmental Science*, vol. 32, no. 1, pp. 114–120, 2018.

[23] F. Y. Zheng, L. Tan, X. Chen, B. Li, T. T. Zhong, and Q. D. Cai, "Spatial distribution of nitrogen and phosphorus and pollution evaluation for sediment in Xiangxi Bay," *Asian Journal of Ecotoxicology*, vol. 13, no. 4, pp. 49–59, 2018.

[24] R. W. Li, "Sediment pollution and environmental sedimentology," *Advances in Earth Science*, vol. 13, no. 4, pp. 81–85, 1998.

[25] W. Yang and X. H. Yan, "Soil phosphorus cycle and its impact on soil phosphorus loss," *Soil and Environment*, vol. 34, no. 3, pp. 256–258, 2001.

[26] C. H. Meng and B. Zhao, "Vertical distribution of species of nitrogen and phosphorus in the sediments of Donghu Lake," *Environmental Science*, vol. 34, no. 7, pp. 1831–1837, 2008.

[27] B. Zhu, Z. Wang, and X. Zhang, "Phosphorus fractions and release potential of ditch sediments from different land uses in a small catchment of the upper Yangtze River," *Journal of Soils and Sediments*, vol. 12, no. 2, pp. 278–290, 2012.

[28] Q. X. He, S. Zhang, Z. X. Fang, and Y. Q. He, "Geochemical morphological distribution characteristics of nitrogen and phosphorus in sediments of Daya Bay," *Tropical Ocean*, vol. 8, no. 2, pp. 38–45, 1992.

[29] L. Zhao, X. Jiang, W. W. Wang, S. H. Wang, L. Chang, and J. Y. Chen, "Occurrence characteristics and bioavailability of different forms of nitrogen in surface sediments of Danjiangkou Reservoir," *Journal of Yangtze River Resources and Environment*, vol. 25, no. 4, pp. 630–637, 2016.

[30] S. L. Wen, Y. Q. Gong, T. Wu et al., "Characteristics and exchange flux of nitrogen and phosphorus in sediment-water interface of Yuqiao Reservoir," *Environmental Science*, vol. 39, no. 5, pp. 2154–2164, 2018.

[31] M. S. Bai, Y. Ban, P. Diplas, and F. Xiao, "Quantitative assessment of hydrological spatiotemporal changes in the middle and lower reaches of the Hanjiang River after Danjiangkou reservoir impoundment and its ecological impact," *Journal of Yangtze River Resources and Environment*, vol. 26, no. 9, pp. 1476–1487, 2017.

[32] R. N. Glud, J. K. Gundersen, N. P. Revsbech, and B. B. Jørgensen, "Effects on the benthic diffusive boundary layer imposed by microelectrodes," *Limnology and Oceanography*, vol. 39, no. 2, pp. 462–467, 1994.

[33] Z. Q. Wang, B. Li, and R. J. Liang, "Comparative study on endogenous release of nitrogen and phosphorus in Nansi Lake, China," *Journal of Environmental Science*, vol. 33, no. 2, pp. 487–493, 2013.

[34] N. V. Vladimir, *Statistical Learning Theory*, Publishing House of Electronics Industry, Beijing, China, 2004.

[35] J. J. Liu, C. Y. Dong, Y. Q. Song, and P. D. Sun, "The seasonal variations of nitrogen and phosphorus release and its fluxes from the sediments of the Beili Lake in the Hangzhou West Lake," *Chinese Journal of Ecology*, vol. 32, no. 24, pp. 7932–7939, 2012.

[36] Z. Q. Wang, B. Li, X. H. Hu, and J. B. Liang, "Distribution characteristics of nitrogen, phosphorus, organic matter and their correlation analyses in the sediments of Nansi Lake China," *Soil Science Bulletin*, vol. 44, no. 4, pp. 867–874, 2013.

[37] P. Hohener and R. Gachter, "Nitrogen cycling across the sediment-water interface in an eutrophic, artificially oxygenated lake," *Aquatic Sciences*, vol. 56, no. 2, pp. 115–132, 1994.

[38] B. Li, Z. Q. Wang, Q. S. Wang, and J. B. Cuan, "Distribution characteristics and correlations of phosphorus in sediment and interstitial water of Nansi Lake, Shandong Province of East China in summer and winter," *Chinese Journal of Applied Ecology*, vol. 24, no. 6, pp. 1699–1706, 2013.

[39] C. Fan, L. Zhang, X. Bao et al., "Migration mechanism of biogenic elements and their quantification on the sediment-water Interface of Lake Taihu: I. spatial variation of the ammonium release rates and its source and sink fluxes," *Journal of Lake Science*, vol. 16, no. 1, pp. 11–21, 2004.

[40] B. Li, S. M. Ding, C. X. Fan et al., "Estimation of releasing fluxes of sediment nitrogen and phosphorus in Fubao Bay in Dianchi Lake," *Environmental Science*, vol. 31, no. 1, pp. 114–120, 2008.

[41] L. J. Hou, M. Liu, and S. Y. Xu, "Effects of environmental factors on endogenous phosphorus release from sediment in Suzhou City," *Shanghai Environmental Science*, vol. 290, no. 4, pp. 258–260, 2003.

[42] H. Xu, L. Zhang, J. Shang, and C. Fan, "Study on ammonium and phosphate fluxes at the sediment-water Interface of Lake Taihu using flow-through incubation," *Journal of Ecology and Rural Environment*, vol. 25, no. 4, pp. 66–71, 2009.

[43] L. Zhang, C. X. Fan, J. J. Wang, and C. H. Zheng, "Space-time dependent variances of Ammonia and phosphorus flux on sediment-water Interface in Lake Taihu," *Environmental Science*, vol. 11, no. 8, pp. 1537–1543, 2006.

[44] J. Wang, Y. Y. Yuan, H. M. Ye, X. F. Yang, and L. Tao, "Phosphorus forms and bioavailability in sediments of different rivers entering the lake in Hongze Lake," *China Environmental Science*, vol. 40, no. 10, pp. 4568–4579, 2020.

[45] X. Wang and F. Hao, "Zhang optimization of the best management measures for non-point source pollution in Danjiangkou Reservoir Basin," *China Environmental Science*, vol. 33, no. 7, pp. 1335–1343, 2013.

[46] T. Q. Yu, L. Wang, Y. Han, P. D. Ma, H. L. Wang, and J. M. Dong, "Fuzzy evaluation of water eutrophication in Xiaojiang River basin of three gorges reservoir area," *Journal of Agro-Environment Science*, vol. 45, no. 4, pp. 1427–1431, 2008.

Hindawi
Journal of Sensors
Volume 2021, Article ID 8875606, 14 pages
https://doi.org/10.1155/2021/8875606

Research Article

Unmanned Aircraft System- (UAS-) Based High-Throughput Phenotyping (HTP) for Tomato Yield Estimation

Anjin Chang[1], **Jinha Jung**[2], **Junho Yeom**[3], **Murilo M. Maeda**[4], **Juan A. Landivar**[5,6], **Juan M. Enciso**[6], **Carlos A. Avila**[6,7] and **Juan R. Anciso**[6,7]

[1]*School of Engineering and Computing Science, Texas A&M University-Corpus Christi, Corpus Christi, TX 78412, USA*
[2]*Lyles School of Civil Engineering, Purdue University, West Lafayette, IN 47907, USA*
[3]*Department of Civil Engineering, Gyeongsang National University, Jinju, Gyeongsangnam-do 52828, Republic of Korea*
[4]*Texas A&M AgriLife Research & Extension Center at Lubbock, Lubbock, TX 79403, USA*
[5]*Texas A&M AgriLife Research & Extension Center at Corpus Christi, Corpus Christi, TX 78406, USA*
[6]*Texas A&M AgriLife Research & Extension Center at Weslaco, Weslaco, TX 78596, USA*
[7]*Department of Horticultural Sciences, Texas A&M University, College Station, TX 77843, USA*

Correspondence should be addressed to Junho Yeom; junho.yeom@gnu.ac.kr

Received 1 August 2020; Revised 8 January 2021; Accepted 25 January 2021; Published 9 February 2021

Academic Editor: Jingwei Wang

Yield prediction and variety selection are critical components for assessing production and performance in breeding programs and precision agriculture. Since plants integrate their genetics, surrounding environments, and management conditions, crop phenotypes have been measured over cropping seasons to represent the traits of varieties. These days, UAS (unmanned aircraft system) provides a new opportunity to collect high-quality images and generate reliable phenotypic data efficiently. Here, we propose high-throughput phenotyping (HTP) from multitemporal UAS images for tomato yield estimation. UAS-based RGB and multispectral images were collected weekly and biweekly, respectively. The shape of the features of tomatoes such as canopy cover, canopy, volume, and vegetation indices derived from UAS imagery was estimated throughout the entire season. To extract time-series features from UAS-based phenotypic data, crop growth and growth rate curves were fitted using mathematical curves and first derivative equations. Time-series features such as the maximum growth rate, day at a specific event, and duration were extracted from the fitted curves of different phenotypes. The linear regression model produced high R^2 values even with different variable selection methods: all variables (0.79), forward selection (0.7), and backward selection (0.77). With factor analysis, we figured out two significant factors, growth speed and timing, related to high-yield varieties. Then, five time-series phenotypes were selected for yield prediction models explaining 65 percent of the variance in the actual harvest. The phenotypic features derived from RGB images played more important roles in prediction yield. This research also demonstrates that it is possible to select lower-performing tomato varieties successfully. The results from this work may be useful in breeding programs and research farms for selecting high-yielding and disease-/pest-resistant varieties.

1. Introduction

Vegetable production is one of the most important components in agriculture, also with grain foods. Commercial vegetable production in the United States was approximately 33.9 million tons and $12.9 billion in 2018 [1]. Notably, tomatoes have the highest values of utilized production, and the value of tomatoes increased by over 10 percent ($1.9 billion) in 2018. Recently, tomato production has faced constant pressure from biotic and abiotic stresses such as climate, disease, and pest that can cause significant loss of production and fruit quality [2]. To identify the potential yield performance in a tomato, advanced phenotyping that can effectively map, monitor, and predict plant traits is required. Despite the importance of vegetable production, the traditional method to develop new cultivars in breeding programs, monitor crop growth/disease, and predict yield has still employed hand-sampling measurements, which are

destructive, labor-intensive, time-consuming, and expensive [3, 4].

Precision agriculture requires large amounts of data to ensure informed decision-making at the specific crop and plot level. Remotely sensed data have been used to collect data in a timely or near real-time manner for agricultural applications because uncontacted measurements by sensors have become nondestructive and more efficient in recent decades [5]. However, satellite-based and airborne remote sensing is often unable to provide the suitable data required for plant- or plot-level assessment due to data acquisition being affected by cloud cover, cost, low spatial resolution, and limited temporal resolution [6]. In recent years, the unmanned aerial systems (UASs), namely, unmanned aerial vehicles (UAVs) or drones, have been regarded as a promising technology with high potential for agricultural applications such as crop growth monitoring, disease monitoring, yield prediction, and biomass estimation [7, 8]. UAS also provides new opportunities to collect data with finer spatiotemporal resolution for high-throughput phenotyping (HTP). Additionally, the hardware cost of UAS platforms and sensors is decreasing, creating a lower entry barrier so that students, researchers, and stakeholders can easily adopt UAS. These new technologies are an alternative solution to address the limitations of manual or conventional remote sensing methods to measure crop characteristics [3, 4].

In several studies, it has been proven that UAS-based remotely sensed data could measure crop traits such as canopy cover, plant height, and vegetation indices more frequently and consistently over a larger area than manual measurement [3, 9, 10]. The aboveground biomass (AGB) of arable crops has also been estimated by the UAV-based height model [11]. Jiang et al. [12] and Li et al. [13] also estimated AGB using UAV-based multispectral and hyperspectral images for rice and potatoes, respectively. Yield prediction using UAS data is another main topic in precision agriculture. Jung et al. [14] showed that UAS-based HTP could provide the rank of cotton genotypes, and the top high-yield varieties could produce yields 10 percent higher, while Maimaitijiang et al. [15] estimated soybean biomass from a UAS-based canopy volume model. Recent research has also adopted the artificial intelligence (AI) technique for biomass and yield estimation [16, 17]. Plant stresses such as drought, disease, nutrition deficiencies, pests, and weeds have been monitored and assessed by UAVs [18]. Previous studies extracted crop parameters from UAS data and used the variables directly to develop various methods, but UAS-based measurements could fluctuate due to errors depending on data collection conditions such as weather, sensors, date, and time.

Despite the commercial importance of tomatoes, few studies have employed UAS data for yield estimation. Enciso et al. [19] validated UAV measurements compared with field data for tomato varieties. Johansen et al. [20] used a time series of UAS imagery to monitor phenotypic traits of individual tomato plants, including canopy area, condition, and growth rate, to quantify responses to salinity stress and identify tomato plant accessions that performed the best in terms of yield. Johansen et al. [21] also proposed modelling and predicting the biomass and yield of individual tomato plants on the farm scale through field- and UAS-based phenotyping. In recent years, a machine learning framework was developed for tomato yield estimation using multitemporal remote sensing data collected from UAS [22]. However, these initial works directly used limited time-series data over the entire cropping season and phenotypes.

In this study, we propose a novel method to extract advanced phenotypic features from UAS data in the tomato field for yield estimation and variety selection. The growth and growth rate curves of phenotypic data were generated from multitemporal UAS data to extract crop traits indicating growth timing and speed over the whole cropping season. Factor analysis was applied to analyse more valuable phenotypic features. Finally, we generated a yield estimation model in the tomato field and then demonstrated the possibility of selecting the high-performing varieties and eliminating the lower-performing varieties.

2. Study Area and Materials

2.1. Study Area. The study area was located at the Texas A&M (Agriculture and Mechanical) AgriLife Research and Extension Center in Weslaco, Texas, USA (latitude: 26°9′24″N, longitude: 97°57′46″W) (Figure 1(a)). Tomato fields consist of two major components for identifying/characterizing resistance against insect-vector transmitted diseases and evaluating planting dates and mulch cover to extend tomato production. The western side of the study area was selected to apply the UAS-based phenotyping method for high-yielding variety selection. Each experimental plot which consisted of four individual tomato plants was established with three planting dates (Feb. 29, Mar. 16, and Mar. 31, 2016), plastic mulch covers (black, white, and bare), and cultivars (9 different varieties). Each variety was replicated three times per planting date and mulch cover in randomized deployment. Tomatoes were harvested 3 times from each plot, and the sum (total yield) of the three harvests was used for the yield prediction model and evaluation.

Ground control points (GCPs) were installed around the study area for precise georeferencing and coregistration of processed UAS data, including orthomosaic images and digital surface models (DSMs) [3]. Although the approximate location of all images was recorded by onboard GPS of UAV, a total of 9 GCPs were installed in this study (Figures 1(b) and 1(c)). Eight GCPs were located around the tomato site, and one GCP was installed in the middle of the study area to correct bowling effects by structure from motion (SfM), which is the most frequently used algorithm to generate orthomosaic images from UAS data [23]. The center coordinate of all GCPs was measured by using an APS-3 Real-Time Kinematic (RTK) GPS (Altus Positioning System, Inc., California, USA).

2.2. UAS Platforms and Sensors. DJI Phantom Products (DJI, Shenzhen, China), which is the most popular commercialized model, and the UAV platform developed by the research team consisting of an Iris quadcopter (3DR, Berkeley, USA) and a Canon S110 digital camera (Canon, Tokyo, Japan),

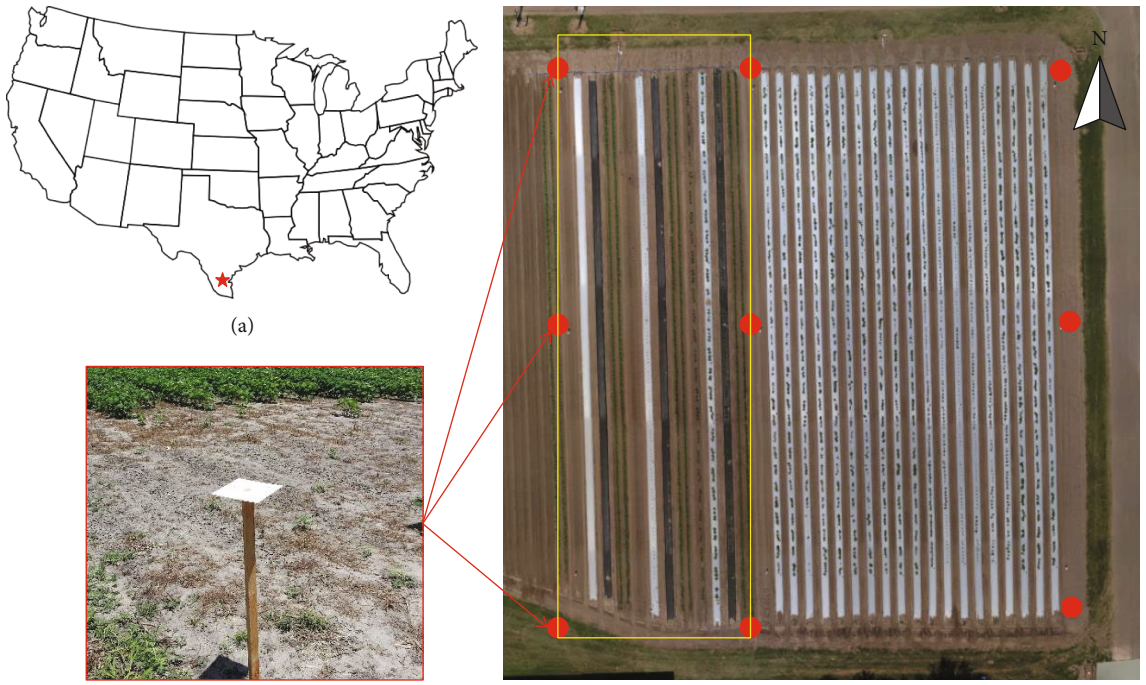

Figure 1: (a) The approximate location of the study area in Texas and (b) a ground photo of the GCP in the field. (c) Overall orthomosaic image of the tomato area covered by UAS. The yellow rectangle indicates the selected field for the high-throughput phenotyping experiment in this study. Red dots are the locations of 9 GCPs.

Figure 2: The UAS systems developed to collect (a) RGB and (b) multispectral imagery.

Table 1: The specification of RGB and multispectral camera.

Sensor	Platform	Camera	Sensor size (mm)	Focal length (mm)	FOV (°)	Image size (pixels)
RGB	Phantom 2 Vision+	FC200	6.17 × 4.55	2.5 mm	120°	4384 × 3288
	Phantom 4	FC330	6.17 × 3.47	20 mm	94°	4000 × 3000
	3DR Iris	Cannon S110	7.6 × 5.7	24 mm	84°	4000 × 3000
Multispectral	3DR X8	Tetracam ADC Snap	6.59 × 4.9	8.43 mm	38°	1280 × 1024

which is a 12-megapixel camera, were used to collect RGB (Figure 2(a)). For multispectral data, another UAS system was developed with X8 octocopter (3DR, Berkeley, USA) and ADC Snap (Tetracam, Chatsworth, UAS) (Figure 2(b)), which can collect 3 bands, including the wavelengths of green, red, and near-infrared (NIR). The Corpus Christi research group designed a mount to integrate the multispectral camera to the bottom of the X8 platform. The mount was printed out by a 3D printer and assembled with dampers. The developed systems collected geotagged RGB and

Table 2: The flight log of RGB datasets.

Date	Platform (sensor)	Altitude (m)	Overlap (%)	Resolution (cm)
2016/03/23	Iris (S110)	40	80 × 70	1.26
2016/03/28	Iris (S110)	30	80 × 70	0.98
2016/03/29	Iris (S110)	30	80 × 70	0.99
2016/03/31	Phantom 2 Vision+ (FC200)	30	84	0.84
2016/04/14	Phantom 4 (FC330)	30	90	1.32
2016/04/19	Iris (S110)	30	80 × 70	0.96
2016/04/21	Phantom 4 (FC330)	30	90	1.35
2016/04/25	Iris (S110)	30	80 × 70	1.04
2016/05/04	Phantom 4 (FC330)	30	90	1.34
2016/05/10	Iris (S110)	30	80 × 70	0.95
2016/05/12	Phantom 4 (FC330)	30	90	1.40
2016/05/16	Iris (S110)	30	80 × 70	0.96
2016/05/23	Iris (S110)	30	80 × 70	1.00
2016/05/24	Iris (S110)	30	80 × 70	0.93
2016/05/25	Phantom 4 (FC330)	30	90	1.34
2016/06/09	Phantom 4 (FC330)	30	90	1.01
2016/06/16	Phantom 4 (FC330)	30	90	1.00
2016/06/22	Phantom 4 (FC330)	20	85	0.82

Table 3: The flight log of multispectral datasets.

Date	Platform (sensor)	Altitude (m)	Overlap (%)	Resolution (cm)
2016/03/31	X8+ (Tetracam ADC Snap)	40	65 × 60	2.40
2016/04/14		40	65 × 65	2.07
2016/04/21		40	65 × 65	2.05
2016/05/04		40	65 × 85	2.17
2016/05/12		50	73 × 65	2.68
2016/05/25		40	65 × 60	2.18
2016/06/09		50	73 × 65	2.65
2016/06/22		40	75 × 80	1.88

multispectral images. Table 1 shows the specification of the UAS-based RGB and multispectral system used in this study for data collection.

2.3. UAS Data Collection. Two flight teams operated separate UAV platforms and collected data for more frequent time-series datasets. The Corpus Christi research group used the DJI Phantom series (Phantom 2 and 4) and X8 platform with a multispectral camera to collect RGB and a multispectral imagery, respectively, every 2 weeks. RGB and multispectral UAS systems operated separately for more efficient flights. The flight conditions including altitude, flight speed, and camera setting should be different since RGB and multispectral cameras have different specifications such as field of view (FOV) and focal length. Another flight team in Weslaco collected RGB imagery using the Iris platform with a Canon camera.

Tables 2 and 3 show the flight logs for RGB and multispectral images, including parameters such as flight altitude, image overlap, and resolution. 18 flights were conducted to collect RGB images for 3 months (March~June 2016), while the multispectral UAS system flew every other week. The resolution is the ground sampling distance (GSD) of the orthomosaic image generated by the SfM algorithm.

3. UAS-Based High-Throughput Phenotyping (HTP)

3.1. Preprocessing of UAS Images

3.1.1. Orthomosaic Image DSM Generation. PhotoScan Pro software (Agisoft LLC, St. Petersburg, Russia) was used to apply the SfM algorithm to generate DSM and orthomosaic images from UAS raw images. The SfM algorithm is one of the most frequently used commercial software to generated

(a) (b)

Figure 3: (a) Ground photos of reflectance panels (5%, 12%, 33%, and 52%) and (b) subset image of reflectance panes in color-infrared (CIR) orthomosaic image. The colored rectangles indicate the region of interest (ROI) to calculate the average DN of the panels.

3D point clouds, DSMs, and orthomosaics from UAS raw images. The GPS coordinates of GCPs were input into the software for precision georeferencing and coregistration of DSM and orthomosaic. Although the image location of UAS raw images was recorded in the metadata of geotagged images, the precision level was not enough, which could cause the bowl effect, one major error of the SfM algorithm. GCPs with high accuracy and good deployment can solve these problems when the SfM algorithm is applied to UAS raw images [24]. DSM and orthomosaics of RGB and multispectral images were generated using PhotoScan Pro with GCPs. The geolocation accuracy of DSM and orthomosaics was less than one pixel.

3.1.2. Radiometric Calibration for Multispectral Image. Radiometric calibration for multispectral images was conducted to calculate more accurate vegetation index such as NDVI. In this study, we used radiometric calibration panels to convert the digital number (DN) in the multispectral orthomosaic image to the reflectance value using the empirical line method (ELM) [25]. Four reflectance panels (5%, 12%, 33%, and 52%) were placed in the tomato field before flying the multispectral platform. The average DN of each reflectance panel in the multispectral orthomosaic image was compared with the actual reflectance values measured in the laboratory (Figure 3). The empirical line (EL) was generated for each flight. The entire pixel value of the multispectral orthomosaic image was converted to reflectance by the developed EL.

3.2. Product Generation from UAS Data

3.2.1. Plot Polygon Generation. The rectangular polygons were generated as plot boundaries for each variety to extract plot-based phenotypic information (Figure 4(a)). To create rectangles of the same size (1×2 meters) according to plot design, the centerline of four individual plants in each plot was manually delineated by using the canopy area in the orthomosaic image on March 28, 2018. The angle and center of the line were considered to determine the polygons automatically. The plot boundary properly included four individual plants (Figure 4(b)). The pixels within the polygon were selected to extract phenotypic data of a single variety. In the study area, there were 81 polygons (9 cultivars $\times$ 3 mulches $\times$ 3 replications) per planting date.

3.2.2. Geospatial Product Generation. Canopy cover (CC), canopy volume (CV), excessive greenness index (ExG), and normalized difference vegetation index (NDVI) were generated from RGB and multispectral orthomosaic images and DSMs. The canopy is the aboveground portion of a plant or crop. As the canopy is strongly related to crop status, health, and environment, canopy cover is a useful way of monitoring crop development and productivity. Although the canopy cover has been measured using subjective methods [26, 27], canopy pixels in RGB images, which mean green areas, can be extracted nondestructively and easily. The Canopeo algorithm, defined as Equation (1), was employed to classify canopy pixels from RGB orthomosaic images [28]. Since there are three plastic mulch covers (black, white, and bare) in the study area, two more conditions to determine noncanopy pixels were considered as Equation (2):

$$\text{Canopy} = \left(\frac{\text{Red}}{\text{Green}} < P_1\right) \text{and} \left(\frac{\text{Blue}}{\text{Green}} < P_2\right) \text{and} \quad (2\text{Green} - \text{Red} - \text{Blue} > P_3), \tag{1}$$

$$(\text{Red} + \text{Green} + \text{Blue} < P_4) \text{ and } (\text{Green} - \text{Blue} > P_5), \tag{2}$$

where P_1 and P_2 are parameters to classify green pixels and P_3 is a parameter that sets the minimum excess green index. P_1 and P_2 indicate the predominant green of each pixel. P_3 effectively classifies dark or gray pixels that cannot be adequately discriminated using P_1 and P_2. Basically, we used the suggested P_1, P_2, and P_3 values (0.95, 0.95, and 20) in a previous study [28]. P_4 is the sum of the digital number (DN) of all bands at each pixel, while P_5 indicates the difference between the green and blue bands. Nevertheless, the parameters were empirically adjusted depending on the color tone and hue of each RGB orthomosaic image. P_4 and P_5 were used to remove white and black plastic mulch covers,

Figure 4: The generated polygons of the plot boundary for HTP in (a) the experimental area of three planting dates and mulch cover. (b) The subset of a single polygon on white plastic, including four individual plants of the same cultivar and centerline of plants (yellow line).

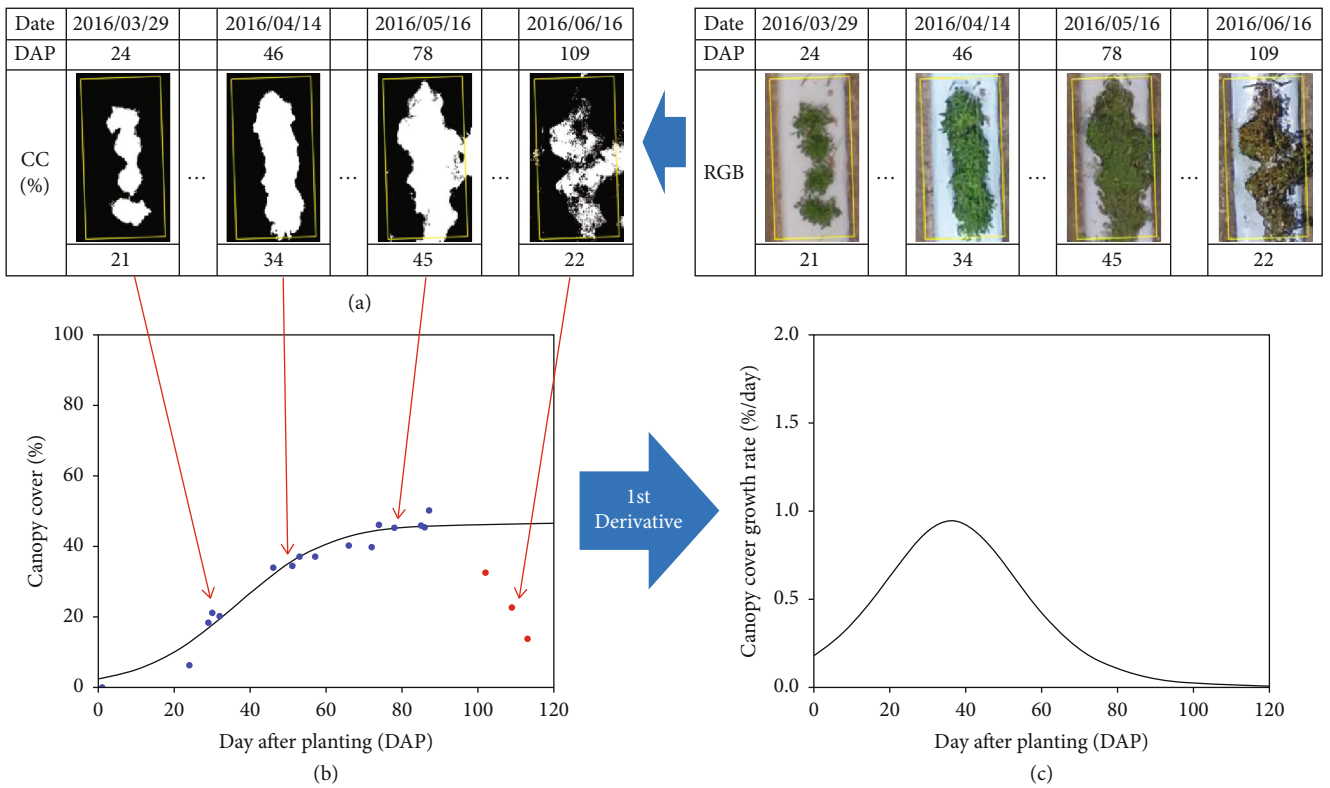

Figure 5: Example of CC growth and growth rate curve from RGB. (a) CC in individual plot polygons was calculated with different dates and days after planting (DAPs). Scatter plot and sigmoid curve are generated in (b). Each point means UAS measurement. The last 3 UAS measurements acquired in June were not used to fit the sigmoid curve. (c) The 1st derivative was calculated as the growth rate curve.

respectively. As white and black mulch showed very high or low DN, P_4 and P_5 with values 600 and 30 were employed to filter out, respectively. A CC map indicating canopy and noncanopy pixels was generated. The canopy area in each plot polygon was divided by polygon size to calculate the CC value of all varieties.

To calculate the CV, a canopy height model (CHM) was generated by subtracting the digital terrain model (DTM) from DSM for each UAS flight. DTM was created from the 3D point cloud data generated from earlier UAS flights on March 23, 2016. The 3D points were classified into ground and nonground points using LAStools, and DTM was generated by the natural neighbor interpolation algorithm from the ground points. The pixel value from CHM, which means canopy height, was multiplied by pixel size to calculate pixel volume. The sum of the pixel volume in the plot polygon was considered CV of each variety.

Two vegetation indices, ExG and NDVI, were generated from RGB and multispectral orthomosaic images, respectively. ExG was calculated from RGB color with Equation (3), while NDVI was generated from multispectral image with Equation (4) [29]. Only ExG and NDVI values of the

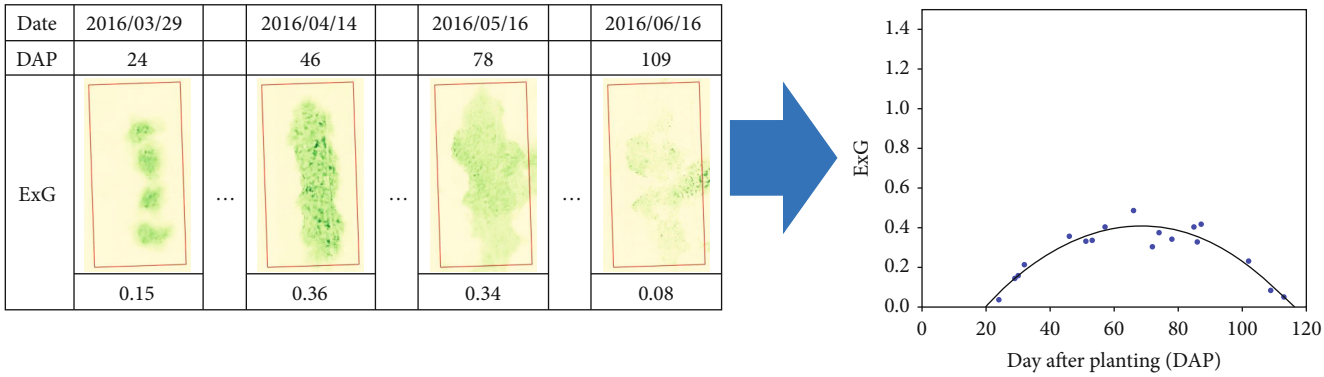

Figure 6: Example of ExG progression curve. (a) ExG in individual plot polygons was calculated with different dates and DAPs. Heath leaves are indicated as greener pixels. (b) All 18 UAS measurements were used to fit the 3rd polynomial curve.

canopy area in the plot polygon were selected to calculate the average of ExG and NDVI values as the representative for each variety:

$$\mathrm{ExG} = 2g - r - b, \tag{3}$$

where

$$\begin{aligned} r &= \frac{\mathrm{Red}}{\mathrm{Red} + \mathrm{Green} + \mathrm{Blue}}, \\ g &= \frac{\mathrm{Green}}{\mathrm{Red} + \mathrm{Green} + \mathrm{Blue}}, \\ b &= \frac{\mathrm{Blue}}{\mathrm{Red} + \mathrm{Green} + \mathrm{Blue}}, \\ \mathrm{NDVI} &= \frac{\mathrm{Red} - \mathrm{NIR}}{\mathrm{Red} + \mathrm{NIR}}. \end{aligned} \tag{4}$$

3.3. Feature Extraction from Time-Series UAS Data

3.3.1. Growth and Growth Rate Curve. Multitemporal phenotypes including CC, CV, ExG, and NDVI enabled advanced phenotypic features. Time-series measurements of these phenotypes were used to model the growth pattern of each variety. Sigmoidal and polynomial functions were adopted to fit the optimal curve depending on the input variables. CC and CV measurements over the growing season were fitted with a sigmoid function to generate growth curves (Figure 5). Although there were 18 UAS observations, the last three measurements were not selected for sigmoidal curve fitting. The first derivatives of the growth curve were generated as the growth rate curves.

The 3rd polynomial function was fitted for 18 ExG observations as ExG progression curves (Figure 6). The ExG progression curve was divided into two parts by the date at the maximum ExG value. The left and right sides from the date indicate the increasing and decreasing canopy growth periods, respectively. In terms of NDVI, due to weather conditions and data acquisition time, four multispectral images were selected based on the data quality to fit the 2nd polynomial curve. The multispectral images collected early in the morning contained a significant amount of shadow and saturated pixels caused by a low sun angle and effect from the surrounding windbreaker plot. The NDVI progression curve was also divided into two parts, ExG.

3.3.2. Phenotypic Feature Extraction. In this study, a total of 22 phenotypic features were extracted from growth and progression models derived from time-series UAS measurements (Table 4). The maximum CC (F1) and maximum CV (F5) were extracted from the sigmoid curve (Figure 7(a)). From the growth rate curves, features including the maximum growth rate (F2 and F6), day after planting (DAP) at the maximum growth rate (F3 and F7), and duration over the half maximum period (F4 and F8) from DAPs of half maximum were calculated (Figure 7(b)). The maximum ExG value (F9) and DAP at the maximum ExG value (F10) were extracted from the ExG progression curve. The ExG measurements of both periods were then fitted with linear models to calculate the slopes of increasing and decreasing canopy periods (F11 and F15). The maximum values of the increasing and decreasing lines at the maximum ExG DAP (F12 and F16), duration (F13 and F17), and area of each period (F14 and F18) were calculated from the fitted curves (Figure 7(c)). Four features were extracted from the NDVI progression curve. The maximum NDVI (F19) and DAP at maximum NDVI (F20) were also extracted from the NDVI progression curve. The increasing NDVI slope (F21) and decreasing NDVI slope (F22) were also calculated from the progression curve by connecting the first observation with the maximum NDVI value and the last NDVI observation with the maximum NDVI value.

4. Results and Discussion

4.1. Correlation Coefficient of Phenotypic Features and Harvested Yield. Most researches have tried to find the features highly correlated with yield using UAV data and reported a positive correlation between vegetation indices and both biomass and yield [30–32]. A few studies also focus on extracting discrete phenotypic data, such as canopy cover, canopy height, and vegetation indices, related to biomass and yield for tomato [21, 33]. Although they could predict biomass and yield using UAV-derived phenotypes and

Table 4: Description of features extracted from CC, CV, ExG, and NDVI models.

Variable name	UAS product	Feature description
F1	CC	Maximum value of CC
F2		Maximum growth rate of CC
F3		DAP at maximum growth rate of CC
F4		Duration over the half maximum period of CC
F5	CV	Maximum value of CV
F6		Maximum growth rate of CV
F7		DAP at maximum growth rate of CV
F8		Duration over the half maximum period of CV
F9	ExG	Maximum of ExG value
F10		DAP at maximum of ExG value
F11		Increasing slope of ExG
F12		Maximum value of increasing line at maximum ExG DAP
F13		Duration of increasing ExG period
F14		Area of increasing period of ExG
F15		Decreasing slope of ExG
F16		Maximum value of decreasing line at maximum ExG DAP
F17		Duration of decreasing ExG period
F18		Area of decreasing period of ExG
F19	NDVI	Maximum NDVI value
F20		DAP at maximum NDVI value
F21		Increasing slope of NDVI
F22		Decreasing slope of NDVI

environment conditions, data volume was limited to consider the whole growing cycle. It is impossible to collect UAV data at the same DAP in different seasons. In addition, the discrete phenotype values such as vegetation indices should be varied according to the conditions of the surrounding environment and UAV (platform and sensors).

Despite these challenges, UAS-based phenotypic features can play an important role in assisting plant breeding efforts. As supports such as tomato cages and wooden sticks should be installed in tomato fields, the plant height (PH) does not show significant variability to indicate the difference in tomato varieties. We calculated the correlation coefficient between the phenotypic features from CC, CV, ExG, and NDVI in Table 4 and the actual yield in 81 plots on the 1st planting (Table 5). The DAP at the maximum growth rate of CV (F7) and the DAP at the maximum value of ExG (F10) were highly correlated with the actual yield (both 0.63). Both features are likely related to robust early crop growth and development phases to expand plant size and likely also indicate a healthy (green) canopy. A high fruit load would cause a stronger shift in the source-sink relationship of the plants because photosynthesis produced at the canopy (leaf) level will be consumed mostly to produce tomato fruits instead of growing. Thus, we expect a high fruit load to cause faster canopy deterioration as the fruits take priority over vegetative growth for carbohydrates. This shift in the source-sink relationship, which will ultimately lead to crop maturity, is usually expressed as a change in leaf color, leaf senescence, or a combination of both. Interestingly, when looking at ExG, the decreasing slope after the maximum for the latter part of the season (F15) also showed a good correlation with crop yield (-0.63). As the decreasing slope is a negative value, this correlation indicates that plants shifting energy to fruits faster can produce high yields.

4.2. Yield Estimation Modelling. In most recent years, AI techniques such as machine and deep learning have received great attention and derived remarkable results for predicting biomass and yield in various crops [21, 31, 34]. The AI-based biomass and yield prediction models resulted in high accuracy of over 90 percent; a critical issue of AI algorithms is that a large number of training datasets are required to obtain robust and accurate machine learning algorithms. However, building a large number of training samples requires a long time and heavy labor [35]. For example, Johansen et al. [21] predicted biomass and yield using 81 UAV-derived variables and a random forest algorithm for 1,200 tomato plants. Although the AI algorithm provides very accurate yield prediction, it cannot be adopted for this study area because of the limited plot numbers causing the singularity. Therefore, we used linear regression to estimate tomato yield using UAV data for 81 tomato varieties.

81 plots on the first planting date with three ground cover conditions (white and black plastic and bare ground) were selected for linear regressions. Yield estimation models were developed by using the actual tomato yield as a dependent variable and the corresponding multitemporal phenotypic features as independent variables in the linear regression.

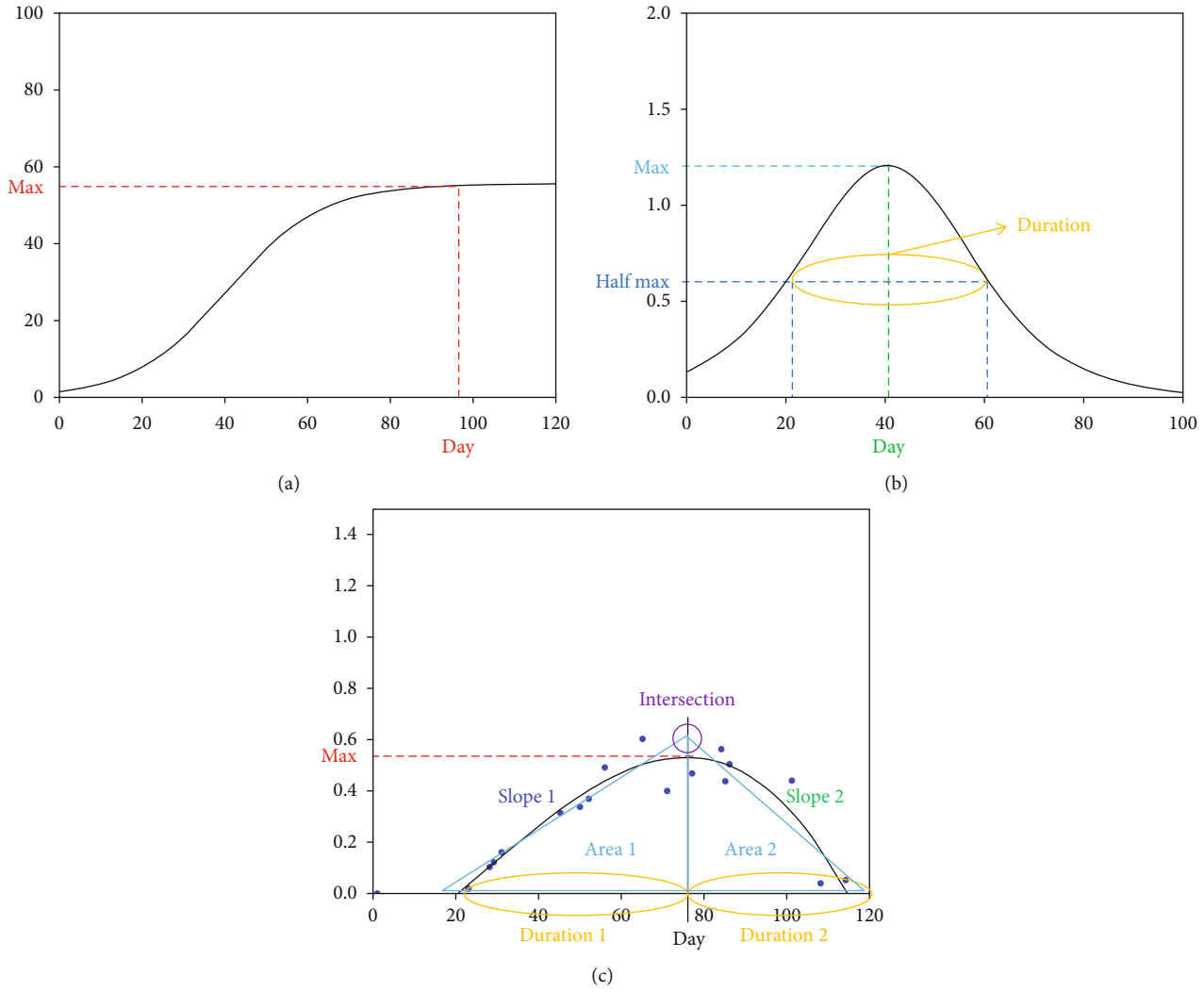

Figure 7: Concept of feature extraction from (a) the growth curve and (b) the growth rate curve of CC and CV. 10 features were extracted from the (c) ExG progression curve.

All 22 phenotypic features from UAS data were selected to develop the yield estimation model. In addition, two different feature selection approaches were employed—(1) a forward feature selection approach starting from a null model and (2) a backward feature elimination approach starting from a full model—to automatically select features and develop statistically significant models (Table 6). All yield estimation models resulted in high R^2 (>0.7) between the actual and estimated yields. Although the AI algorithm might show higher accuracy, linear regression can be alternative according to field conditions and data specs. In general, the backward elimination approach resulted in a higher R^2 than the forward selection, but the number of input variables that automatically remained in the final models was significantly greater than that of the forward selection approach. As the backward elimination approaches tend to overfit with many variables, the forward selection method can be simpler and more efficient.

In the forward selection model, the day at maximum value of ExG (F10), decreasing slope value of ExG (F15), day at maximum growth rate of CC (F3), day at maximum growth rate of CV (F7), duration over the half maximum period of CV (F8), and duration of increasing ExG period (F13) were selected sequentially. Three phenotypic features (F7, F10, and F15) highly correlated with actual yield were entered in the forward selection model. The selected variables in the model can be divided into two groups, crop growth timing (F3, F7, and F10) and crop growth duration (F8, F13, and F15). Crop growth timing indicates the specific day after planting when the plant reaches the status of the greenest canopy and fastest growth. Crop growth timing has positive relationships with actual yield, implying that maturity timing is strongly related to yield performance, as later maturity can make the plant size larger. In crop growth duration, the period of crop growth is a critical variable affecting the yield, while the deterioration speed is also correlated.

4.3. Factor Analysis for UAS-Based Phenotypic Features. Although the variable importance can be calculated to predict biomass and yield, it cannot be consistent for biomass and yield prediction according to the UAV dataset and its specs [21]. In addition, as a few of 22 phenotypic features

Table 5: Correlation coefficient of the UAV-derived features and harvested tomato yield.

Variables	Correlation coefficient
F1	0.52
F2	-0.12
F3	0.35
F4	0.46
F5	0.54
F6	-0.02
F7	0.63
F8	0.35
F9	0.51
F10	0.63
F11	0.24
F12	0.50
F13	0.45
F14	0.58
F15	-0.63
F16	0.55
F17	-0.24
F18	0.38
F19	0.46
F20	0.53
F21	0.09
F22	-0.33

proposed in this study were highly correlated with each other, factor analysis was performed to avoid collinearity and overfitting issues in the regression model and identify statistically significant phenotypic features. Factor analysis is used to describe the covariance relationships among many variables in terms of a few underlying, but unobservable, random quantities [36]. In this study, the maximum likelihood (ML) method was employed, and two major factors having over 75 percent cumulative explanations were selected using the rotated factor matrix calculated by the Varimax method after seven iterations. The final two factors explained 75 percent of the variance and consisted of nine phenotypic features showing two crop traits (Table 7). The first factor included six phenotypic features, including days after planting when the ExG value was maximum (F10), duration of half maximum canopy cover (F4), days after planting when the canopy volume growth rate was maximum (F7), days after planting when the NDVI was maximum (F20), days after planting when the canopy cover growth rate was maximum (F3), and duration of half maximum canopy volume (F8). These are kinds of days and durations closely related to the "timing of crop growth event." Four of six variables selected in the linear regression models with the forward selection method were included in the first factor. As mentioned above, crop growth timing and duration strongly affect tomato yield performance. The six variables of the first factors imply that the plant growing faster and longer until canopy deterioration can produce more fruits since the larger plant can use more energy to produce tomato fruits. The second factor included the increasing slope of ExG (F11), the increasing slope of NDVI (F21), and the triangular area of the decreasing slope of ExG (F18), which indicate the "speed of crop growth." In factor analysis, the other features (F11, F18, and F21) were selected in the crop growth speed group instead of the duration of the increasing ExG period (F13) and decreasing slope value of ExG (F15). F13 and F15 alternated to F11 and F18, indicating similar crop characteristics of growing speed. A very interesting fact is that the phenotypic features from multispectral images were included in both first and second factors. As the fitted curves of ExG and NDVI have similar trends, NDVI-related features have a high correlation with the features of ExG. Two NDVI-based features also represented the timing of crop growth and growth speed. The results of factor analysis found that growth timing, duration, and growth speed were the main traits affecting tomato yield. Our results showed what crop characteristics should be considered in breeding programs for cultivar improvement.

The nine phenotypic features selected by factor analysis were input into the linear regression model to estimate tomato yield. A forward feature selection approach was used, and five phenotypic features were selected for the final model. The features remaining in the final regression model were days after planting when the ExG value was maximum (F10), days after planting when the canopy volume growth rate was maximum (F7), days after planting when the canopy cover growth rate was maximum (F3), duration of the half maximum canopy volume period (F8), and triangle area of the decreasing ExG slope (F18). The yield prediction model, as shown in Equation (5), explained 65 percent of the variation in the actual harvested yield (Figure 8). Four features (F3, F7, F8, and F10) are related to the crop growth time. We realized that the phenotypic features related to crop growth time play a more important role in predicting yield. In addition, the number of days after planting when ExG (F10) was the most critical crop parameter for yield estimation was determined not only by factor analysis but also by general linear regression models.

All variables in the yield prediction model from factor analysis can be extracted from time-series CC, CV, and ExG derived from RGB images at similar accuracy with the phenotypic features from both RGB and multispectral imagery. The results indicated that RGB images can provide enough information to predict yield at the field level. As UAS platforms with RGB sensors are relatively cheaper and easier to operate for data collection and calibration, they should be a good alternative to collect a large number of crop parameters for precision agriculture. As CC and CV can be calculated from multispectral images and NDVI has a trend similar to ExG, it will be possible to adopt either RGB or multispectral images for predicting tomato yield at the field level:

$$\begin{aligned}\text{Tomato yield} = {} & 1.841 \times \text{F10} + 0.875 \times \text{F18} - 2.546 \\ & \times \text{F3} + 2.026 \times \text{F7} - 0.902 \times \text{F8}.\end{aligned} \quad (5)$$

4.4. Tomato Variety Selection. Based on the estimated yield from the final regression model in factor analysis, the rank

Table 6: Tomato yield prediction model with a linear regression model. The variables are arranged at the significance level.

Features	Regression model	R square
All (22 features)	Yield = −0.858 × F1 − 4.14 × F2 + 7.07 × F3 + 0.80 × F4 − 13.21 × F5 + 1.70 × F6 − 1.19 × F7 −0.18 × F8 + 50.82 × F9 − 0.49 × F10 − 524.20 × F11 + 901.31 × F12 + 323.92 × F13 +2.68 × F14 − 10777.49 × F15 + 399.90 × F16 − 0.95 × F17 − 10.63 × F18 − 5534.03 × F19 − 222.49 × F20 − 0.25 × F21 − 0.26 × F22 − 2.28	0.79
Forward selection (6 features)	Yield = 2.25 × F10 − 1500.15 × F15 − 3.29 × F3 + 1.83 × F7 − 0.71 × F8 − 0.58 × F13 − 50.80	0.70
Backward selection (13 features)	Yield = −4.01 × F2 − 20.49 × F5 + 2.20 × F6 + 30.54 × F19 + 996.360 × F22 + 394.07 × F9 +1.93 × F10 − 9873.48 × F11 + 424.37 × F12 − 12.65 × F14 − 6775.12 × F15 −315.69 × F16 − 0.37 × F17 − 42.845	0.77

Table 7: Rotated factor matrix of selected phenotypic features through factor analysis.

Phenotypic features	Factor 1	Factor 2
DAP at maximum of ExG value (F10)	0.911	0.056
Duration over the half maximum period of CC (F4)	0.899	0.063
Maximum growth rate of CV (F7)	0.870	0.116
DAP at maximum NDVI value (F20)	0.858	0.025
Maximum growth rate of CC (F3)	0.833	0.188
Duration over the half maximum period of CV (F8)	0.747	-0.066
Increasing slope of ExG (F11)	0.087	0.885
Increasing slope of NDVI (F21)	-0.036	0.822
Area of decreasing period of ExG (F18)	0.115	0.758

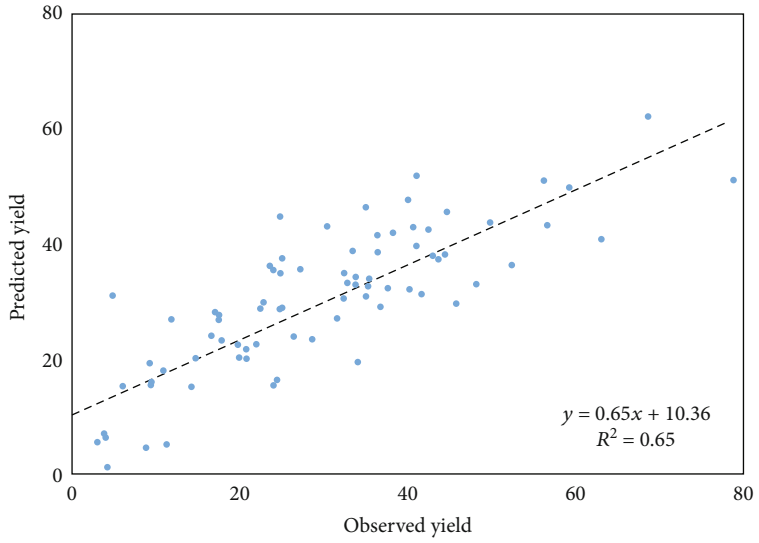

Figure 8: The linear regression results between the predicted yield by five selected features from factor analysis and the harvested yield.

of the best performing tomato genotype was determined by the precited yield. The top 10, 20, 30, and 40 performing varieties based on the estimation were compared with the rank by the actual harvested yield to find matched varieties. Figure 9(a) shows how many varieties selected by the proposed method are correctly matched in the same number of varieties based on the actual yield. When the estimator selects the top 10 varieties (blue line), five of them were included in the top 10 of the high actual yield varieties, which means a 50 percent match ratio. All top 10 varieties by the estimator were included in the top 40 high-performing varieties by actual yield. In terms of the top 20 varieties selected by the estimation model, we could achieve 100 percent selection accuracy in the top 50 varieties of actual yield. When 40 varieties were selected with the developed model in this study, 34 varieties, which is 85 percent of the 40, were included in the list of the top 40 actual yields. Although we could not select high-performing varieties perfectly, our result shows that the

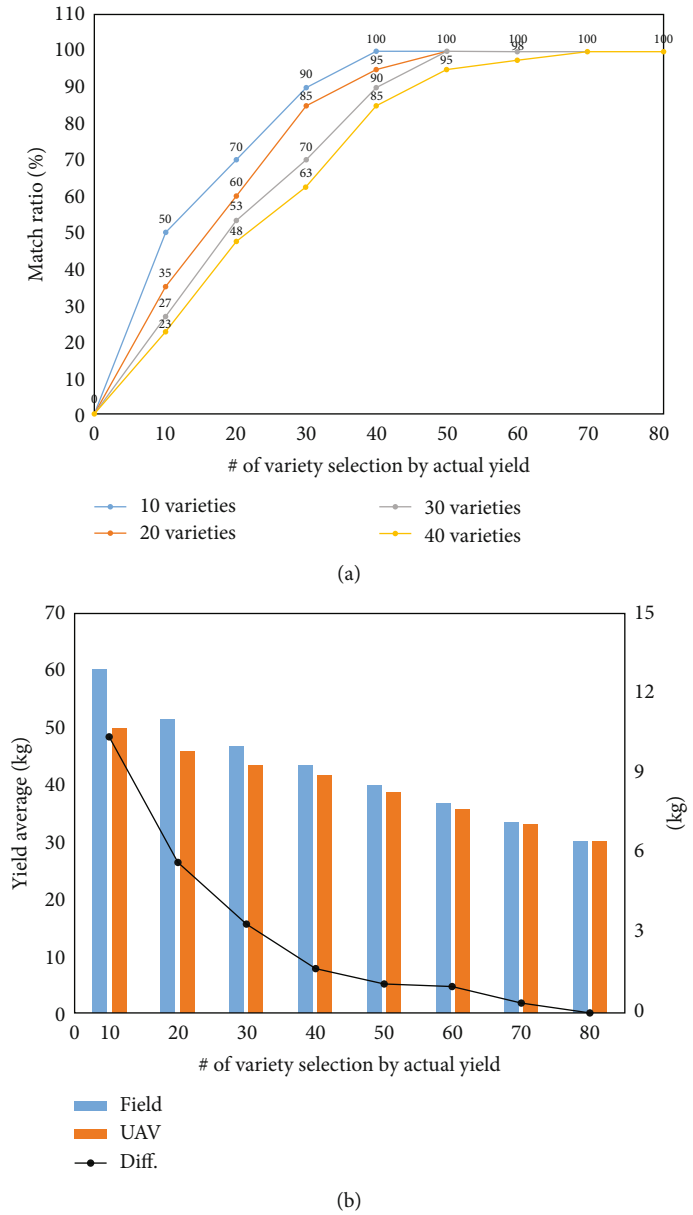

Figure 9: (a) Match ratio curve of the best performing tomato variety according to the number of selections based on the estimated and actual yield. (b) Average of the actual harvested yield of selected varieties based on the estimated and actual yield. The black dots indicate the difference in the yield average of the varieties selected by UAV-estimated and actual yield.

low-performing varieties could be successfully eliminated by the proposed framework. For example, scientists can select and eliminate the bottom 10 varieties by the proposed framework without losing any high-performance varieties. The advantage of this work is that it is not necessary to harvest the eliminated varieties in the field. In other words, we can save economic resources, human power, and time to make breeding programs more efficient.

Jung et al. [14] compared the average cotton lint yield among the remaining varieties after variety selection based on the UAV-derived phenotypes to verify the performance of the UAV-based variety selection framework. In the cotton field, the average lint yield increased by 10 percent compared to the original population after variety selection using UAV data. UAV-selected varieties matched over 70 percent of the same lists ranked by actual field harvest measurements. In this study, to see more details of eliminating low-performing varieties, the average actual yield of the selected varieties by UAV-estimated and actual yield was calculated (Figure 9(b)). When the top 10 high-yield varieties by UAV-estimated and actual yield are selected, the average tomato yield is different by about 10 kg. More variety selection decreases the disparity of the average yield between UAV and field groups. After selecting more than 50 varieties, the difference is less than 1 kg. The average tomato yield increased by 100 and 53 percent compared to all varieties after variety selection using actual and UAV data, respectively. It implies that the proposed method could provide

feasible information for selecting high- or low-performance varieties without destructive hand-sampling and actual harvesting.

5. Conclusions

In this study, a novel HTP framework of data was proposed to predict tomato yield using multitemporal UAS data. Shape features, including canopy cover, canopy volume, and vegetation indices derived at the plot level, were determined to fit the mathematical curves. Time-series phenotypes were extracted from the growth and growth rate curves. Although the time-series phenotypic features were individually correlated with actual yield, linear regression models produced high R^2 values (>0.7). Based on the factor analysis, two significant factors, growth speed and timing, were figured out to be strongly related to the yield performance of tomato varieties. Finally, five time-series phenotypes were selected for the yield prediction model explaining 65 percent of the variance of the actual harvest. The phenotypic features derived from RGB images played important roles in providing enough information to predict yield. We compared the actual yield with the estimated yield to determine the possibility of UAS-based variety selection in breeding programs. Although the high-performance variety could not be perfectly selected using the estimator, the low-performance varieties were exactly matched between UAS-based and actual yields. Ultimately, the proposed variety selection/elimination process using UAV data increased the average tomato yield of the remaining varieties by 53 percent. The results from this work can be useful in breeding programs to select high-yielding and disease-/pest-resistant varieties for tomato fields. In the future, we will adopt the AI algorithm to develop a more elaborate model for yield prediction and variety selection in agricultural applications.

Data Availability

The data used to support the findings of this study have not been made available because it is only available for researchers and collaborators of Texas A&M AgriLife Research and Extension.

Conflicts of Interest

The authors declare no conflict of interest.

Acknowledgments

This research was supported by Texas AgriLife Research.

References

[1] USDA, *Vegetables 2018 Summary (March 2019)*, USDA National Agricultural Statistics Service, DC, USA, 2019.

[2] S. Oh, A. Ashapure, T. G. Marconi, J. Jung, and J. Landivar, "UAS Based Tomato Yellow Leaf Curl Virus (TYLCV) Disease Detection System," in *Autonomous Air and Ground Sensing Systems for Agricultural Optimization and Phenotyping IV*, Baltimore, Maryland, USA, 2019.

[3] A. Chang, J. Jung, M. Maeda, and J. Landivar, "Crop height monitoring with digital imagery from unmanned aerial system (UAS)," *Computers and Electronics in Agriculture*, vol. 141, pp. 232–237, 2017.

[4] A. Ashapure, J. Jung, J. Yeom et al., "A novel framework to detect conventional tillage and no-tillage cropping system effect on cotton growth and development using multi-temporal UAS data," *ISPRS Journal of Photogrammetry and Remote Sensing*, vol. 152, pp. 49–64, 2019.

[5] D. J. Mulla, "Twenty five years of remote sensing in precision agriculture: key advances and remaining knowledge gaps," *Biosystems Engineering*, vol. 114, no. 4, pp. 358–371, 2013.

[6] P. Nevavuori, N. Narra, and T. Lipping, "Crop yield prediction with deep convolutional neural networks," *Computers and Electronics in Agriculture*, vol. 163, article 104859, 2019.

[7] Y. Shi, J. A. Thomasson, S. C. Murray et al., "Unmanned aerial vehicles for high-throughput phenotyping and agronomic research," *PLoS ONE*, vol. 11, no. 7, article e0159781, 2016.

[8] D. C. Tsouros, S. Bibi, and P. G. Sarigiannidis, "A review on UAV-based applications for precision agriculture," *Information*, vol. 10, no. 11, 2019.

[9] A. Ashapure, J. Jung, A. Chang, S. Oh, M. Maeda, and J. Landivar, "A comparative study of RGB and multispectral sensor-based cotton canopy cover modelling using multi-temporal UAS data," *Remote Sensing*, vol. 11, no. 23, article 2757, 2019.

[10] J. Yeom, J. Jung, A. Chang et al., "Comparison of vegetation indices derived from UAV data for differentiation of tillage effects in agriculture," *Remote Sensing*, vol. 11, no. 13, p. 1548, 2019.

[11] M. L. Gil-Docampo, M. Arza-García, J. Ortiz-Sanz, S. Martínez-Rodríguez, J. L. Marcos-Robles, and L. F. Sánchez-Sastre, "Above-ground biomass estimation of arable crops using UAV-based SfM photogrammetry," *Geocarto International*, vol. 35, no. 7, pp. 687–699, 2020.

[12] Q. Jiang, S. Fang, Y. Peng et al., "UAV-based biomass estimation for rice-combining spectral, TIN-based structural and meteorological features," *Remote Sensing*, vol. 11, no. 7, p. 890, 2019.

[13] B. Li, X. Xu, L. Zhang et al., "Above-ground biomass estimation and yield prediction in potato by using UAV- based RGB and hyperspectral imaging," *ISPRS Journal of Photogrammetry and Remote Sensing*, vol. 162, pp. 161–172, 2020.

[14] J. Jung, M. Maeda, A. Chang, J. Landivar, J. Yeom, and J. McGinty, "Unmanned aerial system assisted framework for the selection of high yielding cotton genotypes," *Computers and Electronics in Agriculture*, vol. 152, pp. 74–81, 2018.

[15] M. Maimaitijiang, V. Sagan, P. Sidike et al., "Vegetation index weighted canopy volume model (CVM_{VI}) for soybean biomass estimation from unmanned aerial system-based RGB imagery," *ISPRS Journal of Photogrammetry and Remote Sensing*, vol. 151, pp. 27–41, 2019.

[16] B. Duan, S. Fang, R. Zhu et al., "Remote estimation of rice yield with unmanned aerial vehicle (UAV) data and spectral mixture analysis," *Frontiers in Plant Science*, vol. 10, 2019.

[17] L. Han, G. Yang, H. Dai et al., "Modeling maize above-ground biomass based on machine learning approaches using UAV remote-sensing data," *Plant Methods*, vol. 15, no. 1, 2019.

[18] J. G. A. Barbedo, "A review on the use of unmanned aerial vehicles and imaging sensors for monitoring and assessing plant stresses," *Drones*, vol. 3, no. 2, p. 40, 2019.

[19] J. Enciso, C. A. Avila, J. Jung et al., "Validation of agronomic UAV and field measurements for tomato varieties," *Computers and Electronics in Agriculture*, vol. 158, pp. 278–283, 2019.

[20] K. Johansen, M. J. L. Morton, Y. M. Malbeteau et al., "Unmanned aerial vehicle-based phenotyping using morphometric and spectral analysis can quantify responses of wild tomato plants to salinity stress," *Frontiers in Plant Science*, vol. 10, 2019.

[21] K. Johansen, M. J. L. Morton, Y. Malbeteau et al., "Predicting biomass and yield in a tomato phenotyping experiment using UAV imagery and random forest," *Frontiers in Artificial Intelligence*, vol. 3, 2020.

[22] A. Ashapure, S. Oh, T. G. Marconi et al., "Unmanned aerial system based tomato yield estimation using machine learning," in *Autonomous Air and Ground Sensing Systems for Agricultural Optimization and Phenotyping IV*, Baltimore, Maryland, USA, 2019.

[23] F.-J. Mesas-Carrascosa, J. Torres-Sánchez, I. Clavero-Rumbao et al., "Assessing optimal flight parameters for generating accurate multispectral orthomosaicks by UAV to support site-specific crop management," *Remote Sensing*, vol. 7, no. 10, pp. 12793–12814, 2015.

[24] T. Su and H. Chou, "Application of multispectral sensors carried on unmanned aerial vehicle (UAV) to trophic state mapping of small reservoirs: a case study of Tain-Pu reservoir in Kinmen, Taiwan," *Remote Sensing*, vol. 7, no. 8, pp. 10078–10097, 2015.

[25] C. Wang and S. W. Myint, "A simplified empirical line method of radiometric calibration for small unmanned aircraft systems-based remote sensing," *IEEE Journal of Selected Topics in Applied Earth Observations and Remote Sensing*, vol. 8, no. 5, pp. 1876–1885, 2015.

[26] M. D. Richardson, D. E. Karcher, and L. C. Purcell, "Quantifying turfgrass cover using digital image analysis," *Crop Science*, vol. 41, no. 6, pp. 1884–1888, 2001.

[27] P. R. H. Robson, K. Farrar, A. P. Gay, E. F. Jensen, J. C. Clifton-Brown, and I. S. Donnison, "Variation in canopy duration in the perennial biofuel crop *Miscanthus* reveals complex associations with yield," *Journal of Experimental Botany*, vol. 64, no. 8, pp. 2373–2383, 2013.

[28] A. Patrignani and T. E. Ochsner, "Canopeo: a powerful new tool for measuring fractional green canopy cover," *Agronomy Journal*, vol. 107, no. 6, pp. 2312–2320, 2015.

[29] D. M. Woebbecke, G. E. Meyer, K. Von Bargen, and D. A. Mortensen, "Color indices for weed identification under various soil, residue, and lighting conditions," *Transactions of the ASAE*, vol. 38, no. 1, pp. 259–269, 1995.

[30] M. A. Hassan, M. Yang, A. Rasheed et al., "A rapid monitoring of NDVI across the wheat growth cycle for grain yield prediction using a multi-spectral UAV platform," *Plant Science*, vol. 282, pp. 95–103, 2019.

[31] Y. Liu, X. Chen, Z. Wang, Z. J. Wang, R. K. Ward, and X. Wang, "Deep learning for pixel-level image fusion: recent advances and future prospects," *Information Fusion*, vol. 42, pp. 158–173, 2018.

[32] H. Zheng, T. Cheng, M. Zhou et al., "Improved estimation of rice aboveground biomass combining textural and spectral analysis of UAV imagery," *Precision Agriculture*, vol. 20, no. 3, pp. 611–629, 2019.

[33] K. Oaddoum, E. L. Hines, and D. D. Iliescu, "Yield prediction for tomato greenhouse using EFuNN," *International Scholarly Research Notices*, vol. 2013, Article ID 430986, 9 pages, 2013.

[34] M. Maimaitijiang, V. Sagan, P. Sidike, S. Hartling, F. Esposito, and F. B. Fritschi, "Soybean yield prediction from UAV using multimodal data fusion and deep learning," *Remote Sensing of Environment*, vol. 237, article 111599, 2020.

[35] Z. Lin and W. Guo, "Sorghum panicle detection and counting using unmanned aerial system images and deep learning," *Frontiers in Plant Science*, vol. 11, article 534853, 2020.

[36] R. A. Johnson and D. W. Wichern, *Applied Multivariate Statistical Analysis*, Pearson Education, New Jersey, 2002.

Hindawi
Journal of Sensors
Volume 2021, Article ID 6617437, 12 pages
https://doi.org/10.1155/2021/6617437

Research Article

Effects of Subsurface Drip Irrigation on Water Consumption and Yields of Alfalfa under Different Water and Fertilizer Conditions

Xuesong Cao,[1] **Yayang Feng**,[2] **Heping Li**,[1] **Hexiang Zheng**,[1] **Jun Wang**,[1] **and Changfu Tong**[1]

[1]*Institute of Water Resources for Pastoral Area, China Institute of Water Resources and Hydropower Research, Huhhot 010020, China*
[2]*Water Conservancy and Civil Engineering, Inner Mongolia Agricultural University, Hohhot 010018, China*

Correspondence should be addressed to Xuesong Cao; cxsmks@126.com

Received 2 November 2020; Revised 10 January 2021; Accepted 20 January 2021; Published 3 February 2021

Academic Editor: Jingwei Wang

A field experiment was conducted for the purpose of examining the effects of different combinations of water and fertilizer applications on the water consumption and yields of alfalfa under subsurface drip irrigation (SDI). The results showed that the jointing and branching stages were the key stages for alfalfa water requirement. The water consumption had varied greatly (from 130 to 170 mm) during the growth period of each alfalfa crop. The water consumption during the whole growth period was approximately 500 mm, and the maximum water consumption intensity was 3.64 mm·d^{-1}. The overall changes in water consumption and yields during the growth period of the alfalfa displayed trends of first increasing and then decreasing. The sensitivities of the yields to water changes were much higher than that of fertilizer. The water use efficiency (WUE) of the alfalfa was determined to range from 1.68 to 3.20 kg·m^{-3}, and the rate of growth had ranged from 4.85% to 51.77%. The WUE and rate of growth of the alfalfa indicated the following trend: second crop > third crop > first crop. The results of frequency analysis based on the water-nitrogen-yield regression equation are the following: irrigation amounts of 142~165 mm and nitrogen application of 61~80 kg·hm^{-2} have a 95% probability of obtaining a hay yield of alfalfa of more than 11903 kg·hm^{-2}. These results suggest that SDI is a promising irrigation method, which can increase the WUE and hay yield of alfalfa under the condition of SDI within an appropriate amount of water and nitrogen fertilizer, and too low or too high water and nitrogen fertilizer will adversely affect the WUE and hay yield of alfalfa.

1. Introduction

With the global economic development, population growth, and regional water shortages, agricultural production, as the world's primary consumer of water resources, is increasingly focused on agricultural water conservation, environmental protection, and improving crop quality and yield, which is also increasingly squeezed by the demands from other society sectors and threatened by potential climatic change [1]. SDI, as a new irrigation method in recent years, has attracted much attention in agricultural production in arid and semi-arid areas due to its improving WUE and ability to minimize the adverse effects of excessive irrigation on the environment [2, 3]. Studies have shown that SDI saves water resources and does not interfere with ground production of alfalfa and can improve crop water productivity and hay yield [4–7]. In modern precision agricultural activities, two of the three "precisions" (precision sowing, precision fertilization, and precision irrigation) are implemented through SDI. The technical characteristics of SDI include small flow, local moistening, and frequent irrigation. When compared with surface irrigation methods, SDI has been found to have outstanding advantages, such as water conservation, lower amounts of required fertilizer, reducing evaporation losses, increasing crop WUE, irrigation WUE and crop yield, good adaptability to various terrain, uniform irrigation, and ease of technology integration [8–15].

Alfalfa (*Medicago sativa L.*) is a type of high-quality perennial leguminous forage, with the characteristics of good palatability, high stress resistance, high yield, rich nutrition,

and so on [16–22]. Throughout the world, alfalfa enjoys the reputation as the " Queen of Forage" [16] and is one of the main high-quality forage crops planted in pastoral areas and occupies a very important position in agricultural production. Alfalfa is not suitable for aboveground drip irrigation due to its mowing multiple times per year and its growth characteristics; therefore, alfalfa under SDI technology came into being. With the development of new water-saving irrigation technology, artificial grass SDI technologies with increased water-saving potential have become important directions for the current development projects in arid and semiarid pastoral regions. Studies have shown that alfalfa has better adaptability to SDI in arid and semiarid areas [23–25]. Furthermore, as a form of engineered water-saving irrigation, SDI has been widely applied in actual production processes. It has been found to have the ability to improve farmland production environments, along with regulating the physiological processes of crops, and also have certain positive effects, such as increasing hay yield [26, 27] and saving water [28]. In a previous study, Kou et al. [29] examined the effects of subsurface regulated deficit drip irrigation on the water consumption, yields, and quality of alfalfa and also pointed out that with increases in the water deficit and yields, the water consumption of the alfalfa had been reduced. Meanwhile, the water usage efficiency had been increased. However, some studies have shown that the fresh and dried yield of alfalfa decreases with the decrease of water supply, and the WUE increases instead [30, 31]. SDI can also greatly reduce surface evaporation and deep percolation; studies had shown that using SDI can save a quarter of total water transfers in the season [32, 33]. Similarly, alfalfa under SDI can increase crop yields by improving precise control of water and fertilizer. Compared with the conventional method of irrigation, the water-saving ratio due to SDI that precisely regulates water and fertilizer ranges from 30 to 70 per cent whereas gain in productivity for different crops ranges from 20 to 90 per cent as well as reduces the requirement of labors and fertilizers [34]. Stavarache et al. [35] determined that nitrogen applications had a significant promoting effect on the yields of alfalfa grown in the same year. In another related study, Liu et al. [36] proposed a precision regulation model of water and fertilizer for irrigation and fertilizer management in alfalfa. Therefore, a comprehensive understanding of crop water needs and water and fertilizer precise control ratio under SDI conditions is of great significance for vigorously developing efficient water-saving agricultural methods, alleviating water shortages, and improving crop water and fertilizer usage efficiency.

In the current experiment, the water and fertilizer were transported directly to the roots of the alfalfa plants using an SDI belt. The irrigation and fertilization processes for the alfalfa were strictly controlled in order to effectively analyze the water consumption rule of the alfalfa under SDI conditions. The effects of the different irrigation and fertilization treatments on the yields and water usage efficiency of the alfalfa were studied in order to obtain the best combination points for the water and fertilizer application amounts. The results of this study provided a theoretical basis for the development of irrigation in artificial forage land, improvements in the forage quality and efficiency; protection of grassland ecological environments, adjustments in the livestock industry structures, and promotion of the sustainable development of grassland animal husbandry in the arid and semiarid pastoral areas of western Inner Mongolia. This paper provides findings for the enrichment of the alfalfa SDI technology system and offers valuable data support and theoretical basis by field experiment data analysis for water saving, yield enhancement, and quality improvement of agricultural crops in this region.

2. Materials and Methods

2.1. Experimental Site. This study's experiment was carried out at the Hengfeng water-saving irrigation experimental base in Otog Front Banner, Ordos City, Inner Mongolia (Figure 1(a)) from April to October 2019. The Otog Front Banner is located in the abdomen of Mu Us Sandland and at the junction of Inner Mongolia, Shaanxi, and Ningxia Provinces. Its geographic coordinates are eastern longitude $106°30' - 108°30'$ and northern latitude $37°38' - 38°45'$, with an altitude ranging between 1,300 and 1,400 m. The study area is characterized by the semiarid continental climate of a middle temperate zone, which includes hot summers, cold winters, dry conditions with little rainfall, strong evaporation conditions, and abundant sunlight. The annual average temperature is 7.9°C; annual average precipitation is 260.6 mm; annual average evaporation is 2,497.9 mm; and the annual prevailing wind direction is south, followed by west and east wind directions, with an average annual wind speed of 2.6 $m \cdot s^{-1}$. In the study area, the average number of sandstorm days is 16.9 days, and the average relative humidity is 49.8%. Also, the number of annual average sunshine hours ranges between 2,500 and 3,200 hours, with an average of 2,958 hours, and the frost-free period is 171 days. The maximum frozen soil depth is 1.54 m. The 40 cm deep soil type in the experimental area was determined to be sandy soil with a bulk density of 1.62 $g \cdot cm^{-3}$. The soil mechanical composition of 0~40 cm soil layer is shown in Table 1.

2.2. Test Material and Planting Method. SDI material: the SDI belts were embedded at a depth of 20 cm, as part of a patch-type SDI belt system. The wall thicknesses were 0.4 mm; drip discharge was 2.0 $L \cdot h^{-1}$; and the drip spacing was 0.3 m. Each SDI belt controlled four rows of alfalfa, and the spacing between the SDI belts was 60 cm.

Varieties of alfalfa: the alfalfa which was used in this study was in its third year of planting. The alfalfa variety was Grassland No. 2. The alfalfa was sown using drills, with the seeding amount set as 30 $kg \cdot hm^{-2}$ and the line spacing set at 15 cm.

Planting method: alfalfa was artificially sown using drills with line spacings of 15 cm. In order to ensure the nutritional value and palatability of the alfalfa, the alfalfa was harvested and stored at the initial flowering stage. The alfalfa was harvested in three crops a year. The alfalfa strikes rooted in early April of each year, and the third crop was harvested at the end of September.

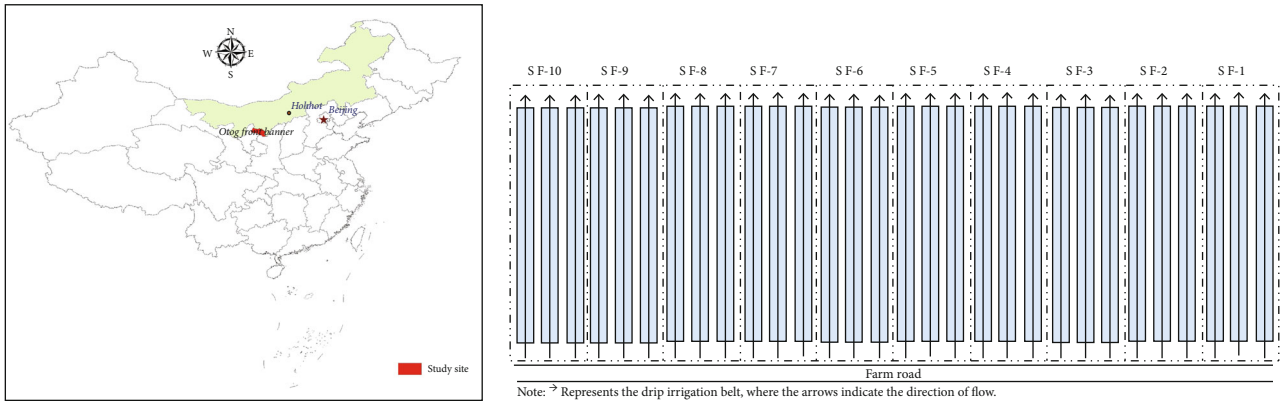

(a) (b)

Figure 1: Study site on the map of China (a) and experimental plot layout of the studied field (b).

Table 1: Soil mechanical composition of 0~40 cm soil layer in the test area.

Bulk density (g·cm^{-3})	Proportion	Soil particle distribution (%)			Soil type
		0.05~2 mm	0.002~0.05 mm	<0.002 mm	
1.62	2.71	76.85	21.69	1.46	Sandy soil

Fertilizers used in the experiment: in this study, the nitrogen fertilizer was urea (N 46.4%).

2.3. Experimental Design. A 2-factor and 3-level orthogonal combination design was used in this study's experiment. The designs of the specific experimental factors and levels are shown in Table 2. Nine different orthogonal design treatments and one conventional field control treatment were set up in the experimental area, with a total of ten experimental treatments being conducted in this study. Each treatment was repeated three times, for a total of 30 experimental plots. Each experimental treatment had a length of 60 m, width of 8 m, and area of 480 m^2. The total area of the experimental plots was 4,800 m^2. In order to avoid the mutual impact of the treatments, a 2 m wide isolation belt was set up between every two treatments (Figure 1(b)). Each treatment was divided into three experimental plots during the experiment monitoring process. For example, each experimental plot had a length of 20 m, width of 8 m, and area of 160 m^2. When the soil moisture content of the SF-5 treatment was reduced to 65% of the field water holding capacity, each treatment was irrigated according to the irrigation quota (the amounts of irrigated water were recorded by a rotor digital water meter), and each experimental treatment had the same irrigation date and frequency.

2.4. Measurement Indexes and Method. Observations of the meteorological factors: a farmland meteorological station (HOBO U30 Onset, Onset Computer Corporation, Bourne, MA, USA) was set up in the experimental area for the purpose of observing the temperature, rainfall, wind speeds, relative humidity, air pressure, wind directions, and other factors occurring during the growing period of the alfalfa crops. The effective rainfall was determined to be 182.10 mm during the entire alfalfa growth period, and the details are shown in Figure 2 (the red line in Figure 2 represents the two-period moving average trend line).

Table 2: Designs of the experimental factors and levels for the fertilization of the alfalfa under SDI conditions.

Treatment	Levels and factors for production target	
	Irrigation quota (mm)	N (kg·hm^{-2})
SF-1	20	0
SF-2	20	60
SF-3	20	120
SF-4	25	0
SF-5	25	60
SF-6	25	120
SF-7	30	0
SF-8	30	60
SF-9	30	120
SF-10	A local herdsman's traditional alfalfa planting field was taken as the control treatment	

Observations of the groundwater levels: the groundwater level changes in the experimental area were measured using a HOBO automatic groundwater level meter (HOBO U30 Onset, Onset Computer Corporation, Bourne, MA, USA). The groundwater burial depths in the experimental area were determined to be between 1.2 and 2.0 m.

Irrigation amounts: the soil moisture levels of each plot were automatically monitored by the HOBO soil moisture automatic measuring instrument (HOBO U30 Onset, Onset Computer Corporation, Bourne, MA, USA). When the soil moisture content had reached the lower water limit, irrigation was implemented in time for the treatment. The irrigation for the local control treatment (SF-10) was based on the irrigation experiences of the local herdsmen, and the amounts of the irrigation were measured using water meter

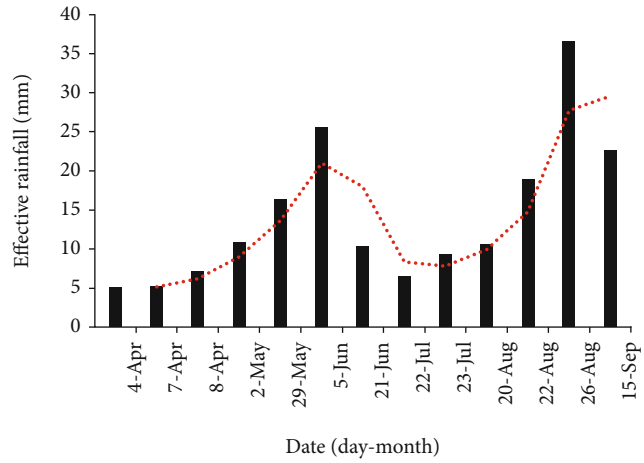

Figure 2: Effective rainfall during the entire growth period of the alfalfa.

Table 3: Irrigation amounts of each alfalfa crop during each growth period.

Treatment	Irrigation amounts (mm) (the first/second/third crop)				
	Seedling establishment stage	Jointing stage	Branching stage	Flowering stage	Total irrigation
SF-1	20/20/20	40/20/20	40/40/0	20/20/20	120/100/60
SF-2	20/20/20	40/20/20	40/40/0	20/20/20	120/100/60
SF-3	20/20/20	40/20/20	40/40/0	20/20/20	120/100/60
SF-4	25/25/25	50/25/25	50/50/0	25/25/25	150/125/75
SF-5	25/25/25	50/25/25	50/50/0	25/25/25	150/125/75
SF-6	25/25/25	50/25/25	50/50/0	25/25/25	150/125/75
SF-7	30/30/30	60/30/30	60/60/0	30/30/30	180/150/90
SF-8	30/30/30	60/30/30	60/60/0	30/30/30	180/150/90
SF-9	30/30/30	60/30/30	60/60/0	30/30/30	180/150/90
SF-10	0/0/0	80/80/80	80/80/80	0/0/0	160/160/160

readings. The irrigation amounts of each growth period of the experiment are detailed in Table 3.

Soil moisture content levels: the field water holding capacity of undisturbed soil samples which were taken using a cutting ring from the experimental area was measured in this study's laboratory facilities. Then, the results were compared with the field experiment results, and the field water holding capacity of the 0 to 40 cm soil layer in the experimental area was determined to be 22.86%. The soil moisture content of each experimental plot was measured by instrument measurement methods and checked by an oven-drying method. The instrument used in the measurement method was the HOBO soil moisture automatic measuring instrument, and the measured depth of the soil layer was 10, 20, 30, 40, 50, and 60 cm, respectively. The oven-drying method utilized a soil auger to extract the soil samples, and an oven was used for the drying process.

Hay yields of the alfalfa crops: the growth stage of the alfalfa was divided into the seedling establishment stage, branching stage, squaring stage, and flowering stage. The alfalfa hay was cut when it had entered the flowering stage, and three crops were harvested each year. A quadrat sampling method was used for measurements of the hay yields. The quadrat area was set as 1 m × 1 m. The fresh weight of the alfalfa after cutting was determined, and the fresh hay samples were placed into an oven. A water removal treatment was conducted for 30 minutes at a high temperature of 105°C, and then, the temperature was adjusted to 65°C in order to dry the samples for a period of 48 hours under constant temperature conditions. The samples were then taken out of the oven; the dry weights of the samples were calculated after the samples had cooled.

2.5. Calculation and Analysis of the Water Consumption of the Alfalfa. Water consumption: the water consumption of the alfalfa was calculated using a water balance equation as follows:

$$ET_a = P + I - \Delta W - Q, \quad (1)$$

where ET_a represents the water consumption (mm) during each period, P is the effective precipitation (mm) during the corresponding period, I denotes the irrigation amount during the corresponding period, ΔW represents the changes in the soil water storage (mm) during the corresponding period, and Q is the water flux (mm) of the lower boundary during the corresponding period.

Changes in the soil water storage levels: the changes in the soil water storage levels during each growth stage were calculated according to soil moisture content of each experimental treatment, and the formula was as follows:

$$\Delta W = \frac{\theta_{i+1} - \theta_i}{100} \times \gamma \times h, \tag{2}$$

where θ_i denotes the initial soil water content (%) during the corresponding period, θ_{i+1} is the final soil water content (%) during the corresponding period, γ represents the soil bulk density (cm^3/g), and h is the planned depth (mm) of the wetting layer.

Soil water fluxes of the lower boundary: the soil water fluxes at the lower boundary of the alfalfa were the deep soil leakage or recharge during each growth period which was calculated according to the soil's negative pressure measured during the experiment. The recharge and leakage of the soil moisture at the lower boundary of the planned wetting layer were calculated using an oriented flux method, and the measuring instrument was a negative pressure gauge. The calculation formula of the oriented flux method was as follows:

$$q(z_{1-2}) = -k(\bar{H}) \times \left(\frac{H_2 - H_1}{\Delta z} + 1\right), \tag{3}$$

where $k(\bar{H})$ represents the permeability coefficient of the soil at $\bar{H}$, $\Delta z = z_2 - z_1$, $\bar{H} = (H_1 + H_2)/2$, and H_1 and H_2 indicate the negative pressure values of the soil at the locations z_1 and z_2, respectively. Therefore, the soil water flow $q(z_{1-2})$ per unit area during the period from t_1 to t_2 could be obtained. Similarly, the flow $q(z)$ on each section could be calculated according to $q(z_{1-2})$ as follows:

$$q(z) = q(z_{1-2}) + \int_z^{z_{1-2}} [q(z, t_2) - q(z, t_1)]dz. \tag{4}$$

WUE: WUE refers to the output per unit of water consumption of crops, the value of which is equal to the ratio of the crop yields to the net water consumption of crops. In this study, the crop WUE was calculated using the following formula:

$$\mathrm{WUE} = \frac{Y}{ET_a}, \tag{5}$$

where WUE is the water use efficiency ($kg \cdot m^{-3}$), Y represents the crop yields ($kg \cdot hm^{-2}$), and the meanings of the other symbols are the same as previously mentioned.

2.6. Statistical Analysis. Analysis of variance was performed using the SPSS22.0 (IBM Corp., Armonk, New York, NY, USA) to determine the least significant difference (LSD) among treatments at $P < 0.05$, and Duncan's multiple range test was applied for comparing the means. OriginPro2019 (Origin Lab Corporation, Northampton, MA, USA) was used to draw the picture.

3. Results

3.1. Changes in the Soil Water Storage and Soil Water Fluxes. The changes in the soil water storage and water flux levels at the lower boundaries of the three alfalfa crops during each growth period are detailed in Tables 4 and 5, respectively. Results indicated that some treatments had a positive soil water storage capacity, which indicated a soil water surplus during growing seasons, whereas some treatments had a negative soil water storage capacity, which indicated a soil water deficit during growing seasons. According to the current irrigation system, in the SF-1~SF-9 treatments, the largest soil water surplus and soil water deficit during growing seasons occurred in the jointing stage of the first crop of SF-7 treatment and that of the third crop of SF-5 treatment, and the values were 19.25 and -10.67 mm, respectively. For the control treatment (SF-10), soil water surplus during growing seasons occurred in the jointing stage and branching stage, due to the irrigation during the two periods, whereas soil water deficit occurred in the seedling establishment stage and flowering stage, as there was no irrigation during this time. The changes in the soil water fluxes at the lower boundaries of each crop of alfalfa displayed similar laws and changes.

3.2. Water Consumption. The results of the calculated water consumption of the three crops of alfalfa during each growth stage are shown in Figure 3. Results indicated that the level of water consumption of the first crop of alfalfa during each growth stage under low, medium, and high water treatment conditions showed a trend of first increasing and then decreasing, and the relationship pattern of the water consumption during each growth stage was as follows: branching stage > jointing stage > seedling establishment stage > flowering stage. Furthermore, in accordance with the results of this study's comparison of total water consumption of the first crop of alfalfa (upper layer of Figure 3), the water consumption of the high water treatment (SF-7, SF-8, and SF-9) was greater than the water consumption of the medium water treatment (SF-4, SF-5, and SF-6), which was greater than the water consumption of the low water treatment (SF-1, SF-2, and SF-3). Furthermore, the water consumption during each growth period was observed to have increased with the increases in the irrigation amounts. The water consumption levels of the alfalfa during each growth period under the low, medium, and high water treatments were found to be lower than those of the local control treatment (SF-10). The control treatment (SF-10) was a one-time irrigation of alfalfa without applied fertilization treatments by the local herdsman for the purpose of pursuing a low input and high output scenario. In this study, by utilizing the results of this study's analyses of the water consumption levels of the alfalfa at different growth stages under the same water treatments and different fertilizer application rates, and according to the results of the comparison of a, b, and c detailed in the upper layer of Figure 3, it could be seen that under the same water treatment conditions, the water consumption levels of the alfalfa during the different growth stages were greatly affected by the amounts of the fertilizer applications.

Table 4: Changes in the soil water storage levels of each crop of alfalfa during each growth stage.

Treatment	Soil water storage (mm) (the first/second/third crop)				
	Seedling establishment stage	Jointing stage	Branching stage	Flowering stage	Total
SF-1	1.54/9.59/3.36	9.97/-3.27/-6.18	1.35/-3.95/13.35	3.83/-6.17/6.79	16.69/-3.80/17.32
SF-2	0.54/7.53/1.64	8.97/-5.97/-9.73	0.35/-3.61/12.46	2.83/-5.37/2.49	12.69/-7.42/6.86
SF-3	0.55/8.46/1.87	7.36/-5.48/-10.13	0.93/-2.92/14.61	2.63/-4.67/3.01	11.47/-4.61/9.36
SF-4	3.63/6.58/3.99	14.27/-3.37/-5.63	6.61/0.72/14.76	6.48/-4.38/5.47	30.99/-0.45/18.59
SF-5	3.36/5.69/3.01	12.23/-4.92/-10.67	3.85/-0.18/11.85	4.65/-4.55/3.13	24.09/-3.96/7.32
SF-6	3.68/5.99/3.05	12.87/-4.46/-8.81	6.37/0.25/13.16	4.49/-4.27/3.61	27.41/-2.49/11.01
SF-7	5.18/10.87/8.25	19.25/-1.14/-4.73	11.27/5.88/15.83	7.84/-1.62/8.36	43.54/13.99/27.71
SF-8	3.94/9.76/6.45	15.34/-2.07/-5.68	7.27/4.87/11.79	6.59/-1.86/5.16	33.14/10.70/17.72
SF-9	3.68/10.37/5.74	17.35/-1.48/-4.57	10.54/5.17/12.66	7.59/-1.25/5.63	39.16/12.81/19.46
SF-10	-9.68/-7.46/-8.89	23.35/23.75/17.65	19.56/13.69/56.08	-8.59/-15.18/-5.67	24.64/14.80/59.17

Table 5: Changes in the soil water fluxes of each crop of alfalfa during each growth stage.

Treatment	Water flux at the lower boundaries (mm) (the first/second/third crop)				
	Seedling establishment stage	Jointing stage	Branching stage	Flowering stage	Total
SF-1	1.29/8.06/2.89	8.76/-4.54/-7.23	1.19/-2.67/15.01	3.55/-4.34/3.58	14.79/-3.49/14.25
SF-2	0.29/6.72/0.83	6.76/-4.71/-11.29	0.19/-3.49/11.35	1.55/-5.88/2.08	8.79/-7.36/2.97
SF-3	0.76/7.09/1.16	8.64/-5.03/-9.78	0.17/-3.64/11.07	4.15/-5.18/2.16	13.72/-6.76/4.61
SF-4	3.78/7.24/4.87	14.34/-4.65/-7.88	6.31/0.83/12.27	6.19/-3.95/5.36	30.62/-0.53/14.62
SF-5	1.95/6.78/3.47	13.91/-4.74/-8.13	5.62/-0.35/9.39	3.97/-4.16/2.86	25.45/-2.47/7.59
SF-6	3.03/6.82/3.36	13.52/-4.81/-7.86	4.16/0.55/10.15	5.54/-3.99/3.37	26.25/-1.43/9.02
SF-7	5.61/11.36/6.42	18.18/-0.96/-3.06	10.48/6.43/12.14	8.85/-1.15/8.15	43.12/15.68/23.65
SF-8	5.82/10.85/5.18	19.61/-1.39/-7.67	9.69/5.52/10.18	7.86/-1.72/6.29	42.98/13.26/13.98
SF-9	6.27/10.89/5.99	18.26/-1.17/-6.76	8.91/5.58/11.19	8.17/-1.69/6.98	41.61/13.61/17.40
SF-10	-10.27/-6.19/-8.62	25.68/22.46/15.28	16.91/15.73/51.16	-8.17/-14.85/-6.42	24.15/17.15/51.40

The water consumption intensity of three alfalfa crops during each growth stage under different water and fertilizer combination applications was detailed in Table 6. Results showed that the value of water consumption intensity of alfalfa ranged from 1.84 to 3.27 mm/d at the seedling establishment stage, from 1.97 to 3.75 mm/d at the jointing stage, from 2.21 to 3.89 mm/d at the branching stage, and from 1.90 to 3.75 mm/d at the flowering stage, respectively. The value of average water consumption intensity of alfalfa throughout its growth period ranged from 1.98 to 3.64 mm/d. Secondly, the average water consumption intensity of the alfalfa had first increased and then decreased with the increases in the irrigation quota. The average water consumption intensity of the second alfalfa crop treatment was observed to be the lowest at 3.12 mm d^{-1}. The average water consumption intensity of the SF-8 treatment was observed to be the largest at 3.64 mm d^{-1}, which was 16.67% higher than that of the SF-1 treatment. The water consumption intensity pattern of the three crops of alfalfa during each growth stage was as follows: branching stage > jointing stage > flowering stage > seedling establishment stage. Thirdly, it was determined that the water consumption of the second crop was greater than that of the first crop, which was higher than that of the third crop (second crop > first crop > third crop). The alfalfa had tended to grow vigorously due to the high temperatures during the second crop period and was observed to grow more slowly during the third crop period due to the lower temperatures. Finally, it was found that under the same water treatment conditions, with the increases in the fertilizer applications, the average water consumption intensity of the alfalfa had first increased and then decreased, and the water consumption intensity pattern of the alfalfa was as follows: medium fertilization > high fertilization > low fertilization.

Note: different letters within the same column indicate significant differences in 0.05 level, the same as below.

3.3. Hay Yield and WUE. In this research, in order to make the test results more obvious, the WUE and growth rates of the three alfalfa crops during each treatment period were calculated based on the control treatment (SF-10). The calculation results are shown in Tables 7 and 8. Results showed that the hay yield of the first alfalfa crop ranged from 2576.29 to 3326.66 kg·hm^{-2}, of the second alfalfa crop ranged from 3526.76 to 5352.68 kg·hm^{-2}, and of the third alfalfa crop ranged from 3051.53 to 4352.18 kg·hm^{-2}, respectively. Similarly, the WUE of the first alfalfa crop ranged from 1.68 to 2.34 kg·m^{-3}, of the second alfalfa crop ranged from 2.15 to 3.20 kg·m^{-3}, and of the third alfalfa crop ranged from 1.98 to 2.65 kg·m^{-3} (Table 7), respectively. Obviously, the WUE of the alfalfa ranged between 1.68 and 3.20 kg·m^{-3}, and the

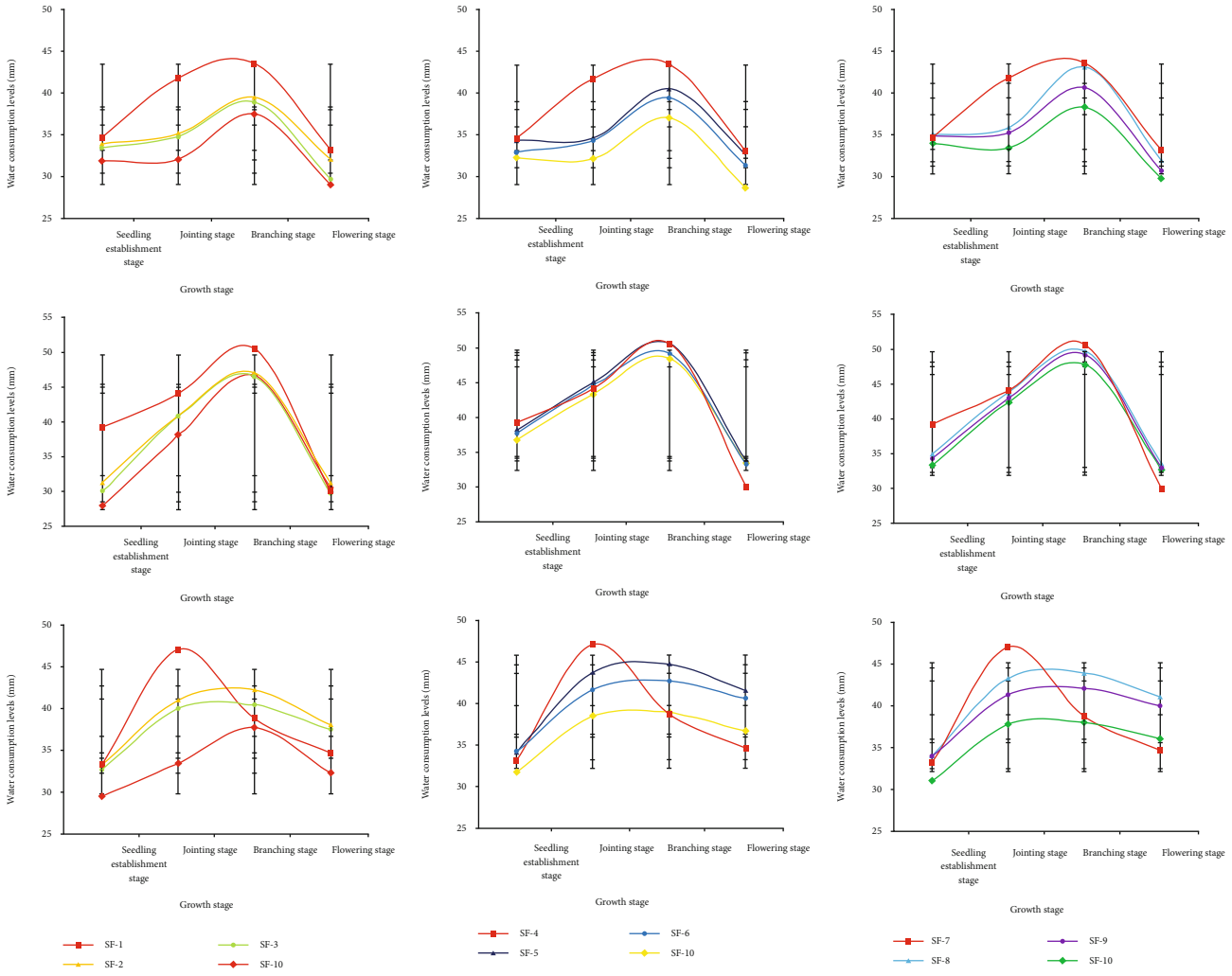

Figure 3: Water consumption levels of alfalfa during each growth stage. Note: the water consumption of the first, second, and third crops of alfalfa is plotted in the upper, middle, and lower layers in order, and (a–c) represent the low, medium, and high water level treatments in turn.

Table 6: Water consumption intensity levels of each crop of alfalfa during each growth stage.

Treatment	Water consumption intensity levels (mm/d) (the first/second/third crop)				
	Seedling establishment stage	Jointing stage	Branching stage	Flowering stage	Average value
SF-1	$1.99^{b}/2.33^{e}/1.84^{c}$	$2.29^{c}/3.18^{c}/1.97^{e}$	$2.34^{c}/3.59^{b}/2.21^{c}$	$2.23^{c}/3.39^{b}/1.90^{d}$	$2.21^{c}/3.12^{c}/1.98^{d}$
SF-2	$2.12^{a}/2.61^{d}/2.08^{a}$	$2.51^{b}/3.42^{b}/2.41^{c}$	$2.47^{b}/3.62^{b}/2.48^{b}$	$2.46^{a}/3.47^{b}/2.24^{b}$	$2.39^{b}/3.28^{b}/2.30^{b}$
SF-3	$2.09^{a}/2.50^{d}/2.04^{a}$	$2.49^{b}/3.40^{b}/2.35^{c}$	$2.43^{b}/3.58^{b}/2.37^{b}$	$2.28^{c}/3.32^{b}/2.20^{b}$	$2.32^{c}/3.20^{c}/2.24^{b}$
SF-4	$2.02^{b}/3.07^{b}/1.99^{b}$	$2.30^{c}/3.61^{a}/2.27^{d}$	$2.32^{c}/3.73^{a}/2.29^{c}$	$2.21^{c}/3.70^{a}/2.16^{b}$	$2.21^{c}/3.53^{a}/2.18^{c}$
SF-5	$2.15^{a}/3.18^{a}/2.14^{a}$	$2.48^{b}/3.75^{a}/2.58^{b}$	$2.53^{b}/3.89^{a}/2.63^{a}$	$2.52^{a}/3.75^{a}/2.45^{a}$	$2.42^{b}/3.64^{a}/2.45^{a}$
SF-6	$2.06^{b}/3.15^{a}/2.14^{a}$	$2.46^{b}/3.71^{a}/2.45^{c}$	$2.47^{b}/3.78^{a}/2.51^{a}$	$2.41^{b}/3.70^{a}/2.39^{a}$	$2.35^{b}/3.59^{a}/2.37^{a}$
SF-7	$2.12^{a}/2.78^{c}/1.94^{b}$	$2.38^{c}/3.53^{b}/2.22^{d}$	$2.39^{c}/3.67^{b}/2.24^{c}$	$2.29^{b}/3.64^{a}/2.12^{c}$	$2.29^{c}/3.41^{b}/2.13^{c}$
SF-8	$2.18^{a}/2.92^{b}/2.13^{a}$	$2.56^{b}/3.65^{a}/2.55^{b}$	$2.69^{a}/3.82^{a}/2.59^{a}$	$2.46^{a}/3.73^{a}/2.42^{a}$	$2.47^{b}/3.53^{a}/2.42^{a}$
SF-9	$2.17^{a}/2.86^{c}/2.12^{a}$	$2.51^{b}/3.58^{a}/2.43^{c}$	$2.53^{b}/3.79^{a}/2.48^{b}$	$2.36^{b}/3.66^{a}/2.35^{a}$	$2.39^{b}/3.47^{a}/2.35^{a}$
SF-10	$2.17^{a}/3.27^{a}/2.08^{a}$	$2.98^{a}/3.67^{a}/2.77^{a}$	$2.72^{a}/3.89^{a}/2.28^{c}$	$2.55^{a}/3.34^{b}/2.04^{c}$	$2.61^{a}/3.54^{a}/2.29^{b}$

growth rate was between 4.85 and 51.77%. It was found that the second crop of the SF-5 treatment had the highest WUE and growth rate, which were 3.20 $kg \cdot m^{-3}$ and 51.77%, respectively. It was determined that both the WUE and growth rates showed the following trend: second crop > third crop > first crop. The second crop of the SF-5 treatment was found

Table 7: Yields, WUE, and growth rates of each crop of alfalfa (the first/second/third crop).

Treatment	Total water consumption (mm)	Yield ($kg \cdot hm^{-2}$)	WUE ($kg \cdot m^{-3}$)	Yield increasing rate (%)
SF-1	$130.42^{c}/143.19^{c}/132.73^{d}$	$2701.35^{c}/4077.04^{d}/3351.68^{d}$	$2.07^{b}/2.85^{b}/2.52^{b}$	4.85/15.60/9.84
SF-2	$140.42^{b}/150.68^{b}/154.47^{b}$	$3201.60^{a}/4752.38^{c}/4127.06^{b}$	$2.28^{a}/3.15^{a}/2.67^{a}$	24.27/34.75/35.25
SF-3	$136.71^{b}/147.27^{c}/150.33^{b}$	$3076.54^{b}/4627.31^{c}/3951.98^{b}$	$2.25^{a}/3.14^{a}/2.63^{a}$	19.42/31.21/29.51
SF-4	$130.29^{c}/161.88^{a}/146.09^{c}$	$3026.51^{b}/5152.58^{a}/3801.90^{c}$	$2.32^{a}/3.18^{a}/2.60^{a}$	17.48/46.10/24.59
SF-5	$142.36^{b}/167.33^{a}/164.39^{a}$	$3326.66^{a}/5352.68^{a}/4352.18^{a}$	$2.34^{a}/3.20^{a}/2.65^{a}$	29.13/51.77/42.62
SF-6	$138.24^{b}/164.82^{a}/159.27^{a}$	$3226.61^{a}/5252.63^{a}/4177.09^{a}$	$2.33^{a}/3.19^{a}/2.62^{a}$	25.24/48.94/36.89
SF-7	$135.24^{c}/156.23^{b}/142.94^{c}$	$2801.40^{c}/4802.40^{b}/3676.84^{c}$	$2.07^{b}/3.07^{a}/2.57^{a}$	8.74/36.17/20.49
SF-8	$145.78^{a}/161.94^{a}/162.60^{a}$	$3076.54^{b}/5027.51^{b}/4227.11^{a}$	$2.11^{b}/3.10^{a}/2.60^{a}$	19.42/42.55/38.52
SF-9	$141.13^{b}/159.48^{a}/157.44^{a}$	$2976.49^{b}/4927.46^{b}/4077.04^{b}$	$2.11^{b}/3.09^{a}/2.59^{a}$	15.53/39.72/33.61
SF-10	$153.11^{a}/163.95^{a}/153.73^{b}$	$2576.29^{d}/3526.76^{e}/3051.53^{e}$	$1.68^{c}/2.15^{c}/1.98^{c}$	0/0/0

Table 8: Total yield, average WUE, and growth rates of the three alfalfa crops.

Treatment	Total water consumption (mm)	Yield ($kg \cdot hm^{-2}$)	WUE ($kg \cdot m^{-3}$)	Yield increasing rate (%)
SF-1	406.34^{c}	10130.06^{d}	2.49^{b}	10.66
SF-2	445.57^{b}	12081.04^{b}	2.71^{a}	31.97
SF-3	434.31^{b}	11655.83^{c}	2.68^{a}	27.32
SF-4	438.26^{b}	11980.99^{b}	2.73^{a}	30.87
SF-5	474.08^{a}	13031.51^{a}	2.75^{a}	42.35
SF-6	462.33^{a}	12656.33^{a}	2.74^{a}	38.25
SF-7	434.41^{b}	11280.64^{c}	2.60^{b}	23.22
SF-8	470.32^{a}	12331.16^{b}	2.62^{a}	34.70
SF-9	458.05^{a}	11980.69^{b}	2.61^{b}	30.87
SF-10	470.79^{a}	9154.58^{e}	1.94^{c}	0.00

to have the highest WUE and growth rate, at 3.20 $kg \cdot m^{-3}$ and 51.77%, respectively. It was observed that both the WUE and growth rates displayed the trend pattern of second crop > third crop > first crop. Tables 7 and 8 also showed that the yield and WUE level of the first crop of alfalfa control treatment (SF-10) were the lowest, at 2576.29 $kg \cdot hm^{-2}$ and 1.68 $kg \cdot m^{-3}$, respectively. The yield and WUE level of the SF-5 treatment were found to be the highest, at 3326.66 $kg \cdot hm^{-2}$ and 2.34 $kg \cdot m^{-3}$, respectively, which indicated that the yield and WUE had increased by 29.13% and 38.88%, respectively. When compared with the control treatment (SF-10), the growth rates of the alfalfa crops were 4.85% to 29.13% higher under the different water and fertilizer application treatments, which indicated obvious yield increase effects. The second and third crops of the alfalfa displayed similar results. It was found that under the same water treatment conditions, the hay yields and WUE levels of the alfalfa undergoing the medium fertilization treatment were the largest. Also, under the same fertilization treatment conditions, the hay yields and WUE levels of the alfalfa undergoing the medium fertilization treatment were the largest. Therefore, it was determined that with the increases in the water or fertilization treatments, both the crop yields and WUE levels had shown the phenomenon of "diminishing returns."

The frequency statistical analysis on the different levels of irrigation and nitrogen application (Figure 4) showed that there was a 95% probability that an irrigation water of 141.11~165.75 mm and a nitrogen application of 60.52~80.70 $kg \cdot hm^{-2}$ could obtain a hay yield of alfalfa of more than 11903.17 $kg \cdot hm^{-2}$.

4. Discussion

4.1. Effects of Subsurface Drip Irrigation on Water Consumption of Alfalfa. Water is one of the most important factors which affect alfalfa growth in arid and semiarid areas, where irrigation is required for crop production, and growers are seeking methods to save water by increasing irrigation efficiency. Water consumption, water consumption intensity, and WUE are important criteria for determining whether the irrigation application amounts are reasonable, especially WUE, which is considered to describe the physiological indicators of alfalfa growth, especially the relationship between harvest yield and crop water consumption [30]. In this study, the water consumption of alfalfa showed an increasing trend with the increase of irrigation. Most importantly, it could be seen that under the same water treatment conditions, the water consumption levels of the alfalfa during the different growth stages were greatly affected by the amounts of the fertilizer applications (Figure 3). This result indicated that fertilization was a sensitive factor, which had obvious water regulating effect, and proper fertilization could improve water consumption and WUE. Our findings were comparable to those obtained by Thompson et al. [37] and Agami et al. [38], who suggested that exogenous N-supply was effective in mitigating the adverse effects of drought stress, and understanding the water consumption rule of crops is significant for the prevention of unnecessary water losses. Similarly, al-Naeem [39] also reported that alfalfa dry yield could be severely affected under water stress irrigation management.

In this study, we also found that the water consumption of alfalfa during each growth stage under low, medium, and high water treatment conditions showed a trend of first increasing and then decreasing. This was because the coverage of the alfalfa plants was low during the seedling establishment stage, and the water consumption of the alfalfa during

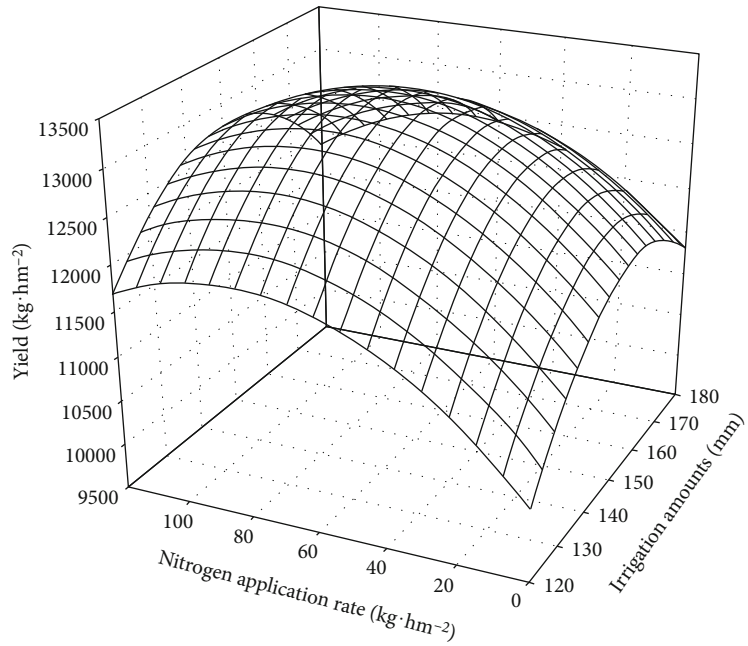

Figure 4: Relationship curve between the hay yield and the total irrigation amounts and fertilizer amount.

that stage was mainly soil evaporation. With the growth and development of the crops, the alfalfa entered a vigorous growth stage and rapid plant growth had occurred. As the plant coverage began to reach the maximum, the bare field surfaces gradually decreased, and crop transpiration was the main form of crop evapotranspiration. At this time, the water consumption reached a maximum. Since the alfalfa was cut at the beginning of the flowering stage and quickly entered the seedling establishment stage of the next crop, this led to the water consumption being the lowest during the flowering stage. Our findings were in consensus with that of Li et al. [40], who suggested that the increased vegetation coverage induced a decrease in surface albedo and resulted in an increase in temperature, and this positive effect could be counteracted by higher evapotranspiration, and the net effect was a decrease in daytime land surface temperature. It should be noted that the water consumption of each experiment plot of the third crop of alfalfa during the branching and flowering stages was observed to be higher than that of the control treatment (SF-10). The reasons for these results were determined to be that the temperature was relatively low and nitrogen application caused alfalfa to still grow vigorously, which consumed more water under relatively low temperature conditions. These findings indicated that the fertilization treatments had potentially promoted the growth and development of alfalfa under low temperature conditions, which is consistent with Hannaway and Shuler [41], who suggested that a yield increase due to fertilizer N is even more likely when alfalfa is established in low N soils and relatively cool less than 60°F for several weeks after planting.

Water consumption intensity is defined as the water consumption per unit area of plant population per unit time. Under the current study, the supplied water was based on the actual water consumption in the root zone, where irrigation water was automatically supplied when needed. The results (Table 6) showed that the value of average water consumption intensity of alfalfa throughout its growth period ranged from 1.98 to 3.64 mm/d. These findings were comparable to those obtained by Jackson [42], Stanberry et al. [43], Daigger et al. [44], Krogman and Hobbs [45], and Wang et al. [25], who suggested that the water consumption intensity of alfalfa throughout the growing season ranged from 2.00 to 7.00 mm/d. Furthermore, the maximum water consumption intensity of alfalfa appeared at the branching stage and then decreased at the flowering stage. Our findings were in consensus with Wang et al. [25], who suggested that the water consumption intensity was also high for reproductive growth and nutrition growth at the bud stage and then decreased at the flowering stage when alfalfa grew slowly due to reproductive growth. Generally, the trend of water consumption of alfalfa during the fertility period in an arid and semiarid desert region was similar compared to other regions in which water consumption has been studied [46, 47].

4.2. Effects of Subsurface Drip Irrigation on Hay Yield and WUE of Alfalfa. WUE refers to the output per unit of water consumption of crops. Previous studies had shown that drought was an important environmental factor that influences growth and physiological processes in plants [48], there were a positive link between WUE and hay yield [49] and synergistic effects between water and fertilizer, and an appropriate N-supply had an obvious water regulating effect [50, 51], which could stimulate plant growth, improve WUE, and alleviate the effects of drought stress [52, 53]. The irrigation amount and nitrogen application rate had significant effects on the total hay yield of alfalfa. In the case of water deficit, crop root development is hindered, nutrient absorption capacity is reduced, and fertilizer efficiency is limited. When water is excessive, soil nutrient leaching occurs, soil permeability is reduced, and root respiration and nutrient

uptake by crops are hindered [54], thereby reducing the hay yield of alfalfa. Therefore, it should be irrigated in small increments and frequently in order to attain high yields when an alfalfa crop is grown under arid and semiarid conditions [55]. In this study, we found that additional applications of fertilizer under the same water treatment conditions had an obvious effect of increasing hay yields of the alfalfa, which was in consensus with Wang et al. [56] and Liu et al. [57], who observed higher WUE under moderate water stress and a decrease of WUE under severe water stress conditions. Abd el–Mageed et al. [58] conducted field experiments for two years at the experimental farm of the Faculty of Agriculture, in EI Fayoum Province of Egypt, and found that application of higher levels of potassium fertilizer in an arid environment improves plant water status as well as growth and yield of soybean under water stress. In this study, we found that an appropriate amount of water and nitrogen fertilizer can increase the WUE of alfalfa under the condition of SDI and increase the hay yield, and too low or too high water and nitrogen fertilizer will adversely affect the WUE and hay yield of alfalfa. These were in consensus with Wang et al. [59], who suggested that partial root-zone drying could be a promising technique for alfalfa production in the arid area of Northwest China, with improved crop water productivity and positive effect on quality characteristics.

In the research, we also found that the second crop of alfalfa had the largest hay yield and WUE, and both appeared in the SF-5 treatment (Table 7). The reason for this phenomenon was that the second crop of alfalfa was in the season from late June to early August each year, when the temperature was higher, the metabolism of alfalfa was faster, and the growth was vigorous. Our findings were in consensus with Karimzadeh Soureshjani et al. [60], who suggested that cool weather during the emergence of first flower buds and first flowering stages led to forage yield loss of alfalfa. In this experiment, hay yield and WUE of alfalfa both increased first and then decreased with the increase of irrigation amount and increased first and then decreased with increasing nitrogen application (Table 8). This result indicated that fertilization had obvious water regulating effect, and proper fertilization could improve WUE [37]. Furthermore, fertilization can increase the soil water holding capacity [61], and successfully matching fertilizer availability with crop absorption improves water-use efficiency and increases yield [38]. Thus, SF-5 treatment is recommended for subsurface drip irrigation of alfalfa in Mu Us Sandland of Northwest China.

5. Conclusions

Overall, the larger the irrigation quota, the greater the water consumption of the alfalfa during each growth stage. The overall changes in the water consumption levels displayed a trend of first increasing and then decreasing. The water consumption during each growth period of each crop of alfalfa had changed within a range of 130 to 170 mm and had displayed a large amplitude of change, with the water consumption during the entire growth period measuring approximately 500 mm. The water consumption intensity of the alfalfa had first increased and then decreased with the increases in the irrigation quota. The average water consumption intensity of alfalfa ranged from 1.98 to 3.64 mm d^{-1}. The WUE of alfalfa ranged between 1.68 and 3.20 $kg{\cdot}m^{-3}$, and the growth rates were between 4.85% and 51.77%. The results indicated that there was a 95% probability of obtaining a hay yield of alfalfa of more than 11903 $kg{\cdot}hm^{-2}$ under SDI with the irrigation amounts of 142~165 mm and nitrogen application of 61~80 $kg{\cdot}hm^{-2}$. Our results demonstrated that SDI was a promising irrigation method, which can increase the WUE and hay yield of alfalfa under the condition of SDI within an appropriate amount of water and nitrogen fertilizer, and too low or too high water and nitrogen fertilizer will adversely affect the WUE and hay yield of alfalfa.

Data Availability

The raw/processed data required to reproduce the results obtained in this study cannot be shared at this time because they are used in an ongoing study.

Conflicts of Interest

The authors declare no conflict of interest.

Authors' Contributions

Xuesong Cao and Yayang Feng contributed equally to this work.

Acknowledgments

This study was supported financially by the China Institute of Water Resources and Hydropower Research (grant No. MK2018J05) and Natural Science Foundation of China (No. 41901052).

References

[1] S. Sun, P. Wu, Y. Wang, J. Liu, X. Zhang, and X. Zhao, "The impacts of interannual climate variability and agricultural inputs on water footprint of crop production in an irrigation district of China," *Science of the Total Environment*, vol. 444, pp. 498–507, 2013.

[2] A. D. McHugh, S. Bhattarai, G. Lotz, and D. J. Midmore, "Effects of subsurface drip irrigation rates and furrow irrigation for cotton grown on a vertisol on off-site movement of sediments, nutrients and pesticides," *Agronomy for Sustainable Development*, vol. 28, no. 4, pp. 507–519, 2008.

[3] T. L. Thompson, T. A. Doerge, and R. E. Godin, "Subsurface drip irrigation and fertigation of broccoli," *Soil Science Society of America Journal*, vol. 66, no. 1, pp. 178–185, 2002.

[4] J. E. Ayars, C. J. Phene, R. B. Hutmacher et al., "Subsurface drip irrigation of row crops: a review of 15 years of research at the Water Management Research Laboratory," *Agricultural Water Management*, vol. 42, no. 1, pp. 1–27, 1999.

[5] M. P. Palacios-Díaz, V. Mendoza-Grimón, J. R. Fernández-Vera, F. Rodríguez-Rodríguez, M. T. Tejedor-Junco, and J. M. Hernández-Moreno, "Subsurface drip irrigation and reclaimed water quality effects on phosphorus and salinity

distribution and forage production," *Agricultural Water Management*, vol. 96, no. 11, pp. 1659–1666, 2009.

[6] J. W. Heard, M. J. Porker, D. P. Armstrong et al., "The economics of subsurface drip irrigation on perennial pastures and fodder production in Australia," *Agricultural Water Management*, vol. 111, pp. 68–78, 2012.

[7] M. M. Kandelous, T. Kamai, J. A. Vrugt, B. Hanson, J. W. Hopmans, and J. Šimůnek, "Evaluation of subsurface drip irrigation design and management parameters for alfalfa," *Agricultural Water Management*, vol. 109, pp. 81–93, 2012.

[8] F. R. Lamm, "Cotton, tomato, corn, and onion production with subsurface drip irrigation: a review," *Transactions of the ASABE*, vol. 59, no. 1, pp. 263–278, 2016.

[9] M. L. Wood and L. Finger, "Influence of irrigation method on water use and production of perennial pastures in northern Victoria," *Australian Journal of Experimental Agriculture*, vol. 46, no. 12, pp. 1605–1614, 2006.

[10] M. Gil, L. Rodríguez-Sinobas, L. Juana, R. Sánchez, and A. Losada, "Emitter discharge variability of subsurface drip irrigation in uniform soils: effect on water-application uniformity," *Irrigation Science*, vol. 26, no. 6, pp. 451–458, 2008.

[11] Y. Mo, G. Li, and D. Wang, "A sowing method for subsurface drip irrigation that increases the emergence rate, yield, and water use efficiency in spring corn," *Agricultural Water Management*, vol. 179, pp. 288–295, 2017.

[12] D. Geisseler, B. J. Aegerter, E. M. Miyao, T. Turini, and M. D. Cahn, "Nitrogen in soil and subsurface drip-irrigated processing tomato plants (*Solanum lycopersicum* L.) as affected by fertilization level," *Scientia Horticulturae*, vol. 261, no. 3, article 108999, 2020.

[13] A. Gupta, K. Rao, S. Singh, K. Soni, and C. Sawant, "Water productivity and yield of baby corn (*Zea mays* L.) as influenced by irrigation levels under subsurface drip irrigation," *International Journal of Chemical Studies*, vol. 7, no. 5, pp. 128–135, 2019.

[14] M. Umair, T. Hussain, H. Jiang et al., "Water-saving potential of subsurface drip irrigation for winter wheat," *Sustainability*, vol. 11, no. 10, pp. 2978–3015, 2019.

[15] J. P. Bordovsky and D. O. Porter, "Effect of subsurface drip irrigation system uniformity on cotton production in the Texas High Plains," *Applied Engineering in Agriculture*, vol. 24, no. 4, pp. 465–472, 2008.

[16] D. Barnes, "Alfalfa," in *Hybridization of crop plants. Crop Science Society of America and American Society of Agronomy*, pp. 177–187, Madison, WI, USA, 1980.

[17] Y. Chen, X. Gong, G. Li et al., "Effects of dietary alfalfa flavonoids extraction on growth performance, organ development and blood biochemical indexes of Yangzhou geese aged from 28 to 70 days," *Animal Nutrition*, vol. 2, no. 4, pp. 318–322, 2016.

[18] S. Kumar, "Biotechnological advancements in alfalfa improvement," *Journal of Applied Genetics*, vol. 52, no. 2, pp. 111–124, 2011.

[19] N. P. Martin and D. R. Mertens, "Reinventing alfalfa for dairy cattle and novel uses," in *Proceedings, California alfalfa and forage symposium*, pp. 12–14, California, America, 2005.

[20] K. I. Rovkina, S. V. Krivoshchekov, A. M. Guryev, M. S. Yusubov, and M. V. Belousov, "Water-soluble polysaccharides of alfalfa (*Medicago sativa* (Fabaceae)) of flora of Krasnoyarsk Krai," *Russian Journal of Bioorganic Chemistry*, vol. 44, no. 7, pp. 854–859, 2018.

[21] P. A. N. Wei-cang, "Main composition of alfalfa and its application in animal husbandry," *Journal of Traditional Chinese Veterinary Medicine*, vol. 34, no. 2, 2015.

[22] D. Wang, M. Khurshid, Z. Min Sun, M. Liang Zhou, Y. Min Wu, and Y. Xiong Tang, "Genetic engineering of alfalfa (*Medicago sativa* L.)," *Protein and Peptide Letters*, vol. 23, no. 5, pp. 495–502, 2016.

[23] F. Lamm, "Subsurface drip irrigation and possibilities in alfalfa," 2016.

[24] D. Zaccaria, M. T. Carrillo-Cobo, A. Montazar, D. H. Putnam, and K. Bali, "Assessing the viability of sub-surface drip irrigation for resource-efficient alfalfa production in central and southern California," *Water*, vol. 9, no. 11, 2017.

[25] S. Wang, X. Jiao, W. Guo, Y. Bai, L. Wang, and J. Lu, "Adaptability of shallow subsurface drip irrigation of alfalfa in an arid desert area of northern Xinjiang," *PLoS One*, vol. 13, no. 4, article e0195965, 2018.

[26] C. Godoy-Avila, A. Perez-Gutierrez, C. A. Torres, L. J. Hermosillo, and I. Reyes, "Water use, forage production and water relations in alfalfa with subsurface drip irrigation," *Agrociencia*, vol. 37, no. 2, pp. 107–115, 2003.

[27] S. Kazumba, L. Gillerman, Y. DeMalach, and G. Oron, "Sustainable domestic effluent reuse *via* subsurface drip irrigation (SDI): alfalfa as a perennial model crop," *Water Science and Technology*, vol. 61, no. 3, pp. 625–632, 2010.

[28] C. R. Camp, "Subsurface drip irrigation: a review," *Transactions of the ASAE*, vol. 41, no. 5, 1998.

[29] D. Kou, D. Su, D. Wu, and Y. Li, "Effects of regulated deficit irrigation on water consumption, hay yield and quality of alfalfa under subsurface drip irrigation," *Transactions of the Chinese Society of Agricultural Engineering*, vol. 30, no. 2, pp. 116–123, 2014.

[30] F. R. Lamm, K. R. Harmoney, A. A. Aboukheira, and S. K. Johnson, "Alfalfa production with subsurface drip irrigation in the Central Great Plains," *Transactions of the ASABE*, vol. 55, no. 4, pp. 1203–1212, 2012.

[31] S. M. Ismail and M. H. Almarshadi, "Maximizing productivity and water use efficiency of alfalfa under precise subsurface drip irrigation in arid regions," *Irrigation and Drainage*, vol. 62, no. 1, pp. 57–66, 2013.

[32] M. Alam, T. P. Trooien, D. H. Rogers, and T. J. Dumler, "An efficient irrigation technology for alfalfa growers," *Journal of Extension*, vol. 40, no. 3, pp. 1–9, 2002.

[33] F. R. Lamm, H. L. Manges, L. R. Stone, A. H. Khan, and D. H. Rogers, "Water requirement of subsurface drip-irrigated corn in Northwest Kansas," *Transactions of the ASAE*, vol. 38, no. 2, pp. 441–448, 1995.

[34] K. S. Reddy, R. Singh, K. V. R. Rao, and D. M. Bhandarkar, "Economic feasibility of drip irrigation systems in India," *Agricultural Engineering Today*, vol. 28, no. 2, pp. 65–69, 2004.

[35] M. Stavarache, I. Muntianu, V. Vîntu, C. Samuil, and C. I. Popovici, "Research on the influence of inoculation and fertilization on the alfalfa (*Medicago sativa* L.), in first year of vegetation, under conditions of Moldavian forest steppe," *Lucrări Ştiinţifice - Universitatea de Ştiinţe Agricole Şi Medicină Veterinară Seria Zootehnie*, vol. 56, pp. 176–181, 2011.

[36] R. Liu, Y. Zhang, Y. Ge, W. Hu, and B. Sha, "Precision regulation model of water and fertilizer for alfalfa based on agriculture cyber-physical system," *IEEE Access*, vol. 8, pp. 38501–38516, 2020.

[37] T. L. Thompson, T. A. Doerge, and R. E. Godin, "Nitrogen and water interactions in subsurface drip-irrigated cauliflower I. Plant response," *Soil Science Society of America Journal*, vol. 64, no. 1, pp. 406–411, 2000.

[38] R. A. Agami, S. A. Alamri, T. A. Abd el-Mageed, M. Abousekken, and M. Hashem, "Role of exogenous nitrogen supply in alleviating the deficit irrigation stress in wheat plants," *Agricultural Water Management*, vol. 210, pp. 261–270, 2018.

[39] M. A. al-Naeem, "Influence of water stress on water use efficiency and dry hay production of alfalfa in Al-Ahsa, Saudi Arabia," *International Journal of Soil Science*, vol. 3, no. 3, pp. 119–126, 2008.

[40] S. Li, W. Liang, B. Fu et al., "Vegetation changes in recent large-scale ecological restoration projects and subsequent impact on water resources in China's Loess Plateau," *Science of the Total Environment*, vol. 569-570, pp. 1032–1039, 2016.

[41] D. B. Hannaway and P. E. Shuler, "Nitrogen fertilization in alfalfa production," *Journal of Production Agriculture*, vol. 6, no. 1, pp. 80–85, 1993.

[42] E. Jackson, "Water consumption by lucerne in Central Australia," *Australian Journal of Agricultural Research*, vol. 11, no. 5, pp. 715–722, 1960.

[43] C. Stanberry, C. Converse, H. Haise, and O. Kelley, "Effect of moisture and phosphate variables on alfalfa hay production on the Yuma Mesa," *Soil Science Society of America Journal*, vol. 19, no. 3, pp. 303–310, 1955.

[44] L. Daigger, L. Axthelm, and C. Ashburn, "Consumptive use of water by alfalfa in Western Nebraska1," *Agronomy Journal*, vol. 62, no. 4, pp. 507-508, 1970.

[45] K. Krogman and E. Hobbs, "Evapotranspiration by irrigated alfalfa as related to season and growth stage," *Canadian Journal of Plant Science*, vol. 45, no. 4, pp. 309–313, 1965.

[46] H. X. Liu and Z. G. Guo, "Forage yield and water use efficiency of alfalfa applied with silicon under water deficit conditions," *PHILIPP AGRIC SCIENTIST*, vol. 96, pp. 370–376, 2013.

[47] I. Borza, C. Domuța, M. Șandor, R. Brejea, and E. Jude, "The irrigation influence on water use efficiency in alfalfa 2nd year, Oradea 2010-2013," *Analele Universității din Oradea, Fascicula: Protecția Mediului*, vol. 23, pp. 25–30, 2014.

[48] N. Loutfy, M. A. el-Tayeb, A. M. Hassanen, M. F. M. Moustafa, Y. Sakuma, and M. Inouhe, "Changes in the water status and osmotic solute contents in response to drought and salicylic acid treatments in four different cultivars of wheat (*Triticum aestivum*)," *Journal of Plant Research*, vol. 125, no. 1, pp. 173–184, 2012.

[49] S. Tandoh, B. Coulman, and B. Biligetu, "Assessment of crested wheatgrass (*Agropyron cristatum* L.) accessions with different geographical origins for agronomic and phenotypic traits and nutritive value," *Euphytica*, vol. 215, no. 10, 2019.

[50] Y. Li and D. Su, "Alfalfa water use and yield under different sprinkler irrigation regimes in north arid regions of China," *Sustainability*, vol. 9, no. 8, 2017.

[51] V. S. Rathore, N. S. Nathawat, S. Bhardwaj et al., "Yield, water and nitrogen use efficiencies of sprinkler irrigated wheat grown under different irrigation and nitrogen levels in an arid region," *Agricultural Water Management*, vol. 187, pp. 232–245, 2017.

[52] F. Wu, W. Bao, F. Li, and N. Wu, "Effects of drought stress and N supply on the growth, biomass partitioning and water-use efficiency of *Sophora davidii* seedlings," *Environmental and Experimental Botany*, vol. 63, no. 1-3, pp. 248–255, 2008.

[53] H. Brueck, K. Erdle, Y. Gao et al., "Effects of N and water supply on water use-efficiency of a semiarid grassland in Inner Mongolia," *Plant and Soil*, vol. 328, no. 1-2, pp. 495–505, 2010.

[54] M. Abid, E. Mansour, L. B. Yahia, A. Ben Khaled, A. Ferchichi, and K. Bachar, "Alfalfa nutritive quality as influenced by drought in South-Eastern Oasis of Tunisia," *Italian Journal of Animal Science*, vol. 15, no. 2, pp. 334–342, 2016.

[55] I. Saeed and A. H. el-Nadi, "Irrigation effects on the growth, yield, and water use efficiency of alfalfa," *Irrigation Science*, vol. 17, no. 2, pp. 63–68, 1997.

[56] F. Wang, S. Kang, T. Du, F. Li, and R. Qiu, "Determination of comprehensive quality index for tomato and its response to different irrigation treatments," *Agricultural Water Management*, vol. 98, no. 8, pp. 1228–1238, 2011.

[57] H. Liu, A. W. Duan, F. S. Li, J. S. Sun, Y. C. Wang, and C. T. Sun, "Drip irrigation scheduling for tomato grown in solar greenhouse based on pan evaporation in North China Plain," *Journal of Integrative Agriculture*, vol. 12, no. 3, pp. 520–531, 2013.

[58] T. A. Abd el–Mageed, A. M. A. el-Sherif, M. M. Ali, and M. H. Abd el-Wahed, "Combined effect of deficit irrigation and potassium fertilizer on physiological response, plant water status and yield of soybean in calcareous soil," *Archives of Agronomy and Soil Science*, vol. 63, no. 6, pp. 827–840, 2016.

[59] Y. Wang, C. Liu, P. Cui, and D. Su, "Effects of partial root-zone drying on alfalfa growth, yield and quality under subsurface drip irrigation," *Agricultural Water Management*, vol. 245, article 106608, 2021.

[60] H. Karimzadeh Soureshjani, A. Ghorbani Dehkordi, and M. Bahador, "Temperature effect on yield of winter and spring irrigated crops," *Agricultural and Forest Meteorology*, vol. 279, article 107664, 2019.

[61] J. Wang, W. Liu, and T. Dang, "Responses of soil water balance and precipitation storage efficiency to increased fertilizer application in winter wheat," *Plant and Soil*, vol. 347, no. 1–2, pp. 41–51, 2011.

Hindawi
Journal of Sensors
Volume 2021, Article ID 8872947, 8 pages
https://doi.org/10.1155/2021/8872947

Research Article

Weighted Mask R-CNN for Improving Adjacent Boundary Segmentation

SungMin Suh[1], **Yongeun Park**[2], **KyoungMin Ko**[1], **SeongMin Yang**[1,3], **Jaehyeong Ahn**[1], **Jae-Ki Shin**[4] **and SungHwan Kim**[1,3]

[1]*Department of Applied Statistics, Konkuk University, Seoul, Republic of Korea*
[2]*Department of Social and Environmental Engineering, Konkuk University, Seoul, Republic of Korea*
[3]*AI Analytics Team, DeepVisions, Seoul, Republic of Korea*
[4]*Korea Water Resources Corporation, Busan, Republic of Korea*

Correspondence should be addressed to Jae-Ki Shin; shinjaeki@gmail.com and SungHwan Kim; shkim1213@konkuk.ac.kr

Received 16 August 2020; Revised 23 November 2020; Accepted 14 December 2020; Published 23 January 2021

Academic Editor: Zhenxing Zhang

In the recent era of AI, instance segmentation has significantly advanced boundary and object detection especially in diverse fields (e.g., biological and environmental research). Despite its progress, edge detection amid adjacent objects (e.g., organism cells) still remains intractable. This is because homogeneous and heterogeneous objects are prone to being mingled in a single image. To cope with this challenge, we propose the weighted Mask R-CNN designed to effectively separate overlapped objects in virtue of extra weights to adjacent boundaries. For numerical study, a range of experiments are performed with applications to simulated data and real data (e.g., *Microcystis*, one of the most common algae genera and cell membrane images). It is noticeable that the weighted Mask R-CNN outperforms the standard Mask R-CNN, given that the analytic experiments show on average 92.5% of precision and 96.4% of recall in algae data and 94.5% of precision and 98.6% of recall in cell membrane data. Consequently, we found that a majority of sample boundaries in real and simulated data are precisely segmented in the midst of object mixtures.

1. Introduction

The identification of genera in water samples is of central importance in assessing water quality in vision. Over the years, this procedure has mainly relied on manual counting [1], which inevitably suffers limitations in consuming time, manpower, and energy. Thus, it is urgent to develop vision sensing-based automatic tools capable of expediting the detection and quantification process. Commonly, previous studies on algae genera have focused on developing accurate classification models. For identifying labels, the model is designed to predict the corresponding taxa, learning on images containing genera of interest. Large-scale data by augmentation technique have been exploited to fine-tune a model on the basis of the AlexNet architecture [2]. It is remarkable that they have achieved performance of overall accuracy 99.51% of 80 genera, each of which contains more than 2000 samples. Different from deep learning-based methods, various predictive models based on hand-crafted features also reported promising results. Importantly, Schulze et al. and Bueno et al. [3, 4] have obtained 95% and 98% accuracy, respectively. Given that the accuracies of the studies nearly come to 100%, seemingly it seems that classification of genera is conquered. Apart from this, Park et al. [5] have proposed the Bayesian optimization-based neural architecture search (BO-NAS) for a better classification of cyanobacteria with the convolutional neural networks (CNN). Using the flow cytometer and microscope (FlowCAM; [6]), they collected the image data of cyanobacteria including *Microcystis* characterized in interfering effects due to crowded cells and diatoms. It is remarkable that this CNN model effectively classified the algal genus with an F1 score,

which is the harmonic mean of precision and recall, of 0.95 for the eight genera. Interestingly, leveraging all of the CNN, the grayscale surface direction angle model (GSDAM; [7]) and Canny edge detection [8, 9] have identified algae in an unsupervised fashion. Mary and Prabakaran [10] segmented and classified 70 genera of 1531 images using Canny edge detection and the Inception V4 [11]. Previous studies have achieved significant classification results on some genera images, but they were limited in scope to classification [12]. To detect and quantify genera furthermore, several intractable problems still remained. As discussed in [1], it is required to locate genera presented in the image since the taxonomist handles images containing multiple taxa. For doing this, we necessarily introduce both Region of Interest (ROI) detection and instance segmentation algorithm.

Recently, image classification has been applied in a variety of fields such as geoscience and remote sensing (RS). In the hyperspectral (HS) images containing specialties on spatial information, several research projects have been successfully made [13]. Hong et al. [14] address the HS images focusing on RS images with the multimodal deep learning framework (MDL-RS). The MDL-RS networks propose five plug-and-play fusion modules making possible to submit the image information effectively through the modalities. In the two extraction subnetworks (Ex-Net) based on pixel-wise or spatial-spectral architectures, each modality extracts the feature map through the CNN-based networks. Embedding the Ex-Net outputs to the input of fusion network (Fu-Net), the Fu-Net binds the feature maps using concatenation- and compactness-based methods. The nonlocal graph convolutional network (nonlocal GCN) classifies the HS images with a novel graph-based semisupervised learning [15].

Furthermore, the recent studies also pay attention to detecting the precise boundary in the midst of the complex image data. Xie et al. [16] utilize the hyperparameters to train and used transfer learning to reduce the training time of the GlacierNet CNN modified from the SegNet [17]. In [18], the deep fully convolutional network dilated kernel (FCN-DK) based on the supervised pixel-wise image classification for improving cadastral boundary detection in urban and semi-urban areas is proposed. The performance of the model is compared with the state-of-the-art techniques, including Multiresolution Segmentation (MRS; [19]) and Globalized Probability of Boundary (gPb; [20]). For the medical image segmentation especially in CT images, the adaptive fully dense (AFD) neural network adding the horizontal connections in U-Net structure [21] is known to perform outstanding boundary detection [22].

Instance segmentation is the simultaneous task of detecting and delineating each distinguishable object in an image. Breaking through the Faster R-CNN [23], the model used object detection with a parallel branch for predicting segmentation masks, namely, the Mask R-CNN [24], surpassing all the previous state-of-the-art methods on the COCO instance segmentation data set [25], and has been widely applied to diverse academic domain. Although its superior performance is unquestionable, it still has difficulty in handling densely crowded and overlapping instances.

To address these obstacles, we propose a novel way of improving the Mask R-CNN by accommodating extra weights in the model that integrates prior known knowledge. In the experiments, we apply weights to neighboring boundaries of algae especially in *Microcystis* genus which are quite complex to classify because of the variety form of algae. Notably, it is also shown worthy of effectively counting cells (i.e., vision sensing) through calculating objective areas for the measurement of concentration in algae. Moreover, we leverage heavy weights to adjacent boundaries of objects in multiple cell membrane images for improved accuracy.

The rest of this paper is organized as follows. In Section 2, the proposed methods are given. Next, in Section 3, we describe how we acquire the image data sets, preprocess, and provide experiment results. In Section 4, we discuss our results comparing with existing works and address future works.

2. Methods

2.1. Mask R-CNN Network Architecture. Network architectures of the Mask R-CNN largely consist of two parts: (1) feature extraction and (2) instance segmentation. First, the ResNet101 module [24] pretrained by the COCO data set is used. The backbone network and feature pyramid network (FPN) architecture designed to extract features are used for better accuracy and processing speed. Next, in the head of network architecture, the model detects ROI, and from the derived ROI detection and classification are made. With these frameworks, the fully convolutional mask prediction is lastly implemented for instance segmentation.

2.2. Integration of Distance Weight with Mask R-CNN. Here, standing on the shoulder of the Mask R-CNN, we propose the weighted Mask R-CNN specially designed to accommodate *a priori* known weights to the main objective function. This method is mainly aimed at precisely separating the boundary of multiple samples in the context of instance segmentation. Putting in a nutshell, the tasks of the Mask R-CNN achieve largely three goals: (1) classifying class labels, (2) detecting bounding boxes, and (3) segmenting instances. Firstly, the model extracts feature maps by passing resized images through the CNN. On the basis of the feature maps, the Region Proposal Network (RPN) stage allows for the candidates of objective bounding box among generated anchor boxes. Subsequent to this, the ROI align is performed to gather the precise pixel location data. The ROI align serves as a building block to detect objects as well as to segment instances. Focusing on ROI align, the model extracts feature maps of interest areas by using exact coordinates through fully convolutional network (FCN [26]). Afterwards, through the process of minimizing the objective function, we optimize the Mask R-CNN model. The model defines the objective function as the aggregation of the loss functions of classification, localization, and segmentation [27]. Moreover, each loss function is optimized by the softmax function, box offset regressor, and mask FCN predictor, respectively. In this process, the novelty of the Mask R-CNN comes into play in advancing the former image recognition models (e.g., Fast

R-CNN [28] and Faster R-CNN). While deriving the objective function, the Mask R-CNN implements the pixel-wise binary classification and decouples mask prediction with both category classification and bounding box detection. Notably, the binary classification method has merits in terms of reduction computation costs. The ROI align precisely masks, aiming at approximating ground truth areas.

For the weighted Mask R-CNN, below is the proposed objective function:

$$\begin{aligned} L &= L_{\text{cls}} + L_{\text{box}} + w \cdot L_{\text{mask}} \\ &= \frac{1}{N_{\text{cls}}} \sum_i \{-p_i^* \cdot \log p_i - (1 - p_i^*) \cdot \log (1 - p_i)\} + \frac{\lambda}{N_{\text{box}}} \sum_i p_i^* \cdot L_1^{\text{smooth}}(t_i - t_i^*) \\ &\quad - w \cdot \frac{1}{m^2} \sum_{1 \le i,j \le m} \left\{ y_{ij} \cdot \log \hat{y}_{ij}^k + \left(1 - y_{ij}\right) \cdot \log \left(1 - \hat{y}_{ij}^k\right) \right\}, \end{aligned} \tag{1}$$

where p_i is the predicted probability of anchor i being an object, p_i^* is the ground truth label (binary) of whether anchor i is an object, t_i is the predicted four parameterized coordinates, t_i^* is the ground truth coordinates, N_{cls} is the normalization term set to be minibatch size (0~256), N_{box} is the normalization term set to the number of anchor locations (0~2400), λ is the balancing parameter set to be (0~10 such that both L_{cls} and L_{box} terms are roughly, equally weighted), k is the number of ground truth class, w is the weight matrix assigned to pixel instances, and

$$L_1^{\text{smooth}}(x) = \begin{cases} 0.5x^2, & \text{if } |x| \le 1, \\ |x| - 0.5, & \text{otherwise.} \end{cases} \tag{2}$$

In addition, we integrate both image representations and *a priori* known knowledge of adjacency in the model. Inspired by the U-Net, this weight induces strong separation across samples as boundaries get closer. In theory, the closer the boundary the bigger the weight:

$$\begin{aligned} w(x) &= w_c(x) + w_0 \cdot e^{-(d_1(x) + d_2(x))^2 / 2\sigma^2}, \\ w &= 1 + \frac{w(x) - \min\left(w(x)\right)}{\max\left(w(x)\right) - \min\left(w(x)\right)} \cdot \delta, \end{aligned} \tag{3}$$

where $w_c : \Omega \to R$ is the weight map to balance the class frequencies, $d_1 : \Omega \to R$ denotes the distance to the border of the nearest cell, $d_2 : \Omega \to R$ denotes the distance to the border of the second nearest cell, and δ refers to the weight adjusting parameter, respectively.

In principle, $w(x)$ is subject to size of objects, distance between objects, and shape of the objects in an image. To account for variability, we scale each weight map separately to the range from 0 to 1. Next, we consider the parameter δ to determine the power of the weight matrix. The weight parameter δ can be used for adding the extra emphasis on the boundary of object especially when the distance between objects is too narrow so that we hardly distinguish boundaries. Subsequent to this, we impose this weight matrix to the objective function of masks in the fashion of element-wise computation. Taken together, Figure 1 displays the end-to-end architecture of the proposed model.

Moreover, the stochastic gradient descent (SGD) algorithm is used as an optimizer and minibatch size is fixed to 1 in this study, and we set the learning rate of 0.001 and 100 epochs. Validation processes with comparing ground truth masks to assess predictive performance. For implementation, the Mask R-CNN adopts the PyTorch packages for simplicity [29].

3. Numerical Experiments

3.1. Data Sets. In what follows, we describe the data sets for numerical study. First and foremost, it is essential to generate well-preprocessed data sets to produce reliable experiment results. To this end, we apply several preprocessing techniques such as standardization or scaling to raw data and matching each preprocessed image with precise annotations.

3.1.1. Simulated Data. In simulation I, we generate circle images each of which includes inside 4 and 6 circled objects for train data sets, respectively, where all images have resolution of $512 \times 512 \times 3$ pixels. Similarly, we generate circle images including the prespecified number of objects for test data set (i.e., 4 and 6). Subsequent to this, we divide each image both in horizontal and vertical direction in the way that each circle is exclusively placed one at a diagonal slot and the radius of each circle is limited to the boundary of slots. Simulation II emulates the nature of real data, for which we generate the shape of ellipses in accommodating randomness and complexity to the simulation data sets. More precisely, we randomly choose the center points of objects and generate ellipses of random sizes for experiment data sets assigned to the diagonal slots. This configuration makes distance between objects arbitrarily determined and promotes adequate complexity.

3.1.2. Microalgae and Cell Membrane Data. Freshwater microalgae samples used in this work were collected at 11 weirpools and five reservoirs located in the four major rivers (e.g., Han, Nakdong, Geum, and Yeongsan) in Korea. Water (quantitative) or net (qualitative) samples were taken from the surface and immediately fixed to the final 1% concentration with acidified Lugol's iodine solution [30]. Quantitative samples were allowed to stand in the dark place of the laboratory for more than one week, and then, the supernatant was carefully siphoned and concentrated an appropriate cell density (above 104 cells/mL). Image acquisition was performed using photomicroscopes (Zeiss AXIO Scope.A1 and Vert.A1 model, Germany) attached camera (Axiocam 506 color) assisted with computer software (ZEN lite 2012), and captured images have resolution of $1936 \times 1460 \times 3$ pixels at 200x or 400x magnification of a microscope. A manual identification of algae species was carried out based on their taxonomic characteristics by [31].

In the experiment, 469 *Microcystis* images are used in total. Since the images are collected insufficiently, the performance of segmentation model can be severely deteriorated.

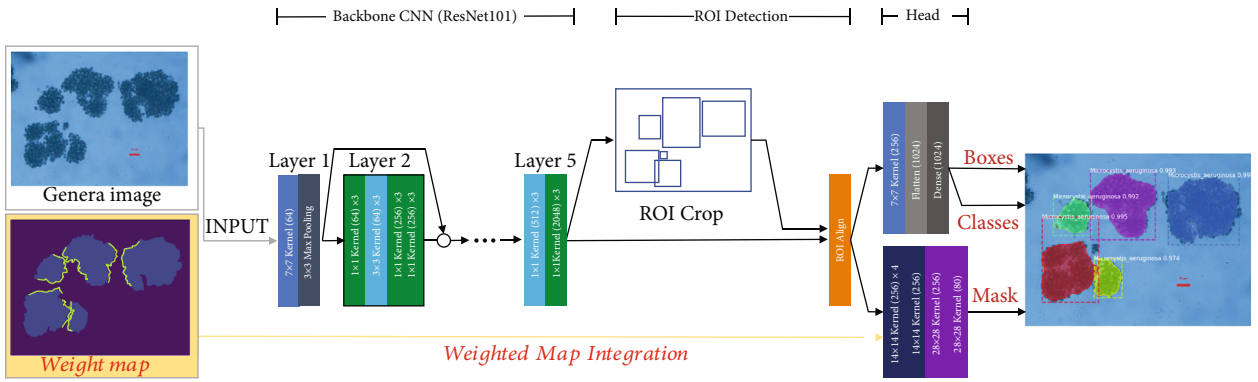

Figure 1: Integration of the weight map under the architecture of the Mask R-CNN.

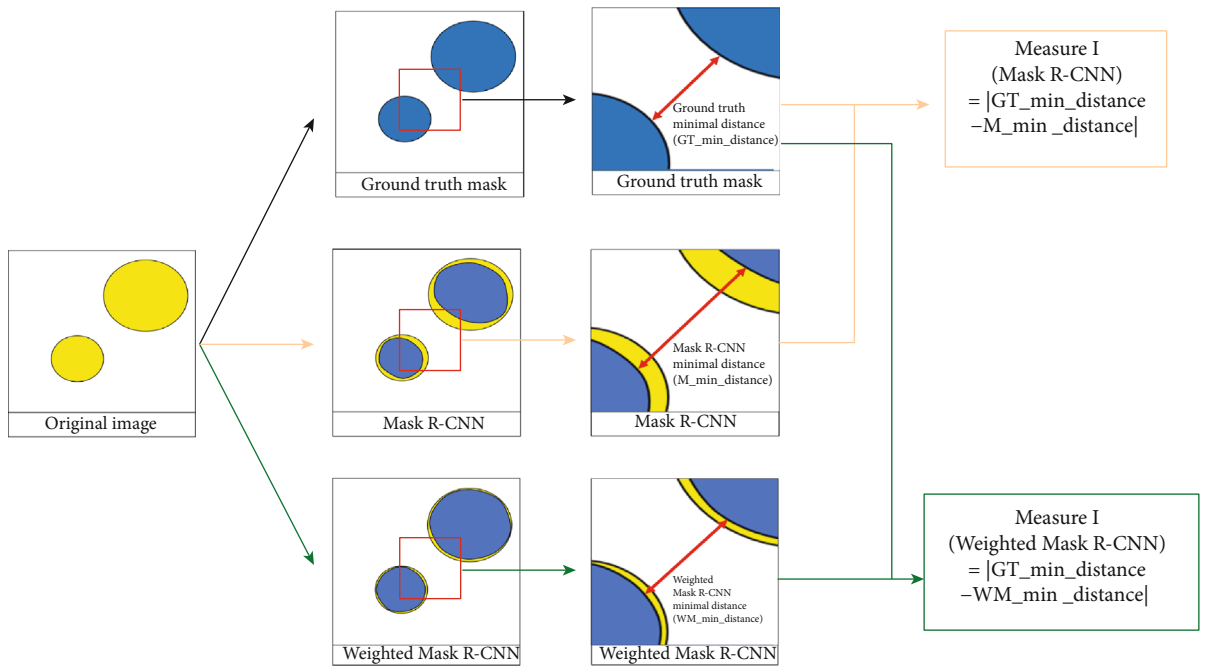

Figure 2: Examples of calculating Measure I from two ellipse images.

However, we fine-tune by means of the CNN pretrained with the COCO data set in order to tackle the degrading performance problem. In addition to this, we also analyze 30 cell membrane images in electron microscopic (EM; [32]) segmentation challenge at the International Symposium on Biomedical Imaging (ISBI). After that, taxonomists elaborately assess the consistency of labeling and annotations. LabelMe (https://github.com/wkentaro/labelme) is used as an annotation tool widely accepted for segmentation tasks. Importantly, it is very useful to annotate polygons simply by marking points and labeling genus taxa challenging due to the complexity and variety of shapes of algae and cell membrane. Thus, we annotate one by one to accurately delineate sophisticated boundaries. Finally, the annotation files are automatically saved in the JSON file format. For algae data set, we split the whole data into the training set of 319 images and the test set of 150 images.

3.2. Results

3.2.1. Evaluation Metrics. True positive (TP) pixels are ground truth target pixels and also predicted as target pixels. True negative (TN) pixels are not ground truth target pixels and also not predicted as target pixels. False positive (FP) pixels are not ground truth target pixels but predicted as target pixels known as Type II Error. False negative (FN) pixels are ground truth target pixels but not predicted as target pixels called as Type I Error. Precision and recall are defined as

$$\text{Precision} = \frac{\text{TP}}{\text{TP} + \text{FP}}, \qquad \text{Recall} = \frac{\text{TP}}{\text{TP} + \text{FN}}. \tag{4}$$

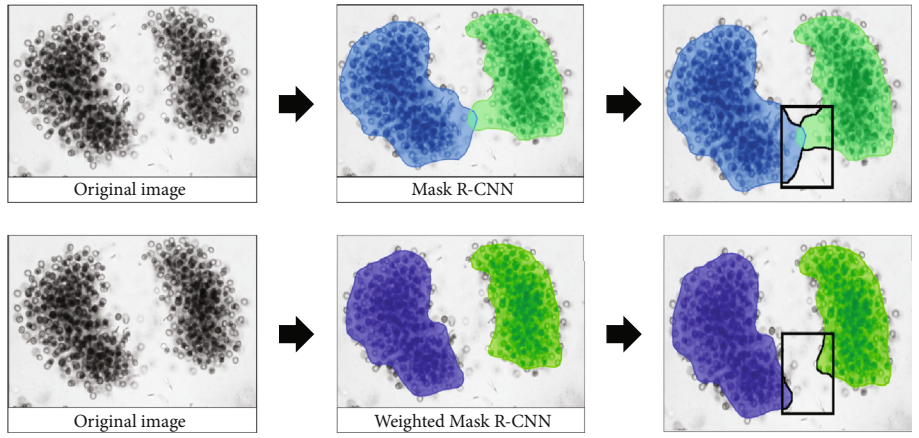

Figure 3: Examples of calculating Measure II from algae images.

Table 1: The comparison of Mask R-CNN, weighted Mask R-CNN, and MEInst in simulation I.

# of circles	4					6				
Model	MEInst	Mask R-CNN	Weighted Mask R-CNN			MEInst	Mask R-CNN	Weighted Mask R-CNN		
			$\delta = 0.1$	$\delta = 0.5$	$\delta = 1$			$\delta = 0.1$	$\delta = 0.5$	$\delta = 1$
Mean	0.768	1.110	0.629	0.857	0.984	0.834	0.936	0.659	0.830	1.008
se	0.062	0.056	0.048	0.052	0.052	0.036	0.034	0.031	0.035	0.033

Table 2: The comparison of Mask R-CNN, weighted Mask R-CNN, and MEInst in simulation II.

# of ellipses	4					6				
Model	MEInst	Mask R-CNN	Weighted Mask R-CNN			MEInst	Mask R-CNN	Weighted Mask R-CNN		
			$\delta = 0.1$	$\delta = 0.5$	$\delta = 1$			$\delta = 0.1$	$\delta = 0.5$	$\delta = 1$
Mean	1.212	1.154	0.787	0.941	1.039	0.895	0.947	0.745	0.941	0.942
se	0.073	0.068	0.055	0.047	0.062	0.068	0.075	0.068	0.075	0.059

Table 3: Comparison of the performance of object detection between Mask R-CNN and weighted Mask R-CNN in algae and cell membrane images.

	Mask R-CNN		Weighted Mask R-CNN	
	Algae	Cell membrane	Algae	Cell membrane
mAP50	0.862	0.899	0.925	0.945
mAP75	0.688	0.796	0.786	0.852
mAP	0.603	0.625	0.673	0.677
Recall50	0.945	0.970	0.964	0.986
Recall75	0.785	0.867	0.843	0.908
Recall	0.699	0.704	0.734	0.739
mIoU	0.801	0.579	0.845	0.636

A precision-recall curve is a plot of precision (y-axis) and recall (x-axis) with varied thresholds. Average Precision (AP) is the under area of the precision-recall curve and is calculated as the mean precision given recall measures. mAP is the mean of Average Precision calculated by the multiple objects in an image. Intersection over Union (IoU) is a well-known measure from ground truth mask (gt_{mask}) and predicted mask ($\text{pred}_{\text{mask}}$) in evaluating image segmentation methods:

$$\text{IoU} = \frac{\text{gt}_{\text{mask}} \cap \text{pred}_{\text{mask}}}{\text{gt}_{\text{mask}} \cup \text{pred}_{\text{mask}}}. \quad (5)$$

In this study, we further define the mean IoU of multiple objects in an image (mIoU (mean of Intersection over Union)). In this paper, we compute mAP and recall at the given IoU threshold (default 0.5). Without the given IoU threshold, we compute mAP and recall over a range of IoU threshold (as default 0.5 to 0.95 with an increment of 0.05).

The first measurement in the boundary detection in this paper called as Measure I is defined as the absolute value of difference, that is, a minimal distance of adjacent two objects between the ground truth mask and predicted mask. Figure 2 describes the example of Measure I.

The second measurement in the boundary detection called as Measure II gauges the proportion of mask pixels among predesignated areas. We compare Measure II in both models with algae and cell membrane images, where the Mask R-CNN produces overlapping inferred masks of two

Table 4: Comparison between Mask R-CNN and weighted Mask R-CNN by Measure II in algae and cell membrane images.

Image names	Mask R-CNN	Weighted Mask R-CNN	Image names	Mask R-CNN	Weighted Mask R-CNN
Microcystis 1	0.38	0.09	Cell membrane 1	0.81	0.68
Microcystis 2	0.58	0.23	Cell membrane 2	0.82	0.82
Microcystis 3	0.82	0.74	Cell membrane 3	0.81	0.75
Microcystis 4	0.85	0.45	Cell membrane 4	0.68	0.60
Microcystis 5	0.41	0.18	Cell membrane 5	0.91	0.73
Microcystis 6	0.61	0.30	Cell membrane 6	0.62	0.50
Microcystis 7	0.77	0.35	Cell membrane 7	0.65	0.46
Microcystis 8	0.66	0.36	Cell membrane 8	0.80	0.74
Microcystis 9	0.80	0.18	Cell membrane 9	0.76	0.52
Microcystis 10	0.72	0.72	Cell membrane 10	0.86	0.75
Microcystis 11	0.57	0.31	Cell membrane 11	0.88	0.76
Microcystis 12	0.59	0.35	Cell membrane 12	0.35	0.34
Microcystis 13	0.67	0.15	Cell membrane 13	0.79	0.66
Microcystis 14	0.76	0.61	Cell membrane 14	0.88	0.83
Mean	0.66	0.36	Mean	0.76	0.65

objects separable in truth. Under this scheme, the lower Measure II, the better model in predictive power. Figure 3 illustrates the examples of Measure II.

3.2.2. Experiment Data. We compare the Mask R-CNN, weighted Mask R-CNN, and Mask Encoding for Single Shot Instance Segmentation (MEInst; [33]) models via Measure I and present the mean and standard errors given the prespecified number of circles and ellipses (i.e., 4 and 6) in Tables 1 and 2. The results indicate that the predicted mask of the weighted Mask R-CNN model is superior across simulation scenarios when we estimate the ground truth mask compared to the Mask R-CNN and MEInst. We train on the ResNet-50-FPN model as the backbone implemented in the PyTorch package for both the MEInst and weighted Mask R-CNN. The Mask RCNN runs at 67.47 ms per image with almost the same as the weighted Mask R-CNN records, and MEInst runs at 77.69 ms per image using our workstation (Intel i7-7800X, RAM 128GB, Geforce GTX 1080 Ti GPUs).

3.2.3. Real Data. In Table 3, we compare the performance of the Mask R-CNN and weighted Mask R-CNN models in real data. In algae data, mAP50 and Recall50 are 0.862 and 0.945 in the Mask R-CNN and 0.925 and 0.964 in the weighted Mask R-CNN, where mAP50 and Recall50 refer to mean AP and recall under IoU threshold of 0.5. In the same manner, mIoU in the Mask R-CNN is 0.801, and in the weighted Mask R-CNN, it is 0.845. In cell membrane data, mAP50 and Recall50 are 0.899 and 0.970 in the Mask R-CNN and 0.945 and 0.986 in the weighted Mask R-CNN. As a whole, it is evident that the weighted Mask R-CNN performs better than the Mask R-CNN in both microalgae and cell membrane data.

Furthermore, in Table 4, the comparisons in detecting borders between two models are given. We choose 14 algae images and 14 cell membrane images each. Hence, we can evaluate the area of images under the following conditions. First, the objects in images are detected in both the Mask R-CNN and weighted Mask R-CNN models. Second, the masks inferred from the Mask R-CNN are overlapped. This is reasonable in the sense that most of microalgae in an image are jumbled and many have put efforts to separating individual algae in vision to facilitate counting. Third, the specified objects are taxonomized as different groups. In Table 3, we observe that the weighted Mask R-CNN (i.e., the mean of 0.36 and 0.65 for algae and cell membrane) consistently outperforms the Mask R-CNN (i.e., the mean of 0.66 and 0.76 for algae and cell membrane) in separating boundaries of adjacent objects with respect to all target images. See the supplementary material (available here) for additional results.

4. Discussion

In this paper, we introduce the weighted Mask R-CNN specially designed to accurately segment instances. Simply put, this method accommodates in theory *a priori* known knowledge of boundary information in the midst of multiple objects. In numerical experiments, it is shown that the weighted Mask R-CNN model performs better than the Mask R-CNN and MEInst models in the boundary detection as stated in Tables 1 and 2. However, it is shown in the experiment that δ is required to be tuned properly to improve performance. In particular, we hardly perform the clear-cut for algae (e.g., *Microcystis*) and cell membrane images, in the sense that they are commonly mingled in an image and are formed with heterogeneous figures. To overcome this, the weighted Mask R-CNN is worth to implement the precise segmentation tasks. On top of that, it is also noteworthy that the proposed method can advance in microalgae research domain in keeping with improving instance segmentation. Surprisingly, this technique obviously contributes to quantify each single cell in vision sensing approaches. In reality, there are urgent needs in freshwater analysis to quantify the number of algae cells and the concentration of algae. This utility enables to monitor water quality in seas or rivers [34]. When

it comes to the model configuration, the weight in the model only builds on distance basis between objects, but yet this weight can be extended to other known knowledge in spirit of data integration. It is also interesting to exploit cutting-edge network architectures and modules in improving accuracy and accelerating the computational speed. We leave this subject for future study.

Data Availability

All data sets are available at the author's website (http://www.hifiai.pe.kr).

Conflicts of Interest

The authors declare that they have no conflicts of interest.

Acknowledgments

This paper was supported by Konkuk University in 2019. This research was supported by the Basic Science Research Program through the National Research Foundation of Korea (NRF) funded by the Ministry of Science, ICT & Future Planning and Konkuk University Researcher Fund in 2020 and the National Research Foundation of Korea (NRF) funded by the Ministry of Education, Science and Technology (NRF-2019R1C1C1011366 and 2020R1C1C1A01005229).

Supplementary Materials

Figure S1: the instance segmentation examples of Mask R-CNN (left) and weighted Mask R-CNN (right). Figure S2: the instance segmentation examples of Mask R-CNN (left) and weighted Mask R-CNN (right). Figure S3: the instance segmentation examples of Mask R-CNN (left) and weighted Mask R-CNN (right). Figure S4: the instance segmentation examples of Mask R-CNN (left) and weighted Mask R-CNN (right). Figure S5: the instance segmentation examples of Mask R-CNN (left) and weighted Mask R-CNN (right). Figure S6: the instance segmentation examples of Mask R-CNN (left) and weighted Mask R-CNN (right). Figure S7: the instance segmentation examples of Mask R-CNN (left) and weighted Mask R-CNN (right). Figure S8: the instance segmentation examples of Mask R-CNN (left) and weighted Mask R-CNN (right). Figure S9: the instance segmentation examples of Mask R-CNN (left) and weighted Mask R-CNN (right). Figure S10: the instance segmentation examples of Mask R-CNN (left) and weighted Mask R-CNN (right). Figure S11: the instance segmentation examples of Mask R-CNN (left) and weighted Mask R-CNN (right). Figure S12: the instance segmentation examples of Mask R-CNN (left) and weighted Mask R-CNN (right). *(Supplementary Materials)*

References

[1] J. Ruiz-Santaquiteria, G. Bueno, O. Deniz, N. Vallez, and G. Cristobal, "Semantic versus instance segmentation in microscopic algae detection," *Engineering Applications of Artificial Intelligence*, vol. 87, article 103271, 2020.

[2] A. Krizhevsky, I. Sutskever, and G. E. Hinton, "Imagenet classification with deep convolutional neural networks," *Communications of the ACM*, vol. 60, no. 6, pp. 84–90, 2017.

[3] K. Schulze, U. M. Tillich, T. Dandekar, and M. Frohme, "PlanktoVision-an automated analysis system for the identification of phytoplankton," *BMC Bioinformatics*, vol. 14, no. 1, pp. 1–10, 2013.

[4] G. Bueno, O. Deniz, A. Pedraza et al., "Automated diatom classification (part A): handcrafted feature approaches," *Applied Sciences*, vol. 7, no. 8, p. 753, 2017.

[5] J. Park, H. Lee, C. Y. Park, S. Hasan, T. Y. Heo, and W. H. Lee, "Algal morphological identification in watersheds for drinking water supply using neural architecture search for convolutional neural network," *Water*, vol. 11, no. 7, p. 1338, 2019.

[6] N. J. Poulton, "FlowCam: quantification and classification of phytoplankton by imaging flow cytometry," in *Imaging Flow Cytometry. Methods in Molecular Biology, vol 1389*, N. Barteneva and I. Vorobjev, Eds., Humana Press, New York, NY, USA, 2016.

[7] H. Zheng, H. Zhao, X. Sun, H. Gao, and G. Ji, "Automatic setae segmentation from *Chaetoceros* microscopic images," *Microscopy Research and Technique*, vol. 77, no. 9, pp. 684–690, 2014.

[8] N. Tang, F. Zhou, Z. Gu, H. Zheng, Z. Yu, and B. Zheng, "Unsupervised pixel-wise classification for *Chaetoceros* image segmentation," *Neurocomputing*, vol. 318, pp. 261–270, 2018.

[9] J. Canny, "A computational approach to edge detection," *IEEE Transactions on Pattern Analysis and Machine Intelligence*, vol. 6, pp. 679–698, 1986.

[10] A. Victoria Anand Mary and G. Prabakaran, "An Efficient Automated Deep Learning Model For Diatom Image Segmentation And Classification," *International Journal of Innovative Technology and Exploring Engineering (IJITEE)*, vol. 8, no. 11, pp. 446–454, 2019.

[11] C. Szegedy, S. Ioffe, V. Vanhoucke, and A. Alemi, "Inception-v4, inception-resnet and the impact of residual connections on learning," 2016, http://arxiv.org/abs/1602.07261.

[12] A. C. Jalba, M. H. Wilkinson, and J. B. Roerdink, "Automatic segmentation of diatom images for classification," *Microscopy Research and Technique*, vol. 65, no. 1-2, pp. 72–85, 2004.

[13] B. Rasti, D. Hong, R. Hang et al., "Feature extraction for hyperspectral imagery: the evolution from shallow to deep," 2020, http://arxiv.org/abs/2003.02822.

[14] D. Hong, L. Gao, N. Yokoya et al., "More diverse means better: multimodal deep learning meets remote-sensing imagery classification," *IEEE Transactions on Geoscience and Remote Sensing*, pp. 1–15, 2020.

[15] L. Mou, X. Lu, X. Li, and X. X. Zhu, "Nonlocal graph convolutional networks for hyperspectral image classification," *IEEE Transactions on Geoscience and Remote Sensing*, vol. 58, no. 12, pp. 8246–8257, 2020.

[16] Z. Xie, U. K. Haritashya, V. K. Asari, B. W. Young, M. P. Bishop, and J. S. Kargel, "GlacierNet: a deep-learning approach for debris-covered glacier mapping," *IEEE Access*, vol. 8, pp. 83495–83510, 2020.

[17] V. Badrinarayanan, A. Kendall, and R. Cipolla, "Segnet: a deep convolutional encoder-decoder architecture for image segmentation," *IEEE Transactions on Pattern Analysis and Machine Intelligence*, vol. 39, no. 12, pp. 2481–2495, 2017.

[18] X. Xia, C. Persello, and M. Koeva, "Deep fully convolutional networks for cadastral boundary detection from UAV images," *Remote Sensing*, vol. 11, no. 14, article 1725, 2019.

[19] L. Drăguţ, O. Csillik, C. Eisank, and D. Tiede, "Automated parameterisation for multi-scale image segmentation on multiple layers," *ISPRS Journal of Photogrammetry and Remote Sensing*, vol. 88, no. 100, pp. 119–127, 2014.

[20] P. Arbelaez, M. Maire, C. Fowlkes, and J. Malik, "Contour detection and hierarchical image segmentation," *IEEE Transactions on Pattern Analysis and Machine Intelligence*, vol. 33, no. 5, pp. 898–916, 2010.

[21] O. Ronneberger, P. Fischer, and T. Brox, "U-net: convolutional networks for biomedical image segmentation," in *Medical Image Computing and Computer-Assisted Intervention – MICCAI 2015. MICCAI 2015. Lecture Notes in Computer Science, vol 9351*, N. Navab, J. Hornegger, W. Wells, and A. Frangi, Eds., pp. 234–241, Springer, Cham, 2015.

[22] E. K. Wang, C. M. Chen, M. M. Hassan, and A. Almogren, "A deep learning based medical image segmentation technique in Internet-of-Medical-Things domain," *Future Generation Computer Systems*, vol. 108, pp. 135–144, 2020.

[23] S. Ren, K. He, R. Girshick, and J. Sun, "Faster R-CNN: towards real-time object detection with region proposal networks," *IEEE Transactions on Pattern Analysis and Machine Intelligence*, vol. 39, no. 6, pp. 1137–1149, 2017.

[24] K. He, X. Zhang, S. Ren, and J. Sun, "Deep residual learning for image recognition," in *Proceedings of the IEEE conference on computer vision and pattern recognition*, pp. 770–778, Caesar's Palace in Las Vegas, Nevada, USA, 2016.

[25] T. Y. Lin, M. Maire, S. Belongie et al., "Microsoft coco: common objects in context," in *Computer Vision – ECCV 2014. ECCV 2014. Lecture Notes in Computer Science, vol 8693*, D. Fleet, T. Pajdla, B. Schiele, and T. Tuytelaars, Eds., pp. 740–755, Springer, Cham, 2014.

[26] J. Long, E. Shelhamer, and T. Darrell, "Fully convolutional networks for semantic segmentation," in *Proceedings of the IEEE conference on computer vision and pattern recognition*, pp. 3431–3440, Hynes Convention Center in Boston, Massachusetts, USA, 2015.

[27] L. Weng, *Object Detection for Dummies Part 3: R-CNN Family*, Lilianweng. Gihub. Io/lil-log, 2017.

[28] R. Girshick, "Fast R-CNN," in *Proceedings of the IEEE international conference on computer vision*, pp. 1440–1448, Las Condes Araucano Park, Región Metropolitana, Chile, 2015.

[29] F. Massa and R. Girshick, "maskrcnn-benchmark: Fast, Modular Reference Implementation of Instance Segmentation and Object Detection Algorithms in PyTorch," Mask R-CNN in PyTorch, 2018, Accessed: Apr, 29, 2019 https://github.com/facebookresearch/maskrcnn-benchmark.

[30] R. G. Wetzel and G. E. Likens, *Limnological Analyses*, Springer-Verlag, New York, NY, USA, 2 edition, 1991.

[31] J. K. Shin and K. J. Cho, "Distribution and population dynamics of *Microcystis* (Cyanophyta) in the Naktong River," *Algae*, vol. 12, no. 4, pp. 283–2903, 1997.

[32] D. Ciresan, A. Giusti, L. Gambardella, and J. Schmidhuber, "Deep neural networks segment neuronal membranes in electron microscopy images," *Advances in Neural Information Processing Systems*, vol. 25, pp. 2843–2851, 2012.

[33] R. Zhang, Z. Tian, C. Shen, M. You, and Y. Yan, "Mask encoding for single shot instance segmentation," in *Proceedings of the IEEE/CVF Conference on Computer Vision and Pattern Recognition*, pp. 10226–10235, Washington State Convention Center in Seattle, Washington, USA, 2020.

[34] J. Park, D. Wang, and W. H. Lee, "Evaluation of weir construction on water quality related to algal blooms in the Nakdong River," *Environmental Earth Sciences*, vol. 77, no. 11, p. 408, 2018.

[35] K. He, G. Gkioxari, P. Dollár, and R. Girshick, "Mask R-CNN," *ICCV*, vol. 1, no. 6, 2017.

[36] Q. Zhou, W. Chen, H. Zhang et al., "A flow cytometer based protocol for quantitative analysis of bloom-forming cyanobacteria (*Microcystis*) in lake sediments," *Journal of Environmental Sciences*, vol. 24, no. 9, pp. 1709–1716, 2012.

[37] A. Pedraza, G. Bueno, O. Deniz, G. Cristóbal, S. Blanco, and M. Borrego-Ramos, "Automated diatom classification (part B): a deep learning approach," *Applied Sciences*, vol. 7, no. 5, p. 460, 2017.

[38] A. Pedraza, G. Bueno, O. Deniz et al., "Lights and pitfalls of convolutional neural networks for diatom identification," in *Proceedings Volume 10679, Optics, Photonics, and Digital Technologies for Imaging Applications V*, Strasbourg, France, May 2018.

[39] M. Everingham, L. Van Gool, C. K. Williams, J. Winn, and A. Zisserman, "The Pascal visual object classes (voc) challenge," *International Journal of Computer Vision*, vol. 88, no. 2, pp. 303–338, 2010.

[40] K. Simonyan and A. Zisserman, "Very deep convolutional networks for large-scale image recognition," 2014, http://arxiv.org/abs/1409.1556.

Hindawi
Journal of Sensors
Volume 2021, Article ID 6658059, 16 pages
https://doi.org/10.1155/2021/6658059

Research Article

Effects of Micropore Group Spacing and Irrigation Amount on Soil Respiration and Yield of Tomato with Microsprinkler Irrigation under Plastic Film in Greenhouse

Mingzhi Zhang[1,2] **Xiaoqun Yan**[3] **Zhenguang Lu**[2] **Qingjun Bai**[1] **Yushun Zhang**[2] **Donglin Wang**[4] **Yuangang Zhou**[5] **and Yuqing Yin**[2]

[1]*State Key Laboratory of Eco-Hydraulics in Northwest Arid Region of China, Xi'an University of Technology, Xi'an 710048, China*
[2]*Henan Provincial Water Conservancy Research Institute, Zhengzhou 450000, China*
[3]*College of Water Conservancy and Hydropower Engineering, Hohai University, Nanjing 210098, China*
[4]*School of Water Conservancy, North China University of Water Resources and Electric Power, Zhengzhou, Henan, China*
[5]*Xi'an Water Group Co. Ltd., Xi'an, Shaanxi 710061, China*

Correspondence should be addressed to Qingjun Bai; bqj@xaut.edu.cn

Received 8 November 2020; Revised 8 December 2020; Accepted 6 January 2021; Published 21 January 2021

Academic Editor: Liang Xu

Microsprinkler irrigation under a plastic film in the greenhouse (MSPF) is a water-saving way which adopts the porous discharge form of a pipe under the plastic film. The effects of different micropore group spacings (L1:30 cm, L2: 50 cm) and irrigation amounts [I1: 0.7 Epan; I2: 1.0 Epan; and I3: 1.2 Epan (Epan is the diameter of 20 cm standard pan evaporation, mm)] of the MSPF on the soil respiration and yield of tomato were studied. A completely randomized trial design was used, and drip irrigation under plastic film (CK1) and microsprinkler irrigation (CK2) were also used as controls. The results showed that under the same irrigation amount, the soil respiration rate, tomato yield, and water use efficiency (WUE) of MSPF in spring and autumn are 8.09% and 6.74%, 19.39% and 4.54%, and 10.03% and 2.32% higher than those of CK1, respectively; they are significantly increased by 31.02% and 20.46%, 49.22% and 38.38%, and 58.05% and 34.66% compared with those of CK2, respectively, indicating that MSPF increased the amount of CO_2 emission, but tomato yield and WUE were effectively improved, and a dynamic balance was reached among them. Compared with the 50 cm micropore group spacing, the spring and autumn tomato yields and WUE under the 30 cm micropore group spacing were significantly increased by 16.00% and 13.01% and 20.85% and 14.25%, respectively, and the micropore group spacing had no significant effect on the soil respiration rate in both root and nonroot zones. When the I increased from 0.7 Epan to 1.2 Epan, the soil respiration rate and yield in the root and nonroot zones of the spring and autumn tomatoes increased at first and then decreased, and the WUE showed a decreasing trend. The relationship of soil respiration rate between the nonroot and root zones obeys a logarithmic function, and the soil respiration rate in the nonroot zone has a quadratic curve relationship with the yield of tomato. This study can provide data support for the development of water-saving irrigation and yield increase of facility agricultural tomato and the analysis of the soil carbon cycling mechanism.

1. Introduction

With global warming, research on global carbon cycling has become the focus of the scientific community. Soil respiration is an important circulation pathway of the global carbon cycle, and it plays a key role in regulating atmospheric CO_2 concentration. According to the IPCC2012 report, agricultural soil is a major contributor to carbon emissions in global carbon cycling, accounting for about 19-29% of global cumulative carbon emissions [1]. Water is one of the five elements in agricultural production, which plays an important role in the carbon cycling of agricultural soil. Rainfall is scarce in arid and semiarid areas of northwest China [2]. Irrigation water accounts for more than 60% of the total water

consumption in this area, which is the main way for local crops to grow, and it is also the focus of this paper [3, 4]. The development of facility agriculture provides a strong guarantee for vegetable production in northwest China. However, the irrigation water for facility agriculture in this area mainly comes from groundwater, and the progress in the exploitation of groundwater resources aggravates the water resource crisis in this region [5–7]. Therefore, under the background of the sharp increase in atmospheric carbon emissions and the shortage of water resources [8], it is of great significance to explore the water-saving technology of facility agriculture for crop growth and soil carbon cycling.

As one of the main microirrigation methods in facility agriculture, microsprinkler irrigation under plastic film (MSPF, see Figure 1; Figure 1 is reproduced from Zhang et al. [9]) is used to irrigate tomato with multiple groups of small holes under the plastic film [10]. The MSPF has obtained good application effects in the facility agriculture tomato irrigation. Compared with the traditional drip irrigation in facility agriculture, under the same working pressure, the single micropore velocity of MSPF is about 15 times that of labyrinth drip irrigation, which has stronger sediment carrying capacity and anticlogging performance, and the MSPF can solve the clogging problem of some drip irrigation emitters [11, 12]. When the irrigation amount is the same, the single group flow of MSPF is about 40 times that of drip irrigation, and the irrigation duration is short, so it is easy to increase the ratio of horizontal and vertical migration distances of the soil water wetting peak. As a result, the soil wetting body per unit area of the tillage layer can be increased, which can reduce the deep transport of soil water and limit the lateral development of roots under water stress [13, 14]. The soil carbon cycle was also changed due to the increase in the soil dry-wet cycle [15, 16]. Compared with the field microsprinkler pipe, the MSPF in facility agriculture can reduce the influence of the external environment on the soil wetting body [17–19]. The MSPF can solve the spray atomization of microsprinkler irrigation, which is easy to increase air humidity. At the same time, it can solve the problems of crop diseases and insect pests caused by high temperature and humidity in the facility's agricultural environment [20–22]. Therefore, the exploration of MSPF is of great significance for enriching the technical system of greenhouse microirrigation, expanding the scope of application of microsprinkler irrigation, saving water and increasing production of crops, and emitting greenhouse gas from the soil.

As one of the main vegetables planted in facility agriculture, the tomato has rich nutrition and health care value. Tomato in the greenhouse belongs to sparse planting crops. The selection of the distance between orifices in the capillary and the irrigation amount has a direct impact on soil water and heat, ventilation, mineralization and decomposition rate of organic matter, nitrogen transformation, microbial biomass, activity, etc. [23, 24]. Therefore, the study on the emission of greenhouse gases in greenhouse tomato farmland and the formation mechanism of tomato yield is of great significance to obtain the best balance point of water saving and yield increase of greenhouse tomato and to formulate measures to reduce greenhouse gas CO_2 emissions in vegetable

Figure 1: Microsprinkler irrigation under plastic film (MSPF).

fields of MSPF. In the practice of facility agricultural production, the capillary distance between orifice outflow and the irrigation amount are often selected according to their own experience. Studies have shown that under the same emitter flow, the smaller the emitter spacing is, the closer the horizontal wetting shape is, the shorter the confluence time of wetting peaks between emitters is, and the larger the soil surface wetting area is [14, 25]. In addition, there is a positive correlation between soil moisture and soil respiration rate, which leads to an increase of CO_2 emission per unit area of soil respiration [1]. The research of Enciso et al. showed that the onion yield increased first and then decreased as the distance between the emitters decreased from 30 to 15 cm [26]. It should be noted that when the emitter spacing is small, the investment and operation cost of drip irrigation equipment will also increase. In practical application, the amount of empirical irrigation by farmers is often much higher than the actual water demand of crops, and the deep leakage of irrigation water is serious, which leads to the waste of water resources [27, 28]. Studies have shown that under the same emitter spacing, the greater the emitter flow rate is, the higher the ratio of the distance between the horizontal and vertical transports of soil water content is [13]. The larger the amount of drip irrigation is, the larger the soil wetting volume is and the lower the ratio of horizontal and vertical migration distance of soil water is. There is a positive correlation between the amount of irrigation and soil water content [14, 29, 30]. Suitable soil water content can enhance root respiration and microbial activity, thus accelerating the decomposition of soil organic matter and increasing yield, as well as increasing CO_2 emission from soil respiration [31–33]. Previous studies have found that reducing the irrigation amount can reduce the soil respiration rate, and excessive irrigation will also inhibit the increase of the soil respiration rate [34, 35]. In tomato and maize under drip irrigation, the irrigation amount was positively correlated with yield and soil CO_2 emission [36–38] and negatively correlated with water use efficiency [23].

At present, the research on soil respiration of facility agriculture is mainly focused on drip irrigation with small flow, but there are few studies on water management of MSPF on soil respiration of facility agriculture. Furthermore, there is a lack of qualitative and quantitative descriptions of the correlation between nonroot zone soil respiration and root zone soil respiration in tomato soil respiration, and there is also a lack of quantitative analysis of the relationship between soil respiration rate and yield. Therefore, it is necessary to

study the soil respiration and yield of tomato by changing the distance between capillary orifice outflow (micropore group spacing) and irrigation water quantity of microsprinkler irrigation under plastic film. In this study, the experiment of MSPF was conducted to explore the effects of different micropore group spacing and irrigation amounts on soil respiration, root zone microenvironment, and yield of greenhouse tomato. The method of regression analysis was used to make a quantitative study in order to obtain the best combination model of micropore group spacing and irrigation amount for reducing soil respiration rate (CO_2 emission) and increasing yield and water use efficiency of tomato in greenhouse under MSPF in northwest China. Through greenhouse experiment and regression analysis, this paper is aimed at enriching the greenhouse tomato microirrigation technology system and providing data support for water saving and high yield of protected agricultural crops and soil carbon cycle in this area.

2. Materials and Methods

2.1. Experimental Site and Management. This study was carried out in the greenhouse of Modern Agricultural Science and Technology Convention and Exhibition Center in Xi'an, Shaanxi Province (108°52′E, 34°03′N, 435 m above sea level). The greenhouse is 85 m long and 15 m wide (see Figure 2; Figure 2 is reproduced from Zhang et al. [9]). The average annual temperature is 13.3°C, and the rainfall is about 613.75 mm. The soil type is sandy loam in this area, and the mass fractions of sand, silt, and clay are 63.9%, 29.63%, and 6.47%, respectively. The average bulk density of a 1.0 m soil layer is 1.48 g/cm^3, the field capacity is 27.40%, and the buried depth of the groundwater table is more than 30 m [9]. The content of organic matter, namely, total phosphorus (P), total potassium (K), total nitrogen, available nitrogen, available phosphorus, and available potassium, in the plough layer before sowing was 15.53 g/kg, 10.12 g/kg, 2.01 g/kg, 1.36 g/kg, 0.70 g/kg, 0.11 g/kg, and 0.08 g/kg, respectively. The irrigation water originated from groundwater, the pH of which was 6.8, the chemical oxygen demand (COD) was 53.2 mg/L, the anionic surfactant content was 3.2 mg/L, and the chloride content was 0.48 mg/L [9].

The Jingfan 401 of tomato (Jingyan Yinong seed Technology Co., Ltd., Beijing) is planted on a ridge, in which the ridge is 3.4 m long and 1.2 m wide, and the irrigated plot is shown in Figure 2. The row spacing of the tomato is 50 cm and the plant spacing is 40 cm. The distance between each plot is 4 m, and a layer of styrene-butadiene-styrene block copolymer building waterproof film with a depth of 1.0 m is embedded in the middle to prevent the horizontal infiltration and movement of soil moisture and avoid the influence on other plot tests. The pipe of MSPF (Hebei Plentirain Irrigation Equipment Technology Co., Ltd., Hebei, China) adopted thin-walled oblique 3 micropores; the pipe of MSPF structure parameters is shown in Figure 3 (Figure 3 is reproduced from Zhang et al. [9]) and Table 1. The control drip irrigation under plastic film (CK1, Hebei Plentirain Irrigation Equipment Technology Co., Ltd., Hebei, China) with a thin-wall labyrinth tooth channel was selected. The geometric parameters of the channel were 54.3 mm × 1.1 mm × 0.83 mm, the pipe diameter was 16 mm, the distance between drippers was 30 cm, and the dripper flow rate was 2 L/h. The control of the pipe of the microsprinkler irrigation (CK2, Hebei Plentirain Irrigation Equipment Technology Co. Ltd, Hebei, China) adopted thin-walled oblique 3 micropores in which the pipe diameter was 32 mm and the micropore diameter was 0.8 mm. The micropore group spacing was 10 cm [9].

The experiment of planting tomatoes in a greenhouse during spring and autumn was conducted. Spring tomato and autumn tomato were planted on March 27, 2019, and August 23, 2019; irrigation began on April 4, 2019, and August 30, 2019; irrigation was stopped on July 15, 2019, and January 17, 2019; and the tomatoes were harvested on July 25, 2019, and January 30, 2020. The field management measures of all treatments of greenhouse tomato were consistent. In order to ensure the survival rate of tomato, irrigation was done uniformly after planting with reference to the planting experience of local farmers [9].

2.2. Experimental Design. Factors including the micropore group spacing (see Figure 3) and irrigation amount (see Figure 4 and see Table 1) were set up in this study. Among them, the micropore group spacing (L) is set to 2 levels: 30 cm (L1) and 50 cm (L2); the irrigation amount was controlled based on the cumulative evaporation from a 20 cm diameter standard pan (Epan) [39], which was realized by a control coefficient (k_{cp}), The k_{cp} (the crop-pan coefficient) was set to 3 levels: 0.7 (I1), 1.0 (I2), and 1.2 (I3) Epan. The CK1 and CK2 were used as the control treatment. There were a total of 8 treatments, each of which was repeated 3 times, for a total of 24 test areas.

The evaporation amount was measured at 08:00 AM for each irrigation frequency; the irrigation was initiated after the measurement. The irrigation amount (W) was calculated according to formula (1) [23, 40]. The irrigation times and amounts were recorded (see Table 1), taking $k_{cp} = 1.0$ as an example to draw the irrigation time and irrigation amount (see Figures 4 and 5].

$$W = A \times E_{pan} \times k_{cp}. \quad (1)$$

In the given formula, E_{pan} represents the evaporation within the interval between 2 irrigations (mm), A is the capillary control area, and k_{cp} is the crop pan coefficient. The k_{cp} of control CK1 and CK2 was 1.0 [9].

3. Measurements and Computational Methods

3.1. Soil Respiration Rate (CO_2 Emission). The soil respiration rate under different treatments was measured by an Li-8100 (LI-COR, Inc., USA) infrared gas analyzer. The PVC soil survey ring of diameter 20 cm was injected into the soil 2 days before the measurement and did not destroy the undisturbed soil on the surface. During the measurement, each measuring ring was measured twice to monitor the respiration rate of nonroot zone soil (soil without plant main roots) and root zone soil (soil containing plant main roots) (see Figure 6).

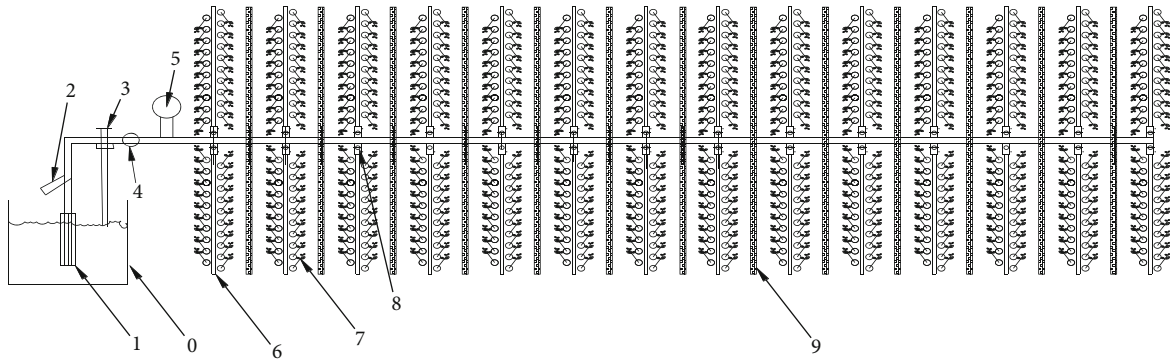

Figure 2: Schematic diagram of the greenhouse plot layout. Note: 0: water tank; 1: the pump (WQD10-12-0.75S, People Pump, Corp., Shanghai, China); 2: filter; 3: backwater valve; 4: electromagnetic flowmeter; 5: pressure gauge; 6: capillary; 7: tomato; 8: capillary valve; 9: plastic screens.

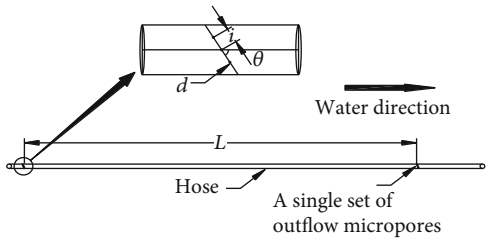

Figure 3: Schematic diagram of microporous group (inside) spacing structure parameters. Note: diameter of micropore is d = 0.8 mm; the internal spacing of the microporous group was I = 0.4 cm; the angle of micropores is equal to 68; the micropore group spacing is L.

Table 1: Experimental factor and design.

No.	Treatment	Micropore group spacing cm	k_{cp}	Irrigation amount (mm)	
				Spring	Autumn
1	L1I1	30	0.7	247.12	152.73
2	L1I2	30	1.0	353.03	218.19
3	L1I3	30	1.2	423.64	261.83
4	L2I1	50	0.7	247.12	152.73
5	L2I2	50	1.0	353.03	218.19
6	L2I3	50	1.2	423.64	261.83
7	CK1	30	1.0	353.03	218.19
8	CK2	10	1.0	353.03	218.19

Note: L: micropore group spacing of MSPF; I: irrigation amount of MSPF; CK1: drip irrigation under plastic film; CK2: microsprinkler irrigation.

When measuring root zone soil, the aboveground plants were cut. The soil respiration rate was measured at 11:00 AM on the 98th day of the planting of spring tomato and 97th day of the planting of autumn tomato.

3.2. Soil Microenvironment

3.2.1. Soil CO_2 Concentration. The soil CO_2 concentration in the nonroot zone and root zone of tomato was measured by the injector method (see Figure 7), and 0 (CO_2-0) and 20 cm (CO_2-20) samples were taken from the surface. The CO_2 concentration in the sample was determined by gas chromatography, and the determination time was the same as the soil respiration rate.

3.2.2. Soil Temperature and Soil Volume Moisture Content. The soil temperature of the nonroot zone and root zone of tomato was measured by a 15 cm geothermometer. TZS-W (Shanghai Heyi Instruments & Meters Co., Ltd., China) soil moisture meter was used to measure the soil moisture on the same day as the soil respiration rate. Firstly, the soil plane surface of the nonroot zone and root zone of 0~20 cm tomato was dug out, and then the probe was inserted into the 15 cm area away from the surface to determine the soil volume moisture content (see Figure 7) in the nonroot zone and root zone of tomato.

3.2.3. The Water-Filled Pore Space of Soil (WFPS). The nonroot zone and root zone of WFPS were calculated by dividing volumetric water content by total soil porosity. Total soil porosity was calculated by measuring the bulk density of the soil according to the relationship: soil porosity 1/4 (1 soil bulk density/2.65), assuming a particle density of 2.65 mg/m^3 [39].

3.2.4. The Tomato Nonrhizosphere and Rhizosphere Soil Total Organic Carbon (TOC), Microbial Biomass Carbon (MBC), Humic Acid Carbon (HA-C), and Fulvic Acid Carbon (FA-C) in Greenhouse. The nonrhizosphere soil adopts the conventional soil drilling method, which is to take out the soil in Figure 7 and mix it well; the rhizosphere soil was collected by the shaking soil method (randomly selecting a plant, digging out the 10~20 cm root system from the soil (see Figure 7), shaking off the soil loosely combined with the root system, and then brushing the root topsoil with a soft brush as the rhizosphere soil sample). The nonrhizosphere and rhizosphere soils were randomly sampled 3 times, and the samples were taken back to the room immediately. The plant residues were removed from the fresh soil and stored in the refrigerator at 20°C after 2 mm sieving. The contents of TOC, MBC, HA-C, and FA-C in the soil were measured within 10 days, and the sampling time was the same as the soil respiration rate. The TOC and MBC were determined by the fumigation extraction method as outlined by Chatterjee et al.

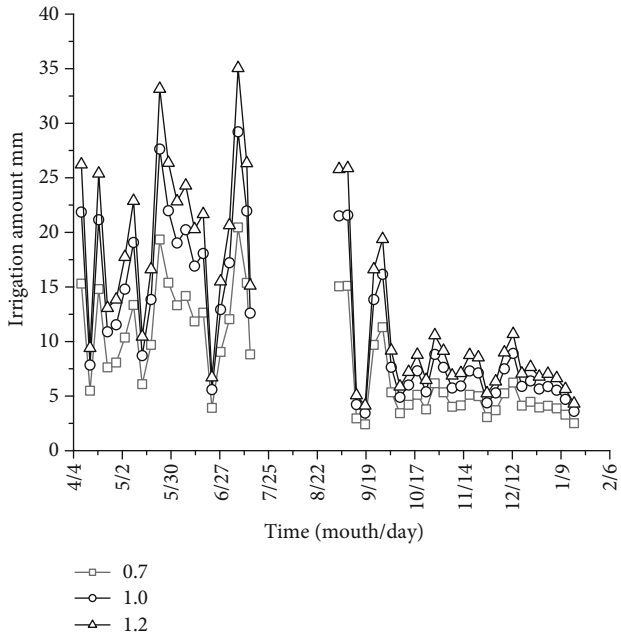

Figure 4: Irrigation records.

[40]. The HA-C and FA-C were extracted from soil samples according to the procedure of Sun et al. [41].

3.3. Yield and Water Use Efficiency. Four tomatoes were randomly selected from each plot, and the yield was measured by 0.01 g precision electronic scale after ripening. After the yield per plant was obtained, the tomato yield per hectare was calculated [9].

The volumetric soil water content of 0~10 cm, 10~20 cm, 20~30 cm, 30~40 cm, 40~50 cm, 50~60 cm, 60~70 cm, and 70~80 cm was measured by a soil moisture sensor (TRIME-PICO-IPH, IMKO, Inc., Ettlingen, Germany). Monitoring before and after planting, two monitoring points were selected in each district (monitoring point 1 was arranged at the outflow micropore, and monitoring point 2 was arranged at the distance m between the two groups of micropores in the vertical flow direction, in which $m = 25$ cm, Figure 6). Crop water consumption (ET_a) and crop water use efficiency (WUE) were obtained by formula (2) and formula (3) [9, 42]:

$$ET_a = I \pm 1000 \times H \times (\theta_{t1} - \theta_{t2}). \quad (2)$$

In the formula: ET_a is the crop water consumption during the growth period, mm; I is the irrigation quota of crop growth period, mm; H is the depth of the wetting layer with plan, $H = 0.8$ m; and θ_{t1} and θ_{t2} are the 80 cm average soil volumetric water contents at times $t1$ and $t2$, respectively (cm^3/cm^3).

$$WUE = \frac{1000 * Y}{ET_a}. \quad (3)$$

In the formula, WUE is the crop water use efficiency, kg/m^3; Y is the crop grain yield, kg/hm^2.

4. Data Analysis

The significant difference of SPSS22.0 (IBM Crop., Armonk, New York, NY, USA) was analyzed by the F test, and the significance level was set to $P < 0.05$. OriginPro2019 (OriginLab Corporation, Northampton, MA, USA) was used to draw the picture. Mathematica12.0 (Wolfram Research, New York, NY, USA) was used for regression analysis.

5. Results

5.1. Effects of Different Treatments on Soil Water and Heat of Tomato in Greenhouse. The micropore group spacing (L) had no significant effect on soil water and heat in the nonroot zone and root zone of tomato ($P > 0.05$, see Table 2). The irrigation amount (I) also exhibited a significant effect on soil water and heat in the nonrhizosphere and root zone of tomato ($P \leq 0.05$).

The nonroot zone soil temperature and root zone soil temperature of spring and autumn tomatoes treated with L1I2 increased by 6.16% and 6.38% and 1.78% and 8.36%, respectively, compared with those of CK1 and 7.58% and 9.45% and 8.58% and 14.78% higher than those of CK2, respectively. The volume water content of the nonroot zone and root zone of tomato treated with L1I2 increased by 8.75% and 3.64% and 0.57% and 3.64%, compared with that of CK1, respectively, and increased by 9.85% and 9.34% and 14.83% and 16.80% compared with that of CK2, respectively. With an increase in irrigation amount, the volume water content of the nonroot zone and root zone of tomato first increased, while the soil nonroot zone temperature and root zone temperature of tomato decreased. The soil nonroot zone temperature, root zone temperature, nonroot zone volume water content, and root zone volume water content of tomato with the micropore group spacing of 30 cm were slightly higher than those of 50 cm by about 0.19% and 2.55%, 2.71% and 2.02%, 2.22% and 6.69%, and 5.59% and 7.38%, respectively.

5.2. Effects of Different Treatments on the Soil CO_2 Concentration in Nonroot Zone and Root Zone of Tomato. The micropore group spacing (L) had no significant effect on CO_2 concentration in the nonroot zone and root zone of tomato soil at different depths (see Table 3). The irrigation amount (I) also exhibited a significant effect on CO_2 concentration in the nonroot zone and root zone of tomato soil at different depths. The interaction between them had no significant effect on the concentration of CO_2 in the nonroot zone and root zone of soil at different depths.

The soil CO_2 concentration of 0 cm of tomato was significantly lower than the depth of the 20 cm soil layer, indicating that as the depth of the soil layer increased, the soil CO_2 concentration increased. With the seasonal change, the soil CO_2 concentration of autumn tomato was lower than that of spring tomato. The CO_2 concentration in the nonroot zone of the 0 cm soil layer and the CO_2 concentration in the root zone of 0 cm soil treated with L1I2 were 2.69% and 1.79% and 0.47%and 1.24% higher than those of CK1 and 6.55% and 4.96% and 7.74% and 12.43% higher than those of

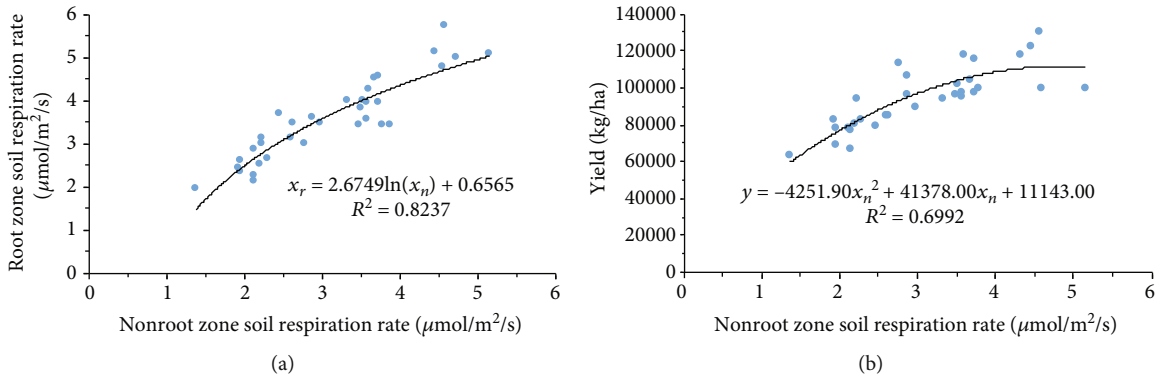

Figure 5: Regression analysis of nonroot zone soil respiration rate (x_n), root zone soil respiration rate (x_r), and yield (y) of spring tomato (a) and autumn tomato (b).

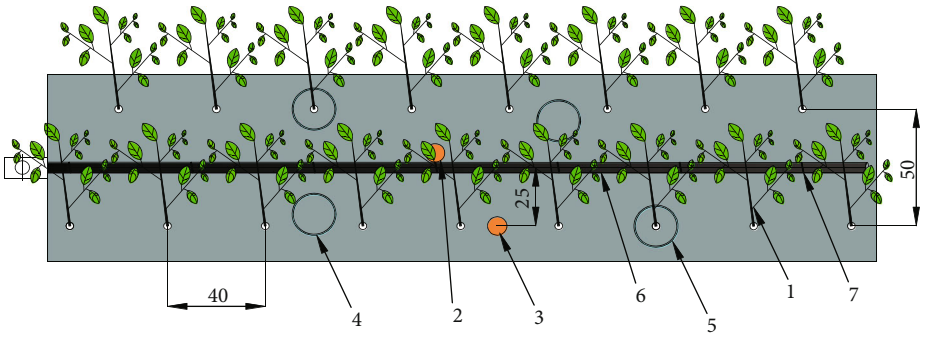

Figure 6: The distribution map of soil respiration monitoring points for greenhouse tomato (unit: cm). Note: 1: tomato; 2: TRIME 1; 3: TRIME 2; 4: nonroot zone soil respiration rate PVC measurement ring; 5: root zone soil respiration rate PVC measurement ring; 6: capillary; 7: single group outflow location.

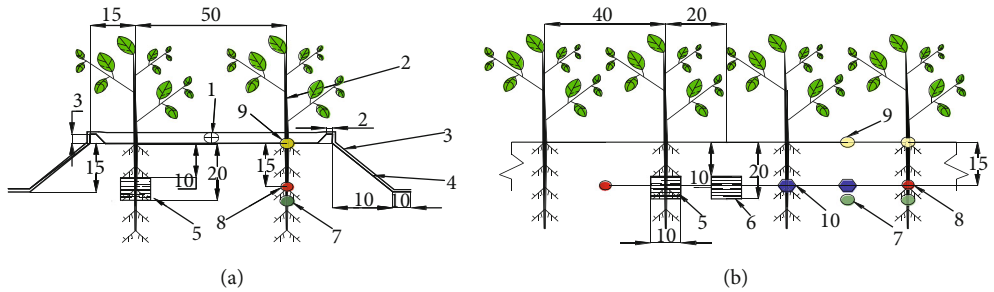

Figure 7: Schematic diagram of the position of sampling points (unit: cm). Note: 1: pipe; 2: tomato; 3: plastic film; 4: surface soil; 5: root zone of soil sampling point; 6: nonroot zone of soil sampling points; 7: the CO_2 concentration of 20 cm measurement point; 8: temperature measurement point; 9: the CO_2 concentration of 0 cm measurement point; 10: soil volume moisture content measurement point.

CK2, respectively. The CO_2 concentration in the nonroot zone of the 20 cm soil layer and the CO_2 concentration in the root zone of the 20 cm soil treated with L1I2 were 4.06% and -1.32% and 1.68% and 3.89% higher than those of CK1 and 11.03% and 2.20% and 8.07% and 20.97% higher than those of CK2, respectively.

With the increase of irrigation amount, the soil CO_2 concentration in the nonroot zone and root zone of tomato at different depths increased first and then decreased. The CO_2 concentration in the nonroot zone of 0 cm soil, the CO_2 concentration in the root zone of 0 cm soil, the CO_2 concentration in the nonroot zone of 20 cm soil, and the CO_2 concentration in the root zone of 20 cm soil were higher than those of 50 cm in tomato soil with a micropore group spacing of 30 cm.

5.3. Effects of Different Treatments on Soil Respiration Rate of Greenhouse Tomato. Figure 8 shows that the micropore group spacing had no significant effect on the respiration rate of the nonroot zone and root zone of tomato soil. The irrigation amount had a significant effect on the respiration rate of the nonroot zone and the root zone of tomato soil ($P \leq 0.05$).

Table 2: Effects of different treatments on soil moisture and temperature in nonroot zone and root zone of tomato in greenhouse.

Treatment	Spring				Autumn			
	Temperature (°C)		Soil volume moisture content (%)		Temperature (°C)		Soil volume moisture content (%)	
	Nonroot zone soil	Root zone soil	Nonroot zone soil	Root zone soil	Nonroot zone soil	Root zone soil	Nonroot zone soil	Root zone soil
L1I1	26.1 ± 0.71^{abc}	25.07 ± 0.87^{ab}	20.55 ± 5.97^{c}	19.56 ± 3.18^{c}	20.14 ± 0.52^{a}	18.69 ± 0.5^{ab}	22.04 ± 3.92^{bc}	20.55 ± 3.44^{cd}
L1I2	26.99 ± 0.22^{a}	25.57 ± 1.18^{a}	27.73 ± 7.56^{ab}	27.48 ± 3.84^{ab}	20.15 ± 0.93^{a}	19.61 ± 2.75^{a}	28.22 ± 3.98^{a}	28.22 ± 3.39^{ab}
L1I3	25.32 ± 1.13^{bc}	23.31 ± 2.49^{bc}	31.44 ± 3.31^{a}	29.21 ± 5.12^{a}	17.57 ± 1.66^{c}	16.91 ± 1.48^{bc}	28.72 ± 4.67^{a}	28.72 ± 2.77^{a}
L2I1	26.37 ± 2.34^{abc}	24.93 ± 1.8^{ab}	20.06 ± 4.28^{c}	18.32 ± 3.34^{c}	19.67 ± 1.53^{ab}	19.25 ± 0.61^{a}	19.81 ± 3.83^{ab}	18.32 ± 2.92^{d}
L2I2	26.77 ± 0.81^{ab}	24.84 ± 1.97^{ab}	27.73 ± 4.06^{ab}	26.91 ± 3.35^{ab}	19.34 ± 1.14^{ab}	18.49 ± 1.07^{ab}	25.75 ± 2.24^{c}	25.62 ± 3.37^{ab}
L2I3	25.12 ± 1.36^{c}	22.23 ± 1.37^{c}	30.2 ± 3.07^{ab}	26.99 ± 3.69^{ab}	17.41 ± 0.98^{c}	16.37 ± 1.98^{c}	28.47 ± 2.18^{a}	28.22 ± 3.51^{ab}
CK1	25.43 ± 1.13^{abc}	25.12 ± 1.66^{ab}	25.5 ± 1.74^{bc}	27.32 ± 2.35^{ab}	18.94 ± 0.6^{abc}	18.09 ± 1.01^{abc}	27.23 ± 5.12^{a}	27.23 ± 3.47^{ab}
CK2	25.09 ± 1.14^{c}	23.55 ± 0.93^{abc}	25.24 ± 2.28^{bc}	23.93 ± 2.25^{b}	18.41 ± 1.91^{bc}	17.08 ± 0.31^{bc}	25.81 ± 2.02^{ab}	24.16 ± 2.01^{bc}
F value								
L	0.014^{ns}	1.311^{ns}	0.091^{ns}	1.124^{ns}	1.456^{ns}	0.464^{ns}	1.588^{ns}	2.697^{ns}
I	5.168^{*}	7.567^{**}	13.453^{**}	21.070^{**}	15.497^{**}	8.708^{**}	17.142^{**}	26.607^{**}
L ∗ I	0.145^{ns}	0.230^{ns}	0.043^{ns}	0.143^{ns}	0.223^{ns}	0.851^{ns}	0.173^{ns}	0.362^{ns}

Note: L: micropore group spacing; I: irrigation amount. The data are all average ± standard deviation in the chart; different letters in the same column mean significant difference at 0.05 level, $^{*}P < 0.05$; $^{**}P < 0.01$; ns: $P > 0.05$, the same as below.

The soil nonroot zone and root zone respiration rates of autumn tomato were about 2.81% and 4.14% lower than those of spring tomato, respectively. The soil respiration rate in the root zone of spring tomato and autumn tomato was about 14.66% and 16.25% higher than that in the nonroot zone, respectively.

Compared with CK1, the soil nonroot zone respiration rate and root zone respiration rate of L1I2 spring tomato and an autumn tomato increased by 11.39% and 6.22% and 4.80% and 7.26%, respectively, and increased by 27.08% and 39.70% and 42.25% and 37.06%, respectively, compared with CK2. With the increase of irrigation amount, the respiration rate of tomato soil nonroot zone and root zone increased first and then showed a slight decreasing trend. The soil respiration rate of 30 cm with the micropore group spacing is higher than 50 cm.

5.4. Effects of Different Treatments on the Related Carbon Content of Soil in Greenhouse Tomato. It can be seen from Table 4 that the micropore group spacing has no significant effect on TOC, MBC, HA-C, and FA-C in the nonrhizosphere and rhizosphere of soil with spring tomato and autumn tomato; irrigation amount has a significant effect on TOC, MBC, HA-C, and FA-C in the nonrhizosphere and rhizosphere of soil with spring tomato and autumn tomato. The TOC, MBC, HA-C, and FA-C of the rhizosphere soil of spring tomato and autumn tomato were 27.94% and 26.97%, 19.47% and 25.23%, 19.47% and 22.20%, and 8.15% and 2.78% higher than those of the nonrhizosphere soil, respectively.

In terms of nonrhizosphere of soil with spring tomato and autumn tomato, the TOC, MBC, HA-C, and FA-C of L1I2 treatments were higher than those of CK1 by about 8.24% and 4.44%, 2.36% and 6.03%, 2.09%and 6.23%, and 0.36% and 2.72%, respectively, and also higher than those of CK2 by about 13.19% and 5.59%, 7.22% and 10.69%, 9.72% and 16.15%, and 6.89% and 11.24%, respectively. For the rhizosphere soil of spring tomato and autumn tomato, the TOC, MBC, HA-C, and FA-C of L1I2 treatments were higher than those of CK1 by about 6.64% and 1.60%, 2.38% and 1.14%, 3.37% and 3.49%, and 1.32% and 2.57%, respectively, and also higher than those of CK2 by about 10.12% and 10.31%, 11.39% and 11.30%, 17.55% and 7.55%, and 6.39% and 12.86%, respectively. With the increase of irrigation amount, the TOC, MBC, HA-C, and FA-C of nonrhizosphere and rhizosphere soils of spring tomato and autumn tomato increased at first and then decreased. The TOC, MBC, HA-C, and FA-C of nonrhizosphere and rhizosphere soils of spring tomato and autumn tomato in the micropore group spacing of 30 cm was higher than 50 cm.

5.5. Effects of Different Treatments on Tomato Yield and Water Use Efficiency. As can be seen from Figure 9, the micropore group spacing had a significant effect on the yield and water use efficiency of spring and autumn tomatoes ($P \leq 0.05$). The irrigation amount had a significant effect on the yield and water use efficiency of spring and autumn tomatoes.

Compared with CK1, the yield and water use efficiency of spring tomato and autumn tomato treated with L1I2 increased by 19.39% and 4.54% and 10.03% and 2.32%, respectively. Compared with CK2, the yield and water use efficiency of spring tomato and autumn tomato treated with L1I2 increased by 20.46% and 49.22% and 31.02% and 58.05%, respectively. The yield of spring tomato and autumn tomato treated with L1I2 was about 31.88% and 28.03%, 0.96% and 1.43%, 47.73% and 44.49%, 24.74% and 21.09%, and 12.21% and 7.48% higher than that of L1I1, L1I3, L2I1, L2I2, and L2I3, respectively. With the increase of irrigation amount, the yield of spring tomato and autumn tomato increased, while the water use efficiency of spring tomato and autumn tomato decreased. The yield and water use efficiency of spring tomato and autumn tomato with micropore group spacing 30 cm were higher than those of 50 cm by about 16.00% and 13.01% and 20.85% and 14.25%, respectively.

Table 3: Effects of different treatments on soil CO_2 concentration of greenhouse tomato at different depths.

Treatment	Spring				Autumn			
	The CO_2 concentration of 0 cm (μmol/mol)		The CO_2 concentration of 20 cm (μmol/mol)		The CO_2 concentration of 0 cm (μmol/mol)		The CO_2 concentration of 20 cm (μmol/mol)	
	Nonroot zone soil	Root zone soil	Nonroot zone soil	Root zone soil	Nonroot zone soil	Root zone soil	Nonroot zone soil	Root zone soil
L1I1	430.93 ± 22.38^{b}	448.28 ± 37.33^{ab}	11549.36 ± 3088.94^{b}	15387.65 ± 3353.14^{b}	354.37 ± 17.44^{b}	362.06 ± 33.02^{b}	9911.93 ± 1542.99^{b}	12220.01 ± 2087.97^{b}
L1I2	460.74 ± 14.86^{a}	475.31 ± 32.63^{a}	$13909.31 \pm 2817.28^{ab}$	$18369.31 \pm 3474.77^{ab}$	409.53 ± 25.36^{a}	457.31 ± 53.35^{ab}	$11910.05 \pm 2638.63^{ab}$	$14832.84 \pm 3354.07^{ab}$
L1I3	445.51 ± 23.51^{ab}	468.43 ± 19.07^{ab}	15238.13 ± 4111.09^{a}	19529.57 ± 3560.48^{a}	406.69 ± 42.87^{a}	424.605 ± 45.46^{ab}	13106.25 ± 3051.99^{a}	15800.78 ± 2645.28^{a}
L2I1	429.97 ± 29.42^{b}	$433.85 \pm 32.33b$	11116.69 ± 1199.53^{b}	15209.09 ± 3858.32^{b}	347.53 ± 27.89^{b}	356.79 ± 47.27^{b}	9894.33 ± 2011.61^{b}	12087.22 ± 2232.93^{b}
L2I2	450.31 ± 19.7^{ab}	476.66 ± 24.27^{a}	13466.39 ± 4681.6^{ab}	$17815.02 \pm 5512.68^{ab}$	402.3 ± 32.05^{a}	435.43 ± 32.39^{ab}	$11663.94 \pm 3104.59^{ab}$	$14547.37 \pm 3466.27^{ab}$
L2I3	446.74 ± 23.26^{ab}	474.06 ± 30.25^{a}	14979.31 ± 2576.25^{a}	19353.99 ± 2662.52^{a}	402.22 ± 47.14^{a}	421.88 ± 63.02^{ab}	12829.23 ± 2418.95^{a}	15614.11 ± 3259.88^{a}
CK1	448.66 ± 13.2^{ab}	473.11 ± 17.92^{a}	$13366.68 \pm 1382.84^{ab}$	$18065.81 \pm 2218.28^{ab}$	402.34 ± 18.45^{a}	451.73 ± 44.67^{ab}	$12069.23 \pm 2366.66^{ab}$	$14276.91 \pm 3646.29^{ab}$
CK2	432.44 ± 5.09^{b}	441.15 ± 17.82^{ab}	$12527.66 \pm 2109.63^{ab}$	$16997.02 \pm 2780.95^{ab}$	390.18 ± 12.52^{a}	406.75 ± 27.51^{ab}	$11653.99 \pm 2744.25^{ab}$	12261.35 ± 1285.67^{b}
F value								
L	0.202^{ns}	0.062^{ns}	0.180^{ns}	0.084^{ns}	0.303^{ns}	0.405^{ns}	0.069^{ns}	0.066^{ns}
I	3.766^{*}	4.810^{*}	6.101^{**}	5.458^{*}	10.369^{**}	11.013^{**}	6.756^{**}	7.202^{**}
L * I	0.225^{ns}	0.374^{ns}	0.004^{ns}	0.014^{ns}	0.006^{ns}	0.146^{ns}	0.014^{ns}	0.003^{ns}

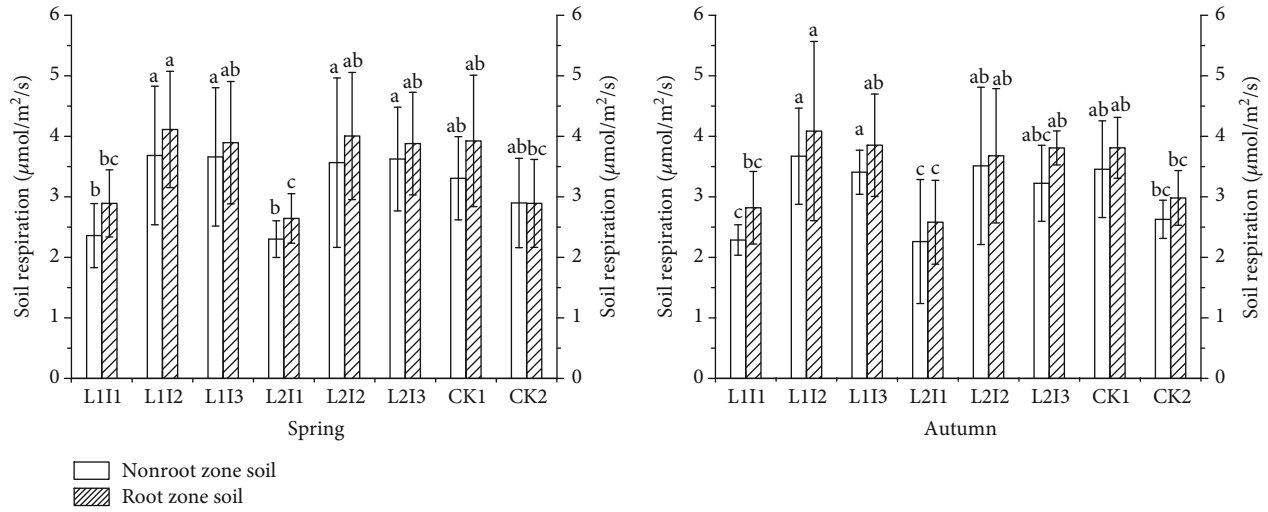

Figure 8: Effects of different treatments on soil respiration rate of tomato in greenhouse. Note: the data are all average ± standard deviation in the figure; different letters in the same column meant significant difference at 0.05 level, the same as below.

5.6. Regression Analysis of Soil Respiration Rate and Yield of Microsprinkler Irrigation under Plastic Film. As can be seen from Figure 5, there is a logarithmic relationship between x_n and x_r (formula (4)) and a conic relationship between x_n and y (formula (5)).

$$x_r = 2.6749 \ln (x_n) + 0.6565, \quad (4)$$

$$y = -0.425.90x_n^2 + 41378x_n + 11143. \quad (5)$$

Through the simultaneous establishment of the above two equations, the relationship between x_r and y can be obtained, that is, $y = 2602.13e^{0.7478x_r} + 32370.01e^{0.3739x_r} + 11143$. In the regression model (4), the determination coefficient of x_n and x_r regression is $R^2 = 0.8237$, indicating that the degree to which x_n can explain x_r in this model is up to 82%, and the coefficient x_r can be predicted by x_n. In the regression model (5), the determination coefficient of x_n and y regression is $R^2 = 6992$, indicating that the degree to which x_n can explain y in this model is up to 69%, and the coefficient y can be predicted by x_n.

6. Discussion

6.1. Effects of Irrigation Methods on Soil Microenvironment and Soil Respiration Rate. Previous studies have shown that different irrigation methods lead to different forms of water entering the soil. It can change the shape of the soil wetting body, the size of the dry and wet zones, and the number of cycles and affect the mineralization decomposition rate of soil organic matter, microbial biomass, and soil enzyme activity and then increase or decrease the concentration of CO_2 in soil. Under the concentration gradient drive, the diffusion rate of soil CO_2 to the surface increases or slows down [38, 43]. There is a positive correlation between soil respiration rate and soil moisture in arid and semiarid areas, in which the limitation of soil moisture is mainly reflected in reducing the availability of soil organic matter and the death of soil microorganisms caused by low water potential [44, 45]. In this study, the soil respiration rate of tomato with MSPF was higher than that of drip irrigation under plastic film (see Figure 8). It is possible that under the same working pressure and irrigation amount, the effluent velocity of drip irrigation under plastic film is about 0.067 times that of MSPF, and the irrigation duration increases, so that the ratio of horizontal to vertical migration distance of soil water in drip irrigation under plastic film is smaller than that of MSPF, and the higher horizontal movement of soil water is easy to increase the wetting volume of the tillage layer (0~40 cm) per unit area [46]. The soil moisture of tomato with drip irrigation under a plastic film is mainly concentrated under the emitter, and there is an obvious dry-wet zone and a long dry-wet duration, which restricts the activities of microorganisms and enzymes in the dry area, and the soil water content is too high in the wet area, which reduces the soil gas exchange. As a result, the soil respiration rate of drip irrigation under plastic film is lower than that of MSPF. Burger et al. found that the peak of CO_2 emission from tomato soil respiration occurred when WFPS was about 60% [47]. It is mainly due to the fact that soil moisture is the main factor limiting soil respiration when WFPS < 60%. Too high or low soil moisture will reduce the stability of soil aggregates. The destruction of soil aggregates is usually accompanied by the increase of the utilization rate of organic carbon sources, which can increase the activities of microorganisms and enzymes and increase the mineralization of soil carbon [48, 49]. At the same time, the increase of soil moisture increased microbial activity and plant physiological activities; increased soil TOC, MBC, HA-C, and FA-C; and further supplied energy sources for microbial activities and increased soil microbial respiration. When WFPS > 60%, higher soil moisture occupies a large number of soil pores, reducing soil oxygen content, and limiting soil gas diffusion rate [39]. In this study, the WFPS of MSPF is close to 60%, and the moisture and temperature of MSPF are higher than 5.77% and 4.30% and 3.99% and 13.47% (see Table 5) of drip

Table 4: Effects of different treatments on soil related carbon content of greenhouse tomato.

			Treatment								*F* value		
			L1I1	L1I2	L1I3	L2I1	L2I2	L2I3	CK1	CK2	L	I	L ∗ I
Spring	TOC (%)	Nonrhizosphere	0.96 ± 0.12^{c}	1.18 ± 0.11^{a}	1.16 ± 0.09^{a}	0.95 ± 0.17^{c}	1.17 ± 0.07^{a}	1.16 ± 0.09^{a}	1.09 ± 0.04^{ab}	1.04 ± 0.07^{bc}	0.032^{ns}	21.533^{**}	0.016^{ns}
		Rhizosphere	1.31 ± 0.09^{b}	1.46 ± 0.14^{a}	1.45 ± 0.11^{a}	1.3 ± 0.17^{ba}	1.46 ± 0.09^{a}	1.46 ± 0.1^{a}	1.37 ± 0.05^{ab}	1.33 ± 0.09^{b}	0.001^{ns}	9.964^{**}	0.029^{ns}
	MBC (mg/kg)	Nonrhizosphere	108.27 ± 17.47^{bc}	121.53 ± 8.38^{a}	121.31 ± 10.36^{a}	107.35 ± 13.48^{c}	120.78 ± 6.35^{a}	121.55 ± 11.58^{a}	108.17 ± 4.7^{ab}	115.34 ± 7.53^{abc}	0.022^{ns}	7.804^{**}	0.012^{ns}
		Rhizosphere	128.11 ± 14.12^{c}	147.64 ± 10.26^{a}	145.27 ± 15.19^{a}	125.88 ± 10.7^{c}	142.4 ± 12.98^{ab}	145.56 ± 15.5^{a}	144.21 ± 8.09^{ab}	132.55 ± 8.21^{bc}	0.439^{ns}	11.295^{**}	0.196^{ns}
	HA-C (g/kg)	Nonrhizosphere	1.63 ± 0.29^{b}	2.07 ± 0.14^{a}	2.04 ± 0.24^{a}	1.64 ± 0.5^{b}	2.05 ± 0.24^{a}	2.07 ± 0.36^{a}	2.03 ± 0.3^{a}	1.89 ± 0.12^{ab}	0.001^{ns}	10.806^{**}	0.021^{ns}
		Rhizosphere	2.07 ± 0.6^{b}	2.47 ± 0.18^{a}	2.39 ± 0.26^{ab}	2.08 ± 0.43^{b}	2.4 ± 0.23^{ab}	2.37 ± 0.15^{ab}	2.39 ± 0.31^{ab}	2.1 ± 0.37^{b}	0.073^{ns}	5.721^{*}	0.060^{ns}
	FA-C (g/kg)	Nonrhizosphere	2.15 ± 0.45^{bc}	2.66 ± 0.31^{a}	2.59 ± 0.4^{a}	2.06 ± 0.34^{c}	2.57 ± 0.37^{a}	2.57 ± 0.34^{a}	2.65 ± 0.38^{a}	2.48 ± 0.37^{ab}	0.386^{ns}	10.462^{**}	0.053^{ns}
		Rhizosphere	2.46 ± 0.27^{ab}	2.82 ± 0.26^{a}	2.72 ± 0.46^{ab}	2.36 ± 0.43^{b}	2.77 ± 0.39^{a}	2.76 ± 0.37^{a}	2.79 ± 0.26^{a}	2.65 ± 0.42^{ab}	0.156^{ns}	5.760^{*}	0.162^{ns}
Autumn	TOC (%)	Nonrhizosphere	0.92 ± 0.07^{b}	1.07 ± 0.05^{a}	1.07 ± 0.07^{a}	0.9 ± 0.07^{b}	1.07 ± 0.05^{a}	1.05 ± 0.05^{a}	1.03 ± 0.07^{a}	1.01 ± 0.11^{a}	0.657^{ns}	39.2936^{**}	0.225^{ns}
		Rhizosphere	1.18 ± 0.08^{b}	1.34 ± 0.06^{a}	1.35 ± 0.07^{a}	1.16 ± 0.09^{b}	1.34 ± 0.07^{a}	1.35 ± 0.07^{a}	1.32 ± 0.08^{a}	1.22 ± 0.11^{b}	0.034^{ns}	33.320^{**}	0.045^{ns}
	MBC (mg/kg)	Nonrhizosphere	92.31 ± 6.01^{b}	107.48 ± 7.51^{a}	107.14 ± 8.85^{a}	94.5 ± 17.2^{b}	107.52 ± 10.74^{a}	106.96 ± 7.42^{a}	101.37 ± 11.89^{ab}	97.1 ± 7.65^{ab}	0.060^{ns}	10.881^{**}	0.073^{ns}
		Rhizosphere	119.39 ± 7.6^{c}	134.61 ± 9.5^{a}	134.31 ± 11.2^{a}	118.83 ± 20.62^{c}	133.68 ± 13.96^{a}	134.08 ± 9.39^{a}	132.74 ± 16.58^{ab}	120.94 ± 6.66^{bc}	0.027^{ns}	8.320^{**}	0.003^{ns}
	HA-C (g/kg)	Nonrhizosphere	1.7 ± 0.31^{bc}	2.05 ± 0.12^{a}	1.94 ± 0.26^{ab}	1.63 ± 0.31^{c}	1.95 ± 0.19^{ab}	1.96 ± 0.26^{ab}	1.93 ± 0.3^{ab}	1.76 ± 0.36^{abc}	0.530^{ns}	9.415^{**}	0.240^{ns}
		Rhizosphere	2.13 ± 0.39^{c}	2.49 ± 0.16^{a}	2.46 ± 0.21^{a}	2.15 ± 0.27^{bc}	2.29 ± 0.18^{abc}	2.36 ± 0.27^{abc}	2.41 ± 0.18^{ab}	2.32 ± 0.29^{abc}	1.6767^{ns}	6.337^{**}	0.871^{ns}
	FA-C (g/kg)	Nonrhizosphere	2.14 ± 0.21^{b}	2.58 ± 0.46^{a}	2.57 ± 0.39^{a}	2.12 ± 0.36^{b}	2.52 ± 0.44^{ab}	2.55 ± 0.39^{a}	2.51 ± 0.43^{ab}	2.32 ± 0.39^{ab}	0.090^{ns}	7.410^{**}	0.017^{ns}
		Rhizosphere	2.3 ± 0.25^{ab}	2.65 ± 0.4^{a}	2.57 ± 0.38^{ab}	2.21 ± 0.26^{b}	2.59 ± 0.4^{ab}	2.59 ± 0.36^{ab}	2.58 ± 0.42^{ab}	2.35 ± 0.3^{ab}	0.188^{ns}	6.041^{*}	0.096^{ns}

Note: TOC: soil total organic carbon; MBC: soil microbial biomass carbon; HA-C: soil humic acid carbon; FA-C: soil fulvic acid carbon.

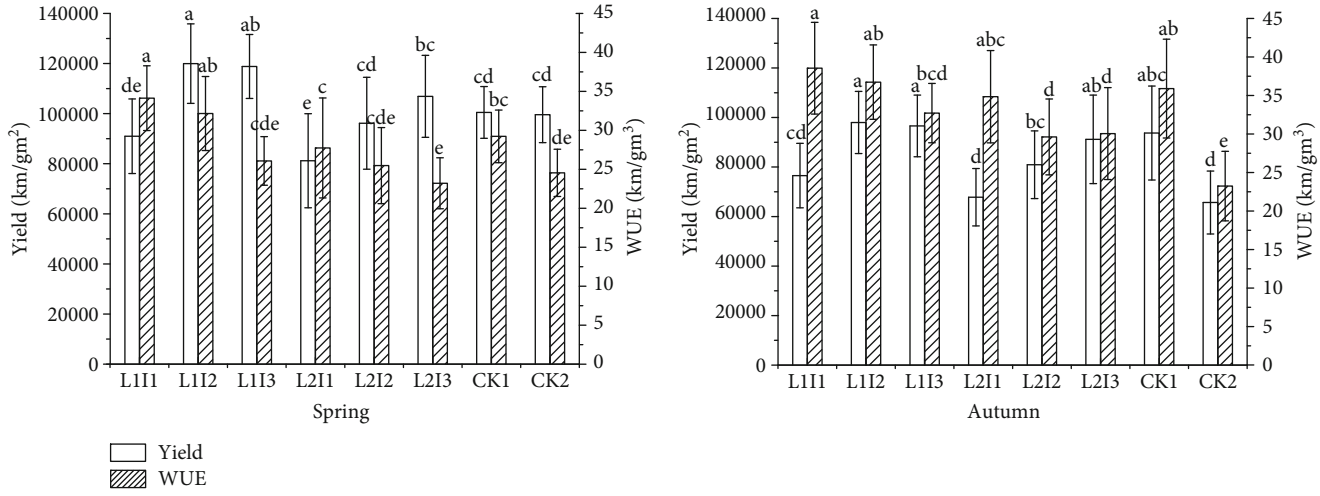

Figure 9: Effects of different treatments on tomato yield and water use efficiency.

irrigation under plastic film, respectively, which may also be one of the reasons for the higher soil respiration of MSPF.

It was found that the soil respiration rate of the tomato root zone was higher than that of the nonroot zone. It may be due to the fact that the soil in the crop root zone contains plant roots. Previous studies have shown that the diversity, abundance, and activity of microorganisms in the plant rhizosphere soil are high [50], and the respiration of microorganisms and plant roots is easy to increase soil respiration rate (CO_2 emission) [51, 52]. In this study, it was also found that the soil respiration rate of spring tomato was higher than that of autumn tomato. Mainly because the soil temperature of spring tomato is 32.19% higher than that of autumn tomato (L1I2, see Table 2), lower temperature can reduce cell activity, which is not conducive to microorganisms and crop respiration [53]. Previous studies have found that the effect of irrigation on the soil respiration rate is attributed to the increase of crop yield to stimulate root autotrophic respiration and the change of soil water content to stimulate soil heterotrophic respiration [54]. In this study, the yield of tomato and soil moisture of MSPF were higher than those of drip irrigation under plastic film by 19.39 and 4.54% (see Figure 9) and 5.77 and 4.30% (see Table 2), respectively, indicating that MSPF can increase soil respiration rate and lead to the increase of the soil CO_2 emission rate. The increase of the soil respiration rate in greenhouse agriculture contributes to the formation of greenhouse tomato yield, which can achieve a new dynamic balance among tomato crop water use efficiency, yield, and CO_2 emission from greenhouse vegetable fields.

This study found that the humidity of spring tomato and autumn tomato canopy under MSPF was about 36.03% and 25.20% lower than that of microsprinkler irrigation (see Figure 10), respectively. This may be due to the large number of micropores per unit length of microsprinkler irrigation, so the water spray is easy to atomize, and the increase of surface wetting area also easily increases ineffective water transpiration, which leads to a significant increase in air humidity in the microenvironment of tomato growth, which is consistent with the finding of Man et al. [15] who explored the mechanism of action of microsprinkler irrigation. The results also showed that the soil respiration rate of tomato under MSPF was higher than that of microsprinkler irrigation, and the yield of tomato under MSPF was 4.69% and 49.22% higher than that of microsprinkler irrigation (see Figure 9), which was consistent with the conclusion of Scheer et al. [54]. Mainly due to the low oxygen content of the air humidity, it will reduce the soil aerobic respiration microbial activity, and its byproduct CO_2 emissions will also be reduced. The increase in crop yield will further stimulate the autotrophic respiration of roots, resulting in a higher soil respiration rate of MSPF. This study also found that the soil WFPS of 0~10 cm under MSPF was about 60%, which was higher than 10.15% and 6.33% of microsprinkler irrigation. At the same time, the soil moisture volume content of 20 cm under MSPF was 7.96% and 7.22% (see Table 2) higher than that of microsprinkler irrigation, indicating that soil moisture was also one of the main reasons affecting the soil respiration rate of tomato under MSPF.

6.2. Effects of Micropore Group Spacing and Irrigation Amount on Soil Respiration Rate. In this study, the micropore group spacing has little effect on the soil respiration rate, which may be due to the large flow rate and short irrigation duration of the single group of MSPF. When the flow of WFPS is greater than the soil infiltration rate, it is easy to produce local microrunoff, which increases the soil water horizontal transport distance and reduces the effect of relatively small micropore group spacing. There is no significant difference in 0~10 cm soil WFPS between the two groups ($P > 0.05$). It was also found that the micropore group spacing had no significant effect on soil moisture and temperature. Previous studies have found that water and heat changes directly affect soil microorganisms and enzyme activities, thus changing soil TOC, MBC, HA-C, and FA-C cycles [38, 55]. There was no significant difference in soil TOC, MBC, HA-C, and FA-C among different micropore group spacings, which further indicated

Table 5: Effects of different treatments on soil water-filled porosity of tomato.

Treatment	Spring		Autumn	
	Nonroot zone soil (%)	Root zone soil (%)	Nonroot zone soil (%)	Root zone soil (%)
L1I1	55.69 ± 10.04^{ab}	54.41 ± 10.89^{ab}	54.25 ± 9.78^{ab}	49.85 ± 12.37^{b}
L1I2	62.55 ± 9.26^{ab}	61.76 ± 5.81^{a}	60.52 ± 8.52^{ab}	58.05 ± 7.4^{ab}
L1I3	63.2 ± 5.35^{a}	62.29 ± 8.05^{a}	63.49 ± 10.09^{a}	63.09 ± 8.88^{a}
L2I1	53.72 ± 8.72^{b}	50.82 ± 7.17^{b}	50.47 ± 8.79^{b}	47.85 ± 13.4^{b}
L2I2	56.77 ± 6.99^{ab}	57.17 ± 6.54^{ab}	55.39 ± 12.51^{ab}	54.34 ± 8.03^{ab}
L2I3	63.92 ± 9.08^{a}	58.56 ± 8.79^{ab}	63.55 ± 9.63^{a}	62.34 ± 8.91^{a}
CK1	62.63 ± 6.31^{ab}	61.84 ± 4.79^{a}	60.13 ± 7.72^{ab}	57.82 ± 13.7^{ab}
CK2	57.68 ± 11.19^{ab}	55.18 ± 9.51^{ab}	56.82 ± 7.96^{ab}	54.69 ± 7.44^{ab}
F value				
L	1.052^{ns}	3.289^{ns}	1.181^{ns}	0.617^{ns}
I	5.039^{*}	5.042^{*}	5.635^{**}	8.516^{**}
L ∗ I	0.682^{ns}	0.021^{ns}	0.328^{ns}	0.097^{ns}

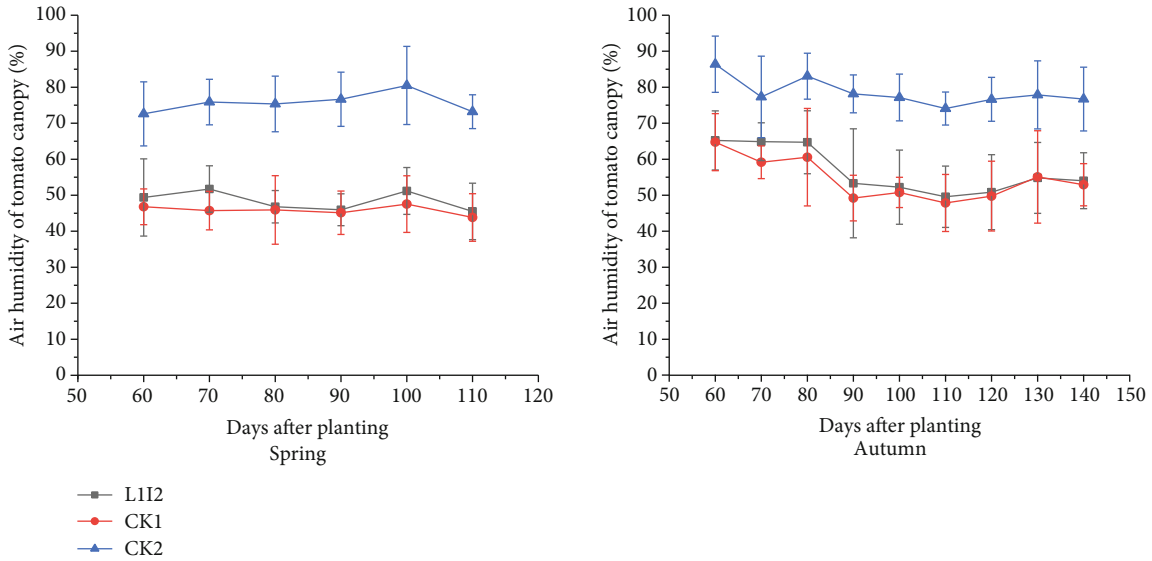

Figure 10: Effects of different treatments on air humidity in tomato canopy with spring and autumn.

that the micropore group spacing had little effect on soil respiration rate.

Previous studies have found that properly reducing the irrigation amount can reduce the soil respiration rate. With the increase of irrigation amount, soil water stimulates root respiration and soil microbial activity, resulting in an increase in the soil respiration rate [34, 35]. However, when the irrigation amount increased to a certain extent, crop root aerobic respiration and soil microbial activity were gradually inhibited and further inhibited soil respiration rate [56, 57]. This may also be one of the reasons why the soil respiration rate increased at first and then decreased with the increase of irrigation amount in this study. Chen et al.'s [39] study shows that the soil respiration rate increases with the increase of the irrigation amount, which is inconsistent with the conclusion of this paper. It may be caused by the difference in irrigation amount. The highest irrigation amount in Chen et al.'s study was 1.0 Epan, while the highest in this study was 1.2 Epan. Agbna et al. [58] and Zhu et al. [59] found that when the irrigation amount of drip irrigation with tomato increased from 0.5 Epan to 1.0 Epan, the yield increased while the WUE decreased. It shows that the effect of MSPF on tomato yield and water use efficiency was similar to drip irrigation, and the MSPF was suitable for greenhouse tomato irrigation.

6.3. Correlation between Soil Microenvironment, Soil Respiration Rate, and Yield of Tomato with Microsprinkler Irrigation under Plastic Film. Previous studies have shown that when the protected agricultural space is relatively closed and the irrigation water is limited, reducing the irrigation amount and increasing greenhouse CO_2 concentration can improve the yield and quality of greenhouse tomato [60, 61]. In this study, it was found that there was a significant

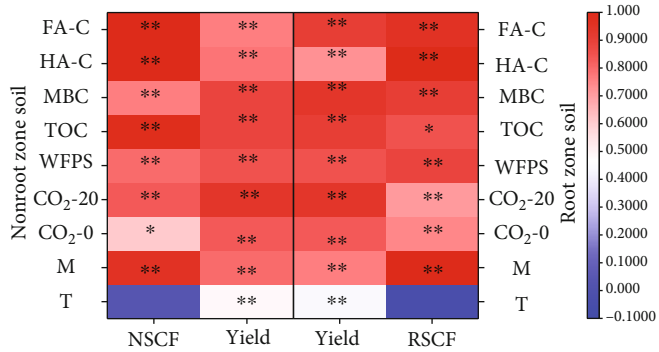

FIGURE 11: Correlation between soil microenvironment, soil respiration rate, and yield of tomato. Note: WFPS: water-filled pore space of soil; CO_2-20: soil CO_2 concentration of 20 cm; CO_2-0: soil CO_2 concentration of 0 cm; M: soil moisture; T: soil temperature; NSCF: soil respiration rate in nonroot zone; RSCF: soil respiration rate in root zone. Different color depth means correlation difference; correlation value is showed by the value of the number from -0.1 to 1. $*$ means significance correlation ($P < 0.05$); $**$ means significance correlation ($P < 0.01$), the same below.

positive correlation between the soil respiration rate and yield (see Figure 11), which was consistent with the conclusion that Mancinelli et al. [62] found that there is a positive correlation between the CO_2 emission rate of tomato soil and yield under drip irrigation. It may be because the greenhouse microenvironment is relatively closed and the CO_2 content is limited. For tomatoes with a high photorespiration rate, increasing atmospheric CO_2 concentration in a certain range can not only provide more sufficient raw materials for photosynthesis but also increase the activity of (RuBP) carboxylase of ribulose 5-diphosphate, which is beneficial to accelerate the binding of RuBP in chloroplasts to CO_2 entering chloroplasts, thus enhancing the ability of photosynthesis to fix CO_2, formatting 3-phosphoglyceric acid (PGA), and further synthesizing photosynthetic carbohydrate through C3 cycling [63, 64]. In this study, there was a positive correlation between soil moisture and soil respiration rate (see Figure 11), which was consistent with that obtained by Wei et al. [65] when soil moisture content in maize planting under drip irrigation was lower than the field water holding capacity. This study also found that there was a synergistic change of TOC and MBC in the soil of tomato under MSPF, which was positively correlated with the soil respiration rate (see Figure 11). It is consistent with the finding of Han et al. [66] to study the changes of soil TOC and MBC under drip irrigation, which shows that the effect of MSPF on soil TOC and MBC is similar to that of drip irrigation under plastic film.

Previous studies have found that there is a significant positive correlation between the soil temperature and soil respiration rate [34, 65, 67]. However, there was no significant difference in the positive effect of temperature on the soil respiration rate in this study. It may be that the soil water distribution of MSPF is relatively uniform, the soil moisture in the root zone and the nonroot zone of tomato is not too high or too low, and the soil microenvironment is relatively stable, which lead to the decrease of the effect of temperature on the soil respiration rate. Wang et al. [68] believe that when the WFPS of the soil is less than 60%, there is a positive correlation between the soil respiration rate and soil WFPS; otherwise, there is a negative correlation between them. In this study, there was a positive correlation between soil WFPS and the soil respiration rate of greenhouse tomato, which is inconsistent with the conclusion that there was a negative correlation between the soil respiration rate and soil WFPS under drip irrigation [69]. It is possibly due to the differences in soil types, irrigation methods, and the irrigation amount controlled by the experiment. Chen used drip irrigation of tomato in *Yangling* soil (brown loam), and the irrigation amount increased from 0.6 Epan to 1.0 Epan. However, in this study, tomato was irrigated with MSPF on sandy loam (yellow cinnamon soil), and the irrigation amount increased from 0.7 Epan to 1.2 Epan.

7. Conclusion

In this paper, by exploring the response mechanism of greenhouse soil microenvironment, soil respiration rate, and yield of tomato under different micropore group spacing and irrigation amount of MSPF, the suitable micropore group spacing and irrigation amount of MSPF for greenhouse tomato growth were obtained. The results showed that compared with drip irrigation under a plastic film, and the yield of spring tomato and autumn tomato increased by 19.39% and 4.54%, respectively. Compared with microsprinkler irrigation, tomato yield, water use efficiency, and soil respiration rate under MSPF for spring and autumn were increased by 20.46% and 49.22%, 31.02% and 58.05%, and 34.66% and 38.38%, respectively. In this study, greenhouse tomato under MSPF increased the soil respiration rate (CO_2 emission); however, the tomato yield and WUE were also improved, indicating that the MSPF could achieve an effective dynamic balance among greenhouse CO_2, yields and WUE. The micropore group spacing had no significant effect on the soil respiration rate. Compared with 50 cm of micropore group spacing, the 30 cm micropore group spacing increased the yield and WUE of tomato by 16.00% and 13.01% and 20.85% and 14.25%, respectively. With the increase of irrigation amount, the soil respiration rate in the root and nonroot zones and the yield of spring tomato and autumn tomato

increased at first and then decreased, and the WUE showed a decreasing trend. As for the soil respiration rate, it is higher in the root zone than it is in the nonroot zone, and there exists a logarithmic function relationship between the soil respiration rate in the nonroot zone and the soil respiration rate in the root zone, and there is a quadratic relationship between the soil respiration rate and the yield in the nonroot zone. Considering our results comprehensively, the combination of the 30 cm micropore group spacing and 1.0 Epan is recommended for greenhouse tomato under MSPF in northwest China. This study can provide theoretical data and experimental support for water-saving irrigation and yield increase of facility agricultural tomato and analysis of the soil carbon cycle mechanism of MSPF. Although the results of this study explain the effects of different micropore group spacings and irrigation amounts on the soil respiration rate and yield of tomato, it is still an open question how to change the soil enzyme activity and microbial community structure to further drive the change of the soil respiration rate and yield under different micropore spacings and irrigation amounts.

Data Availability

The data used to support the findings of this study are available from the corresponding author upon request.

Conflicts of Interest

The authors declare no conflict of interest.

Acknowledgments

This work is supported jointly by the Natural Science Foundation of China (No. 41807041), Shaanxi Provincial Water Conservancy Science and Technology Project (2015slkj-07), Henan Water Conservancy Science and Technology Project (GG202043), Scientific and Technological Project of Henan Province (212102110069), Science and Technology Program of Xi'an (20193052YF040NS040), Natural Science Foundation of Guangdong Province (No. 2018A0303130149), and Science and Technology Program of Guangzhou (No. 20181002SF0530).

References

[1] R. Zong, Z. Wang, Q. Wu, L. Guo, and H. Lin, "Characteristics of carbon emissions in cotton fields under mulched drip irrigation," *Agricultural Water Management*, vol. 231, article 105992, 2020.

[2] H. Zhang, R. Zong, H. He et al., "Biogeographic distribution patterns of algal community in different urban lakes in China: insights into the dynamics and co-existence," *Journal of Environmental Sciences*, vol. 100, pp. 216–227, 2021.

[3] T. Du, S. Kang, X. Zhang, and J. Zhang, "China's food security is threatened by the unsustainable use of water resources in North and Northwest China," *Food and Energy Security*, vol. 3, no. 1, pp. 7–18, 2014.

[4] F. T. de Vries, R. I. Griffiths, C. G. Knight, O. Nicolitch, and A. Williams, "Harnessing rhizosphere microbiomes for drought-resilient crop production," *Science*, vol. 368, no. 6488, pp. 270–274, 2020.

[5] L. Mu, C. Wang, B. Xue, H. Wang, and S. Li, "Assessing the impact of water price reform on farmers' willingness to pay for agricultural water in Northwest China," *Journal of Cleaner Production*, vol. 234, pp. 1072–1081, 2019.

[6] S. Kang, F. Zhang, X. Hu, and J. Zhang, "Elevated carbon dioxide and soil moisture on early growth response of soybean," *Plant and Soil*, vol. 238, no. 1, pp. 69–77, 2002.

[7] H. Q. Wang, M. S. Zhang, X. Y. Dang, and H. Zhu, "The response of agricultural water demand to climate change in Shiyang river basin, in Northwest China," *Advanced Materials Research*, vol. 347-353, pp. 1964–1972, 2011.

[8] H. Zhang, L. Xu, T. Huang et al., "Combined effects of seasonality and stagnation on tap water quality: changes in chemical parameters, metabolic activity and co-existence in bacterial community," *Journal of Hazardous Materials*, vol. 403, article 124018, 2021.

[9] M. Z. Zhang, W. Q. Niu, Q. J. Bai et al., "Improvement of quality and yield of greenhouse tomato (*Solanum lycopersicum* l.) plants by micro-sprinkler irrigation under plastic film," *Applied Ecology and Environmental Research*, vol. 18, no. 5, pp. 6905–6926, 2020.

[10] M. Zhang, Z. Lu, Q. Bai et al., "Effect of microsprinkler irrigation under plastic film on photosynthesis and fruit yield of greenhouse tomato," *Journal of Sensors*, vol. 2020, Article ID 8849419, 14 pages, 2020.

[11] J. Feng, Y. Li, W. Wang, and S. Xue, "Effect of optimization forms of flow path on emitter hydraulic and anti-clogging performance in drip irrigation system," *Irrigation Science*, vol. 36, no. 1, pp. 37–47, 2018.

[12] Y. Yu, G. Shihong, D. Xu, W. Jiandong, and X. Ma, "Effects of Treflan injection on winter wheat growth and root clogging of subsurface drippers," *Agricultural Water Management*, vol. 97, no. 5, pp. 723–730, 2010.

[13] Á. Del Vigo, S. Zubelzu, and L. Juana, "Numerical routine for soil water dynamics from trickle irrigation," *Applied Mathematical Modelling*, vol. 83, pp. 371–385, 2020.

[14] A. V. O. M. El-Hafedh, H. Daghari, and M. Maalej, "Analysis of several discharge rate–spacing–duration combinations in drip irrigation system," *Agricultural Water Management*, vol. 52, no. 1, pp. 33–52, 2001.

[15] J. Man, J. Yu, P. J. White et al., "Effects of supplemental irrigation with micro-sprinkling hoses on water distribution in soil and grain yield of winter wheat," *Field Crops Research*, vol. 161, pp. 26–37, 2014.

[16] J. Li, Z. Zhang, Y. Liu et al., "Effects of micro-sprinkling with different irrigation amount on grain yield and water use efficiency of winter wheat in the North China Plain," *Agricultural Water Management*, vol. 224, article 105736, 2019.

[17] J. Li, Y. Wang, M. Zhang et al., "Optimized micro-sprinkling irrigation scheduling improves grain yield by increasing the uptake and utilization of water and nitrogen during grain filling in winter wheat," *Agricultural Water Management*, vol. 211, pp. 59–69, 2019.

[18] J. Man, D. Wang, and P. J. White, "Photosynthesis and dry-mass production of winter wheat in response to micro-sprinkling irrigation," *Agronomy Journal*, vol. 109, no. 2, pp. 549–561, 2017.

[19] J. Man, D. Wang, P. J. White, and Z. Yu, "The length of micro-sprinkling hoses delivering supplemental irrigation affects

photosynthesis and dry matter production of winter wheat," *Field Crops Research*, vol. 168, pp. 65–74, 2014.

[20] M. K. Er and A. Gökçe, "Effects of selected pesticides used against glasshouse tomato pests on colony growth and conidial germination of *Paecilomyces fumosoroseus*," *Biological Control*, vol. 31, no. 3, pp. 398–404, 2004.

[21] J. Camara, V. Logah, E. A. Osekre, and C. Kwoseh, "Leaf nutrients content of tomato and incidence of insect pests and diseases following two foliar applications," *Journal of Plant Nutrition*, vol. 159, 167 pages, 2017.

[22] O. Gómez-Rodríguez, E. Zavaleta-Mejía, V. A. González-Hernandez, M. Livera-Muñoz, and E. Cárdenas-Soriano, "Allelopathy and microclimatic modification of intercropping with marigold on tomato early blight disease development," *Field Crops Research*, vol. 83, no. 1, pp. 27–34, 2003.

[23] H. Liu, H. Li, H. Ning et al., "Optimizing irrigation frequency and amount to balance yield, fruit quality and water use efficiency of greenhouse tomato," *Agricultural Water Management*, vol. 226, no. 12, article 105787, 2019.

[24] S. Malherbe and D. Marais, "Economics, yield and ecology," *Outlook On Agriculture*, vol. 44, no. 1, pp. 37–47, 2015.

[25] S. Elmaloglou and E. Diamantopoulos, "Soil water dynamics under surface trickle irrigation as affected by soil hydraulic properties, discharge rate, dripper spacing and irrigation duration," *Irrigation and Drainage*, vol. 59, no. 3, pp. 254–263, 2010.

[26] J. Enciso, J. Jifon, and B. Wiedenfeld, "Subsurface drip irrigation of onions: effects of drip tape emitter spacing on yield and quality," *Agricultural Water Management*, vol. 92, no. 3, pp. 126–130, 2007.

[27] H. Sun, X. Zhang, X. Liu et al., "Impact of different cropping systems and irrigation schedules on evapotranspiration, grain yield and groundwater level in the North China Plain," *Agricultural Water Management*, vol. 211, pp. 202–209, 2019.

[28] X. Yang, Y. Chen, S. Pacenka et al., "Effect of diversified crop rotations on groundwater levels and crop water productivity in the North China Plain," *Journal of Hydrology*, vol. 522, pp. 428–438, 2015.

[29] L. Chen, Q. Feng, F.-R. Li, and C.-S. Li, "A bidirectional model for simulating soil water flow and salt transport under mulched drip irrigation with saline water," *Agricultural Water Management*, vol. 146, pp. 24–33, 2014.

[30] H. Guan, J. Li, and Y. Li, "Effects of drip system uniformity and irrigation amount on cotton yield and quality under arid conditions," *Agricultural Water Management*, vol. 124, pp. 37–51, 2013.

[31] H. Liu, A. Duan, F.-s. Li, J.-s. Sun, Y.-c. Wang, and C.-t. Sun, "Drip irrigation scheduling for tomato grown in solar greenhouse based on pan evaporation in North China Plain," *Journal of Integrative Agriculture*, vol. 12, no. 3, pp. 520–531, 2013.

[32] D. D. Nangare, Y. Singh, P. S. Kumar, and P. S. Minhas, "Growth, fruit yield and quality of tomato (*Lycopersicon esculentum* Mill.) as affected by deficit irrigation regulated on phenological basis," *Agricultural Water Management*, vol. 171, pp. 73–79, 2016.

[33] B. Trost, A. Prochnow, A. Meyer-Aurich, K. Drastig, M. Baumecker, and F. Ellmer, "Effects of irrigation and nitrogen fertilization on the greenhouse gas emissions of a cropping system on a sandy soil in Northeast Germany," *European Journal of Agronomy*, vol. 81, pp. 117–128, 2016.

[34] Y. Zhong, J. Li, and H. Xiong, "Effect of deficit irrigation on soil CO_2 and N_2O emissions and winter wheat yield," *Journal of Cleaner Production*, vol. 279, article 123718, 2021.

[35] X. Wang, H. Cai, L. Li, J. T. Xu, and H. Chen, "Effects of water deficit on greenhouse gas emission in wheat field in different periods," *Huanjing kexue*, vol. 40, no. 5, article 2413, 2019.

[36] H. Chen, H. J. Hou, H. J. Cai, Y. Zhu, and C. Wang, "Effects of aerated irrigation on CO_2 emissions from soils of tomato fields," *Scientia Agricultura Sinica*, vol. 49, no. 17, pp. 3380–3390, 2016.

[37] C. Li, Y. Xiong, Q. Huang, X. Xu, and G. Huang, "Impact of irrigation and fertilization regimes on greenhouse gas emissions from soil of mulching cultivated maize (*Zea mays* L.) field in the upper reaches of Yellow River, China," *Journal of Cleaner Production*, vol. 259, article 120873, 2020.

[38] Y. Xu, Y. Wang, X. Ma et al., "Ridge-furrow mulching system and supplementary irrigation can reduce the greenhouse gas emission intensity," *Science of the Total Environment*, vol. 717, article 137262, 2020.

[39] H. Chen, H. Hou, X. Wang et al., "The effects of aeration and irrigation regimes on soil CO_2 and N_2O emissions in a greenhouse tomato production system," *Journal of Integrative Agriculture*, vol. 17, no. 2, pp. 449–460, 2018.

[40] S. Chatterjee, K. K. Bandyopadhyay, S. Pradhan, R. Singh, and S. P. Datta, "Effects of irrigation, crop residue mulch and nitrogen management in maize (*Zea mays* L.) on soil carbon pools in a sandy loam soil of Indo-Gangetic plain region," *Catena*, vol. 165, pp. 207–216, 2018.

[41] C. Y. Sun, J. S. Liu, Y. Wang, N. Zheng, X. Q. Wu, and Q. Liu, "Effect of long-term cultivation on soil organic carbon fractions and metal distribution in humic and fulvic acid in black soil, Northeast China," *Soil Research*, vol. 50, no. 7, pp. 562–562, 2012.

[42] Y. Du, H. Cao, S. Liu, X.-b. Gu, and Y.-x. Cao, "Response of yield, quality, water and nitrogen use efficiency of tomato to different levels of water and nitrogen under drip irrigation in Northwestern China," *Journal of Integrative Agriculture*, vol. 16, no. 5, pp. 1153–1161, 2017.

[43] S. Franco-Luesma, J. Álvaro-Fuentes, D. Plaza-Bonilla, J. L. Arrúe, C. Cantero-Martínez, and J. Cavero, "Influence of irrigation time and frequency on greenhouse gas emissions in a solid-set sprinkler-irrigated maize under Mediterranean conditions," *Agricultural Water Management*, vol. 221, pp. 303–311, 2019.

[44] B. Jia, G. Zhou, F. Wang, Y. Wang, and E. Weng, "Effects of grazing on soil respiration of Leymus chinensis steppe," *Climatic Change*, vol. 82, no. 1-2, pp. 211–223, 2007.

[45] R. T. Conant, P. Dalla-Betta, C. C. Klopatek, and J. M. Klopatek, "Controls on soil respiration in semiarid soils," *Soil Biology and Biochemistry*, vol. 36, no. 6, pp. 945–951, 2004.

[46] L. Zotarelli, J. M. Scholberg, M. D. Dukes, R. Muñoz-Carpena, and J. Icerman, "Tomato yield, biomass accumulation, root distribution and irrigation water use efficiency on a sandy soil, as affected by nitrogen rate and irrigation scheduling," *Agricultural Water Management*, vol. 96, no. 1, pp. 23–34, 2009.

[47] M. Burger, L. E. Jackson, E. J. Lundquist et al., "Microbial responses and nitrous oxide emissions during wetting and drying of organically and conventionally managed soil under tomatoes," *Biology and Fertility of Soils*, vol. 42, no. 2, pp. 109–118, 2005.

[48] A. Morugán-Coronado, F. García-Orenes, J. Mataix-Solera, V. Arcenegui, and J. Mataix-Beneyto, "Short-term effects of treated wastewater irrigation on Mediterranean calcareous soil," *Soil and Tillage Research*, vol. 112, no. 1, pp. 18–26, 2011.

[49] J. H. Ma, X. H. Ye, B. Han et al., "Effects of different controlled irrigation low limits on the size distribution of soil aggregates with drip irrigation under film mulching in a greenhouse soil," *Scientia Agricultura Sinica*, vol. 50, no. 18, pp. 3561–3571, 2017.

[50] R. Zhang, J. M. Vivanco, and Q. Shen, "The unseen rhizosphere root-soil-microbe interactions for crop production," *Current Opinion in Microbiology*, vol. 37, pp. 8–14, 2017.

[51] Y. Liu, P. Li, T. Wang, Q. Liu, and W. Wang, "Root respiration and belowground carbon allocation respond to drought stress in a perennial grass (*Bothriochloa ischaemum*)," *Catena*, vol. 188, p. 104449, 2020.

[52] K. Zhang, M. Duan, Q. Xu, Z. Wang, B. Liu, and L. Wang, "Soil microbial functional diversity and root growth responses to soil amendments contribute to CO_2 emission in rainfed cropland," *Catena*, vol. 195, p. 104747, 2020.

[53] Z. Luo, Z. Tang, X. Guo, J. Jiang, and O. J. Sun, "Non-monotonic and distinct temperature responses of respiration of soil microbial functional groups," *Soil Biology and Biochemistry*, vol. 148, p. 107902, 2020.

[54] C. Scheer, P. R. Grace, D. W. Rowlings, and J. Payero, "Soil N_2O and CO_2 emissions from cotton in Australia under varying irrigation management," *Nutrient Cycling in Agroecosystems*, vol. 95, no. 1, pp. 43–56, 2013.

[55] X. Li, S. Kang, X. Zhang, F. Li, and H. Lu, "Deficit irrigation provokes more pronounced responses of maize photosynthesis and water productivity to elevated CO_2," *Agricultural Water Management*, vol. 195, pp. 71–83, 2018.

[56] W. Zhongmei, S. Changchun, G. Yuedong, W. Li, and H. Jingyu, "Effects of water gradients on soil enzyme activity and active organic carbon composition under *Carex lasiocarpa* marsh," *Acta Ecologica Sinica*, vol. 28, no. 12, pp. 5980–5986, 2008.

[57] R. Zornoza, R. M. Rosales, J. A. Acosta et al., "Efficient irrigation management can contribute to reduce soil CO_2 emissions in agriculture," *Geoderma*, vol. 263, pp. 70–77, 2016.

[58] G. H. D. Agbna, S. Dongli, L. Zhipeng, N. A. Elshaikh, S. Guangcheng, and L. C. Timm, "Effects of deficit irrigation and biochar addition on the growth, yield, and quality of tomato," *Scientia Horticulturae*, vol. 222, pp. 90–101, 2017.

[59] Y. Zhu, H. Cai, L. Song et al., "Aerated irrigation of different irrigation levels and subsurface dripper depths affects fruit yield, quality and water use efficiency of greenhouse tomato," *Sustainability*, vol. 12, no. 7, article 2703, 2020.

[60] X. Yang, P. Zhang, Z. Wei, J. Liu, X. Hu, and F. Liu, "Effects of CO_2 fertilization on tomato fruit quality under reduced irrigation," *Agricultural Water Management*, vol. 230, p. 105985, 2020.

[61] P. T. Pazzagli, J. Weiner, and F. Liu, "Effects of CO_2 elevation and irrigation regimes on leaf gas exchange, plant water relations, and water use efficiency of two tomato cultivars," *Agricultural Water Management*, vol. 169, pp. 26–33, 2016.

[62] R. Mancinelli, S. Marinari, P. Brunetti, E. Radicetti, and E. Campiglia, "Organic mulching, irrigation and fertilization affect soil CO_2 emission and C storage in tomato crop in the Mediterranean environment," *Soil and Tillage Research*, vol. 152, pp. 39–51, 2015.

[63] R. T. Avila, W. L. de Almeida, L. C. Costa et al., "Elevated air [CO_2] improves photosynthetic performance and alters biomass accumulation and partitioning in drought-stressed coffee plants," *Environmental and Experimental Botany*, vol. 177, p. 104137, 2020.

[64] S. S. Anapalli, D. K. Fisher, K. N. Reddy, J. L. Krutz, S. R. Pinnamaneni, and R. Sui, "Quantifying water and CO_2 fluxes and water use efficiencies across irrigated C_3 and C_4 crops in a humid climate," *Science of the Total Environment*, vol. 663, pp. 338–350, 2019.

[65] C. Wei, S. Ren, P. Yang et al., "Effects of irrigation methods and salinity on CO_2 emissions from farmland soil during growth and fallow periods," *Science of the Total Environment*, vol. 752, p. 141639, 2021.

[66] L. Han, Y. Zhang, S. Jin et al., "Effect of different irrigation methods on dissolved organic carbon and microbial biomass carbon in the greenhouse soil," *Agricultural Sciences in China*, vol. 9, no. 8, pp. 1175–1182, 2010.

[67] R. Elgaddafi, R. Ahmed, and S. Shah, "Corrosion of carbon steel in CO_2 saturated brine at elevated temperatures," *Journal of Petroleum Science and Engineering*, vol. 196, p. 107638, 2021.

[68] X. Wang, Y. Jiang, B. Jia, F. Wang, and G. Zhou, "Comparison of soil respiration among three temperate forests in Changbai Mountains, China," *Canadian Journal of Forest Research*, vol. 40, no. 4, pp. 788–795, 2010.

[69] H. Chen, Z. H. Shang, Y. F. Wang et al., "Effects of irrigation amounts on soil CO_2, N_2O and CH_4 emissions in greenhouse tomato field," *Chinese Journal of Applied Ecology*, vol. 30, no. 9, pp. 3126–3136, 2019.

Hindawi
Journal of Sensors
Volume 2020, Article ID 8815940, 11 pages
https://doi.org/10.1155/2020/8815940

Research Article

Estimation of Leaf Water Use Efficiency Threshold Values for Water Stress in Winter Wheat (*Triticum aestivum* L.)

Qiu Xinqiang, Zhang Yushun, Qin Haixia, Wang Min, Wang Yanping, Yang Haochen, and Lu Zhenguang

Henan Provincial Water Conservancy Research Institute/Center of Efficient Irrigation Engineering and Technology Research of Henan Province, Zhengzhou 450003, China

Correspondence should be addressed to Lu Zhenguang; skslzg@hnsl.gov.cn

Received 18 September 2020; Revised 3 November 2020; Accepted 8 December 2020; Published 31 December 2020

Academic Editor: Yuan Li

Drought significantly threatens crop productivity and food security worldwide. However, the severity of drought is predicted to increasingly intensify in the future. To provide an antidrought strategy for farmers and breeders, the response of stomatal behavior of crops to water stress should be well studied. In this study, a lysimeter experiment was conducted to study the relationship between gas exchange parameters and grain yields of winter wheat. Light, moderate, and severe drought levels were imposed at seedling, jointing, heading, and filling stages. The results showed that crop evapotranspiration (ET_c, mm) of winter wheat during the entire growing season was limited by drought imposed at any growth stage, and ET_c under severe drought treatment was always the lowest. The stomatal limitation value had a significant linear correlation with the stomatal conductance (Gs, μmol mol H_2O m^{-2} s^{-1}) and transpiration rate (Tr, mmol H_2O m^{-2} s^{-1}). Light and moderate drought levels at the seedling stage did not generate irreversible physiological stress on wheat plants, while severe drought at any growth stage caused significant reduction in gas exchange parameters and grain yields. Theoretical threshold values of leaf water use efficiency (WUE_l) for light, moderate, and severe drought levels were 2.62, 3.36, and 4.11 μmol $mmol^{-1}$, respectively. The threshold values are useful to provide theoretical reference for achieving smart irrigation in the North China Plain.

1. Introduction

Drought is one of the most common factors threatening food security worldwide. It is predicted that the severity of drought will continue in the future under the current climate change scenarios [1]. Nevertheless, global demand for major grains such as wheat and maize is projected to increase by 70% by 2050 due to the ever-increasing population [2]. This means the agricultural sector will double the present consumption of the water resources on the planet under the current water use efficiency (WUE) level [3]. To mitigate the conflict between water consumption for food production and water supply for agriculture, modern irrigation technology should be developed toward smart and precision irrigation with efficient use of water [4]. However, the present efficiency of irrigation in the world is relatively low, especially in Southeast Asia, North Africa, and South America [5–7]. Taking China, for example, the mean utilization coefficient of irrigation water was 0.45 in 2019 [8]. Precision irrigation according to the crop water requirement is the key to achieving high leaf water use efficiency (WUE_l). However, the main difficulty for precision irrigation lies in real-time and rapid monitoring of gas exchange parameters of crop leaves, such as the stomatal conductance (Gs, μmol mol H_2O m^{-2} s^{-1}) and transpiration rate (Tr, mmol H_2O m^{-2} s^{-1}), and WUE_l [9].

The North China Plain (NCP) is one of the most important granaries in China, accounting for 30 and 60% of the domestic maize (*Zea mays* L.) and wheat (*Triticum aestivum* L.) production [10]. Over recent years, NCP has been subjected to serious water shortages due to the rapid development of irrigated agriculture. For example, groundwater for irrigated agriculture in the NCP has accounted for nearly 70% of total water use in 2015 [11]. Consequently, every year's decline of the groundwater table reached 1.0 m over

the past decade, causing the deepest groundwater table of 105 m in the groundwater depression cone [12]. During winter wheat growing seasons, only 25–40% of the crop water requirement can be met by seasonal precipitation, which is around 100–180 mm in the NCP [3]. Generally, the crop needs 2–4 times of irrigation to meet the water requirement and achieve high yield formation of wheat. Therefore, timely irrigation according to the water requirement of crops is the key to high productivity of winter wheat. However, the main difficulty for timely irrigation remains in real-time and rapid monitoring of crop water status. Some scholars developed a probabilistic method for modeling the dynamics of soil water content to guide irrigation, but the model is too complicated to be of wide practical use [13–15]. Using a crop canopy temperature monitoring system which measured real-time data at a 1 h interval, Jiabing et al. [16] adopted the difference between canopy temperature and air temperature to identify the crop water deficit, which could be further used to trigger irrigation. However, how to reasonably separate canopy temperature from surface temperature when the vegetation coverage is low caused overestimation of crop transpiration [17]. Moreover, how to accurately determine dependable threshold values for irrigation decision-making is also a difficult point for automatic irrigation [18]. So far, few publications have been found using WUE_l as the threshold value of wheat to support data-driven automatic irrigation. In practice, less is known about how to quantitatively analyze the soil moisture status through monitoring crop water status and other photosynthetic parameters, which is critical to determine the irrigation timing and amount.

Accurate identification and measurement of crop water status is the basis for smart irrigation [19]. In order to make crops grow normally without water stress, timely irrigation should be conducted before excessive drought occurs. Studies have shown that, when subjected to drought stress, crop leaves always make the first and rapid response to water stress [20]. Besides, the leaf is a major carrier where photosynthesis and crop transpiration occur. Crops regulate the transpiration rate through adjusting stomatal conductance so that they can maintain the balance of plant water status and intercellular CO_2 concentration [21] and cool down themselves when exposed to high temperature [22]. Also, leaf water potential is one of the most important indicators that is associated with stomatal conductance [23], and it will change immediately after the change of stomatal conductance [24]. Leaf water use efficiency (WUE_l) is defined as the ratio of photosynthesis to transpiration, which reflects the change of related quantity in the process of leaf gas exchanges [25]. Moreover, intercellular CO_2 concentration (Ci) is an important decision basis to determine whether the main reason for the change of the photosynthetic rate is attributable to stomatal factors [26]. Under soil water stress, there is a "threshold" response of photosynthesis of wheat leaves to soil water content [27]. When the intercellular CO_2 concentration of leaves changes from decreasing to increasing, it indicates that the main reason for the decrease of the photosynthetic rate is caused by water stress changes from stomatal limitation to nonstomatal limitation [28, 29]. It is known that the moderate water deficit in a specific growth period does not reduce crop yield but increases crop productivity and WUE [30, 31].

We hypothesize that timely and appropriate irrigation can be achieved based on the real-time crop water requirement by monitoring gas exchange parameters such as WUE_l as threshold values of crops. The objectives of this study are as follows: (i) to compare the difference of gas exchange parameters of winter wheat leaves under different water stress conditions in a lysimeter experiment, (ii) to clarify the response of leaf stomatal behavior to water stress, and (iii) to figure out the threshold values of WUE_l, providing guidance for water-saving and smart irrigation of winter wheat in the NCP.

2. Materials and Methods

2.1. Site Description. The experiment was carried out at the Maozhuang Experimental Station of Henan Water-Saving Irrigation Engineering Technology Research Center, Central Station of Henan Irrigation Experiment, China (34°16′N, 112°42′E, a.s.l. 85 m) (see Figure 1). The place has a continent temperate monsoon climate. The mean annual temperature is 14.0–14.3°C, mean annual precipitation is 640.9 mm, frost-free period is 220 d, and annual sunshine hours are about 2400 h. The soil was a silty loam soil. The field water holding capacity in 0–100 cm soil layers is 23% (by weight), average bulk density in the same layers is 1.42 g cm^{-3}, and water table was detected more than 5 m below the soil surface. The content of organic matter, total phosphorus, total potassium, total nitrogen, alkali hydrolyzable nitrogen, available phosphorus, and potassium in 0–30 cm soil layers was 5.62 g kg^{-1}, 0.44 g kg^{-1}, 15.12 g kg^{-1}, 0.37 g kg^{-1}, 24.91 mg kg^{-1}, 23.89 mg kg^{-1}, and 75 mg kg^{-1}, respectively.

2.2. Experimental Design. The field experiments were carried out in a lysimeter facility equipped with an automatic rainproof shelter. The research facility consisted of 24 lysimeters (3.3 m long × 2.0 m wide × 2.0 m deep) packed uniformly with silty loam soil. These lysimeters were arranged in two rows, and between the rows of each system, a 2.5 m wide concrete platform was constructed level with the top of the lysimeters. The electrically operated double rain shelters were installed for the lysimeters. The rainproof shelters were moved over all lysimeters before precipitation happened.

Popularly used wheat seeds (*c.v.* Zhoumai 22) were selected as the experimental materials. Nine rows were sown in each lysimeter with a row spacing of 20 cm and a sowing rate of 150 kg h m^{-2}. The experiment was conducted in two wheat growing seasons (2012–2013 and 2013–2014). Wheat was sown on October 17, 2012, and October 12, 2013, and harvested on May 30, 2013, and 2014. The whole growth period was 225 d and 230 d, respectively. Before sowing, the soil was deeply ploughed. While ploughed, compound fertilizer (15-15-15 of N-P_2O_5-K_2O, Shandong Kingenta Ecological Engineering Group Company, LY, China) was applied at the rate of 750 kg ha^{-1}. In the meantime, 10 t ha^{-1} of dry chicken manure was applied as amendment fertilizer. After sowing, full irrigation of 65 mm was applied to guarantee seed germination. Each plot was irrigated independently,

Figure 1: Photos of the field experiments.

and the type of irrigation was surface irrigation. To measure and control irrigation amount, a precision flow meter (Shanghai Water Meter Manufacturing Ltd., Co., Shanghai, China) was adopted. Weed and pest control was applied according to local governmental recommendations. The field crop management was kept the same during the two growing seasons of winter wheat.

In this experiment, 3 drought levels expressed in percentage of field holding capacity (%FC) were arranged, including the light drought level (55%FC), moderate drought level (45%FC), and severe drought level (35%FC), respectively. Irrigation was ceased once relative soil moisture content (%FC) reached the 3 corresponding drought levels for each treatment. Furthermore, the 3 drought levels were separately imposed at the seedling stage, jointing stage, heading stage, and filling stage, respectively. Furthermore, to investigate the effects of continuous drought on crop growth, the moderate drought level (45%FC) was continuously imposed in the early growth period (i.e., seedling+jointing stages), middle growth period (jointing+heading stages), and late growth period (heading+filling stages), respectively, whereas the suitable soil moisture level, whose relative soil water content was kept ≥65%FC in the whole growth period, was taken as control (CK). Consequently, a total of 18 irrigation treatments were set up (see Figure 2).

2.3. Data Collection and Measurements

2.3.1. Soil Water Content. Soil water content (%) was measured at 20 cm increments to a depth of 100 cm using the soil core method. Soil samples were taken every 7 d and were oven-dried at 105°C for 24 h for analysis of the gravimetric soil water content. Additional measurement was conducted before and after irrigation.

2.3.2. Grain Yield. At maturity, 9 middle rows in 3.3 m long were selected from each plot to determine grain yield. All the plants in each plot were hand-harvested and air-dried for 2 weeks until constant mass, and then the grain was separated, cleaned, and weighed. Grain yield was calculated on a dry matter basis (13%). Besides, ten representative winter wheat plants were randomly selected for the investigation of yield components.

2.3.3. Leaf Gas Exchange Parameters. Relevant leaf gas exchange parameters, including the photosynthetic rate (Pn, μmol CO_2 m^{-2} s^{-1}), transpiration rate (Tr, mmol-H_2O m^{-2} s^{-1}), stomatal conductance (Gs, mol H_2O m^{-2} s^{-1}), and intercellular CO_2 concentration (Ci, μmol CO_2 mol^{-1} air), were measured from 9:30 to 12:30 a.m. at each major growth stage on the top full leaves before flag leaves appeared and on the flag leaves after their appearance. Three uniform plants from three selected sampling areas in each plot were measured using a Li-6400XT Portable Photosynthesis System (Li-Cor Inc., Lincoln, NE, USA). The chamber was adjusted to 25°C (temperature), ambient CO_2 concentration (Ca) was 360 μM mol^{-1}, and photosynthetic photon flux density is 800 μM m^{-2} s^{-1}. Leaf water use efficiency (WUE_l = Pn/Tr, μmol $mmol^{-1}$) and stomatal limitation (Ls = 1 – Ci/Ca) were calculated accordingly.

2.4. Statistical Analysis. All data were subjected to analysis of variance (ANOVA) using SPSS version 24.0 (IBM Corp., Armonk, NY), and differences between the means were tested by the least significant difference (Duncan's multiple comparison method). Significance was declared at the probability level of 0.05 unless otherwise stated. All figures were illustrated using Origin 9.0 software (OriginLab, Northampton, USA). Relationships between WUE_l, Ls, and gas exchange parameters were estimated by means of regression using the Levenberg–Marquardt algorithm.

3. Results and Discussion

3.1. Effects of Water Stress at the Seedling Stage on Leaf Gas Exchange of Winter Wheat. In this experiment, leaf gas exchange parameters, including Pn, Tr, Ci, and Gs, were measured at the seedling stage during the two growing seasons (see Figure 3). Pn, Tr, Ci, and Gs of winter wheat leaves during the drought period (March 22–27) decreased continuously with the intensification of drought levels. T4 treatment showed the greatest effects on suppressing gas exchange parameters. In detail, T4 decreased Pn by 35.4%, Tr by 55.0%, Ci by 16.5%, and Gs by 43.6%, respectively, compared with CK (T1). The difference was also significant between T2 and T4. After rewatering at the jointing stage, gas exchange parameters of each drought treatment increased. Crop growth performance of T2 and T3 treatments was generally better than that of CK. What is more, the growth performance of T4 treatment was only slightly weaker than that of CK. Therefore, although drought at the seedling stage weakened the gas exchange process of winter wheat leaves to a certain extent, it had nonsignificant adverse effects on photosynthetic rates after rewatering at the jointing stage. Previous studies have shown that moderate water

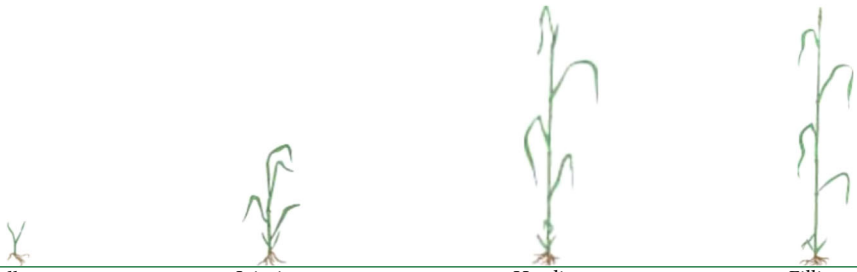

Growth stages	Seedling	Jointing	Heading	Filling
T1 (CK)	Non-stress (65%FC)	Non-stress (65%FC)	Non-stress (65%FC)	Non-stress (65%FC)
T2	Light drought (55%FC)	Non-stress (65%FC)	Non-stress (65%FC)	Non-stress (65%FC)
T3	Moderate drought (45%FC)	Non-stress (65%FC)	Non-stress (65%FC)	Non-stress (65%FC)
T4	Sever drought (35%FC)	Non-stress (65%FC)	Non-stress (65%FC)	Non-stress (65%FC)
T5	Non-stress (65%FC)	Light drought (55%FC)	Non-stress (65%FC)	Non-stress (65%FC)
T6	Non-stress (65%FC)	Moderate drought (45%FC)	Non-stress (65%FC)	Non-stress (65%FC)
T7	Non-stress (65%FC)	Sever drought (35%FC)	Non-stress (65%FC)	Non-stress (65%FC)
T8	Non-stress (65%FC)	Non-stress (65%FC)	Light drought (55%FC)	Non-stress (65%FC)
T9	Non-stress (65%FC)	Non-stress (65%FC)	Moderate drought (45%FC)	Non-stress (65%FC)
T10	Non-stress (65%FC)	Non-stress (65%FC)	Sever drought (35%FC)	Non-stress (65%FC)
T11	Non-stress (65%FC)	Non-stress (65%FC)	Non-stress (65%FC)	Light drought (55%FC)
T12	Non-stress (65%FC)	Non-stress (65%FC)	Non-stress (65%FC)	Moderate drought (45%FC)
T13	Non-stress (65%FC)	Non-stress (65%FC)	Non-stress (65%FC)	Sever drought (35%FC)
T14	Moderate drought (45%FC)	Moderate drought (45%FC)	Non-stress (65%FC)	Non-stress (65%FC)
T15	Non-stress (65%FC)	Moderate drought (45%FC)	Moderate drought (45%FC)	Non-stress (65%FC)
T16	Non-stress (65%FC)	Non-stress (65%FC)	Moderate drought (45%FC)	Moderate drought (45%FC)

Figure 2: Diagram of the nonstress (T1, CK), the three drought stress levels (light, moderate, and severe) separately imposed at seedling (T2, T3, and T4), jointing (T5, T6, and T7), heading (T8, T9, and T10), and filling (T11, T12, and T13) stages, and the moderate drought stress continuously imposed at seedling and jointing stages (T14), jointing and heading stages (T15), and heading and filling stages (T16), respectively. FC: field holding capacity ($cm^3\ cm^{-3}$). %FC in the table represents the lower limit for triggering irrigation.

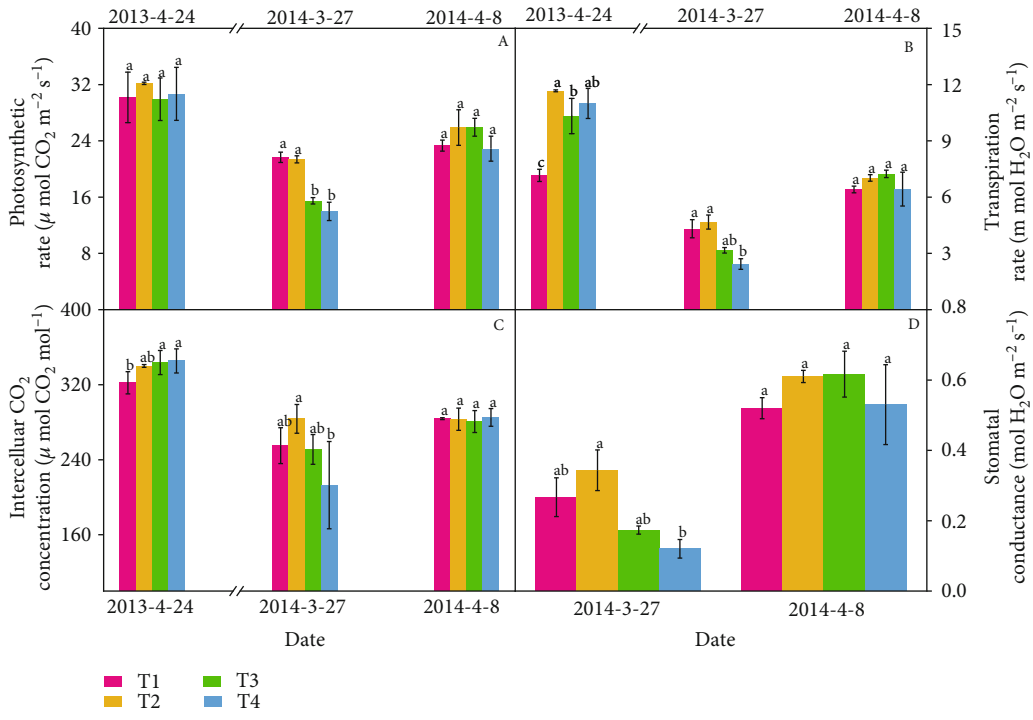

Figure 3: Variations in leaf gas exchange parameters of winter wheat under well-watered control treatment (T1), light drought (T2), moderate drought (T3), and severe drought (T4) stress at the seedling stage. Data are the means ± standard errors (SE) of three replicates, where $n = 3$ for the photosynthetic rate (Pn), transpiration rate (Tr), intercellular CO_2 concentration (Ci), and stomatal conductance (Gs). Different letters above the bars indicate statistical significance ($p \leq 0.05$).

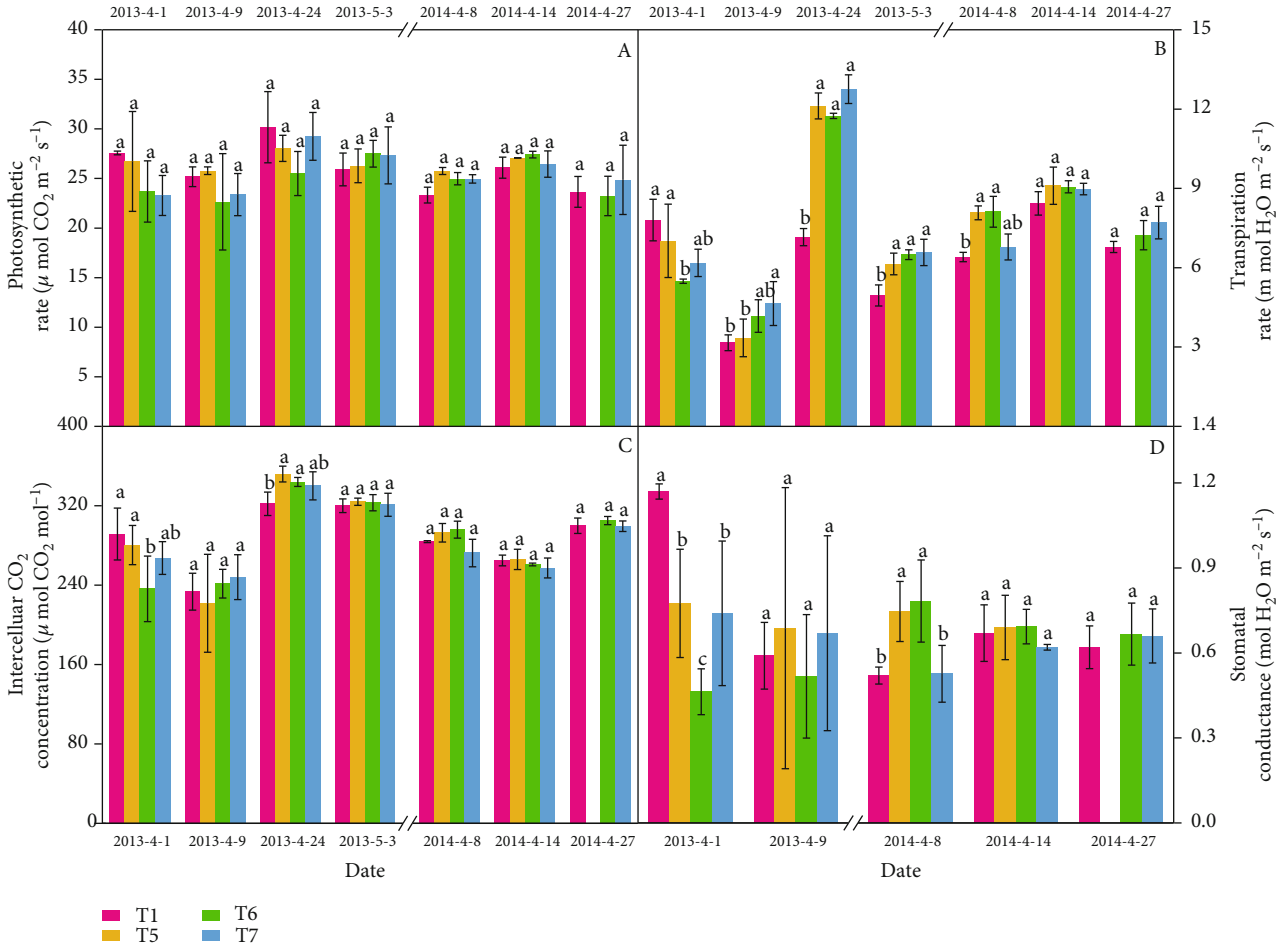

FIGURE 4: Variations in leaf gas exchange parameters of winter wheat under well-watered control treatment (T1), light drought (T5), moderate drought (T6), and severe drought (T7) stress at the jointing stage. Data are the means ± standard errors (SE) of three replicates, where $n = 3$ for the photosynthetic rate (Pn), transpiration rate (Tr), intercellular CO_2 concentration (Ci), and stomatal conductance (Gs). Different letters above the bars indicate statistical significance ($p \leq 0.05$).

stress in the early stage could ensure a higher photosynthetic rate of wheat leaves and helped to improve WUE, while the severe water deficit had a significant negative effect on the stomatal opening [32, 33]. Also, grain yield of light and moderate drought treatments at the seedling stage was not significantly affected, which was consistent with the results of previous studies [34, 35]. Consequently, properly intensifying soil water stress at the seedling stage of winter wheat not only is conducive to water saving but also can achieve the purpose of "promoting root penetration" in the early growth stage.

3.2. Effects of Water Stress at the Jointing Stage on Leaf Gas Exchange of Winter Wheat. Pn, Tr, and Ci of winter wheat leaves decreased at first and then increased from jointing to flowering (see Figure 4). At the jointing stage of the 2012–2013 growing season, Pn of drought treatments was generally lower than that of CK. The maximum reduction in Pn was 7.1% (light drought), 15.5% (moderate drought), and 15.6% (severe drought), respectively, compared with CK. The difference in Pn between drought treatments and CK in the 2013–2014 growing season was relatively small. Compared with CK, Ci, Tr, and Gs decreased by 10.4%, 20.2%, and 43.6%, respectively, for light, moderate, and severe treatments, before irrigation (April 1, 2014). After irrigation, the above indexes returned to normal levels rapidly (April 9, 2014), and Tr values increased by 16.5% (T5), 31.9% (T6), and 46.7% (T7), respectively, showing a rapid stomatal response to soil moisture restoration. Therefore, we pointed out that appropriate drought stress at the jointing stage helped promote crop root growth and improve water uptake. Our study demonstrated that physiological indexes (e.g., Pn, Tr, and Ci) of winter wheat (*c.v.* Zhoumai 24) were rapidly compensated after light water stress rewatering, and the supercompensation effect was observed after moderate water stress rewatering at the jointing stage. Similar results were also observed in another lysimeter experiment using another winter wheat variety (*c.v.* Shijiazhuang 8) as experimental material [36].

3.3. Effects of Water Stress at the Heading Stage on Leaf Gas Exchange of Winter Wheat. There were significant differences between treatments T8 and T10 (see Figure 5). During the 2013–2014 growing season, Pn of T10 treatment decreased by 14.3% compared with CK. Under treatments

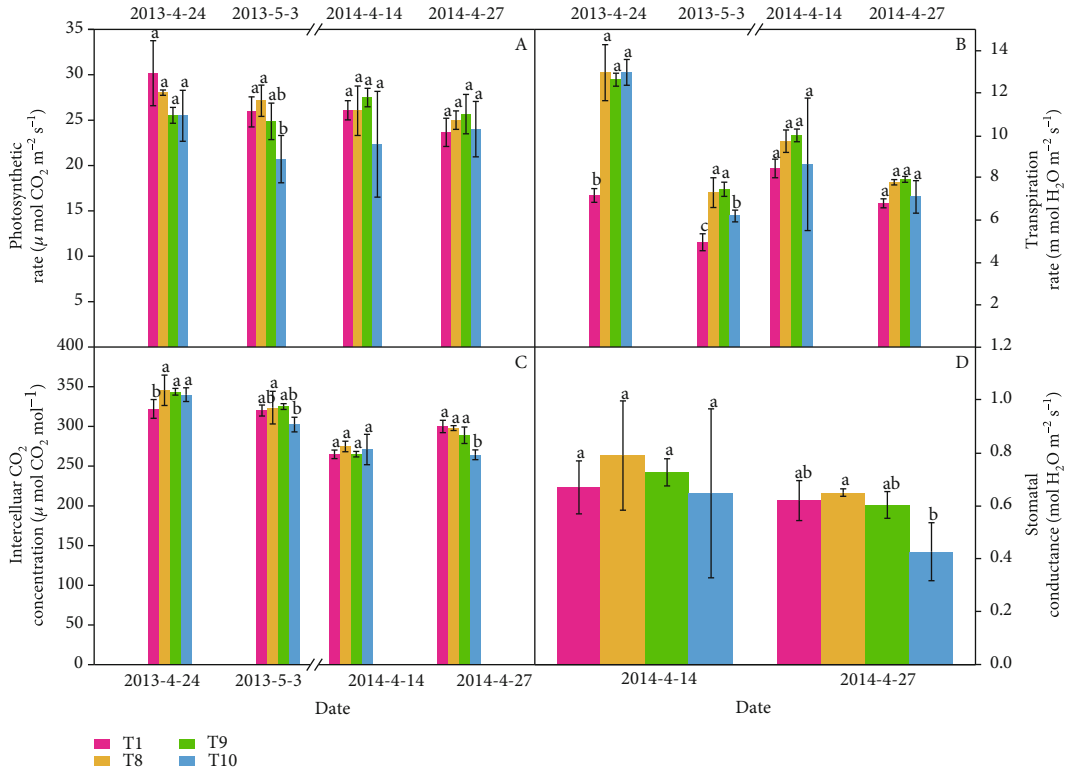

FIGURE 5: Variations in leaf gas exchange parameters of winter wheat under well-watered control treatment (T1), light drought (T8), moderate drought (T9), and severe drought (T10) stress at the heading stage. Data are the means ± standard errors (SE) of three replicates, where $n = 3$ for the photosynthetic rate (Pn), transpiration rate (Tr), intercellular CO_2 concentration (Ci), and stomatal conductance (Gs). Different letters above the bars indicate statistical significance ($p \leq 0.05$).

T8 and T9, gas exchange parameters did not significantly decrease, while Tr was increased by 15.3% and 18.5%, respectively, compared with CK. Under continuous water stress, Pn, Tr, and Gs of all treatments decreased, while Ci increased (except for that of severe drought treatment). The results showed that Pn and Tr of T10 treatment were significantly lower than those of other drought treatments. Furthermore, compared with CK, Ci and Gs of T10 treatment were significantly decreased by 11.9% and 31.2%, respectively. Severe drought at the heading stage had significant negative effects on gas exchange parameters of winter wheat leaves, and the variability of the above parameters was large.

3.4. Effects of Water Stress at the Filling Stage on Leaf Gas Exchange of Winter Wheat. With the intensification of water stress, Pn, Tr, and Gs of drought treatments decreased significantly at the filling stage (see Figure 6). Pn, Tr, Ci, and Gs of T13 treatment decreased by 74.9%, 73.2%, 7.64%, and 87.1%, respectively, compared with CK at the filling stage. However, Pn, Tr, Ci, and Gs of T11 and T12 treatments did not significantly decrease. Under continuous water stress, Pn, Tr, Ci, and Gs of each drought treatment decreased significantly by 40.6% (Pn), 47.7% (Tr), 11.1% (Ci), and 69.6% (Gs), respectively. Severe drought had the greatest decreasing effect on Pn, Tr, and Gs at the filling stage.

3.5. Effects of Continuous Water Stress on Leaf Gas Exchange of Winter Wheat. During the drought period of the 2012–2013 growing season, Tr, Ci, and Gs of continuous drought treatments in the early growth stage decreased by 19.6%, 17.3%, and 50.4%, respectively (see Figure 7). Similarly, those of continuous drought treatments in the late growth stage decreased by 45.2% (Tr), 15.7% (Ci), and 78.9% (Gs), respectively. After rewatering, differences of Tr, Ci, and Gs between the drought treatments and CK were significantly reduced. Ci and Gs returned to the level of CK treatment, whereas Tr "rebounded" to 1.92 times (2012–2013) and 1.28 times (2013–2014) the CK treatment. The differences between continuous drought treatments and CK began to be significant at the filling stage, and they gradually increased with time and reached the maximum in the late filling stage.

3.6. Correlations of Leaf Water Use Efficiency and Stomatal Limitation Values Related to Leaf Gas Exchange Parameters. Stomatal limitation (Ls) was defined as 1 – Ci/Ca. Ls had a quadratic relationship with Pn and a linear relationship with Gs and Tr (see Figure 8). Ls mainly concentrated at the level below 0.3. Leaf water use efficiency (WUE_l) had a quadratic relationship with Pn and Tr and a nonlinear ellipse relationship with Gs. Furthermore, Tr decreased under drought stress, and the decreasing rates of Tr became larger with the intensification of water stress. Our study showed that moderate water stress led to the increase of WUE_l, and WUE_l continued to increase even if wheat crops suffered severe drought stress. Under soil water stress, the plant stomatal regulation mechanism is considered to be feedback to make plants

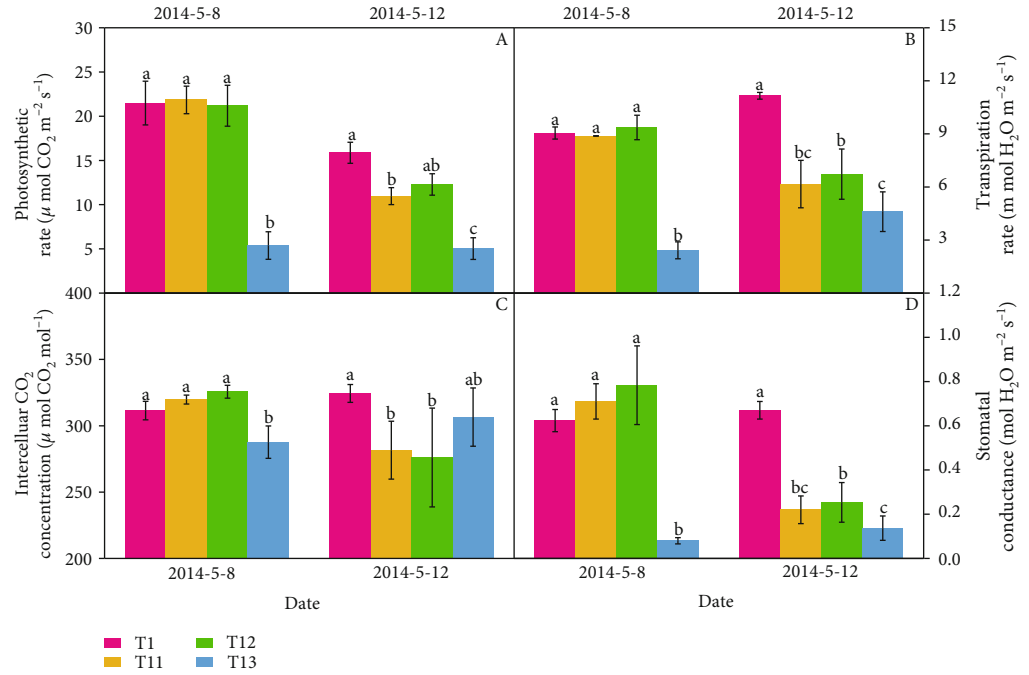

Figure 6: Variations in leaf gas exchange parameters of winter wheat under well-watered control treatment (T1), light drought (T11), moderate drought (T12), and severe drought (T13) stress at the filling stage. Data are the means ± standard errors (SE) of three replicates, where $n = 3$ for the photosynthetic rate (Pn), transpiration rate (Tr), intercellular CO_2 concentration (Ci), and stomatal conductance (Gs). Different letters above the bars indicate statistical significance ($p \leq 0.05$).

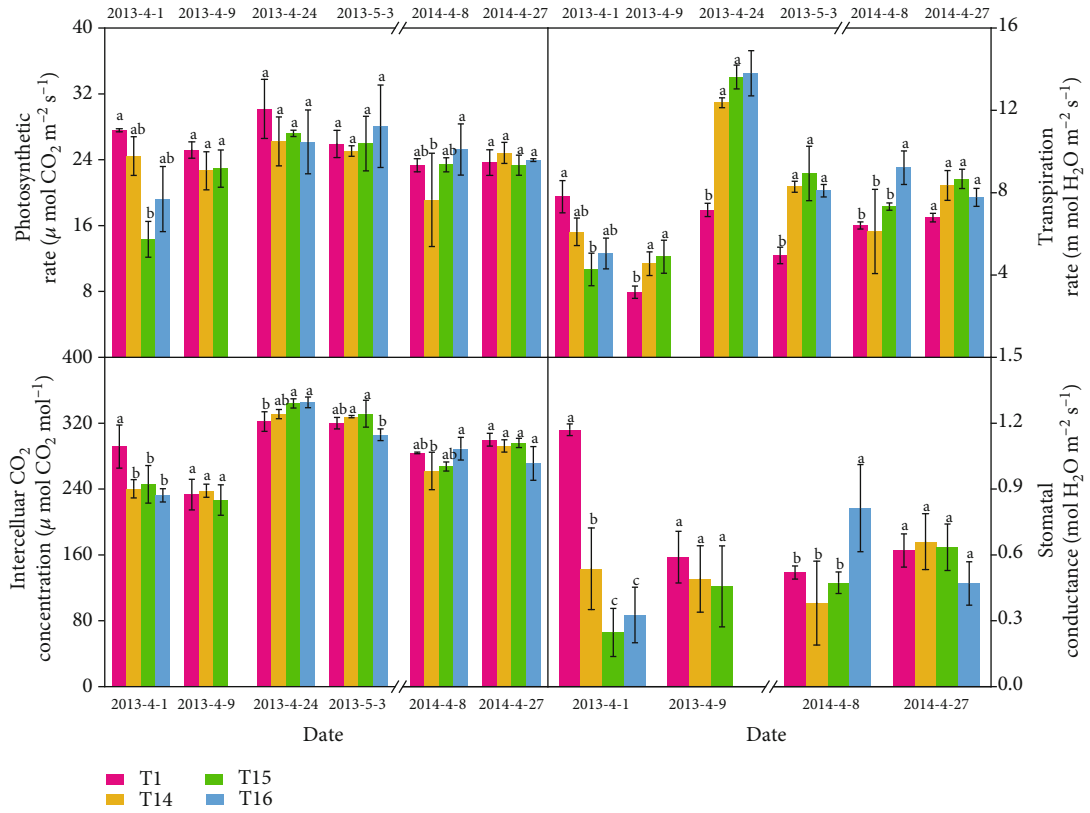

Figure 7: Variations in leaf gas exchange parameters of winter wheat under well-watered control treatment (T1), continuous moderate drought stress at seedling and jointing stages (T14), at jointing and heading stages (T15), and at heading and filling stages (T16), respectively. Data are the means ± standard errors (SE) of three replicates, where $n = 3$ for the photosynthetic rate (Pn), transpiration rate (Tr), intercellular CO_2 concentration (Ci), and stomatal conductance (Gs). Different letters above the bars indicate statistical significance ($p \leq 0.05$).

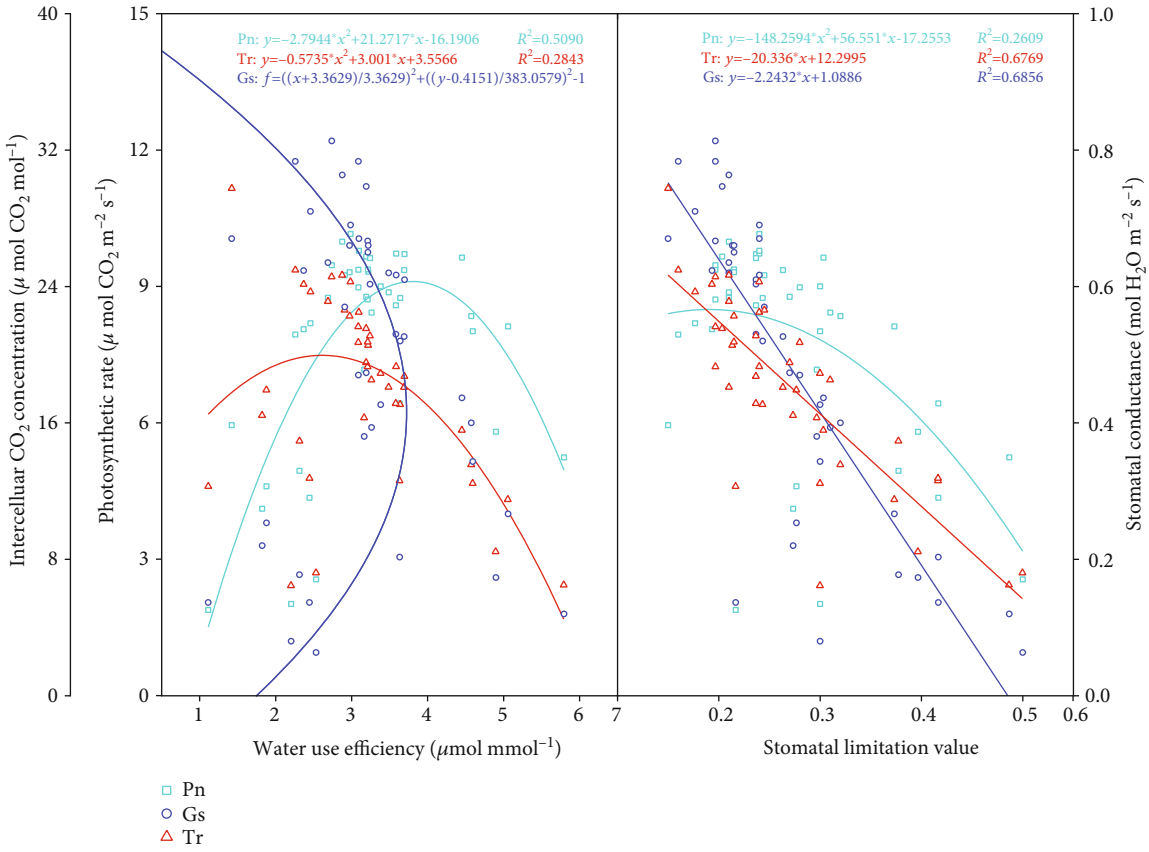

Figure 8: Relationships between leaf water use efficiency, stomatal limitation values, and gas exchange parameters of winter wheat.

adaptable to drought stress [37, 38]. When soil water is sufficient, stomatal conductance increases with the increase of photosynthetic active radiation intensity. Under severe drought, plants will suffer excessive water loss through transpiration, resulting in changes in leaf water potential and the decrease of the stomatal opening. However, under moderate water stress, the photosynthetic rate did not decrease or even became higher than that of nonstress treatment.

In this study, WUE_l decreased until nonstomatal restriction became a main limiting factor for leaf gas exchange, which was consistent with the previous studies [39, 40]. With the increase of WUE_l, Pn and Tr both increased first and then decreased. When WUE_l was about 2.62 μmol mmol^{-1}, Tr reached the maximum value. When WUE_l reached 3.36 μmol mmol^{-1}, the drought level increased from light to moderate water stress. Similarly, when WUE_l exceeded 3.81 μmol mmol^{-1}, Pn reached the maximum value. It was when WUE_l reached 4.11 μmol mmol^{-1} that it began to decrease quickly, indicating that crops had suffered from severe water stress. At the same time, the nonstomatal factor had become a main limiting factor of leaf photosynthesis [41]. The recommendation of WUE_l threshold values (i.e.,WUE_l of 2.62, 3.36, and 4.11 μmol mmol^{-1} represents light, moderate, and severe drought levels, respectively) that define different levels of drought stress will be of more practical significance for realizing the unification of water-saving and high yield of wheat.

3.7. Crop Evapotranspiration, Grain Yield, and Water Use Efficiency. Crop evapotranspiration (ET_c) was limited by drought at any growth stage (Table 1). Generally, ET_c decreased with the intensification of drought. Compared with light and moderate drought treatments, ET_c of severe drought treatment at any growth stage was always the lowest. On average, grain yield and ET_c of winter wheat in the 2012–2013 growing season were decreased by 7.38% and 6.63% (light drought), 10.3% and 7.94% (moderate drought), and 15.3% and 31.8% (severe drought), respectively, compared with CK. Similar results were also observed in 2013–2014. Grain yield of light and moderate drought treatments at the seedling stage generally decreased within 5%, while water use efficiency (WUE) was generally higher, which indicated that moderate drought at the seedling stage was beneficial to improve WUE of winter wheat, and did not lead to significant yield reduction. Compared with CK, WUE of drought treatments at heading and filling stages was decreased by up to 21.7% (2012–2013) and 27.5% (2013–2014), respectively. WUE was lowest under continuous drought conditions at middle growth stages. Under moderate water stress, the stomatal opening decreased significantly, and the transpiration rate decreased faster than the photosynthetic rate, giving rise to the highest WUE. Under severe water stress, the photosynthetic activity of mesophyll cells decreased, leading to stomatal limitation.

Table 1: Crop evapotranspiration, grain yield, and water use efficiency of winter wheat under well-watered control conditions and light, moderate, and severe drought stress at different key growth stages during the 2012–2013 and 2013–2014 growing seasons.

Treatments	Grain yield ($kg\,ha^{-1}$)		Crop evapotranspiration (mm)		Water use efficiency ($kg\,m^{-3}$)	
	2012–2013	2013–2014	2012–2013	2013–2014	2012–2013	2013–2014
T1 (CK)	7545a	8023a	569.8a	531.1ab	1.33abc	1.51ab
T2	7318a	7682a	569.2a	539.8ab	1.29bc	1.42bc
T3	7318a	7886a	541.7ab	484.5bc	1.36abc	1.64a
T4	7227ab	5886e	490.7bcde	421.6d	1.48ab	1.40bcd
T5	7091ab	7023b	513.8abcd	510.8ab	1.38abc	1.38bcde
T6	6818abc	5864e	526.6abcd	526.6ab	1.30bc	1.11fghi
T7	6909ab	5114f	470.1defg	515.4ab	1.48ab	0.99i
T8	6818abc	6614bcd	530.8abc	559.7a	1.28bc	1.19efgh
T9	6818abc	6205cde	518abcd	517.3ab	1.32abc	1.21efgh
T10	6045cd	6227cde	473.9cdef	512.4ab	1.28bc	1.22fefg
T11	6727abc	6795bc	514.3abcd	532.4ab	1.30bc	1.29cdef
T12	6091cd	6023de	512.1bcd	447.8cd	1.19c	1.35bcde
T13	5364d	4636fg	415.8g	423.6d	1.29bc	1.09ghi
T14	6455bc	4614fg	418.2g	452.3cd	1.54a	1.02hi
T15	5500d	4000g	426.6fg	493.9bc	1.29bc	0.81j
T16	6455bc	6000de	438.9efg	491.7bc	1.47ab	1.22defg

Note: treatment means followed by the different letters are significantly different at $p \leq 0.05$.

4. Conclusion

Grain yield of light and moderate drought treatments at the seedling stage was similar to CK, indicating that light and moderate water stress levels at the seedling stage did not generate an irreversible effect on wheat plants. However, severe drought in any growth stage caused significant negative effects on gas exchange parameters, WUE_l, and grain yields of winter wheat. Based on the correlation between WUE_l and Pn, Tr, and Gs, the theoretical threshold values of WUE_l for light, moderate, and severe drought levels were 2.62, 3.36, and 4.11 $\mu mol\,mmol^{-1}$, respectively. Photosynthetic rates of wheat leaves reached their maximum values when WUE_l was 3.81 $\mu mol\,mmol^{-1}$. The WUE_l threshold values are useful to identify different levels of drought stress the crops suffered from and provide a theoretical reference threshold to achieve smart irrigation for winter wheat in the North China Plain.

Data Availability

The data used to support the findings of the study can be available upon request to the corresponding author.

Conflicts of Interest

All the authors declare no conflict of interest.

Acknowledgments

This study was financially supported by the Henan Water Conservancy Science and Technology Project (GG201509, GG201602), and Scientific and Technological Project of Henan Province (212102110069). The page fee for this manuscript comes from the project undertaken by the author.

References

[1] C. Su, S. Song, Y. Lu et al., "Potential effects of changes in climate and emissions on distribution and fate of perfluorooctane sulfonate in the Bohai Rim, China," *Science of the Total Environment*, vol. 613-614, pp. 352–360, 2018.

[2] D. Tilman, C. Balzer, J. Hill, and B. L. Befort, "Global food demand and the sustainable intensification of agriculture," *Proceedings of the National Academy of Sciences of the United States of America*, vol. 108, no. 50, pp. 20260–20264, 2011.

[3] Q. Fang, L. Ma, T. R. Green, Q. Yu, T. D. Wang, and L. R. Ahuja, "Water resources and water use efficiency in the North China Plain: current status and agronomic management options," *Agricultural Water Management*, vol. 97, no. 8, pp. 1102–1116, 2010.

[4] S. Sun, J. Liu, P. Wu, Y. Wang, X. Zhao, and X. Zhang, "Comprehensive evaluation of water use in agricultural production: a case study in Hetao Irrigation District, China," *Journal of Cleaner Production*, vol. 112, pp. 4569–4575, 2016.

[5] M. Giuliani, F. Carucci, E. Nardella et al., "Combined effects of deficit irrigation and strobilurin application on gas exchange, yield and water use efficiency in tomato (*Solanum lycopersicum* L.)," *Scientia Horticulturae*, vol. 233, pp. 149–158, 2018.

[6] T. Oda, K. Moriwaki, K. Tanigaki, Y. Nomura, and T. Sumi, "Irrigation ponds in the past, present, and future: a case study of the Higashi Harima Region, Hyogo Prefecture, Japan," *Journal of Hydro-Environment Research*, vol. 26, pp. 19–24, 2019.

[7] H. Kazem Attar, H. Noory, H. Ebrahimian, and A.-M. Liaghat, "Efficiency and productivity of irrigation water based on water balance considering quality of return flows," *Agricultural Water Management*, vol. 231, p. 106025, 2020.

[8] S. M. Ismail and K. Ozawa, "Improvement of crop yield, soil moisture distribution and water use efficiency in sandy soils by clay application," *Applied Clay Science*, vol. 37, no. 1-2, pp. 81–89, 2007.

[9] T. Améglio, P. Archer, M. Cohen et al., "Significance and limits in the use of predawn leaf water potential for tree irrigation," *Plant and Soil*, vol. 207, no. 2, pp. 155–167, 1998.

[10] A. Qin, D. Ning, Z. Liu et al., "Structural equation modeling of soil moisture effects on evapotranspiration of maize in the North China Plain," *National Academy Science Letters*, vol. 43, no. 3, pp. 219–224, 2020.

[11] J. Zou, Z. Xie, C. Zhan et al., "Effects of anthropogenic groundwater exploitation on land surface processes: a case study of the Haihe River Basin, northern China," *Journal of Hydrology*, vol. 524, pp. 625–641, 2015.

[12] D. Feng, J. Zhang, C. Cao et al., "Soil salt accumulation and crop yield under long-term irrigation with saline water," *Journal of Irrigation and Drainage Engineering*, vol. 141, no. 12, pp. 04015025–04015729, 2015.

[13] G. D. Salvucci, "Estimating the moisture dependence of root zone water loss using conditionally averaged precipitation," *Water Resources Research*, vol. 37, no. 5, pp. 1357–1365, 2001.

[14] A. Porporato, F. Laio, L. Ridolfi, and I. Rodriguez-Iturbe, "Plants in water-controlled ecosystems: active role in hydrologic processes and response to water stress: III. Vegetation water stress," *Advances in Water Resources*, vol. 24, no. 7, pp. 725–744, 2001.

[15] G. R. Miller, D. D. Baldocchi, B. E. Law, and T. Meyers, "An analysis of soil moisture dynamics using multi-year data from a network of micrometeorological observation sites," *Advances in Water Resources*, vol. 30, no. 5, pp. 1065–1081, 2007.

[16] C. Jiabing, X. Di, S. Nan, and W. E. I. Zheng, "Real-time monitoring system of crop canopy temperature and soil moisture for irrigation decision-making," *Transactions of the Chinese Society for Agricultural Machinery*, vol. 46, no. 12, pp. 133–139, 2015.

[17] M. Han, H. Zhang, J. L. Chávez, L. Ma, T. J. Trout, and K. C. DeJonge, "Improved soil water deficit estimation through the integration of canopy temperature measurements into a soil water balance model," *Irrigation Science*, vol. 36, no. 3, pp. 187–201, 2018.

[18] M. Culman, C. M. de Farias, C. Bayona, and J. D. Cabrera Cruz, "Using agrometeorological data to assist irrigation management in oil palm crops: a decision support method and results from crop model simulation," *Agricultural Water Management*, vol. 213, pp. 1047–1062, 2019.

[19] Y. Zhang, E. Kendy, Y. Qiang, L. Changming, S. Yanjun, and S. Hongyong, "Effect of soil water deficit on evapotranspiration, crop yield, and water use efficiency in the North China Plain," *Agricultural Water Management*, vol. 64, no. 2, pp. 107–122, 2004.

[20] S. Hao, H. Cao, H. Wang, and X. Pan, "The physiological responses of tomato to water stress and re-water in different growth periods," *Scientia Horticulturae*, vol. 249, no. 1, pp. 143–154, 2019.

[21] X. Fang, Y. Li, J. Nie et al., "Effects of nitrogen fertilizer and planting density on the leaf photosynthetic characteristics, agronomic traits and grain yield in common buckwheat (*Fagopyrum esculentum* M.)," *Field Crops Research*, vol. 219, no. 4, pp. 160–168, 2018.

[22] A. Saryoko, Y. Fukuda, I. Lubis, K. Homma, and T. Shiraiwa, "Physiological activity and biomass production in crop canopy under a tropical environment in soybean cultivars with temperate and tropical origins," *Field Crops Research*, vol. 216, no. 12, pp. 209–216, 2018.

[23] A. B. Heinemann, L. F. Stone, and N. K. Fageria, "Transpiration rate response to water deficit during vegetative and reproductive phases of upland rice cultivars," *Scientia Agricola*, vol. 68, no. 1, pp. 24–30, 2011.

[24] T. Zenone, M. Fischer, N. Arriga et al., "Biophysical drivers of the carbon dioxide, water vapor, and energy exchanges of a short-rotation poplar coppice," *Agricultural and Forest Meteorology*, vol. 209-210, pp. 22–35, 2015.

[25] G. Shao, J. Cui, S. Yu et al., "Impacts of controlled irrigation and drainage on the yield and physiological attributes of rice," *Agricultural Water Management*, vol. 149, pp. 156–165, 2015.

[26] X. Li, S. Kang, X. Zhang, F. Li, and H. Lu, "Deficit irrigation provokes more pronounced responses of maize photosynthesis and water productivity to elevated CO_2," *Agricultural Water Management*, vol. 195, pp. 71–83, 2018.

[27] R. A. C. Mitchell, V. J. Mitchell, and D. W. Lawlor, "Response of wheat canopy CO_2 and water gas-exchange to soil water content under ambient and elevated CO_2," *Global Change Biology*, vol. 7, no. 5, pp. 599–611, 2001.

[28] L. Zheng, J. Ma, X. Sun et al., "Responses of photosynthesis, dry mass and carbon isotope discrimination in winter wheat to different irrigation depths," *Photosynthetica*, vol. 56, no. 4, pp. 1437–1446, 2018.

[29] S. Zhang, Q. Li, K. Ma, and L. Chen, "Temperature-dependent gas exchange and stomatal/non-stomatal limitation to CO_2 assimilation of Quercus liaotungensis under midday high irradiance," *Photosynthetica*, vol. 39, no. 3, pp. 383–388, 2001.

[30] J. Lampurlanés, D. Plaza-Bonilla, J. Álvaro-Fuentes, and C. Cantero-Martínez, "Long-term analysis of soil water conservation and crop yield under different tillage systems in Mediterranean rainfed conditions," *Field Crops Research*, vol. 189, pp. 59–67, 2016.

[31] A. Qin, Y. Fang, D. Ning et al., "Incorporation of manure into ridge and furrow planting system boosts yields of maize by optimizing soil moisture and improving photosynthesis," *Agronomy*, vol. 9, no. 12, p. 865, 2019.

[32] H. Ozaki, R. Oguchi, and K. Hikosaka, "Dependence of functional traits related to growth rates and their CO_2 response on multiple habitat climate factors across Arabidopsis thaliana populations," *Journal of Plant Research*, vol. 131, no. 6, pp. 987–999, 2018.

[33] Y. Qu, P. Song, Y. Hu et al., "Regulation of stomatal movement by cortical microtubule organization in response to darkness and ABA signaling in Arabidopsis," *Plant Growth Regulation*, vol. 84, no. 3, pp. 467–479, 2018.

[34] A. Sallam, A. M. I. Mourad, W. Hussain, and P. Stephen Baenziger, "Genetic variation in drought tolerance at seedling stage and grain yield in low rainfall environments in wheat (*Triticum aestivum* L.)," *Euphytica*, vol. 214, no. 9, 2018.

[35] J. Niu, S. Zhang, S. Liu et al., "The compensation effects of physiology and yield in cotton after drought stress," *Journal of Plant Physiology*, vol. 224-225, pp. 30–48, 2018.

[36] L. Liu, W. Hao, Q. Bai, X. R. Mei, and Y. L. Yan, "Differential compensatory effects of winter wheat in water stress and rewatering during jointing stage in North China," *Journal of Irrigation and Drainage*, vol. 30, no. 2, pp. 37–40, 2011.

[37] E. Lefi, H. Medrano, and J. Cifre, "Water uptake dynamics, photosynthesis and water use efficiency in field-grown *Medicago* arborea and *Medicago citrina* under prolonged Mediterranean drought conditions," *Annals of Applied Biology*, vol. 144, no. 3, pp. 299–307, 2004.

[38] X. Cheng, F. Zhang, and S. Chai, "Stomatal response of spring wheat and related affecting factors under different irrigation treatments," *Chinese Journal of Applied Ecology*, vol. 21, no. 1, pp. 36–40, 2010.

[39] J. R. Ehleringer and C. S. Cook, "Carbon and oxygen isotope ratios of ecosystem respiration along an Oregon conifer transect: preliminary observations based on small-flask sampling," *Tree Physiology*, vol. 18, no. 8-9, pp. 513–519, 1998.

[40] M. E. Salvucci and S. J. Crafts-Brandner, "Inhibition of photosynthesis by heat stress: the activation state of Rubisco as a limiting factor in photosynthesis," *Physiologia Plantarum*, vol. 120, no. 2, pp. 179–186, 2004.

[41] R. B. Thompson, M. Gallardo, L. C. Valdez, and M. D. Fernández, "Using plant water status to define threshold values for irrigation management of vegetable crops using soil moisture sensors," *Agricultural Water Management*, vol. 88, no. 1-3, pp. 147–158, 2007.

Hindawi
Journal of Sensors
Volume 2020, Article ID 8874468, 15 pages
https://doi.org/10.1155/2020/8874468

Research Article

Computational Fluid Dynamics-Based Simulation of Crop Canopy Temperature and Humidity in Double-Film Solar Greenhouse

Wei Jiao,[1,2] Qi Liu,[1] Lijun Gao,[1] Kunyu Liu,[2] Rui Shi,[3,4] and Na Ta[1]

[1]*College of Mechanical and Electrical Engineering, Inner Mongolia Agricultural University, Hohhot 010018, China*
[2]*Institute of Grassland Research of CAAS, Hohhot 010010, China*
[3]*Collage of Grassland, Resources and Environment, Inner Mongolia Agricultural University, Hohhot 010018, China*
[4]*Baotou Medical College, Baotou 014040, China*

Correspondence should be addressed to Na Ta; jdtana@163.com

Received 24 July 2020; Revised 14 September 2020; Accepted 19 September 2020; Published 17 October 2020

Academic Editor: Yuan Li

The microenvironment of the crop area in a greenhouse is the main factor that affects its growth, quality, and pest control. In this study, we propose a double-layer film solar greenhouse microenvironment testing system based on computational fluid dynamics simulations of a celery canopy with a porous medium. A real greenhouse was examined with a sensor system for soil, air, radiation, and carbon dioxide detection to verify the simulation results. By monitoring the internal environment of celery canopies with heights of 0.8 and 1 m during a period of temperature fluctuations, we found the temperature and humidity of the canopy interior changed spatially and differed greatly from the those in the greenhouse under solar radiation conditions. The temperature and humidity of the celery canopy were 4–14°C lower and 10%–30% higher than those of the surroundings. As the canopy grew, the differences in temperature and humidity between the canopy and other parts of the greenhouse increased. The root mean square errors of the temperature and humidity with the 0.8 m high celery canopy were found to be 0.56 and 2.86 during the day and 0.24 and 0.81 at night, respectively; the corresponding values for the 1 m high celery canopy were found to be 0.51 and 2.26 during the day and 0.26 and 0.78 at night. The porous medium model expressed the temperature and humidity characteristics of the celery crop appropriately, and the simulation method was shown to be effective and feasible. With the simulation method proposed in this study, the production of crops in complex microenvironments in greenhouses can be modeled and digitized.

1. Introduction

Solar greenhouses are the most important type of greenhouse used in cold and arid areas of northern China [1]. They are either closed or semienclosed thermal systems and are composed of an enveloped structure, indoor air, crops, and soil. The environment in a solar greenhouse is affected by the external temperature, humidity, solar radiation intensity, wind speed, greenhouse structure, and planted crops [2]. The microenvironment in which a crop is grown affects the plant efficiency, healthy growth rate, pest control, greenhouse ventilation, irrigation, and other related aspects of the growth. The study of the temperature and humidity distribution in crop canopies is important for the crop production and quality [3–5]. However, research based on computational fluid dynamics (CFD) simulations of a greenhouse has mainly focused on the greenhouse environment in relation to the crop growth demand [6–8]. With the rapid development of computer technology, CFD-based numerical simulations have been widely used to study the spatial and temporal distribution of climate-related characteristics (e.g., temperature) of microenvironments in greenhouses [9–12]. In recent years, more scholars have paid attention to the microenvironment of greenhouse crops. The changes in temperature and humidity inside greenhouses during crop growth has become a hot research topic [13–15]. Boulard and Roy used a CFD approach to model the micrometeorology of a closed greenhouse at the canopy level [16]. They visualized the distribution of solar radiation and found good agreement between the experimental and simulation

measurements of crop transpiration. Tadj used the CFD method to simulate the microclimate in a closed vaulted greenhouse where tomatoes were grown and discussed the influence of different heating systems on the microclimate of tomatoes in the greenhouse [17]. Yue Zhang developed a method to evaluate the microlight climate and thermal performance of Liaoshen-type solar greenhouses, including a detailed 3D tomato canopy structure simulated using a functional–structural plant model [18]. Nebbali simulated the distributed climate parameters of a ventilated tunnel tomato greenhouse using a biband discrete ordinate (DO) model with the plant canopy considered a porous medium [19]. They considered the impact of the sun position and wind on the greenhouse microclimate.

In this study, we investigate the temperature and humidity distribution of a celery crop in a solar greenhouse with a double-layer cover film using the CFD method. We designed a contrasting experiment with two celery canopies of different heights set as isotropic porous media with different parameters. Then, we used the ANSYS Fluent to simulate the crop canopy temperature and humidity. A simple and efficient greenhouse sensor test system was designed to provide the boundary and verification conditions required for the simulation. The accuracy of the CFD model was verified by comparing the values obtained with the ANSYS Fluent with the measured results. Furthermore, we investigate the distribution of the temperature, and humidity in the celery crop canopies with different heights is explored.

2. Materials and Methods

2.1. Study Site and Sensor System Settings. The experiment was carried out at the Hailiutu solar greenhouse experimental site of the Inner Mongolia Agricultural University. The geographic coordinates were as follows: 40.68° N latitude and 111.37° E longitude. Figure 1 shows the study site on the map of Hohhot and a photograph of the studied greenhouse.

The experiments were performed on a solar greenhouse with a double-layer cover film. The greenhouse faced south from the north and had a length of 70 m and a span of 9 m. The back wall had a brick-and-soil structure and was 1.4 m thick and 3.5 m high. As shown in Figure 2, the greenhouse sensing detection system was composed of three parts: data acquisition, data storage, and data transmission [20]. Briefly, carbon dioxide (CD, model: CD10), air temperature and humidity (ATH, model: FLEX1000TH), solar radiation (SR, model: YJ-SR200), and soil temperature and moisture (STM, model: MS10) sensors, provided by Dalian Zheqin Technology Co., Ltd., were connected to a low-frequency half-duplex Lora serial port (LG207P) for data collection. The Lora data transmission terminal supports the point-to-point communication protocol with a working frequency band of 410–441 MHz. The computer server stored the collected data and was connected to the G780 data transmission module. The G780 is a product developed for the transmission of data between serial devices and network servers through the operator's network. Through simple attention command settings, the G780 can be used to achieve two-way serial transparent data transmission to the network. The data were transferred to a laboratory analysis workstation through 4G wireless communication for the simulation analysis [21, 22].

The ATH sensors provide 14 bits air temperature (aTp) and 12 bits air humidity (aHd) measurements. The temperature measurement range was from −20 to 85°C with an accuracy of ±0.3°C. The humidity measurement range was from 0% to 100% RH with an accuracy of ±2% RH. The STM sensors measured temperatures between −40 and 80°C and humidity between 0 and 100% RH with accuracies of ±0.5 and ±3%, respectively. The SR sensors measured the spectral range from 0.3 to 3 μm. The core device of the radiation sensor was a high-precision sensor, and a quartz glass cover made using precision optical cold processing was installed outside the sensor to effectively prevent environmental factors from affecting its performance. Figure 3 shows the arrangement of the measuring points in the solar greenhouse and a photograph of the greenhouse sensor system.

The outdoor temperature, humidity, solar radiation, wind speed, and wind direction were measured by the weather station. In order to focus on the crop canopy, groups of sensors were arranged at the center of the span cross-section of the crop canopy at a two-meter (2 m) distance on both sides. Each group consisted of four ATH sensors arranged in the vertical direction. These sensors could be adjusted according to the canopy height. Specifically, for a 0.8 m canopy height, the sensors could be adjusted to 0.1, 0.4, 0.6, or 0.8 m from the ground level, and for a 1 m high canopy height, they can be adjusted to 0.1, 0.4, 0.8, and 1 m from the ground level. Seven ATH sensors were arranged in the inner arch shed, inner membrane, outer membrane, north and south sides of the ceiling, two meters above the ceiling, and rear wall. These sensors were used to set the boundary conditions to observe aTp and aHd in the greenhouse. Three STM sensors were arranged on the soil surface layer to set the boundary conditions of the soil surface temperature and moisture content. The SR sensors were arranged in air and inside the canopy to observe the radiation of the sun inside the greenhouse. The CD sensors were arranged in the middle of the canopy and approximately 1.9 m above the ground to observe changes in the carbon dioxide concentration in the canopy and air.

2.2. CFD Model Procedure. The CFD simulation of the greenhouse energy dynamics is primarily based on the porous medium model, air turbulence model, solar radiation model, and energy component transport model [23]. Porous media consist of a combination of heterogeneous materials, in which solids serve as the backbone of the media, and liquids or gases are dispersed through the pores. In this study, the celery canopy was set as an isotropic porous medium model following the Darcy law. This was based on the physical structure of the canopy and the microenvironment of the experimental area [24]. Thus, the porous medium model simulated the resistance of the porous material to the fluid in the calculation domain by adding the source term to the momentum equation. The

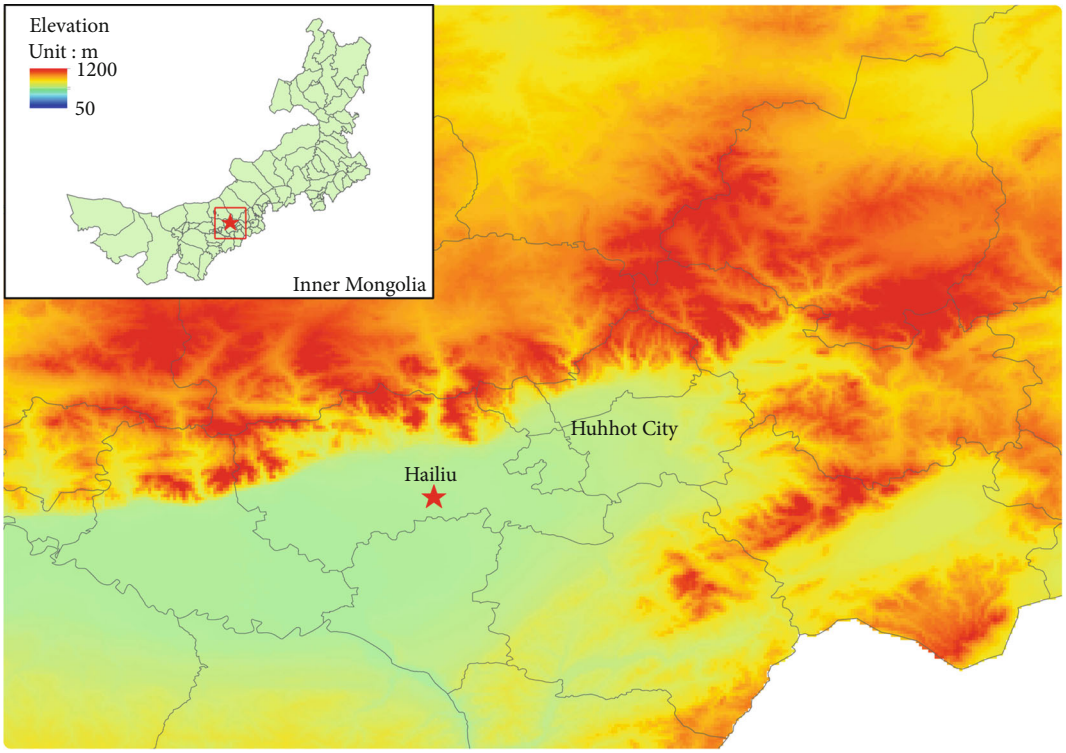

(a)

(b)

Figure 1: (a) Study site on the map of Inner Mongolia and Hohhot and (b) photograph of the greenhouse.

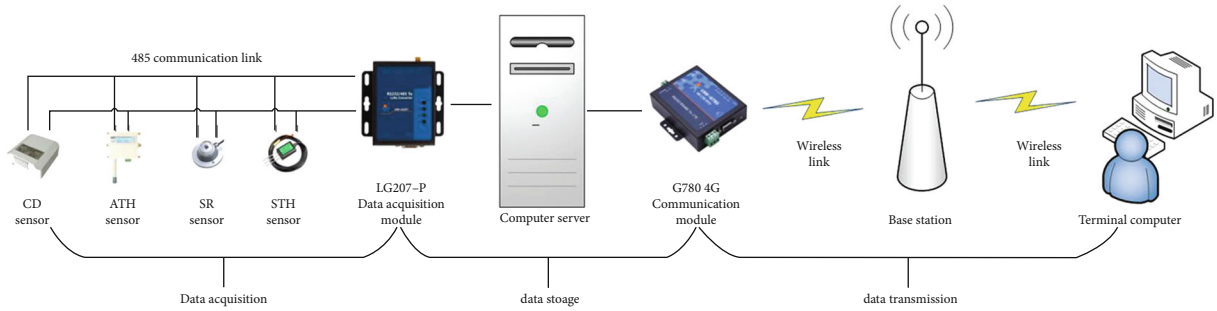

Figure 2: Connection diagram of the greenhouse sensing detection system.

source term is composed of a viscous resistance term and an inertial loss term. The apparent velocity formula of the porous medium model is as follows:

$$S_i = -\left(\frac{\mu}{\alpha} v_i + C_2 \frac{1}{2} \rho |v| v_i\right), \tag{1}$$

where S_i is the momentum source term in the i direction (x, y, z), μ is the viscous coefficient, v_i is the speed in the i direction (m/s), $|v|$ is the absolute value of the speed, ρ is the fluid density (kg/m^3) in the greenhouse, $1/\alpha$ is the viscous resistance coefficient, and C_2 is the inertial resistance coefficient. Because the fluid flow inside the canopy is laminar, the inertial resistance coefficient can be solved using the Blake–Kozeny equation:

$$\frac{|\Delta p|}{L} = \frac{150\mu}{D_p^2} \frac{(1-\varepsilon)^2}{\varepsilon^3} v_\infty, \tag{2}$$

where $|\Delta p|$ is the pressure gradient (Pa), L is the canopy thickness (m), D_p is the average particle diameter (m), ε is the porosity, and v_∞ is the incoming speed (m/s). By incorporating Equation (1) into Equation (2), we obtain

$$\frac{1}{\alpha} = \frac{150}{D_p^2} \frac{(1-\varepsilon)^2}{\varepsilon^3}, \tag{3}$$

$$C_2 = \frac{3.5}{D_p} \frac{(1-\varepsilon)}{\varepsilon^3}. \tag{4}$$

In a previous study, Ha reported that porous media with 0.8 and 1 m heights had a porosity of 0.35 and 0.3, respectively [25]. Table 1 shows the calculation results of the celery crop parameters.

By considering the viscosity of fluids in low Reynolds number flows, the renormalization group $k-\varepsilon$ turbulence model, which consider an additional term to improve accuracy [26–28], was used for the simulation. The renormalization group model equation is as follows:

$$\frac{\partial(pu\varnothing)}{\partial t} + \text{div}\,(pu\varnothing) = \text{div}\,(\Gamma_\varnothing\ \text{grad}\varnothing) + S_\varnothing, \tag{5}$$

where the subscript Φ indicates the quantity, i.e., temperature or humidity, designated as aTp or aHd, respectively, Γ_Φ is the diffusion coefficient (m^2/s), which was set as a constant, and u is the fluid velocity vector (m/s).

When the solar radiance passes through the translucent film in the greenhouse, the rays are reflected and refracted. Considering the translucent film characteristics and the sunshine intensity in Inner Mongolia, the DO model was selected to simulate the effect of solar radiation on the thermal environment in the greenhouse. The Do model equation is as follows:

$$\frac{dI\left(\vec{r}, \vec{s}\right)}{ds} + K_p \bullet I\left(\vec{r}, \vec{s}\right) = K_p \bullet I_p, \tag{6}$$

where r is the vector direction, s is the position vector, K_p is the absorption rate of the film, I is the solar radiation intensity (W/m^2), $K_p \cdot I$ is the solar radiant energy absorbed by the film (MJ/m^2), $K_p \cdot I_p$ is the radiant energy emitted by the film (MJ), and I_p is the intensity of radiation passing through the film (W/m^2).

In the ANSYS Fluent simulation, the greenhouse gas was set as a mixture of water vapor and air. Energy transfer was achieved using a moisture transfer, volume fraction, and water evaporation model. From these models, we obtain

$$\frac{\partial}{\partial t}(\rho c_i) + \text{div}\,(puc_i) = \text{div}\,(D_i\ \text{grad}\,(\rho c_i)) + S_j, \tag{7}$$

where c_i is the volume concentration of component i in the mixed gas (ml/m^3), pc_i is the mass concentration of the component (mg/m^3), D_i is the mass diffusivity of the component (m^2/s), and S_j is the additional generalized source (m/s).

2.3. Analytical Setting and Meshing Grid. We monitored the changes in the microenvironment in the central section of the greenhouse canopy. Specifically, the two-dimensional physical model in the middle section of the double-layer film solar greenhouse was established using computer-aided design and was subsequently used for the CFD simulations using ANSYS Fluent. Notably, when the same crop with high canopy height was planted without external interference, the simulation results of the middle section can represent the overall trend of the microenvironmental factors (e.g., temperature) in the greenhouse [29]. In this study, we used a 2D simulation model to monitor the distribution of the canopy microenvironment characteristics because the model

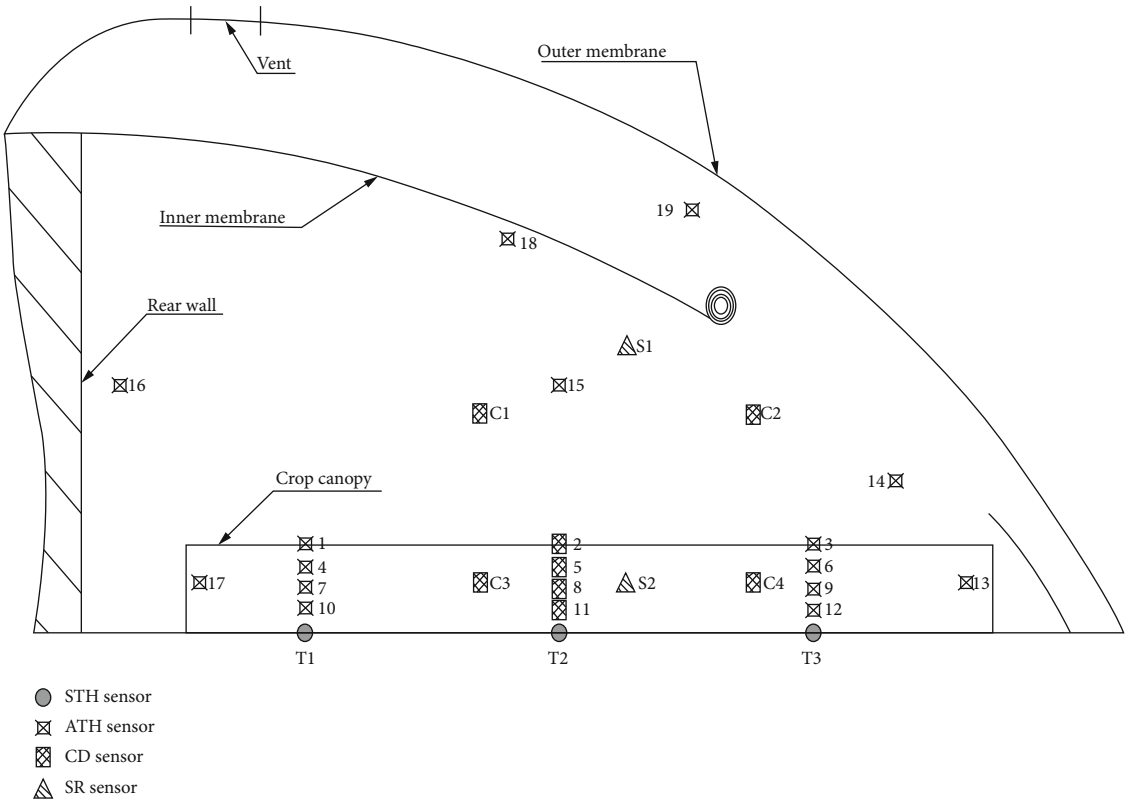

(a)

(b)

Figure 3: (a) Arrangement of sensors in the middle section of the greenhouse and (b) photograph of the sensors in the greenhouse.

Table 1: Celery porous media parameters.

Celery crop height (m)	Permeability (m^2)	Inertial resistance coefficient	Viscous resistance coefficient
0.8	6.766×10^{-10}	5.306×10^{4}	1.478×10^{9}
1.0	3.674×10^{-10}	9.074×10^{4}	2.722×10^{9}

could reflect the temperature and humidity distribution under the canopy with low interference and few test data. We used Jinnan Shiqin No.1 Benqin celery, which is a variety that originates from the Shandon province, China, and is widely cultivated in this region. We planted 162 rows of 11 plants of celery in the east-west direction on September 15, 2018. The growth pattern of the celery canopies with heights of 0.8 m (November 25, 2018) and 1 m (December 20, 2018) were compared. Jinnan Shiqin No.1 Benqin can grow to approximately 1.2 m; it forms a relatively uniform-high canopy at 0.8 m and is suitable for harvesting at 1 m heights. Hence, celery heights of 0.8 and 1 m are the most suitable for comparison for this variety relative to having considering the porosity and other related microenvironmental factors considered in this study. The greenhouse sensor system started operating at 12:00 on September 23 and collected data every half an hour. The data were selected at 11:00 a.m. (i.e., the warm-up period in the greenhouse) and 0:00 a.m. (i.e., the cool-down period in the greenhouse) for systematic energy dynamics analysis.

In the analysis, we used CFD (ICEM-CFD) to divide the grid and calculate the simulation domain. The crop canopy area and the noncanopy air portion in the greenhouse were set as the calculation domain. The boundary of the inner and outer membrane arcs was encrypted by the grid part and subsequently discretized in the computational domain. The quality of the grid calculation was above 0.35, and the maximum grid size was set to 0.02 m. This setting not only enhances the accuracy of the calculation but also improves the calculation speed [30]. The temperature of the area between the inner and outer membranes was close to the outdoor temperature at night after the inner membrane was closed. Therefore, this region was ignored. We set up the same measuring point as the sensors in the ANSYS Fluent and imported the obtained measuring point data and detection data into origin for verification and analysis.

In the ANSYS Fluent solution methods, the semi-implicit method for pressure-linked equation (SIMPLE) algorithm was set to analog computing. We set the least squares cell-based for the gradient and standard for the pressure. The momentum, energy, and H_2O were set to the second order upwind, turbulent dissipation rate, turbulent kinetic energy, and the DOs were set to first order upwind [31]. The underrelaxation factors of pressure, momentum, turbulent dissipation rate, and turbulent kinetic energy were set to 0.3, 0.7, 0.8, and 0.8, respectively, and the others were set to 1. The standard of energy and DO-intensity convergence residual was set to 10^{-6}, and the other convergence residuals were set to 10^{-3} [32].

2.4. Boundary Conditions. The boundary conditions included the outdoor climate, ground soil, back walls, crop area boundaries, and the inside and outside of the plastic films. The crop was set as a porous medium, and the border was set as a porous-jump boundary. The other borders were set as a wall, while the plastic films and the inner arch shed were set as translucent media [33]. Table 2 presents the thermal performance parameters of the various materials in the solar greenhouse.

3. Results

3.1. Energy-Flux Dynamics Simulation. Figure 4 shows the daytime and nighttime error iteration curves during the continuous-time step simulation and CFD calculation iterations. Owing to the accuracy of the model and grid settings, the error iteration curves converge quickly and smoothly. We can obtain simulation results before obtaining new test data (half an hour), so this model can be used in conjunction with the greenhouse test system to achieve real-time simulation and monitoring of the greenhouse environment throughout the day.

3.2. Energy-Flux Dynamics Simulation. Figures 5 and 6 show the CFD simulation results of the temperature and humidity distributions with the different celery canopy heights at 11:00 and 0:00 a.m., respectively. From Figure 5, it can be seen that at 11:00 a.m., heat is exchanged through the opening of the inner membrane, and the temperature between the inner and outer membranes reaches the highest value. The lowest temperature is measured at the bottom of the canopy layers. The temperature difference between the middle position of the 0.8 and 1 m high celery crop canopies, and the internal environment are 7.6 and 9.3°C, respectively, and the corresponding lowest soil surface temperatures are 11.0 and 9.3°C. The temperature difference in the canopy area of the 1 m high celery crop is larger than that in the canopy area of the 0.8 m high celery crop. The internal humidity of the canopy is higher than 80%; it forms a gradient from the bottom to the top, with the highest humidity approaching 95%. By comparing the simulated cloud maps, it can be found that the humidity distribution of the 0.8 m high celery canopy is similar to that of the 1 m high one.

From the top to the bottom of the celery canopy, the temperature decreases while the humidity increases during heating through solar radiation; in the horizontal direction (from the wall to the opening of the inner membrane), the temperature increases while the humidity decreases. These results indicate that low-porosity canopies have large differences in temperature and humidity.

Because the inner membrane was closed at 16:00, the greenhouse was in a cooling stage at night. The main sources of heat in the greenhouse were the radiant heat of the soil, walls, and crop canopy. As can be seen in Figure 6, the lowest temperature measured at night in the plastic film part near the outer soil with the 0.8 and 1 m high canopies is 4.9 and 5.1°C, respectively. The highest temperature recorded at the bottom of the 0.8 and 1 m high crop canopies is 8.1 and 8.3°C, respectively. The humidity inside the greenhouse

Table 2: Boundary condition parameters.

Material	Density ($kg\,m^{-3}$)	Thermal conductivity ($W\,m^{-1}\,K^{-1}$)	Specific heat capacity ($J\,kg^{-1}\,K^{-1}$)	Absorption rate (%)	Refractive index (%)
Plastic film	420	0.14	1380	0.1	7.5
Curtain	650	0.09	2512	0.9	—
Wall	1860	0.56	1240	0.9	—
Soil	1700	0.9	2010	0.9	—
Cement	2100	1.3	880	0.9	
Air	1.29	0.023	1007	—	1
Celery	1070	0.3	2800	0.9	—

reaches values above 90%. At this time, the greenhouse is in the cooling stage, and the overall humidity difference in the greenhouse is small. The humidity in the area of the porous medium layer is the same as that inside the greenhouse. With the 0.8 and 1 m high canopies, the highest humidity recorded in the cover film near the southern boundary is 94% and 96%, and the lowest humidity recorded near the north wall is 87% and 85%, respectively. The difference in the humidity between the bottom and the area 5 cm above the 0.8 and 1 m high canopies is 1.1% and 0.5%, respectively.

From the bottom to the top of the canopy, the internal temperature of the celery canopy decreases, and the humidity does not change significantly during cooling (without solar radiation). From the wall to the opening of the greenhouse (horizontal direction), the temperature increases and the humidity decreases. These results indicate that the canopy porosity and height do not affect the temperature and humidity significantly.

3.3. Simulation Verification Analysis. To verify the simulation model, we compared the simulation and measured results of the temperature and humidity with the canopies with different heights at 11:00 and 0:00 a.m. We selected the ATH sensors with number labels 2, 5, 7, 8, 9, 11, and 15 for temperature and humidity verification [34]. The horizontal and vertical temperature and humidity distributions of the crop canopy could be observed through selected measuring points. The ATH sensor No. 2, 5, 8, and 11 were used for the verification of the temperature and humidity results in the vertical direction of the canopy, while sensor No. 7, 8, and 9 were used for the verification in the horizontal direction. ATH sensor No. 15 was used as the environmental comparison point in the greenhouse. Figure 7 shows the validation results.

From the figure, it can be observed the overall trends of temperature and humidity distribution are consistent in the 0.8 and 1 m high canopies. Except for test point No. 9, the simulation temperature values are lower than the measured ones. The simulated humidity values at test points 2, 5, 7, 8, and 9 are lower than the measured values, while the opposite trend is observed at test points 11 and 15. At 11:00 and 0:00 a.m., the relative errors of the temperature are 7.06% and 6.64%, respectively; the corresponding values of the humidity are 4.34% and 6.35. The root mean square errors of the temperature and humidity with the 0.8 m high celery canopy are 0.56 and 2.86 during the day and 0.24 and 0.81 at night, respectively; the corresponding values for the 1 m high celery canopy are 0.51 and 2.26 during the day and 0.259 and 0.78 at night.

4. Discussion

The double-layer film solar greenhouse was found to control the solar radiant energy transmitted through the area between the inner and outer membranes. The opening size and time of the inner membrane were found to affect the temperature and humidity distribution of the greenhouse environment and crop microenvironment. The temperature and humidity in the crop microenvironment with the canopy structure were found to differ from the greenhouse environment. Under solar radiation, the crop canopy temperature was lower than the ambient temperature, and its humidity was higher than the ambient humidity. Boulard and Roy argued that the characteristic parameters of the porous medium on the canopy are the main factors affecting the mass and heat exchange between the crop and the environment. However, they regarded the crop canopy as a whole and studied the temperature and humidity of the canopy surface. Using advanced light modeling techniques, Zhang simulated the surface temperature of each greenhouse component and the crop at the organ level down to individual leaves. An accurate and complex modeling of crops was carried out, but the long period of simulation was not conducive to timely guidance and suggestions for crop production. Xu et al. developed a radiation model of a solar greenhouse and found that the temperature and humidity of the crop canopy are significantly affected by solar radiation [35]. Adeyemi used the water stress index to describe the temperature and humidity distribution characteristics of the crop canopy under irrigation conditions [36]. Xu and Adeyemi conducted research on solar radiation and water transport, respectively, but lacked analysis of canopy physical properties and model construction. Our study further verifies that the crop canopy surface effectively blocked solar radiation and that there was a difference in temperature and humidity distribution inside the canopy.

From the above mentioned studies and the results of this study, it can be concluded that under radiation, the internal temperature and humidity of the canopy are mainly affected by the canopy structure and parameters. Mass and heat were

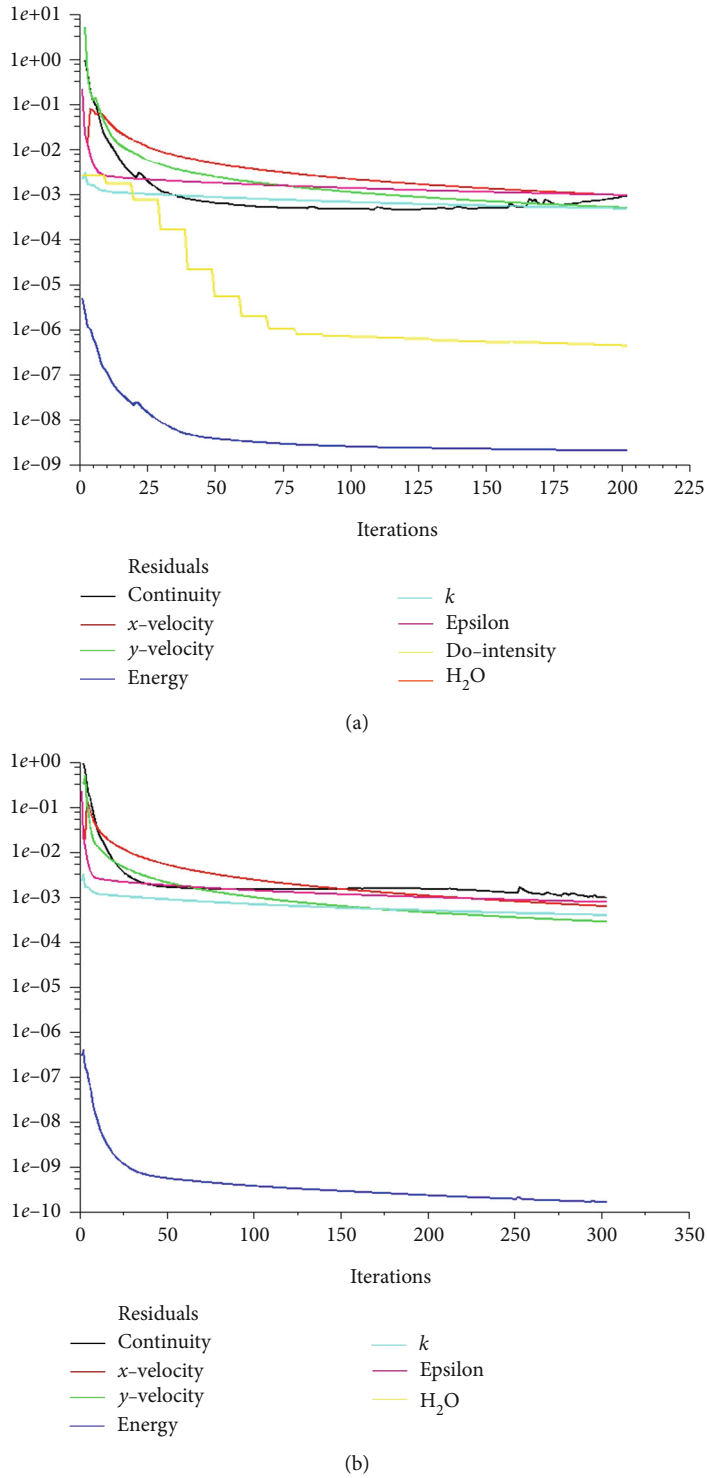

Figure 4: (a) Daytime and (b) nighttime error iteration curves.

exchanged through the canopy surface. The temperature and humidity inside the canopy formed a layered distribution according to the structure of the canopy. This suggests that the distribution of temperature and humidity can be modeled relatively easily by setting the plant porosity of crops appropriately. While some studies [37–39] reported that the crop growth can be enhanced by controlling the environmental conditions in the greenhouses, our results indicate that crops grown in the greenhouse require environmental conditions somewhat different from those of the greenhouse. Therefore, we conclude that the growth of greenhouse crops can be enhanced by setting a controlled temperature and humidity

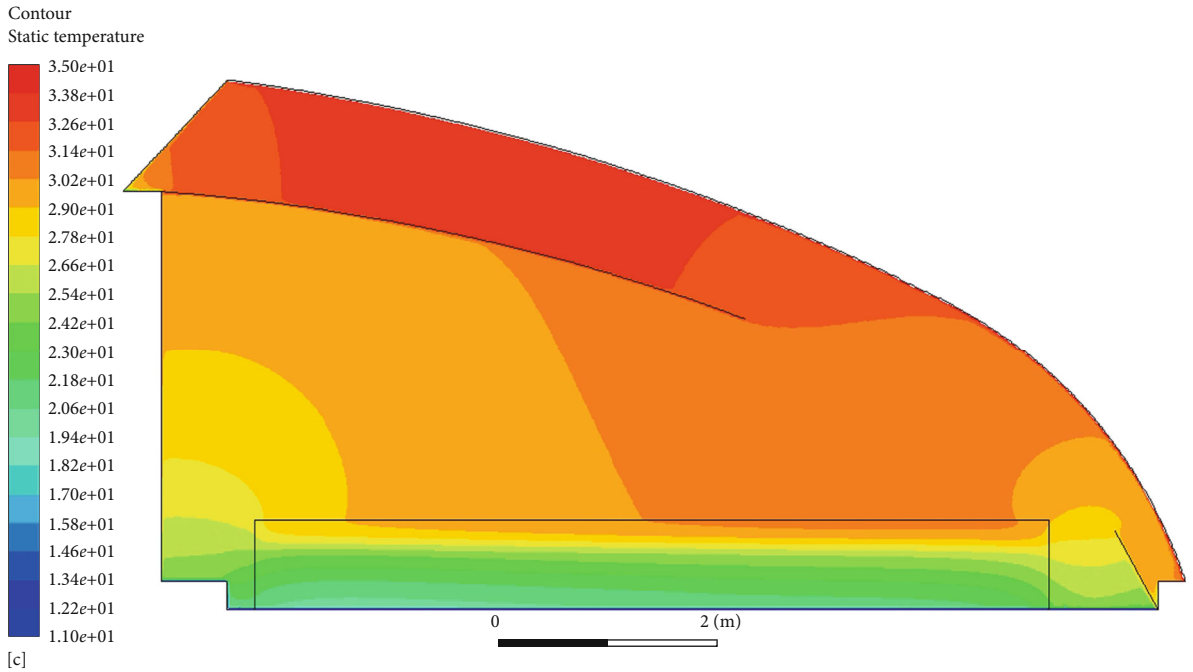

(a)

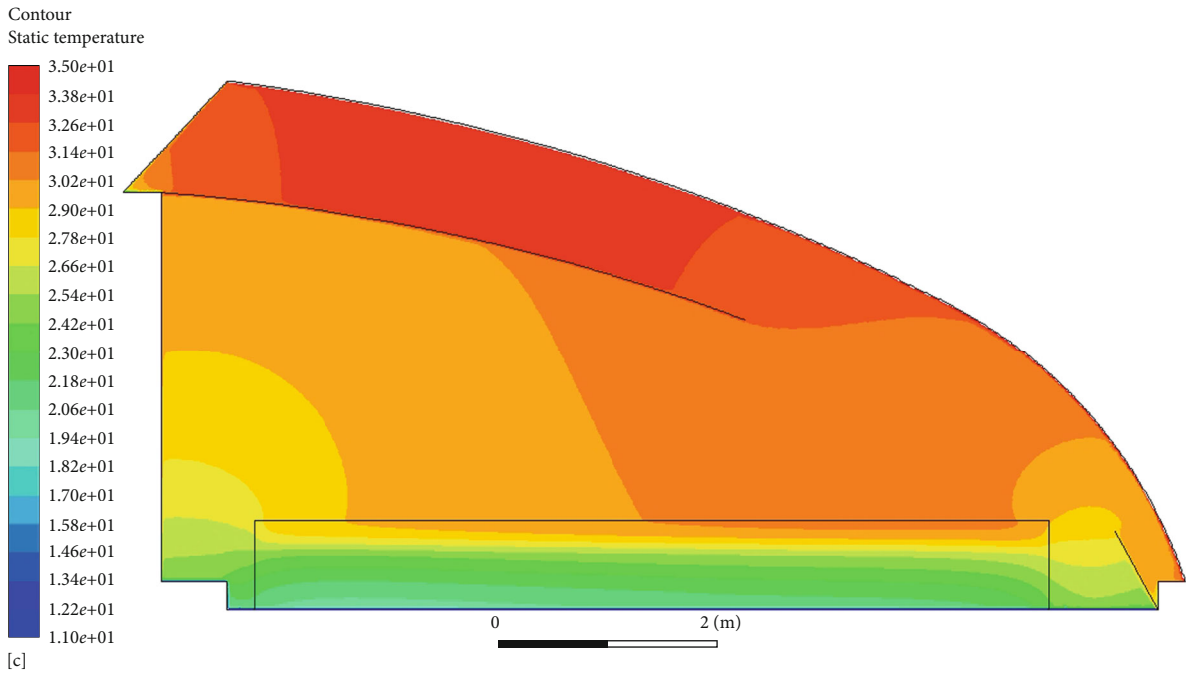

(b)

Figure 5: Continued.

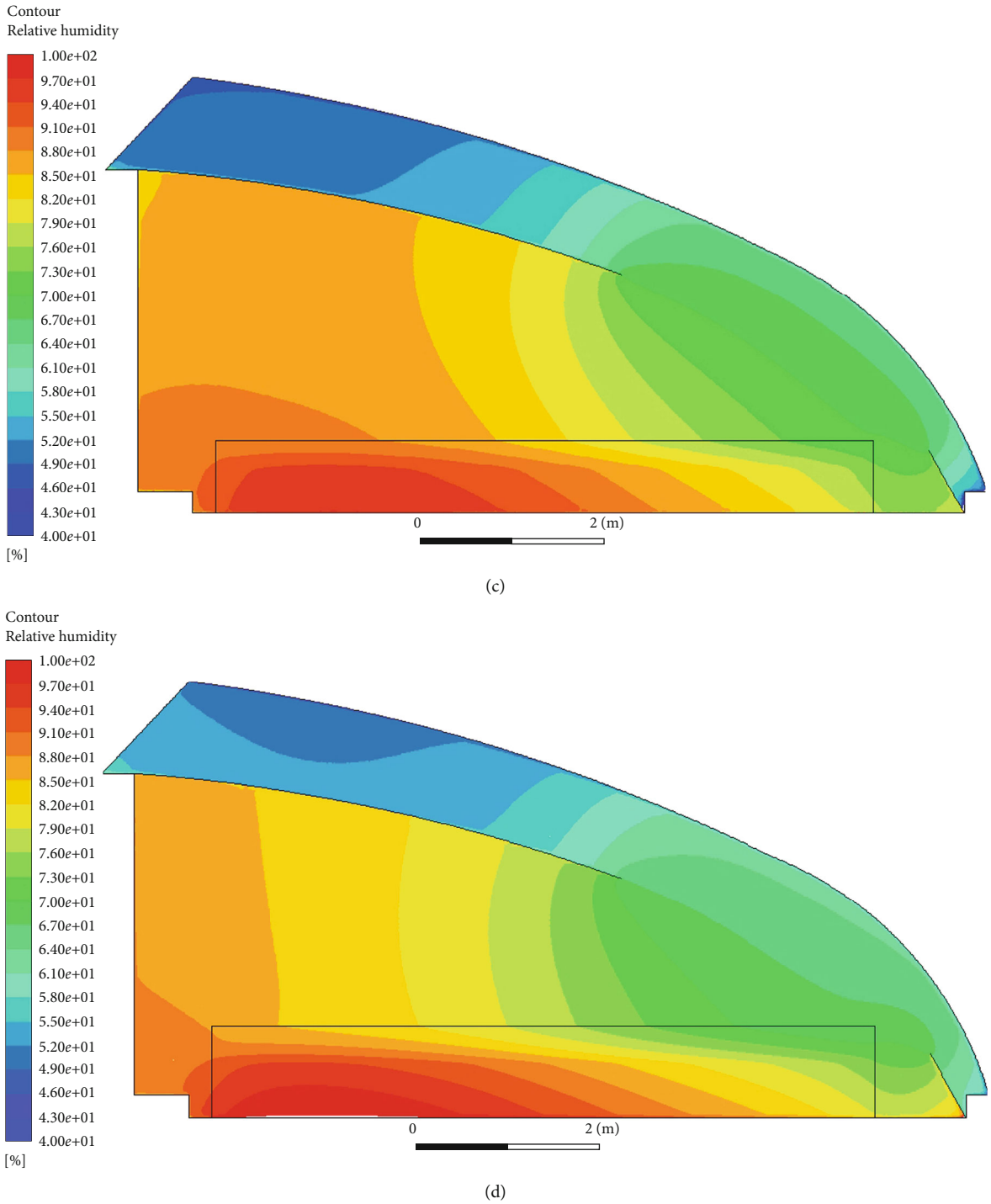

Figure 5: Temperature and humidity distributions at 11:00 a.m.: temperature distribution with canopy height of (a) 0.8 m and (b) 1 m; humidity distribution with canopy height of (c) 0.8 m and (d) 1 m.

range through the use of auxiliary equipment, such as heating, ventilation, and irrigation systems, different crop irrigation systems, and by trimming the shape of the crop canopy to facilitate light interception.

Unlike the traditional greenhouse monitoring and analysis system, the CFD simulation with the porous media canopy model can be used to record the internal microenvironment status of the canopy using a greenhouse detection system. Furthermore, the CFD method allows faster collection and analysis of the results, which is important for pest control, greenhouse ventilation, irrigation, and other aspects of intensive crop production. However, there are some issues that should be investigated further. First, the porous media model uses the average porosity of the celery crop canopy,

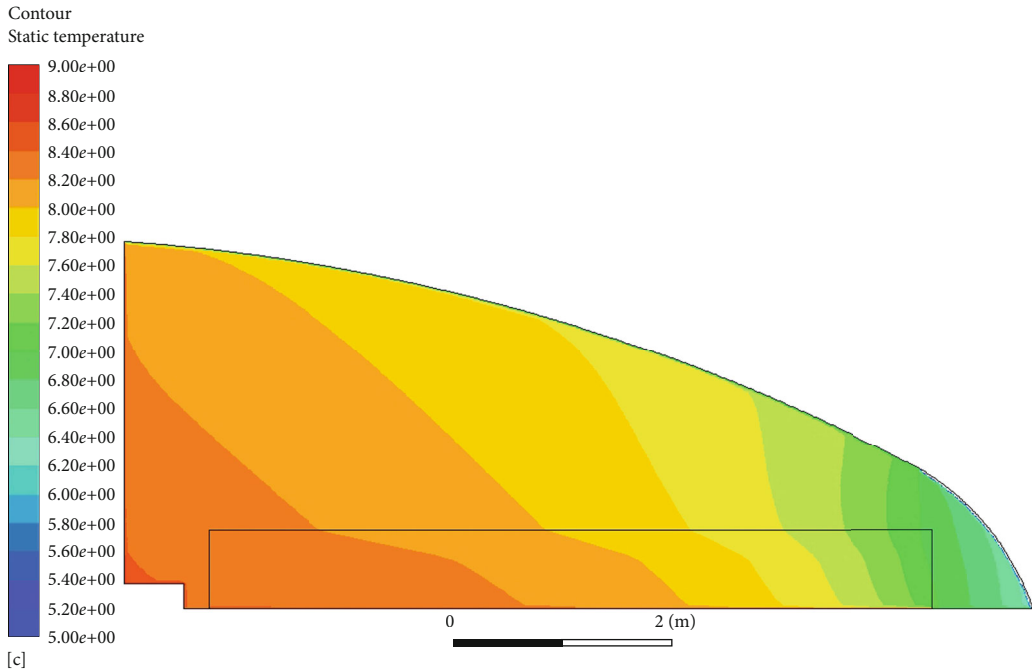

(a)

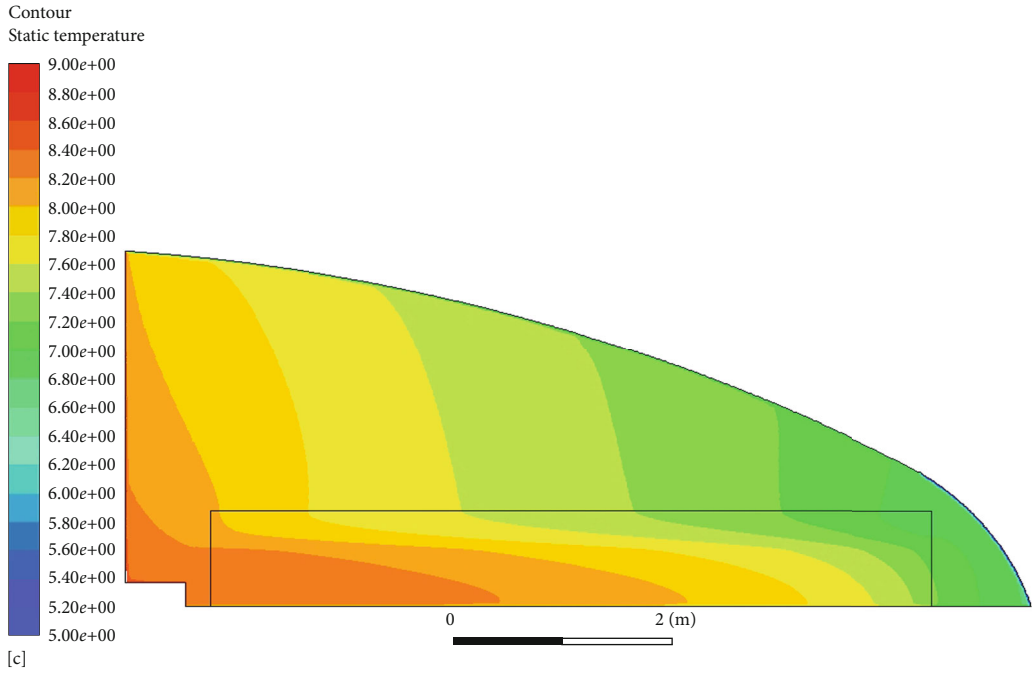

(b)

Figure 6: Continued.

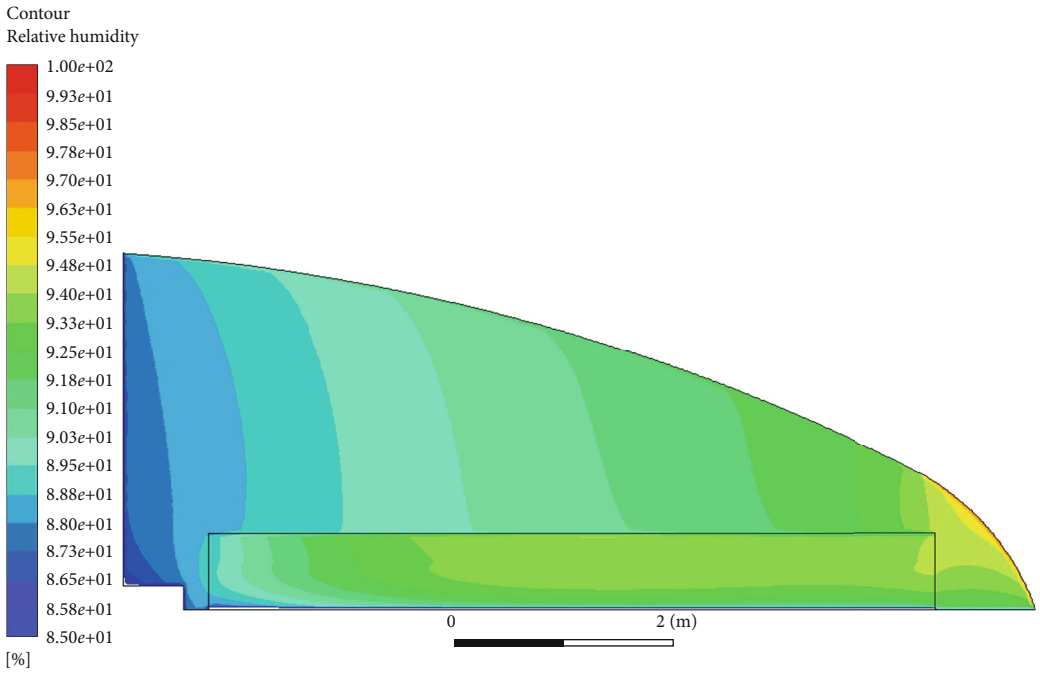

(c)

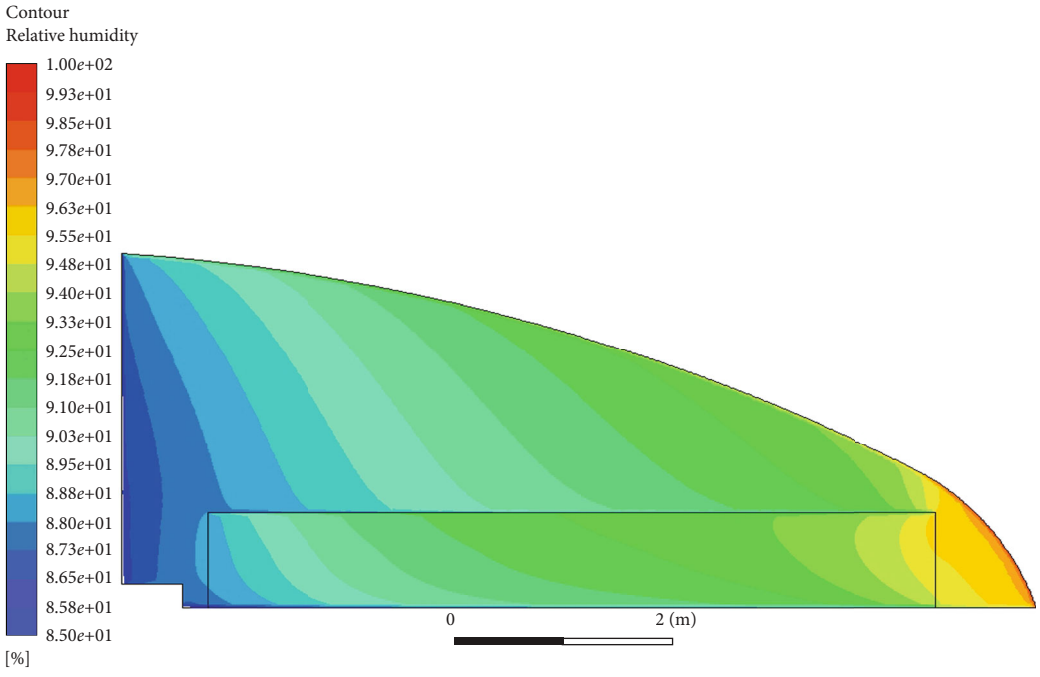

(d)

Figure 6: Temperature and humidity distributions at 0:00 a.m.: temperature distribution with canopy height of (a) 0.8 m and (b) 1 m; humidity distribution with canopy height of (c) 0.8 m and (d) 1 m.

and errors may occur in areas where the porosity varies greatly. Furthermore, the simulation regards the boundary conditions of the greenhouse environment as a whole; however, there are certain differences in space. These two issues are the main factors that cause simulation errors. Second, obtaining data through the greenhouse detection system requires human operation to import the ANSYS Fluent for CFD simulation analysis [40].

In the future, the accuracy of the simulation could be improved by dividing the canopy model into multiple combined layers with different porosities. Based on the results of this study, three-dimensional CFD simulation studies with auxiliary facilities should be carried out to further explore the spatial distribution of microenvironmental factors in a crop canopy under greenhouse conditions.

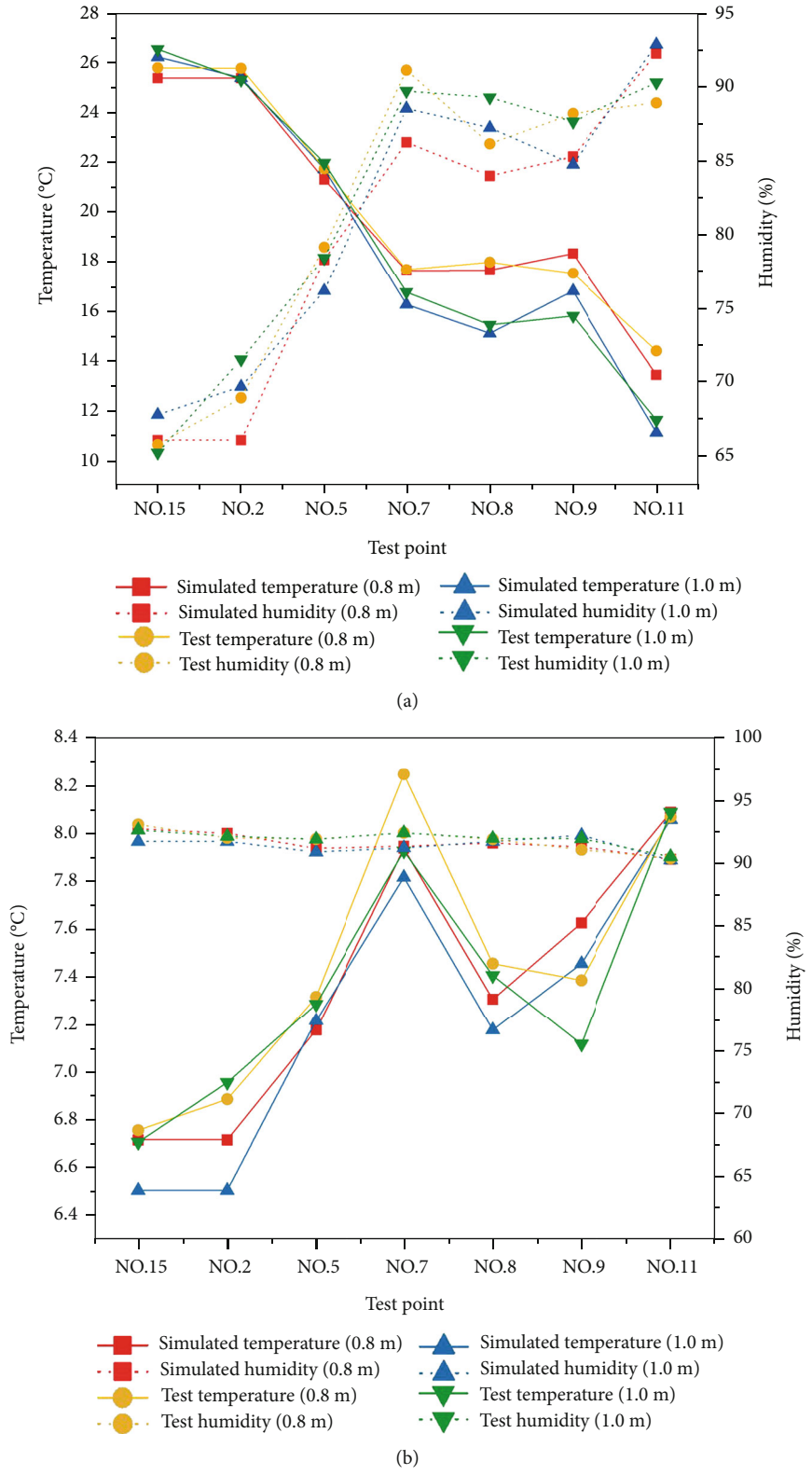

Figure 7: Comparison of simulated and actual measured results on temperature and humidity with canopy height of 0.8 (a) and (b) 1.0 m.

5. Conclusions

We proposed a greenhouse microenvironment testing system that can monitor environmental factors (i.e., temperature and humidity) using CFD simulations with the porous media canopy model in ANSYS Fluent.

The results of this study showed that the temperature and humidity of the canopy interior changed spatially and

differed greatly from those in the greenhouse under solar radiation conditions. The temperature and humidity of the celery canopy were found to be approximately 4–14°C lower and 10%–30% higher than those of the surroundings. As the canopy grew, the differences in temperature and humidity between the canopy and other parts of the greenhouse increased.

The porous medium model could accurately simulate the heat and mass transfer between the celery crop and greenhouse air and soil. With the simulation method proposed in this study, the production of crops in greenhouses can be modeled and digitized.

Data Availability

The raw/processed data required to reproduce the results obtained in this study cannot be shared at this time because they are used in an ongoing study.

Conflicts of Interest

The authors declare no conflicts of interest.

Authors' Contributions

Wei, J is responsible for the conceptualization, methodology, validation, resources, spatial analysis, writing (original draft preparation), writing (review and editing), visualization, and funding acquisition. Qi, L and Rui, S are responsible for the resources, writing (original draft preparation), and data curation. Lijun, G is responsible for the resources, software, and formal analysis. Kunyu, L is responsible for the resources, software, and investigation. Na, T is responsible for the funding acquisition, writing (review and editing), and visualization. All authors approved the final version of the manuscript.

Acknowledgments

This research was funded by the National Natural Science Foundation of China (No. 61663038) and the Inner Mongolia Natural Science Foundation of China (No. 2019MS05027). The authors are grateful to the editor and reviewers for their constructive comments. We also thank Mr. Qin H, School of Energy Power and Mechanical Engineering, North China Electric Power University, for his assistance with the simulation by ANSYS Fluent and ICEM.

References

[1] G. Tong, D. M. Christopher, and B. Li, "Numerical modelling of temperature variations in a Chinese solar greenhouse," *Computers and Electronics in Agriculture*, vol. 68, pp. 129–139, 2009.

[2] H. Fatnassi, T. Boulard, and L. Bouirden, "Simulation of climatic conditions in full-scale greenhouse fitted with insect-proof screens," *Agricultural and Forest Meteorology*, vol. 118, no. 1-2, pp. 97–111, 2003.

[3] E. Tamimi and M. Kacira, "Analysis of climate uniformity in a naturally ventilated greenhouse equipped with high pressure fogging system using computational fluid dynamics," *Acta Horticulturae*, vol. 1008, pp. 177–183, 2013.

[4] A. Kichah, P.-E. Bournet, C. Migeon, and G. Chasséria, "Experimental and numerical study of heat and mass transfer occurring at plant level inside a greenhouse," *Acta Horticulturae*, vol. 893, pp. 621–628, 2011.

[5] C. Kittas and T. Bartzanas, "Greenhouse microclimate and dehumidification effectiveness under different ventilator configurations," *Building and Environment*, vol. 42, no. 10, pp. 3774–3784, 2007.

[6] F. Zhang, H. Fang, Q. C. Yang et al., "Ventilation simulation in a large-scale greenhouse based on CFD," *Chinese Journal of Agrometeorology*, vol. 38, no. 4, pp. 221–229, 2017.

[7] J. C. Roy, H. Fatnassi, T. Boulard, J. B. Pouillard, and A. Grisey, "CFD determination of the climate distribution in a semi closed greenhouse with air cooling," *Acta Horticulturae*, vol. 1170, pp. 103–110, 2017.

[8] R. Salazar, I. L. López-Cruz, A. M. Mauricio, U. Schmidt, and L. Miranda, "A physical model for water balance in a semi-closed greenhouse," *Acta Horticulturae*, vol. 1170, pp. 183–191, 2017.

[9] J. C. Roy, J. B. Pouillard, T. Boulard, H. Fatnassi, and A. Grisey, "Experimental and CFD results on the CO_2 distribution in a semi closed greenhouse," *Acta Horticulturae*, vol. 1037, pp. 993–1000, 2014.

[10] F. D. Molina-Aiz, D. L. Valera, and A. López, "Numerical and experimental study of heat and mass transfers in an Almería-type greenhouse," *Acta Horticulturae*, vol. 1170, pp. 209–217, 2017.

[11] S. Li, D. H. Willits, and C. A. Yunker, "Experimental study of a high pressure fogging system in naturally ventilated greenhouses," *Acta Horticulturae*, vol. 719, pp. 393–400, 2006.

[12] P. Zhao, G. Li, and Y. Yu, "Numerical simulation and experimental study of heat and mass transfer in fuel droplet evaporation," *Heat and Mass Transfer*, vol. 50, no. 8, pp. 1145–1154, 2014.

[13] R. Salazar, I. López, A. Rojano, U. Schmidt, and D. Dannehl, "Tomato yield prediction in a semi-closed greenhouse," *Acta Horticulturae*, vol. 1107, pp. 263–269, 2015.

[14] D. Piscia, J. I. Montero, E. Baeza, and B. J. Bailey, "A CFD greenhouse night-time condensation model," *Biosystems Engineering*, vol. 111, pp. 141–154, 2012.

[15] T. Bartzanas, T. Boulard, and C. Kittas, "Effect of vent arrangement on windward ventilation of a tunnel greenhouse," *Biosystems Engineering*, vol. 88, no. 4, pp. 479–490, 2004.

[16] T. Boulard and S. Wang, "Experimental and numerical studies on the heterogeneity of crop transpiration in a plastic tunnel," *Computers and Electronics in Agriculture*, vol. 34, pp. 173–190, 2002.

[17] M. Teitel, M. Atias, and M. Barak, "Gradients of temperature, humidity and CO_2 along a fan-ventilated greenhouse," *Biosystems Engineering*, vol. 106, no. 2, pp. 166–174, 2010.

[18] Y. Zhang, M. Henke, Y. Li et al., "High resolution 3D simulation of light climate and thermal performance of a solar greenhouse model under tomato canopy structure," *Renewable Energy*, vol. 160, pp. 730–745, 2020.

[19] R. Nebbali, J. C. Roy, and T. Boulard, "Dynamic simulation of the distributed radiative and convective climate within a cropped greenhouse," *Renewable Energy*, vol. 43, pp. 111–129, 2012.

[20] A. Vergara, E. Martinelli, E. Llobet, A. D'Amico, and C. Di Natale, "Optimized feature extraction for temperature-modulated gas sensors," *Journal of Sensors*, vol. 2009, Article ID 716316, 10 pages, 2009.

[21] S. Nomura, M. Arake, Y. Morimoto et al., "Thermal sensor circuit using thermography for temperature-controlled laser hyperthermia," *Journal of Sensors*, vol. 2017, Article ID 3738046, 7 pages, 2017.

[22] R. Zhao, G. Shao, N. Li, C. Xu, and L. An, "Development of a wireless temperature sensor using polymer-derived ceramics," *Journal of Sensors*, vol. 2016, Article ID 8624817, 5 pages, 2016.

[23] H. B. Ali, P. E. Bournet, V. Danjou, and C. Migeon, "CFD analysis of the climate inside a closed greenhouse at night including condensation and crop transpiration," *Acta Horticulturae*, vol. 1170, pp. 53–60, 2017.

[24] O. Kolditz and O. Kolditz, "Porous Media," in *Computational Methods in Environmental Fluid Mechanics*, International Society for Horticultural Science, 2002.

[25] T. Bartzanas, T. Boulard, and C. Kittas, "Numerical simulation of the airflow and temperature distribution in a tunnel greenhouse equipped with insect-proof screen in the openings," *Computers and Electronics in Agriculture*, vol. 34, pp. 207–221, 2002.

[26] S. Hussain, P. H. Oosthuizen, and A. Kalendar, "Evaluation of various turbulence models for the prediction of the airflow and temperature distributions in atria," *Energy and Buildings*, vol. 48, pp. 18–28, 2012.

[27] M. Córdova and B. Stoffel, "Comparison of various turbulence models in respect to their suitability for CFD calculations of diffuser flows," in *Proceedings of the ASME Turbo Expo, vol. 6 PART B*, pp. 1343–1353, Barcelona, Spain, 2006.

[28] M. Lateb, C. Masson, T. Stathopoulos, and C. Bédard, "Comparison of various types of k-ε models for pollutant emissions around a two-building configuration," *Journal of Wind Engineering and Industrial Aerodynamics*, vol. 115, pp. 9–21, 2013.

[29] K. Kim, J. Y. Yoon, H. J. Kwon et al., "3-D CFD analysis of relative humidity distribution in greenhouse with a fog cooling system and refrigerative dehumidifiers," *Biosystems Engineering*, vol. 100, no. 2, pp. 245–255, 2008.

[30] E. Santolini, B. Pulvirenti, S. Benni, L. Barbaresi, D. Torreggiani, and P. Tassinari, "Numerical study of wind-driven natural ventilation in a greenhouse with screens," *Computers and Electronics in Agriculture*, vol. 149, pp. 41–53, 2018.

[31] Y. Li, G. Sun, and X. Wang, "Temperature field-wind velocity field optimum control of greenhouse environment based on CFD model," *Mathematical Problems in Engineering*, vol. 2014, Article ID 949128, 9 pages, 2014.

[32] S.-z. Liu, Y. He, Y.-b. Zhang, and X.-w. Miao, "Prediction and analysis model of temperature and its application to a natural ventilation multi-span plastic greenhouse equipped with insect-proof screen," *Journal of Zhejiang University: Science*, vol. 6B, no. 6, pp. 523–529, 2005.

[33] A. Kichah, P. E. Bournet, C. Migeon, and T. Boulard, "Measurement and CFD simulation of microclimate characteristics and transpiration of an Impatiens pot plant crop in a greenhouse," *Biosystems Engineering*, vol. 112, no. 1, pp. 22–34, 2012.

[34] J. K. Valiunas, M. Tenuta, and G. Das, "A gas cell based on hollow-core photonic crystal fiber (PCF) and its application for the detection of greenhouse gas (GHG): Nitrous oxide (N_2O)," *Journal of Sensors*, vol. 2016, Article ID 7678315, 9 pages, 2016.

[35] H. J. Xu, Y. F. Cao, Y. R. Li, J. Gao, W. J. Jiang, and Z. R. Zou, "Establishment and application of solar radiation model in solar greenhouse," *Transactions of the Chinese Society of Agricultural Engineering*, vol. 35, no. 7, pp. 160–169, 2019.

[36] O. Adeyemi, I. Grove, S. Peets, Y. Domun, and T. Norton, "Dynamic modelling of the baseline temperatures for computation of the crop water stress index (CWSI) of a greenhouse cultivated lettuce crop," *Computers and Electronics in Agriculture*, vol. 153, pp. 102–114, 2018.

[37] T. Jia, H. Y. Wang, D. Y. Chen et al., "3D temperature distribution model based on thermal infrared image," *Journal of Sensors*, vol. 2017, Article ID 4815021, 10 pages, 2017.

[38] T. Kuroyanagi, "Prediction of leakage rate of a greenhouse using computational fluid dynamics," *Acta Horticulturae*, vol. 1170, pp. 87–94, 2017.

[39] J. Chen, F. Xu, D. Tan, Z. Shen, L. Zhang, and Q. Ai, "A control method for agricultural greenhouses heating based on computational fluid dynamics and energy prediction model," *Applied Energy*, vol. 141, pp. 106–118, 2015.

[40] Y. Zhou, Y. Xie, and L. Shao, "Simulation of the core technology of a greenhouse-monitoring system based on a wireless sensor network," *International Journal of Online Engineering*, vol. 12, no. 5, pp. 43–47, 2006.

Hindawi
Journal of Sensors
Volume 2020, Article ID 8849419, 14 pages
https://doi.org/10.1155/2020/8849419

Research Article

Effect of Microsprinkler Irrigation under Plastic Film on Photosynthesis and Fruit Yield of Greenhouse Tomato

Mingzhi Zhang,[1,2] **Zhenguang Lu**,[2] **Qingjun Bai**,[1] **Yushun Zhang**,[2] **Xinqiang Qiu**,[2] **Haixia Qin**,[2] **Haochen Yang**,[2] **and Yanping Wang**[2]

[1]*State Key Laboratory of Eco-Hydraulics in Northwest Arid Region of China, Xi'an University of Technology, Xi'an 710048, China*
[2]*Henan Provincial Water Conservancy Research Institute, Zhengzhou 450000, China*

Correspondence should be addressed to Qingjun Bai; bqj@xaut.edu.cn

Received 10 August 2020; Revised 16 September 2020; Accepted 30 September 2020; Published 9 October 2020

Academic Editor: Liang Xu

The aim of this study is to exam the effect of microsprinkler irrigation technology under plastic film (MSPF) and to evaluate the reasonable micropore group spacing and capillary arrangement density in the greenhouse. Compared with drip irrigation under plastic film (DIPF) and microsprinkling irrigation (MSI) conditions, the effects of different micropore group spacing (L1: 30 cm micropore group spacing, L2: 50 cm micropore group spacing) and capillary arrangement density (C1: one pipe for one row, C2: one pipe for two rows, and C3: one pipe for three rows) with the MSPF on photosynthetic characteristics and fruit yield of tomatoes were studied using completely randomized trial design. The results showed that under the same irrigation amount, compared with DIPF and MSI, the photosynthetic rate of tomatoes treated with L1C2 increased by 8.24% and 13.55%, respectively. The total dry matter accumulation, yield, and water use efficiency at condition of L1C2 increased by 12.16%, 19.39%, and 10.03% compared with DIPF and 26.38%, 20.46%, and 31.02% compared with MSI, respectively. The results provide evidence that the MSPF can be applied to greenhouse tomatoes. The photosynthetic rate, total dry matter accumulation, yield, and water use efficiency of tomato leaves cultivated at a micropore group spacing of 30 cm were 1.07, 1.13, 1.14, and 1.13 times higher than those of 50 cm, respectively. With the decrease in capillary arrangement density, the photosynthetic characteristics of the tomato leaves, the total dry matter accumulation, and yield of tomatoes all experienced a decline. It is recommended to use a combination of one pipe for two rows of capillaries at a 30 cm micropore group spacing as the technical parameter of greenhouse tomato with MSPF in arid and semiarid sandy loam soils.

1. Introduction

The development of facility agriculture provides a strong guarantee for vegetable production in arid and semiarid sandy loam. However, the irrigation water for facility agriculture in this area mainly comes from groundwater, and the resulting development of groundwater resources aggravates the water crisis in these arid and semiarid areas, so there is an urgent need to alleviate the overuse of irrigation water in this area [1]. Saving water resources has become a current research hotspot. As a common irrigation method of tomato in this area, drip irrigation is an advantageous approach owing to its water-saving, fertilizer-saving, and labor-saving features. It has been widely used to cultivate tomato, pepper, melon, and other crops [2–4]. Owing to the existence of sediment, chemical precipitates, or biomass in the irrigation water body, it is easy to cause blockage of drip irrigation system, reduce irrigation uniformity, reduce crop yield, increase cost, and so on [5, 6]. Drip irrigation belongs to local irrigation, and the soil wetting body per unit plough layer is limited, which restricts the growth of crop roots [7, 8].

Microsprinkler irrigation is an irrigation form, where sprinkler (micro) pores are arranged in groups on the wall of a thin-walled drip irrigation plastic pipe (flat strip after coiling) [9]. The energy dissipation structure of the emitter is removed. Under the same working pressure, the flow rate of microsprinkler irrigation is about 15 times that of labyrinth drip irrigation, and it has a strong sediment-carrying capacity and anticlogging performance. This technique can solve the clogging problem of drip irrigation emitters [5, 6].

At the same time, the flow rate of a single microsprinkler is much higher than that of drip irrigation, which is easy to increase the ratio of soil water peak horizontal to vertical migration distance and improve the water uniformity of soil wetting body and unit tillage layer [10, 11]. It has advantages of decreasing the restriction of horizontal root growth and short irrigation duration [12, 13]. For this reason, microsprinkler irrigation has achieved good results with total growth amount and yield in winter wheat, summer corn, lawn, seedlings, and other crops [12, 14–16]. However, the shape, area, and uniformity of soil wetting in the microsprinkler irrigation area are affected by wind speed. In addition, there are still some problems, such as difficulties in weed control and high damage rate of microsprinklers, which hinder the treatment of microsprinkler irrigation [17–19]. The development of facility agriculture provides a good application environment for microsprinkler irrigation, such as flat land, wind-free chamber, and short capillary laying distance [20]. However, the facility agricultural space is relatively closed, and microsprinkler irrigation spray atomization is easy to increase air humidity. High temperature and high humidity have been proved beneficial to the occurrence of crop diseases and insect pests [21–23], resulting in less use of microsprinkler irrigation in facility agriculture. Plastic film mulching provides a solution for the application of microsprinkler irrigation in facility agriculture. Plastic film mulching can restrain the water jet of microsprinkler irrigation, reduce spray atomization and ineffective evaporation, and improve the utilization efficiency of irrigation water [24, 25]. Therefore, the combination of microsprinkler irrigation and plastic film technology can make up for the deficiency of micropores used in the greenhouse. This technique is called microsprinkler irrigation under plastic film (MSPF, see Figure 1). The exploration of MSPF is of great significance for enriching the greenhouse microirrigation technology system, reducing crop water requirement, and improving crop yield and quality.

Tomato, as one of the main vegetables grown in facility agriculture, has rich nutritional value [26, 27]. Photosynthesis is the basis of tomato growth, increasing yield and improving quality. Photosynthesis is affected by heredity, leaf age, leaf angle, leaf shape, and other internal factors, also affected by the external environment, soil water content is one of the main influencing factors of the external environment [18, 28]. In production practice, farmers often use different ways of irrigation, which can not only save water resources but also change the form of irrigation water into the soil, which indirectly affects the distribution of water in the soil and near the ground. Compared with conventional drip irrigation, drip irrigation under plastic film can change soil microenvironment, increase soil volume water content, and help to increase photosynthesis and yield [29]. The emitter spacing of the pipe and capillary arrangement density of the pipe directly determine the distribution of water in the irrigated soil, altering the soil water use efficiency (WUE) and creating a microenvironment for plant growth. Consequently, a foundation was laid out for water-saving crops with high yield, a larger capillary arrangement density results in a more uniform horizontal water content distribution and

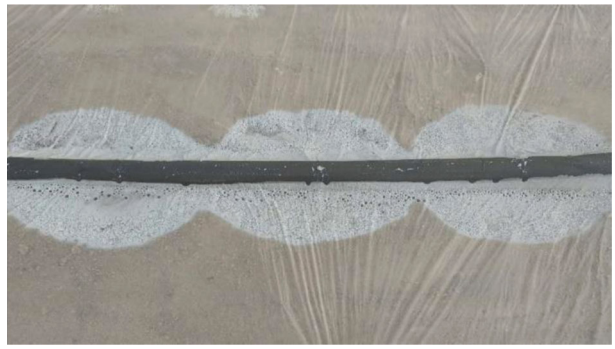

Figure 1: Microsprinkler irrigation under plastic film (MSPF).

a higher the leaf photosynthetic rate, chlorophyll, leaf area index, dry matter accumulation, and crop yield. However, the higher capillary arrangement density generally can increase investment cost and reduce crop WUE [8, 30–32]. Previous studies have also shown that different emitter spacing can adjust the volume shape and moisture of moist soil. At the same emitter flow rate, the time for the average soil moisture content between emitters to reach the peak is shorter. When the spacing between emitters is reduced from 80 to 30 cm, the horizontal wetting shape between emitters is approximately rectangular and the more uniform the wetting body is between the two emitter [11]. The application can reduce the irrigation water consumption, improving photosynthesis of leaves and the irrigation water utilization efficiency [33–35]. When the emitter spacing increased from 15 to 30 cm, the onion yield increased at first and then decreased [33–35].

At present, the related studies on crop photosynthetic characteristics, dry matter accumulation, yield, and WUE are mainly focused on emitter spacing and capillary arrangement density with a small flow rate of drip. However, there are few studies evaluating the effects of different micropore group spacing and capillary arrangement density of MSPF on photosynthetic characteristics, dry matter accumulation, yield, and WUE of greenhouse crops. As the focus of tomato yield research in this area, there are a variety of models for analyzing the effects on tomato yield, such as linear regression, principal component analysis, simple correlation analysis, and channel analysis [36–38]. Nonetheless, these methods are difficult to simultaneously obtain the strength of the causal relationships among multiple variables in the system. The AMOS structural equation provides a solution to determine the intensity of causality among multiple variables. It has been widely used in the social science field [39] and ecological field [40]. However, relatively few studies were performed to analyze the relationship between photosynthetic characteristics, dry matter accumulation, and yield of tomato by using AMOS structural equation under plastic film microsprinkler irrigation.

Therefore, this study intends to take the effects of drip irrigation under plastic film (DIPF) and microsprinkler irrigation (MSI) as controls to explore the effects of different micropore group spacing and capillary arrangement density on photosynthetic characteristics, dry matter accumulation,

and yield of greenhouse tomato with the MSPF. The relationships among photosynthetic characteristics, dry matter accumulation, and yield of tomato in greenhouse under MSPF was determined by the AMOS structure equation. The most suitable capillary arrangement density and micropore group spacing combination model of MSPF for tomato in arid and semiarid sandy loam soil of facility agriculture was obtained. This paper provides findings for the enrichment of tomato microirrigation technology system and offers valuable data support and theoretical basis by greenhouse experiment data analysis for water saving, yield enhancement, and quality improvement of agricultural crops in this region.

2. Materials and Methods

2.1. Experimental Site and Management. The experiment was carried out from 27 March 2019 to 30 January 2020 in a greenhouse at the Modern Agricultural Science and Technology Exhibition Centre, Xi'an City, Shaanxi Province (108°52′E, 34°03′N). The region exhibits a warm temperate semihumid continental monsoon climate and located at an altitude of 435 m above sea level. The annual average temperature of the region is 13.3°C, and the annual average rainfall is 507.7–719.8 mm. The precipitation from August to October accounts for more than 60% of the annual precipitation and the frost-free period ranges from 219 to 233 days. The soil is sandy loam, and the mass fractions of sand, silt, and clay are 63.9%, 29.63%, and 6.47%, respectively. The average bulk density of the 1.0 m soil layer was 1.48 g/cm^3, the water holding capacity of field weight was 27.40%, and the depth of groundwater table on the site exceeded 30 m. The content of organic matter, total phosphorus (P), total potassium (K), total nitrogen, available nitrogen, available P, and available K in the plough layer before sowing were 15.53 g/kg, 10.12 g/kg, 2.01 g/kg, 1.36 g/kg, 70.45 mg/kg, 112 mg/kg, and 85.23 mg/kg, respectively. The irrigation water originated from groundwater, the pH of which was 6.8, the chemical oxygen demand (COD) was 53.2 mg/L, the anionic surfactant content was 3.2 mg/L, and the chloride content was 0.48 mg/L.

The greenhouse (85 m long and 15 m wide) was oriented from north to south. The tomato variety 'Jingfan 401' (Jingyan Yinong Seed Sci-tech Co. Ltd., Beijing, China), with a 50 cm row spacing and a 40 cm plant spacing, was planted on a ridge. The length of the ridge was 3.4 m. The width was 1.2 m. The irrigation plot is shown in Figure 2. The distance between each plot was 4 m; one 1.0 m deep building waterproof film made up of styrene-butadiene-styrene block copolymer was buried in the middle to prevent the horizontal infiltration and movement of soil moisture, thus avoiding their effect on other plot experiments. The source of irrigation water in the region was groundwater. To ensure the survival of seedlings on the day of planting, the irrigation was unified with reference to the local tomato planting experience. The microsprinkler pipe of MSPF (Hebei Plentirain Irrigation Equipment Technology Co., Ltd., Hebei, China) adopts thin-walled oblique 3 micropore with a diameter of 32 mm and a micropore diameter of 0.8 mm. The micropore group spacing is shown in the experimental design (see Table 1). The control drip irrigation under plastic film (DIPF, CK1, Hebei Plentirain Irrigation Equipment Technology Co., Ltd., Hebei, China) with thin-wall labyrinth tooth channel was selected. The geometric parameters of the channel were 54.3*1.1*0.83 mm^3, the distance between emitters was 30 cm, and the emitter flow rate was 2 L/h. The control microsprinkler irrigation (MSI, CK2, Hebei Plentirain Irrigation Equipment Technology Co. Ltd., Hebei, China) adopts thin-walled oblique 3 micropore pipe with a diameter of 32 mm and a micropore diameter of 0.8 mm. The micropore group spacing is 10 cm.

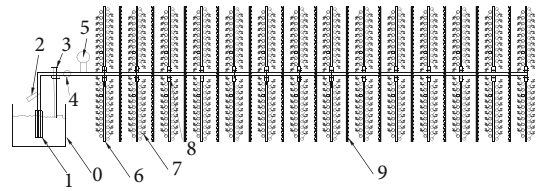

Figure 2: Schematic diagram of greenhouse layout. Note: 0: water tank; 1: the pump (WQD10-12-0.75S, PEOPLE PUMB, Corp., Shanghai, China); 2: filter; 3: backwater valve; 4: electromagnetic flowmeter; 5: pressure gauge; 6: capillary; 7: tomato; 8: capillary valve; 9: plastic screens.

Tomato plants were topped when the four-eared fruit were retained, and the field management measures such as fertilizer irrigation, irrigation, and medicine were the same in all treatments. The irrigation water comes from the groundwater in this area. In order to ensure the survival of the seedlings on the day of planting, the irrigation was unified with reference to the local tomato planting experience. It was planted on March 27, 2019; the irrigation treatment began on April 4, 2019 and stopped on July 15, 2019.

2.2. Experimental Design. Two factors were considered in this study: micropore group spacing L (see Figure 3) and capillary arrangement density C (see Figure 4). The micropore group spacing (L) used two levels: 30 cm (L1) and 50 cm (L2); the capillary arrangement density (C) used three levels: one pipe for one row (one capillary pipe irrigated one crop, C1), one pipe for two rows (one capillary pipe irrigated two rows of crops, C2) and one pipe for three rows (one capillary pipe irrigated three rows of crops, C3). One pipe for two rows were used for both CK1 and CK2 control treatments. A total of eight treatments were implemented, each of which was repeated three times, for total of 24 test areas (see Table 1).

The irrigation amount was controlled on the basis of the cumulative evaporation from a 20 cm diameter standard pan (E_{pan}, DY.AM3, Weifang Dayu Hydrology Technology Co., Ltd., Shandong, China) following Dinc et al. and Liu et al. [41, 42]. The evaporation amount was measured at 08:00 am every 5 d. The irrigation amount was evaluated after the measurement. The W of irrigation quota was calculated according to formula (1) [43], and the irrigation times and amounts were recorded (see Figure 5).

$$W = A \times E_{pan} \times k_{cp}, \quad (1)$$

where E_{pan} represents the evaporation within the interval

Table 1: Experimental factor and design.

No.	Treatment	Irrigation method	Micropore group spacing (cm)	Capillary arrangement density	Irrigation amount (mm)
1	L1C1	MSPF	30	One pipe for one row	353.30
2	L1C2		30	One pipe for two rows	
3	L1C3		30	One pipe for three rows	
4	L2C1		50	One pipe for one row	
5	L2C2		50	One pipe for two rows	
6	L2C3		50	One pipe for three rows	
7	CK1	DIPF	30	One pipe for two rows	
8	CK2	MSI	10	One pipe for two rows	

Note: *L*: micropore group spacing; *C*: capillary arrangement density.

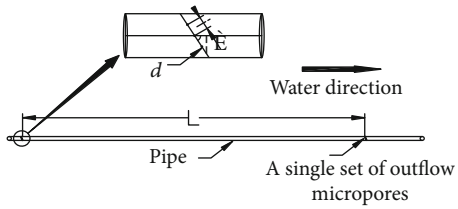

Figure 3: Schematic diagram of micropore group (inside) spacing structure parameters. Note: diameter of micropore is $d = 0.8$ mm. The internal spacing of the micropore group was $I = 0.4$ cm. The angle of micropores is 68°. The micropore group spacing is *L*.

of two irrigation, basing on the cumulative evaporation from a 20 cm diameter pan (mm); *A* represents the capillary control area (mm); and k_{cp} represents the crop-pan coefficient. In this paper, adopting adequate irrigation mode, the crop-pan coefficient of k_{cp} is 1.0 [43].

2.3. Measurements and Computational Methods

2.3.1. Photosynthesis. Three conjoined healthy leaves with sufficient light and consistent leaf position were randomly selected, and the gas exchange parameters such as net photosynthetic rate (Pn), stomatal conductance (Gs), intercellular CO_2 concentration (Ci), and transpiration rate (Tr) were measured by the LI-6400 (Li-Cor, Inc., Lincoln, Nebraska, USA) automatic portable photosynthesis system. The CO_2 gas was collected from a relatively stable air of 2 ~ 3 m. The light intensity was set at 800 μmol/(m^2·s) and the flow rate was set at μmol/s. All the samples were measured at the time of 15, 29, 56, 79, 95, and 110 days after planting (DAP) [44].

2.3.2. Chlorophyll. The leaf pigment was extracted with acetone extract, and the absorption values were measured at 665 nm, 649 nm, and 470 nm by spectrophotometer colorimetry, and the contents of chlorophyll a, chlorophyll b, carotenoid, and chlorophyll (chlorophyll = chlorophyll a + chlorophyll b) were calculated, respectively [45]. The same leaf position was selected to determine the chlorophyll test and photosynthesis.

2.3.3. Dry Matter Accumulation. During the tomato maturity period (112 DAP), three tomato plants were randomly selected in each plot, the stem of the plant was assumed as the center, and a hole was dug with a straight diameter of about 0.2 m and a depth of about 0.4 m to obtain the root system of the plant. Rhizosphere soil was carefully shaken off, and the residual root system was slowly washed to remove the soil, using a weak water flow. Then, the root system and soil were placed on a 100-mesh steel screen during flushing to minimize root loss. After washing, the stems, leaves, fruits, and roots were dried in an oven at 105°C for 15 min, followed by drying at 75°C to constant weight. Finally, the dry matter mass was obtained [46].

2.3.4. Yield and Water Use Efficiency. During the maturity period, 4 tomatoes were randomly selected from each plot and the quality of mature tomatoes was measured using an electronic scale. After obtaining yield per plant, the yield per hectare was derived.

Time-domain reflectometry soil moisture sensor (TRIME-PICO-IPH, IMKO, Inc., Ettlingen, Germany) was used to measure the soil volume moisture content at different layers of soil (0–10, 10–20, 20–30, 30–40, 40–50, 50–60, 60–70, and 70–80 cm, respectively). It was measured once before and after each growth period. Two monitoring points were selected in each district as shown in Figure 6 (monitoring point 1 was arranged at the outflow micropore; monitoring points 2 was arranged at distance m between the two groups of micropore in the vertical flow direction, where $m = 25$ cm). Water consumption (ET_a) and crop water use efficiency (WUE) were calculated using formulas (2) and (3), respectively [47]:

$$ET_a = I \pm 1000 \times H \times (\theta_{t1} - \theta_{t2}), \quad (2)$$

where ET_a represents crop water consumption during growth period (mm), *I* represents the irrigation quota of crop growth period (mm), *H* represents the depth of the wetting layer with plan ($H = 0.8$ m), and θ_{t1} and θ_{t2} represent 80 cm average soil volumetric water contents at times $t1$ and $t2$ (cm^3/cm^3), respectively.

$$WUE = 1000 * \frac{Y}{ET_a}, \quad (3)$$

where *Y* indicates crop grain yield (t/hm^2).

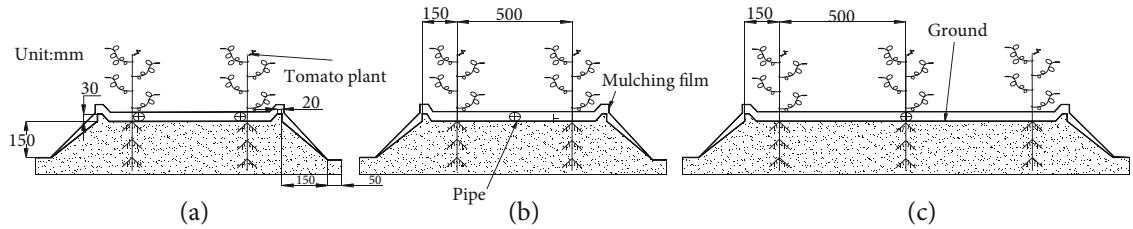

Figure 4: Schematic diagram of capillary arrangement: (a) one pipe for one row, (b) one pipe for two rows, and (c) one pipe for three rows.

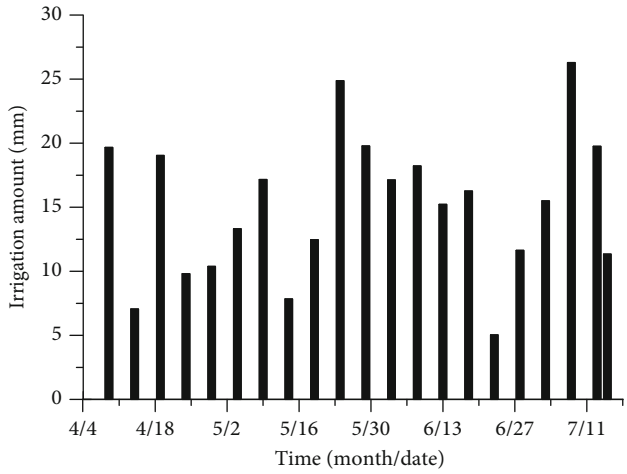

Figure 5: Irrigation records.

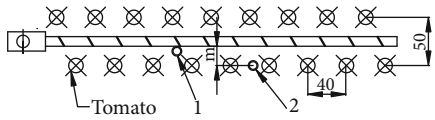

Figure 6: Schematic diagram of capillary and TRIME pipe arrangement (unit: cm).

2.3.5. AMOS Structural Equation Analysis. The mean value of photosynthetic rate (Pn), stomatal conductance (Gs), intercellular carbon dioxide concentration (Ci), transpiration rate (Tr), chlorophyll a, chlorophyll b, carotenoid of tomato leaves at 56, 79, 95, and 110 DAP, and total dry matter accumulation at maturity and yield at maturity were measured under MSPF. First of all, the reliability analysis was performed on 9 sets of data (alpha = 0.845, suggesting the reliability is good and AMOS structural equation analysis can be applied here); secondly, the averaging method is used for dimensional processing to eliminate the dimensional influence; finally, the AMOS structural equation analysis is carried out.

2.3.6. Meteorological and Field Microclimate Observations. The meteorological parameters such as air temperature, relative humidity, wind speed, solar radiation intensity, and precipitation were collected by automatic weather station.

2.3.7. Data Analysis. The significant differences between data were analyzed using SPSS22.0 (IBM Crop., Armonk, New York, NY, USA) with F test, and the significant level was set at $P < 0.05$. OriginPro2019 (Origin Lab Corporation, Northampton, MA, USA) was used to draw the picture. Except for special annotations, the data are all average ± standard deviation in the chart. AMOS25.0 (Amos Development Corporation, Chicago, IL, USA) was used to draw the structural equation.

3. Results

3.1. Photosynthetic Characteristics of Leaves. Figure 7 shows that the Pn of tomato leaves increased at first and then decreased with the increase of planting days and reached the peak at 72 DAP, and Pn showed a linear and rapid increasing trend from 13 to 56 DAP. One-way ANOVA showed that there were significant differences among treatments 56 days after planting. The mean values of 56, 79, 95, and 110 days after planting showed that L1C1 treatment was the best (20.478 μmol·m^{-2}·s^{-1}), followed by L1C2 treatment (19.92 μmol·m^{-2}·s^{-1}). The Pn of L1C2 treatment is higher than that of DIPF about 1.09%, 8.24% 1.67%, and 2.03% at 56, 72, 95, and 110 DAP, respectively. The Pn of L1C2 treatment is higher than that of MSI about 1.04%, 13.55%, 7.58%, and 8.94% at 56, 72, 95, and 110 DAP, respectively. The Pn of tomato leaves of 30 cm micropore group spacing was 1.04, 1.11, 1.07, and 1.07 times higher than that of 50 cm. With the decrease of capillary arrangement density, Pn showed a significant downward trend, in which the Pn of C3 was significantly lower than that of C1 and C2 about 12.01% and 7.91%, 14.35% and 10.55%, 15.48% and 12.20%, and 12.73% and 8.78%. The change trend of Gs is similar to that of Pn, because stomata are the main channels for gas exchange between plant leaves and the outside world; O_2, CO_2, and H_2O are diffused through stomata, and their closure directly affects Pn and Tr. The increasing trend of Tr was similar to that of Pn and Gs. In the same growth period of tomato, the stronger the Pn of leaves, the lower the Ci. With the advance of growth period, Ci increased at first and then decreased and reached the peak at 56 DAP.

3.2. Chlorophyll Content. Figure 8 shows that with the increase of planting days, chlorophyll a, chlorophyll b, carotenoid, and chlorophyll in tomato leaves increased at first and then decreased, reaching the peak about 79 DAP. The means of the leaf pigment measured at 56 DAP showed that chlorophyll a, chlorophyll b, carotenoids, and chlorophyll in L1C2 treatment were higher than those in DIPF and MSI about 3.56% and 16.86%, 0.99% and 1.20%, 1.21% and 1.50%, and

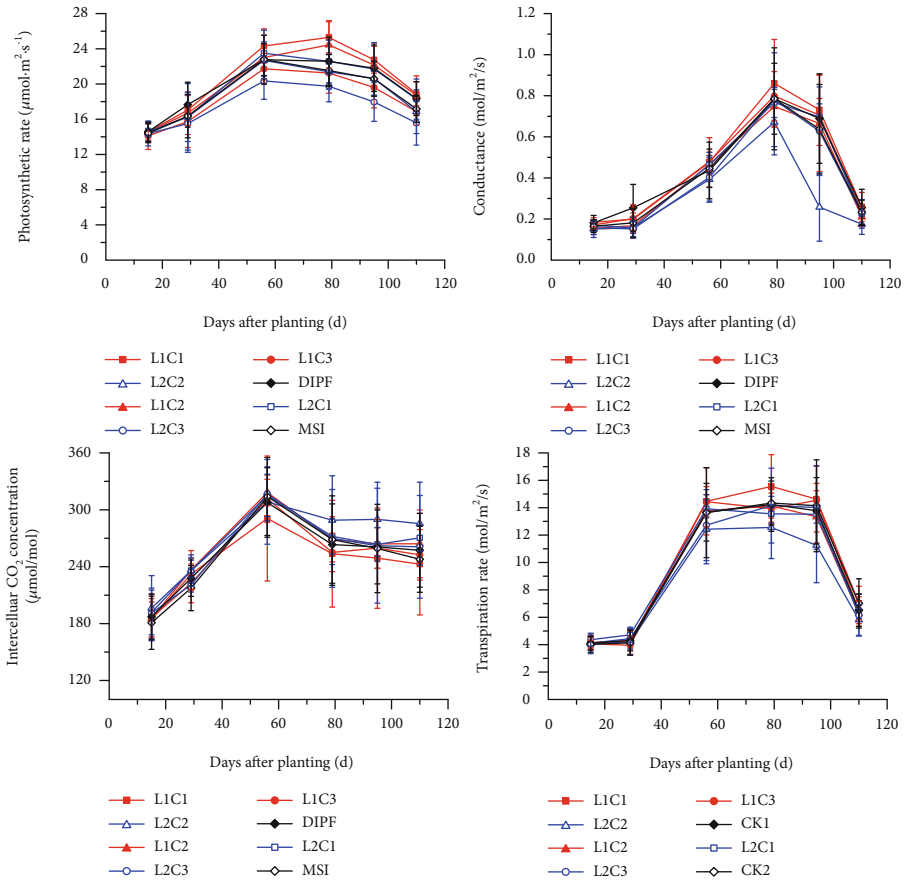

Figure 7: Effects of different treatments on photosynthetic characteristics of Tomato leaves. Note: the data are all average ± standard deviation in the figure.

1.04% and 1.12%, respectively. The levels of chlorophyll a, chlorophyll b, carotenoid, and chlorophyll of 30 cm micropore group spacing were about 13.22%, 9.47%, 15.75%, and 11.24% higher than those of 50 cm. With the decrease of capillary arrangement density, chlorophyll a, chlorophyll b, carotenoids, and chlorophyll showed a decreasing trend. Among them, the levels of chlorophyll a, chlorophyll b, carotenoids, and chlorophyll in C3 treatment were lower than those in C1 and C2 by 23.77% and 20.19%, 20.44% and 13.69%, 40.25% and 36.15%, and 21.27% and 19.76%, respectively.

3.3. Dry Matter Accumulation. Figure 9 shows that the accumulation of fruits, leaves, stems, roots, and total dry matter in L1C2 treatment were higher than those in DIPF and MSI about 6.46% and 14.84%, 7.84% and 18.53%, 10.56% and 30.05%, 24.56% and 24.93%, and 12.16% and 26.38%, respectively. The accumulations of fruit, leaf, stem, root, and total dry matter of tomatoes cultivated at a micropore group spacing of 30 cm were 1.15, 1.15, 1.10, 1.23, and 1.13 times as much as those cultivated at spacing of 50 cm. With the decrease in capillary arrangement density, the accumulation of fruit, leaf, stem, and total dry matter showed a decrease, while the accumulation of root dry matter increased at first and then decreased. The accumulation of fruit, leaf, stem, and total dry matter of C1 was significantly higher than that of C3 about 16.63%, 34.87%, 21.26%, 29.56%, and 32.04%, respectively. The accumulation of fruit, leaf, stem, and total dry matter of C2 was significantly higher than that of C3 about 30.57%, 29.62%, 36.63%, 37.83%, and 33.18%, respectively.

3.4. Yield and Water Use Efficiency. Table 2 shows that the relative contributions of micropore group spacing to yield, water consumption, and WUE were 16.30%, 2.10%, and 11.80%, respectively. The relative contributions of capillary arrangement density to yield, water consumption, and WUE were 47.40%, 21.6%, and 36.9%, respectively. The relative contributions of the interaction of 2 factors to yield, water consumption, and WUE were 7.70%, 3.30%, and 8.90%, respectively. Compared with L1C1, L1C3, L2C1, L2C2, and L2C3, the L1C2 of yield increased by about 0.99%, 47.18%, 13.69%, 24.74%, and 52.08%, respectively. Compared with L1C1, L1C3, L2C1, L2C2, and L2C3, the L1C2 of WUE increased by about 6.62%, 46.70%, 16.74%, 26.22%, and 47.76%, respectively.

The yield of L1C2 was significantly higher than that of DIPF by about 19.39%, and the WUE was improved (10.03%), but there was no significant difference; the yield was about 20.46% higher than that of MSI, and the WUE was significantly increased by 31.02%. The yield, water consumption, and WUE of tomato cultivated at a micropore

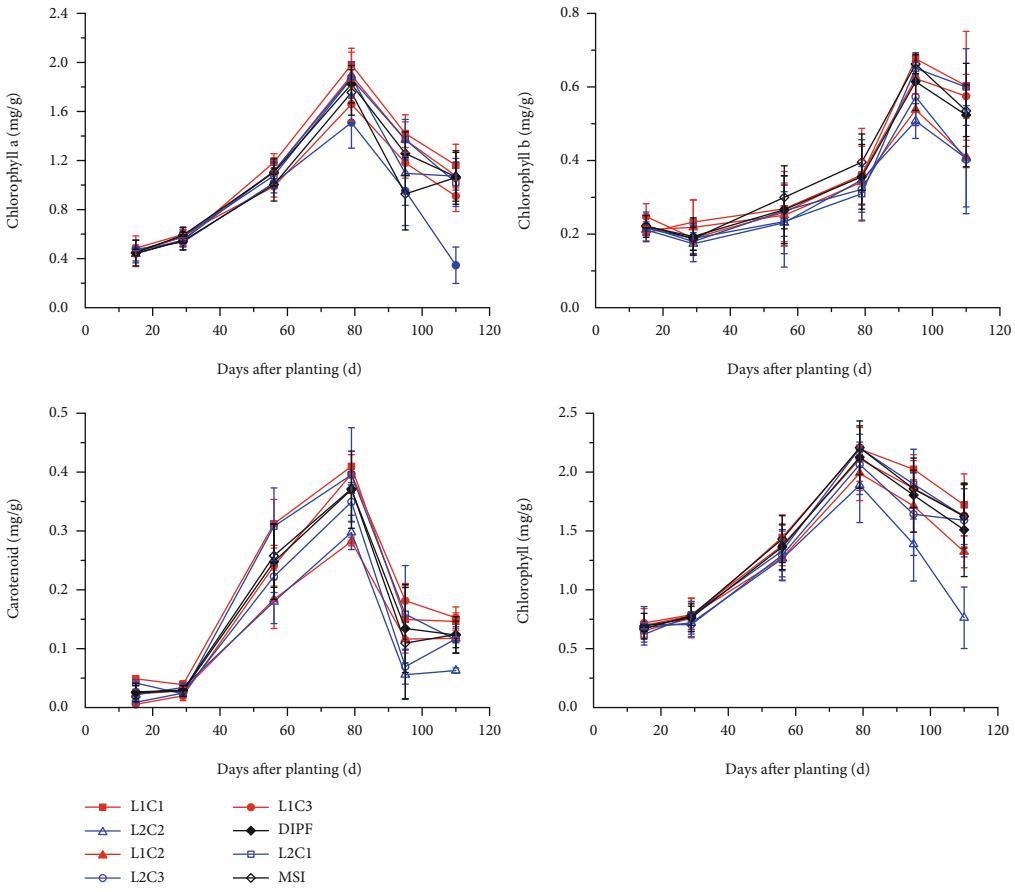

Figure 8: Effects of different treatments on chlorophyll content of functional leaves. Note: the data are all average ± standard deviation in the figure.

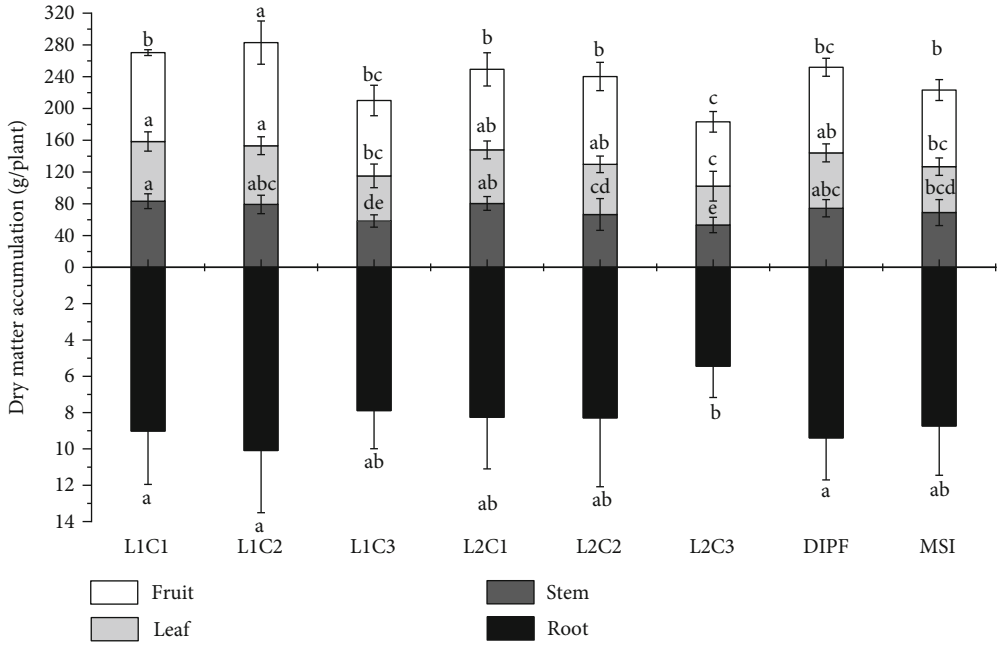

Figure 9: Effects of different treatments on dry matter accumulation of tomato. Note: the data are shown as average ± standard deviation in the figure, different letters in the same color column meant significant difference at 0.05 level, the same as below.

Table 2: Effects of different treatments on tomato yield and WUE.

Treatment	Yield (t/hm^2)	Water consumption (mm)	WUE (kg/m^3)
L1C1	118.79 ± 10.10^{a}	394.6 ± 20.63^{ab}	30.16 ± 2.84^{ab}
L1C2	119.96 ± 15.86^{a}	374.12 ± 15.82^{cd}	32.16 ± 4.75^{a}
L1C3	81.50 ± 13.96^{c}	373.05 ± 12.7^{cd}	21.92 ± 4.11^{d}
L2C1	105.51 ± 22.85^{b}	384.93 ± 15.34^{bc}	27.55 ± 6.54^{bc}
L2C2	96.17 ± 18.34^{b}	377.93 ± 10.89^{cd}	25.48 ± 4.88^{cd}
L2C3	78.88 ± 7.77^{c}	364.18 ± 25.2^{d}	21.76 ± 2.73^{d}
DIPF	100.48 ± 10.35^{b}	344.94 ± 22.42^{e}	29.23 ± 3.38^{ab}
MSI	99.58 ± 11.17^{b}	406.69 ± 22^{a}	24.54 ± 3.03^{cd}
F value			
L	$12.884^{**}(16.3)$	$1.425^{ns}(2.1)$	$8.814^{**}(11.80)$
C	$29.683^{**}(47.4)$	$9.080^{**}(21.6)$	$19.304^{**}(36.9)$
$L \times C$	$2.747^{ns}(7.7)$	$1.127^{ns}(3.3)$	$3.212^{*}(8.9)$

Notes: WUE: water use efficiency; the bracketed number is total variance relative contribution %, $^{*}P < 0.05$; $^{**}P < 0.01$; and $^{ns}P > 0.05$.

group spacing of 30 cm were 1.14, 1.01, and 1.13 times higher than that of 50 cm. With the decrease in capillary arrangement density, the yield and water consumption decreased, while the value of WUE increased. Overall, compared with C3, the yield and WUE of C2 were significantly increased by 34.76% and 31.94%.

3.5. Analysis of the AMOS Structural Equation. In the structural equation model (see Figure 10), the value of RMSEA is less than 0.08, the value of CFI is higher than 0.90, and the value of CMIN/DF is less than 3.00. The results indicated that the model has a good fitness. The structural equation model explains the interaction between photosynthetic characteristics with leaves, chlorophyll content with leaves, and total dry matter accumulation of tomato, including direct effects, indirect effects, and the total effect of the sum of the two. In this model, Pn, Tr, Ci, chlorophyll a, chlorophyll b, carotenoids, and total dry matter accumulation can explain 66% of the yield variability. In terms of direct effect, Pn, Tr, chlorophyll a, chlorophyll b, carotenoids, and total dry matter accumulation all had positive effects on yield, among which Tr had the greatest effect (0.39); Ci and Gs had a negative effect on yield, among which Gs had the greatest effect. There was also an interaction between Pn, Tr, Ci, chlorophyll a, chlorophyll b, and carotenoids. There was a negative correlation between Pn and Ci, Ci and Gs, and Ci and chlorophyll a and a positive correlation between chlorophyll and carotenoids. The positive correlation between chlorophyll a and carotenoids was the highest, followed by Pn and Gs.

In addition to direct effects, Pn, Tr, Ci, chlorophyll a, chlorophyll b, and carotenoids also play an important role in yield through various indirect effects. Pn, Tr, chlorophyll a, and carotenoids all had positive effects on yield through dry matter accumulation, among which chlorophyll a and carotenoids had significant effects (0.096); Gs and Ci all had negative effects on yield through dry matter accumulation, and Gs had a greater effect (-0.042). The total effects of various factors on yield were as follows: Gs > Tr > Pn > carotenoids > total dry matter accumulation > Ci > chlorophyll a > chlorophyll b.

4. Discussion

4.1. Effects of Irrigation Methods on Photosynthetic Characteristics, Dry Matter Accumulation, and Yield of Tomato in Greenhouse. Previous studies have shown that there is a positive correlation between chlorophyll content and leaf photosynthetic rate. Under drought conditions, soil water content limits the water supply of roots, promotes root production of ABA, reduces stomatal opening, restricts leaf gas and water exchange [48, 49], and reduces leaf net photosynthetic rate [50]. Through the experimental determination, it was found that the average soil volume moisture content of the 0-40 cm soil layer under MSPF was 9.34% higher than that of DIPF (see Figure 11). The appropriate increase of soil moisture created stable conditions for the increase of photosynthetic rate of microsprinkler irrigation leaves under plastic film (see Figure 7) and further led to the increase of tomato dry matter accumulation by 12.16%. This study also found that the yield and WUE of tomato plants under MSPF were 19.39% and 10.03% higher compared with DIPF (see Table 2). This may be ascribed to the flow rate of MSPF that was about 45 times higher than that of the single group with DIPF and identical working pressure.

Under identical irrigation amount, the flow rate of the single group of MSPF exceeded that of drip irrigation with smaller orifice flow, and the irrigation time was shorter, so that the ratio of soil water horizontal to vertical migration distance increased. The larger surface wetting area increases the wetting volume and irrigation uniformity per unit area of the tillage layer and decreases the deep transport of soil water [51]. This provided a strong guarantee for the stable yield of greenhouse tomato [11, 51, 52], resulting in higher yield of tomato under MSPF. However, because of the large surface wetting area of MSPF and the vigorous growth of tomato plants, soil water evaporation was further intensified. Compared with drip irrigation under plastic film, the water consumption of tomato under MSPF increased by 8.46% (see Table 2). The yield increase of MSPF (19.39%) was about 2.29 times that of its water consumption (8.46%); therefore, the WUE of crops under MSPF was higher than that of drip irrigation under plastic film.

In this study, the average volume water content in layer 0 ~ 40 cm under MSI was lower than that of MSPF at maturity stage of tomato about 7.48% (see Figure 11). At the same time, the canopy humidity of tomato in MSI was more than 70%, which was 1.56 times higher than that of MSPF (see Figure 12). The results show that under the same irrigation amount, MSI can reduce irrigation amount, and part of irrigation water was used to increase air humidity [53]. Previous studies have shown that leaf water condensation easily occurs in high humidity environment, causing leaf surface cell rupture, reducing leaf photosynthesis, and limiting dry matter accumulation and fruit morphological development [54, 55]. The aforementioned information may be one of the reasons for the decrease of tomato yield under microsprinkler irrigation in this study. We also found that the WUE of

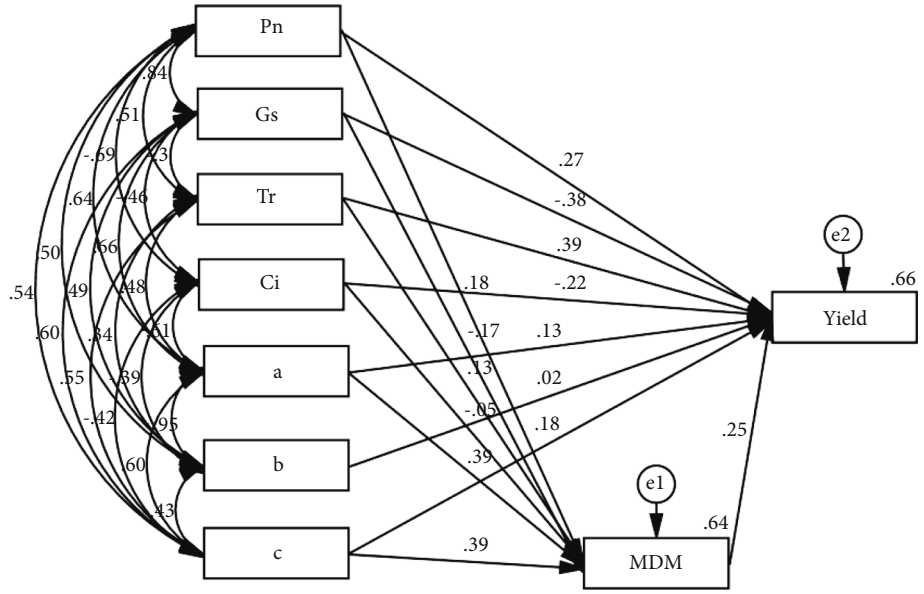

Figure 10: AMOS of structural equation model. Note: the rectangular box indicates the observation variable; e1 ~ e2 are the random values of the observation variables; one-way arrow represents the causal relationship between variables, starting as the cause and pointing to the result. The number above the variable box is the determination coefficient, which indicates the total interpretation rate of the independent variable on the dependent variable. The number on the one-way arrow is the direct effect of standardization. Pn: photosynthetic rate; Ci: intercellular CO_2 concentration; Tr: transpiration rate; Gs: conductance; a: chlorophyll a; b: chlorophyll b; c: carotenoids; MDM: total dry matter accumulation; and Yield: yield.

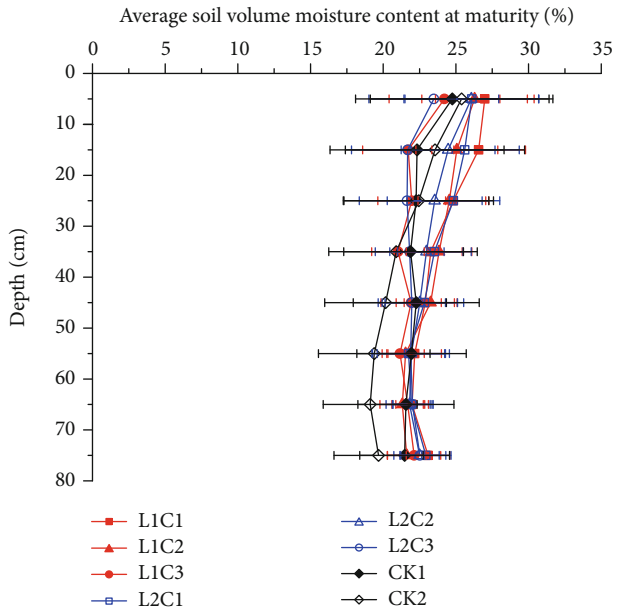

Figure 11: Average soil volume moisture content in different treatments at maturity stage (70 days after transplant). Note: the data are all average ± standard deviation in the figure.

tomato MSPF was significantly higher than that of MSI by 31.02%, possibly due to the large number of micropores per unit length of MSI, high atomization of water droplets, and increase of ineffective water transpiration [12]. As a result, the water consumption of tomato under MSI was significantly higher than that of MSPF 8.71% (see Table 2).

4.2. Effects of Micropore Group Spacing on Photosynthetic Characteristics, Dry Matter Accumulation, and Yield of Tomato in Greenhouse. Compared with the tomato cultivated at a micropore group spacing of 50 cm, the average soil volumetric moisture content of the 0 ~ 40 cm soil layer of the 30 cm during tomato maturity stage was increased by 1.60% (see Figure 11). It may be that that the effect of the change of micropore group spacing of MSPF on soil wetting body is similar to that of DIPF, and there is a phenomenon of intersection of wetting peaks between two groups of adjacent micropores on the pipe. The difference is that the single group flow of MSPF is higher than that of DIPF under the same working pressure and irrigation amount, and a larger flow rate is easy to increase the ratio of horizontal to vertical migration distance of soil water wetting peak and reduce the confluence time of adjacent wetting peaks. It has the phenomenon of the overall migration of soil moisture between the two groups of micropores on the pipe, which improves the soil volumetric water content and water dispersion per unit area of the tillage layer [10, 11]. The higher soil volumetric moisture content of the tillage layer provides a strong guarantee for the photosynthetic rate, dry matter accumulation, and yield of tomatoes [56–58]. It may also be one of the reasons why the photosynthetic rate (see Figure 7), dry matter accumulation (see Figure 9), and yield (see Table 2) of 30 cm micropore group spacing are better than 50 cm.

In this study, it was found that the tomato yield at a micropore group spacing of 30 cm was significantly higher than that of 50 cm (14.15%), which was inconsistent with the conclusion that there was no significant difference between the cucumber yield of 50 cm drip irrigation and 30 cm by Wang et al. [59] drip irrigation, which may be due

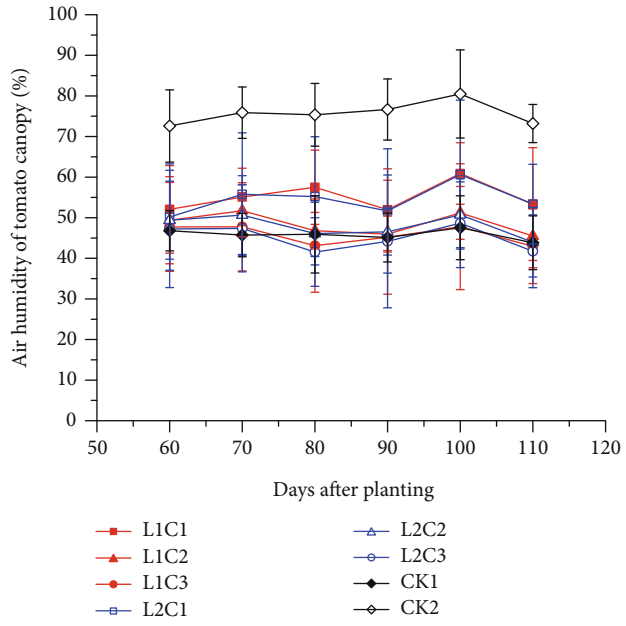

Figure 12: Effects of different treatments on air humidity in tomato canopy. Note: the data are all average ± standard deviation in the figure.

to the difference of irrigation amount in the experiment, the irrigation amount was controlled by evaporation pan, the cumulative irrigation water was 353 mm in growth period, while Wang controlled the lower limit of soil irrigation and irrigated 385 mm during growth period. It is also inconsistent with the conclusion that there is no significant difference in the onion yield under different drip irrigation spacing by Enciso et al. [60]. The maximum spacing of emitters set by Enciso et al. is 30 cm, which is much smaller than that of 50 cm in this study. The soil water distribution in the smaller spacing is uniform, and it is not easy to cause yield difference due to drought stress on crops [11, 61]. It is consistent with the conclusion of Meshram et al. [62] that the pomegranate yield of 50 cm emitter spacing is significantly lower than that of 30 cm. This study also found that the WUE of the 30 cm of micropore group spacing was 1.13 times higher than that of 50 cm. Due to the micropore spacing 30 cm, the tillage layer soil volume is moist and uniform and there is no obvious high water and small water area, which can meet the water needs of plants more timely and accurately [63]. It led to a significant increase in tomato yield (1.14 times), while there was no significant increase in water consumption between 30 cm of micropore group spacing (see Table 2), which finally showed a significant improvement in WUE [44, 59]. Elmaloglou and Diamantopoulos [35] believes that reducing the spacing between the emitters can shorten the irrigation duration and increase the irrigation efficiency, which is consistent with the conclusion that reducing the 30 cm of micropore group spacing can improve water use efficiency.

4.3. Effects of Capillary Arrangement Density on Photosynthetic Characteristics and Dry Matter Accumulation and Yield of Tomato in Greenhouse. It was found that the total dry matter accumulation of tomato in C1 and C2 was significantly higher than that in C3 (approximately, 32.04% and 33.18%, respectively, see Figure 9). This is mainly due to the fact that under the same single group flow rate, micropore group spacing, and irrigation amount, the denser the capillary arrangement density, the larger the unit area flow, which is easy to increase the surface wetting area and increase the soil volume moisture content of the tillage layer. The results showed that the average soil volumetric moisture content of C1 and C2 at mature stage was significantly higher than that of C3 about 8.07 and 5.81% (see Figure 11). Higher soil volumetric moisture content reduced root drought stress, limited root ABA accumulation, and promoted leaf photosynthesis (see Figure 7) [64, 65], leading to an increase in dry matter accumulation [66]. Zhou et al. [8] found that the dry matter accumulation of C2 of maize under drip irrigation was less than that of C1; it is inconsistent with the conclusion that the total dry matter accumulation of C2 tomato under MSPF is higher than that of C1. It may be due to the fact that the soil volume moisture content of the 0-20 cm soil layer in the C1 layout mode is about 3.31% higher than that of the C2. Higher shallow soil moisture tends to increase soil water-filled porosity and reduce soil aeration, making the total dry matter accumulation of C1 is slightly lower than C2 by about 0.86% [8]. Wang et al. [46] study found that Pn and Gs of muskmelon leaves increased at first and then decreased with the increase of capillary arrangement density, which was inconsistent with the conclusion that Pn and Gs of tomato leaves increased with the increase of capillary arrangement density. It may be due to the fact that the difference of irrigation control methods, Wang et al. adopt the percentage control of field water holding rate, so it is difficult to ensure that the irrigation quantity of different capillary arrangement density is the same. This study is based on evaporation control, and different capillary arrangement density irrigation quantity is the same.

Liu et al. [67] found that the cotton yield of one pipe and two rows was not significantly higher than that of one pipe and four rows. However, Zhou et al. [8] found that the yield of maize in one pipe of two rows in drip irrigation was significantly lower than that in one pipe and one row. The reasons for the above differences may be due to differences in soil types, crop types, climate, precipitation, and other factors. Whether the capillary arrangement density of MSPF has a consistent effect on yield under different environments needs to be demonstrated by further experiments. Wang et al. [4] found that the yield of muskmelon under drip irrigation in the greenhouse increased at first and then decreased with the increase of capillary arrangement density, which was inconsistent with the conclusion that tomato yield decreased with the decrease of capillary arrangement density in this study. It is mainly due to the difference of total irrigation amount, soil type, and irrigator during the growth period. It may also be caused by the difference of capillary arrangement density of drip irrigation. In this study, the maximum distance between one pipe and two rows of Wang et al. is the maximum distance between the arrangement of one pipe and two rows of drip irrigation. The difference of tomato yield between three pipes and four rows of MSPF needs to be demonstrated by further experiments. Cantrell et al. [68]

studied the yield of drip irrigation bermudagrass, Lv et al. [32] drip irrigation spring wheat yield, and Bozkurt et al. [31] drip irrigation corn yield showed a decreasing trend with the decrease of capillary arrangement density. These conclusions are consistent with the conclusion of this study on the yield change of MSPF. It shows that MSPF and drip irrigation have similar effects on crops in terms of capillary arrangement density. This study also found that the WUE of tomato showed a decreasing trend with the increase of capillary arrangement density. It may be due to the increase of soil wetting area and ineffective water consumption in the tillage layer with the increase of capillary arrangement density. At the same time, when the soil water stress decreased, the vegetative growth of tomato was exuberant and the photosynthetic rate increased. The effective evapotranspiration of plant water [69] also increased, resulting in the tomato water consumption increasing by 5.74% (see Table 2). The increase of tomato yield (29.85%) was less than that of water consumption (5.74%), which led to the decrease of tomato WUE by 32.1% with the increase of capillary density.

5. Conclusions

By exploring the effects of different micropore group spacing and capillary arrangement density on the photosynthetic characteristics and yield of greenhouse tomato, it was found that the photosynthetic rate of tomato leaves of MSPF increased by 8.24% and 13.55% compared with DIPF and MSI. The yield and WUE of MSPF were higher than those of DIPF and MSI about 19.39% and 20.46% and 10.03% and 31.02%, respectively. It was shown that MSPF is suitable for greenhouse crop irrigation. The yield-increasing effect is better than DIPF, and the water-saving effect is better than MSI. In a certain range, with the decrease in micropore group spacing, the more beneficial it is to the improvement of tomato photosynthetic characteristics of leaves and yield. Along with the decrease of capillary arrangement density, the tomato photosynthetic characteristics of leaves and yield decreased. In AMOS of the structural equation model, Pn, Tr, Ci, chlorophyll a, chlorophyll b, carotenoids, and total dry matter accumulation can explain 66% of the yield variability. Considering comprehensively, MSPF is aimed at saving water and low cost without significantly reducing yield; it is recommended to use the optimal combination mode of micropore group spacing 30 cm and one pipe for two rows is recommended. This study can enrich the water-saving irrigation technology of facility agriculture and provide theoretical basis and technical guidance for the sustainable development of greenhouse tomato industry in arid and semiarid sandy loam soils. This study provides a theoretical basis and data support for the large-scale promotion of MSPF. While the presented results describe the optimum irrigation of greenhouse spring tomato, but it remains an open question that further experiments are needed to investigate of autumn tomato.

Data Availability

The data used to support the findings of this study are available from the corresponding author upon request.

Conflicts of Interest

The authors declare no conflict of interest.

Acknowledgments

This work is supported jointly by Natural Science Foundation of China (No. 41807041), Shaanxi Provincial Water Conservancy Science and Technology Project (2015slkj-07), Henan Water Conservancy Science and Technology Project (GG201931, GG202043), Science and Technology Program of Xi'an (20193052YF040NS040), Natural Science Foundation of Guangdong Province (No. 2018A0303130149), Science and Technology Program of Guangzhou (No. 20181002SF0530), and Fundamental Research Funds for the Central Universities (GK201903115).

References

[1] T. Du, S. Kang, X. Zhang, and J. Zhang, "China's food security is threatened by the unsustainable use of water resources in North and Northwest China," *Food and Energy Security*, vol. 3, no. 1, pp. 7–18, 2014.

[2] H. Liu, H. Yang, J. Zheng et al., "Irrigation scheduling strategies based on soil matric potential on yield and fruit quality of mulched-drip irrigated chili pepper in Northwest China," *Agricultural Water Management*, vol. 115, pp. 232–241, 2012.

[3] H. Zhang, Y. Xiong, G. Huang, X. Xu, and Q. Huang, "Effects of water stress on processing tomatoes yield, quality and water use efficiency with plastic mulched drip irrigation in sandy soil of the Hetao Irrigation District," *Agricultural Water Management*, vol. 179, pp. 205–214, 2017.

[4] J. Wang, W. Niu, M. Dyck, M. Zhang, and Y. Li, "Drip irrigation with film covering improves soil enzymes and muskmelon growth in the greenhouse," *Soil Research*, vol. 56, no. 1, p. 59, 2018.

[5] J. Feng, Y. Li, W. Wang, and S. Xue, "Effect of optimization forms of flow path on emitter hydraulic and anti-clogging performance in drip irrigation system," *Irrigation Science*, vol. 36, no. 1, pp. 37–47, 2018.

[6] Y. Yu, G. Shihong, D. Xu, W. Jiandong, and X. Ma, "Effects of Treflan injection on winter wheat growth and root clogging of subsurface drippers," *Agricultural Water Management*, vol. 97, no. 5, pp. 723–730, 2010.

[7] N. Michelakis, E. Vougioucalou, and G. Clapaki, "Water use, wetted soil volume, root distribution and yield of avocado under drip irrigation," *Agricultural Water Management*, vol. 24, no. 2, pp. 119–131, 1993.

[8] L. Zhou, H. Feng, Y. Zhao et al., "Drip irrigation lateral spacing and mulching affects the wetting pattern, shoot-root regulation, and yield of maize in a sand-layered soil," *Agricultural Water Management*, vol. 184, pp. 114–123, 2017.

[9] X. Zhang, Z. Wu, X. Ding, and X. Li, "Experimental analysis of water distribution characteristics of micro-sprinkling hose," *Transactions of the CSAE*, vol. 25, pp. 66–69, 2009.

[10] Á. Del Vigo, S. Zubelzu, and L. Juana, "Numerical routine for soil water dynamics from trickle irrigation," *Applied Mathematical Modelling*, vol. 83, pp. 371–385, 2020.

[11] A. O. M. El-Hafedh, H. Daghari, and M. Maalej, "Analysis of several discharge rate–spacing–duration combinations in drip

irrigation system," *Agricultural Water Management*, vol. 52, no. 1, pp. 33–52, 2001.

[12] J. Man, J. Yu, P. J. White et al., "Effects of supplemental irrigation with micro-sprinkling hoses on water distribution in soil and grain yield of winter wheat," *Field Crops Research*, vol. 161, pp. 26–37, 2014.

[13] J. Li, Z. Zhang, Y. Liu et al., "Effects of micro-sprinkling with different irrigation amount on grain yield and water use efficiency of winter wheat in the North China Plain," *Agricultural Water Management*, vol. 224, p. 105736, 2019.

[14] J. Li, X. Xu, G. Lin et al., "Micro-irrigation improves grain yield and resource use efficiency by co-locating the roots and N-fertilizer distribution of winter wheat in the North China Plain," *Science of the Total Environment*, vol. 643, pp. 367–377, 2018.

[15] E. Fletcher, K. T. Morgan, J. A. Qureshi, J. A. Leiva, and P. Nkedi-Kizza, "Imidacloprid soil movement under micro-sprinkler irrigation and soil-drench applications to control Asian citrus psyllid (ACP) and citrus leafminer (CLM)," *Plos One*, vol. 13, no. 3, pp. 1–16, 2018.

[16] S. Baram, S. Dabach, D. Jerszurki, C. M. Stockert, and D. R. Smart, "Upscaling point measurements of N_2O emissions into the orchard scale under drip and microsprinkler irrigation," *Agriculture, Ecosystems & Environment*, vol. 265, pp. 103–111, 2018.

[17] J. Li, Y. Wang, M. Zhang et al., "Optimized micro-sprinkling irrigation scheduling improves grain yield by increasing the uptake and utilization of water and nitrogen during grain filling in winter wheat," *Agricultural Water Management*, vol. 211, pp. 59–69, 2019.

[18] J. Man, D. Wang, and P. J. White, "Photosynthesis and Dry-mass production of winter wheat in response to micro-sprinkling irrigation," *Agronomy Journal*, vol. 109, no. 2, pp. 549–561, 2017.

[19] J. Man, D. Wang, P. J. White, and Z. Yu, "The length of micro-sprinkling hoses delivering supplemental irrigation affects photosynthesis and dry matter production of winter wheat," *Field Crops Research*, vol. 168, pp. 65–74, 2014.

[20] I. Tsitsimpelis, I. Wolfenden, and C. J. Taylor, "Development of a grow-cell test facility for research into sustainable controlled-environment agriculture," *Biosystems Engineering*, vol. 150, pp. 40–53, 2016.

[21] M. K. Er and A. Gökçe, "Effects of selected pesticides used against glasshouse tomato pests on colony growth and conidial germination of Paecilomyces fumosoroseus," *Biological Control*, vol. 31, no. 3, pp. 398–404, 2004.

[22] J. Camara, V. Logah, E. A. Osekre, and C. Kwoseh, "Leaf nutrients content of tomato and incidence of insect pests and diseases following two foliar applications," *Journal of Plant Nutrition*, vol. 41, no. 2, pp. 159–167, 2017.

[23] O. Gómez-Rodrıguez, E. Zavaleta-Mejıa, V. A. Gonzalez-Hernandez, M. Livera-Munoz, and E. Cárdenas-Soriano, "Allelopathy and microclimatic modification of intercropping with marigold on tomato early blight disease development," *Field Crops Research*, vol. 83, no. 1, pp. 27–34, 2003.

[24] K. Massatbayev, N. Izbassov, D. Nurabaev, K. Musabekov, A. Shomantayev, and M. Massatbayev, "Technology and regime of sugar beet drip irrigation with plastic mulching under the conditions of the Jambyl region," *Irrigation And Drainage*, vol. 65, no. 5, pp. 620–630, 2016.

[25] Z. Wang, B. Fan, and L. Guo, "Soil salinization after long-term mulched drip irrigation poses a potential risk to agricultural sustainability," *European Journal of Soil Science*, vol. 70, no. 1, pp. 20–24, 2019.

[26] H. Liu, H. Li, H. Ning et al., "Optimizing irrigation frequency and amount to balance yield, fruit quality and water use efficiency of greenhouse tomato," *Agricultural Water Management*, vol. 226, no. 12, p. 105787, 2019.

[27] S. Malherbe and D. Marais, "Economics, yield and Ecology," *Outlook On Agriculture*, vol. 44, no. 1, pp. 37–47, 2015.

[28] E. H. Murchie, M. Pinto, and P. Horton, "Agriculture and the new challenges for photosynthesis research," *New Phytologist*, vol. 181, no. 3, pp. 532–552, 2009.

[29] Y.-L. Zhang, F.-X. Wang, C. C. Shock et al., "Influence of different plastic film mulches and wetted soil percentages on potato grown under drip irrigation," *Agricultural Water Management*, vol. 180, no. 5, pp. 160–171, 2017.

[30] R. Chen, W. Cheng, J. Cui et al., "Lateral spacing in drip-irrigated wheat: the effects on soil moisture, yield, and water use efficiency," *Field Crops Research*, vol. 179, pp. 52–62, 2015.

[31] Y. Bozkurt, A. Yazar, B. Gençel, and M. S. Sezen, "Optimum lateral spacing for drip-irrigated corn in the Mediterranean Region of Turkey," *Agricultural Water Management*, vol. 85, no. 1-2, pp. 113–120, 2006.

[32] Z. Lv, M. Diao, W. Li et al., "Impacts of lateral spacing on the spatial variations in water use and grain yield of spring wheat plants within different rows in the drip irrigation system," *Agricultural Water Management*, vol. 212, pp. 252–261, 2019.

[33] J. Z. Xu, Q. Wei, S. Z. Peng, Y. Yu, and X. Zhang, "Distribution characteristics of soil water under partial wetted irrigation and it is potential environmental effects," *Journal of Water Resources & Water Engineering*, vol. 23, 2012.

[34] J. Sui, J. Wang, S. Gong, D. Xu, Y. Zhang, and Q. Qin, "Assessment of maize yield-increasing potential and optimum N level under mulched drip irrigation in the Northeast of China," *Field Crops Research*, vol. 215, pp. 132–139, 2018.

[35] S. Elmaloglou and E. Diamantopoulos, "Soil water dynamics under surface trickle irrigation as affected by soil hydraulic properties, discharge rate, dripper spacing and irrigation duration," *Irrigation And Drainage*, vol. 59, no. 3, pp. 254–263, 2010.

[36] T. Xie and P. Su, "Canopy and leaf photosynthetic characteristics and water use efficiency of sweet sorghum under drought stress," *Russian Journal of Plant Physiology*, vol. 59, no. 2, pp. 224–234, 2012.

[37] M. A. Muhamman, S. G. Mohammed, A. Lado, and M. D. Belel, "Interrelationship and path coefficient analysis of some growth and yield characterestics in sesame (Sesamum Indicum L.)," *Journal of Agricultural Science*, vol. 2, no. 4, pp. 100–105, 2010.

[38] E. S. Köksal, "Hyperspectral reflectance data processing through cluster and principal component analysis for estimating irrigation and yield related indicators," *Agricultural Water Management*, vol. 98, no. 8, pp. 1317–1328, 2011.

[39] T. F. Alam, N. Sultana, and M. I. Rayhan, "Structural equation modeling: an application of broadband penetration and GDP growth in Asia," *Journal of Economic Structures*, vol. 8, no. 1, 2019.

[40] E. Lamb, S. Shirtliffe, and W. May, "Structural equation modeling in the plant sciences: an example using yield components in oat," *Canadian Journal of Plant Science*, vol. 91, no. 4, pp. 603–619, 2011.

[41] N. Dinc, K. Aydinsakir, M. Isik et al., "Assessment of different irrigation strategies on yield and quality characteristics of drip

irrigated pomegranate under mediterranean conditions," *Irrigation Science*, vol. 36, no. 2, pp. 87–96, 2018.

[42] H. LIU, A.-w. DUAN, L. I. Fu-sheng, J.-s. SUN, Y.-c. WANG, and C.-t. SUN, "Drip irrigation scheduling for tomato grown in solar greenhouse based on pan evaporation in north china plain," *Journal of Integrative Agriculture*, vol. 12, no. 3, pp. 520–531, 2013.

[43] Y. Zhu, H. Cai, L. Song, X. Wang, Z. Shang, and Y. Sun, "Aerated irrigation of different irrigation levels and subsurface dripper depths affects fruit yield, quality and water use efficiency of greenhouse tomato," *Sustainability*, vol. 12, no. 7, 2020.

[44] Y. Li, W. Niu, X. Cao et al., "Effect of soil aeration on root morphology and photosynthetic characteristics of potted tomato plants (*Solanum lycopersicum*) at different NaCl salinity levels," *BMC Plant Biology*, vol. 19, no. 1, p. 331, 2019.

[45] Y. Li, Y. Sun, J. Jiang, and J. Liu, "Spectroscopic determination of leaf chlorophyll content and color for genetic selection on Sassafras tzumu," *Plant Methods*, vol. 15, no. 1, pp. 73–81, 2019.

[46] J. Wang, W. Niu, and Y. Li, "Effects of drip irrigation with plastic on photosynthetic characteristics and biomass distribution of muskmelon," *Agriculture*, vol. 10, no. 3, pp. 84–94, 2020.

[47] D. U. Ya-dan, H.-x. CAO, S.-q. LIU, G. U. Xiao-bo, and Y.-x. CAO, "Response of yield, quality, water and nitrogen use efficiency of tomato to different levels of water and nitrogen under drip irrigation in Northwestern China," *Journal of Integrative Agriculture*, vol. 16, no. 5, pp. 1153–1161, 2017.

[48] X. Luo, H. Croft, J. M. Chen, L. He, and T. F. Keenan, "Improved estimates of global terrestrial photosynthesis using information on leaf chlorophyll content," *Global Change Biology*, vol. 25, no. 3, pp. 2499–2514, 2019.

[49] Q. Xia, J. Tan, S. Cheng, Y. Jiang, and Y. Guo, "Method article sensing plant physiology and environmental stress by automatically tracking Fj and Fi features in PSII chlorophyll fluorescence induction," *Photochemistry and Photobiology*, vol. 20, pp. 1–9, 2019.

[50] R. Sivakumar, D. Durga Devi, C. N. Chandrasekar, R. Santhi, and R. M. Vijayakumar, "Impact of drought on gas exchange and physiological parameters and yield in contrasting genotypes of tomato (*Solanum Lycopersicum*)," *Indian Journal of Plant Physiology*, vol. 19, no. 1, pp. 1–7, 2014.

[51] L. Zotarelli, J. M. Scholberg, M. D. Dukes, R. Muñoz-Carpena, and J. Icerman, "Tomato yield, biomass accumulation, root distribution and irrigation water use efficiency on a sandy soil, as affected by nitrogen rate and irrigation scheduling," *Agricultural Water Management*, vol. 96, no. 1, pp. 23–34, 2009.

[52] S. Manzoni, G. Vico, S. Palmroth, A. Porporato, and G. Katul, "Optimization of stomatal conductance for maximum carbon gain under dynamic soil moisture," *Advances in Water Resources*, vol. 62, pp. 90–105, 2013.

[53] M. K. Singh and T. Sasahara, "Photosynthesis and transpiration in rice as influenced by soil moisture and air humidity," *Annals of Botany*, vol. 48, no. 4, pp. 513–518, 1981.

[54] L. M. Mortensen, "Effects of ozone concentration on growth of tomato at various light, air humidity and carbon dioxide levels," *Scientia Horticulturae*, vol. 49, no. 1-2, pp. 17–24, 1992.

[55] S. Panchal, R. Chitrakar, B. K. Thompson et al., "Regulation of stomatal defense by air relative humidity," *Plant Physiology*, vol. 172, no. 3, pp. 2021–2032, 2016.

[56] A. T. Abdelhafeez, H. Harssema, and K. Verkerk, "Effects of air temperature, soil temperature and soil moisture on growth and development of tomato itself and grafted on its own and egg-plant rootstock," *Scientia Horticulturae*, vol. 3, no. 1, pp. 65–73, 1975.

[57] L. K. Silveira, G. C. Pavão, C. T. dos Santos Dias, J. A. Quaggio, and R. C. . M. Pires, "Deficit irrigation effect on fruit yield, quality and water use efficiency: a long-term study on Pêra-IAC sweet orange," *Agricultural Water Management*, vol. 231, p. 106019, 2020.

[58] W. H. Sun, Y. Y. Wu, X. Y. Wen et al., "Different mechanisms of photosynthetic response to drought stress in tomato and violet orychophragmus," *Photosynthetica*, vol. 54, no. 2, pp. 226–233, 2016.

[59] S. Wang, G. Li, G. Meng et al., "Effects of dripper discharge and spacing on growth of cucumber in Chinese solar greenhouse under drip irrigation," *Transactions of the Chinese Society of Agricultural Engineering*, vol. 21, no. 10, pp. 167–170, 2005.

[60] J. Enciso, J. Jifon, and B. Wiedenfeld, "Subsurface drip irrigation of onions: effects of drip tape emitter spacing on yield and quality," *Agricultural Water Management*, vol. 92, no. 3, pp. 126–130, 2007.

[61] M. Jiménez, J. A. de Juan, J. M. Tarjuelo, and J. F. Ortega, "Effect of irrigation uniformity on evapotranspiration and onion yield," *The Journal of Agricultural Science*, vol. 148, no. 2, pp. 139–157, 2010.

[62] D. T. Meshram, S. D. Gorantiwar, N. V. Singh, and K. D. Babu, "Response of micro-irrigation systems on growth, yield and WUE of pomegranate (*Punica granatum L.*) in semi-arid regions of India," *Scientia Horticulturae*, vol. 246, pp. 686–692, 2019.

[63] X. Li, M. Jin, N. Zhou, S. Jiang, and Y. Hu, "Inter-dripper variation of soil water and salt in a mulched drip irrigated cotton field: advantages of 3-D modelling," *Soil and Tillage Research*, vol. 184, pp. 186–194, 2018.

[64] N. Sreenivasulu, V. T. Harshavardhan, G. Govind, C. Seiler, and A. Kohli, "Contrapuntal role of ABA: does it mediate stress tolerance or plant growth retardation under long-term drought stress?," *Gene*, vol. 506, no. 2, pp. 265–273, 2012.

[65] M. Xu, W. Duan, P. G. Fan et al., "Low sink-induced stomatal closure alters photosynthetic rates of source leaves in beans as dependent on H_2O_2 and ABA accumulation in guard cells," *Russian Journal of Plant Physiology*, vol. 61, no. 3, pp. 397–408, 2014.

[66] S. R. Tracy, C. R. Black, J. A. Roberts, and S. J. Mooney, "Exploring the interacting effect of soil texture and bulk density on root system development in tomato (*Solanum lycopersicum L.*)," *Environmental And Experimental Botany*, vol. 91, pp. 38–47, 2013.

[67] M. Liu, J. Yang, X. Li, G. Liu, M. Yu, and J. Wang, "Effects of drip irrigation strategy on cotton root distribution and water use efficiency," *Transactions of the Chinese Society of Agricultural Engineering*, vol. 28, no. S1, pp. 98–105, 2012.

[68] K. B. Cantrell, K. C. Stone, P. G. Hunt, K. S. Ro, M. B. Vanotti, and J. C. Burns, "Bioenergy from coastal bermudagrass receiving subsurface drip irrigation with advance-treated swine wastewater," *Bioresource Technology*, vol. 100, no. 13, pp. 3285–3292, 2009.

[69] C. Patanè, S. Tringali, and O. Sortino, "Effects of deficit irrigation on biomass, yield, water productivity and fruit quality of processing tomato under semi-arid Mediterranean climate conditions," *Scientia Horticulturae*, vol. 129, no. 4, pp. 590–596, 2011.

[70] H. CHEN, H. J. HOU, X. Y. WANG et al., "The effects of aeration and irrigation regimes on soil CO_2 and N_2O emissions in a greenhouse tomato production system," *Journal of Integrative Agriculture*, vol. 17, no. 2, pp. 449–460, 2018.